NATO Science for Peace and Security Series - B:
Physics and Biophysics

Light-Matter Interactions Towards the Nanoscale

Edited by
Maura Cesaria
Antonio Calà Lesina
John Collins

Springer

NATO OTAN

This publication is supported by:

The NATO Science for Peace and Security Programme

Light-Matter Interactions Towards the Nanoscale

NATO Science for Peace and Security Series

This Series presents the results of scientific activities supported through the framework of the NATO Science for Peace and Security (SPS) Programme.

The NATO SPS Programme enhances security-related civil science and technology to address emerging security challenges and their impacts on international security. It connects scientists, experts and officials from Alliance and Partner nations to work together to address common challenges. The SPS Programme provides funding and expert advice for security-relevant activities in the form of Multi-Year Projects (MYP), Advanced Research Workshops (ARW), Advanced Training Courses (ATC), and Advanced Study Institutes (ASI). The NATO SPS Series collects the results of practical activities and meetings, including:

Multi-Year Projects (MYP): Grants to collaborate on multi-year R&D and capacity building projects that result in new civil science advancements with practical application in the security and defence fields.

Advanced Research Workshops: Advanced-level workshops that provide a platform for experts and scientists to share their experience and knowledge of security-related topics in order to promote follow-on activities like Multi-Year Projects.

Advanced Training Courses: Designed to enable specialists in NATO countries to share their security-related expertise in one of the SPS Key Priority areas. An ATC is not intended to be lecture-driven, but to be intensive and interactive in nature.

Advanced Study Institutes: High-level tutorial courses that communicate the latest developments in subjects relevant to NATO to an advanced-level audience.

The observations and recommendations made at the meetings, as well as the contents of the volumes in the Series reflect the views of participants and contributors only, and do not necessarily reflect NATO views or policy.

The series is published by IOS Press, Amsterdam, and Springer, Dordrecht, in partnership with the NATO SPS Programme.

Sub-Series

A.	Chemistry and Biology	Springer
B.	Physics and Biophysics	Springer
C.	Environmental Security	Springer
D.	Information and Communication Security	IOS Press
E.	Human and Societal Dynamics	IOS Press

- http://www.nato.int/science
- http://www.springer.com
- http://www.iospress.nl

Series B: Physics and Biophysics

Light-Matter Interactions Towards the Nanoscale

edited by

Maura Cesaria
Department of Mathematics and Physics
University of Salento
Lecce, Italy

Antonio Calà Lesina
Hannover Centre for Optical Technologies
Leibniz University Hannover
Hannover, Germany

and

John Collins
Norton, MA, USA

Published in Cooperation with NATO Emerging Security Challenges Division

Proceedings of the NATO Advanced Study Institute on Light-Matter Interactions Towards the Nanoscale Erice, Sicily
July 20 – August 4, 2019

ISBN 978-94-024-2140-8 (PB)
ISBN 978-94-024-2137-8 (HB)
ISBN 978-94-024-2138-5 (eBook)
https://doi.org/10.1007/978-94-024-2138-5

Published by Springer,
P.O. Box 17, 3300 AA Dordrecht, The Netherlands.

www.springer.com

Printed on acid-free paper

The Organizing Team: Prof. Sergey Gaponenko, Dott. Maura Cesaria, Prof Antonio Calà Lesina, Prof John Collins (from left to right)

The group photo of the participants

Preface

This book presents the Proceedings of the NATO Advanced Study Institute that took place at the Ettore Majorana Center in Erice, Sicily, Italy, from July 20 to August 4, 2019. The subject of the Institute was "Light-Matter Interactions Towards the Nanoscale."

The Institute was an activity of the International School of Atomic and Molecular Spectroscopy, which is part of the Ettore Majorana Centre Foundation and Center for Scientific Culture, and is directed by Professor Baldassare Di Bartolo. This Institute was the 36th activity run by the International School of Spectroscopy at the Ettore Majorana Center.

At the meeting, each main lecturer presented a series of talks lasting from 3 to 6 h. Their lectures began from first principles and proceeded in a didactic fashion reaching the current level of understanding in their field of work. Other lecturers gave 1-h seminar-like talks. All participants were invited to give either short oral talks or poster presentations, and the vast majority of them took the opportunity to do so.

Aside from the scientific aspect of the meeting, the 2 weeks allowed for interactions that led to many new friendships and scientific collaborations. I wish to thank all the participants for their contributions to both the scientific and the social dimensions of the meeting.

This Institute, the 36th activity of the International School of Atomic and Molecular Spectroscopy, was the first one in which Professor Di Bartolo was unable to attend in person. He helped to open the meeting virtually, from his home near Boston, Massachusetts, in the USA, and set a tone by reminding all participants that we are all students, and that we should take time to enjoy what the Erice region has to offer. For many of us at the meeting, his absence was keenly felt. I would like to thank Professor Di Bartolo for allowing me to direct this meeting, for his help throughout the process of organizing the meeting, and for his continued friendship.

There are many others who deserve thanks. First, my sincere gratitude to the co-director of the school, Sergey Gaponenko, for his graciousness and assistance throughout the meeting. I wish to thank all the lecturers for their commitment to the meeting, and in particular for their efforts to make their lectures pedagogically

sound. My sincere thanks to Professor Martin Wegener for his help in suggesting the topics and lecturers of the school. I also wish to acknowledge the dedication, patience, and professionalism of my two colleagues who worked with me throughout the meeting, Dr. Maura Cesaria and Dr. Antonino Calà Lesina. Thank you Maura and Antonino!

I also want to acknowledge the sponsorship of NATO, as well as the sponsorship of the Italian Ministry of Scientific Research and Technology and the Sicilian Regional Government.

Finally, I wish to convey my belief in the power of meetings like this one to promote the culture of science, encourage friendship and collaboration between people from different cultures, and provide opportunities for emerging scientists. The interactions with one another during our two weeks together, the intimate setting offered by Erice, the generous sharing of time from all the lecturers, and the brief formation of a community with a common purpose all contributed to the success of the meeting.

Norton, MA, USA John M. Collins
December 2020

Memorial

This past year, Professor Mark Stockman, passed away. Mark was a lecturer at the 2019 school on "Light-Matter Interactions Towards the Nanoscale." He was an intellectual force at the meeting, willing and able to discuss most any topic, scientific or otherwise. Mark was always generous with his time, and loved having discussions with students. He also understood the importance of engaging with participants socially, and participated in that arena with gusto.

His kindness, generosity, keen understanding of physics, and overall love of life will be missed by those of us who had the good fortune to meet him at the Erice schools.

John Collins
Director of the Course

The International School of Atomic and Molecular Spectroscopy of the Ettore Majorana Center has, since 1974, organized summer schools on topics of interest to researchers in the field of spectroscopy. Over the years, two scientists who contributed a lot to these encounters are Prof. Alexander Kaminskii and Prof. Mark Stockman. They have recently passed away, and in loving memory of them, this letter aims at honoring them and their contribution to the success of the Spectroscopy School.

As a director of the Spectroscopy School, I have known Alexander Kaminskii throughout the years since he came to teach in Erice. I had a great esteem of his influencing publications on laser crystals and I appreciated a lot the very informative lectures he delivered.

We became good friends and he invited me to visit his laboratory in Moscow. I was also a guest in his house where I had the pleasure of meeting his family.

As he wrote in the preface to his book *Laser Crystals*, "The greatest reward for an author is the feeling of satisfaction he gets when it becomes clear to him that the readers find his work useful." I am grateful to him for his contributions and for his friendship.

I met Mark Stockman when he came to Erice to teach at the 2011 School of Spectroscopy. His fame preceded him as a pioneer in the field of nano-optics at Georgia State University. The Stockman I met in Erice was an enthusiastic teacher who gained the attention and the interest of all the participants in the school.

The Stockman I met was also a scientist who could entertain conversations on literature, history, music, and travels. Since his first participation in the Erice school he continued to be a very valuable teacher in the Schools of Spectroscopy that followed with always the same contagious enthusiasm. We remember him with sympathy and gratitude.

I am grateful to them for their enthusiastic participation in the Erice schools and their contribution that greatly helped me to conduct successful meetings and also the students to enjoy very high-level lectures. May they rest in peace.

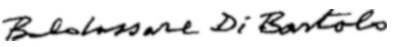

Baldassare Di Bartolo
Director of the School of Spectroscopy

Contents

Part I
Lectures

Chapter 1
Plasmonic Effects on Photonic Processes and Devices

Sergey V. Gaponenko

Abstract Nanoplasmonics represents one of the most extensive research fields in optics on the nanoscale and has emerging applications in sensors, light-emitting and photovoltaic devices. It offers a number of positive effects on photonic materials and devices and can be combined with existing technologies by a number of approaches, the colloidal techniques representing the easiest implementation in the existing and emerging photonic components and devices. Plasmonic effects are discussed in terms of the three major physical phenomena (incident field enhancement, photon density of states enhancement, non-radiative decay rate enhancement) in the context of various photonic processes and devices including absorption, Raman scattering, photo- and electroluminescence, photovoltaics, photochemistry and photodetectors. Pros and contras with respect to every practical task are discussed taking into account interplay of the above plasmonic effects in every task.

Keywords Photonics · Plasmonics · Devices

1.1 Introduction

Plasmonics deals with optical properties of metal nanostructures and effects of metal nanobodies on absorption, emission, scattering, and propagation of light as well as with metal nanostructures effects on photo-induced processes. Because of the negative dielectric permittivity resulting from very high concentration of free electrons (treated as electron plasma) metals shine since negative permittivity prevent penetration of light waves inside and makes them to be reflected. E. g., silver, gold and copper feature different colors owing to the difference in the spectral position of the crossover point where permittivity changes sign from the positive to the negative one. Subwavelength-sized metal particles (i.e. *nano*particles) when

S. V. Gaponenko (✉)
B. I. Stepanov Institute of Physics, National Academy of Sciences, Minsk, Belarus
e-mail: s.gaponenko@ifanbel.bas-net.by

M. Cesaria et al. (eds.), *Light-Matter Interactions Towards the Nanoscale*,
NATO Science for Peace and Security Series B: Physics and Biophysics,
https://doi.org/10.1007/978-94-024-2138-5_1

dispersed in a transparent dielectric give rise to specific extinction (i.e. a sum of absorption and scattering processes) spectra in accordance with the efficient medium theory known for many decades [1–4]. Plasmonics represents actually an old field in optical materials technology dating back to application of tiny metal inclusions in glass to get colors starting from the famous Lycurgus cap in the IV-th century and then remarkably developed in stained glasses for church windows in the Middle Ages. Optical studies of metal particles dispersed in transparent media (in solutions) have been pioneered by M. Faraday in 1857. Nowadays the field experiences a boom-like renaissance owing to development of nanoscience with new insight to many seemingly familiar phenomena in optics and predictions of the new ones and nanotechnology promising novel devices and improvement of the existing ones.

In this paper, a variety of optical, photophysical and photo-induced processes in plasmonics will be discussed in terms of the *weak* light—matter interaction which implies that light and matter are considered separately, and light—matter interaction can be then correctly described in terms of light absorption, scattering, and emission. This case is inherent in basic optical materials and devices like, e.g., LEDs or solar cells. The alternative case is referred to as the *strong* light—matter interaction regime, and with respect to plasmonics its manifestations can be retrieved in the recent literature [5, 6]. We also will not consider here the propagational phenomena in complex nanostructures for which the reader is advised to use the other sources [7–9]. We shall focus at relatively simple cases when a quantum absorber or emitter (an atom, a molecule or a quantum dot) interacts with light in presence of a metal nanobody and will pay attention how different and sometime opposite or counterbalancing effects interplay with respect to desirable impact on device performance. In the context of technology these cases correspond pretty well to colloidal nanostructures [10].

1.2 Spectral Range of Plasmonic Phenomena

Plasmonic effects which will be discussed in what follows occur in the range where optical response of metal material involved features negative permittivity but still dissipation losses are negligible, so that, if ones imagine metal nanoparticles dispersed in a dielectric medium, the resulting transmission spectrum will mainly result from the light scattering contribution to the overall extinction coefficient. This corresponds to the wavelengths close to or bigger than the zero-crossover point of the dielectric permittivity for a given metal. For shorter wavelengths dissipative losses in metal will mask other effects whereas for much longer wavelengths the actual size of nanoparticles appears to be very small compared to wavelength and their effect on optical processes diminishes. In accordance with these arguments when considering common metals one can see that aluminum can be treated as plasmonic material in the range from the near UV to longer wavelengths and silver – from the blue towards green and red whereas gold and copper are not suitable for the blue-violet range but rather should be used in the orange-red domain. Nowadays

the most common metals used in plasmonics are silver and gold and this occurs not only because of their useful spectral features but also because of their chemical stability with respect to oxidation and owing to well- developed colloidal chemistry for these metals. Extension of plasmonic phenomena towards the near infrared can be performed either through large size or by means of shaping, e. g., elongated nanorods readily shift their extinction to the near-infrared.

1.3 Principal Phenomena Affecting Light—Matter Interaction in Presence of Metal Nanobodies

There are three principal phenomena whose interplay defines the net effect of metal nanoparticles on atoms, molecules or quantum dots located nearby (Fig. 1.1):

(i) local concentration of electromagnetic energy at the frequency of incident light, i.e. incident field enhancement;
(ii) local density of photon states enhancement resulting both in radiative decay rate enhancement of the really excited electronic states and photon scattering enhancement (both elastic and inelastic one) since scattering can be viewed as emission of secondary radiation by virtually excited matter;

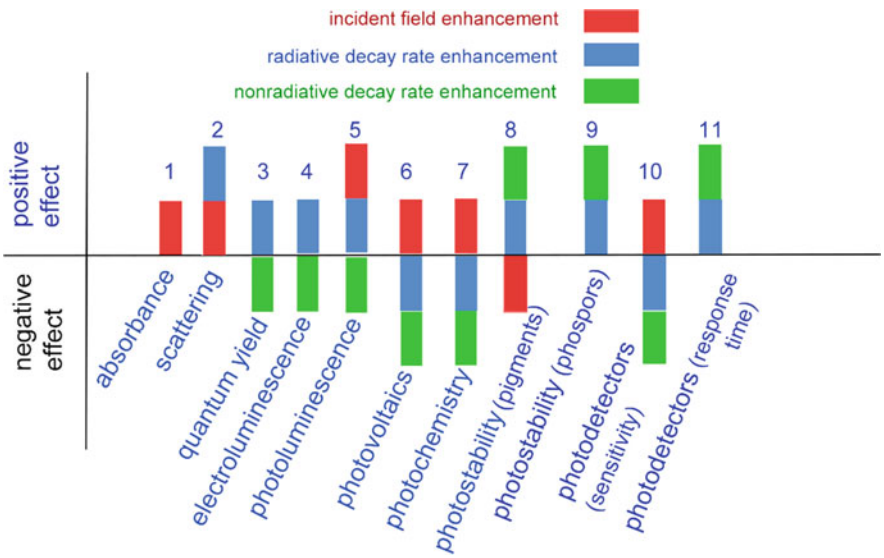

Fig. 1.1 The three major phenomena in plasmonics in the weak light—matter interaction regime and their contribution to optical and photo-induced processes and devices

(iii) non-radiative decay rate enhancement of electronic excited states in the matter resulting in energy transfer to a metal nanobody with corresponding heating and no secondary photon created as emitted or inelastically scattered one.

The principal elementary optical processes are absorption, scattering and emission of photons, and all these processes or part of these then define performance of photoluminescent, photovoltaic, photodetecting, and light-emitting materials and devices, also affecting their photostability and time response. Consider manifestation of plasmonically affected absorption, scattering and emission in various experimental implementations. From the conceptual standpoint it is important to emphasize that local incident field enhancement and elastic light scattering are fully classical phenomena and can be understood and described accurately using classical electrodynamics without involvement of light quanta (photons).

Inelastic light scattering (Raman or Mandelstam—Brillouin scattering) and spontaneous emission of light do need implication of photons and their modification in presence of nanobodies (not necessarily metal ones) but the rate of photon scattering and emission can be successfully computed based on analogy with a classical antennas so that classical electrodynamics here reasonably matches its quantum counterpart [11].

1.4 Absorption of Light

Absorption of light near metal nanobody(ies) simply follows the square of incident field, the latter being the subject of extensive computing in many seminal publications (see, e.g. [4, 12]., and Refs. therein). For example, for a single spherical nanoparticle absorption enhances by one order of the magnitude, for an elongated nanoparticle like a nanorod or a spheroid in a tip area enhancement can reach 2–4 orders of the magnitude and the similar or even higher enhancement occurs with the arrangement of two or three spherical particles. Absorption enhancement gives rise to enhancement of the relevant processes and device performance including photoluminescence, photovoltaics, photochemistry and photodetectors (see Fig. 1.1). A metal nanobody or arrangements of a few metal nanobodies can be treated as an optical antenna, often referred to as *nanoantenna.* In radio physics, antenna enables concentration of incident electromagnetic energy to a receiver. In a similar way, in the optical range a nanoantenna transforms far-field radiation into the near-field one, a quantum absorber (an atom, a molecule, or a quantum dot) is then can be treated as a receiver. The optical antenna (nanoantenna) notion is a very reasonable and instructive approach for understanding light—matter interaction modified by plasmonic effects. It has been extensively elaborated during the last decade [12, 13].

1.5 Local Density of Photon States and Radiative Lifetime Modification

Density of electromagnetic modes evolves to the notion of photon density of states (DOS) when emission of photons is considered. First introduced in the theory at the dawn of quantum statistical physics in 1924 by S. N. Bose [15], photon DOS has become one of the principal conceptions in nanophotonics. Departure from a continuous medium to space with inhomogeneities of permittivity on a wavelength scale immediately results in enhancement or inhibition of the spontaneous decay rate of an excited quantum emitter. This phenomenon has been for the first time suggested by E. M. Purcell in 1946 [16] with respect to the radiofrequency range for an emitter in a cavity where Q-fold enhancement for a cavity with Q factor occurs in an ideal case of a cavity resonance coinciding with a photon energy to be emitted by an excited quantum emitter. Nowadays all cases of spontaneous emission rate modified by an environment of often referred to as the Purcell effect [17]. In other words, radiative lifetime of an excited emitters changes becoming shorter in the certain frequency range by an expense of the opposite changes otherwise, so that the global radiative decay rate and radiative lifetime integrated over the wide frequency range conserves (Barnett—Loudon sum rule) [18]. Modification of radiative lifetimes has been computed and mapped for many model plasmonic systems [4, 9, 10, 12, 19], indicating typically a 10 . . . 100-fold variation in the case of a single nanobody and up to 10^3-fold variations for purposefully arranged nanobodies, like a dimer of two nanospheres or spheroids. A representative example for the case of Ag nanospheres is given in Fig. 1.2. Note the apparent correlation between size-dependent extinction and radiative rate enhancement. Here nanoantenna notion appears to be very instructive and reduction in the excited state lifetime of a quantum emitters in modern optics reasonably merges with enhancement of radiated power by a classical antenna in radio physics.

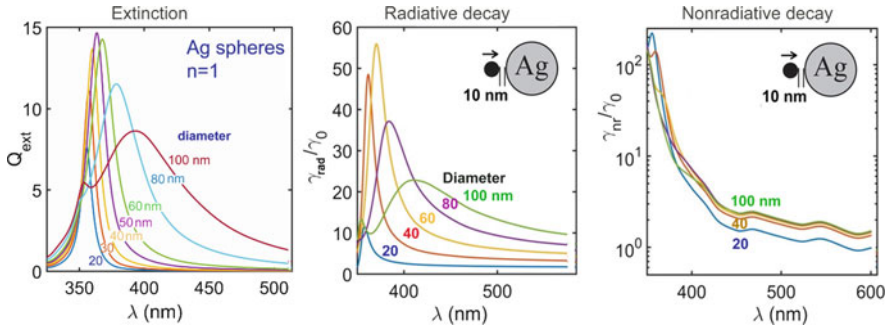

Fig. 1.2 Calculated extinction spectra, radiative decay rate enhancement, and nonradiative decay rate enhancement spectra for Ag nanoparticles with diameter ranging from 20 to 100 nm and metal-emitter spacing 10 nm. Ambient medium refractive index equals 1. (Reprinted from [14] under a Creative Commons Attribution (CC BY) license)

Thus, supposing that a quantum emitter generates a photon in the course of quantum transition, one can nevertheless calculate the rate of this process based on the classical consideration in terms of emitted power per unit time. This analogy is so important that it provides the rationale for local photon DOS definition (see [4] for detail).

1.6 Scattering

In quantum consideration photon scattering is viewed as an emission of a secondary photon by a virtually excited quantum system. It is proportional to the density of electromagnetic modes in classical consideration and to the local photon DOS in quantum representation. This is valid both for Rayleigh (i.e. elastic) scattering when radiation change direction and/or polarization whereas its frequency remains unchanged, and also for inelastic (Raman) scattering when secondary photons gains energy either lower or higher when the incident one [20]. Therefore, scattering rate can be readily enhanced near metal nanobodies by means of both incident field enhancement and local density of states enhancement,

$$F_{Scatt} = \frac{I(\mathbf{r},\omega)}{I_0(\mathbf{r},\omega)} = \frac{|\mathbf{E}(\mathbf{r},\omega_0)|^2}{|\mathbf{E}_0(\mathbf{r},\omega_0)|^2}\frac{D(\mathbf{r},\omega)}{D_0(\omega)} = \frac{|\mathbf{E}(\mathbf{r},\omega_0)|^2}{|\mathbf{E}_0(\mathbf{r},\omega_0)|^2}\frac{\gamma_{rad}(\mathbf{r},\omega)}{\gamma_0(\omega)} \tag{1.1}$$

where $\mathbf{E}_0(\mathbf{r},\omega_0)$ is electric field amplitude in vacuum, $\mathbf{E}(\mathbf{r},\omega_0)$ is electric field amplitude at the point $\mathbf{r}$ in the presence of a metal nanostructure**,** $D_0(\omega)$ is vacuum density of photon states (electromagnetic modes) which reads $D_0(\omega) = \omega^2/\pi^2c^3$ where c is the speed of light in vacuum, γ_{rad} is the radiative decay rate of some probe emitter placed at the same point $\mathbf{r}$, and γ_0 is its radiative decay rate in vacuum. When writing Eq. (1.1) the proportionality of the radiative decay rate change of any emitter placed in the same point $\mathbf{r}$ to the photon density of states change $D(\mathbf{r},\omega)/D_0(\omega)$ was used. In case of Raman scattering the overall enhancement can measure up to several orders of the magnitude like $>10^9$ times for molecules located in the so-called 'hot spots' where the product of incident field enhancement and local photon DOS reach its maxima. Note that incident field should experience enhancement for primary radiation frequency ω_0 whereas local DOS should feature enhancement at secondary radiation frequency ω. Plasmonically enhanced Raman spectroscopy often referred to as SERS (Surface Enhanced Raman Spectroscopy) enables detection of single molecules by Raman scattering [21] and is considered as promising approach to high-sensitive molecular spectroscopy in many applications including medicine [22], ecology [23, 24], forensic [25, 26] and cultural heritage [27, 28] studies. There are attempts to introduce silicon microelectronic techniques to fabricate templates with nanotexture and use them as SERS-active substrates after silver or gold deposition thereon [29–31].

Equation (1.1) gives very important correlation between routine measurements of optical transmission of transparent films containing metal nanoparticles and their

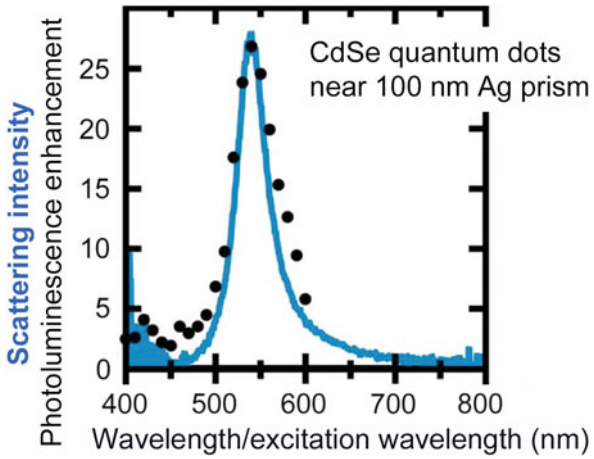

Fig. 1.3 Correlation of the scattering spectrum for 100 nm size Ag prisms and CdSe quantum dots photoluminescence intensity enhancement factor for various excitation wavelengths. (Adapted from Ref. [32] with permission from AIP Publishing (licence number 4985411297233))

potential impact on SERS and radiative decay rate enhancements. Transmission is defined by dissipative and scattering losses; the former being mainly defined by the intrinsic metal dielectric permittivity and the latter featuring pronounced enhancement by means of nanoparticle size and shape control.

Bigger size and complicated shape (like, e.g. tetrapods or rods) readily promote scattering pronounced as size- and shape-dependent transmission losses. The correlation of resonant scattering enhancement with Raman scattering rate and radiative decay rate (note again Fig. 1.1) suggests a reasonable way of engineering SERS-based and fluorescence-based sensors and efficient light-emitting devices [10]. It has been experimentally demonstrated (Fig. 1.3).

1.7 Nonradiative Decay Rate Enhancement

Proximity of metal promotes fast nonradiative path for energy relaxation of an excited quantum emitter bypassing the radiative process. This reduces lifetime but the energy is converted into heat rather than into emitted photons. As a result, internal quantum efficiency, IQE (also often referred to as quantum yield, QY, in case of photoluminescence) for spontaneous photon emission goes down for a perfect emitter. However, if the intrinsic quantum efficiency of an emitter is well less than 1, the interplay of radiative and nonradiative rates may also result in increase of the overall quantum efficiency as was reliably confirmed in many experiments. The same regularities occur in radio physics for perfect and non-perfect emitters whose properties are influenced by an antenna. The relevant equations reads [18],

$$\frac{Q}{Q_0} = \frac{\left(\gamma_{rad}/\gamma_0\right)/Q_0}{\gamma_{rad}/\gamma_0 + \gamma_{nr}/\gamma_0 + \left(1 - Q_0\right)/Q_0}, \tag{1.2}$$

Here Q is emitter quantum yield in presence of a metal nanobody, Q_0 is its intrinsic quantum yield in a free space, γ_0 is intrinsic radiative decay rate of an emitter in question in a free space, γ_{rad} is its value in presence of a metal nanobody, the internal non-radiative rate γ_{nr} is written as $\gamma_{nr} = (1 - Q_0)/Q_0$ to emphasize that enhancement of quantum efficiency is fully defined by the intrinsic value Q_0 (the emitter property) and the radiative and non-radiative decay enhancement factors, γ_{rad}/γ_0 and γ_{nr}/γ_0, respectively (the plasmonic effects which are to be calculated). For an emitter in radio physics the similar relation occurs for the emitted power modified by an antenna [18],

$$F_{antenna} = \frac{(P_{rad}/P_0)}{P_{rad}/P_0 + P_{antenna\ loss}/P_0 + (1 - \eta_i)/\eta_i} \tag{1.3}$$

where P_0 is the emitter power in free space, P_{rad} is the power emitted in presence of an antenna, $P_{\text{antenna loss}}$ describes undesirable losses because of non-ideality of an antenna, and η_{i} stands for the intrinsic internal losses in the emitter itself. Comparing Eqs. (1.2) and (1.3) one can see the apparent similarity. Excited state radiative decay rates in Eq. (1.2) transform into appropriate powers relevant to Eq. (1.3) by multiplying by the energy carried by a photon, $\hbar\omega$. Thus, consideration in terms of radio physics merges with the quantum approach.

For plasmonic nanostructures nonradiative decay enhancement features very low sensitivity to size and shape of metal nanobodies being mainly dependent on dielectric permittivity of the parent metal material. This is clearly seen when the right-hand part of Fig. 1.1 is compared to the left-hand one. Thus, increasing nanoparticle size and modifying its shape enables detune spectral range for radiative decay rate enhancement from the nonradiative counterpart.

1.8 Possible Quantum Yield and Electroluminescence Enhancements

Interplay of nonradiative and radiative decay rates define modification of luminescence internal quantum yield QY (or internal quantum efficiency, IQE) and gives the rationale for possible improvement of electroluminescent devices like semiconductor light-emitting diodes (LED) or organic ones (OLED). These are shown in Fig. 1.1 as processes 3 and 4, respectively. Electroluminescence intensity factor is simply given by the quantum yield factor (Eq. (1.2)). The lower is the intrinsic QY and IQE, the higher is their possible plasmonic enhancement. For perfect emitters (QY = IQE = 1) proximity of metal will always deteriorate performance. Many examples of calculated and experimentally implemented enhancement of LED and OLED efficiency by means of silver and gold nanoparticles can be found elsewhere [10, 14, 19, 33–35]. An example of theoretical predictions of Ag nanoparticles is given in Fig. 1.4 whereas Fig. 1.5 presents the results of experimental implementation for colloidal quantum dot LED.

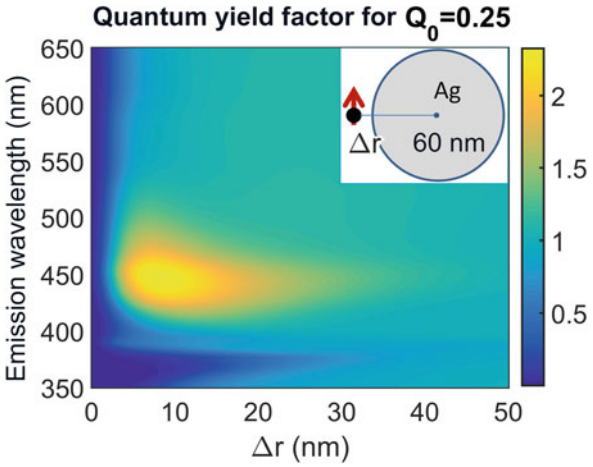

Fig. 1.4 Calculated quantum yield (electroluminescence intensity) enhancement by a 60-nm dimeter Ag sphere for averaged dipole moment orientation of emitters depending om emission wavelength and emitter-metal spacing Δr. Intrinsic quantum yield is taken $Q_0 = 0.25$ and ambient medium refractive index $n = 1.5$. (Reprinted from [14] under Creative Commons Attribution (CC BY) license)

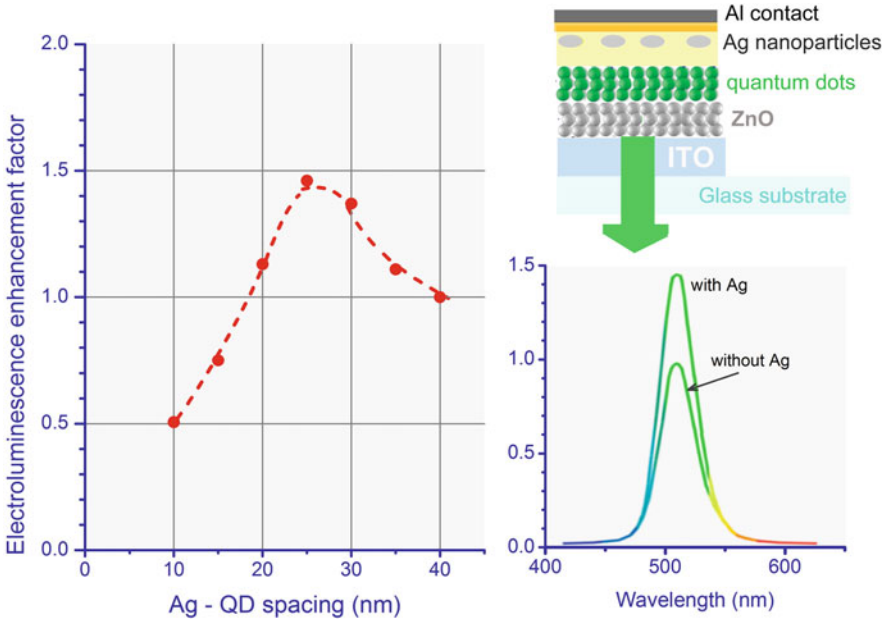

Fig. 1.5 Experimentally observed plasmonic enhancement of electroluminescence for a colloidal quantum dot LED using silver nanoparticles. (Reprinted with permission from Ref. 18 (license number 45887))

In certain applications, time response of electrically driven light source is critical. In laser diodes modulation rate is restricted by stimulated emission rate which is always faster than the spontaneous one because in lasers active medium is always heavily pumped. In LEDs response time is defined by the spontaneous rather than stimulated emission rate. It is plasmonics that opens a way towards faster electric modulation of the optical output and this is important in the context of wireless optical communication (the so-called 'Li-Fi', Light Fidelity scheme by analogy to Wi-Fi counterpart) [36–38].

1.9 Metal Enhanced Fluorescence

Photoluminescence intensity follows a complex interplay of the enhanced absorption owing to incident field enhancement and quantum yield modification, the latter being lower for perfect emitters in presence of metal nanobodies. The corresponding formula reads [10],

$$F_{PL} = \frac{I(\mathbf{r},\omega)}{I_0(\mathbf{r},\omega)} = \frac{|\mathbf{E}(\mathbf{r},\omega_0)|^2}{|\mathbf{E}_0(\mathbf{r},\omega_0)|^2}\frac{Q(\mathbf{r},\omega)}{Q_0(\omega)} = \\ = \frac{|\mathbf{E}(\mathbf{r},\omega_0)|^2}{|\mathbf{E}_0(\mathbf{r},\omega_0)|^2}\frac{(\gamma_{rad}(\mathbf{r},\omega)/\gamma_0(\omega))/Q_0(\omega)}{\gamma_{rad}(\mathbf{r},\omega)/\gamma_0(\omega)+\gamma_{nr}(\mathbf{r},\omega)/\gamma_0(\omega)+(1-Q_0(\omega))/Q_0(\omega)} \tag{1.4}$$

To minimize unwanted nonradiative decay rate enhancement one should either keep on spacing of the order of 10 nm or more between emitting species and metal inclusions or to use larger and/or properly shaped metal nanostructures to move radiative enhancement spectrum apart from the nonradiative ones, but still keeping absorption and emission spectra as close as possible to the scattering component of extinction. Therefore, a design of improved photoluminescent structures needs the accurate account for many parameters including excitation source wavelength and polarization, absorption spectrum, emission spectrum, metal-emitter average spacing, emitter dipole orientation and even its accurate displacement in case of non-symmetric nanostructures. The general field of plasmonic enhancement of photoluminescence gained a notation *Metal Enhanced Fluorescence* (MEF) and represents an active field in nanophotonics [39]. With colloidal nanoparticles approximately ten-fold enhancement of photoluminescence intensity can be realized using multilayer structures (metal-dielectric-emitter) with 5–10 nanometer dielectric spacers (Fig. 1.6). Successful experiments are known for organic molecules, semiconductor quantum dots, and rare-earth ions ([40–48] and Refs. therein). For specially arranged metal nanostructures like nanoparticles dimers, trimers, bowtie antennas or metal nanoarrays much higher enhancement factors can be observed provided that every emitter is placed in certain 'hot spots' and its dipole moment is properly aligned [49].

Figure 1.6 provides insight on the multiparametric problem in question. Here a perfect emitter is considered (QY = 1) with its emission wavelength fixed at 530 nm (e. g. fluorescein of CdSe quantum dots) and then for favorable alignments of

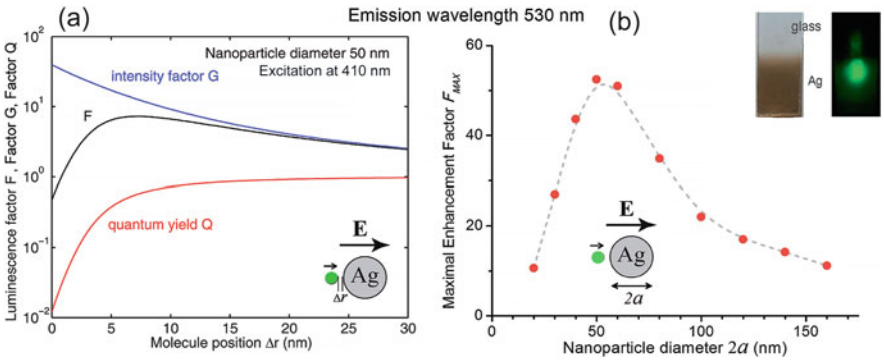

Fig. 1.6 Calculated plasmonic effects on photoluminescence at 530 nm emission wavelength by silver nanosphere. Incident light polarization and emitter dipole moment alignment are shown by arrows in the inserts. Panel (a) shows incident intensity factor G, quantum yield Q and the over emission intensity enhancement factor $F_{PL} = GQ$ (Eq. 1.4) calculated for 410 nm excitation wavelength as functions of emitter—metal spacing Δr. Panel (b) shows maximal evaluated intensity enhancement factor F_{PL} for various Ag sphere diameters from 20 to 160 nm with excitation wavelength and spacing being the adjustable parameters. (Reprinted with permission from [44]. Copyright © 2012, American Chemical Society)

incident light polarization and dipole moment of an emitter (as shown by the arrows) extensive calculations are made using metal nanoparticle diameter and spacing as adjustable parameters.

Though up to 50-fold enhancement is feasible (occurs for 50 nm spheres) this maximal value corresponds to excitation wavelength about 370 nm that might not meet other implementation criteria, like e. g., availability of excitation sources, side photophysical and photochemical effects from high-energy photon absorption, low absorption by molecules emitting in the green. Additionally, metal-emitter spacing is typically controlled using a thin dielectric layer whose permittivity affects extinction spectrum and should be involved in computations in a self-consistent manner [38]. And finally, permittivity of ambient environment and of a substrate should also be involved into consideration [50]. Taking into account the complicated problem of optimal nanostructure topology and emitters displacement along with the desirable emission wavelength and optional excitation conditions, it looks reasonable to extend modern advances in deep learning approach to this problem by analogy to the deep learning analysis of plasmonic colors formed by metal nanoparticles [51].

Plasmonics is extremely efficient for intrinsically poor phosphors since in this case their quantum yield can be readily increased. In the extreme limit of QY < < 1, the photoluminescence intensity enhancement factor can reach several orders of the magnitude and the overall scenario becomes very similar to Raman scattering enhancement. Therefore, it is widely explored in the context of large biomolecules fluorescent detection. Probably, plasmonics can be helpful to enhance performance of technologically feasible semiconductor nanostructures with intrinsically low

quantum yield, e. g., doped semiconductor quantum dots [52] and nanoporous silicon [53, 54].

1.10 Photovoltaics, Photochemistry, and Photodetectors

Photovoltaics, photochemistry and photodetectors sensitivity feature the similar sensitivity to the three principal plasmonic effects in question: these processes gain from enhanced absorption resulting from the incident field enhancement but at the same time loose from increased overall decay rate (see processes 6, 7, and 10 in Fig. 1.1). Probably the reasonable strategy in this case could be keeping metal-absorber spacing large enough to prevent fast recombination rates but still keeping safely certain absorption enhancement, especially important in the spectral range where absorption of the material used is low. This is, e.g. the case for near infrared range in silicon-based photovoltaics. It is also reasonable for extension of photodetectors sensitivity towards longer wavelength. Since discussion of these issues needs a special consideration, the recent reviews are recommended as the starting guide [55–58]. Note, sensitivity of photodetectors can be increased along with acceleration of recombination rate which is favorable for response time shortening (process 11 in Fig. 1.1) [59].

1.11 Photostability of Pigments and Emitters

Photostabilty of pigments (process in Fig. 1.1) when compared to photovoltaics, photochemistry, and photodetectors features the opposite impact from plasmonic structures. From one side it suffers from enhanced absorption which can result in photobleaching enhancement. However, photobleaching occurs by means of photochemical or photophysical processes (e. g., photoionization) that to large extent can be ‘bypassed’ by shorter lifetimes, both radiative and non-radiative ones. Therefore, the overall impact of plasmonics on photostability may be positive, negative or not presenting at all.

Photostability of phosphors should be discussed not in the context of durable operation while being exposed to uncontrollable illumination (then phosphors simply reduce to pigments) but essentially in the context of the emissive properties in the desirable spectral range under condition of due illumination with predefined spectrum and power. In this case, plasmonics does really promise improved stability by means of shorter lifetimes thus preventing side photophysical (like, e. g., photoionization) and photochemical processes. Higher absorption should not be treated as harm since it allows to reduce excitation power while keeping the same emitted power. There are many experimental reports on positive impact of plasmonic nanostructures on luminescing quantum dot stability which is important in the context of ongoing and potential applications of quantum dots in sensors,

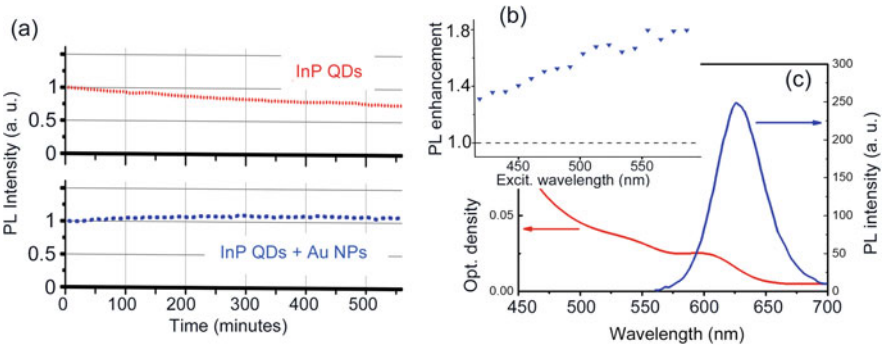

Fig. 1.7 Photostability enhancement along with photoluminescence (PL) intensity enhancement for InP quantum dots (QDs) in presence of Au nanoparticles (NPs). (**a**) PL intensity at 630 nm monitored upon a prolonged period with radiation power of 0.3 mW/mm^2 at 460 nm (the total dose being 10.1 J/mm^2) for reference QDs and QDs + AuNPs. (**b**) PL enhancement factor versus excitation wavelength. (**c**) Absorption and emission spectra of InP quantum dots. (Courtesy of O. Kulakovich)

display devices and LEDs [60–62]. One recent example is presented in Fig. 1.7 where higher stability of emitting InP quantum dots is demonstrated along with simultaneous enhancement in the overall efficiency. Plasmonic enhancement of luminescence photostability can be also considered as potential way to inhibit the known efficacy droop effect in LEDs (lower efficacy at higher currents) which possibly results from Auger recombination [37].

1.12 Conclusions

The brief overview shows that plasmonic effects can be purposefully used to improve performance of various optical materials and devices. Those using light scattering (e.g. sensors) can be readily improved, whereas phosphors and luminescent light converter can be moderately improved in the context of efficacy and modulation rate.

At the same time, photovoltaic, photochemical and photodetecting devices can be improved only provided the certain conditions are met, though response time of detectors can be easily shortened. Therefore, one might expect a transfer of knowledge gained in the labs to industry in the reasonable future.

Acknowledgements Cooperation with D. V. Guzatov, O. S. Kulakovich, E. V. Shabunya-Klyachkovskaya, A. O. Muravitskaya, A. S. Matsukovich, L. L. Trotsiuk, and A. A. Ramanenka is greatly acknowledged.

References

1. Bohren CF, Huffman DR (2008) Absorption and scattering of light by small particles. John Wiley & Sons, NJ
2. Kreibig U, Vollmer M (2013) Optical properties of metal clusters. Springer Science & Business Media, Heidelberg
3. Kelly KL, Coronado E, Zhao LL, Schatz GC (2003) The optical properties of metal nanoparticles: the influence of size, shape, and dielectric environment. J Phys Chem B 107(3):668–677
4. Gaponenko SV (2010) Introduction to nanophotonics. Cambridge University Press, Cambridge
5. Törmä P, Barnes WL (2014) Strong coupling between surface plasmon polaritons and emitters: a review. Rep Prog Phys 78(1):013901
6. Baranov DG, Wersäll M, Cuadra J, Antosiewicz TJ, Shegai T (2018) Novel nanostructures and materials for strong light–matter interactions. ACS Photonics 5(1):24–42
7. Murray WA, Barnes WL (2007) Plasmonic materials. Adv Mater 19(22):3771–3782
8. Zayats AV, Smolyaninov II, Maradudin AA (2005) Nano-optics of surface plasmon polaritons. Phys Rep 408(3–4):131–314
9. Klimov V (2014) Nanoplasmonics. CRC Press, FL
10. Gaponenko SV, Guzatov DV (2020) Colloidal plasmonics for active nanophotonics. Proc IEEE 108(5):704–720
11. Gaponenko SV (2017) Nanophotonics with and without photons. In: NATO ASI on Quantum Nano-Photonics. Springer, Dordrecht, pp 3–16
12. Novotny L, Van Hulst N (2011) Antennas for light. Nat Photonics 5(2):83–90
13. Guzatov DV, Klimov VV (2011) Optical properties of a plasmonic nano-antenna: an analytical approach. New J Phys 13(5):053034
14. Guzatov DV, Gaponenko SV, Demir HV (2018) Plasmonic enhancement of electroluminescence. AIP Adv 8(1):015324
15. Gaponenko SV (2014) Satyendra Nath Bose and nanophotonics. J Nanophotonic 8(1):087599
16. Purcell EM (1946) Spontaneous emission probabilities at radio frequencies. Phys Ther Rev 69(2):681–681
17. Krasnok AE, Slobozhanyuk AP, Simovski CR, Tretyakov SA, Poddubny AN, Miroshnichenko AE, Kivshar YS, Belov PA (2015) An antenna model for the Purcell effect. Sci Rep 5:12956
18. Barnett SM, Loudon R (1996) Sum rule for modified spontaneous emission rates. Phys Rev Lett 77(12):2444–2447
19. Gaponenko SV, Demir HV (2018) Applied nanophotonics. Cambridge University Press, Cambridge
20. Gaponenko SV (2002) Effects of photon density of states on Raman scattering in mesoscopic structures. Phys Rev B 65(14):140303
21. Kneipp J, Kneipp H, Kneipp K (2008) SERS—a single-molecule and nanoscale tool for bioanalytics. Chem Soc Rev 37(5):1052–1060
22. Lane LA, Qian X, Nie S (2015) SERS nanoparticles in medicine: from label-free detection to spectroscopic tagging. Chem Rev 115(19):10489–10529
23. Pang S, Yang T, He L (2016) Review of surface enhanced Raman spectroscopic (SERS) detection of synthetic chemical pesticides. TrAC Trends Anal Chem 85(1):73–82
24. Kulakovich OS, Shabunya-Klyachkovskaya EV, Matsukovich AS, Rasool K, Mahmoud KA, Gaponenko SV (2016) Nanoplasmonic Raman detection of bromate in water. Opt Express 24(2):A174–A179
25. Hakonen A, Wu K, Schmidt MS, Andersson PO, Boisen A, Rindzevicius T (2018) Detecting forensic substances using commercially available SERS substrates and handheld Raman spectrometers. Talanta 189:649–652
26. Muehlethaler C, Leona M, Lombardi JR (2016) Towards a validation of surface-enhanced Raman scattering (SERS) for use in forensic science: repeatability and reproducibility experiments. Forensic Sci Int 268:1–13

27. Shabunya-Klyachkovskaya EV, Kulakovich OS, Gaponenko SV (2019) Surface enhanced Raman scattering of inorganic microcrystalline art pigments for systematic cultural heritage studies. Spectrochim Acta A Mol Biomol Spectrosc 222:117235
28. Shabunya-Klyachkovskaya E, Kulakovich O, Vaschenko S, Guzatov D, Gaponenko S (2016) Surface enhanced Raman spectroscopy application for art materials identification. Eur J Sci Theol 12(3):211–220
29. Bandarenka HV, Girel KV, Zavatski SA, Panarin A, Terekhov SN (2018) Progress in the development of SERS-active substrates based on metal-coated porous silicon. Materials 11(5):852–870
30. Klyachkovskaya E, Strekal N, Motevich I, Vaschenko S, Harbachova A, Belkov M, Gaponenko S, Dais C, Sigg H, Stoica T, Grützmacher D (2011) Enhanced Raman scattering of ultramarine on Au-coated Ge/Si-nanostructures. Plasmonics 6(2):413–418
31. Matsukovich AS, Nalivaiko OY, Chizh KV, Gaponenko SV (2019) Raman scattering enhancement using Au/SiGe and Au/Ge nanostructures. J Appl Spectrosc 86(1):72–75
32. Chen Y, Munechika K, Jen-La Plante I, Munro AM, Skrabalak SE, Xia Y, Ginger DS (2008) Excitation enhancement of CdSe quantum dots by single metal nanoparticles. Appl Phys Lett 93(5):053106
33. Yang X, Hernandez-Martinez PL, Dang C, Mutlugun E, Zhang K, Demir HV, Sun XW (2015) Electroluminescence efficiency enhancement in quantum dot light-emitting diodes by embedding a silver nanoisland layer. Adv Optic Material 3(10):1439–1445
34. Kim NY, Hong SH, Kang JW, Myoung N, Yim SY, Jung S, Lee K, Tu CW, Park SJ (2015) Localized surface plasmon-enhanced green quantum dot light-emitting diodes using gold nanoparticles. RSC Adv 5(25):19624–19629
35. Pan J, Chen J, Zhao D, Huang Q, Khan Q, Liu X, Tao Z, Zhang Z, Lei W (2016) Surface plasmon-enhanced quantum dot light-emitting diodes by incorporating gold nanoparticles. Opt Express 24(2):A33–A43
36. Tsakmakidis KL, Boyd RW, Yablonovitch E, Zhang X (2016) Large spontaneous-emission enhancements in metallic nanostructures: towards LEDs faster than lasers. Opt Express 24(16):17916–17927
37. Guzatov DV, Gaponenko SV, Demir HV (2018) Possible plasmonic acceleration of LED modulation for Li-Fi applications. Plasmonics 13(6):2133–2140
38. Guzatov DV, Gaponenko SV, Tevel OI (2020) Possible enhancement of the modulation ate of light-emitting diodes in wireless optical data transfer networks by means of metal nanoparticles with a dielectric shell. Semiconductors 54(13):1751–1756
39. Geddes CD, Lakowicz JR (2002) Metal-enhanced fluorescence. J Fluoresc 12(2):121–129
40. Strekal N, Maskevich A, Maskevich S, Jardillier JC, Nabiev I (2000) Selective enhancement of Raman or fluorescence spectra of biomolecules using specifically annealed thick gold films. Biopolymer: Original Res Biomol 57(6):325–328
41. Kulakovich O, Strekal N, Artemyev M, Stupak A, Maskevich S, Gaponenko S (2006) Improved method for fluorophore deposition atop a polyelectrolyte spacer for quantitative study of distance-dependent plasmon-assisted luminescence. Nanotechnology 17(20):5201–5206
42. Kulakovich O, Strekal N, Yaroshevich A, Maskevich S, Gaponenko S, Nabiev I, Woggon U, Artemyev M (2002) Enhanced luminescence of CdSe quantum dots on gold colloids. Nano Lett 2(12):1449–1452
43. Van Wijngaarden JT, Van Schooneveld MM, de Mello Donegá C, Meijerink A (2011) Enhancement of the decay rate by plasmon coupling for Eu^{3+} in an Au nanoparticle model system. Europhys Lett 93(5):57005
44. Guzatov DV, Vaschenko SV, Stankevich VV, Lunevich AY, Glukhov YF, Gaponenko SV (2012) Plasmonic enhancement of molecular fluorescence near silver nanoparticles: theory, modeling, and experiment. J Phys Chem C 116(19):10723–10733
45. Sultangaziyev A, Bukasov R (2020) Applications of surface-enhanced fluorescence (SEF) spectroscopy in biodetection and biosensing. Sens Bio-Sens Res 30:100382

46. Koktysh IV, Melnikova YI, Kulakovich OS, Ramanenka AA, Vaschenko SV, Muravitskaya AO, Gaponenko SV, Maskevich SA (2020) Highly sensitive immunofluorescence assay of prostate-specific antigen using silver nanoparticles. J Appl Spectrosc 87(5):870–876
47. Bauch M, Toma K, Toma M, Zhang Q, Dostalek J (2014) Plasmon-enhanced fluorescence biosensors: a review. Plasmonics 9(4):781–799
48. Vaschenko S, Ramanenka A, Kulakovich O, Muravitskaya A, Guzatov D, Lunevich A, Glukhov Y, Gaponenko S (2016) Enhancement of labeled alpha-fetoprotein antibodies and antigen-antibody complexes fluorescence with silver nanocolloids. Procedia Eng 140:57–66
49. Akselrod GM, Argyropoulos C, Hoang TB, Ciracì C, Fang C, Huang J, Smith DR, Mikkelsen MH (2014) Probing the mechanisms of large Purcell enhancement in plasmonic nanoantennas. Nat Photonics 8(11):835–840
50. Muravitskaya AO, Trotsiuk LL, Kulakovich OS, Gurinovich LI, Gaponenko SV, Antanovich AV (2019) Refractive index influence on the quantum dots fluorescence near the gold nanorods. Int J Nanosci 18(3–4):1940003
51. Baxter J, Lesina AC, Guay JM, Weck A, Berini P, Ramunno L (2019) Plasmonic colours predicted by deep learning. Sci Rep 9(1):1–9
52. Artemyev MV, Gurinovich LI, Stupak AP, Gaponenko SV (2001) Luminescence of CdS nanoparticles doped with Mn. Phys Status Solidi B 224(1):191–194
53. Gaponenko SV, Germanenko IN, Petrov EP, Stupak AP, Bondarenko VP, Dorofeev AM (1994) Time-resolved spectroscopy of visibly emitting porous silicon. Appl Phys Lett 64(1):85–87
54. Abu-Thabit N, Ratemi E (2020) Hybrid porous silicon biosensors using plasmonic and fluorescent nanomaterials: a mini review. Front Chem 8:454
55. Moakhar RS, Gholipour S, Masudy-Panah S, Seza A, Mehdikhani A, Riahi-Noori N, Tafazoli S, Timasi N, Lim YF, Saliba M (2020) Recent advances in plasmonic perovskite solar cells. Adv Sci 7(13):1902448
56. Zada A, Muhammad P, Ahmad W, Hussain Z, Ali S, Khan M, Khan Q, Maqbool M (2020) Surface plasmonic-assisted photocatalysis and optoelectronic devices with Noble metal nanocrystals: design, synthesis, and applications. Adv Funct Mater 30(7):1906744
57. Gaponenko SV, Adam PM, Guzatov DV, Muravitskaya AO (2019) Possible nanoantenna control of chlorophyll dynamics for bioinspired photovoltaics. Sci Rep 9(1):1–14
58. Chen M, Lu H, Abdelazim NM, Zhu Y, Wang Z, Ren W, Kershaw SV, Rogach AL, Zhao N (2017) Mercury telluride quantum dot based phototransistor enabling high-sensitivity room-temperature photodetection at 2000 nm. ACS Nano 11(6):5614–5622
59. La JA, Kang J, Byun JY, Kim IS, Kang G, Ko H (2021) Highly sensitive and fast perovskite photodetector functionalized by plasmonic Au nanoparticles-alkanethiol assembly. Appl Surf Sci 538:148007
60. Song F, Tang PS, Durst H, Cramb DT, Chan WC (2012) Nonblinking plasmonic quantum dot assemblies for multiplex biological detection. Angew Chem Int Ed 51(35):8773–8777
61. Donehue JE, Wertz E, Talicska CN, Biteen JS (2014) Plasmon-enhanced brightness and photostability from single fluorescent proteins coupled to gold nanorods. J Phys Chem C 118(27):15027–15035
62. Kulakovich O, Gurinovich L, Li H, Ramanenka A, Trotsiuk L, Muravitskaya A, Wei J, Li H, Matveevskaya N, Guzatov DV, Gaponenko S (2020) Photostability enhancement of InP/ZnSe/ZnSeS/ZnS quantum dots by plasmonic nanostructures. Nanotechnology 32(3):035204

Chapter 2
Surface Plasmon-Mediated Decay Processes of Ions in Solids

John Collins and Kailash Mishra

Abstract This chapter focuses on how the emission characteristics of luminescent systems are affected by the presence of a smooth metallic layer. First, we examine the case of a metallic layer nearby to the most fundamental luminescent system — an isolated atom/ion or molecule. Because the metallic layer will adjust the photonic modes in the region near the layer, the radiative decay rate of a nearby excited atom will be altered. Additionally, the presence of the metallic layer allows the atom to interact with the plasmon field of the layer, which will in principle provide additional modes into which the atom could decay. It is this latter affect that is discussed in the first part of this chapter where we show that a modest increase in the radiative decay rate, and hence a corresponding increase in the Purcell factor, can be obtained. The dependence of the Purcell factor on the emission wavelength and on the atom-layer separation are explored. We next discuss another important luminescence-related process — ion-ion energy transfer — in the case when the ion pair is proximate to a smooth metallic surface. When the mirror is present, the energy transfer process may be mediated by surface plasmons, in addition to the traditional energy transfer process, which is mediated by virtual photons, at least in a quantum electrodynamic (QED) formulation of the problem. We find that though the plasmon-mediated energy transfer rate is much less than the traditional energy transfer rate for closely spaced ions, the plasmon mediated transfer rate could be the dominant process for certain experimental conditions.

2.1 Introduction

Optically active ions in solids have formed the basis for much of the lighting and display materials for over 70 years, and continue to be extremely important in modern lighting technology, i.e. light emitting diode (LED)-based solid-state

J. Collins (✉) · K. Mishra
Department of Physics, Wheaton College, Norton, MA, USA
e-mail: jcollins@wheatonma.edu

M. Cesaria et al. (eds.), *Light-Matter Interactions Towards the Nanoscale*,
NATO Science for Peace and Security Series B: Physics and Biophysics,
https://doi.org/10.1007/978-94-024-2138-5_2

lighting. The processes of primary interest in these systems are radiative decay, multiphonon decay, and non-radiative energy transfer. It has been observed that the radiative decay and nonradiative energy transfer rates can be affected when the optical ions are nearby a metallic surface. This is because the metal surface spatially redistributes of the photonic modes into which the ion can decay and also allows for the ion to decay into the surface plasmon modes of the metallic surface. These observations have motivated a plethora of studies on the optical properties of ions in the presence of metallic surfaces for the purpose of improving photon extraction from LEDs [1–10] and for extracting more photons from both LEDs and the phosphor composites [11–22].

This chapter describes the theoretical background necessary for understanding the role of surface plasmons on radiative decay and energy transfer, and is organized as follows. In Sect. 2.2 we discuss some general considerations of the luminescence properties of optical ions in solids, and also present an overview of how the radiative rate is influenced by a nearby metal surface. Next, we develop an expression of the radiative decay rate due to the ion-surface plasmon interaction using the formalism of quantum electrodynamics (QED), and obtain the Purcell factor for the radiative decay rate of an ion nearby a planar metallic surface. In Sect. 2.3 we present the theory for ion-ion energy transfer mediated by surface plasmon modes. The dependence of the energy transfer rate on the distance of the ions from the metallic surface and on the relative positions of the two ions are discussed. These dependencies are consistent with both the symmetry of the system and the known behavior of the surface plasmon field. Finally, the plasmon-mediated energy transfer rate is compared with the Förster-Dexter transfer rate between two ions in the absence of a metallic surface, and the conditions under which the plasmon-mediated energy transfer process could be experimentally observed are discussed.

2.2 Radiative Decay of an Ion into Surface Plasmon Modes

2.2.1 Ion Near a Metallic Surface: General Considerations

When an ion is located near a flat metallic surface, the lifetime of the ion depends on the distance of the ion from the surface. Drexhage clearly showed that that the field established by the excited ion (or molecule) senses the presence of the mirror, and that interference between the reflected field and the field of the ion results in a luminescence pattern that exhibits an angular dependence [23, 24]. Thus, the presence of the mirror adjusts the effective density of photonic modes into which the ion can emit, which changes the lifetime of the ion. Depending on the distance from the mirror, the lifetime could either increase or decrease. At distances less than or on the order of a few tens to 100 nm contributions of the surface plasmon modes on the metallic layer will tend to decrease in the lifetime. It is this contribution that is the main topic of this section. At very close distances, (less than a few nm) other lossy

modes associated with the surface are found to dominate. The reader is referred to the work of Ford and Weber for a fuller description of the various ion-metal interactions and their relative importance [25]. For the remainder of this section, we describe in detail the ion-plasmon interaction and its effect on the radiative decay rate. In practice, this interaction is most relevant for the ion-surface distances between few nm and 100 nm.

2.2.2 *Einstein Coefficients for Surface Plasmon Modes*

In this section, we express the lifetime of the ion due to surface plasmons using the Einstein A and B coefficient formalism. The reader is referred to the work by Mishra et al. for the details of the derivations presented here [26].

For an ion in free space, the ratio of the A and B coefficients is given by

$$\frac{\mathrm{A}}{\mathrm{B}} = \frac{8\pi \mathrm{h}\nu^3}{\mathrm{c}^3} = \overline{\mathrm{M}}(\nu)\,\mathrm{h}\nu \tag{2.1}$$

where

$$\overline{\mathrm{M}}(\nu) = \frac{8\pi\nu^2}{\mathrm{c}^3} \tag{2.2}$$

is the density of photon modes of free space. The coefficient B can be calculated using quantum mechanical methods, and is given by

$$\mathrm{B} = \frac{2\pi}{3\hbar^2}|\mu_{12}|^2 \tag{2.3}$$

for electric dipole transitions of randomly oriented dipoles, where μ_{12} is given by

$$\mu_{12} = \mathrm{e}\left\langle 1|\,\vec{\mathrm{r}}\,|2\right\rangle \tag{2.4}$$

and where $|i\rangle$, $i = 1, 2$ correspond to the initial and final electronic states of the transition. The spontaneous emission rate for the ion to decay into a photonic mode is simply the A coefficient:

$$\frac{1}{\tau_{\mathrm{rad}}} \equiv \mathrm{A} = \overline{\mathrm{M}}(\nu)\,\mathrm{h}\nu\mathrm{B} \tag{2.5}$$

In Eq. (2.5), τ_{rad} is the radiative lifetime of an isolated ion.

We shall assume that an expression similar to Eq. (2.5) can be written for the spontaneous decay rate of the ion into the surface plasmon modes associated with the metallic surface. Thus, we write

$$\frac{1}{\tau_{sp}} \equiv A_{sp} = \overline{M}_{sp}(\nu)\, h\nu B_{sp} \tag{2.6}$$

where $\overline{M}_{sp}(\nu)$ is the density of surface plasmon modes and A_{sp} and B_{sp} are the Einstein A and B coefficients, respectively, associated with the decay into surface plasmon modes. In order to determine the spontaneous rate in Eq. (2.6), we must obtain expressions for $\overline{M}(\nu)$ and B_{sp}.

We first note that $\overline{M}(\nu)$ is the number of photon modes per unit volume. Because the surface plasmons constitute a two-dimensional system, then in order to keep the units correct, we write $\overline{M}_{sp}(\nu)$ as

$$\overline{M}_{sp}(\nu) = \frac{\sigma(\omega)}{L(\omega, d)} \tag{2.7}$$

where, $\sigma(\omega)$ is the number of allowed surface plasmon states per unit area per unit frequency on the surface of the metal, L is a length parameter, and d is the distance of the ion from the metallic layer. $\sigma(\nu)$ can be calculated in the usual manner, and is given by

$$\sigma(\omega) = p\frac{dp}{d\omega} \tag{2.8}$$

where p is the wavevector of the surface plasmon and $\omega = 2\pi\nu$. Also, the appropriate dispersion relation for a surface plasmon is

$$p = \left(\frac{\omega}{c}\right)^2 \frac{\varepsilon_1\varepsilon_2}{\varepsilon_1 + \varepsilon_2}. \tag{2.9}$$

The length parameter, $L(\omega, d)$, is found in reference 26 to be

$$L(\omega, d) = \frac{\omega^3}{2c^2}\frac{\varepsilon_2^{3/2}(\varepsilon_2 - \varepsilon_1)}{(-\varepsilon_1)^{1/2}}\frac{1}{p^4}\frac{dp}{d\omega}e^{2\alpha_2 d} \tag{2.10}$$

where ε_1 and ε_2 are the dielectric constants of the metal and of the dielectric material in which the ion is located, and α_2 is given by

$$\alpha_2 = i\frac{\omega}{c}\frac{\varepsilon_2}{(\varepsilon_1 + \varepsilon_2)^{1/2}}. \tag{2.11}$$

We note that $1/2\alpha_2$ is the characteristic length at which the electric field of the plasmon extends away from the metal surface. Using Eqs. (2.8), (2.9) and (2.10),

Eq. (2.7), which represents the number of plasmon states per unit volume per unit frequency available to the ion, can be rewritten as

$$\overline{M}_{sp}(\nu) = \frac{8\pi^2}{c^3}\nu^2 \left(\frac{(-\varepsilon_1)^{5/2}(\varepsilon_1)^{1/2}\varepsilon_2}{(\varepsilon_1+\varepsilon_2)^{5/2}(\varepsilon_2-\varepsilon_1)} \right) e^{-2\alpha_2 d}. \tag{2.12}$$

We see that the available density of plasmon states decreases exponentially as the ion-metallic layer increases. Note also the explicit dependence on the frequency of the plasmon as well as an implicit frequency dependence through the dielectric constants.

To find the decay rate of the ion into the surface plasmon modes using Eq. (2.6), we need an expression for the appropriate Einstein B-coefficient, B_{sp}. We use the following expression [26]

$$B_{sp} = \frac{2\pi}{\hbar^2}\left(\mu_\perp^2 - \frac{\varepsilon_2}{2\varepsilon_1}\mu_\parallel^2\right), \tag{2.13}$$

where $\mu_\perp$ and $\mu_\parallel$ are the dipole moments at the site of the ions perpendicular and parallel to the metallic layer. Inserting Eq. (2.12) into Eq. (2.6), we obtain an expression for the rate of the decay of the excited ion into surface plasmon modes,

$$\frac{1}{\tau_{sp}} = B_{sp}h\nu\left(\frac{8\pi^2}{c^3}\nu^2\right)\left[\frac{(-\varepsilon_1)^{5/2}(\varepsilon_1)^{1/2}\varepsilon_2}{(\varepsilon_1+\varepsilon_2)^{5/2}(\varepsilon_2-\varepsilon_1)}\right] e^{-2\alpha_2 d} \tag{2.14}$$

where B_{sp} is given in Eq. (2.13).

2.2.3 *Purcell Factor for Radiative Decay into Surface Plasmon Modes*

In 1946, Purcell recognized that placing a resonant circuit near an emitting ion atomic system would add an additional mode into which the system could decay, and therefore would increase the radiative decay rate of the atomic system [27]. The metal surface with its surface plasmon modes constitutes such a resonant circuit. In the previous section we determined the rate as which an ion can decay into the surface plasmon modes. In this section we determine the "Purcell factor" for an ion near a metallic surface, which we will define as the ratio of the decay rate of an ion in the presence of the metallic surface to the decay rate of an isolated ion. The reader is referred to the work of Collins et al. for details of the following treatment [28].

Case 1. Dipole Perpendicular to Metal Surface We first examine the case when the dipole moment of the ion is oriented perpendicular to the metallic surface. In

this case the Einstein B coefficient corresponding to the decay via surface plasmons given in Eq. (2.6) reduces to,

$$B_{sp} = \frac{2\pi}{\hbar^2}\left(\mu_{\perp}^2\right). \tag{2.15}$$

The total decay rate of the ion into electromagnetic modes (photonic modes and surface plasmon modes) is found by summing Eqs. (2.5) and (2.6), using the expressions for the appropriate densities of states given in Eqs. (2.2) and (2.12) and the B-coefficients given in Eqs. (2.3) and (2.15). The result is

$$\frac{1}{\tau_{rad}} + \frac{1}{\tau_{sp}} = B\overline{M}\,(\nu)\,h\nu + B_{sp}\,(\nu)\,\overline{M}_{sp}\,(\nu)\,h\nu$$

$$= Bh\nu\frac{8\pi^2}{c^3}\,\nu^2\,\left[1 + f\,(\varepsilon_1, \varepsilon_2)\;e^{-2\alpha_2 d}\right] \tag{2.16}$$

where

$$f\,(\varepsilon_1, \varepsilon_2) = \left[\frac{(-\varepsilon_1)^{5/2}(\varepsilon_1)^{1/2}\,\varepsilon_2}{(\varepsilon_1 + \varepsilon_2)^{5/2}\;(\varepsilon_2 - \varepsilon_1)}\right] \tag{2.17}$$

By dividing Eq. (2.16) by Eq. (2.5), we obtain the Purcell factor $F_{\perp}$, which gives the fractional increase of the spontaneous decay rate of an ion with its dipole oriented perpendicular to the surface into the surface plasmon modes. The result is

$$F_{\perp} = \frac{\left(\frac{1}{\tau_{rad}} + \frac{1}{\tau_{sp}}\right)}{\frac{1}{\tau_{rad}}} = 1 + \left(\frac{\frac{1}{\tau_{sp}}}{\frac{1}{\tau_{rad}}}\right) = 1 + f\,(\varepsilon_1, \varepsilon_2)\;e^{-2\alpha_2 d}. \tag{2.18}$$

Thus, the contribution of the decay of the ion due to the surface plasmon modes is determined by the term $f\,(\varepsilon_1, \varepsilon_2)\;e^{-2\alpha_2 d}$, which is given in Eq. (2.17).

Figure 2.1 shows the behavior of the Purcell factor as a function wavelength for the ion-surface distances, d, of 20 nm and 50 nm, and for the cases when ε_2 is equal to 1.0 and to 2.25. We have assumed a silver layer, so that ε_1 varies roughly between -3 and -20 moving from the 400 nm to 700 nm. [29] The results shown in Fig. 2.1 indicate that the contribution of the surface plasmon modes to the decay rate of the ion increases as the wavelength decreases throughout the visible region, and that the decay rate increases as the as the dielectric constant of the material in which the ion is located (ε_2) increases.

Case 2. Average Orientation of Dipole with Respect to the Metallic Surface In many systems, we expect the dipole to be randomly oriented with respect to the surface. Thus, it is of interest to find the Purcell factor when the dipole has

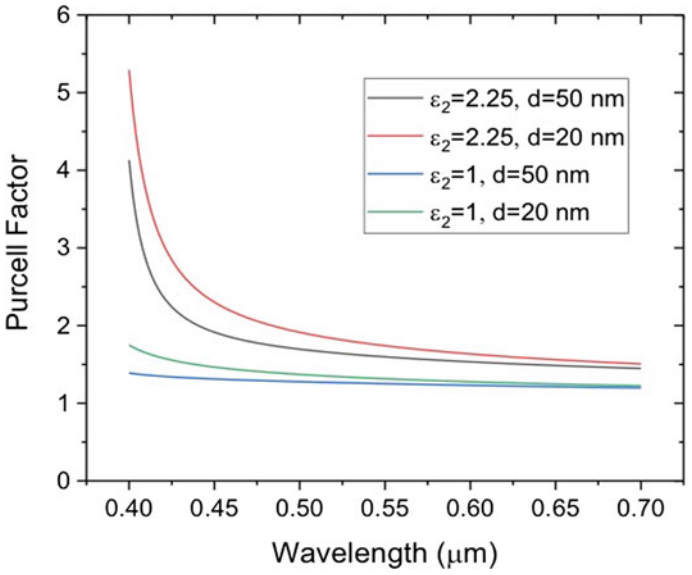

Fig. 2.1 Purcell factors vs. wavelength for ε_2 of 2.25 and 1.0 and distances (d) from the silver surface of 20 and 50 nm for dipoles oriented perpendicular to the surface (Eq. (2.18))

contributions from $\mu_\perp$ *and* $\mu_\parallel$, averaged over all angles. We first begin with the observation that

$$\left\langle \mu_x^2 \right\rangle = \left\langle \mu_y^2 \right\rangle = \left\langle \mu_z^2 \right\rangle = \frac{1}{3}\left\langle \mu^2 \right\rangle. \tag{2.19}$$

As seen in Eq. 2.13, the $\mu_\parallel$ term includes a factor of $\varepsilon_2/2\varepsilon_1$, and since there are two distinct parallel orientations, we write the relevant B-coefficient, given in Eq. (2.13), as

$$B_{sp} = \frac{2\pi}{\hbar^2}\left(\frac{1}{3}\right)\left(1 - \frac{\varepsilon_2}{\varepsilon_1}\right)\left\langle \mu^2 \right\rangle \tag{2.20}$$

We note that since $-\varepsilon_2/\varepsilon_1$ is usually much less than one for a metallic layer, it is the dipole oriented perpendicular to the surface that dominates the decay process.

Inserting Eqs. (2.12) and (2.16) into Eq. (2.6), the decay rate of the ion into surface plasmon modes is

$$\frac{1}{\tau_{sp}} = \left(\frac{64\pi^5}{3hc^3}\,\nu^3\right)\mu^2\,\left(1-\frac{\varepsilon_2}{\varepsilon_1}\right)\left[\frac{(-\varepsilon_1)^{\frac{5}{2}}(\varepsilon_1)^{\frac{1}{2}}\,\varepsilon_2}{(\varepsilon_1+\varepsilon_2)^{\frac{5}{2}}\,(\varepsilon_2-\varepsilon_1)}\right]\,e^{-2\alpha_2 d} \tag{2.21}$$

Before finding the total decay rate, we note that the B coefficient for spontaneous emission into the vacuum photon modes is

$$B = \frac{2\pi}{3\hbar^2}\left\langle \mu^2 \right\rangle. \tag{2.22}$$

Inserting Eqs. (2.22), (2.21), and (2.20) into (2.12), one obtains

$$\frac{1}{\tau_{rad}} + \frac{1}{\tau_{sp}} = \frac{64\pi^5}{3hc^3}\, \nu^3 \left\langle \mu^2 \right\rangle \left\{ 1 + \left(\frac{1}{3}\right)\left(1 - \frac{\varepsilon_2}{\varepsilon_1}\right) f\left(\varepsilon_1, \varepsilon_2\right)\ e^{-2\alpha_2 d} \right\}. \tag{2.23}$$

The Purcell factor for when the dipoles have been averaged over all angles is

$$F = 1 + \left(\frac{\frac{1}{\tau_{sp}}}{\frac{1}{\tau_{rad}}} \right) = \left\{ 1 + \left(\frac{1}{3}\right)\left(1 - \frac{\varepsilon_2}{\varepsilon_1}\right) f\left(\varepsilon_1, \varepsilon_2\right)\ e^{-2\alpha_2 d} \right\}. \tag{2.24}$$

In comparing Eqs. (2.24) and (2.18), we see that the contribution of the surface plasmons to the decay rate differs by a factor of $\left(\frac{1}{3}\right)\left(1 - \frac{\varepsilon_2}{\varepsilon_1}\right)$. For a silver surface and for $\varepsilon_2 = 2.25$, this factor is between 0.45 to 0.58 from 700 nm to 400 nm. Thus, for randomly oriented dipoles the surface plasmon contribution is roughly one-half that when the dipoles are perpendicular to the surface.

Conclusions We have examined the decay of an optically active ion in the vicinity of a flat, smooth metallic surface. Using an Einstein B coefficient appropriate to the ion-surface plasmon interaction and the density of surface plasmon modes, we obtain an expression for the decay rate of the ion into the surface plasmon modes. The decay rate of the ion into the surface plasmon modes decreases exponentially as the ion-metal surface distance increases, and is also dependent on the orientation of the dipole at the ion site relative to the surface. For a silver metallic layer, the ω dependence shows the decay rate increasing as the wavelength decreases in the visible region, with the decay rate increasing more rapidly as the photon frequency approaches the plasmon frequency of the metal, which for silver is near 330 nm. The Purcell factor shows the effect of the surface plasmons to be modest throughout much of the visible region, but can dominate over the photon decay rate in the violet region of the spectrum.

2.3 Non-radiative Ion-Ion Energy Transfer Mediated by Surface Plasmons

In this section we describe the transfer of energy from an excited ion to an unexcited ion. First, in Sect. 2.3.1 we briefly describe the ion-ion (or molecule-molecule) energy transfer process in the absence of a metallic surface. In Sect. 2.3.2 we discuss

in detail the energy transfer process mediated by surface plasmons, which requires the presence of a metallic surface. We shall see that the two types of energy transfer processes show very different characteristics, and it is not at first clear under what conditions might the plasmon-mediated process dominate. Thus, we also examine the question of how determine which energy transfer will be dominant in a particular experimental situation.

2.3.1 Photon-Mediated Energy Transfer

Traditional energy transfer, as formulated by Dexter [30], is the process in which an excited ion (the donor) transfers its energy to a nearby unexcited ion (the acceptor). In the Dexter's treatment, the interaction responsible for the energy transfer is the static Coulomb electron-electron interaction. A multipolar expansion of that interaction leads to dipole-dipole, dipole-quadrupole, quadrupole-quadrupole, etc. interaction terms that drive the energy transfer process. In most systems, the dipole-dipole term is the most important. It is a short-range interaction, with a $(1/R)^6$ dependence, where R is the donor-acceptor distance. Because it is due to the (static) Coulomb interaction, the interaction is said to be "non-radiative", in that no real photon is emitted or absorbed in the process. Dexter's formulation of the dipole-dipole energy transfer rate between ions a donor and acceptor ion in free space is given by

$$\Gamma_{dd} = \frac{3\hbar^4 c^3}{4\pi R^6} \frac{Q_A}{\tau_D} \int \frac{f_D(E) F_A(E)}{E^4} dE \tag{2.25}$$

In Eq. (2.25), Q_A is the integrated absorption cross section of the acceptor ion, τ_D is the radiative lifetime of the donor, and the integral is the overlap of the normalized donor emission line, $f_D(E)$, and the normalized acceptor absorption line, $F_A(E)$.

In a QED approach, the electric field is quantized and the electron-electron interaction is mediated by photons, either real or virtual. Usually, if the donor-acceptor distance is shorter than the wavelength of a photon, then energy transfer is considered to be mediated by virtual photons. The short-range terms in the QED treatment match well the corresponding terms from Dexter's treatment. Longer range energy transfer terms also emerge from the QED treatment, and long-range energy transfer processes involve real photons [31].

2.3.2 Plasmon-Mediated Energy Transfer

The energy transfer process of interest in this section occurs when the donor and acceptor ions are proximate to a flat, metallic surface. The traditional Dexter-type energy transfer will still be present, but an additional energy transfer process, one

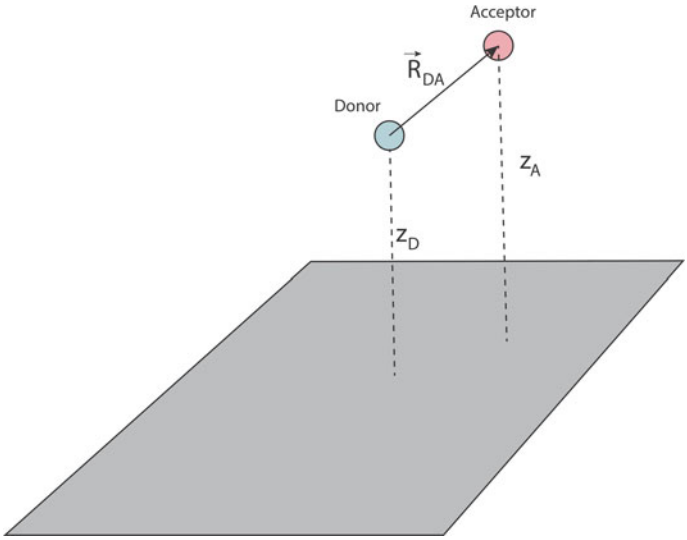

Fig. 2.2 Donor and acceptor ions located at distances $z_D$and $z_A$above the metallic surface, respectively. $\vec{R}_{DA}$ is a vector from the donor to the acceptor

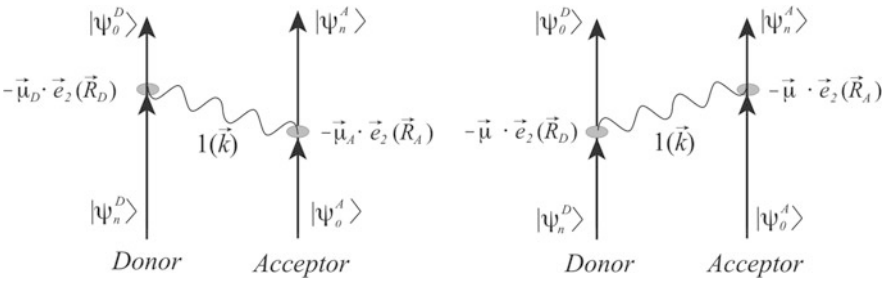

Fig. 2.3 Two Feynman diagrams relevant to the energy transfer process

mediated by the surface plasmons on the metallic layer, may also occur. A diagram of the set up for this type of transfer is shown in Fig. 2.2. The goal of this section is to derive an expression for the surface plasmon-mediated donor-acceptor energy transfer rate, which can then be compared with the transfer rate in the absence of the metal layer, as given in Eq. (2.25). We will use the QED treatment to find the rate of transfer mediated by surface plasmons .

The two relevant Feynman diagrams for the spontaneous energy-transfer process are shown in Fig. 2.3. Both diagrams in Fig. 2.3 has the initial state

$$|\, i\rangle = \Big|\, \psi_n^D, \psi_0^A; 0\Big\rangle, \tag{2.26}$$

with the donor in the excited state (n), the acceptor in the ground state (0), and no surface plasmons are present. The final state of the system for both diagrams is given by

$$\mid f\rangle = \mid \psi_0^D, \psi_n^A; 0\Big\rangle, \tag{2.27}$$

which consists of the donor in its ground state, the acceptor in its excited state and no surface plasmons. The two possible intermediate states are shown in the Fig. 2.3. The first intermediate state, corresponding to the diagram on the left in Fig. 2.3, is

$$\mid I\rangle = \mid \psi_0^D, \psi_0^A; 1\left(\vec{k}\right)\Big\rangle, \tag{2.28}$$

which has both the donor and acceptor in the ground state, and one surface plasmon of wavevector $\vec{k}$. The second intermediate state (see diagram on the right in Fig. 2.3), is

$$\mid I\rangle = \mid \psi_n^D, \psi_n^A; 1\left(\vec{k}\right)\Big\rangle \tag{2.29}$$

has both donor and acceptor in their excited states, and one surface plasmon of wavevector $\vec{k}$.

For dipole-dipole energy transfer, the relevant interaction Hamiltonian is given by

$$H_{int} = -\vec{\mu}(D) \cdot \vec{e}_2\left(\vec{R}_D\right) - \vec{\mu}(A) \cdot \vec{e}_2\left(\vec{R}_A\right) \tag{2.30}$$

where $\vec{\mu}(D)$ and $\vec{\mu}(A)$ are the dipole operators for the donor and acceptor, respectively, and $\vec{e}_2\left(\vec{R}_D\right)$ and $\vec{e}_2\left(\vec{R}_A\right)$ are the corresponding electric fields at the donor and acceptor locations.

In order to determine the energy transfer rate, one must first know the behavior of the surface plasmon fields at the donor and acceptor locations. The fields are well known, and have characteristics shown if Fig. 2.4. The diagram on the left shows the fields oscillating along the surface, and extending both into the nearby dielectric layer and into the metal. The diagram on the right in Fig. 2.3 shows that the field strength decays exponentially with the distance from the surface.

The vector potential associated with the surface plasmon field can be expressed as [32]

$$\vec{a}\left(\vec{r}, t\right) = \sum_{\vec{k}} \left(a_{\vec{k}}(t)\, \vec{u}_{2\vec{k}}(z)\, e^{i\vec{k}\cdot\vec{\rho}} + \bar{a}_{\vec{k}}(t)\, \overline{\vec{u}}_{2\vec{k}}(z)\, e^{-i\vec{k}\cdot\vec{\rho}} \right) \tag{2.31}$$

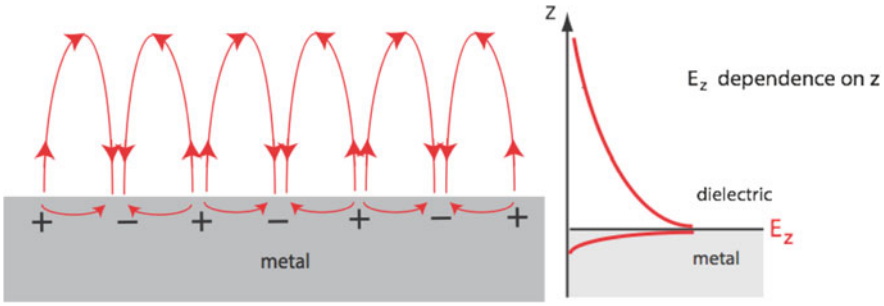

Fig. 2.4 The behavior of the electric field due to surface plasmons in the vicinity of the metallic layer. The diagram on the left shows the fields oscillating with the wavelength of the surface plasmon, and that on the right shows the magnitude of the field decreasing exponentially with the distance z away from the surface into the dielectric and into the metal

where

$$\vec{u}_{\vec{k}}(z) = \left(\hat{k} + i\frac{k}{\alpha_2}\hat{z}\right)\frac{e^{-\alpha_2 z}}{\sqrt{L(k)}} \tag{2.32}$$

and

$$\vec{r} = \vec{\rho} + z\hat{z} \tag{2.33}$$

In the above equations, $\vec{\rho}$ represents a radius vector in the x-y plane (the plane of the metallic surface), $\hat{z}$, the unit vector perpendicular to this plane, and α_2 is given in Eq. (2.11) in Sect. 2.2 of this chapter. Also, a unit vector along $\vec{k}$, the plasmon wavevector, is denoted by $\hat{k}$. Finally, in Eq. (2.31) we have introduced a length parameter, L, which is a function of the wavevector $\vec{k}$ and serves as a thickness to the surface plasmon modes. This allows for the surface plasmon modes to be assigned a volume density (modes per unit volume), which is necessary for use in the Fermi Golden Rule. Essentially, the thickness L is an effective thickness into which the plasmons modes extend into the dielectric.

The next step is to quantize the fields. We follow the method done by Archambault et al. [33]. The energy associated with the surface plasmon wave can be expressed as

$$U = \sum_{\vec{k}} \varepsilon_0 \omega^2 s \left(a_{\vec{k}} a^*_{\vec{k}} + a^*_{\vec{k}} a_{\vec{k}}\right) \tag{2.34}$$

Associating the quantum mechanical annihilation, $\hat{a}_{\vec{k}}$ and creation $\hat{a}^{\dagger}_{\vec{k}}$ operators with the field amplitudes, $a_{\vec{k}}$ and $a^{*}_{\vec{k}}$ in the following manner,

$$a_{\vec{k}} \rightarrow \left(\frac{\hbar}{2\varepsilon_0 \omega s}\right)^{1/2} \hat{a}_{\vec{k}} \tag{2.35}$$

$$a^{*}_{\vec{k}} \rightarrow \left(\frac{\hbar}{2\varepsilon_0 \omega s}\right)^{1/2} \hat{a}^{\dagger}_{\vec{k}} \tag{2.36}$$

the Hamiltonian for the surface waves can written as

$$H_{sp} = \sum_{\vec{k}} \frac{\hbar\omega}{2} \left(\hat{a}_{\vec{k}} \hat{a}^{\dagger}_{\vec{k}} + \hat{a}^{\dagger}_{\vec{k}} \hat{a}_{\vec{k}}\right) \tag{2.37}$$

The annihilation and creation operators in Eq. (2.32) satisfy the following relations,

$$\hat{a}^{\dagger}_{\vec{k}} \mid n_{\vec{k}} \rangle = \sqrt{n_{\vec{k}} + 1} \mid n_{\vec{k}} + 1 \rangle \tag{2.38}$$

$$\hat{a}_{\vec{k}} \mid n_{\vec{k}} \rangle = \sqrt{n_{\vec{k}}} \mid n_{\vec{k}} - 1 \rangle \tag{2.39}$$

In Eq. (2.38) and Eq. (2.39), $n_{\vec{k}}$ is the occupation number for the plasmon mode, $\vec{k}$ and thus an eigenvalue of the (occupation) number operator, $\hat{a}^{\dagger}_{\vec{k}} \hat{a}_{\vec{k}}$ corresponding to the eigenvector, $\mid n_{\vec{k}} \rangle$. Then the operator form of the vector potential can be expressed as

$$\hat{a}_2\left(\vec{r}\right) = \sum_{\vec{k}} \left(\frac{\hbar}{2\varepsilon_0 \omega s}\right)^{1/2} \left(\hat{a}_{2\,\vec{k}} \vec{u}_{2\,\vec{k}} e^{i\,\vec{k}\cdot\vec{\rho}} + \hat{a}^{\dagger}_{\vec{k}} \overline{\vec{u}}_{2\,\vec{k}} e^{-i\,\vec{k}\cdot\vec{\rho}}\right) \tag{2.40}$$

and the electric field is

$$\hat{e}_2\left(\vec{r}\right) = i \sum_{\vec{k}} \left(\frac{\hbar\omega}{2\varepsilon_0 s}\right)^{1/2} \left(\hat{a}_{2\,\vec{k}} \vec{u}_{2\,\vec{k}} e^{i\,\vec{k}\cdot\vec{\rho}} - \hat{a}^{\dagger}_{\vec{k}} \overline{\vec{u}}_{2\,\vec{k}} e^{-i\,\vec{k}\cdot\vec{\rho}}\right). \tag{2.41}$$

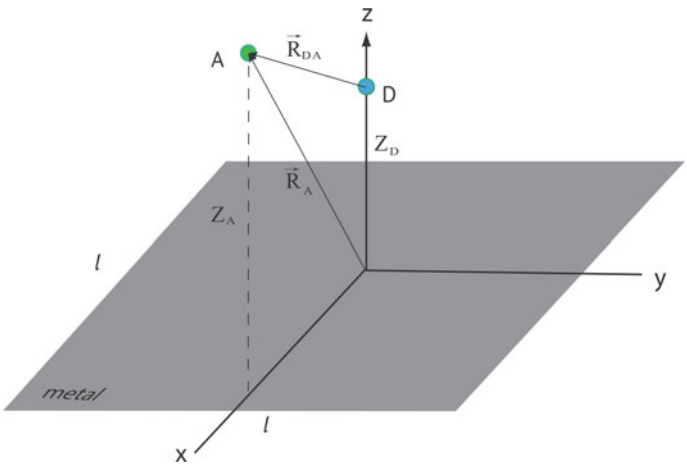

Fig. 2.5 The coordinate system used in calculating energy transfer rate

We now choose a coordinate system, shown in Fig. 2.5, such that the origin is on the interface and the z axis is normal to the plane of the interface. The donor ion is chosen to be on the z-axis so that its position vector, $\vec{R}_D$, is given by

$$\vec{R}_D = Z_D \hat{z} \tag{2.42}$$

We then choose the position vector of acceptor ion as

$$\vec{R}_A = X_{DA}\hat{x} + Z_A \hat{z} \tag{2.43}$$

Thus, the interionic vector from D to A, $\vec{R}_{DA}$ is given by

$$\vec{R}_{DA} = X_{DA}\hat{x} + (Z_D - Z_A)\,\hat{z}. \tag{2.44}$$

The x-axis is defined by the projection of $\vec{R}_{DA}$ on the x-y plane, i.e., the plane of the interface. The y-axis is then chosen to be perpendicular to the x-z-plane, defined by $\vec{R}_{DA}$ and the z-axis, to yield a right-handed coordinate system. Any surface plasmon wavevector, $\vec{k}$ lies in the x-y-plane, i.e.

$$\vec{k} = \hat{k}k, \quad \hat{k} = \cos\theta\hat{x} + \sin\theta\hat{y} \tag{2.45}$$

where θ denotes the angle between the x-axis and the plasmon wavevector, $\vec{k}$. In this coordinate system, $\vec{u}_{2\vec{k}}$ from Eq. (2.28) can be expressed as

$$\vec{u}_{2\vec{k}}(z) = \left(\cos\theta\hat{x} + \sin\theta\hat{y} + i\frac{k}{\alpha_2}\hat{z}\right)\frac{e^{-\alpha_2 z}}{\sqrt{L(k)}} \tag{2.46}$$

In second order perturbation theory, the matrix element for transition from the initial state, $|i\rangle$, to the final state, $|f\rangle$, has the form

$$M_{fi} = \sum_I \frac{\langle f|H_{int}|I\rangle\langle I|H_{int}|i\rangle}{E_i - E_I} \tag{2.47}$$

where the initial, final, and two intermediate states are given in Eqs. (2.26–2.29). Eq. (2.47) contains the sum over intermediate states, of which there are only two. These are shown Fig. 2.3. Using the states in Eqs. (26–28), the contribution of the first intermediate state, shown on the left side of Fig. 2.3, can be written as

$$\mathrm{M}_{\mathrm{fi}}^{1} = \frac{\left\langle\psi_{\mathrm{n}}^{\mathrm{A}}|\vec{\mu}|\psi_{0}^{\mathrm{A}}\right\rangle\left\langle 0\left(\vec{\mathrm{k}}\right)|\hat{\mathrm{e}}_2\left(\vec{\mathrm{R}}_{\mathrm{A}}\right)|1\left(\vec{\mathrm{k}}\right)\right\rangle\left\langle\psi_{0}^{\mathrm{D}}|\vec{\mu}|\psi_{\mathrm{n}}^{\mathrm{D}}\right\rangle\left\langle 1\left(\vec{\mathrm{k}}\right)|\hat{\mathrm{e}}_2\left(\vec{\mathrm{R}}_{\mathrm{A}}\right)|0\left(\vec{\mathrm{k}}\right)\right\rangle}{\mathrm{E}_{\mathrm{no}}-\hbar\omega(\mathrm{k})} \tag{2.48}$$

where E_{no} is the energy of the excited donor. Similarly, the contribution of the second intermediate state (Eq. (2.27), shown on the right side of Fig. 2.3, is

$$M_{fi}^{2} = \frac{\left\langle\psi_{n}^{A}|\vec{\mu}|\psi_{n}^{A}\right\rangle\left\langle 0\left(\vec{k}\right)|\hat{e}_2\left(\vec{R}_{A}\right)|1\left(\vec{k}\right)\right\rangle\left\langle\psi_{n}^{D}|\vec{\mu}|\psi_{n}^{D}\right\rangle\left\langle 1\left(\vec{k}\right)|\hat{e}_2\left(\vec{R}_{A}\right)|0\left(\vec{k}\right)\right\rangle}{-E_{no}-\hbar\omega(k)} \tag{2.49}$$

To evaluate Eqs. (2.48) we insert the quantized field $(\hat{e}_2)$, as given in Eq. (2.41), which yields

$$\begin{aligned}\mathrm{M}_{\mathrm{fi}}^{1} = &\sum\nolimits_{\vec{\mathrm{k}}}\left(\frac{\hbar\omega}{2\varepsilon_0 \mathrm{s}}\right)\frac{\mathrm{e}^{-\alpha_2(\mathrm{Z_D}+\mathrm{Z_A})}}{\mathrm{L}}\frac{\mathrm{e}^{\mathrm{ikX_{DA}}\cos\theta}}{\mathrm{E_{n0}}-\hbar\omega}\\ &\times\left(\mu_{\mathrm{x}}^{0\mathrm{n}}(\mathrm{D})\cos\theta+\mu_{\mathrm{y}}^{0\mathrm{n}}(\mathrm{D})\sin\theta-\mathrm{i}\frac{\mathrm{k}}{\alpha_2}\mu_{\mathrm{z}}^{0\mathrm{n}}(\mathrm{D})\right)\\ &\times\left(\mu_{\mathrm{x}}^{\mathrm{n0}}(\mathrm{A})\cos\theta+\mu_{\mathrm{y}}^{\mathrm{n0}}(\mathrm{A})\sin\theta+\mathrm{i}\frac{\mathrm{k}}{\alpha_2}\mu_{\mathrm{z}}^{\mathrm{n0}}(\mathrm{A})\right)\end{aligned} \tag{2.50}$$

Proceeding in a similar manner, we can express Eq. (2.49) as

$$\begin{aligned}M_{fi}^{2} = &-\sum\nolimits_{\vec{k}}\left(\frac{\hbar\omega}{2\varepsilon_0 s}\right)\frac{e^{-\alpha_2(Z_D+Z_A)}}{L}\frac{e^{-ikX_{DA}\cos\theta}}{E_{n0}+\hbar\omega}\\ &\times\left(\mu_x^{n0}(A)\cos\theta+\mu_y^{n0}(A)\sin\theta-i\frac{k}{\alpha_2}\mu_z^{n0}(A)\right)\\ &\times\left(\mu_x^{0n}(D)\cos\theta+\mu_y^{0n}(D)\sin\theta+i\frac{k}{\alpha_2}\mu_z^{0n}(D)\right)\end{aligned} \tag{2.51}$$

Both Eqs. (2.50) and (2.51) involve a summation over k-vectors of the plasmon modes on the metallic surface. We replace the sum by the integral using:

$$\sum_{\vec{k}} \frac{1}{s} = \int_0^{\infty} \int_0^{2\pi} k dk d\theta \tag{2.52}$$

Integrating over the polar angle, the only nonzero terms that survive involve 1, $\cos\theta$, $\sin^2\theta$ and $\cos^2\theta$. Eq. (2.50) becomes

$$\begin{aligned} M_{fi}^1 = & \int_0^{\infty} k dk \left(\frac{\pi\hbar\omega}{\varepsilon_0}\right) \frac{e^{-\alpha_2(Z_D+Z_A)}}{L} \frac{1}{E_{n0}-\hbar\omega} \\ & \times \left(\mu_x^{0n}(D)\mu_x^{n0}(A)\left(J_0(kX_{DA}) - \frac{J_1(kX_{DA})}{kX_{DA}}\right) + \mu_y^{0n}(D)\mu_y^{n0}(A)\frac{J_1(kX_{DA})}{kX_{DA}}\right. \\ & + \frac{k^2}{\alpha_2^2}\mu_z^{0n}(D)\mu_z^{n0}(A)J_0(kX_{DA}) \\ & \left. - \frac{k}{\alpha_2}\left(\mu_x^{0n}(D)\mu_z^{n0}(A) - \mu_z^{0n}(D)\mu_x^{n0}(A)\right)J_1(kX_{DA})\right) \end{aligned} \tag{2.53}$$

Similarly, integrating Eq. (2.51) over the polar angle leads to

$$\begin{aligned} M_{fi}^2 = & -\int_0^{\infty} k dk \left(\frac{\pi\hbar\omega}{\varepsilon_0}\right) \frac{e^{-\alpha_2(Z_D+Z_A)}}{L} \frac{1}{E_{n0}+\hbar\omega} \\ & \times \left(\mu_x^{0n}(D)\mu_x^{n0}(A)\left(J_0(kX_{DA}) - \frac{J_1(kX_{DA})}{kX_{DA}}\right) + \mu_y^{0n}(D)\mu_y^{n0}(A)\frac{J_1(kX_{DA})}{kX_{DA}}\right. \\ & + \frac{k^2}{\alpha_2^2}\mu_z^{0n}(D)\mu_z^{n0}(A)J_0(kX_{DA}) \\ & \left. - \frac{k}{\alpha_2}\left(\mu_x^{0n}(D)\mu_z^{n0}(A) - \mu_z^{0n}(D)\mu_x^{n0}(A)\right)(kX_{DA})\right) \end{aligned} \tag{2.54}$$

In Eqs. (2.53) and (2.54), J_n is a Bessel function of the first kind of order n. Moving forward we will designate X_{DA}, the donor-acceptor distance projected onto the x-y plane, as ρ.

The total matrix element responsible for the energy transfer is the sum of Eqs. (2.53) and (2.54).

$$M_{fi} = M_{fi}^1 + M_{fi}^2 \tag{2.55}$$

Defining p to be the wavevector satisfying

$$E_{no} = \hbar\omega(p) \tag{2.56}$$

and assuming that the plasmon phase velocity is only weakly dependent on the plasmon wavevector, then Eq. (2.55) can be expressed as

$$M_{fi} = \int_0^\infty \frac{f(k)}{k^2 - p^2} dk \tag{2.57}$$

where

$$\begin{aligned} f(k) = &- \left(\frac{2\pi}{\varepsilon_0}\right) k^3 \frac{e^{-\alpha_2(Z_D+Z_A)}}{L} \\ &\times \left(\mu_x^{0n}(D)\mu_x^{n0}(A)\left(J_0(k\rho) - \frac{J_1(k\rho)}{k\rho}\right) + \mu_y^{0n}(D)\mu_y^{n0}(A)\frac{J_1(k\rho)}{k\rho}\right. \\ &\left. + \frac{k^2}{\alpha_2^2}\mu_z^{0n}(D)\mu_z^{n0}(A)J_0(k\rho) - \frac{k}{\alpha_2}\left(\mu_x^{0n}(D)\mu_z^{n0}(A) - \mu_z^{0n}(D)\mu_x^{n0}(A)\right)J_1(k\rho)\right) \end{aligned} \tag{2.58}$$

The integral in Eq. (2.58) cannot be solved analytically. To estimate this integral, we will assume that the maximum contributions will come from near the pole at $k = p$. Evaluating near the pole we obtain

$$\begin{aligned} M_{fi} \cong &\left(\frac{\pi}{\varepsilon_0}\right) p^2 \frac{e^{-\alpha_2(Z_D+Z_A)}}{L} \\ &\times \left(\mu_x^{0n}(D)\mu_x^{n0}(A)\left(J_0(p\rho) - \frac{J_1(p\rho)}{p\rho}\right) + \mu_y^{0n}(D)\mu_y^{n0}(A)\frac{J_1(p\rho)}{p\rho}\right. \\ &\left. + \frac{p^2}{\alpha_2^2}\mu_z^{0n}(D)\mu_z^{n0}(A)J_0(p\rho) - \frac{p}{\alpha_2}\left(\mu_x^{0n}(D)\mu_z^{n0}(A) - \mu_z^{0n}(D)\mu_x^{n0}(A)\right)J_1(p\rho)\right) \end{aligned} \tag{2.59}$$

2.3.3 The Plasmon-Mediated, Ion-Ion Energy Transfer Rate

In order to calculate the energy transfer rate using the Fermi Golden Rule for randomly oriented electric dipole moments of the optical ions, we calculate $|M_{fi}|^2$ averaged over all orientations. It can be shown that

$$\langle \mu_x \mu_y \rangle = \langle \mu_y \mu_z \rangle = \langle \mu_z \mu_x \rangle = 0 \tag{2.60}$$

where μ represents the magnitude of the dipole moment of the ion. Using Eq. (2.60) and Eq. (2.13) it can be shown that $|M_{fi}|^2$ averaged over all orientations is

$$\left\langle |M_{fi}|^2 \right\rangle = \frac{\pi^2}{9\varepsilon_0^2} p^4 |\mu(A)|^2 |\mu(B)|^2 \frac{e^{-2\alpha_2(Z_D+Z_A)}}{L^2} F(p, \rho) \tag{2.61}$$

where $F(p, \rho)$ is given by

$$F\left(p\rho\right) = J_0^2\left(p\rho\right)\left(1 + \frac{p^4}{\alpha_2^4}\right) + \frac{2J_1^2\left(p\rho\right)}{p^2\rho^2}\left(1 + \frac{p^4\rho^2}{\alpha_2^2}\right) - 2J_0\left(p\rho\right)\frac{J_1\left(p\rho\right)}{p\rho} \tag{2.62}$$

and where L is a length parameter defined in the work of Archambault et al. [33] as

$$L = -\frac{\varepsilon}{2\alpha_1} + \frac{1}{4\alpha_2}\left[\frac{1-\varepsilon}{-\varepsilon}\frac{d\left(\omega\varepsilon\right)}{d\omega} - 1 - \varepsilon\right] \tag{2.63}$$

and where α_1 is defined as

$$\alpha_1 = \frac{\omega}{c}\sqrt{\frac{\varepsilon^2}{|\varepsilon|}} \tag{2.64}$$

Given the dispersion relation for the surface plasmons,

$$p = \frac{E_{no}}{\hbar c}\sqrt{\frac{\varepsilon}{1+\varepsilon}} \tag{2.65}$$

and the definition of α_2 in Eq. (2.11), Eq. (2.61) may be written as

$$\left\langle \left|M_{fi}\right|^2 \right\rangle = \frac{\pi^2}{9\varepsilon_0^2}\left(\frac{E_{no}}{\hbar c}\right)^4\left(\frac{\varepsilon}{1+\varepsilon}\right)^2 |\mu(D)|^2|\mu(A)|^2\frac{e^{-2\alpha_2(Z_D+Z_A)}}{L^2}F\left(p,\rho\right) \tag{2.66}$$

Also, using Eq. (2.11), Eq. (2.62) can be rewritten so as to show more explicitly the dependence of $F(p, \rho)$ on the dielectric constant of the metal:

$$\begin{aligned} F\left(p\rho\right) = {} & J_0^2\left(p\rho\right)\left(1 + \tfrac{p^4c^4}{\omega^4(p)}\left(|\varepsilon| - 1\right)^2\right) \\ & + \tfrac{2J_1^2(p\rho)}{p^2\rho^2}\left(1 + \tfrac{p^4c^2\rho^2}{\omega^2(p)}\left(|\varepsilon| - 1\right)\right) - 2J_0\left(p\rho\right)\tfrac{J_1(p\rho)}{p\rho} \end{aligned} \tag{2.67}$$

Thus far we have not considered the fact that the energy levels of the optical ions are usually broadened for a variety of reasons. The effect of broadening of the energy levels can be described by the line shape function for the donor ion, D for emission, $f_D(E)$, and that for the absorption by acceptor ion A, $F_A(E)$. The line shape functions satisfy the following relations

$$\int f_D(E)\,dE = 1; \int f_D(E)E^n dE = E_{no}^n \tag{2.68}$$

$$\int F_A(E)\, dE = 1; \int F_A(E) E^n dE = E_{no}^n \tag{2.69}$$

The differential transition rate for energy transfer from the donor to the acceptor is then given by the Fermi Golden rule,

$$d\Gamma = \frac{2\pi}{\hbar} \left\langle \left| M_{fi} \right|^2 \right\rangle f_A(E) F_B(E) dE \tag{2.70}$$

Inserting $\langle |M_{fi}|^2 \rangle$ from Eq. (2.66) in Eq. (2.70), one obtains

$$d\Gamma = \frac{2\pi^3}{9\varepsilon_0^2 \hbar^5 c^4} E_{n0}^4 \left(\frac{\varepsilon(p)}{1+\varepsilon(p)} \right)^2 |\mu(D)|^2 |\mu(A)|^2 \frac{e^{-2\alpha_2(Z_D+Z_A)}}{L^2} F(p\rho)\, f_A(E) F_B(E) dE. \tag{2.71}$$

We can obtain $|\mu(D)|^2$ and $|\mu(A)|^2$ from the lifetime of the donor ion, τ_D and integrated absorption intensity of acceptor ion, $Q(A)$. They are given by

$$|\mu(D)|^2 = \frac{3\pi\varepsilon_0 c^3 \hbar^4}{E_{no}^3} \frac{1}{\tau_D} \tag{2.72}$$

and

$$|\mu(A)|^2 = \frac{3\varepsilon_0 \hbar c}{\pi E_{n0}} Q(A) \tag{2.73}$$

Using $|\mu(D)|^2$ and $|\mu(A)|^2$ from Eq. (2.72) and Eq. (2.73) respectively in Eq. (2.71), one obtains,

$$d\Gamma = 2\pi^3 \left(\frac{\varepsilon(p)}{1+\varepsilon(p)} \right)^2 \frac{e^{-2\alpha_2(Z_D+Z_A)}}{L^2} \frac{Q(A)}{\tau_D} F(p\rho)\, f_D(E) F_A(E) dE \tag{2.74}$$

Upon integrating the right-hand side of Eq. (2.75) over E, one obtains the transition rate, Γ, as

$$\Gamma = 2\pi^3 \left(\frac{\varepsilon(p)}{1+\varepsilon(p)} \right)^2 \frac{e^{-2\alpha_2(Z_D+Z_A)}}{L^2} \frac{Q(A)}{\tau_D} F(p\rho) \int f_D(E) F_A(E) dE \tag{2.75}$$

where we have ignored any explicit dependence of L on energy.

2.3.4 Distance Dependence of the Energy Transfer Rate

Let us compare Eq. (2.71), the energy transfer rate for plasmon-mediated energy transfer, with the Forster-Dexter type energy transfer rate given in Eq. (2.25). We note that both equations have terms relating to the conservation of energy, that is the overlap integral of the lineshape functions of the absorption band of the acceptor and the emission band of the donor. Also, both equations have terms related to the absorption strength of the acceptor and the radiative decay rate of the excited donor. The main difference between the two equations is the dependence of the energy transfer rate on the position of the acceptor relative to the donor. In the dipole approximation of the Forster-Dexter type energy transfer, the dependence is $(1/R_{DA})^6$. In the plasmon-mediated energy transfer, we see two different distance dependencies, one perpendicular to the metallic layer (z-direction) and a second distance dependence in the plane parallel to the interface, determined by ρ. These two dependencies, which we now examine, occur because of the manner in which, the interface has destroyed the isotropy of space.

First, the exponential term in Eq. (2.72), $e^{-2\alpha_2(Z_D+Z_A)}$, shows that the transfer rate depends on the sum of the z distances of donor and the acceptor from the metallic layer; the closer these ions get to the surface of the metal, the higher will be the transfer rate. Given the fact that the strength of the plasmon fields decay exponentially with distance from the metallic layer, and that energy transfer requires both the donor and the acceptor to interact with the plasmon fields, then the exponential decay of the transfer rate is hardly surprising. The term $2\alpha_2$ in the exponent will determine the characteristic distance over which the energy transfer occurs. For example, for a silver layer and for a plasmon wavelength of 550 nm, we estimate α_2 to be on the order of 3.7 μm^{-1}, which implies a characteristic distance of a few hundred nm, which is relatively long range.

The second distance dependency is contained in the term $F(p\rho)$. To uncover the behavior of $F(p\rho)$, we note first that it is a function of the ratio p/α_2, which has the form

$$\frac{p}{\alpha_2} = \left(\frac{\omega}{c}\sqrt{\frac{\varepsilon}{1+\varepsilon}}\right) \div \left(\frac{\omega}{c}\sqrt{(|\varepsilon|-1)}\right) = \left(\sqrt{\frac{\varepsilon}{1+\varepsilon}}\right)\sqrt{(|\varepsilon|-1)} \tag{2.76}$$

For metal in the frequency range of interest, $\varepsilon \leq -1$, so that $1+\varepsilon = -(|\varepsilon|-1)$. This leads to

$$\frac{p}{\alpha_2} = \sqrt{-\varepsilon} \tag{2.77}$$

Thus, for $\varepsilon \leq -1$, $F(p\rho)$ in Eq. (106) can be simplified to

$$F(p\rho) = J_0^2(p\rho)\left(1+\varepsilon^2\right) + \frac{2J_1^2(p\rho)}{p^2\rho^2}\left(1+\varepsilon p^2\rho^2\right) - 2J_0(p\rho)\frac{J_1(p\rho)}{p\rho} \tag{2.78}$$

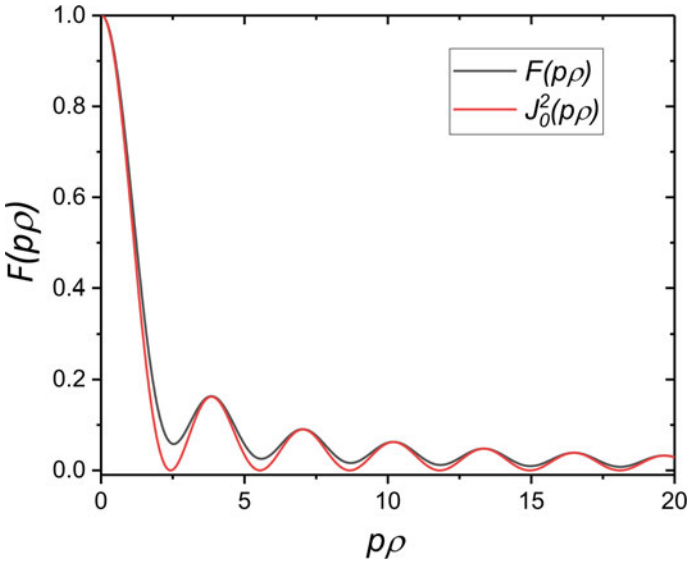

Fig. 2.6 A plot of the function $F(p\rho)$ (black line) for a silver interface. A plot of $J_0^2(p\rho)$ (red line), the first term in $F(p\rho)$, is also shown

In order to observe the behavior of this function, we choose a photon energy $E_{n0} = \hbar\omega$ corresponding to $\lambda = 500$ nm. For a silver interface, the dielectric constant corresponding to $\lambda = 500$ nm is $\varepsilon \approx -9$ [29].Under these conditions, $\varepsilon^2 \approx 81$ so that $F(p\rho)$ becomes

$$F(p\rho) = J_0^2(p\rho)(1+81) + \frac{2J_1^2(p\rho)}{p^2\rho^2}\left(1+9p^2\rho^2\right) - 2J_0(p\rho)\frac{J_1(p\rho)}{p\rho} \tag{2.79}$$

A plot of $F(p\rho)$, normalized to unity at $\rho = 0$, is given in Fig. 2.6. For comparison, also shown in Fig. 2.6 is the plot of $J_0^2(p\rho)$, the first term in $F(p\rho)$. A comparison of the two plots shows that the $J_0^2(p\rho)\epsilon^2$ is the dominant term in Eq. (2.80), with the other terms playing a minor role. In the visible region, the dielectric constant of silver ranges from $\varepsilon \approx -3$ at $\lambda = 400$ nm to $\varepsilon \approx -22$ at $\lambda = 700$ nm. Thus, at wavelengths longer than 500 nm, ε becomes more negative, and the first term in Eq. (2.80) becomes even more dominant. At shorter wavelengths, ε becomes less negative, and the first term Eq. (2.80) becomes less dominant.

2.3.5 *Estimating the Energy Transfer Rate*

To date, there is little definitive experimental evidence of plasmon-mediated energy transfer in the presence of a flat metallic layer. Perhaps the work that comes closest to definitive experimental evidence is the work by Andrew and Barnes [34], who studied the energy transfer from the donor molecule Alq to acceptor molecule R6G near a silver layer. Due to the dearth of data available on this topic, it is of interest to investigate under what circumstances plasmon-mediated transfer could be observed in an experiment. To explore this, we first estimate the transfer rate from a single donor and to a single acceptor.

We assume the following; the donor and acceptor distances from the metallic layer are $Z_D = 10\ nm$ and $Z_A = 20\ nm$; a silver layer; a plasmon wavelength of 550 nm, the acceptor absorption integrated intensity $Q(A) = 10^{-16}\ cm^2 eV$; the x-y distance between donor and acceptor, $\rho, = 0$; $\alpha_2 = 3.7\ \mu m^{-1}$, $F(p\rho)$=107; the overlap integral $\int f_A(E) F_B(E) dE = \frac{1}{3}\ eV^{-1}$. Finally, the distance parameter, L, is given by

$$L = \frac{\varepsilon}{2\alpha_1} + \frac{1}{4\alpha_2}\left[\frac{1-\varepsilon}{-\varepsilon}\frac{d\omega(\varepsilon)}{d\varepsilon} - 1 - \varepsilon\right] \approx 2.2\ \mu m \tag{2.80}$$

With the above assumptions, we see that

$$\Gamma_{sp}\tau_D \approx 10^{-6}\text{–}10^{-5} \tag{2.81}$$

Since $1/\tau_D$ is the radiative decay rate of the donor ion, Γ_D , the

$$\frac{\Gamma_{sp}}{\Gamma_D} \approx 10^{-6}\text{–}10^{-5} \ll 1 \tag{2.82}$$

Thus, we expect that the energy transfer from a donor to any single acceptor will not be able to compete with radiative decay.

Recent computational work on plasmon-mediated energy transfer shows that plasmon-mediated energy transfer can compete with the radiative decay when a large number of acceptors present. Compared with the Forster-Dexter type energy transfer, plasmon mediated energy transfer is a long-range interaction. Thus, any donor may interact with acceptors within a few hundred nanometers or more of the donor ion. Thus, for example, suppose one places a donor nearby to a silver layer, and slightly further from the layer is placed a volume of donors at reasonable doping levels (a few percent). Suppose also that absorption band of the acceptor, overlaps significantly with the emission band of the donor. Under such conditions, if the volume of the acceptor region is greater than or on the order of (0.005) μm^3, then the plasmon-mediated transfer can be on the order of the radiative decay, and so can easily be measured experimentally. Of course, increasing the acceptor region to larger volumes or higher dopant levels will cause the plasmon-mediated transfer to be the dominant decay process. Thus, we expect that the plasmon-mediated energy

transfer could be the dominant decay mechanism in a properly designed experiment, and so should be easily observable experimentally.

2.4 Conclusions

We have outlined the theory of energy transfer from a donor to an acceptor that is mediated by the surface plasmons on a nearby flat, metallic surface. As expected, the energy transfer rate reflects the symmetry of the situation; it is isotropic in the plane of the interface, and exponentially decreases as one moves away from the interface, similar to the behavior of the plasmon fields. The dependence of the transfer rate on the donor-acceptor distance as projected on the plane of the metallic layer is a complicated function that shows and relatively strong distance-dependence for the first few hundred nanometers followed by oscillations that continue over very long distances (micrometers). Over short distances, plasmon mediated transfer much less probable than the typical Dexter-type transfer. However, it is more prominent in the long range, and it is straightforward to create systems where the plasmon-mediated energy transfer becomes the dominant decay mechanism of the donor.

References

1. Chao W-H, Wu R-J, Tsai C-S, Wu T-B (2010) J. Appl. Phys. 107:013101
2. Lee SM, Choi KC (2010) Opt. Express 18:12144
3. Cohen-Hoshen E, Bryant GW, Pinkas I, Sperling J, Bar-Joseph I (2012) Nano Lett. 12:4260
4. Munechika K, Chen Y, Tillack AF, Kulkarni AP, Jen-La Plante I, Munro AM, Ginger DS (2011) Nano Lett. 11:2725
5. Mertens H, Biteen JS, Atwater HA, Polman A (2006) Nano Lett. 6:2623
6. Gopinath A, Boriskina SV, Yerci S, Li R, Dal Negro L (2010) Appl. Phys, Lett. 96:071113
7. Jang C, Lee SM, Choi KC (2012) Opt. Express 20:2143
8. Mertens H, Polman A (2006) Appl. Phys. Lett. 89:211107
9. Xu L, Qiang Y, Xiao K, Zhang Y, Xie J, Cui C, Lin P, Wang P, Yu X, Wu F, Yang D (2017) Appl. Phys. Lett. 110:233113
10. Ye W, Huang Q, Jiao X, Liu X, Hu G (2017) J. Alloy. Compd. 719:159
11. Muskens OL, Gómez-Rivas J (2008) Mater. Sci. Eng. B 149:216
12. Nikitin A, Remezani M, Gómez-Rivas J (2016) ECS J. Solid State Sci. Technol. 5:R3164
13. Kwon M-K, Kim J-Y, Kim B-H, Park I-K, Cho C-Y, Byeon CC, Park S-J (2008) Adv. Mater. 20:1253
14. Okamoto K, Niki I, Shvartser A, Maltezos G, Narukawa Y, Mukai T, Kawakami Y, Scherer A (2007) Phys. Stat. Sol. A 204:2103
15. Okamoto K, Niki I, Shvartser A, Narukawa Y, Mukai T, Scherer A (2004) Nat. Mater. 3:601
16. Vučković J, Lončar M, Scherer A (2000) IEEE J. Quantum Electron. 36:1131
17. Henson J, DiMaria J, Dimakis E, Moustakas TD, Paiella R (2012) Opt. Lett. 37:79
18. Henson J, Heckel JC, Dimakis E, Abell J, Bhattacharyya A, Chumanov G, Moustakas TD, Paiella R (2009) Appl. Phys. Lett. 95:151109
19. Gontijo I, Boroditsky M, Yablonovitch E, Keller S, Mishra UK, DenBaars SP (1999) Phys. Rev. B 60:11564

20. Hecker NE, Höpfel RA, Sawaki N (1998) Physica E 2:98
21. Neogi A, Lee C-W, Everitt HO, Kuroda T, Tackeuchi A, Yablonovitch E (2002) Phys. Rev. B 66:153305
22. Lozano G, Rodriguez SRK, Verschuuren MA, Rivas JG (2016) Light Sci. Appl. 5:e16080
23. Drexhage KH (1970) Luminescence 1(2):693
24. Drexhage KH (1974) In: Wolf E (ed) "Interaction of Light with Monomolecular Dye Layers", Progress in Optics. North Holland Press
25. Ford GW, Weber WH (1984) Physics Reports 113(4):195–287
26. Mishra KC, Collins J, Piquette A (2018) ECS J. Solid State Sci. Technol. 7(5):R42
27. Purcell EM (1946) Phys. Rev. 69:681
28. Collins J, Mishra K (2019) ECS Journal of Solid State Science and Technology 9:016002
29. Yang H, D'Archangel J, Sundheimer M, Tucker E, Boreman G, Raschke M (2015) Phys. Rev. B 91:253157
30. Dexter DL (1953) J Chem. Phys. 21:836
31. Andrews DA, Bradshaw DS (2004) Eur. J. Phys. 25:845–858. https://doi.org/10.1088/0143-0807/25/6/017
32. Mishra KC, Collins J (2019) ECS Journal of Solid State Science and Technology 8B(2):R27–R35. https://doi.org/10.1149/2.0121902jss
33. Archambault A, Marquier F, Greffet J-J, Arnold C (2010) Phys. Rev B 82:035411–035591
34. Andrew P, Barnes WL (2004) Science 306:1002–1004

Chapter 3
Workshop in Computational Nanophotonics

Antonio Calà Lesina and Lora Ramunno

Abstract This chapter summarizes the "Workshop in Computational Nanophotonics" presented in 2019 at the NATO Advanced Study Institute on "Light-Matter Interactions Towards the Nanoscale" in Erice, Italy. The workshop began with a pedagogical introduction to the fundamentals of the FDTD method as applied to nanophotonics simulations, and proceeded to describing nonlinear nanophotonics simulations via both nonlinear scattering theory and direct nonlinear FDTD simulations. The lectures included an active component wherein participants applied their knowledge to three in-class labs using commercial FDTD software, thanks to licenses provided by Lumerical Solutions. The topics of the three labs were: (1) scattering from a gold nanosphere; (2) transmittance through a silver gap nanoantenna array; and (3) third harmonic generation from a hybrid plasmonic/dielectric metasurface. We describe these labs in detail.

A. Calà Lesina (✉)
Department of Physics and Centre for Research in Photonics, University of Ottawa, Ottawa, ON, Canada

School of Electrical Engineering and Computer Science, University of Ottawa, Ottawa, ON, Canada

A. C. Lesina (✉)
Faculty of Mechanical Engineering (Institut für Transport- und Automatisierungstechnik), Hannover Centre for Optical Technologies, and Cluster of Excellence PhoenixD, Leibniz Universität Hannover, Hannover, Germany
e-mail: antonio.calalesina@hot.uni-hannover.de

L. Ramunno (✉)
Department of Physics and Centre for Research in Photonics, University of Ottawa, Ottawa, ON, Canada
e-mail: lora.ramunno@uottawa.ca

M. Cesaria et al. (eds.), *Light-Matter Interactions Towards the Nanoscale*,
NATO Science for Peace and Security Series B: Physics and Biophysics,
https://doi.org/10.1007/978-94-024-2138-5_3

3.1 Introduction

Computational science can be considered a "third pillar" of science alongside theory and experiment. In nanophotonics, there are only a handful of problems for which analytical solutions exist. Thus simulations play a critical role both in facilitating and understanding underlying physical mechanisms, as well as acting as a stand-in for experiments, especially for device design. Indeed, many advances in nanoscience and nanofabrication would not be possible without the development of sophisticated simulation tools. Computational electromagnetics methods [1], which were originally developed for radio- and microwave simulations, have been adapted to the optical regime, and are used widely in nanophotonics. Computational nanophotonics identifies the set of computer-aided techniques for the simulation of light-matter interaction at the nanoscale [2] with the finite-difference time-domain (FDTD) method [3–5] the most popular. FDTD is relatively easy to implement while having very broad applicability. Indeed, it is capable of simulating light interaction with materials possessing complex properties and/or geometries (see, e.g., our recent work in Refs. [6–8]). Being a time-domain method, FDTD naturally allows the generation of movies, providing a unique tool to access and visualize physical processes at the nanoscale. As FDTD is well-suited to parallelization via domain decomposition, it can run in parallel on massive supercomputers with nearly linear scalability [9], allowing the simulation of optically large devices and mitigating limitations imposed by the strict requirements regarding grid cell size and time step.

This chapter is based upon the "Workshop in Computational Nanophotonics", presented in 2019 at the NATO Advanced Study Institute on "Light-Matter Interactions Towards the Nanoscale" in Erice, Italy. The lectures focussed on the FDTD method as applied to nanophotonics, and began with a pedagogical introduction to the basics of the Yee algorithm, including the discretization of Maxwell's equations via central differencing, and the resultant numerical dispersion and stability criteria. Beyond the basics, the other "ingredients" needed for an FDTD simulation were also discussed, including: sources of light, material models, boundary conditions, and time- and frequency-domain monitors for the efficient collection of data. Further, advanced topics such as meshing strategies and high-performance computing [9] were also highlighted in lecture. These topics are not presented here, as they can be found elsewhere [4, 5, 10].

We present here a detailed discussion of the three in-class labs that comprised the active component of the workshop. Participants applied the knowledge they gained in the introductory lectures by performing the following three exercises:

Lab I calculate the scattering, absorption and extinction coefficients for a spherical gold nanoparticle, comparing simulation results with Mie theory in order to validate the software and explore computational parameters such as grid cell size;

Lab II calculate the transmittance of an array of plasmonic gap nanoantennas on a substrate, as a practical example of how one might use such simulations for metasurface device design; and

Lab III determine the nonlinear generation efficiency for a hybrid metal/dielectric metasurface, as a demonstration of how to perform nonlinear FDTD simulations, and how these differ from linear simulations.

Participants first had the task of determining which "ingredients" were needed for the three simulations. These were then implemented using Lumerical Solutions FDTD software (www.lumerical.com), for which each participant received a temporary licence, generously provided by Lumerical. The ingredients and specific set-up for these three labs are described in detail in Sects. 3.2–3.4, respectively, where the ingredients needed to progress from Lab I to Lab II, and from Lab II to Lab III, are highlighted.

Finally, in Sect. 3.5, we describe not only how to implement nonlinear optical processes directly within FDTD (as in Lab III), but, as a complement, we also describe an alternate method of obtaining nonlinear generation efficiencies based on the postprocessing of two or more linear simulations via nonlinear scattering theory [11].

3.2 Lab I: Scattering from a Gold Nanosphere

The first lab consists of calculating the scattering, absorption and extinction coefficients (also referred to as efficiencies) as a function of wavelength for a gold nanosphere of radius 60 nm. This example is chosen to highlight that when one starts using a new numerical/computational technique, it is highly advisable to assess the quality of the simulation by comparing the computed results against an analytical solution. Here such a solution exists, the so-called "Mie theory" that presents a rigorous solution of Maxwell's equations for the interaction of a plane wave with a sphere in a homogeneous medium [12, 13]. Though over a century old, this theory is still of prime importance in nanophotonics, including, for example, recent interest in multipole decomposition for applications in linear and nonlinear metasurfaces [14, 15].

In order to build the simulation illustrated in Fig. 3.1, here are step-by-step instructions. For convenience, the units have been set to nm (Settings → Length units → nm).

1. **Check the material models** that are implemented for gold, to be sure that the experimental data and its fitting are as expected. First, select the dispersive model for the linear susceptibility of gold (Check → Material Explorer), e.g., as obtained from Johnson and Christie data. Then, click "fit and plot" to see the data that is used, as well as the fit to the data that will be implemented in the simulation. Adjust the fit as necessary for your requirements. We consider vacuum as the background material (this is the default setting: Edit FDTD simulation → background material index set to 1).
2. **Insert the object**, which is a gold sphere with radius 60 nm (Structures → Sphere). Assign to it the material identified in the previous step.
3. **Insert the FDTD simulation domain** (Simulation → Region) and adjust its parameters. We set its size large enough to contain the object as well as the near

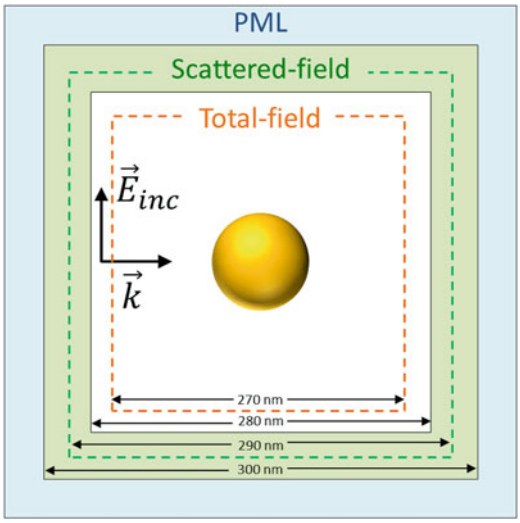

Fig. 3.1 Lab I: Schematic of the simulation setup comprising a gold nanosphere in a simulation domain that includes PML boundaries and TF/SF regions

fields around the object. We force a uniform mesh in order to see more clearly the effect of step size on accuracy, though Lumerical's other mesh settings can also be used and would likely lead to more efficient calculations. Finally, as we would like to simulate the scattered fields going to infinity, we surround the simulation domain with absorbing boundary conditions on all sides. The instructions are:

(a) *Geometry tab:* insert a 300 nm FDTD domain box to contain the sphere (see Fig. 3.1). Note that the simulation will ignore anything placed outside of this domain.
(b) *Mesh settings tab:* choose the mesh type as staircase, and the space-step as $\Delta x = 5$ nm for initial quick simulations; this can be decreased later for higher accuracy. Note the "dt stability factor" satisfying the stability condition, i.e., $c\Delta t = 0.99\Delta x/\sqrt{3}$, where c is the speed of light, and Δt is the time-step.
(c) *Boundary conditions tab:* insert perfectly matched layer (PML) absorbing boundary conditions on all sides.

4. **Insert the source**, which we choose to be a total-field/scattered-field (TF/SF) plane wave source (Sources → Total-field/Scattered-field). This will create a "total-field" region within the simulation domain that contains the incoming plane wave and all the scattered fields, and a "scattered-field" region between the total-field region and the PML boundary, where the incoming plane wave is removed and thus contains only scattered fields. The separation into these two regions prevents the incoming plane wave from touching the boundaries, enabling the employment of PML boundary conditions. It also makes convenient the calculation of the scattering, absorption and extinction coefficients, as we will see. We choose a broadband pulse in time, which allows us to obtain frequency domain information over a large frequency range in a single time-

domain run. The software determines the pulse shape automatically, but shape does not affect the frequency domain results of a linear simulation, as it is effectively divided out. The instructions are:

(a) *Geometry tab:* insert a 280 nm box inside the simulation domain for the TF/SF boundary (see Fig. 3.1). Note that this must be smaller than the simulation domain.
(b) *General tab:* set polarization and direction of propagation of the incident plane wave. Note that the value of the amplitude does not matter for linear simulations, and can be set to 1.
(c) *Frequency/Wavelength tab:* set wavelength range from 400 to 1000 nm to run a broadband simulation.

5. **Insert a refractive index monitor** (Monitors → Refractive index) so that the actual simulated object may be examined after the simulation is run. This will clearly show, for example, the staircasing effect on the sphere.
6. **Insert a time-domain monitor** (Monitors → Movie) in a 2D plane to generate a movie of the simulation.
7. **Insert frequency-domain monitors** (Monitors → Frequency-domain field and power) in 2D planes to visualize the frequency-domain fields at different wavelengths of interest, to be chosen here in advance. These frequency-domain electric field distributions are obtained with a discrete Fourier transform (DFT)

$$\vec{E}(\vec{r},\omega) = \sum_{n=0}^{N_{steps}} \vec{E}(\vec{r}, n\Delta t) e^{-i\omega n\Delta t}\,\Delta t, \tag{3.1}$$

where N_{steps} is the total number of time steps and ω the frequency of interest. At each spatial position in the monitor, and for each frequency of interest, this is calculated "on the fly" as the code runs via

$$\vec{E}(\vec{r},\omega) \mathrel{+}= \vec{E}(\vec{r}, n\Delta t) e^{-i\omega n\Delta t}\,\Delta t. \tag{3.2}$$

At the end of the simulation, the DFTs are normalized with respect to the DFT of the incident plane wave. This explains why the amplitude and shape of the incident field do not matter in a linear simulation.
8. **Insert power monitors** in the total-field and scattered-field regions to calculate the absorption and scattered coefficients, respectively. (Object library → Analysis → Optical power → Cross sections). This is done internally by integrating the outgoing Poynting vector over closed boxes in the total-field and scattered-field regions. As we indicate in Fig. 3.1, 270 nm and 290 nm boxes are chosen, respectively.
9. **Check simulation setup and run** (Check → Check simulation and memory requirements, and then click Run).
10. **Inspect simulations results** by examining the structure, movie and DFT near fields via the monitors, to visualize if there were any obvious problems with the simulation.

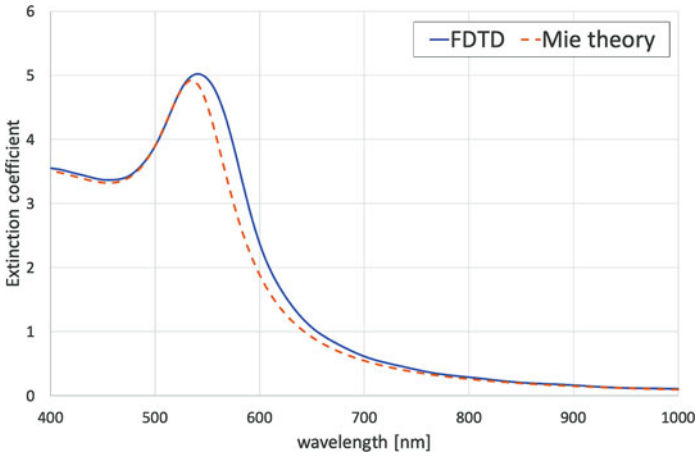

Fig. 3.2 Lab I: Extinction coefficient of a 60 nm radius gold nanosphere versus wavelength calculated via FDTD and Mie theory for a step size of 5 nm

11. **Compare results to Mie Theory.** Calculate the extinction, scattering and absorption coefficients via the power monitor data (see formulas described in Ref. [9]) and compare with Mie theory. A script file for this is available on the Lumerical website (see "Mie scattering (FDTD)" (www.lumerical.com)).

The extinction coefficient for the simulation as detailed above is plotted versus wavelength in Fig. 3.2. One can clearly see that 5 nm is not a sufficiently small step size; in fact, for uniform staircasing a much smaller step size is required (below 1 nm for less than 2% error [16]). After this first simulation is completed and verified, one can alter the mesh size and mesh type, material fitting, and simulation domain size to get the desired accuracy in the minimum compute time. To get a feel for the underlying physics, one can then run additional simulations, for example, changing the size of the sphere to understand when scattering dominates, and when absorption dominates, changing the background index from vacuum to see its effect on resonance, changing the material of the sphere, choosing other metals or dielectrics, and changing the shape.

3.3 Lab II: Transmittance from a Plasmonic Metasurface

The second lab consists of calculating the transmittance of a plasmonic metasurface. In the last decade, the interest in metasurfaces has grown exponentially as they offer a platform for realizing flat optical components [17, 18], including with tunable optical properties [19]. Lab II introduces the foundations for the simulation of metasurfaces. In particular, it demonstrates how to find the resonance frequency of

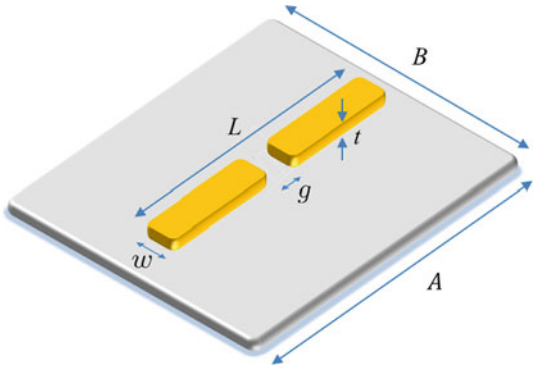

Fig. 3.3 Lab II: Schematic of the nanostructure to simulate, consisting of a Ag nanoantenna containing a gap between two branches ($L = 400\,\text{nm}$, $g = 20\,\text{nm}$, $t = 40\,\text{nm}$, $w = 40\,\text{nm}$) on a SiO_2 substrate; above the metasurface is vacuum. The unit cell dimensions are $A = 600\,\text{nm}$ and $B = 300\,\text{nm}$

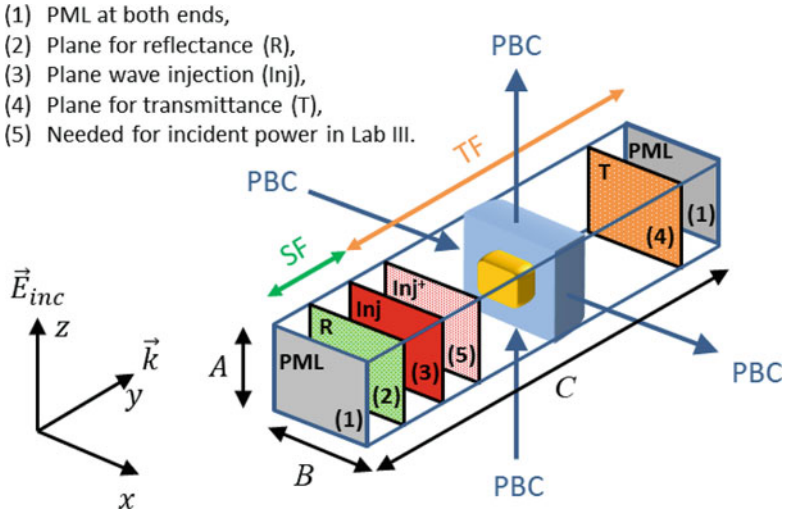

Fig. 3.4 Lab II: Generic schematic of a unit cell of a metasurface. Note that for the simulation of Lab II, the nanoantenna depicted in the centre would be replaced by that detailed in Fig. 3.3

a nanostructure within a unit cell (meta-atom) of an array; this frequency generally corresponds to the frequency of operation of the metasurface.

In Fig. 3.3, we show a schematic drawing of the unit cell of the metasurface we consider for Lab II, consisting of a silver dipole (gap) nanoantenna on a glass substrate. The actual device to be simulated is an array of such meta-atoms with lattice spacing A and B. The size C is such that the R and T planes are in the far-field of the meta-atom. To simulate this metasurface under plane wave excitation, we only need to simulate one unit cell of the array and apply periodic boundary

conditions; overview of how to simulate a unit cell is illustrated in Fig. 3.4. This is a different setup than for Lab I, where we were interested in the optical response of a single nanoparticle. We now detail how to build the simulation by describing the differing and/or extra steps with respect to the setup of Lab I:

1. **Insert the object**. Using the pre-defined structures contained within Lumerical, build the meta-atom composed of two silver nanoantenna branches on a glass substrate, as described in the caption of Fig. 3.3. A linear susceptibility for Ag (e.g., Palik, 0–2 μm) and SiO_2 need to be selected, for the branches and substrate, respectively.
2. **Insert the FDTD simulation domain** with size $A = 600\,\text{nm}$ along z, $B = 300\,\text{nm}$ along x, and $C = 600\,\text{nm}$ along y. Apply periodic boundary conditions (PBCs) to the unit cell along the x and z directions, and apply PML boundary conditions along the y direction, as in Fig. 3.4.
3. **Insert the source**, which in this case is a plane wave (Sources → Plane wave). We do not need the TF/SF source, which operates over the six faces of the simulation domain box, as the PBCs are compatible with plane wave propagation; note that a TF/SF boundary at the plane wave source injection plane is automatically applied by Lumerical. We inject the plane wave at a plane in front of the meta-atom (i.e., incident from vacuum; see plane (3) in Fig. 3.4). The instructions are:
   (a) *Geometry tab:* the location of the plane wave injection separates scattered-field and total-field regions, as illustrated in Fig. 3.4. Set this plane at 40 nm from the edge of the simulation domain along y.
   (b) *General tab:* set the plane wave to be polarized in z, so that it is aligned with the axis of the dipole nanoantenna, and to propagate along y.
   (c) *Frequency/Wavelength tab:* set the wavelength range from 600 to 1600 nm for broadband analysis.
4. **Insert power monitors** in the frequency domain to obtain the transmittance and reflectance (Monitors → Frequency-domain field and power). The transmittance is calculated from a power monitor inserted in the total-field region of the substrate, behind the metasurface (see plane (4) in Fig. 3.4); Lumerical's "T" function automatically calculates the transmittance from the data collected by this transmittance monitor. The reflectance is calculated from a power monitor inserted in the scattered-field region in vacuum, in front of the metasurface (see plane (2) in Fig. 3.4). Note that Lumerical always calculates the Poynting vector as the energy flux flowing *into* the simulation domain. Thus, to obtain the reflectance, we need to reverse the sign of "T" from the reflectance monitor.

We plot in Fig. 3.5 the transmittance and reflectance versus wavelength, and from inspection we can see the transmittance exhibits a minimum (and the reflectance a maximum) at $\lambda_{res} \sim 1050\,\text{nm}$, which gives an indication of the resonance frequency of the nanostructure array. It is also instructive to examine the near fields in the DFT monitors, particularly within the gap, to see how they change for frequencies close to and away from the resonance frequency. One can perform follow-up simulations

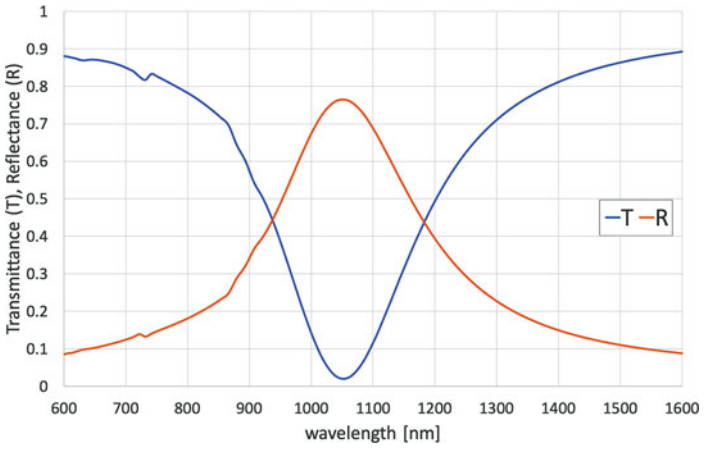

Fig. 3.5 Lab II: Transmittance and reflectance for the simulation of Lab II

to determine how the fields and resonance condition changes for different materials, different nanostructure geometries, and different array periodicities, and to optimize the structure for a desired resonance wavelength and other attributes of interest.

3.4 Lab III: Nonlinear Efficiency of Hybrid Metasurfaces

Nonlinear metasurfaces allow us to perform nonlinear optics over nanometric thicknesses, thus avoiding cumbersome phase matching requirements. The nonlinear generation can be boosted at the nanoscale by exploiting the linear field enhancement due to resonances in metallic and dielectric nanostructures [20]. Furthermore, these resonances can be used to control the phase, amplitude and polarization of nonlinear emission [21, 22]. Numerical tools for simulating nonlinear processes are not nearly as established as for the linear regime, and particular care is required during the setup of a nonlinear simulation, even (and perhaps especially) in commercial software.

In the simulation exercise of Lab III, we use a direct nonlinear simulation approach (described in more detail in Sect. 3.5) to calculate the third harmonic generation (THG) from a nonlinear material placed in the gap of the nanoantenna introduced in Lab II, as shown in Fig. 3.6. Our goal is to calculate the nonlinear efficiency of the metasurface. We begin with the Lab II simulation file, needing to perform the following additional steps to achieve the nonlinear simulation:

1. **Create a nonlinear material** (Materials → add → Chi3/Chi2). We assume the material has an instantaneous, isotropic third order susceptibility and choose $\chi^{(3)} = 1 \cdot 10^{-18}$ m^2/V^2, which has a value similar to that of, e.g., ITO. Note that leaving $\chi^{(1)} = 0$ implies we are choosing a linear refractive index of

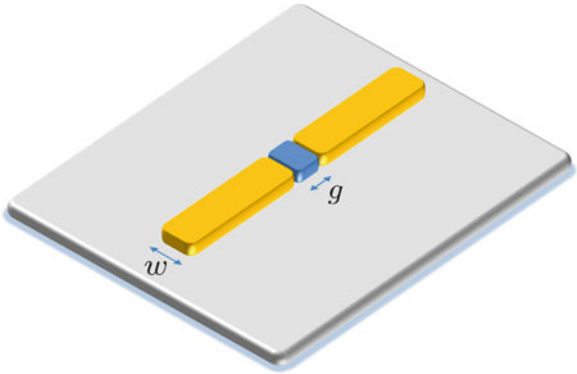

Fig. 3.6 Lab III: Schematic of the hybrid nanostructure to simulate, a gap nanoantenna with a nonlinear material within the gap

1 for this material. We do this here for convenience only, so that the linear resonance wavelength of the gap nanoantenna analysed in Lab II does not change ($\lambda_{res} = 1050\,\text{nm}$). However, this is not realistic, and can be changed later.

2. **Insert a nonlinear element in the gap** of the silver nanoantenna (Structures → Rectangle), and choose its material to be that created in step 1.
3. **Remove CW normalization** (Setting → Normalization state → No normalization). Because this is a nonlinear simulation, it is nonsensical to normalize all simulation data with respect to the Fourier transform of the exciting signal. However, the units of the electric field in frequency domain are not V/m, but rather Vs/m. This translates to all other data, including powers and Poynting vectors.
4. **Update simulation domain**. We cannot use an arbitrary broadband pulse for nonlinear simulations, as the actual amplitude of each frequency component matters. There are two approaches we can take. Either we need to use the actual pulse we would use in an experiment, or we need to use a narrowband pulse which is effectively CW (and thus requires a much longer simulation time). Here, we do the latter. The instructions are:

   (a) *General tab:* change simulation time to 3000 fs.
   (b) *Mesh settings tab:* decrease mesh accuracy to 3 to reduce simulation time. This can be changed later to a higher number.
   (c) *Advanced options tab → set simulation bandwidth:* choose min = 300 nm, max = 1200 nm, as we need a spectral range that includes the wavelength of the nonlinear signal at 350 nm.

5. **Update the plane wave source** to be narrowband, centred at the resonant wavelength $\lambda_{res} = 1050\,\text{nm}$, and with an amplitude that is realistic. This ensures that the fields at 3ω (350 nm) are due to the nonlinear generation process, rather than to the presence of spectral components at 3ω in the input signal. The instructions are:

   (a) *General tab:* set amplitude to $1 \cdot 10^7$ V/m.

(b) *Frequency/Wavelength tab:* click "set time domain", then set frequency = 285.517 THz, pulse length = 500 nm, offset = 1500 nm. Unclick "optimize for short pulse".

6. **Update global monitor settings**. We want to make sure we collect data at both 350 nm (third harmonic) and 1050 nm (pump), so we need to change the global monitor settings in one of the monitors. This change will automatically apply to all monitors.
7. **Insert a new power monitor** right after the plane wave source (see plane (5), i.e., Inj^+, in Fig. 3.4). This is necessary as a consequence of the non-normalized units discussed in step 3. This monitor allows us to calculate the incident power (in those units) at the pump wavelength of 1050 nm, so that we can correctly calculate the nonlinear conversion efficiency. The incident power $P_{inc}(\omega)$ (in those units) is obtained by calculating the power flow through the $Inj^+(\omega)$ plane, and by adding to it what was lost due to reflection, which we obtain from the reflectance monitor, i.e., $R(\omega)$.
8. **Calculate conversion efficiency**. To get the outgoing power at 3ω, we need its forward signal (transmittance $T(3\omega)$), plus its backward signal (reflectance $R(3\omega)$). The conversion efficiency is then calculated via

$$\eta_{THG} = \frac{T(3\omega) + R(3\omega)}{P_{inc}(\omega)}, \tag{3.3}$$

giving a value, for this simulation setup, of $\eta_{THG} = 8.5 \cdot 10^{-6}$.

It is instructive to examine the near and far field distributions at the pump and nonlinear wavelengths, and investigate increasing the incoming field strength to see the change in efficiency and the effect on convergence. Further exercises could include changing the gap material properties to see the effect on nonlinear generation, and the linear permittivity; the latter would change the linear resonance frequency, so Lab II would need to be repeated to identify the dip in the transmission curve for the new structure. Finally, one could try performing this calculation using the nonlinear scattering theory described in the next section, by running two linear simulations rather than one nonlinear simulation.

3.5 Nonlinear Simulations Methods

We summarize in this section two different strategies for simulating perturbative nonlinear optical processes: (i) nonlinear scattering theory, that is based on post-processing the results of two or more linear simulations [23, 24], and (ii) the direct calculation of the nonlinear generation within FDTD [7, 25] which was used "under the hood" in Lab III.

Nonlinear scattering theory is derived from the Lorentz reciprocity theorem [11] that relates the electric field $\vec{E}_1$ resulting from one current source $\vec{J}_1$, to the

electric field $\vec{E}_2$ resulting from a second current source $\vec{J}_2$, for the same physical system via

$$\iiint \vec{J}_2(\vec{r},\omega)\cdot\vec{E}_1(\vec{r},\omega)dV = \iiint \vec{J}_1(\vec{r}',\omega)\cdot\vec{E}_2(\vec{r}',\omega)dV'. \tag{3.4}$$

While reciprocity does not hold in general for nonlinear optical processes, we may calculate the generation of nonlinear optical fields by applying Eq. (3.4) only to the nonlinear frequency of interest, ω_{NL}, under the undepleted pump approximation. For an undepleted pump, it is straightforward to obtain the nonlinear polarization at ω_{NL} within the nonlinear material, $\vec{P}_{NL}(\vec{r},\omega_{NL})$, from a linear simulation of the input field(s). Setting our first current source as $\vec{J}_1(\vec{r},\omega_{NL}) = i\omega_{NL}\vec{P}_{NL}(\vec{r},\omega_{NL})$, the electric field $\vec{E}_1(\vec{r},\omega_{NL})$ generated from this nonlinear polarization is the field we seek.

To calculate nonlinear generation efficiency, we need $\vec{E}_1$ at some point in the far field, say at the location of a distant detector, $\vec{r}_{detector}$; this is illustrated in the upper half of Fig. 3.7. If we set $\vec{J}_2$ to be a dipole current at $\vec{r}_{detector}$ oscillating at ω_{NL}, then it will contain a delta function that will pull out $\vec{E}_1(\vec{r}_{detector},\omega_{NL})$ from the integral on the left hand side of Eq. (3.4), which is exactly the field required.

To complete the theory, we need to obtain the field generated by $\vec{J}_2$, that is, $\vec{E}_2(\vec{r},\omega_{NL})$, for $\vec{r}$ within the nonlinear material (i.e., the volume that contains $\vec{J}_1$). As we purposely set $\vec{r}_{detector}$ far from the nanostructure, the field radiated by $\vec{J}_2$ will be effectively a plane wave by the time it reaches the nanostructure; this is illustrated in the lower half of Fig. 3.7. Thus, $\vec{E}_2(\vec{r},\omega_{NL})$ can be found from calculating—via a linear simulation—the field within the nanostructure upon plane wave excitation at ω_{NL}.

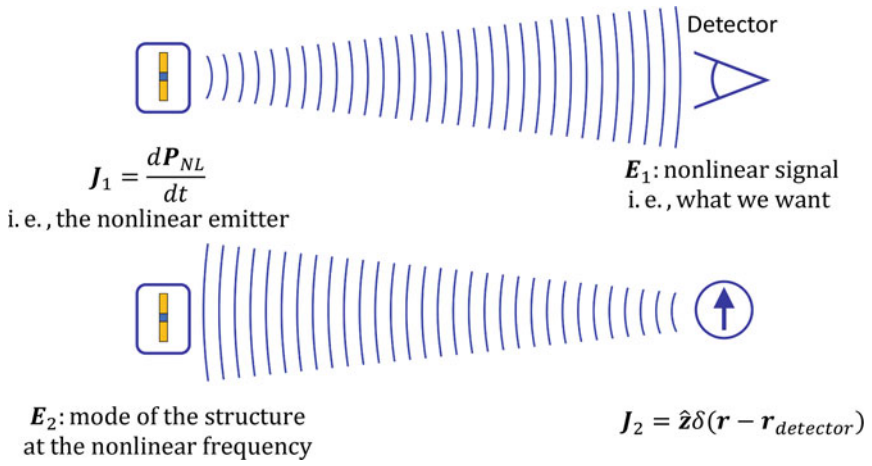

Fig. 3.7 Illustration of the nonlinear scattering theory by using the Lorentz reciprocity theorem

With these considerations, Eq. (3.4) becomes

$$\vec{E}_1(\vec{r}_{detector}, \omega_{NL}) = \iiint i\omega \vec{P}_{NL}(\vec{r}', \omega_{NL}) \cdot \vec{E}_2(\vec{r}', \omega_{NL}) dV'. \tag{3.5}$$

As an example, this approach was used to calculate the second harmonic generation from a gold split ring resonator in [24], and in that case, Eq. (3.5) becomes:

$$E_{nl}(2\omega) \propto \iint \chi_{nnn} E_n^2(\omega) \cdot E_n(2\omega) dS, \tag{3.6}$$

where $E_{nl}(2\omega)$ is the desired nonlinear emission, χ_{nnn} is the dominant second order surface nonlinear susceptibility component, and $E_n(\omega)$ and $E_n(2\omega)$ are the field distributions of the fundamental mode and the mode at the second harmonic frequency, respectively, as obtained via linear simulations.

Direct nonlinear simulation within FDTD requires the derivation of a time-domain update equation via the discretization of the Ampère-Maxwell equation with a nonlinear polarization $\vec{P}_{NL}$,

$$\epsilon_0 \frac{\partial \vec{E}}{\partial t} = \nabla \times \vec{H} - \frac{\partial \vec{P}_L}{\partial t} - \frac{\partial \vec{P}_{NL}}{\partial t}. \tag{3.7}$$

The linear polarization, $\vec{P}_L$, is commonly updated by solving an auxiliary differential equation. As an example, consider a linear dispersive material with a Lorentz susceptibility given by

$$\chi^{(1)}(\omega) = \frac{\omega_0^2}{\omega_0^2 - i\omega\gamma - \omega^2}, \tag{3.8}$$

where ω_0 is the resonance frequency, and γ a damping coefficient. In this case, the linear polarization $\vec{P}_L = \epsilon_0 \chi^{(1)}(\omega) \vec{E}$ is updated in the time-domain via

$$\frac{\partial^2 \vec{P}_L}{\partial t^2} + \gamma \frac{\partial \vec{P}_L}{\partial t} + \omega_0^2 \vec{P}_L = \omega_0^2 \epsilon_0 \vec{E}. \tag{3.9}$$

The nonlinear polarization is often assumed to be given by an instantaneous nonlinear process in the perturbative nonlinear regime. In this case, one can write

$$\vec{P}_{NL}(t) = \epsilon_0 \chi^{(2)} \vec{E}^2(t) + \epsilon_0 \chi^{(3)} \vec{E}^3(t) + \ldots, \tag{3.10}$$

where in general the nonlinear susceptibilities $\chi^{(n)}$ of order n are tensorial. This is already a time domain equation, and one may use it directly to update $\vec{P}_{NL}$, where iteration is often required to solve an implicit updating equation [4]. An explicit updating equation for $\vec{P} = \vec{P}_L + \vec{P}_{NL}$, which takes into account both linear

and nonlinear contributions, is given by the nonlinear generalization of the Lorentz dispersion model of Eq. (3.9):

$$\frac{\partial^2 \vec{P}}{\partial t^2} + \gamma \frac{\partial \vec{P}}{\partial t} + \omega_0^2 \vec{P} = \omega_0^2 \epsilon_0 \left(\chi^{(1)} \vec{E} + \chi^{(2)} \vec{E}^2 + \chi^{(3)} \vec{E}^3 + \dots \right), \tag{3.11}$$

where this expression has been derived from the quantum mechanical two-level atom model in the under-resonant, adiabatic-following, and weak-field limit [25].

3.6 Conclusions

We presented a detailed overview of the in-class labs presented at the "Workshop in Computational Nanophotonics" presented in 2019 at the NATO Advanced Study Institute on "Light-Matter Interactions Towards the Nanoscale" in Erice, Italy.

Acknowledgments We would like to thank Lumerical Solutions Inc. for providing to each participant a temporary license for their software, NATO for their financial support, and the Ettore Majorana Foundation and Centre for Scientific Culture for their logistical support during the NATO Advanced Study Institute on "Light-Matter Interactions Towards the Nanoscale". Lora Ramunno would like to acknowledge Baldassare Di Bartolo, John Collins, Sergey Gaponenko, Maura Cesaria, and Antonio Calà Lesina, for their tireless work in making this school come together, thank you.

References

1. Rylander, T., Ingelström, P., Bondeson, A.: Computational Electromagnetics. Springer, New York (2013)
2. Gallinet, B., Butet, J., Martin, O.J.F.: Numerical methods for nanophotonics: standard problems and future challenges. Laser Photonics Rev. **9**(6), 577–603 (2015)
3. Yee, K.: Numerical solution of initial boundary value problems involving Maxwell's equations in isotropic media. IEEE Trans. Antennas Propag. **14**(3), 302–307 (1966)
4. Taflove, A., Hagness, S.C.: Computational Electrodynamics: The Finite-Difference Time-Domain Method, 3rd edn. Artech House, Norwood (2005)
5. Taflove, A., Johnson, S.G., Oskooi, A.: Advances in FDTD Computational Electrodynamics: Photonics and Nanotechnology. Artech House, Norwood (2013)
6. Guay, J.M., Calà Lesina, A., Baxter, J., Killaire, G., Ramunno, L., Berini, P., Weck, A.: Topography tuning for plasmonic color enhancement via picosecond laser bursts. Adv. Opt. Mater. **6**(17), 1800189 (2018)
7. Calà Lesina, A., Berini, P., Ramunno, L.: Origin of third harmonic generation in plasmonic nanoantennas. Opt. Mater. Express **7**(5), 1575 (2017)
8. Butt, M.A., Calà Lesina, A., Neugebauer, M., Bauer, T., Ramunno, L., Vaccari, A., Berini, P., Petrov, Y., Danilov, D., Manshina, A., Banzer, P., Leuchs, G.: Investigating the optical properties of a laser induced 3D self-assembled carbon–metal hybrid structure. Small **15**(18), 1900512 (2019)

9. Calà Lesina, A., Vaccari, A., Berini, P., Ramunno, L.: On the convergence and accuracy of the FDTD method for nanoplasmonics. Opt. Express **23**(8), 10481 (2015)
10. Calà Lesina, A., Baxter, J., Berini, P., Ramunno, L.: Quantum nano-photonics. In: Simulations in Nanophotonics, pp. 117–131. Springer, Netherlands (2018)
11. Roke, S., Bonn, M., Petukhov, A.V.: Nonlinear optical scattering: the concept of effective susceptibility. Phys. Rev. B **70**(11), 115106 (2004)
12. Mie, G.: Beiträge zur Optik trüber Medien, speziell kolloidaler Metallösungen. Ann. Phys. **330**(3), 377–445 (1908)
13. Stratton, J.A.: Electromagnetic Theory. John Wiley & Sons, Inc., Hoboken (2015)
14. Decker, M., Staude, I., Falkner, M., Dominguez, J., Neshev, D.N., Brener, I., Pertsch, T., Kivshar, Y.S.: High-efficiency dielectric Huygens' Surfaces. Adv. Opt. Mater. **3**(6), 813–820 (2015)
15. Smirnova, D., Kivshar, Y.S.: Multipolar nonlinear nanophotonics. Optica **3**(11), 1241 (2016)
16. Calà Lesina, A., Vaccari, A., Berini, P., Ramunno, L.: Nano-Optics: Principles Enabling Basic Research and Applications, chap. FDTD Method and HPC for Large-Scale Computational Nanophotonics, pp. 435–439. Springer, Netherlands (2017)
17. Yu, N., Capasso, F.: Flat optics with designer metasurfaces. Nat. Mater. **13**(2), 139–150 (2014)
18. Shaltout, A.M., Kinsey, N., Kim, J., Chandrasekar, R., Ndukaife, J.C., Boltasseva, A., Shalaev, V.M.: Development of optical metasurfaces: emerging concepts and new materials. Proc. IEEE **104**(12), 2270–2287 (2016)
19. Shaltout, A.M., Shalaev, V.M., Brongersma, M.L.: Spatiotemporal light control with active metasurfaces **364**(6441), eaat3100 (2019)
20. Kauranen, M., Zayats, A.V.: Nonlinear plasmonics. Nat. Photonics **6**(11), 737–748 (2012)
21. Calà Lesina, A., Berini, P., Ramunno, L.: Vectorial control of nonlinear emission via chiral butterfly nanoantennas: generation of pure high order nonlinear vortex beams. Opt. Express **25**(3), 2569 (2017)
22. Krasnok, A., Tymchenko, M., Alù, A.: Nonlinear metasurfaces: a paradigm shift in nonlinear optics. Mater. Today **21**(1), 8–21 (2018)
23. Calà Lesina, A., Ramunno, L., Berini, P.: Dual-polarization plasmonic metasurface for nonlinear optics. Opt. Lett. **40**(12), 2874 (2015)
24. O'Brien, K., Suchowski, H., Rho, J., Salandrino, A., Kante, B., Yin, X., Zhang, X.: Predicting nonlinear properties of metamaterials from the linear response. Nat. Mat. **14**(4), 379–383 (2015)
25. Varin, C., Emms, R., Bart, G., Fennel, T., Brabec, T.: Explicit formulation of second and third order optical nonlinearity in the FDTD framework. Comput. Phys. Commun. **222**, 70–83 (2018)

Chapter 4
Interaction Between a Plasmonic Nano-Resonator and a Whispering Gallery Mode Photonic Resonator Described Through Coupled Mode Theory and Experiment

Stephen Arnold, Jiachen Wan, Kaitlynn M. Snyder, and Mohammed Ali Miri

Abstract A Whispering gallery mode (WGM) based micro-spherical resonator driven by an optical fiber and adorned with a plasmonic SiO_2/Au nano-shell receptor is capable of zeptogram sensitivity for cancer marker detection from its frequency shift upon binding, making it an excellent candidate for an ultra-sensitive label-free biosensor. In this chapter we describe the experimental assembly of this hybrid resonator, obtain frequency shift and linewidth broadening data for single nanoshell binding events, and compare this data to coupled mode theory (CMT). A complex interaction $\widetilde{g}$ describes coupling between the photonic and nano-plasmonic resonators. The shift in resonance frequency is Re $\left[\widetilde{g}\right]$ and the spectral line broadening is 2 Im $\left[\widetilde{g}\right]$. The linewidth broadening is found to be consistent with the extinction (scattering and absorption) of the WGM evanescent wave by the nanoshell. Use of the *Reactive Sensing Principle* suggests a new technology for purifying nanoshells by resonance frequency, using light forces that accompany the assembly mechanism.

Keywords Hybrid whispering gallery mode resonator · Plasmonic nano-shell epitope · Coupled mode theory

S. Arnold (✉) · J. Wan · K. M. Snyder
Microparticle Photophysics Lab (MP3Lab), NYU School of Engineering, New York, USA
e-mail: sa1577@nyu.edu

M. A. Miri
Queens College of the City University of New York (CUNY), New York, USA

M. Cesaria et al. (eds.), *Light-Matter Interactions Towards the Nanoscale*,
NATO Science for Peace and Security Series B: Physics and Biophysics,
https://doi.org/10.1007/978-94-024-2138-5_4

4.1 Introduction

Micro-spherical whispering gallery mode (WGM) resonators driven by fiber coupling [1–3], were 1st proposed as a candidate for a biosensor in 1995 [1, 4], and have been used to sense single cancer marker protein with zeptogram sensitivity [5] by using nano-shell plasmonic epitopes [6] as frequency shift enhancers [7, 8] as shown in Fig. 4.1. Surprisingly there has been no detailed experimental description of how this WGM nano-plasmonic hybrid resonator (WGM-nph) is assembled. On the theoretical side Foreman [9, 10] extended the original description [7, 8] of the nano-shell microcavity interaction, in order to understand how the plasmonic epitope may be expected to compromise the Quality (Q) of the bare resonator. The later point is important since nano-shell plasmonic receptors are considered to be viable if they minimally effect Q. It should be pointed out that references 7–10 do not explicitly include the driving fiber in their theoretical descriptions. In addition on the experimental side there is little data that simultaneously measures the frequency shift and linewidth broadening which occurs on the binding of a single nano-shell. Here we seek a more comprehensive theoretical model that includes the fiber, sphere, and nano-shell epitope (pictured below), by using the coupled mode theory (CMT) pioneered by Haus [11]. In addition we describe the experimental assembly of the microsphere nanoshell hybrid by using light forces, and present frequency shift and linewidth broadening data for single nano-shell binding events. Finally in the end we put our CMT model up to nature.

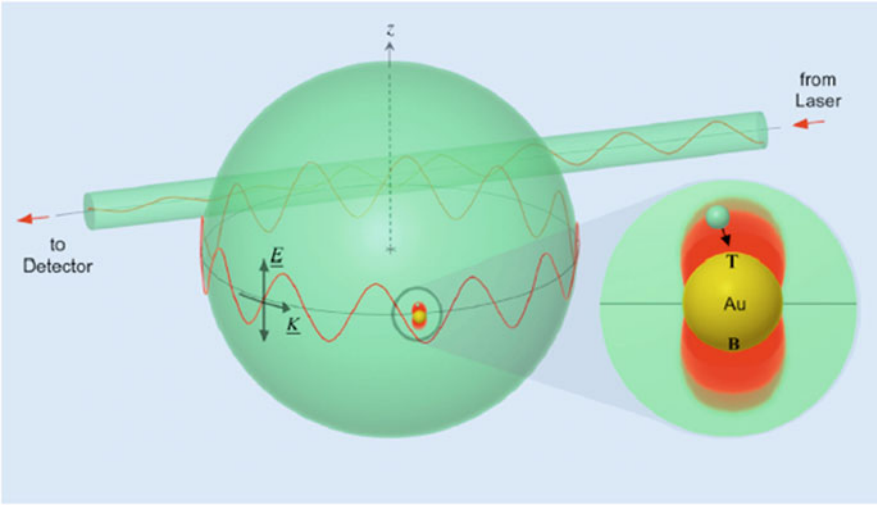

Fig. 4.1 Illustrates a fiber driven WGM interacting with a stationary SiO_2/Au core/shell nanostructure (nanoshell) stimulated near its resonant dipole mode. This generates hot spots north and south of the equator that capture smaller dielectric nanoparticles as the WGM's Carousel forces are transporting them. The effect is an enhanced resonant shift of the microcavity's frequency

4.2 Theoretical Approach: Coupled Mode Theory (CMT)

Coupled Mode Theory (CMT) [11] was borne out of the necessity of understanding complex resonant systems for which detailed analytic solutions are prohibitive. For example, in electromagnetics the difficulty often lies in mixed geometries. A cylindrical fiber coupled to a slightly spheroidal resonator upon which is attached a plasmonic epitope designed from a SiO_2/Au core/shell structure, is just such a system (Fig. 4.1).

To get a feeling for CMT we start with the familiar mechanical harmonic oscillator with displacement x, mass m, and force constant $m\omega_0^2$. Its dynamical equation, $\ddot{x} = -\omega_0^2 x$, is broken up into two 1st order equations

$$\dot{v}/\omega_0 = -\omega_0 x, \quad \text{and} \quad \dot{x} = v \tag{4.1}$$

where v is the velocity. These equations are assembled into a "complex modal amplitude"

$$a = \sqrt{m\omega_0^2/2}\,(x + iv/\omega_0)\,, \tag{4.2}$$

so that the oscillator's energy is aa^*, and its dynamical equation becomes

$$\dot{a} = -i\omega_0 a. \tag{4.3}$$

Here we have a 1st order equation describing the oscillator's motion as a clockwise (CW) rotating vector in the complex plane for which the real part of a allows the position to be determined, and the imaginary part the velocity. If now we drive the oscillator with a force f, and add damping, the dynamical equation becomes

$$\ddot{x} = -\omega_o^2 x - \gamma\dot{x} + f(t)/m. \tag{4.4}$$

In the Fourier domain

$$X(\omega) = \frac{F(\omega)/m}{-\omega^2 + \omega_0^2 - i\omega\gamma} = \frac{F(\omega)/m}{(-\omega + \omega_0)(\omega + \omega_0) - i\omega\gamma} \tag{4.5}$$

For a resonator with $Q \geq 10$, and in the spectral region near the real positive frequency ω_0, it is reasonable to substitute $\omega \cong \omega_0$ in slowly varying parts of the denominator (i.e. $\omega + \omega_0 \cong 2\omega_0$, and $i\omega\gamma \cong i\omega_0\gamma$) with the result

$$\widetilde{X}(\omega) = \frac{F(\omega)/m}{(-\omega + \omega_0)(2\omega_0) - i\omega_0\gamma} = \frac{F(\omega)/(2m\omega_0)}{(-\omega + \omega_0) - i\,\gamma/2} \tag{4.6}$$

Note that in doing this we have not only considered a resonator mode with a reasonably high Q, but we have also expressed the solution in terms of only the positive frequency pole (i.e. positive side band). With only this solution the associated temporal differential equation will be first order. This can readily be seen by writing Eq. 4.6 as

$$-i\omega\widetilde{X}(\omega) + i\omega_0\widetilde{X}(\omega) + \frac{\gamma}{2}\widetilde{X}(\omega) = iF_{(\omega)}/(2m\omega_0) \tag{4.7}$$

and taking its inverse Fourier transform

$$\frac{d\tilde{x}}{dt} = -i\omega_0\tilde{x} - \frac{\gamma}{2}\tilde{x} + if(t)/(2m\omega_0) \tag{4.8}$$

This single side band dynamical equation for the position is complex. The actual position involves adding the conjugate of $\tilde{x}$ to $\tilde{x}$. With that consideration, Eq. 4.3 modified for the inclusion of a driving force and damping becomes

$$\frac{da}{dt} = -i\left(\omega_0 - i\frac{\gamma}{2}\right)a + i\frac{1}{\sqrt{2m}}f(t) \tag{4.9}$$

For a resonator, whether mechanical or optical, the form of Eq. 4.9 is much the same. The difference is in the driving term, although that too can be generalized.

Our interest is in coupling the two resonators shown in Fig. 4.1, consisting of a fiber driven microcavity and a plasmonic nanoparticle with complex modal amplitudes, frequencies, and decay rates a_1, ω_1, γ_1 and a_2, ω_2, γ_2 respectively. In the absence of the fiber, the microcavity mode decays with rate γ_0. The driving fiber loads the microcavity with an additional rate γ_f, so that $\gamma_1 = \gamma_0 + \gamma_f$. The two resonators are coupled by an interaction $\widetilde{g} = g - i\gamma_g/2$, where the real part is described by the frequency shift calculated from the *reactive sensing principle* (RSP), [12] and the imaginary part is due to scattering and absorption of the WGM's evanescent wave by the nanoplasmonic epitope. Equation 4.10 expresses the evolution of the complex modal amplitudes of both the microcavity and nanoplasmonic resonators in matrix form.

$$\frac{d}{dt}\begin{bmatrix} a_1 \\ a_2 \end{bmatrix} = -i\begin{bmatrix} \left(\omega_1 + \widetilde{g} - i\frac{\gamma_1}{2}\right) & \widetilde{g} \\ \widetilde{g} & \left(\omega_2 + \widetilde{g} - i\frac{\gamma_2}{2}\right) \end{bmatrix}\begin{bmatrix} a_1 \\ a_2 \end{bmatrix} + \begin{bmatrix} \sqrt{\gamma_f}s_{in} \\ 0 \end{bmatrix} \tag{4.10}$$

There are several differences in the evolution of the individual complex modal amplitudes in Eq. 4.10 in comparison with Eq. 4.9. First and foremost, the 2 x 2 matrix contains the interaction $\widetilde{g}$ in the off diagonal components that allow for interplay between the modes. In addition in each of the diagonal terms $\widetilde{g}$ appears

in order to dress the modal frequencies. Beyond this, the mechanical driving force in Eq. 4.9 is changed. In the fiber-microsphere case the drive is expressed in terms of s_{in}, a function that is proportional to the electric field in the fiber. This "normalized field" is defined in order that its absolute square $|s_{in}|^2$ is the power injected into the fiber. The drive for the microsphere is associated with fiber coupling and the normalized field, $\sqrt{\gamma_f} s_{in}$. The drive vector on the far right of Eq. 4.10 is not symmetric to be consistent with Fig. 4.1, since only the microsphere is directly driven by the fiber; the plasmonic nanoparticle is driven indirectly through the coupling factor $\widetilde{g}$. Our analysis is nearly done. What is left is to associate this theory with experiment. We experimentally measure the transmission T through the fiber, which we will define as the ratio of the power out of the fiber to the power launched into the fiber; $T = |s_{out}/s_{in}|^2$. So we must connect s_{out} to s_{in}. As a consequence of a 90° phase shift in the evanescently coupled field into the microsphere relative to the wave continuing through the fiber [2, 3] the wave returning from the microsphere finds itself 180° out of phase with the wave in the fiber, causing destructive interference. This interference is described by

$$s_{out} = s_{in} - \sqrt{\gamma_f} a_1 \tag{4.11}$$

The transmission is found by: (1) replacing $\dot{a_1}$ and $\dot{a_2}$ in Eq. 4.10 by $-i\omega a_1$ and $-i\omega a_2$, respectively, solving for a_1, and (2) substituting this solution for a_1 into Eq. 4.11. The result is

$$T = \left|\frac{s_{out}}{s_{in}}\right|^2 = \left|\frac{\left[\omega - \left(\omega_1 + \widetilde{g}\right) + i(\gamma_0 - \gamma_f)/2\right]\left[\omega - \left(\omega_2 + \widetilde{g}\right) + i\gamma_2/2\right] - \widetilde{g}^2}{\left[\omega - \left(\omega_1 + \widetilde{g}\right) + i(\gamma_0 + \gamma_f)/2\right]\left[\omega - \left(\omega_2 + \widetilde{g}\right) + i\gamma_2/2\right] - \widetilde{g}^2}\right|^2 \tag{4.12}$$

Equation 4.12 has notable properties without the nano-plasmonic interaction (i.e. $\widetilde{g} = 0$). As an illustration we have chosen a microcavity resonator with a resonance frequency $f_1 = 194.4343\ THz$, and intrinsic damping rate $\gamma_0 = 63.5\ MHz$. Fig. 4.2 illustrates the effect of changing γ_f. The black curve sets $\gamma_f = \gamma_0$, and we observe critical coupling, with no transmission at resonance. The situation changes abruptly as the fiber coupling is reduced as shown by the red spectral line. With the rate of fiber coupling reduced below the intrinsic damping rate we observe under coupling, a narrower line and transmission at resonance. Finally, with rate of fiber coupling considerably larger than the rate of intrinsic damping, CMT predicts over coupling, a broader spectral line and transmission at resonance, as illustrated by the blue spectral line. These effects are consistent with experiment [3].

Next we describe the experimental assembly of the WGM-nph resonator.

4.3 Experimental Assembly of WGM-nph Resonator

The simulation in Fig. 4.2 is based on a free space wavelength of 1542.621 nm. Our experiments will reduce this wavelength to ~780 nm. A shorter wavelength will allow us to use a smaller microsphere (radius R~45μm), but still have a reasonably high Q in aqueous solution. The smaller sphere and shorter wavelength lead to a smaller mode volume, [13] and thereby generate a larger shift that is more easily quantified [12]. Next we will describe the experimental setup.

The assembly was carried out in a home-made microfluidic cell shown in Fig. 4.3 by using evanescent light forces [14]. The cell included a tapered fiber that guided light from a tunable distributed feedback (DFB) laser with a free space wavelength near 780 nm. An equatorial WGM within a SiO_2 microsphere (radius, R ~ 45 μm at the equator) with $Q = 4 \times 10^5$ was stimulated by contact with this fiber, and detected from a dip in the transmission through the fiber.

The evanescent field extending from the equatorial ring catches nanoplasmonic particles in a carousel orbit around the equator, which eventually leads to depositing a particle near the equator [15]. The attachment to the surface was aided by increasing the salt concentration in solution above 10 mM so as to reduce the Debye length, and thereby reduce the repulsive force between the negatively charged silica surface and the negatively charged nano-shell. The nanoshell with its SiO_2/Au core/shell structure had a nominal dimension of 60 nm/11.5 nm. After several events the resonance dip was measured to shift toward longer wavelength by an average of

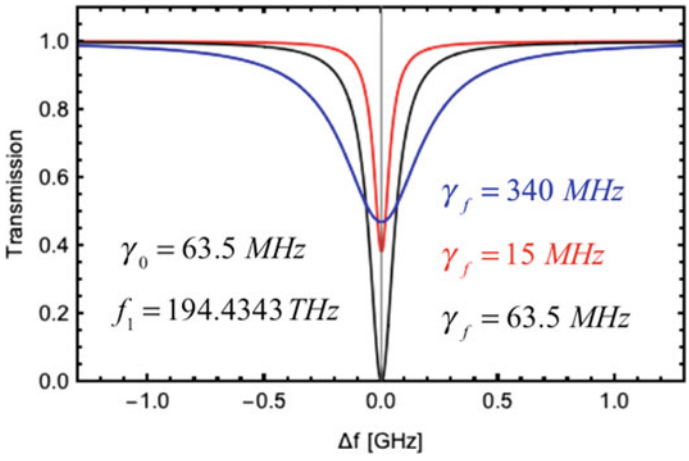

Fig. 4.2 Transmission spectra near resonance predicted from CMT. With the intrinsic rate of decay of a microcavity equal to the rate of fiber coupling, we observe critical coupling at resonance, with no transmitted power (black). With the rate of fiber coupling reduced below the intrinsic damping rate we observe under coupling, a narrower line and transmission at resonance (red). Finally, with rate of fiber coupling considerably larger than the rate of intrinsic damping, CMT predicts over coupling, a broader spectral line and transmission at resonance (blue)

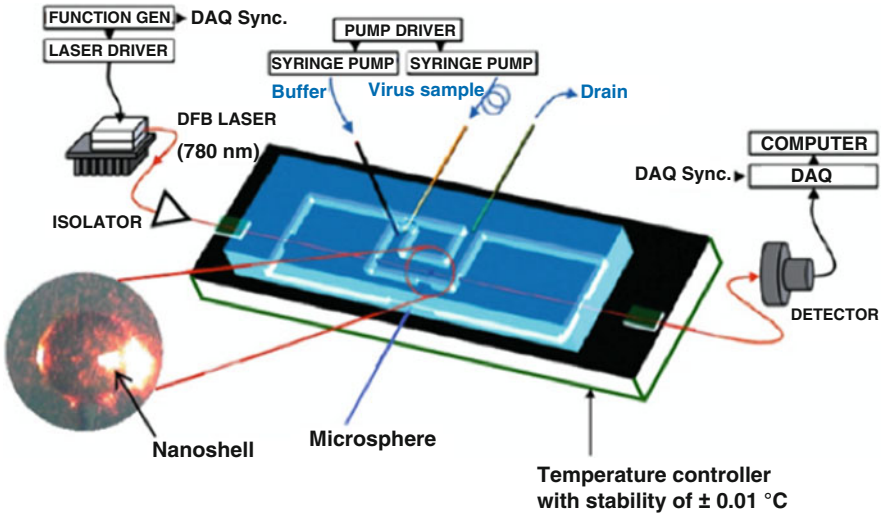

Fig. 4.3 Microfluidic WGM biosensor with the image of an assembled WGM nanoplasmonic hybrid (WGM-nph) resonator

+175 fm (86 MHz), and the linewidth increased by 230 fm (113 MHz). Although the measurements of the shift varied widely (+/−50 fm), the increased linewidth was more consistent (+/− 10 fm).

One can understand the large variations in the resonance shift between different nano-shells within a hydrosol sample based on the *Reactive Sensing Principle*, since the resonance shift should be proportional to the real part of the polarizability $Re[\alpha]$, and our measurements are being done near the plasmonic resonance at ω_2 where $Re[\alpha] \propto (\omega_2 - \omega)$, and small variations in ω_2 have a profound effect. However that is not the case for linewidth broadening, which for a nanoshell, principally arises from scattering and absorption, both of which have a broad resonance peak in the same region in frequency, and as a consequence a much slower variation with ω_2. So the linewidth broadening data is more reliable, and our goal of understanding how Q is compromised by a plasmonic binding event is more accessible.

The linewidth of the microcavity resonance for a Q of 4 x 10^5 is 960 MHz, so the fact that a binding event only increases this width by ~12% is rather small when one considers that the linewidth of the plasmonic particle is 5 orders of magnitude larger than that of the WGM (128 THz in comparison to 960 MHz). Considering the consistency in the linewidth broadening measurement, this minuscule increase in the linewidth broadening compared with the linewidth of the bare nano-shell provides a critical test of the CMT (Eq. 4.12).

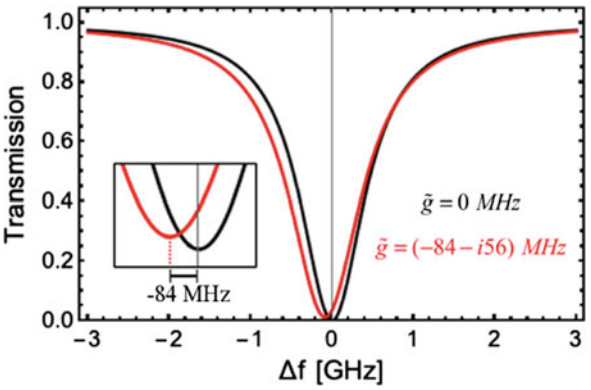

Fig. 4.4 Transmission near resonance predicted from CMT before (black) and after turning on the interaction $\tilde{g}$. These spectra agree well with our experimental results in Sect. 4.4

4.4 Application of CMT to the Experimental Results

Application of Eq. 4.12 to the region of frequency covered by our experiments provides good agreement with our measured spectra. Fig. 4.4 shows a simulation for the following parameters :$f_1 = 384.600\ THz, f_2 = 384.603\ THz$, $\gamma_2 = 128\ THz$, $\gamma_0 = \gamma_f = 480\ MHz$, $\tilde{g} = (-84 - i56)\ MHz$. Indeed the CMT predicts a minuscule increase in the linewidth broadening compared with the linewidth of the bare nanoshell, consistent with experiment. It is the imaginary part of the coupling constant $\tilde{g}$ that controls the change in linewidth of the resonance dip upon coupling. In addition even though we are dealing with a 2 x 2 matrix we see only one discernable dip for this WGM-nph, consistent with our experiments. Beyond this the shift in frequency is essentially the Re $\left[\tilde{g}\right]$, and the linewidth broadening 2Im $\left[\tilde{g}\right]$, as seen in Fig. 4.4. This implies that a simple heuristic approach can be used to estimate the linewidth broadening as we will see next.

4.5 Heuristic Approach for Understanding the Linewidth Broadening Arising from Forming the WGM-nph

If we take the view that linewidth broadening results from a loss of energy from the WGM mode upon the binding of the nanoplasmonic particle, then one can simply ask where the losses are. The intuitive answer is that the loss is due to scattering and absorption, or simply stated extinction. These effects taken together are represented by the extinction cross section, σ_e. The energy lost per unit time due to extinction may be estimated from the circulating intensity at the center of the particle $I(r_p)$ times this extinction cross section; energy loss rate due to extinction $= \sigma_e I(r_p)$. If we associate this with the linewidth broadening $\Delta\gamma$, then

$$(\Delta\gamma)\,\varepsilon = \sigma_e I\left(r_p\right) \tag{4.13}$$

where ε is the photonic energy of the microcavity. Fortunately ε and I are proportional to each other, and σ_e for the nanoshell can be calculated from Mie theory [16]. As to the connection between ε and $I(r_p)$ we recognize that

$$\frac{I\left(r_p\right)}{\varepsilon} = \frac{I(R)\exp\left(-\frac{r_p-R}{L}\right)}{\varepsilon} = \frac{n_m \varepsilon_0 c}{2}\frac{E_0^2(R)}{\varepsilon}\exp\left(-\frac{r_p-R}{\mathrm{L}}\right) \tag{4.14}$$

where R is the radius of the microcavity, n_m is the refractive index of the medium (water), and c is the speed of light in vacuum. The last thing we need to complete our estimate of $\Delta\gamma$ is the ratio of the square of the field on the microcavity surface to the energy in the cavity. Fortunately this result is available for the equatorial mode of a microsphere [12],

$$\frac{E_0^2(R)}{\varepsilon} = \frac{E_0^2(R)}{2\int \varepsilon\left(r_c\right) E_0^2\left(r_c\right) dV} = \frac{\left|Y_{ll}\left(\pi/2,\varphi\right)\right|^2}{\varepsilon_0\left(n_s^2-n_m^2\right)R^3} \tag{4.15}$$

where $|Y_{ll}(\pi/2,\varphi)|^2$ is the square modulus of the equatorial spherical harmonic, and n_s is the refractive index of the microcavity (fused SiO_2, 1.45). Combining Eqs. 4.13–4.15 allows us to arrive an equation for the linewidth broadening,

$$\frac{\Delta\gamma}{\omega_1} = \frac{\sigma_e I\left(r_p\right)}{\varepsilon\,\omega_1} = \frac{\sigma_e\lambda_0}{4\pi}\frac{n_m\left|Y_{ll}\left(\pi/2,\varphi\right)\right|^2}{\left(n_s^2-n_m^2\right)R^3}\exp\left(-\frac{r_p-R}{L}\right) \tag{4.16}$$

The extinction cross-section for our average nanoshell at 780 nm (384.6 THz) is near the dipole peak and equal to 1.4 x 10^5 nm^2. At this peak we calculate a linewidth broadening of 200 MHz using Eq. 4.16, compared to our measured 113 MHz. It is interesting to note that there would be no attractive gradient force at this peak since the $Re[\alpha] = 0$; the gradient force $< F_g >= (\mathrm{Re}\,[\alpha]\,/4)\,\nabla E_0^2$. For a particle to be drawn to the surface the exciting frequency would have to be smaller than the plasmonic resonance frequency. The spectrum for such a particle is shown in Fig. 4.5. It has a slight variation in its core/shell dimension of 55 nm/12.5 nm as compared with the average of 60 nm/11.5 nm. The plasmonic resonance is now shifted to 760 nm (394.7 THz). For this particle the maximum extinction cross section is 1.3 x 10^5 nm^2, and the cross section at an excitation wavelength of 780 nm (384.6 nm) is 1.2 x 10^5 nm^2, which brings our calculation for the linewidth broadening to 171 MHz, that is closer to the measured value of 113 MHz. It also allows for an attractive force; $Re[\alpha] > 0$, consistent with the mechanism for binding the particle to the microcavity surface, and suggests a new technology.

In a sense the gradient force acts to separate particles with a resonance frequency below the excitation frequency from those with a resonance frequency above the excitation frequency; only particles with a plasmonic resonance frequency above the excitation frequency move toward the microcavity, the others are repelled.

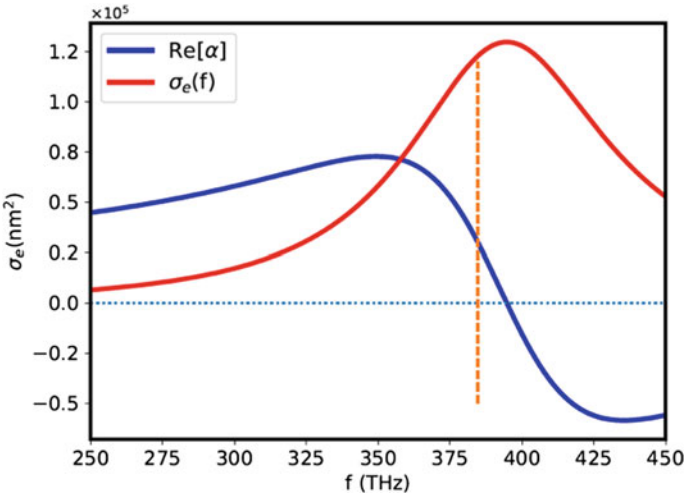

Fig. 4.5 Extinction cross-section σ_e and real part of polarizability $Re[\alpha]$ for a particle with core radius to shell thickness ratio of 55 nm/12.5 nm. The dashed red line at 384.6 THz corresponds to a wavelength of our excitation at 780 nm

This provides a filter for separating particles by plasmonic frequency; the particles reaching the surface will be purified in terms of plasmonic frequency.

4.6 Conclusions

Coupled mode theory at present provides a semi-quantitative means for arriving at an understanding for the interaction between the fiber driven photonic WGM resonator and a nano-plasmonic resonator. Although it is by no means complete, considering the reduction in complexity that is affords, our work shows CMT to be both useful and revealing.

Acknowledgements We thank David Keng for providing the MP3Laser system used in taking the measurements in this paper, and for contributing his time without charge. S.A. would like to thank Lucas Novotny for discussions during the NATO ASI that inspired this chapter. S.A. would also like to thank Rino DiBartolo for his help over the years, and for the introduction to the land of his birth. Finally we all are in debt to John Collins for organizing this NATO ASI.

References

1. Serpengüzel A, Griffel G, Arnold S (1995) Excitation of resonances of microspheres on an optical fiber. Opt Lett 20:654–656
2. Griffel G, Arnold S, Taskent D, Serpengüzel A, Connolly J, Morris N (1996) Morphology-dependent resonances of a microsphere-optical fiber system. Opt Lett 21:695–697
3. Cai M, Painter O, Vahala K (2000) Observation of critical coupling in a fiber taper to a silica-microsphere whispering-gallery mode system. Phys Rev Lett 85:74–77
4. Sun Y, Fan X (2011) Optical ring resonators for biochemical and chemical sensing. Anal Bioanal Chem 399:205–211
5. Dantham VR, Holler S, Barbre C, Keng D, Kolchenko V, Arnold S (2013) Label-free detection of single protein using a nanoplasmonic-photonic hybrid microcavity. Nano Lett 13:3347–3351
6. Arnold S, Dantham VR, Barbre C, Garetz BA, Fan X (2012) Perodic plsmonic enhancing epitopes on a whispering gallery mode biosensor. Opt Expess 20:26147–26159
7. Shopova SI, Rajmangal R, Holler S, Arnold S (2011) Plasmonic enhancement of a whispering-gallery-mode biosensor for single nanoparticle detection. Appl Phys Lett 98:243104
8. Dantham VR, Holler S, Kolchenko V, Wan Z, Arnold S (2012) Taking whispering gallery-mode single virus detection to the limit. Appl Phys Lett 101:043704
9. Foreman MR, Vollmer F (2013) Level repulsion in hybrid photonic-plasmonic microresonators for enhanced biodetection. Phys Rev A 88:023831
10. Foreman MR, Vollmer F (2013) Theory of resonance shifts of whispering gallery modes by arbitrary plasmonic nanoparticles. New J Phys 15:083006
11. Haus HA, Huang W (1991) Coupled-mode theory. Proceedings IEEE 79:1505–1518
12. Arnold S, Khoshsima M, Teraoka I, Holler S, Vollmer F (2003) Shift of whispering-gallery modes in microspheres by protein adsorption. Opt Lett 28:272–274
13. Kim W, Ozdemir SK, Zhu J, Yang L (2011) Observation and characterization of mode splitting in microsphere resonators in aquatic environment. Appl Phys Lett 98:141106
14. Arnold S, Ramjit R, Keng D, Kolchenko V, Teraoka I (2008) Micro particle photophysics illuminates viral bio-sensing. Faraday Discuss 137:65–83
15. Arnold R, Keng D, Shopova SI, Holler S, Zurawsky W, Vollmer F (2009) Whispering gallery mode carousel. Opt Express 17:6230–6238
16. Sarid D, Challener W (2010) Modern introduction to surface plasmons. Cambridge University Press, Cambridge

Chapter 5
Time Reversal Symmetry and Topology in Electromagnetics

Mário G. Silveirinha

Abstract We present an overview of the role of time-reversal symmetry in electromagnetism and highlight how it affects the wave propagation and wave phenomena. It is shown that by combining the time-reversal symmetry with additional symmetries related to parity and duality it is possible to suppress the back-scattering in a generic bi-directional photonic platform. Furthermore, we discuss how by biasing a system with either a linear or an angular momentum one can break the time-reversal symmetry and achieve unidirectional propagation. It is discussed that the time reversal symmetry breaking is often associated with phase transitions characterized by topological invariants that determine a bulk-edge correspondence. Finally, it is highlighted that systems with continuous translation symmetry have an ill-defined topology, and that this property can be exploited to halt abruptly a wave and create energy sinks wherein the electromagnetic field is massively enhanced.

Keywords Symmetry · Electromagnetic reciprocity · Spin hall effect · Topological photonics · Ill-defined topology

5.1 Introduction

Time-reversal is the transformation that flips the arrow of time $t \rightarrow -t$. Notably, the laws that rule the microscopic dynamics of most physical systems are unchanged under a time-reversal. In other words, the time-reversed system state satisfies the same dynamical laws as the original state. This means that under suitable initial conditions, the time reversed dynamics may be generated and observed in a real physical scenario, analogous to a movie played backwards. In last instance, the time-

M. G. Silveirinha (✉)
University of Lisbon, Instituto Superior Técnico and Instituto de Telecomunicações, Lisbon, Portugal
e-mail: mario.silveirinha@co.it.pt

M. Cesaria et al. (eds.), *Light-Matter Interactions Towards the Nanoscale*,
NATO Science for Peace and Security Series B: Physics and Biophysics,
https://doi.org/10.1007/978-94-024-2138-5_5

reversal invariance implies that at a microscopic level the physical phenomena are reversible [1–3].

An important consequence of time-reversal invariance is that the propagation of light in typical guides is inherently bi-directional, even if the system does not have any particular spatial symmetry. For example, if some electromagnetic wave can go through a metallic pipe with no back-reflections, then the time-reversed wave also can, but propagating in the opposite direction independent of the geometry of the guide [1–3].

In this article, we present an overview of the role of time-reversal symmetry in electromagnetism and explain how it affects wave phenomena and the scattering matrix. We give a few modern examples of systems with of a broken time-reversal symmetry. Finally, we highlight the topological nature of some systems with a broken time reversal symmetry.

5.2 Time Reversal

Consider the propagation of an electromagnetic wave in some lossless, dispersion-free, dielectric system described by the Maxwell equations:

$$\nabla \times \mathbf{E} = -\mu_0 \frac{\partial \mathbf{H}}{\partial t}, \quad \nabla \times \mathbf{H} = \mathbf{j} + \varepsilon \frac{\partial \mathbf{E}}{\partial t}, \tag{5.1}$$

with $\varepsilon = \varepsilon(\mathbf{r})$. The time-reversal operation $\mathcal{T}$ transforms the electromagnetic fields $\mathbf{E}$, $\mathbf{H}$ and the current density $\mathbf{j}$ as $\mathbf{E} \xrightarrow{\mathcal{T}} \mathbf{E}^{\mathrm{TR}}$, $\mathbf{H} \xrightarrow{\mathcal{T}} \mathbf{H}^{\mathrm{TR}}$, and $\mathbf{j} \xrightarrow{\mathcal{T}} \mathbf{j}^{\mathrm{TR}}$ with:

$$\mathbf{E}^{\mathrm{TR}}(\mathbf{r}, t) = \mathbf{E}(\mathbf{r}, -t), \quad \mathbf{H}^{\mathrm{TR}}(\mathbf{r}, t) = -\mathbf{H}(\mathbf{r}, -t), \quad \mathbf{j}^{\mathrm{TR}}(\mathbf{r}, t) = -\mathbf{j}(\mathbf{r}, -t). \tag{5.2}$$

The transformed fields satisfy the same equations as the original fields. The sign of the magnetic field and of the current density is flipped under a time-reversal, and thus they are said to be odd under a time-reversal. In contrast, the electric field is unchanged and hence is even under the action of $\mathcal{T}$. Consequently, the Poynting vector $\mathbf{S} = \mathbf{E} \times \mathbf{H}$ also flips sign under a time-reversal, so that the wave dynamics and the direction of propagation are effectively reversed. The time reversal concept is rather general and applies to fields with arbitrary time dynamics.

Consider now time-harmonic solutions of the Maxwell equations, with the electromagnetic fields and the current density given by: $\mathbf{E}(\mathbf{r}, t) = \mathrm{Re}\{\mathbf{E}_\omega(\mathbf{r}) e^{-i\omega t}\}$, $\mathbf{H}(\mathbf{r}, t) = \mathrm{Re}\{\mathbf{H}_\omega(\mathbf{r}) e^{-i\omega t}\}$, $\mathbf{j}(\mathbf{r}, t) = \mathrm{Re}\{\mathbf{j}_\omega(\mathbf{r}) e^{-i\omega t}\}$, with ω the real-valued oscillation frequency. Under a time-reversal the electric field is transformed as $\mathbf{E}(\mathbf{r}, t) \to \mathrm{Re}\left\{\mathbf{E}_\omega(\mathbf{r}) e^{+i\omega t}\right\} = \mathrm{Re}\left\{\mathbf{E}_\omega^*(\mathbf{r}) e^{-i\omega t}\right\}$, where the symbol "*" stands for complex conjugation. Hence, the complex amplitudes of the fields are transformed as:

$$\mathbf{E}_\omega(\mathbf{r}) \xrightarrow{\mathcal{T}} \mathbf{E}_\omega^*(\mathbf{r}), \quad \mathbf{H}_\omega(\mathbf{r}) \xrightarrow{\mathcal{T}} -\mathbf{H}_\omega^*(\mathbf{r}), \quad \mathbf{j}_\omega(\mathbf{r}) \xrightarrow{\mathcal{T}} -\mathbf{j}_\omega^*(\mathbf{r}). \tag{5.3}$$

Thus, in the frequency-domain the time-reversal operation implies a phase conjugation. Similarly, voltages and currents are transformed as:

$$V_\omega \overset{\mathcal{T}}{\rightarrow} V_\omega^*, \quad I_\omega \overset{\mathcal{T}}{\rightarrow} -I_\omega^*. \tag{5.4}$$

5.3 Scattering Matrix Symmetry

The time-reversal symmetry imposes several restrictions on the wave propagation and wave scattering. In what follows, it is shown that the time-reversal invariance is strictly linked to the concept of electromagnetic reciprocity. Furthermore, it is highlighted that the constraints on the scattering matrix are different for electromagnetic and condensed-matter systems.

5.3.1 Electromagnetic Reciprocity

Consider a N-port microwave network such that the complex-amplitudes of the voltages and currents at a generic port i are of the form: $V_{\omega,i} = V_{\omega,i}^+ + V_{\omega,i}^-$ and $I_{\omega,i} = \left(V_{\omega,i}^+ - V_{\omega,i}^-\right)/Z_0$, $i = 1, \ldots, N$. Here, $V_{\omega,i}^+$ represents an incoming (incident) wave and $V_{\omega,i}^-$ an outgoing (scattered) wave. The characteristic impedance of the ports is Z_0. The incident and scattered waves are related as $\mathbf{V}^- = \mathbf{S} \cdot \mathbf{V}^+$, where $\mathbf{V}^\pm = \left[V_{\omega,i}^\pm\right]$ are column vectors and $\mathbf{S} = [S_{ij}]$ is the scattering matrix.

The time reversal operation exchanges the roles of the incident and scattered waves, such that $\mathbf{V}^{\mathrm{TR},\pm} = \mathbf{V}^{\mp,*}$. Therefore, if the system is time-reversal invariant $\mathbf{V}^{+,*} = \mathbf{S} \cdot \mathbf{V}^{-,*}$. Thus, the scattering matrix must satisfy $\mathbf{S} = \mathbf{S}^{-1,*}$. On the other hand, for a lossless system the incident power must be identical to the scattered power: $\mathbf{V}^- \cdot \mathbf{V}^{-,*} = \mathbf{V}^+ \cdot \mathbf{V}^{+,*}$. In order to satisfy this additional constraint the scattering matrix must be unitary $\mathbf{S} \cdot \mathbf{S}^\dagger = \mathbf{1}$. Combining $\mathbf{S} = \mathbf{S}^{-1,*}$ with the unitary property, one finds that the scattering matrix must be symmetric:

$$\mathbf{S} = \mathbf{S}^T. \tag{5.5}$$

Thus, any time-reversal invariant linear lossless system is necessarily reciprocal ($S_{ij} = S_{ji}$). Electromagnetic reciprocity implies that the transmission strength from port i to port j is identical to the transmission strength from port j to port i. Thus, time-reversal invariant platforms are forcibly bi-directional.

In the previous derivation it was assumed that the system under study is lossless. This is not a limitation of the derivation, as lossy reciprocal systems have a hidden time-reversal symmetry and can be regarded as projections in real-space of a

fictitious lossless system with synthetic dimensions [3]. Thus, the constraint $\mathbf{S} = \mathbf{S}^T$ also applies to lossy systems.

5.3.2 Condensed-Matter Systems

In electromagnetic theory the time-reversal operator $\mathcal{T}$ is idempotent, such that $\mathcal{T}^2 = \mathbf{1}$. In other words, a "double" time-reversal leaves the system state unchanged.

In contrast, in condensed matter theory –in the context of Schrödinger equation for spin ½ particles– the time-reversal operator satisfies $\mathcal{T}^2 = -\mathbf{1}$ [4]. The extra minus sign changes the phase of the wave function. This does not have any immediate physical consequences as a change of phase does not affect the expectation of physical observables. However, a careful analysis shows that the extra minus sign implies that the scattering matrix of fermionic systems is anti-symmetric [4],

$$\mathbf{S} = -\mathbf{S}^T. \tag{5.6}$$

This means that a time-reversal symmetric condensed matter system is matched at all its input ports, such $S_{ii} = 0$. Thus, when the number of propagating modes per physical channel is identical to one (or more generally if it is an odd number) the time-reversal symmetry enables the bi-directional propagation of electron waves free of back-scattering. This is known as the quantum spin Hall effect [4, 5].

It is relevant to mention that the minus sign in $\mathcal{T}^2 = -\mathbf{1}$ also implies that the energy states of an electronic system are forcibly degenerate. Hence, the extra minus sign is rooted in the spin degree of freedom.

5.4 $\mathcal{P} \cdot \mathcal{T} \cdot \mathcal{D}$ Invariant Systems

As previously discussed, time-reversal invariant electromagnetic platforms are characterized by a symmetric scattering matrix $\mathbf{S} = \mathbf{S}^T$. Curiously, the time-reversal symmetry does not constraint in any form the diagonal elements of the scattering matrix, which determine the reflection-loss due to the back-scattering. Evidently, it can be highly beneficial for many applications to eliminate the reflection loss. Next, we describe a class of bi-directional electromagnetic systems which are inherently matched at all input ports ($S_{ii} = 0$), analogous to spin ½ condensed matter systems.

To begin with, we write the Maxwell's equations in the frequency domain as:

$$\hat{N} \cdot \mathbf{f} = \omega \mathbf{g}, \quad \text{with} \quad \hat{N} = \begin{pmatrix} \mathbf{0} & i\nabla \times \mathbf{1}_{3\times 3} \\ -i\nabla \times \mathbf{1}_{3\times 3} & \mathbf{0} \end{pmatrix}. \tag{5.7}$$

Here, $\mathbf{1}_{3\times 3}$ is the 3×3 identity matrix, ω is the oscillation frequency, $\mathbf{f} = (\mathbf{E}\ \mathbf{H})^T$ and $\mathbf{g} = \left(\mathbf{D}\ \mathbf{B}\right)^T$ are six-component vector fields written in terms of the standard electromagnetic field vectors, and T denotes the matrix transpose operation. It is assumed that the $\mathbf{f}$ and $\mathbf{g}$ fields are linked as $\mathbf{g} = \mathbf{M}(\mathbf{r}) \cdot \mathbf{f}$ where $\mathbf{M}$ is a space-dependent material matrix of the generic bianisotropic form:

$$\mathbf{M}(\omega) = \begin{pmatrix} \varepsilon_0 \overline{\varepsilon} & \frac{1}{c}\overline{\xi} \\ \frac{1}{c}\overline{\zeta} & \mu_0 \overline{\mu} \end{pmatrix}. \tag{5.8}$$

The tensors $\overline{\varepsilon}(\omega), \overline{\mu}(\omega), \overline{\xi}(\omega), \overline{\zeta}(\omega)$ are dimensionless and determine the permittivity, permeability and the magneto-electric coupling tensors, respectively. In this compact formalism, the time-reversal operator $\mathcal{T}$ is written as $\mathcal{T} = \mathcal{K}\boldsymbol{\sigma}_z$ where $\mathcal{K}$ denotes the complex conjugation operator and $\boldsymbol{\sigma}_z = \begin{pmatrix} \mathbf{1}_{3\times 3} & 0 \\ 0 & -\mathbf{1}_{3\times 3} \end{pmatrix}$. The time-reversal operation transforms the (frequency domain) electromagnetic fields as $\mathbf{f} \to \mathcal{T} \cdot \mathbf{f}$ and $\mathbf{g} \to \mathcal{T} \cdot \mathbf{g}$. The operator $\mathcal{T}$ is anti-linear, i.e., it is the composition of a linear operator and $\mathcal{K}$.

The idea to mimic the behavior of condensed matter systems is to enforce suitable symmetry constraints on the material response. Specifically, it is imposed that the photonic platform is invariant under the action of some anti-linear operator $\tilde{\mathcal{T}}$, which is supposed to imitate the time-reversal operator in condensed-matter theory so that $\tilde{\mathcal{T}}^2 = -\mathbf{1}$. The operator $\tilde{\mathcal{T}}$ is required to transform the electromagnetic fields in such a manner that its action flips the Poynting vector in the relevant propagation directions, similar to the standard time-reversal operation.

A suitable operator $\tilde{\mathcal{T}}$ with the required properties is determined by the composition of the time-reversal ($\mathcal{T}$), parity ($\mathcal{P}$) and a duality transformation ($\mathcal{D}$) [5]:

$$\tilde{\mathcal{T}} = \mathcal{P} \cdot \mathcal{T} \cdot \mathcal{D}. \tag{5.9}$$

The parity (inversion) operator flips the z-spatial coordinate $(x, y, z) \to (x, y, -z)$, i.e., the coordinate perpendicular to the propagation plane (xoy plane). A parity operation transforms the electromagnetic fields as $\mathbf{f} \to \mathcal{P} \cdot \mathbf{f}$ and $\mathbf{g} \to \mathcal{P} \cdot \mathbf{g}$ with $\mathcal{P} = \begin{pmatrix} \mathbf{V} & 0 \\ 0 & -\mathbf{V} \end{pmatrix}$ where $\mathbf{V}$ is a 3×3 diagonal matrix with diagonal entries $V_{11} = V_{22} = -V_{33} = 1$. On the other hand, the duality transformation simply exchanges the electric and magnetic fields as $\mathbf{f} \to \mathcal{D} \cdot \mathbf{f}$ with

$$\mathcal{D} = \begin{pmatrix} 0 & \eta_0 \mathbf{1}_{3\times 3} \\ -\eta_0^{-1}\mathbf{1}_{3\times 3} & 0 \end{pmatrix}, \tag{5.10}$$

without affecting the space and the time coordinates. The $\mathbf{g}$ fields are transformed by the duality transformation as $\mathbf{g} \to -\mathcal{D}^T \cdot \mathbf{g}$. In the above, $\eta_0 = \sqrt{\mu_0/\varepsilon_0}$ is the free-space impedance.

It can be checked that the in-plane components of the Poynting vector are flipped by the $\mathcal{P}\cdot\mathcal{T}\cdot\mathcal{D}$ transformation and that $(\mathcal{P}\cdot\mathcal{T}\cdot\mathcal{D})^2 = -\mathbf{1}$, as it should be. Furthermore, a generic photonic platform is $\mathcal{P}\cdot\mathcal{T}\cdot\mathcal{D}$ invariant when the material matrix satisfies [5].

$$\mathbf{M}(x,y,z) = -\begin{pmatrix} 0 & -\eta_0^{-1}\mathbf{V} \\ \eta_0\mathbf{V} & 0 \end{pmatrix}\cdot\mathbf{M}^T(x,y,-z)\cdot\begin{pmatrix} 0 & -\eta_0\mathbf{V} \\ \eta_0^{-1}\mathbf{V} & 0 \end{pmatrix}. \tag{5.11}$$

For simplicity suppose that the system is formed by lossless isotropic dielectrics, such that $\mathbf{M} = \begin{pmatrix} \varepsilon\mathbf{1}_{3\times3} & 0 \\ 0 & \mu\mathbf{1}_{3\times3} \end{pmatrix}$. Then, the $\mathcal{P}\cdot\mathcal{T}\cdot\mathcal{D}$ invariance requires simply that the relative permittivity and permeability are linked as:

$$\varepsilon(x,y,z) = \mu(x,y,-z). \tag{5.12}$$

An example of a $\mathcal{P}\cdot\mathcal{T}\cdot\mathcal{D}$ invariant guide is shown in Fig. 5.1a. The air channel is delimited by electric walls (perfect electric conductors, PEC, with $\varepsilon = -\infty$) and magnetic walls (perfect magnetic conductions, PMC, with $\mu = -\infty$). In Fig. 5.1, the relevant parity transformation is $(x,y,z)\to(x,-y,z)$. The plane $y=0$ is the mid-plane equidistant from the top and bottom walls. Clearly, the material parameters of two points connected by mirror symmetry are related by a duality transformation. For low frequencies, there is a single propagating mode, which turns out to be a transverse electromagnetic (TEM) wave. Therefore, provided the $\mathcal{P}\cdot\mathcal{T}\cdot\mathcal{D}$ symmetry is preserved, the guide can be arbitrarily deformed without generating any back-reflections (Fig. 5.1b) [5–7].

There is an apparent paradox: the platform of Fig. 5.1a is evidently reciprocal and thereby its scattering matrix should be symmetric $\mathbf{S} = +\mathbf{S}^T$. On the other hand, the same platform is $\mathcal{P}\cdot\mathcal{T}\cdot\mathcal{D}$-invariant and this implies that $\mathbf{S} = -\mathbf{S}^T$. A matrix can be both symmetric and anti-symmetric only if it vanishes: $\mathbf{S}=\mathbf{0}$. However, the result $\mathbf{S}=\mathbf{0}$ is evidently inconsistent with the conservation of energy in the lossless junction.

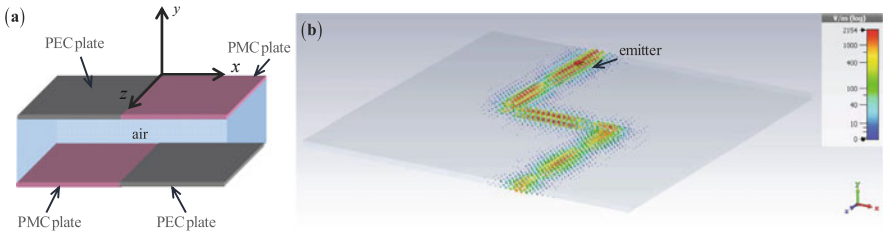

Fig. 5.1 (**a**) Sketch of a $\mathcal{P}\cdot\mathcal{T}\cdot\mathcal{D}$-invariant waveguide formed by PEC and PMC walls. The waveguide supports a mode with fields concentrated near the interface between the PEC and PMC plates. (**b**) Electric field profile for a zig-zag type path. If the $\mathcal{P}\cdot\mathcal{T}\cdot\mathcal{D}$ symmetry is preserved, the propagation path can be arbitrarily deformed without generating any reflections

The solution of the paradox is that the scattering matrix is not an absolute physical object, but rather depends on the basis of modes used to expand the fields. If one chooses a basis such that $\mathbf{f}_n^- = \tilde{\mathcal{T}} \cdot \mathbf{f}_n^+$ the scattering matrix satisfies $\mathbf{S}_{\tilde{\mathcal{T}}} = -\mathbf{S}_{\tilde{\mathcal{T}}}^T$, while if one picks a basis such that $\mathbf{f}_n^- = \mathcal{T} \cdot \mathbf{f}_n^+$ the scattering matrix satisfies $\mathbf{S}_{\mathcal{T}} = +\mathbf{S}_{\mathcal{T}}^T$. Here, $\mathbf{f}_n^-, \mathbf{f}_n^+$ represent the electromagnetic fields associated with the outgoing and incoming waves on port n, respectively. Both scattering matrices describe equally well the relevant wave phenomena, but they are computed using two different bases of outgoing modes. Thus, electromagnetic reciprocity and the $\mathcal{P} \cdot \mathcal{T} \cdot \mathcal{D}$-symmetry are compatible, and the invariance of a system under both $\mathcal{T}$ and $\tilde{\mathcal{T}}$ does not lead to inconsistencies [5].

5.5 Time Reversal Symmetry Breaking

As previously discussed, physical systems are generically time-reversal invariant at the microscopic level. Therefore, the energy-momentum dispersion has even symmetry with respect to the momentum origin: $\varepsilon(p) = \varepsilon(-p)$ (Fig. 5.2). This means that the energy expectation of a certain stationary state is always the same as that of the corresponding time-reversed state. Excluding the exceptional circumstance of a degenerate ground, it follows that the system "ground state" is forcibly time-reversal invariant. This property is the cornerstone of the reciprocity of standard electromagnetic platforms. Interestingly, it is possible to break the time-reversal invariance by applying a "momentum bias" that pushes the equilibrium state away from the "free-system" ground state (Fig. 5.2a). With an "external bias" the input-output transfer relations are not constrained by the time-reversal symmetry. The reason is that the operating point is not anymore time-reversal invariant because under a time-reversal the "momentum bias" is flipped (Fig. 5.2).

There are several solutions to enforce a "momentum bias" and break the time-reversal symmetry of photonic systems [8]. The standard approach consists in biasing a material (e.g., a semiconductor or a ferrimagnetic material) with a static

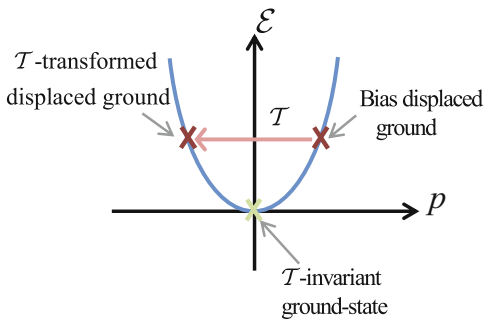

Fig. 5.2 Illustration of time-reversal symmetry breaking due to a "momentum bias"

magnetic field. The magnetic field is transformed as $\mathbf{B} \xrightarrow{\mathcal{T}} -\mathbf{B}$ (odd quantity) under a time-reversal, i.e., similar to a "momentum". Thus, the input-output relations of a magnetically biased system are free of the time-reversal constraint. In contrast, a static electric bias does not lead directly to the time-reversal symmetry breaking because the electric field transforms as $\mathbf{E} \xrightarrow{\mathcal{T}} +\mathbf{E}$ (even quantity). However, the static electric bias can lead indirectly to a time-reversal symmetry breaking. For example, a static electric field can induce a drift-electric current in a material, which is an odd quantity under a time-reversal. Thus, systems with a drift-current bias are nonreciprocal. These ideas are developed in the following.

5.5.1 Static Magnetic Field Bias

A static magnetic bias $\mathbf{B}_0$ modifies the dynamics of the electrons in a plasma through the Lorentz force. With a static magnetic bias, the motion of a generic electron with velocity $\mathbf{v}$ is determined by

$$m\frac{d\mathbf{v}}{dt} = q\left(\mathbf{E} + \mathbf{v} \times \mathbf{B}_0\right) - m\Gamma\mathbf{v}, \tag{5.13}$$

where m is the effective mass, $q = -e$ is the electron charge, Γ is the collision frequency, and $\mathbf{E}$ is the dynamical electric field. Taking $\mathbf{B}_0 = B_0\hat{\mathbf{u}}$ and assuming a time harmonic variation for $\mathbf{v}$ and $\mathbf{E}$, it follows that the averaged response of the electron gas satisfies

$$\left(\mathbf{1} + \frac{-\omega_0 i}{\omega + i\Gamma}\hat{\mathbf{u}} \times \mathbf{1}\right) \cdot \frac{\mathbf{j}}{-i\omega\varepsilon_0} = \frac{-\omega_p^2}{\omega\left(\omega + i\Gamma\right)}\mathbf{E}, \tag{5.14}$$

where $\mathbf{j} = nq\mathbf{v}$ is the electric current density, $\omega_p = \sqrt{nq^2/\varepsilon_0 m}$ is the plasma frequency and $\omega_0 = -qB_0/m = eB_0/m$ is the electron cyclotron frequency.

Solving Eq. (5.14) with respect to $\mathbf{j}$ and substituting the result into Faraday's equation it can be shown that the permittivity response of the biased plasma is determined by [9]:

$$\overline{\overline{\varepsilon}} - \mathbf{1} = \frac{-\omega_p^2\left(\omega + i\Gamma\right)}{\omega(\omega + i\Gamma)^2 - \omega_0^2\omega}\mathbf{1}_t - \frac{i}{\omega}\frac{\omega_0\omega_p^2}{\left(\omega + i\Gamma\right)^2 - \omega_0^2}\hat{\mathbf{u}} \times \mathbf{1} + \frac{-\omega_p^2}{\omega\left(\omega + i\Gamma\right)}\hat{\mathbf{u}} \otimes \hat{\mathbf{u}}. \tag{5.15}$$

This result can be written in a more compact manner as:

$$\overline{\overline{\varepsilon}} = \varepsilon_t\mathbf{1}_t + \varepsilon_a\hat{\mathbf{u}} \otimes \hat{\mathbf{u}} + i\varepsilon_g\hat{\mathbf{u}} \times \mathbf{1}, \tag{5.16}$$

with

$$\varepsilon_t = 1 - \frac{\omega_p^2\,(1 + i\Gamma/\omega)}{(\omega + i\Gamma)^2 - \omega_0^2}, \quad \varepsilon_a = 1 - \frac{1}{\omega}\frac{\omega_p^2}{(\omega + i\Gamma)}, \quad \varepsilon_g = \frac{1}{\omega}\frac{\omega_0\omega_p^2}{\omega_0^2 - (\omega + i\Gamma)^2}. \tag{5.17}$$

The electromagnetic response has a broken time-reversal symmetry. In fact, flipping time requires flipping also $\mathbf{B}_0$, and thereby also the sign of ε_g. As a consequence, the electromagnetic response of a magnetized plasma is nonreciprocal ($\overline{\varepsilon} \neq \overline{\varepsilon}^T$).

The bias magnetic field bias forces the electrons to undergo circular cyclotron orbits in the bulk region with the angular frequency ω_0. The circular motion of the charged particles creates a drag-type effect when the electrons interact with a time varying field, which is at the origin of the Faraday rotation in bulk gyrotropic media. A simple way to picture the wave propagation in a magnetically biased plasma is to imagine that the wave goes through a centrifuge, e.g., rotating drum, and is dragged by the rotation of the walls. The static magnetic field effectively endows the material with an angular momentum. For example, suppose that the bias magnetic field is directed along $\hat{\mathbf{u}} = \hat{\mathbf{z}}$ with $B_0 > 0$ so that $\omega_0 > 0$. In this case, the electrons trail the cyclotron orbits in the anticlockwise direction with respect to $+z$, and thus the angular momentum of the medium is also directed along $+z$.

5.5.2 *Unidirectional Plasmons in Gyrotropic Media*

The plasmons supported by a magnetically biased plasma can have directional properties. To illustrate this idea, consider an interface between air (in the semi-space $z > 0$) and a gyrotropic electric material (in the semi-space $z < 0$; e.g., a magnetized plasma), as depicted in Fig. 5.3. It is supposed that the magnetic bias is oriented along the y-direction ($\mathbf{B}_0 = B_0\hat{\mathbf{u}}$ with $\hat{\mathbf{u}} = \hat{\mathbf{y}}$), i.e., it is parallel to the interface.

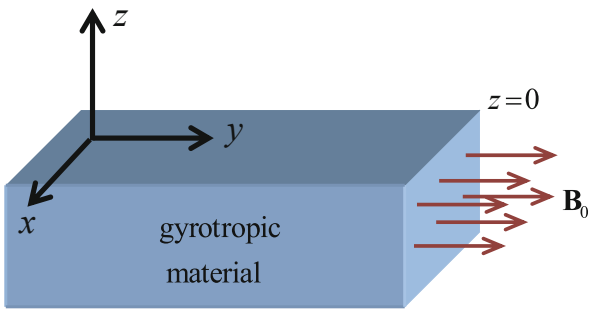

Fig. 5.3 Geometry of an air-gyrotropic material interface with the magnetic bias directed along the y-direction. The rotating motion of the charged particles in the bulk region drags the plasmons towards the $+x$-direction

The short-wavelength plasmons can be found using the quasi-static approximation $\mathbf{E} \approx -\nabla\phi$, and $\mathbf{H} \approx 0$, with the electric potential satisfying $\nabla \cdot (\overline{\varepsilon} \cdot \nabla\phi) = 0$ [10]. The plane wave solutions for the electric potential (with a spatial-variation $e^{i\mathbf{k}\cdot\mathbf{r}}$) in the bulk region of the gyrotropic material must satisfy $\mathbf{k} \cdot \overline{\varepsilon} \cdot \mathbf{k} = 0$. Hence, from Eq. (5.16) it follows that:

$$\varepsilon_t \left(k_x^2 + k_z^2\right) + \varepsilon_a k_y^2 = 0. \tag{5.18}$$

From here, we get $ik_z = \tilde{k}_\parallel$ with $\tilde{k}_\parallel = \sqrt{k_x^2 + \frac{\varepsilon_a}{\varepsilon_t} k_y^2}$. Thus, the electric potential associated with a surface plasmon in the air-gyrotropic material interface is of the form:

$$\phi_{\mathbf{k}} = A_{\mathbf{k}_\parallel} e^{i\mathbf{k}_\parallel \cdot \mathbf{r}} \begin{cases} e^{-k_\parallel z}, & z > 0 \\ e^{+\tilde{k}_\parallel z}, & z < 0 \end{cases} \tag{5.19}$$

with $\mathbf{k}_\parallel = k_x\hat{\mathbf{x}} + k_y\hat{\mathbf{y}}$ the transverse wave vector, $k_\parallel = \sqrt{k_x^2 + k_y^2}$ and $A_{\mathbf{k}_\parallel}$ a normalizing factor. Imposing that the normal component of the electric displacement vector is continuous at the interface, we obtain the following dispersion equation for the natural modes:

$$-k_\parallel = k_x \varepsilon_g + \tilde{k}_\parallel \varepsilon_t. \tag{5.20}$$

When dielectric function elements depend on frequency as in Eq. (5.17), one gets the explicit solution [10]:

$$\omega_{\mathbf{k}} \equiv \omega_\theta = \frac{\omega_0}{2}\cos\theta + \sqrt{\frac{\omega_p^2}{2} + \frac{\omega_0^2}{4}\left(1 + \sin^2(\theta)\right)}. \tag{5.21}$$

Here, θ is the wave vector angle measured with respect to the x-axis. The function $\omega_{\mathbf{k}}$ only depends on θ, but not on the magnitude of the wave vector.

Thus, in a magnetized electron gas the resonance frequency ($\omega_{\mathbf{k}}$) of the short-wavelength plasmons is direction dependent. Furthermore, when $\omega_0 > 0$ it can be checked that $\omega_- \le \omega_{\mathbf{k}} \le \omega_+$ with

$$\omega_+ \equiv \omega_{\theta=0} = \frac{1}{2}\left(\omega_0 + \sqrt{2\omega_p^2 + \omega_0^2}\right), \tag{5.22a}$$

$$\omega_- \equiv \omega_{\theta=\pi} = \frac{1}{2}\left(-\omega_0 + \sqrt{2\omega_p^2 + \omega_0^2}\right). \tag{5.22b}$$

Note that $\omega_\pm$ determine the plasmon resonances for propagation along the x-axis, i.e., along the direction perpendicular to the magnetic bias. The asymmetry between the $+x$ and $-x$ directions is due to the magnetic field bias.

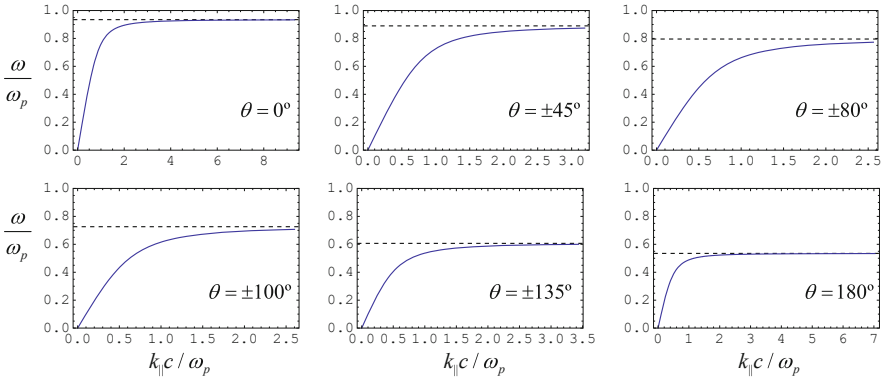

Fig. 5.4 Dispersion of the surface plasmons supported by an air-gyrotropic material interface for $\omega_0 = 0.4\omega_p$ along different directions of propagation θ. Solid blue lines: exact dispersion. Black dashed lines: quasi-static approximation [Eq. (5.21)]. Adapted from Ref. [10]

Figure 5.4 compares the exact plasmon dispersion with the quasi-static approximation for the case $\omega_0 = 0.4\omega_p$, showing that $\omega_\theta = \lim_{k\to\infty}\omega_{\mathbf{k}}^{\text{exact}}$. For frequencies on the order of ω_p the plasmons are effectively dragged to the semi-space $x > 0$ by the rotating motion of the electrons. This effect can lead to a regime where the surface plasmon propagation is allowed only within a sector that contains the positive x-axis [10, 11].

5.5.3 *Drift-Current Bias*

The drift-current bias is another mechanism to break the Lorentz reciprocity. However, it is usually rather impractical because significant nonreciprocal effects require large drift velocities comparable to the phase velocity of the wave. Graphene can offer a truly unique opportunity in this context: its ultra-high electron mobility may enable drift velocities on the order of $v_F = c/300$, which may be several orders of magnitude larger than the drift velocities of typical metals and several times larger than in high-mobility semiconductors [12]. A sketch of a graphene sheet biased with a drift current is shown in Fig. 5.5.

A drift-current endows the material with a linear momentum bias. Based on analogy with moving media, it can be shown that the effect of the drift-current bias on the graphene conductivity can be described by a Galilean-type Doppler transformation [13–15] that leads to $\sigma_{\text{g}}^{\text{drift}} = \sigma_{\text{g}}^{\text{Gal}}$ with

$$\sigma_{\text{g}}^{\text{Gal}}(\omega, k_x) = \frac{\omega}{\tilde{\omega}}\sigma_{\text{g}}(\tilde{\omega}, k_x) = i\,\omega\sigma_0\frac{8}{\pi}\omega_F\frac{1}{\tilde{\omega}\sqrt{\tilde{\omega}^2 - v_F^2k_x^2} + \tilde{\omega}^2 - v_F^2k_x^2}. \tag{5.23}$$

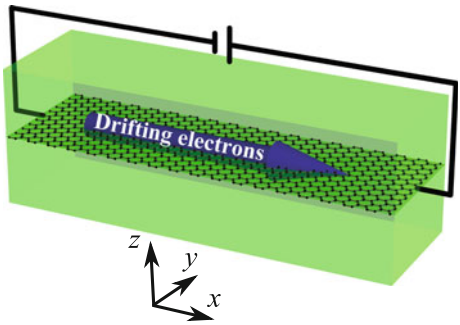

Fig. 5.5 Drift current biasing of graphene. A static voltage generator induces an electron drift in a graphene sheet. Adapted from Ref. [13]

Here, $\sigma_0 = e^2/(4\hbar)$, $\omega_F = E_F/\hbar$ with E_F the Fermi level of graphene, $\sigma_g(\omega, k_x)$ is the nonlocal conductivity of graphene with no drift and $\tilde{\omega} = \omega - k_x v_0$ is the Doppler shifted frequency. We neglect interband transitions and consider the low temperature limit. Since $\sigma_g^{\text{Gal}}(\omega, k_x) \neq \sigma_g^{\text{Gal}}(\omega, -k_x)$, the drift-current biased graphene exhibits a nonreciprocal electromagnetic response.

A different model for the drift-biased conductivity is obtained by evaluating the graphene response with a skewed Fermi distribution [16–18]. The physics predicted by such a model is well captured by a relativistic-type Doppler-shift transformation [15], such that $\sigma_g^{\text{drift}} = \sigma_g^{\text{Rel}}$ with

$$\sigma_g^{\text{Rel}}(\omega, k_x) = i\,\omega\sigma_0 \frac{8}{\pi}\omega_F \frac{1}{\gamma\,(\omega - v_0 k_x)\sqrt{\omega^2 - v_F^2 k_x^2} + \omega^2 - v_F^2 k_x^2}, \tag{5.24}$$

where $\gamma = 1/\sqrt{1 - v_0^2/v_F^2}$ the Lorentz factor in graphene.

With a quasi-static approximation the dispersion of the graphene plasmons is determined by $q - 2\varepsilon_{\text{r,s}}\kappa_g^{\text{drift}} = 0$ with $q = \sqrt{k_x^2}$ and $\kappa_g^{\text{drift}} = i\omega\varepsilon_0/\sigma_g^{\text{drift}}$ [13]. The parameter κ_g^{drift} can be explicitly written as

$$\kappa_g^{\text{Gal}} = \frac{1}{\alpha c 8\omega_F}\left(\tilde{\omega}\sqrt{\tilde{\omega} - v_F k_x}\sqrt{\tilde{\omega} + v_F k_x} + \tilde{\omega}^2 - v_F^2 k_x^2\right), \tag{5.25a}$$

$$\kappa_g^{\text{Rel}} = \frac{1}{\alpha c 8\omega_F}\left(\gamma\,\tilde{\omega}\sqrt{\omega - v_F k_x}\sqrt{\omega + v_F k_x} + \omega^2 - v_F^2 k_x^2\right), \tag{5.25b}$$

for the Galilean Doppler-shift and relativistic Doppler-shift models, respectively.

Figure 5.6 shows the impact of the drift-current bias on the graphene plasmons. As seen, due to the time-reversal symmetry breaking, the dispersion suffers a blue (red) shift for plasmons co-propagating (counter-propagating) with the drifting electrons. The effect is considerably stronger in the Galilean Doppler-shift model, which predicts the emergence of unidirectional plasmon waves (see the blue lines in the right-panel of Fig. 5.6).

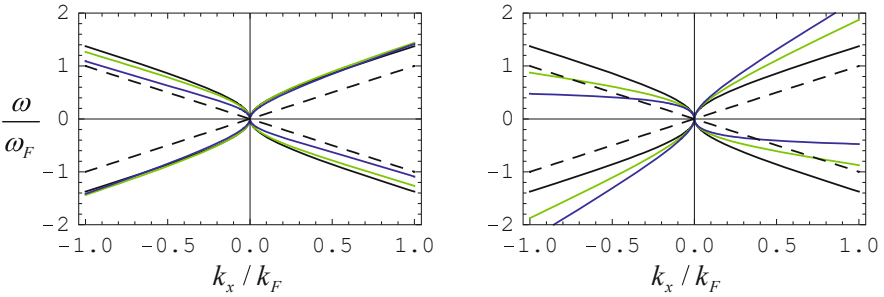

Fig. 5.6 Normalized dispersion of the graphene plasmons with a drift-current bias for $\varepsilon_{\mathrm{r,\,s}} = 4.0$ and $k_F = \omega_F/v_F$. Left: Relativistic Doppler-shift model. Right: Galilean Doppler-shift model. Black lines: $v_0 = 0$; Green lines: $v_0 = 0.5v_F$. Blue lines: $v_0 = 0.9v_F$.The dashed lines represent $\omega = \pm k_x v_F$

5.6 Topological Photonics

Topology studies the properties of objects that stay invariant under a continuous transformation. When some property of a mathematical object is unaffected by a deformation it is called a topological invariant. For example, in the theory of surfaces the number of holes is a topological invariant known as the genus. Any continuous deformation of the surface must preserve the genus, which is thereby a global property fully independent of any local features of the surface.

It is possible to characterize the topology of other more abstract mathematical objects, e.g., Hermitian operators, for which the topological invariants do not have an immediate geometrical visualization [19]. Next, we focus on the characterization of the topological phases of lossless electromagnetic continua.

5.6.1 Topological Classification of Electromagnetic Continua

The topological classification of physical systems is rooted in the cyclic structure of the wave vector space [19]. Indeed, to ensure that the topological invariant –the Chern number– is an integer, it is necessary that the underlying space is a closed surface with no boundary. In a periodic system the relevant space is the Brillouin zone, which is isomorphous to a torus.

It is relevant to extend topological ideas to physical systems with no intrinsic periodicity, e.g., to metamaterials modeled by some effective parameters [20]. Indeed, the electrodynamics of continuous media is much simpler than that of periodic structures, and this simplicity may give additional physical insights and a deeper understanding of topological photonics. Similar to periodic systems, due to the frequency dispersion of the material response, continuous media are also characterized by an intricate band structure. However, unlike in periodic structures,

for continuous media the wave vector space is an unbounded open region (the Euclidean space). In Ref [20], it was shown that despite this unusual feature it is possible to characterize the topological phases of electromagnetic systems when a suitable regularization process is applied to the material response.

Specifically, the response of a material described by the local material matrix $\mathbf{M}(\omega)$ can be regularized as follows:

$$\mathbf{M}_{\text{reg}}(\omega, \mathbf{k}) = \mathbf{M}_\infty + \frac{1}{1 + k^2/k_{\text{max}}^2}\left[\mathbf{M}(\omega) - \mathbf{M}_\infty\right], \tag{5.26}$$

where $\mathbf{M}_\infty = \lim_{\omega \to \infty} \mathbf{M}(\omega)$. Here, k_{max} is a high-frequency wave vector cut-off, which can be arbitrarily large. The regularized material response is evidently spatially dispersive (nonlocal), as it depends on the wave vector $\mathbf{k}$. Clearly, for $k << k_{\text{max}}$ the transformed material matrix is nearly coincident with the original material matrix: $\mathbf{M}_{\text{reg}}(\omega, \mathbf{k}) \approx \mathbf{M}(\omega)$. The cut-off ensures that as $k \to \infty$ the material response approaches that of vacuum ($\lim_{k \to \infty} \mathbf{M}_{\text{reg}}(\omega, \mathbf{k}) = \mathbf{M}_\infty$), similar to what happens in the $\omega \to \infty$ limit.

The physical justification to introduce a cut-off is that in a realistic material a field with a very fast spatial variation cannot effectively polarize the microscopic constituents of the medium, and hence the material response is expected to vanish when $k \to \infty$.

Figure 5.7 depicts the band diagram of an electric gyrotropic material with $\hat{\mathbf{u}} = \hat{\mathbf{z}}$ (see Eq. (5.16)) and the permittivity elements:

$$\varepsilon_t = 1 + \frac{\omega_0 \omega_e}{\omega_0^2 - \omega^2}, \quad \varepsilon_g = \frac{\omega_e \omega}{\omega_0^2 - \omega^2}, \varepsilon_a = 1. \tag{5.27}$$

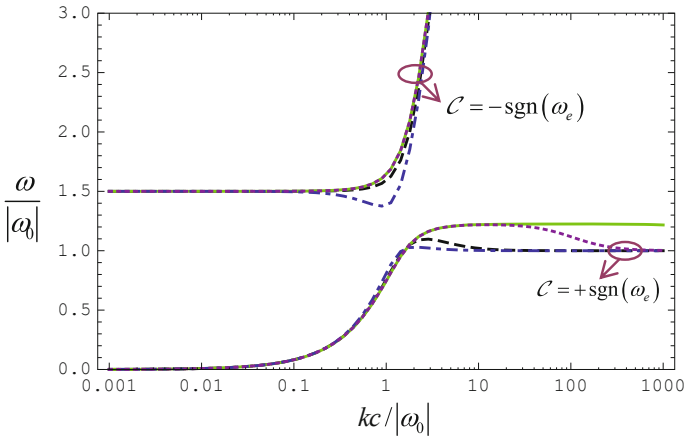

Fig. 5.7 Effect of the high-frequency spatial cut-off on the band structure ω vs. k of a gyrotropic material with $\omega_e = 0.5\omega_0$ and (i) (green solid lines) no spatial-cut off, (*iii*) (purple dotted lines) $k_{\text{max}} = 100|\omega_0|/c$, (*iii*) (black dashed lines) $k_{\text{max}} = 3|\omega_0|/c$, and (*iv*) (blue dot-dashed lines) $k_{\text{max}} = |\omega_0|/c$. Adapted from Ref. [20]

In the above, $|\omega_0|$ is the resonance frequency and ω_e determines the resonance strength. The parameter ω_0 may be either positive or negative and it is necessary that $\omega_0\omega_e > 0$. The dispersion of transverse magnetic (TM) waves with $E_z = 0$ and $H_z \neq 0$ is given by:

$$k_x^2 + k_y^2 = \frac{\varepsilon_t^2 - \varepsilon_g^2}{\varepsilon_t}\left(\frac{\omega}{c}\right)^2. \tag{5.28}$$

As seen in Fig. 5.7, for $k << k_{\max}$ the band structure calculated with the cut-off (purple, black and blue lines) is nearly coincident with the band structure of the original gyrotropic material (green lines, for $k_{\max} = \infty$). By increasing $k_{\max}$ the coincidence can be made as good as one may wish. For $k >> k_{\max}$, the band structure inevitably depends on the spatial cut-off.

Notably, when the spatial cut-off is enforced the Chern numbers are always integer numbers. The Chern invariants are calculated as explained in Ref. [20], including the wave vector cut-off in the permittivity response of the material. It turns out that independent of the value $k_{\max}$ (at least for a sufficiently large $k_{\max}$) the Chern invariant of the high-frequency band is $\mathcal{C}_n = -\operatorname{sgn}(\omega_e)$, and the Chern invariant of the low-frequency band is $\mathcal{C}_n = +\operatorname{sgn}(\omega_e)$. In practice, the sign of ω_e depends on the direction of a bias magnetic field.

5.6.2 Bulk-Edge Correspondence

The most celebrated property of topological systems is the bulk-edge correspondence [21–23]. It establishes that when two inequivalent topological materials are paired the corresponding material interface must forcibly support a net number of *unidirectional* edge states determined by the difference of the gap Chern numbers of the bulk materials. Furthermore, the edge states are gapless and hence their dispersion must cross the common band-gap.

5.6.3 Ill-Defined Topologies and Energy Sinks

From the previous subsections, it is clear that some physical systems cannot be topologically classified even though their spectrum has a full band-gap. This property can be explained in a geometrical way. Specifically, consider the mathematical objects represented in Fig. 5.8a. The objects on the left and right panels have a well defined topology determined by the genus of the corresponding surface. In contrast, the object in the middle panel has an ill-defined topology. Indeed, the cross-sectional cut of a torus with vanishing inner radius consists of two-kissing circles, and, thereby the number of holes of the surface is indefinite.

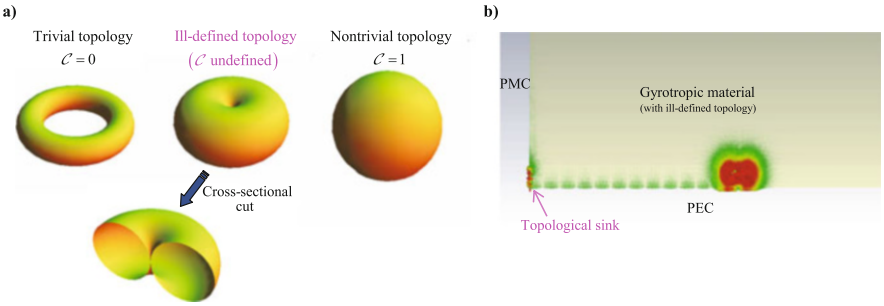

Fig. 5.8 (**a**) Geometrical illustration of the concept of an ill-defined topology. The torus and the sphere on the left and right panels have well defined topologies determined the number holes of each surface. In contrast a torus with a vanishingly small inner radius (middle panel) has an ill-defined topology. (**b**) A nonreciprocal material with a continuous translational symmetry has an ill-defined topology, and can be used to realize a topological energy sink that drags towards its interior the radiation generated in the surroundings

Ill-defined topologies arise naturally in the study of the wave propagation in physical systems with a continuous translational symmetry. Indeed, consistent with Sect. 5.6.1 the topological classification of continuum models requires the regularization of the system response with some high-spatial frequency cut-off. Without the spatial cut-off, the topology is ill-defined in the same manner as the topology of the torus with vanishing inner radius is ill-defined. A practical consequence of this is that the wave propagation in such systems is not constrained by the bulk-edge correspondence principle [22]. Mathematically the pathologic situation arises due to the continuous translational symmetry of the material.

Remarkably, an ill-defined topology creates an opportunity to halt a wave in a carefully designed electromagnetic waveguide, leading to the formation of hotspots where the electromagnetic fields are massively enhanced [24]. This idea is illustrated in Fig. 5.8b which represents an edge-type unidirectional (horizontal) waveguide formed by a PEC wall and a gyrotropic material with an ill-defined topology. Interestingly, an interface of the same gyrotropic material and a PMC wall does not support propagating states. This is only possible due to the breakdown of the bulk-edge correspondence in media with an ill-defined topology [22].

The breakdown of the bulk-edge correspondence creates a deadlock for the unidirectional edge mode propagating in the horizontal guide. At the junction point, the incoming wave has no place to go: it cannot propagate to the vertical PMC wall, it cannot escape to the bulk regions and it cannot be back-reflected because the edge mode is unidirectional and immune to backscattering. Therefore, in the idealized case of lossless materials, the electromagnetic energy is forced to accumulate at the vertex point of the PEC and PMC walls. Thus, ill-defined topologies can lead to the formation of energy sinks with ultra-singular fields that absorb all the energy generated in their surroundings. Such systems can be useful, for example, for energy harvesting or to enhance nonlinearities [24].

References

1. Feynman R, Leighton R, Sands M (1963) The Feynman lectures on physics. California Institute of Technology
2. Silveirinha MG (2019) Time-reversal symmetry in antenna theory. Symmetry 11:486
3. Silveirinha MG (2019) Hidden time-reversal symmetry in dissipative reciprocal systems. Opt Express 27:14328
4. Shen S-Q (2012) Topological insulators, Solid state sciences, vol 174. Springer, Berlin, p 98
5. Silveirinha MG (2017) PTD symmetry protected scattering anomaly in optics. Phys Rev B 95:035153
6. Martini E, Silveirinha MG, Maci S (2019) Exact solution for the protected TEM edge mode in a PTD-symmetric parallel-plate waveguide. IEEE Trans Antennas Propag 67:1035–1044
7. Chen W-J, Zhang Z-Q, Dong J-W, Chan CT (2015) Symmetry-protected transport in a pseudospin-polarized waveguide. Nat Commun 6:8183
8. Caloz C, Alù A, Tretyakov S, Sounas D, Achouri K, Deck-Léger Z-L (2018) Electromagnetic nonreciprocity. Phys Rev Applied 10:047001
9. Bittencourt JA (2010) Fundamentals of plasma physics, 3rd edn. Springer, New York
10. Silveirinha MG, Gangaraj SAH, Hanson GW, Antezza M (2018) Fluctuation-induced forces on an atom near a photonic topological material. Phys Rev A 97:022509
11. Gangaraj SAH, Hanson GW, Silveirinha MG, Shastri K, Antezza M, Monticone F (2019) Truly unidirectional excitation and propagation of difractionless surface plasmon-polaritons. Phys Rev B 99:245414
12. Gonçalves PAD, Peres NMR (2016) An introduction to graphene plasmonics. World Scientific, Hackensack
13. Morgado TA, Silveirinha MG (2018) Drift-induced unidirectional graphene plasmons. ACS Photonics 5:4253
14. Morgado TA, Silveirinha MG (2017) Negative Landau damping in bilayer graphene. Phys Rev Lett 119:133901
15. Morgado TA, Silveirinha MG (2019) Reply to comment on "negative Landau damping in bilayer graphene". Phys Rev Lett 123:219402
16. Borgnia DS, Phan, TV, Levitov LS Quasi-relativistic Doppler effect and non-reciprocal Plasmons in graphene. arXiv 1512.09044
17. Van Duppen B, Tomadin A, Grigorenko AN, Polini M (2016) Current-induced birefrigent absorption and non-reciprocal plasmons in graphene. 2D Materials 3:015011
18. Wenger T, Viola G, Kinaret J, Fogelström M, Tassin P (2018) Current-controlled light scattering and asymmetric plasmon propagation in graphene. Phys Rev B 97:085419
19. Ozawa T, Price HM, Amo A, Goldman N, Hafezi M, Lu L, Rechtsman MC, Schuster D, Simon J, Zilberberg O, Carusotto I (2019) Topological photonics. Rev Mod Phys 91:015006
20. Silveirinha MG (2015) Chern invariants for continuous media. Phys Rev B 92:125153
21. Hatsugai Y (1993) Chern number and edge states in the integer quantum hall effect. Phys Rev Lett 71:3697
22. Silveirinha MG (2016) Bulk edge correspondence for topological photonic continua. Phys Rev B 94:205105
23. Silveirinha MG (2019) Proof of the bulk-edge correspondence through a link between topological photonics and fluctuation-electrodynamics. Phys Rev X 9:011037
24. Fernandes DE, Silveirinha MG (2019) Topological origin of electromagnetic energy sinks. Phys Rev Appl 12:014021

Chapter 6
All-Dielectric Nonlinear Meta-Optics

Giuseppe Marino, Carlo Gigli, Valerio F. Gili, and Giuseppe Leo

Abstract Optical metasurfaces are arrays of coupled optical antennas, with sub-wavelength size and separation. In the past two decades, their optical properties have been mostly demonstrated with either metallic or amorphous dielectric nanostructures. Since the former suffer from strong dissipation near the plasmon resonance and they are both only weakly nonlinear, AlGaAs nanoparticles have recently attracted a great deal of interest because of their huge non-resonant $\chi^{(2)}$ nonlinearity. In this chapter, besides briefly recalling the bases of nonlinear optics, we will first describe the main modeling approaches for linear and nonlinear nano-optics. Finally we will review the recent demonstrations of AlGaAs-on-insulator nanoantennas and metasurfaces as efficient second harmonic emitters, with a focus on their potential for both beam shaping of classical harmonic fields and the generation of engineered quantum photon states.

Keywords Nonlinear optics · Nanophotonics · Metasurfaces

6.1 Introduction

As is well known for metals with plasmonic resonances, also dielectrics can operate at optical frequencies and nanoscale sizes. The different physics of these two systems (the former exhibits the collective oscillation of free conduction electrons, while in the latter the induced currents are generated by the displacement of bound valence electrons) highlights the main issue of plasmonics at optical frequencies: ohmic losses [1]. While in dielectrics the displacement currents generated by

G. Marino · C. Gigli · G. Leo (✉)
Matériaux et Phénomènes Quantiques, Université de Paris & CNRS, Paris, France
e-mail: giuseppe.leo@univ-paris-diderot.fr

V. F. Gili
Institute of Applied Physics, Abbe Center of Photonics, Friedrich-Schiller-Universität Jena, Jena, Germany

M. Cesaria et al. (eds.), *Light-Matter Interactions Towards the Nanoscale*,
NATO Science for Peace and Security Series B: Physics and Biophysics,
https://doi.org/10.1007/978-94-024-2138-5_6

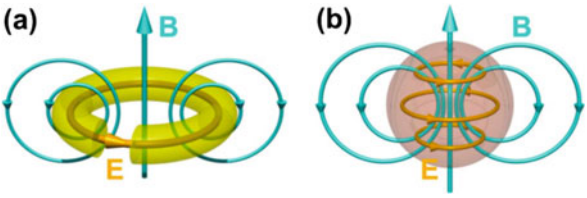

Fig. 6.1 Magnetic dipole resonances supported by plasmonic (**a**) and dielectric (**b**) nanostructures. In the metallic case, optical magnetism is artificially obtained by resorting to particular geometries such as the split-ring resonator. Conversely, for dielectric nanoparticles optical magnetism occurs naturally as a consequence of high field confinement in the bulk. *Reproduced from* [6]. *CC BY-NC-SA 3.0*

bound electrons motion do not dissipate energy, surface plasmons undergo ultrafast dephasing and decay after a few femtoseconds, both by radiative damping and via the formation of hot carriers. These relax in the picosecond timescale by locally increasing the temperature of the nanostructures and their immediate vicinity up to values of 1000 °C [2, 3]. Conversely, losses in dielectric nano-objects can be practically neglected as long as we excite them with energies below the gap.

Another key difference is that metals only support electric type resonances, due to the smaller penetration depth caused by electrostatic screening. This prevents the formation of circulation currents inside the bulk of the metallic nanoparticle, which are necessary to the excitation of magnetic multipole moments. As such, a magnetic response in plasmonic nanostructures can only be achieved through careful engineering of their geometry. The archetypal example in this sense is the split-ring resonator reported in Fig. 6.1 [4, 5], where the real currents excited by an external field produce a transverse oscillating magnetic field in the center of the ring, which simulates an oscillating magnetic dipole. In contrast, high-index dielectric nanostructures naturally offer magnetic resonances as the field is well confined in the bulk due to total internal reflection [6].

Interestingly, in some cases the magnetic response of dielectric nanoparticles can even be higher than the electric one. This happens for example in the case of an AlGaAs nanocylinder with $r = 225$ nm and $h = 400$ nm, where the magnetic dipole (MD) resonance is stronger than the electric dipole (ED) [7]. Such effects have given origin to the concept of "magnetic light".

Despite the advantage of having a mode well confined in the bulk, field enhancements are less important for dielectric nanoparticles. The reason for that is twofold: on the one hand in metals the electromagnetic field does not penetrate much into the bulk, and on the other hand to obtain plasmonic resonances in the visible the typical sizes of the nanostructures are of the order of tens of nanometers. In contrast, for resonances to be excited in dielectric particles we need typical diameters of a few hundreds of nanometers. For these two reasons the electromagnetic field in plasmonic nanostructures is compressed in smaller volumes very near to the surface, giving rise to field enhancements as high as $E/E_0 \approx 10^3$, while for dielectric structures we have $E/E_0 \approx 10$. This handicap does not reduce the potential of

dielectric nanostructures to achieve nonlinear conversion efficiencies many orders of magnitude higher than with plasmonics. This happens thanks to the negligible losses and field confinement inside the structures, allowing for greater effective interaction volume between the incident field and the bulk nonlinearity.

6.2 Theory and Numerical Modeling

This section outlines the theoretical grounds for understanding the nonlinear processes in the most effective optical nanostructures reported in the last few years. First, a quick reminder of nonlinear optics will be given, followed by an introduction to nano-optics, with a focus on the case of dielectric nanostructures dealt with in this chapter.

6.2.1 Principles of Nonlinear Nano-Optics

Since excellent textbooks exist on nonlinear optics [8], let us limit ourselves to recalling its basic notions.

When an electric field is applied to a homogeneous dielectric material, the latter gets polarized according to the law $P_i = \varepsilon_0 \sum_j \chi_{ij}^{(1)} E_j$, where $\chi^{(1)}$ is the linear susceptibility tensor, and ε_0 the free-space permittivity. This simple relation however only holds in the case of linear response of the material. If a higher input intensity allows for a more general super-linear dependence, the induced polarization can be expressed as a Taylor expansion [8] (we neglect dispersion and losses of the medium):

$$P_i = \varepsilon_0 \left(\sum_j \chi_{ij}^{(1)} E_j + \sum_{j,k} \chi_{ijk}^{(2)} E_j E_k + \sum_{j,k,l} \chi_{ijkl}^{(3)} E_j E_k E_l + \dots \right)$$

where we call $\chi_{ijk}^{(2)}$ and $\chi_{ijkl}^{(3)}$ second- and third-order nonlinear susceptibilities. For centrosymmetric materials, it is easily shown that all even terms in the expansion vanish because $\chi^{(2n)} = 0 \; \forall \; n$. Throughout this chapter, we will focus our attention just on $\chi^{(2)}$ processes as they are dominant in non-centrosymmetric materials.

Let us consider as a first approximation a linearly polarized monochromatic plane wave incident field (called pump):

$$E(t) = E_0 e^{-i\omega t} + c.c.$$

then the second-order polarization reads

$$P^{(2)}(t) = 2\varepsilon_0 \chi^{(2)} E E^* + \left(\varepsilon_0 \chi^{(2)} E^2 e^{-i2\omega t} + c.c.\right)$$

The second term corresponds to Second Harmonic Generation (SHG) and can be understood as the creation of one photon with frequency 2ω by simultaneously annihilating two pump photons with frequency ω. The first term instead refers to the generation of a static field, called optical rectification, often used to generate THz radiation. Let us now allow two pump frequency components instead of a single one:

$$E(t) = E_1 e^{-i\omega_1 t} + E_2 e^{-i\omega_2 t} + c.c.$$

We then find a richer second-order nonlinear response:

$$P^{(2)}(t) = 2\varepsilon_0 \chi^{(2)} \left(E_1 E_1^* + E_2 E_2^*\right) + \varepsilon_0 \chi^{(2)} \times \left(E_1^2 e^{-i2\omega_1 t} + E_2^2 e^{-i2\omega_2 t} + 2E_1 E_2 e^{-i(\omega_1+\omega_2)t} + 2E_1 E_2^* e^{-i(\omega_1-\omega_2)t} + c.c.\right)$$

The first line of the equation describes optical rectification, and the first two terms in the second line refer to SHG from the two pump frequencies. The last two terms are absent in the case of monochromatic pump and refer to Sum-Frequency Generation (SFG) and Difference-Frequency Generation (DFG), respectively. One last process to be mentioned is Spontaneous Parametric Down-Conversion (SPDC), the time-reversed process of SFG, which allows the generation of two photons with frequency ω_1 and ω_2 starting from a single pump photon at $\omega_1 + \omega_2$.

This SFG-SPDC correspondence is important for our experimental results and will be described in greater detail in the next chapters. SPDC is widely used in quantum optics to generate entangled photon pairs [9]. All $\chi^{(2)}$ processes are summarized in Fig. 6.2. The nonlinear polarization frequency components act as a source of new electromagnetic waves. Let us therefore look at how Maxwell's equations describe frequency mixing in the nonlinear medium and the generation of the nonlinear fields. In the absence of free charges and currents, the nonlinearity of a non-magnetic medium is expressed by the relation between the displacement and electric fields, $D = \varepsilon_0 E + P$, where $P = P^{(1)} + P^{NL}$ contains both the linear and the nonlinear polarization response of the medium depending on the intensity of the electric field E.

We can alternatively separate the linear and nonlinear electric displacement contributions as $D = D^{(1)} + D^{NL}$, where $D^{(1)} = D = \varepsilon_0 E + P^{(1)} = \varepsilon_0 \varepsilon_r E$ (by

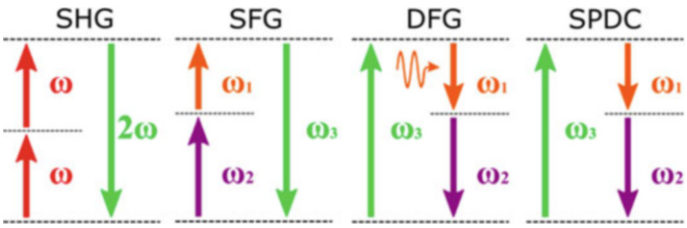

Fig. 6.2 Energy level diagrams of $\chi^{(2)}$ processes. It should be noted that the intermediate energy levels correspond to virtual states

writing ε_r as a real scalar quantity we have implicitly assumed an isotropic and lossless medium as well). Maxwell's equations are then given by

$$\nabla \cdot D = 0$$

$$\nabla \cdot B = 0$$

$$\nabla \times E = -\frac{\partial B}{\partial t}$$

$$\nabla \times H = \frac{\partial D}{\partial t}$$

We then take the curl of the curl of the electric field, change the space and time derivation order on the right side of the equation, and replace it with the curl of the magnetic field. The result of these manipulation is:

$$\nabla \times \nabla \times E = -\mu_0 \frac{\partial^2 D}{\partial t^2}$$

The left-side term can be simplified using the vector relation:

$$\nabla \times \nabla \times E = \nabla (\nabla \cdot E) - \nabla^2 E$$

Under some general assumptions, the divergence term can be neglected even in nonlinear optic where the relation between D and E is not trivial [8]. By now, using the above equations along with $\mu_0 \varepsilon_0 = 1/c^2$, we can finally write:

$$\left[\nabla^2 - \frac{\varepsilon_r}{c^2}\frac{\partial^2}{\partial t^2}\right] E = \frac{1}{\varepsilon_0 c^2}\frac{\partial^2 P^{NL}}{\partial t^2}$$

In this inhomogeneous equation, the nonlinear polarization acts as a source. The fields can now be expressed in terms of the linear and nonlinear frequency components:

$$E = \sum_n E_n(r)e^{-i\omega_n t} + c.c.$$

$$D^{(1)} = \sum_n D_n^{(1)}(r)e^{-i\omega_n t} + c.c.$$

$$P^{NL} = \sum_n P_n^{NL}(r)e^{-i\omega_n t} + c.c.$$

where the summation index n runs over all frequency components present in our system. By substituting the summations in the wave equation, after some manipulation we obtain that each frequency component separately satisfies its own inhomogeneous wave equation:

$$\left[\nabla^2 \frac{\omega_n^2}{c^2}\varepsilon_r\,(\omega_n)\right] E_n(r) = -\frac{\omega_n^2}{\varepsilon_0 c^2} P^{NL}(r)$$

Where material dispersion is taken into account via the dependence of the relative permittivity on the frequency. The wave equation here derived allows to quantitatively describe all the nonlinear optical interactions of Fig. 6.2.

Phase-Matching Considerations If we solve the nonlinear wave equation, for example in case of SHG in a bulk crystal, we will find that the nonlinear field will sinusoidally depend on the position along the propagation direction (for example z): $E_{SHG} \sim e^{i\Delta kz}$, where $\Delta k = k_{2\omega} - 2k_{\omega}$, implying that the nonlinear signal builds up inside the nonlinear medium only for a certain length, and then decreases. This phenomenon can be understood with the following argument: as the generation of nonlinear light is a very weak local process, it is not trivial in general to achieve macroscopically detectable signals. Indeed, after a certain length called coherence length ($L_c = \pi/\Delta k$), the nonlinear light accumulates a π phase difference relative to the pump, thus the nonlinear light generated in the next coherence length will be out of phase with respect to the previous one, resulting in destructive interference. L_c depends on various parameters including pump wavelength, the nature of the nonlinear process and field confinement in the nonlinear medium. For example, in the case of SHG in GaAs from a 1.55 μm pump, L_c can be as small as a few micrometers [10].

In order to induce constructive interference between the local nonlinear sources throughout the whole crystal it is necessary to match the phase velocity of the pump and that of the nonlinear signal. This results in the so-called phase matching (PM) condition between k vectors: $\Delta k = 0$.

If we now go back to the local interpretation of nonlinear processes, this relation can be seen as a momentum conservation condition to apply to the SHG process. By recalling Noether's theorem of classical mechanics, every symmetry in a physical system is accompanied by a conserved quantity and vice versa. Momentum conservation in particular stems from translational invariance, which in first approximation is perfectly consistent with the request that the nonlinear signal propagates throughout the whole nonlinear medium. The reason why this condition is not always easily achieved in real materials becomes evident if we rewrite the PM condition for SHG $k_{2\omega} = 2k_{\omega}$ as $2\omega n(2\omega)/c = 2\omega n(\omega)/c$ or $n(2\omega) = n(\omega)$, insofar as the dispersion of refractive index n makes PM difficult to be obtain. For example, in optical waveguides, a number of techniques have been developed to solve this problem, such as birefringent PM, quasi-PM, and modal PM [10–12].

All the above considerations on PM apply in the case of propagating nonlinear signals, which implies that the dimensions of the host media should be larger than the signal's wavelength. If we now consider nonlinear effects in sub-wavelength structures, which in the case of optical frequencies means dimensions of the order of a few hundred nanometers, it becomes intuitively clear that PM is no longer available to make nonlinear signals macroscopically significant. In other words, as the coherence length L_c is of the order of several micrometers, the nonlinear signal does "not travel enough" in the medium to build up a sufficiently large phase-mismatch to require a condition on wave-vectors. Therefore, if we want to boost nonlinear effects at the nanoscale, we need to benefit from some local enhancement of both the interacting fields and their spatio-temporal overlap.

This approach is common (but not always well understood) in macroscopic intracavity nonlinear optics, where Fabry-Perot (FP) or whispering-gallery-mode (WGM) low-loss cavities have been around for decades. However in those cases, instead of considering the inherently three-dimensional nature of the resonating fields, these are usefully factorized in two terms: a purely propagating one along the coordinate of translational (FP) or azimuthal (WGM) invariance, plus a two-dimensional distribution in the transverse plane. Accordingly, as it is standard in bulk crystals or waveguides, one can use a coupled-mode approach where a slowly-varying amplitude and phase mismatch occur along many-wavelengths-long roundtrips, while two-dimensional overlap integrals can be readily calculated in the transverse plane. All this is not applicable to subwavelength nanoresonators where, despite a strong spatial confinement, losses are huge (low quality-factor) and momentum conservation does not apply.

The above discussion naturally brings us to illustrating what we believe to be the two most powerful modeling approaches for nonlinear nanophotonics: the multipolar expansion associated to Mie theory, and the quasi-normal mode description.

6.2.2 Multi-polar Modelling of Nanoscale Optics

Light scattering from dielectric objects is a broadly studied subject and gives rise to a large number of interesting effects depending on the dimensions of the object(s) compared to the wavelength λ, reflected in the size parameter $x = 1/\lambda$, their refractive index, and the product of these two. For example, in case of λ much larger than the object(s) dimensions ($x << 1$, $x(n\text{-}1) << 1$) we are in Rayleigh scattering regime, while for the opposite case ($x >> 1$) we find geometric optics.

In 1908 Gustav Mie developed a theory describing the case of $x \approx 1$, $(n\text{-}1) \geq 1$ in an effort to understand the various colors assumed by the scattered and absorbed visible light shined on gold nanoparticles in colloidal solution. He considered a homogeneous sphere of radius a and refractive index N_1, embedded in a medium of index N illuminated by a plane wave with amplitude E_0. Starting from Maxwell's equations and introducing a scalar function ψ and two auxiliary vector fields $M(\psi)$ and $N(\psi)$, Mie theory provides a set of solutions $\psi(r,\theta,\varphi)$ of the scalar wave equation in spherical coordinates under the hypothesis of separation of variables. From such solutions, which are given by the product of spherical Bessel functions $Z_n(r)$, sinusoidal functions $\Phi_m(\varphi)$ and the associated Legendre functions $P_n^m(\cos\theta)$, one can develop the incident, internal and scattered electric fields in series of even/odd (e/o) spherical harmonics $M^{(q)}_{e/o,m=1,n}$, $N^{(q)}_{e/o,m=1,n}$, where the superscript (q) indicates qth-type spherical Bessel function ($q = 1$ for the incident and internal fields, to grant for finiteness at the origin; $q = 3$ for the scattered field, to grant for an asymptotic behavior of an outgoing spherical wave). In particular, the scattered field reads:

$$E_{sca} = E_0 \sum_{n=1}^{\infty} i^n \frac{2n+1}{n\,(n+1)} \left(a_n N^{(3)}_{o,1,n} - \mathrm{i} b_n M^{(3)}_{e,1,n} \right)$$

As we have written the internal and scattered fields as infinite series in the vector spherical harmonics N_n and M_n, the latter take on the meaning of electromagnetic normal modes. In particular, N_n give rise to modes with zero radial magnetic field component, called electric type modes, while M_n give rise to modes with zero radial electric field component resonances, i.e. magnetic type modes.

In general, the scattered field is a superposition of normal modes, weighted by appropriate coefficients a_n (electric) and b_n (magnetic). After some math, an explicit expression for a_n and b_n can be found, which depend on Riccati-Bessel functions of the size parameter x (typically $x \approx 1$ for our sub-wavelength optical nanoparticles) and the refractive index. As the coefficients a_n and b_n respectively weight N_n and M_n, (electric and magnetic normal modes), they are respectively called electric and magnetic multipole coefficients. Their role is very important to understand the nonlinear response of optical nanoparticles.

Finally, an extinction cross section can be introduced, defined as the total attenuation of energy from the incident beam flux due to both absorption and scattering by the sphere ($C_{ext} = C_{abs} + C_{sca}$). Let us construct an imaginary

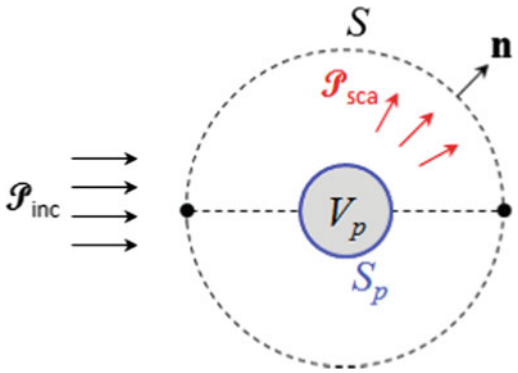

Fig. 6.3 Estimation of extinction and scattering cross sections: an imaginary sphere with surface S is constructed around the nanoparticle and the electromagnetic energy rates across this surface are calculated. S_p and V_p refer to the sphere surface and volume, respectively

sphere with surface S surrounding our spherical particle, and evaluate the rate at which electromagnetic power $\wp_{abs}$ crosses this surface (Fig. 6.3). Assuming that the surrounding medium is non-absorbing, we have $\wp_{abs} = -\wp_{sca} + \wp_{ext}$, where each $\wp_x$ is obtained by calculating the flux of the corresponding Poynting vector S_x over the sphere surface S:

$$\wp_{sca} = \int_S S_{sca} \cdot \hat{n} dS, \quad \wp_{ext} = -\int_S S_{ext} \cdot \hat{n} dS.$$

Finally cross sections can be introduced as $C_{ext} = \wp_{ext}/I_{inc}$. In particular it is possible to derive an expression for the cross sections as a function of the multipole coefficients:

$$C_{sca} = \frac{2\pi}{k^2} \sum_{n=1}^{\infty} (2n+1) \left(|a_n|^2 + |b_n|^2 \right)$$

$$C_{ext} = \frac{2\pi}{k^2} \sum_{n=1}^{\infty} (2n+1) \, Re \{a_n + b_n\}$$

It should be stressed here that the formula for C_{ext} depends on the polarization and propagation direction of the incident plane wave. For example, in the case of a y-polarized illumination, the real part would have been replaced by the imaginary part. On the contrary, C_{sca} is independent of this choice thanks the presence of the square modulus. Sometimes, instead of cross sections, dimensionless quantities misleadingly called efficiencies are used, defined as $Q_j = C_j/\pi r^2$.

Contrarily to what their name suggests, such efficiencies often are greater than 1, meaning for example that the nanoparticle is scattering more than would be geometrically possible. As we will see in the next chapter, despite the handiness of this theory, solutions in a closed form are available only for a few particular geometries other than the sphere.

Therefore, the only viable approach in most cases is either semi-analytical, which includes the expansion of the fields into an infinite multipole series, or numerical, resorting to several techniques such as FDTD [13], FEM [7], or DDA to solve for the fields, followed by multipolar decomposition to identify the involved resonances [14].

In the general case, an analytical model for finding the Mie-type multipolar resonances of a nanostructure is based on multipolar expansion of the incident, scattered and internal fields, with application of the proper boundary conditions on the nanostructure surface. The solution in a closed form is however possible in a very limited number of the nanostructure geometries, such as a sphere, spheroids, a cube and a cylinder of infinite length. Unfortunately the fabrication of such structures with standard lithographic techniques is not an easy task compared to that of other structures like nanocylinders.

Despite this limitation, the linear and nonlinear response of optical nanostructures can be numerically calculated using several methods. Here we will focus on FEM implementation on COMSOL Multiphysics, a commercially available software.

The calculation steps required to implement the FEM on COMSOL and calculate the linear response of a generic nanoparticle can be summarized in the following points:

- The geometry of the problem is defined, comprising the parameters of the nanostructure, a possible substrate, and the host medium, which is usually air. The domain is then surrounded by a perfect matching layer (PML), a perfect absorber introduced to avoid non-physical reflections at the boundaries. Usually the domain is not larger than a few wavelengths.
- The illumination parameters are defined, together with the dispersion of the materials involved.
- The domain is discretized into a set of discrete sub-domains. The nanostructure region is the most finely meshed, with elements having a typical dimension of $\lambda/20$, and a growing factor slightly larger than one, exiting this domain and going towards the PML.
- Initial values and the type of problem are specified.
- Once the field is calculated in every mesh element, scattering and extinction can be evaluated by integrating the relative Poynting vectors.

There exist developed algorithms to evaluate the multipole coefficients a_n and b_n once the field is numerically calculated [14]. The general idea is to build up the scattering density currents, which in turn enable to evaluate the multipole coefficients via analytical formulas.

6.2.3 *Multi-polar Numerical Modelling of the Nonlinear Response*

So far, we explained how to numerically calculate the linear response of a nanostructure. Let us now describe how to calculate its nonlinear response [7]. The idea is to divide the problem in two steps. In the first one the linear response is calculated with COMSOL following the above-mentioned procedure. In the second step, the nonlinear polarization induced by the bulk nonlinearity is employed as a source for a second linear study at the nonlinear frequency of interest.

In order to better illustrate this point, it is appropriate to describe the example of SHG in AlGaAs nanoantennas, as reported in ref. [7]. All simulation settings were chosen so as to be easily recreated in the laboratory: $Al_{0.18}Ga_{0.82}As$ was chosen as a material to avoid TPA at $\lambda = 1.55\ \mu m$, referring to [15] for the material dispersion. For Mie theory regime to hold true, the illumination wavelength choice restricts the cylinder dimensions so as to have $x \approx 1$.

In particular the height was fixed at 400 nm for epitaxial growth reasons, while the radius was spanned in the interval 175–230 nm. Finally, the simulations were performed both in the cases or air host medium, and AlOx substrate ($n \approx 1.6$ at 1.55 μm), as shown in Fig. 6.4. The illumination geometry is such that the pump k-vector is parallel to the cylinder's symmetry axis, as showed in the right inset of Fig. 6.4a. The calculated scattering efficiency of a cylinder with radius 225 nm, decomposed according to [14], shows four main contributions coming from electric and magnetic dipoles and quadrupoles (MD, ED, MQ, EQ). In particular the electric field profile at the magnetic dipole resonance ($\lambda_{MD} = 1640$ nm) is shown in the left inset, forming an electric current loop inside the cylinder, which is the necessary condition to sustain a magnetic dipole [6].

By varying the radius from 175 nm to 230 nm, it can be seen that the resonances redshift as the radius increases (Fig. 6.4b). The presence of AlOx substrate does

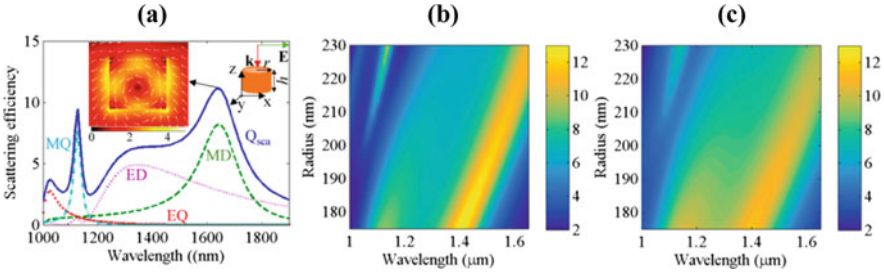

Fig. 6.4 Linear response of an $Al_{0.18}Ga_{0.82}As$ nanocylinder. (**a**) Scattering efficiency of a cylinder with 225 nm radius, decomposed according to [14] to identify the multipole contributions. The left inset shows the electric field profile at the MD resonance. Scattering efficiency map in the case of air (**b**) and AlOx (c) substrate. *Reprinted with permission from* [7], *© 2015 Optical Society of America*

not significantly alter the spectral position of those resonance, with only a slight broadening due to the decreased field confinement in the nanocylinder (Fig. 6.4c).

$Al_{0.18}Ga_{0.82}As$ is a non-centrosymmetric material with a strong bulk $\chi^{(2)}_{ijk} = 200$ pm/V for $i \neq j \neq k$ [16]; as a consequence the nonlinear response of the nanocylinder is calculated by performing a second linear computation at 2ω, by using the SH term in the nonlinear polarization induced by the bulk $\chi^{(2)}$ as an external current source. Finally the conversion efficiency can be evaluated as $\eta_{SHG} = \int_A S_{SH} \cdot \hat{n}\, dA / \left(I_0 \pi r^2\right)$, where S_{SH} is the Poynting vector of the SH field, A is an imaginary surface enclosing the cylinder, and $I_0 = 1$ GW/cm^2 is the incident field intensity. As the strongest resonance in the linear scattering is MD, the expected η_{SHG} should have a maximum when pumping at this frequency. However, Fig. 6.5a shows that the SH efficiency peak is obtained for a slightly higher pump frequency (1680 nm).

This point can be understood by calculating the linear scattering at 2ω. Indeed, a sharp resonance is present at exactly half the maximum SHG frequency (Fig. 6.5b). This behavior shows that the nonlinear conversion efficiency in this system not only depends on the product of the scattering efficiencies at ω and 2ω ($Q^2_{FF} \times Q_{SH}$ in particular), but also on the overlap integral between these two resonances. Finally, Fig. 6.5a (inset) and Fig. 6.5c show that the excited multipolar mode at 2ω has a quadrupolar nature.

As we will see in Section SHG from $Al_{0.18}Ga_{0.82}As$-on-AlO_x nanoantennas was experimentally demonstrated in 2016 [17–19]. Due to the presence of a substrate with a refractive index higher than 1, the measured conversion efficiency was of the order of 10^{-5}. Despite the two-order of magnitude decreased efficiency with respect to the case of a cylinder in air, these results represent a record for nonlinear light generation at the nanoscale, especially with respect to plasmonic nanostructures.

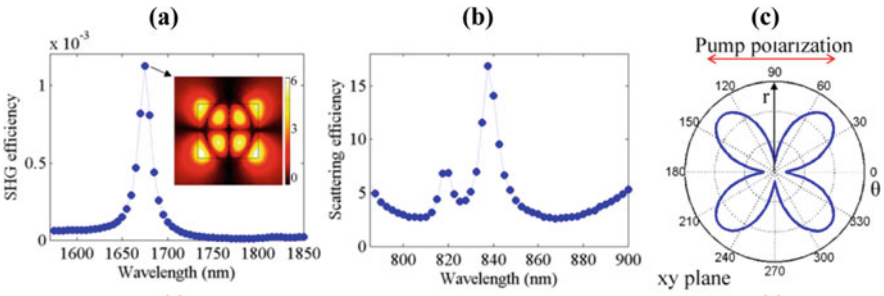

Fig. 6.5 Nonlinear response of an $Al_{0.18}Ga_{0.82}As$ nanocylinder. (**a**) SHG efficiency of a cylinder with 225 nm radius as a function of the pump frequency, with the inset showing a quadrupolar field profile at the efficiency peak. (**b**) Linear scattering efficiency calculated at 2ω. (c) SHG far-field radiation pattern in the *xy*-plane. *Reprinted with permission from* [7], *© 2015 Optical Society of America*

6.2.4 *Quasi-Normal-Mode Description of Nonlinear Nano-Optics*

While the multipolar modeling described in Sect. 6.2.3 provides an intuitive physical insight of nanoantennas response to a well-defined external electromagnetic excitation, hereafter we will focus more on the resonant nature of a scattering nanoparticle. If we consider the latter as an open cavity with huge losses, its interaction with light will rely on its resonant modes. Upon an external electromagnetic excitation, energy is transferred to the leaky modes of the structure which radiate back to the environment by exponentially decaying in time [20]. In contrast to the Hermitian formalism of closed resonators, broadly adopted with optical microcavities, we switch here to a non-conservative open systems description. In this framework the natural modes of resonators, referred to as quasi-normal modes (QNMs), are solutions of a non-Hermitian eigenvalue problem. The electromagnetic eigenstates, hereafter labelled as $\left[\tilde{E}_m(r), \tilde{H}_m(r)\right]$, have complex eigenvalues $\tilde{\omega}_m$ and characterize the system independently of the excitation field. Mathematically they can be found as time-harmonic solutions of source-free Maxwell's equations in an unbounded system [21]:

$$\begin{bmatrix} 0 & -i\mu_0^{-1}\nabla\times \\ i\varepsilon\left(\tilde{\omega}_m\right)\nabla\times & 0 \end{bmatrix} \begin{bmatrix} \tilde{H}_m \\ \tilde{E}_m \end{bmatrix} = \tilde{\omega}_m \begin{bmatrix} \tilde{H}_m \\ \tilde{E}_m \end{bmatrix} \tag{6.1}$$

The complex frequency $\tilde{\omega}_m = \Omega_m - i\Gamma_m/2$ encloses the resonant behavior of the m^{th} mode (Ω_m) and its leaky nature ($\Gamma_m/2$), notably the mode quality factor is $Q_m = \Omega_m/\Gamma_m$ and its lifetime is $\tau_m = 1/\Gamma_m$ [20]. This description is common to many physical systems, from acoustic to gravitational waves. Historically in electromagnetism problem (Eq. 6.1), modes calculation raised remarkable normalization issues. Thanks to the development of theoretical models and numerical tools, such difficulties have been recently overcome. The QNM normalization that we refer to here imposes $\int \left[\tilde{E}_m \cdot \left(\frac{\partial\omega\varepsilon}{\partial\omega}\right)\tilde{E}_m - \tilde{H}_m \cdot \left(\frac{\partial\omega\mu}{\partial\omega}\right)\tilde{H}_m\right] d^3r = 1$ [22] and is numerically implemented with the introduction of PMLs far enough from the resonator. This transforms an unbounded system in a spatially confined analog and solves the mathematical issue of diverging fields at infinity. Moreover, the eigenvalue problem (Eq. 6.1) is dispersive and thereby results in a further difficulty in the analysis. There exist at least two alternative approaches to solve the problem: the first computes QNMs by searching poles in the complex plane where the response to a driving source diverges [21], while the second is based on the introduction of auxiliary fields to linearize the problem (Eq. 6.1) [23].While here we will focus on the latter supposing for the sake of simplicity that the resonator permittivity can be modeled with a single-pole Lorentzian $\varepsilon(\omega) = \varepsilon_\infty\left(1 - \frac{\omega_p^2}{\omega^2 - \omega_0^2 + i\omega\gamma}\right)$, let us

keep in mind that the same approach can be extended to multipolar models and dispersive permeability $\mu(\omega)$. Two auxiliary fields are introduced: the polarization $P = -\varepsilon_\infty \frac{\omega_p^2}{\omega^2 - \omega_0^2 - i\gamma\omega} E$ and the current density $J = -i\omega P$ [20, 23]. By doing so, the eigenvalue problem (Eq. 6.1) can be linearized with new eigenstates $\left[\tilde{E}_m(r), \tilde{H}_m(r), \tilde{P}_m(r), \tilde{J}_m(r)\right]$. The set of numerically computed modes constitutes a complete basis, implying that the field scattered by the system upon background excitation $[E_b(r,\omega), H_b(r,\omega)]$ can be expanded as:

$$E_s(\omega, r) = \sum_{m=1}^{M_1} \alpha_m^{(1)}(\omega)\, \tilde{E}_m(r)$$

Here $\alpha_m(\omega)$ is the excitation coefficient of the m-th mode, which can be retrieved from the scattered field formulation of Maxwell's equations in the presence of an external source [23]:

$$\alpha_m^{(1)}(\omega) = \left\{ \left[\varepsilon(\tilde{\omega}_m) - \varepsilon_b\right] \frac{\tilde{\omega}_m}{(\tilde{\omega}_m - \omega)} + (\varepsilon_b - \varepsilon_\infty) \right\} \int_V \tilde{E}_m(r) \cdot E_b(r,\omega)\, d^3 r \tag{6.2}$$

where ε_b is the permittivity of the background medium and the integral is performed over the resonator volume V. Different formulations can be adopted to reconstruct the total field inside the dispersive material, starting from the auxiliary fields. For convergence rapidity, here we use [24]:

$$E_t(r,\omega) = \sum_{m=1}^{M_1} \alpha_m^{(1)}(\omega) \frac{\varepsilon(\tilde{\omega}_m) - \varepsilon_\infty}{\varepsilon(\omega) - \varepsilon_\infty} \tilde{E}_m(r) \tag{6.3}$$

When the resonator is made of a material with a nonlinear susceptibility, the local confinement of a strong electric field $E_t(r,\omega)$ leads to second-order generation processes as SFG, SHG and DFG, as well as higher-order processes. Here we will apply QNM theory to the particular case of SHG, but of course the formalism can be easily extended to other phenomena. Let us therefore consider a resonator with a quadratic susceptibility such that the dielectric polarization density is described by $P(t) = \varepsilon_0[\chi^{(1)}E(t) + \chi^{(2)}E^2(t)] = P^{(1)}(t) + P^{(2)}(t)$. The total field in Eq. 6.3 generates a nonlinear displacement current inside the resonator:

$$J^{(2)}(r, 2\omega) = -i2\omega P^{(2)}(r, 2\omega) = -i2\omega\varepsilon_0 \chi^{(2)} : [E_t(r,\omega) \otimes E_t(r,\omega)]$$

which acts as a source of a radiation problem at 2ω (symbols "⊗" and ":" stand for tensor and constructed product, respectively [25]). Therefore, analyzing a second order process through QNM formalism implies to apply twice a reconstruction protocol, first for an external excitation $[E_b(r,\omega), H_b(r,\omega)]$ at fundamental frequency

(FF) and later for a localized source $J^{(2)}(r, 2\omega)$ at second harmonic (SH). Both processes can be reconducted to a projection of an electromagnetic field distribution on the same eigenstates of the system. The total field at SH can be therefore written as

$$E_t\,(2\omega) = \sum_{l=1}^{M_2} \alpha_l^{(2)}\,(2\omega)\,\tilde{E}_l$$

with modal excitation coefficients

$$\alpha_l^{(2)}\,(2\omega) = -2\omega/\,(\tilde{\omega}_l - 2\omega) \int_V P^{(2)}\,(r, 2\omega) \cdot \tilde{E}_l(r)\,dr$$

Expanding $P^{(2)}(r, 2\omega)$ one gets:

$$\alpha_l^{(2)}\,(2\omega) = \sum\nolimits_{m,n} \frac{-2\omega^3\;\zeta_{lmn}\;\xi_{mn}\,(\omega)}{(\tilde{\omega}_l - 2\omega)\,(\tilde{\omega}_m - \omega)\,(\tilde{\omega}_n - \omega)} \tag{6.4}$$

with

$$\xi_{mn}\,(\omega) = \frac{\left[\varepsilon\,(\tilde{\omega}_m) - \varepsilon_\infty\right]\left[\varepsilon\,(\tilde{\omega}_n) - \varepsilon_\infty\right]}{\left[\varepsilon\,(\omega) - \varepsilon_\infty\right]^2} \alpha_m^{(1)}\,(\omega)\,\alpha_n^{(1)}\,(\omega) \tag{6.5}$$

$$\zeta_{lmn} = \varepsilon_0 \int_V \tilde{E}_l(r) \cdot \left\{\chi^{(2)} : \left[\tilde{E}_m(r) \otimes \tilde{E}_n(r)\right]\right\}\,dr \tag{6.6}$$

Equations 6.4 to 6.6 capture important notions of nonlinear generation in leaky cavities analogue to guided optics counterparts. Eq. 6.4 illustrates that to efficiently generate SH signal, three resonant conditions have to be fulfilled: two modes, labelled with m and n, have to be efficiently excited at FF and well coupled with a mode at SH. Remarkably, if we settle in the perfectly matched condition $Re\,(\tilde{\omega}_l) = 2\omega$ and $Re\,(\tilde{\omega}_m) = Re\,(\tilde{\omega}_n)$, Eq. 4 can be recast as $\alpha_l^{(2)}\,(2\omega) = 8i\sum_{m,n} Q_l\,Q_m\,Q_n\zeta_{lmn}\;\xi_{mn}\,(\omega)$, an analog formulation of Hermitian systems predictions (in the limit of Q approaching infinity) which sets an intrinsic limit of intracavity nonlinear generation efficiency for low-Q cavities. Eq. 6.5 quantitatively expresses the coupling coefficient between the external excitation at frequency ω and two pump modes labelled m and n, thus representing the ideal figure of merit to maximize the energy transfer to the resonator at FF. Importantly, Eq. 6.5 is analytic, meaning that once the QNMs of the structures are computed, $\xi_{mn}(\omega)$ can be retrieved for any driving source at the low computational cost of a projection of an electric field on another. Finally, the square modulus of ζ_{lmn} (Eq. 6.6) estimates the SHG efficiency, since ζ_{lmn} is the spatial overlap between the two modes (m and n) excited at FF and the mode (l) at SH. This figure of merit is an intrinsic feature of the resonator that only depends on its geometry and orientation relative to

crystalline axes. At variance with Hermitian physics, the overlap integral introduces a triple $\tilde{E}_l \tilde{E}_m \tilde{E}_n$ product instead of $\tilde{E}_l^* \tilde{E}_m \tilde{E}_n$, which is a signature of the different mode normalization introduced above [22].

The total generation efficiency at SH can be analyzed through the ratio between the total power generated at 2ω (P_{SH}) and the excitation power intensity at ω (I_{FF}). Exploiting the formalism of scattering problems, here below we will call this figure of merit nonlinear extinction cross section $\sigma_{ext}^{(2)}$. In analogy with the linear extinction cross section, which through Lorentz reciprocity theorem can be expressed as

$$\sigma_{ext} = -\frac{1}{2S_0}\iint_{\Sigma} Re\left(E_S \times H_b^* + E_b \times H_S^*\right)\cdot n \, d\sigma = -\frac{\omega}{2S_0}\iiint_{V} \mathrm{Im}\left[\Delta\varepsilon E_S \cdot E_b^*\right] d^3r \tag{6.7}$$

a close formula can be derived also for $\sigma_{ext}^{(2)}$ in the case of a plane wave excitation:

$$\sigma_{ext}^{(2)}(2\omega) = \frac{P_{SH}}{I_{FF}} = -\frac{\omega}{S_0}\int_V \mathrm{Im}\left[\sum_{l=1}^{M_2} \alpha_l^{(2)}(2\omega)\, \tilde{E}_l(r)\cdot P^{(2)*}\left(r, 2\omega\right)\right] dr \tag{6.8}$$

Please notice that Eq. 6.8 also allows to separately study the contribution of each resonant mode to the SHG power, and that this figure of merit scales linearly with the incident power for a second order nonlinear process. It is worth stressing a critical difference between the knowledge conveyed by $|\zeta_{lmn}|^2$ and $\sigma_{ext}^{(2)}(2\omega)$: the former quantifies the internal conversion efficiency inside the resonator volume stemming from the sole mode spatial overlap, while the latter also includes both the absorption losses and the energy scattered in the SH far field.

6.2.5 *Practical Application of QNM to Nonlinear Nano-Optics*

To illustrate the potential of the above mode-expansion technique, we will consider in the following the example of SHG in an AlGaAs nanocylinder with radius $r = 220$ nm and height $h = 400$ nm on a dispersion-less AlO_x substrate with refractive index $n_s = 1.6$. Conversely, AlGaAs is dispersive and its refractive index is modeled with a single-pole Lorentzian $\varepsilon(\omega) = \varepsilon_\infty\left[1 - \frac{\omega_p^2}{(\omega^2 - \omega_0^2 + i\omega\gamma)}\right]$.

Restricting our study to the absorption-less part of the spectrum ($\lambda > 740\ nm$), let us set $\gamma = 0$, while $\omega_p = 1.69 \cdot 10^{16}$ rad/s, $\omega_0 = 5.55 \cdot 10^{15}$ rad/s and $\varepsilon_\infty = 1$ are the best-fit parameter to the empirical model in [15]. The QNMs are numerically computed using the eigenmode solver in COMSOL Multiphysics and a freeware toolbox can be found at [26]. Figure 6.6 shows the absolute value of the normalized electric field for a few modes with $Re\left(\tilde{\lambda}_m\right)$ close to $\lambda_{FF} = 1600$ nm and

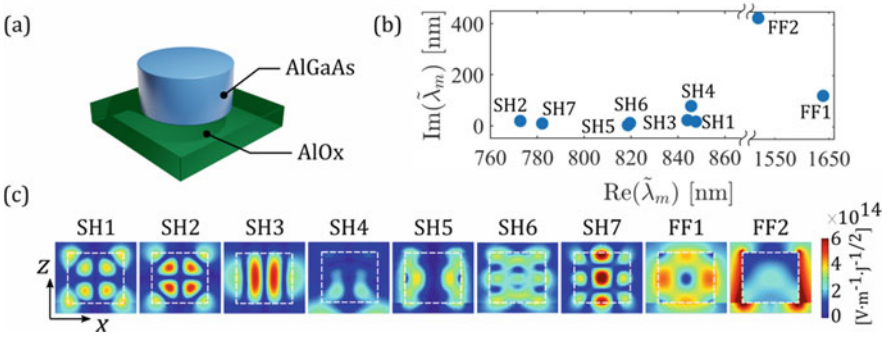

Fig. 6.6 QNM calculation for the AlGaAs nanocylinder on AlOx substrate sketched in (**a**). Radius $r = 220$ nm and height $h = 400$ nm. (**b**) QNM distribution in the complex plane around the real wavelengths $\lambda_{FF} = 1600$ nm and $\lambda_{SH} = 800$nm. (**c**) Electric near-field distribution in the xz-plane at $y = 0$ for the same QNM shown in (**b**). *Reprinted with permission from* [25], *© 2020 American Chemical Society*

λ_{SH}=800 nm. If we excite this resonator with a plane wave with linear polarization along $\hat{x}$ and k vector aligned along the cylinder axis (i.e. antiparallel to $\hat{z}$ unit vector), the background field can be written as:

$$E_b(r,\omega) = \begin{cases} E_0\hat{x}\ \left[\exp(-ik_0n_cz) + r_s\exp(ik_0n_cz)\right]\exp(-i\omega t)\ \ (z \geq 0) \\ E_0 t_s\ \hat{x}\ \exp(-ik_0n_sz)\exp(-i\omega t)\ \ (z \leq 0) \end{cases}$$

Projecting this field on the QNMs at FF shown in Fig. 6.6, we can calculate the excitation coefficients and the linear extinction cross section via Eqs. 6.2 and 6.7. The result is reported in the right side of Fig. 6.7: in Fig. 6.7a the complex plane is displayed as in Fig. 6.6, for the main excited mode FF1; in (b) the contribution of this QNM to the scattered cross section is displayed as a dashed blue line. The contribution of just the two main excited modes (black solid line) suffices to provide a good agreement with fully vectorial computations in COMSOL Multiphysics (right part of Fig. 6.7b, red dots). Hereafter we will refer to this projection process as 'reconstruction', meaning that an increasing number of QNMs is considered to approximate the fully vectorial computation within a desired tolerance. The SH extinction cross section can be reconstructed through Eq. 6.7, and the result is reported in the left part of Fig. 6.7b. Comparably to the behavior at FF, the SH emission is mainly due to one resonant mode (SH1). In such conditions, the QNM formalism is very powerful design tool SHG at the nanoscale. Let us consider for example $m = n$ being the label of FF1 and l the label of SH1. The spatial overlap integral ζ_{lmn} can be separated in its contributions $\tilde{E}_m(r) \otimes \tilde{E}_n(r)$ and $\tilde{E}_l(r)$, and studied in modulus and phase.

Since SH1 electric field is mainly oriented along the y-axis, for the sake of simplicity we consider just the product $\tilde{E}_{m,x}(r)\tilde{E}_{m,z}(r)\tilde{E}_{l,y}(r)$, whose contributions

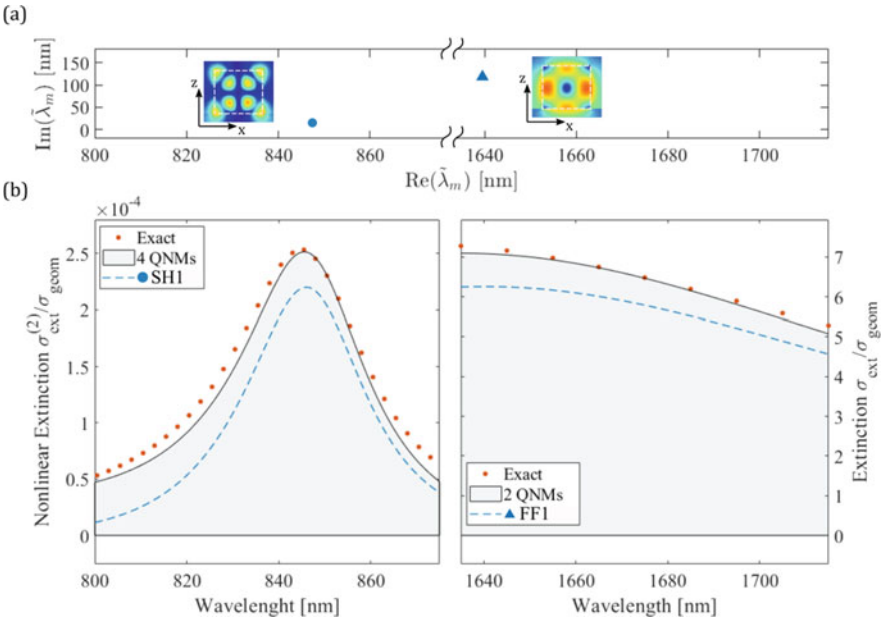

Fig. 6.7 SH extinction cross section of the nanoresonator in Fig. 6.6 excited by a plane wave with $\boldsymbol{k}$ vector along z and linear polarization along x. (**a**) Complex plane distribution of the main QNMs excited around FF and SH. (**b**) Linear (right) and second harmonic (left) extinction cross sections. Blue dotted lines display the reconstruction with just the main modes in (**a**), while black solid lines with 2 and 4 QNMs respectively. Red dots report the fully vectorial result computed with COMSOL Multiphysics. *Reprinted with permission from* [25], *© 2020 American Chemical Society*

in the xz-plane at $y = 0$ are reported in Fig. 6.8. Interestingly, the rightmost plot displays π-shifted contributions to ζ_{lmn} resulting in destructive interference and limiting SHG efficiency.

The above example is instructive insofar as it demonstrates at least two advantages of QNM analysis: a) thanks to a proper open-cavity modes normalization, it enables to quantify some figures of merit that are hard to isolate with common FEM solvers (i.e. overlap integrals in subwavelength resonators); b) it offers guidelines to optimize nonlinear generation efficiencies in terms of coupling between external excitation and cavity modes (Eq. 6.5), modal spatial overlap (Eq. 6.6) and modes scattering/absorption contributions (Eq. 6.8), thereby providing the upper limit of conversion efficiency for a given optical nanoresonator.

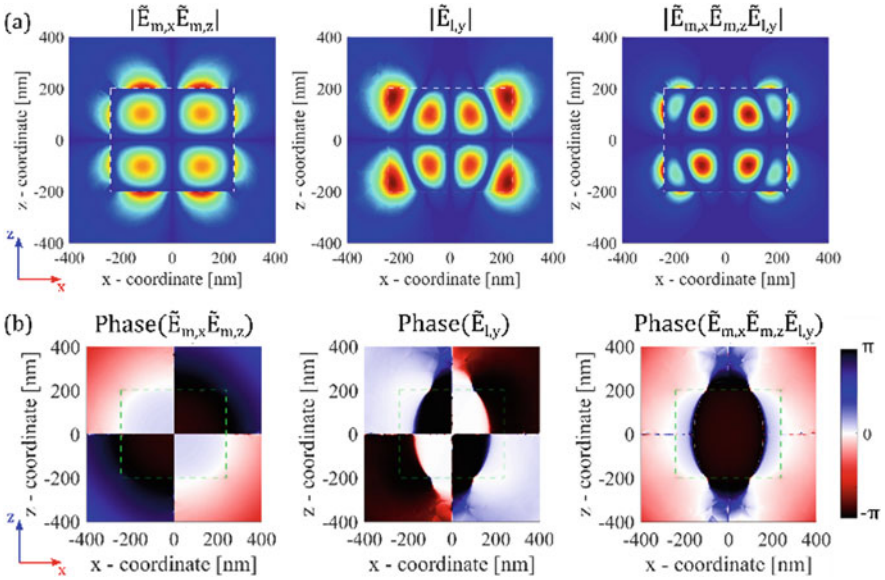

Fig. 6.8 Nonlinear overlap integral for the subwavelength resonator of Fig. 6.6, between the main modes excited at FF and SH reported in Fig. 6.7. The *xz*-plane at $y = 0$ is considered. From left to right the plots displays, respectively in modulus (**a**) and phase (**b**): the product of the main components (x and z) of the mode excited at FF (labelled with m), the y component of the main mode excited at SH (labelled with l), and the product of the three. *Reprinted with permission from* [25]*, © 2020 American Chemical Society*

6.3 Experimental Demonstrations

In this Section, we will describe the nonlinear measurements carried out on single AlGaAs nanoantennas. We will initially recall the first SHG demonstration, then we will introduce the directivity problem. The latter can be addressed by breaking the symmetry of either the excitation, or the crystal, or the nanopillar geometry.

6.3.1 SHG in Semiconductor Nanoantennas

SHG nonlinear measurements on single pillars were carried out on a sample consisting of several arrays, in which a 3 μm spacing is chosen to ensure single-pillar investigation. Nominal radii span from 175 to 225 nm and the 400 nm height is fixed by the epitaxial growth. This sample was patterned with ma-N 2401 e-beam resist, with a dose varying from 100 to 200 $\mu C/cm^2$ (Fig. 6.9).

In order to experimentally test the $\eta_{SHG} \approx 10^{-5}$ theoretical prediction, SHG experiments were performed at Politecnico di Milano with the nonlinear confocal

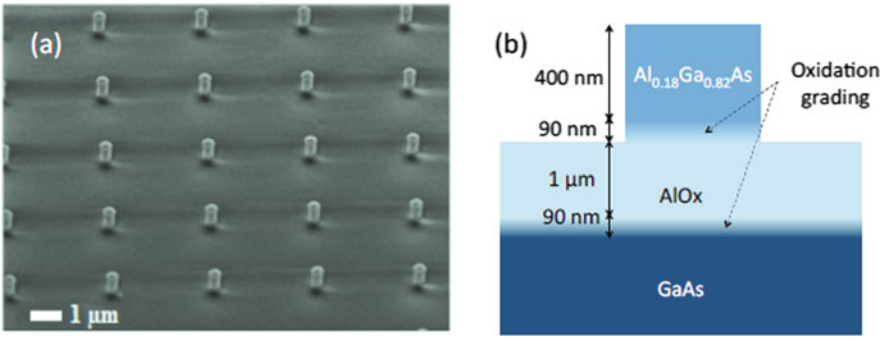

Fig. 6.9 (**a**) SEM image showing an array of AlGaAs nanocylinders. (**b**) Vertical section of the sample showing the layer composition. *Reprinted with permission from* [17], *© 2016 Optical Society of America*

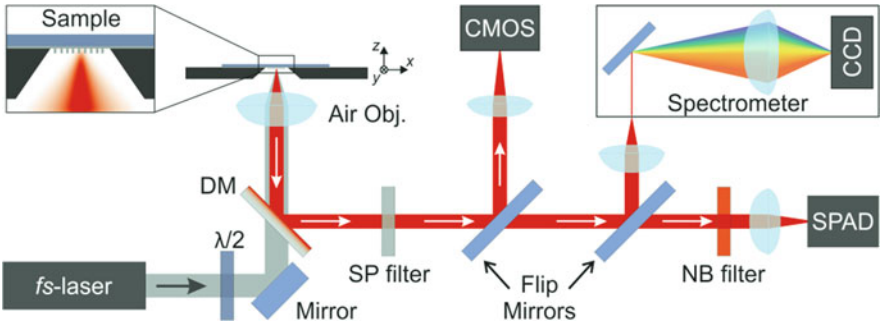

Fig. 6.10 Experimental setup for the nonlinear confocal microscopy experiments. Fs-laser: Er^{+}-doped fiber laser delivering 150-fs pulses centered at 1554 nm (light grey beam). *λ/2* half-waveplate, *Air Obj.* 0.85-NA air objective, *DM* dichroic mirror, *SP and NB filters* short-pass and narrow-band filter respectively, *CMOS* imaging camera, *SPAD* single-photon avalanche detector, *CCD* spectrometer cooled camera. *Reprinted with permission from* [17], *© 2016 Optical Society of America*

microscopy setup described in Fig. 6.10, which allows for 700 pm lateral resolution. Despite the fixed-wavelength pump, it was still possible to access the various resonances involved in the SH process and retrieve spectral information on the system by analyzing nanoantennas with different radii.

This approach is ideal to probe the nonlinear properties of $Al_{0.18}Ga_{0.82}As$ nanostructures, since the chosen Al molar fraction ensures transparency at both the pump and emission wavelengths and TPA-free operation. Results obtained in this way can still be compared with the ones employing a tunable pump since all the relevant phenomena occur at energies well below the material resonances, and other experiments are performed on relatively narrow spectral ranges so as to avoid dispersion. Moreover, as Mie type resonances strictly depend on the size parameter

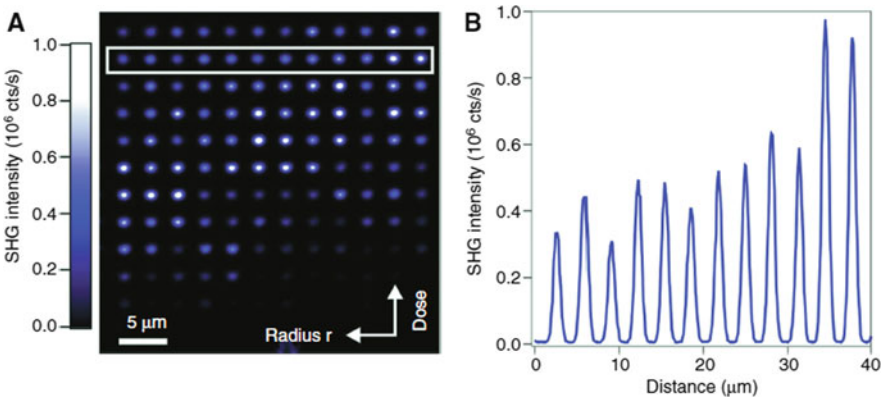

Fig. 6.11 (**a**) SHG intensity map of a nanoantenna array with nominal radii spanning from 175 to 225 nm (x-axis) and e-beam dose varying from 100 to 200 $\mu C/cm^2$ (*y*-axis), obtained by scanning the hollow piezo on which the sample is placed. (**b**) Line profile of the second row of the array, marked by the white box in (**a**). *Reproduced from* [17]. *CC BY-NC-ND 3.0*

x defined in Sect. 6.1, all the meaningful physics is expected to scale as the radius-to-wavelength ratio r/λ, regardless of which of these two parameters is fixed.

The sample was mounted on a 3D-stage with a piezo allowing to move along the *x* and *y* directions with nanometric precision, thus allowing to record 2D SHG intensity maps (Fig. 6.11). Extracting data from a single row in the SHG intensity map (Fig. 6.11b) allowed to confirm that the signal comes from individual pillars, as individual peaks have the same spacing of 3 µm of the nanoantennas, with a signal-to-noise ratio exceeding 10^4. By subtracting the signal coming from the substrate of AlO_x and GaAs, which is however three orders of magnitude lower than that of the pillars, it is possible to reveal the dependence of the experimental SHG on the nanopillar radius (Fig. 6.12a), with a maximum corresponding to a radius around 193 nm. From peak SH count rate of Fig. 6.12c, measured at 750 µW average pump power (corresponding to 1.6 GW/cm^2 peak intensity), gives a peak SHG efficiency of $\eta_{SHG} = 1.1 \cdot 10^{-5}$, corresponding to normalized efficiency $\gamma_{SHG} = 1.5 \cdot 10^{-7}\ W^{-1}$, in good agreement with theoretical predictions and large advantage with respect to record SHG yield in engineered plasmonic nanostructures ($5 \cdot 10^{-10}\ W^{-1}$ [27]).

We next analyzed the SHG polarization properties of the emitted SH signal by inserting a polarizer in the detection path. We observed a significant dependence of SH polarization on nanopillar radius and the field distribution of the high-order multipolar mode at 2ω that best couples to the FF mode. As at 2ω a spectrally dense forest of modes exists, small changes in the antenna geometry can result in great differences in the SH field distribution, and hence the nonlinear emission polarization [28].

A peculiar feature of SHG in [100] AlGaAs nanopillars, which was formerly observed at ANU Canberra and KCL London [18, 29], is that its far field has a two-

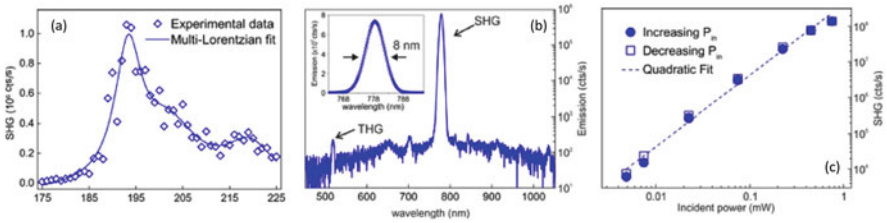

Fig. 6.12 (**a**) Measured SHG rate as a function of the nanoantenna radius. (**b**) Emission spectrum of a pillar with $r = 193$ nm for 500 μW incident power (log scale). Inset: a zoom of the main SHG peak (linear scale). (**c**) Power collected from a nanoantenna. *Reprinted with permission from* [17], *© 2016 Optical Society of America*

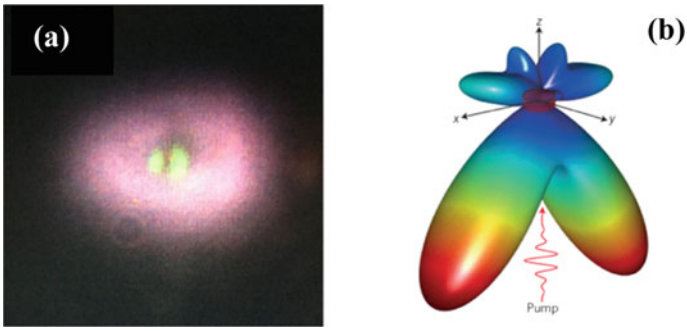

Fig. 6.13 Two-lobe SH far field generated in [100] AlGaAs circular-base nanopillars. (**a**) Camera image of green (532 nm) spot, for FF wavelength 1064 nm, taken at the nanoantenna focal plane Reprinted from [29], *© IOP Publishing. Reproduced with permission.* (**b**) 3D simulation of the SH far field observed with back-focal-plane imaging. *Reprinted with permission from* [18]. *Copyright (2016) American Chemical Society*

lobe structure (see Fig. 6.13). The absence of SHG in the normal direction stems from the symmetry in both the bulk $\chi^{(2)}$ tensor of [100] AlGaAs and the circular-based nanopillar geometry. Since most future applications of nonlinear metasurfaces are likely to require on-axis operation, several strategies have been devised to break such symmetry, by acting on either the excitation, or the crystal orientation, or yet the nanopillar geometry.

For example, it was formerly calculated [29] and then experimentally verified [30] that if the angle of incidence of the pump is varied from 0 to 45°, the two-lobe SHG turns gently into single lobe (see Fig. 6.14). The suppression of SHG null under normal incidence of the pump was also demonstrated in cylindrical nanopillars made of both [111] and [110] AlGaAs on glass [31, 32]. In those cases, the symmetry breaking is at the level of the tensor product between the zinc-blend $\chi^{(2)}$ and the pump field, because it is no longer true that nonlinear coupling is only possible between x, y and z polarized components of the two photons at ω and the photon at 2ω, via the d_{14}, i.e. the only nonzero tensor element.

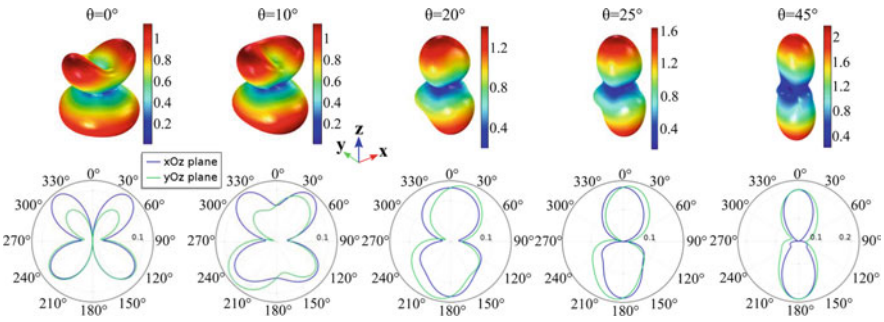

Fig. 6.14 Top: calculated far-field SH radiation patterns vs pump incidence angle. Bottom: Radiation pattern projected in the *xz* plane (blue line) and *yz* plane (green line). *Reprinted from* [29], © *IOP Publishing. Reproduced with permission*

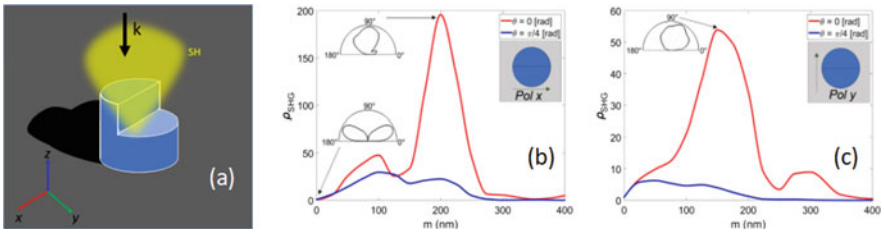

Fig. 6.15 (**a**) Sketch of the proposed structure, where a chair-like notch is etched in a circular basis cylinder. (**b**, **c**) SH gain ρ_{SHG}, for *x*- (**a**) or *y*-polarized (**b**) incident light as a function of the notch (chair back) m. The insets represent the SH radiation diagram in the air region in the *xz* plane at different m values. *Reproduced from* [33]. *CC BY 4.0*

A third possibility, one that allows normal pump incidence on optical nanostructures fabricated in the more popular [100] AlGaAs technological platform, is to act on the geometrical shape of either the nanoantenna, as was recently proposed with the scheme of Fig. 6.15 [33], or its environment. The last case is illustrated in Fig. 6.16, where a single cylindrical nanoantenna is dressed by an asymmetric circular Bragg grating that phase shifts the two lobes of the SH field making them constructively interfere along *z*. In both cases, the collection efficiency of the SH power in a small numerical aperture about *z* was reportedly 2 order-of-magnitude higher than for a bare antenna [34].

6.3.2 *Spontaneous Parametric Down-Conversion in a Sub-λ Nanoantenna*

SPDC in nonlinear crystals is one of the most popular techniques for the generation of entangled photon pairs [35–38] (Fig. 6.17a). In this process a short-wavelength pump photon spontaneously decays into a pair of phase-matched signal and idler

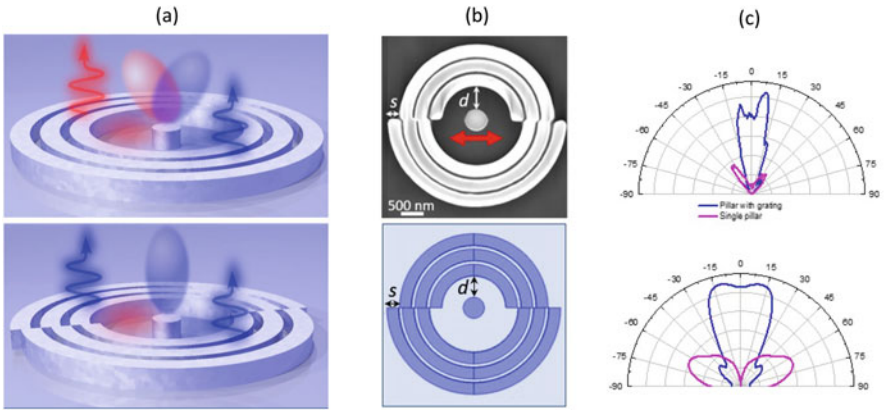

Fig. 6.16 (**a**) Sketch of the SH radiation patterns of an AlGaAs nanocylinder surrounded by either a symmetric (top) or an asymmetric (bottom) Bragg grating. In the latter case, the two p-shifted lobes of the nanopillar are brought in phase in one on-axis lobe. (**b**) schematics (bottom) and electron-microscope picture (top) of the nano-device. (**c**) Experimental (top) and calculated (bottom) radiation diagram for a bare pillar (pink) and a pillar with grating (blue). *Reprinted with permission from* [34], *© 2018 American Chemical Society*

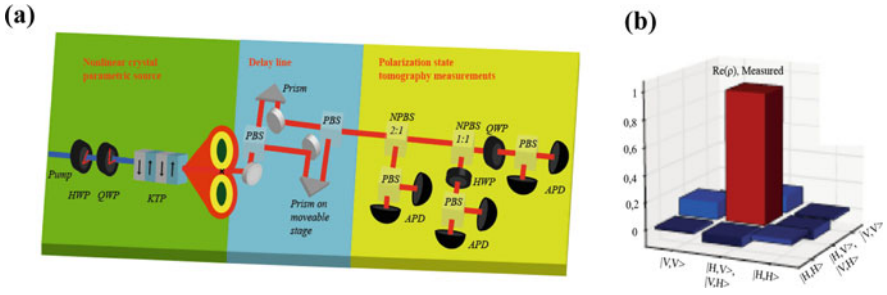

Fig. 6.17 (**a**) Schematic of SPDC generation of orthogonally polarized photon pairs from a nonlinear crystal. In collinear degenerate type-II SPDC, polarization-entangled photons conserve the energy (same ring) and momentum (same direction) and can have either of the two polarizations. A protocol for 2-photon polarization state tomography from Ref. [40] is also reported. On the single-photon level the projective measurements in the distinct paths realized by combinations of wave retarders, polarizing beam splitters (PBS), and photon-number resolving detectors (PNRD), correspond to applying the Stokes operator. (**b**) Reconstructed states using the tomography method proposed in (**a**) from Ref. [40]. *Reproduced from* [40]. *licence number RNP/20/JUN/026858*

photons with longer wavelengths. In theory, signal and idler photons can share the same energy and momentum while having strictly orthogonal polarizations. In actual measurements, they might be in a mixture of polarization pure states. Thus, reconstruction of the density matrix becomes critical to describe the probability that a measured photon can be found in a given pure polarization state (Fig. 6.17b). This analysis is called quantum state tomography. A typical protocol for two-photon polarization state tomography from a nonlinear crystal is shown in Fig.

6.17a [39]. In that case, however, not only the source is several centimeters long, but also quantum state tomography requires bulky optical components such as wave retarders, polarizing beam splitters, and photon-number resolving detectors. An attempt to integrate quantum state tomography in a single miniaturized device was reported in Ref. [40], where a passive linear metasurface is used to carry out multi-photon interference for quantum state reconstruction of photons generated from a centimeter-long nonlinear waveguide. However, the next breakthrough in quantum optics is to use active nonlinear metasurfaces to directly generate polarization entangled photons beyond the use for quantum-state reconstruction. For this scope we propose a nonlinear semiconductor metasurface, made of a non-centrosymmetric material such as AlGaAs, whose high $\chi^{(2)}$ enables the spontaneous generation of photon pairs. Spontaneous photon-pair generation from nanoantennas is alternative to atom-like emitters, such as solid-state fluorescent atomic defects [41], quantum dots [42, 43], and 2D host materials [44, 45]. Some of the advantages of the latter are high degree of frequency indistinguishability, purity and brightness [42, 43]. However they require operation at cryogenic temperatures and do not offer spatial coherence between multiple quantum emitters, thereby reducing the potential for scalability and reproducibility of the devices. Furthermore, the photon extraction efficiency [44] from the small size atomic sources is weak, often requiring complex schemes to couple to optical nanoantennas. It follows that, however brighter the atomic-light emitters are, a nanoscale SPDC source offers complementary advantages such as good scalability, operation at room temperature, shaping of the radiation pattern, and multiplexing.

An overview of nanoscale spontaneous photon pair generation is illustrated in Fig. 6.18 [46]: an s-polarized CW pump laser at a wavelength $\lambda = 785$ nm is focused on a monolithic AlGaAs nanocylinder. The latter exhibits Mie-type resonances at both pump, signal and idler frequencies, and signal/idler photons are collected in reflection geometry. Then the generated photon pairs are spectrally filtered from the pump, first with a dichroic mirror, then with three long pass filters, and finally they are separated with a beam splitter and detected with two distinct single-photon detectors.

Due to the broad magnetic dipole resonance in the IR spectral range (see Fig. 6.18d), signal and idler photons are generated in a large spectral bandwidth of about 150 nm. This bandwidth is broader than conventional SPDC sources, which are typically sub-nm or few-nm. Thus, signal and idler are generated in a sub-100 fs temporal width, which is shorter than the coincidence window of the single photon detector used in the experiment. It follows that the second-order correlation function has a maximum at the time delay of the simultaneous arrival of the two photons with a coincidence window width of one bin. Figure 6.19 shows the coincidence histogram where the peak on top of the red bar is the SPDC rate from the AlGaAs nanoantenna, then a statistical correlation fitted with a green Gaussian curve is detected, which is due to thermal excitation of semiconductor materials. The rate of generated photon-pairs is 35 Hz over an integration time of 24 h. Normalized to the pump energy stored by the nanoantenna, this rate corresponds to 1.4 GHz/Wm, i.e. one order of magnitude higher than best SPDC on-chip and 3 orders of magnitude higher than bulk photon-pair sources [38, 47].

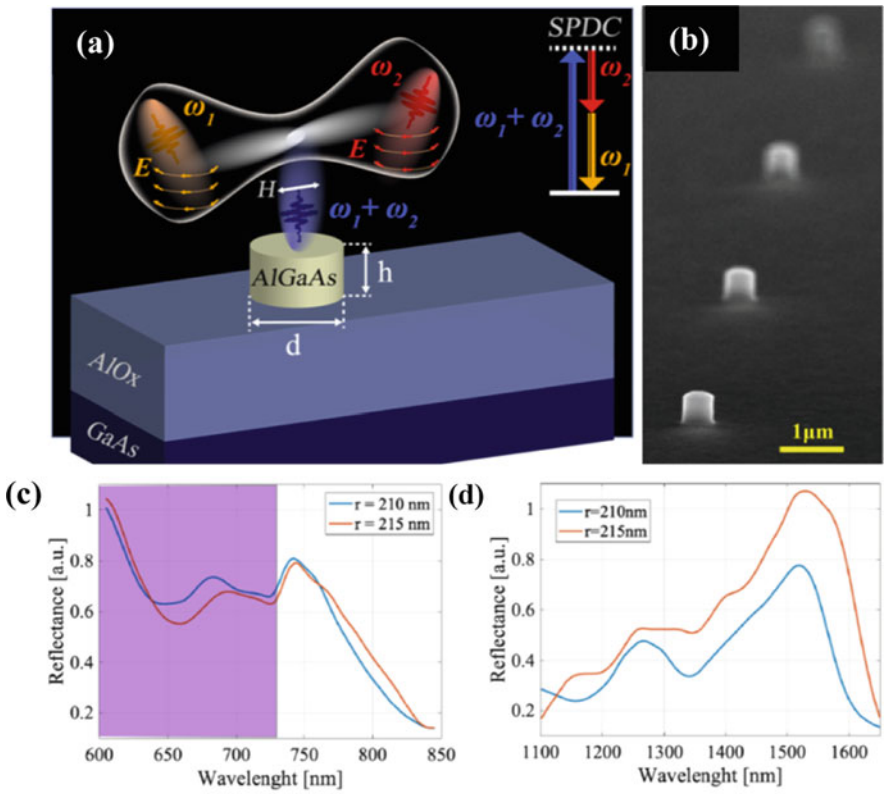

Fig. 6.18 (**a**) Artist's view of the nanoantenna-based source of photon-pairs through the SPDC process, with photon energy diagram in the inset. The pump is horizontally polarized along the [100] AlGaAs crystallographic axis. The signal and idler photons are generated by entangled magnetic dipole moments inside the volume of the AlGaAs nanoantenna, namely m_x and m_z (sketched below the emitted photons). (**b**) A typical scanning electron micrograph (SEM) images of [100] AlGaAs monolithic nanocylinders, 3 μm apart, such that each disk can be excited individually. (**c**) Dark and (**d**) bright field reflectance spectra around the pump/signal and idler frequencies from a metasurface made of an array of nanoantennas. The violet shadow area at wavelengths below 730 nm represents the absorption window of the AlGaAs. *Reprinted with permission from* [46]*, © 2019 Optical Society of America*

Although quantum state tomography is the most important technique for state reconstruction, it is usually time consuming and lacks of precision due to weak bi-photon rates. To solve this issue, a quantum-classical correspondence was established between SPDC and its reversed process, namely SFG. Following Ref. [48], the nanoscale analogy predicts that the spontaneous photon pair rate is:

$$\frac{1}{\Phi_p}\frac{dN_{pair}}{dt} = 2\pi\eta^{SFG}\frac{\lambda_p^4}{\lambda_s^3\lambda_i^3}\frac{c\Delta\lambda}{\lambda_s^2} \tag{6.9}$$

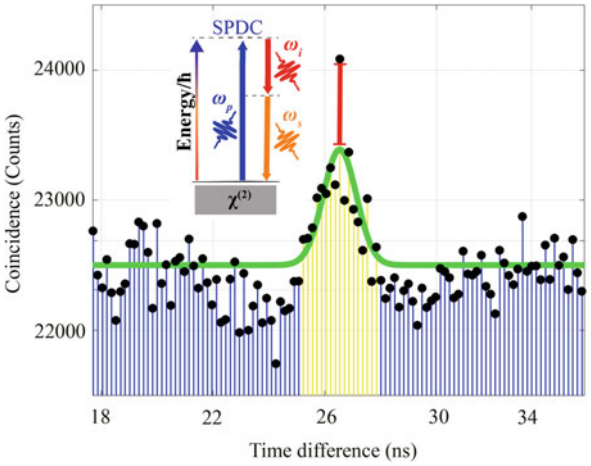

Fig. 6.19 Generation of photon pairs in an AlGaAs disk nanoantenna. A peak, marked by the red bar, appears at a time difference of 26.5 ns, corresponding to the temporal delay between both detectors. Black dots are the measured coincidences, the yellow shadowed area indicates correlation due to thermal excitation of the semiconductor materials, while the green line is its fitted Gaussian curve. Inset: schematic of the SPDC process and energy correlation. *Reprinted with permission from* [46]*, © 2019 Optical Society of America*

where $\eta^{SFG} = \langle P_{SFG} \rangle / \langle \Phi_i \Phi_s \rangle$ is the SFG efficiency given by the ratio of the sum-frequency photon power and the product of incident energy fluxes at signal and idler frequencies. Moreover, Φ_p is the SPDC pump flux, λ_p, λ_s and λ_i are the pump, signal and idler wavelengths, and $\Delta\lambda$ is the nonlinear resonance bandwidth at the signal/idler wavelengths. This equation says that the number of photon pairs generated through SPDC in a given optical mode of the nanostructure, is proportional to the SFG amplitude of the classical signal and idler waves, propagating in the opposite directions. One can then rely on SFG experiments and simulations to predict correlations of the spontaneous photon pairs measured in Fig. 6.19 (the SFG setup is described in Ref. [18]).

Different combinations of incident polarizations for the signal and idler pulses are scanned, including horizontal (H), vertical (V), right circular (R) and left circular (L), and measured the SFG with H polarization, as shown in Fig. 6.20a. The maximum efficiency is obtained for linearly polarized SFG which is cross-polarized to signal and idler as it can be seen from the histogram. Back-focal-plane (BFP) images in Fig. 6.20b reconstruct, instead, the wave-vector space of the SFG radiation: it can be seen that at the maximum efficiency, photons are dominantly emitted at 45° from the backward direction. If we then substitute this efficiency in the rate equation Eq. 6.9, we find a photon pair generation rate equal to 380 Hz. The discrepancy with the measured value of 35 Hz is due to the lack of a strict analogy between the classical and quantum experiments. In fact, the two experiments are not in reversed geometries. This can be clarified by looking at simulations.

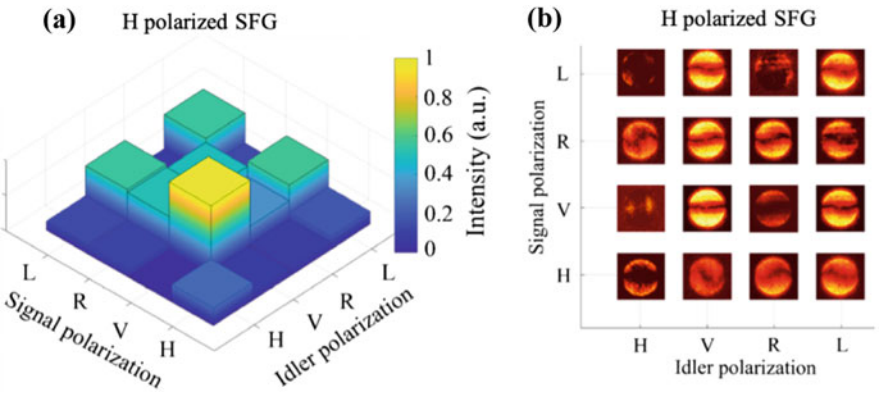

Fig. 6.20 (**a**) Intensity of H-polarized reflected SFG at 770 nm measured with 16 combinations of horizontal (H), vertical (V), right circular (R) and left circular (L) polarizations of signal and idler beams for the nanocylinder geometry in Fig. 6.2. (**b**) Measured reflected SFG images in k-space for the polarization combinations shown in (**a**) and SFG detected with NA = 0.7. *Reprinted with permission from* [46], *© 2019 Optical Society of America*

Figure 6.21c reports the simulated BFP for normal incident co-polarized signal and idler. As in the experiments, a null in the backward direction and a maximum at 45° occur, which is explained by the symmetry of the nonlinear tensor in a wafer with a (100) epitaxial growth. However, the only solution of the SFG emission that satisfies the quantum-classical analogy with the SPDC experiment is the case for which SFG emission overlaps constructively with a linear plane wave emitted normally. This configuration is achieved only when co-polarized signal and idler are incident at oblique angle, and thus SFG is mainly emitted backwards and co-polarized (Fig. 6.21f). This means that in the SPDC experiment the maximum photon pair rate is emitted at 45° from the backward direction and that signal and idler are co-polarized between them and with the pump. This emission is partially detected by the objective NA = 0.7 used in the experiment. These polarizations of signal and idler waves are related to the resonating modes of the AlGaAs nanoantenna.

For example, the SPDC pump linearly polarized will mainly excite an electric dipole which by means of the nonlinear tensor can overlap at signal and idler frequencies with two magnetic dipoles. This correlation is summarized in the two matrices in Figs. 6.22a, b where an SPDC along x or along y generates at signal and idler frequencies only orthogonal Cartesian components of a magnetic dipole. The near field distributions of these modes at pump, signal and idler frequencies are reported in Figs. 6.22c, d, e. This mode correlation at the nanoscale is responsible for the polarization correlation of signal and idler and eventually to their entanglement. The demonstrated nanoscale two-photon emitter allows flexible quantum state engineering by shaping of the spectral and radiation pattern of the nanoantenna and paves the way to more efficient photon pair-generation rates, by either tuning the incident wavelength and angle, or using a doughnut-like cylindrical vector

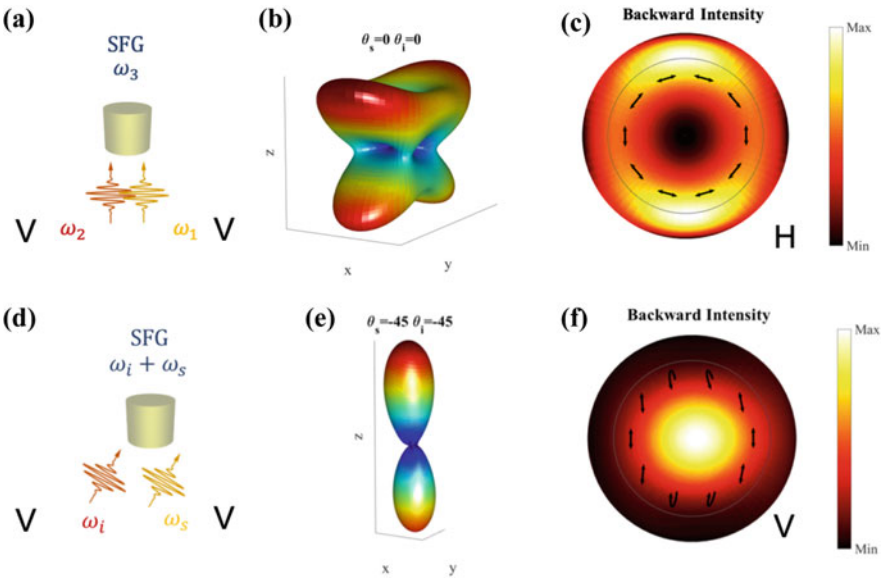

Fig. 6.21 (**a**, **d**) Schematic of the SFG process at normal and oblique incidence, respectively. (**b**, **e**) Calculated SFG radiation pattern, polarized along y (V), for normal and oblique incidence of the signal and idler photons, respectively. (**c**, **f**) Projection of the radiation pattern in backward direction for normal and oblique incidence, respectively. The arrows indicated the polarization of the emitted SFG light. The dotted circles indicate the numerical aperture of our collection objective of NA = 0.7. *Reprinted with permission from* [46]*, © 2019 Optical Society of America*

pump beam, or optimizing the nanoantenna geometry, or performing transmission detection (five-fold enhancement in the SHG efficiency [18]. For example, in a recent work based on QNMs [25], we propose a meta-atom with high $Q_{disk}^{(\omega_1+\omega_2)}$ factor mode at the SPDC pump frequency and we engineer the nonlinear phase so as to maximize the overlap integral between pump and signal and idler modes $\zeta_{disk}^{(\omega_1,\omega_2,\omega_1+\omega_2)}$.

The related photon-pair rate is 550 times higher than the simple nanoantenna shown previously. In this case efficient spatially entangled sources can be achieved along with their spatial multiplexing without occurrence of cross-talk. We can also conceive cross-talk-free spatial multiplexing with the use of multiple nanoantennas or metasurfaces for the generation of complex spatially entangled states [40, 49]. Alternatively, collective response from multiple nanoantennas can be used to enhance the generation rate of polarization-entangled photon pairs, where the occurrence of cross-talk is not detrimental. This is the case of a metasurface working in the photonic crystal regime [50], which will be discussed in details in the following paragraph.

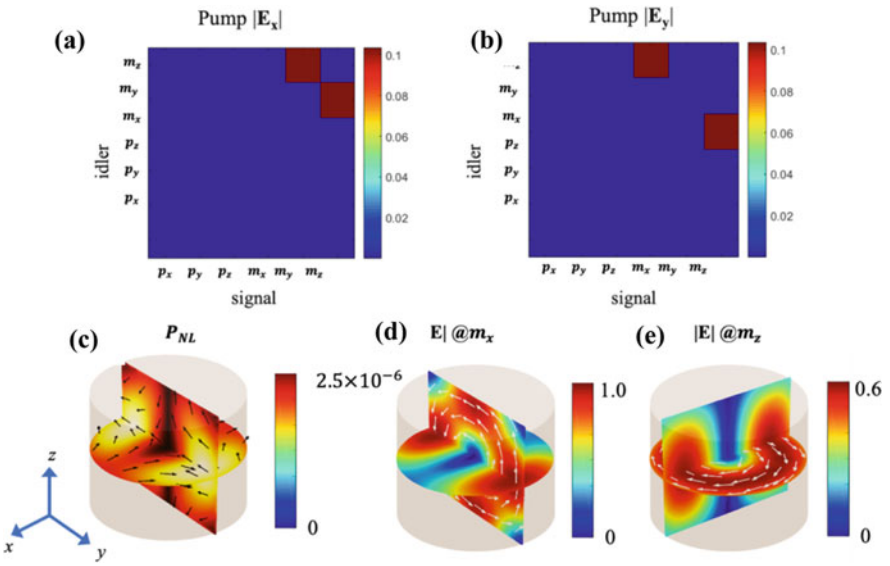

Fig. 6.22 Mode correlation in an AlGaAs nanocylinder for H (**a**) and V (**b**) polarized pump. (**c**) Nonlinear polarization distribution. The field distribution inside the disk when exciting (**d**) m_x and (**e**) m_z at signal and idler wavelengths, respectively. *Reprinted with permission from* [46], *© 2019 Optical Society of America*

6.3.3 From Single Nanoantennas to Quadratically Nonlinear Metasurfaces

Following the first experimental demonstrations on single pillars dealt with in Sects. 6.3.1 and 6.3.2, a few investigations have been performed on more complex structures. The former study of this type focused on AlGaAs nano-dimers, formed by two coupled nanocavities (see Fig. 6.23) [51]. As previously shown in the linear case [52–54], dimers offer more tunability and degrees of freedom for controlling the properties of the generated harmonic fields. One of them is the dependence of the optical response on the linear polarization state of the impinging light with two basic configurations: light polarized parallel and perpendicular to the dimer axis. Moreover, the strong coupling between the induced dipoles at FF affects the SHG process.

While the above dimer structures can be seen as first steps towards the demonstration of $\chi^{(2)}$ metasurfaces, the first demonstration of the latter were reported in 2019 by [50, 55, 56], with a special focus on the possibility of tailoring the SH far field via the interplay between the single nanoantenna radiation diagram

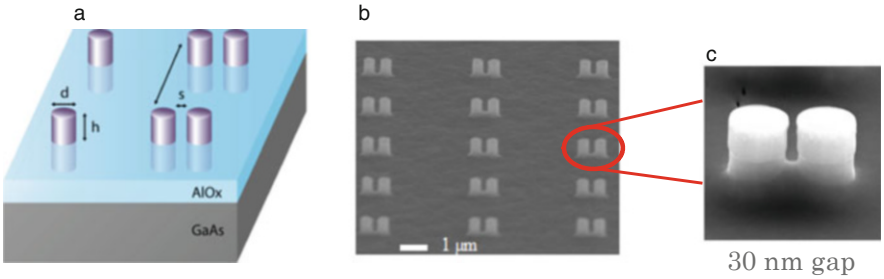

Fig. 6.23 From AlGaAs nano-pillars to nano-dimers: (**a**) scheme; (**b**) scanning-electron-microscope picture; and (**c**) zoom on a single dimer. *Reproduced from* [51]. *Licence number 4850690886866*

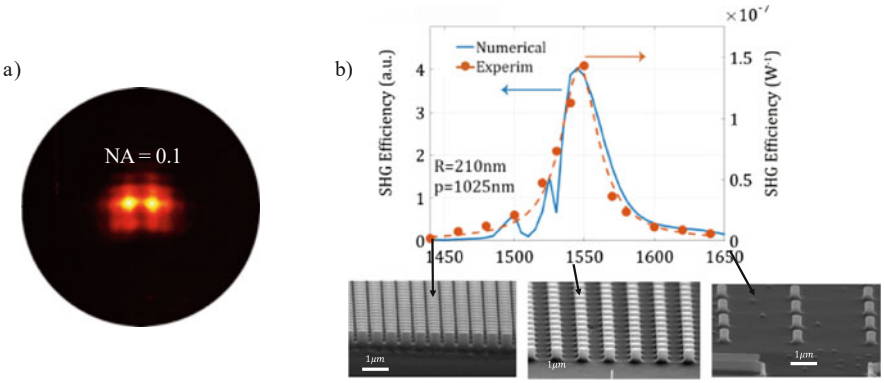

Fig. 6.24 (**a**) Coaxial SHG with a pump beam at normal incidence, and (**b**) SHG efficiency vs the period of a square-lattice metasurface of AlGaAs-on-AlOx circular-basis nanocylinders. Reprinted with permission from [50]. *Copyright (2019) American Chemical Society*

and the array factor of the metasurface in the photonic-crystal regime [57]. These studies have shown that a proper choice of the metasurface periodicity enables both an almost normal SHG despite normal incidence, [100] GaAs orientation and micropillar circular symmetry, and an improvement of the conversion efficiency (see Fig. 6.24). Moreover, using the degree of freedom provided by an elliptical basis of the cylindrical meta-atoms, and their relative orientations with respect to the in-planecrystal axes of a [001]-cut GaAs wafer, a good control on the SH polarization was achieved (see Fig. 6.25).

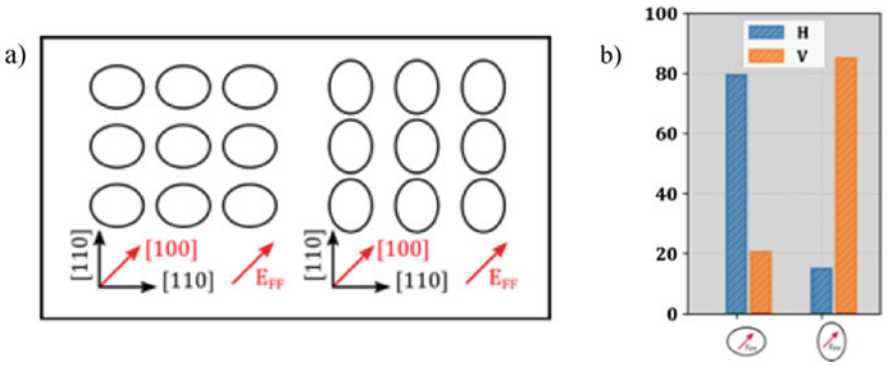

Fig. 6.25 SHG from AlGaAs-on-AlOx metasurfaces consisting of a square array of elliptical-basis nanocylinders: layout (**a**) and experimental SH polarization analysis (**b**), where H and V stand for linear horizontal and vertical polarization, respectively. *Reprinted with permission from* [55]*, © 2019 Optical Society of America*

6.4 Conclusion and Perspectives

This chapter has provided a quick overview of the new field of nonlinear meta-optics [58], with a specific focus on non-metallic metasurfaces and on the most efficient bulk nonlinearity in the near infrared spectral region. Clearly, this well-justified but nonetheless arbitrary choice, has restricted our scope to non-resonant bulk $\chi^{(2)}$, thereby leaving out of the scope both the generally weaker and difficult-to-model surface $\chi^{(2)}$ effects [19] and the promising perspective of metasurface enhanced SHG from the resonant $\chi^{(2)}$ of asymmetric quantum-well intersubband transitions [58].

As this book is being printed, several developments are taking place in nonlinear meta-optics, to combine the frequency generation with more advanced polarization and phase-front shaping of the harmonic field, both with single-layer metasurfaces and multiple layer devices.

Several more developments will occur in the next months and years, for example to endow these nonlinear metasurfaces with exciting reconfigurability properties, as it begins to be the case today with linear meta-optics [59, 60].

Moreover, the future of this exciting research domain will include the combination of topological and nonlinear nanophotonics [61], as well the to-date hardly explored field of quantum metasurfaces. We also believe that an ultra-thin $\chi^{(2)}$ metasurface for the synthesis of two-photon quantum states might introduce a truly revolutionary control over polarization, spectral and spatial properties of entangled quantum states of light, by taking benefit of the extremely large number of modes that are inherently associated to such metasurfaces.

Since the related technology is mostly available and nano-fabrication tolerances appear tough but not impossible to deal with [58], future challenges of nonlinear metasurfaces based on multimode meta-atoms with intricate $\chi^{(2)}$ tensor behavior

will probably occur at the design level. While advanced modelling approaches like the QNM discussed in Sect. 6.2.4 will greatly help, a systematic design approach is urged if pioneer brute-force approach is to give the floor to more subtle strategies. A promising start in this direction is given by the very recent work of Lei Xu et al. [62], but the next years will certainly bring further studies in this direction.

Acknowledgements We are indebted with too many colleagues to cite them all, but special thanks are warmly addressed to Philippe Lalanne, Costantino De Angelis, Dragomir Neshev and Jean-Michel Gérard, for insightful discussions and inspiration.

G.L. acknowledges financial support from ANR projects NOMOS (ANR-18-CE24-0026) and Nanopair (ANR-18-CE92-0043).

References

1. Khurgin JB (2015) How to deal with the loss in plasmonics and metamaterials. Nat Nanotechnol 10:2–6
2. Furube A, Hashimoto S (2017) Insight into plasmonic hot-electron transfer and plasmon molecular drive: new dimensions in energy conversion and nanofabrication. NPG Asia Mater 9:e454
3. Jauffred L, Samadi A, Klingberg H, Bendix PM, Oddershede LB (2019) Plasmonic heating of nanostructures. Chem Rev 119:8087–8130
4. Smith DR, Padilla WJ, Vier DC, Nemat-Nasser SC, Schultz S (2000) Composite medium with simultaneously negative permeability and permittivity. Phys Rev Lett 84:4184–4187
5. Pendry JB, Holden AJ, Robbins DJ, Stewar WJ (1999) Magnetism from conductors and enhanced nonlinear phenomena. IEEE Trans Microw Theory Tech 47:2075–2084
6. Kuznetsov AI, Miroshnichenko AE, Fu YH, Zhang J, Lukyanchukl B (2012) Magnetic light. Sci Rep 2:1–6
7. Carletti L, Locatelli A, Stepanenko O, Leo G, De Angelis C (2015) Enhanced second-harmonic generation from magnetic resonance in AlGaAs nanoantennas. Opt Express 23:26544–26550
8. Boyd R (2008) Nonlinear optics, 3rd edn. Academic
9. Caspani L, Xiong C, Eggleton BJ, Bajoni D, Liscidini M, Galli M, Morandotti R, Moss DJ (2017) Integrated sources of photon quantum states based on nonlinear optics. Light Sci Appl 6:e17100–e17112
10. Fiore A, Janz S, Delobel L, Van Der Meer P, Bravetti P, Berger V, Rosencher E, Nagle J (1998) Second-harmonic generation at λ=1.6 μm in AlGaAs/Al2O3 waveguides using birefringence phase matching. Appl Phys Lett 72:2942–2944
11. Ducci S, Lanco L, Berger V, De Rossi A, Ortiz V, Calligaro M (2004) Continuous-wave second-harmonic generation in modal phase matched semiconductor waveguides. Appl Phys Lett 84:2974–2976
12. Vodopyanov KL, Levi O, Kuo PS, Pinguet TJ, Harris JS, Fejer MM, Gerard B, Becouara L, Lallier E (2004) Optical parametric oscillation in quasi-phasematched GaAs. OSA Trend Opt Photonics Ser 96 A:459–461
13. Grosges T, Vial A, Barchiesi D (2005) Models of near-field spectroscopic studies : comparison between finite-element and finite-difference methods. Opt Express 13:85416–85422
14. Grahn P, Shevchenko A, Kaivola M (2012) Electromagnetic multipole theory for optical nanomaterials. New J Phys 14:1–11
15. Gehrsitz S, Reinhart FK, Gourgon C, Herres N, Vonlanthen A, Sigg H (2000) The refractive index of AlxGa1-xAs below the band gap: accurate determination and empirical modeling. J Appl Phys 87:7825–7837

16. Ohashi M, Kondo T, Ito R, Fukatsu S, Shiraki Y, Kumata K, Kano SS (1993) Determination of quadratic nonlinear optical coefficient of AlxGa1-xAs system by the method of reflected second harmonics. J Appl Phys 74:596–601
17. Gili VF, Carletti L, Locatelli A, Rocco D, Finazzi M, Ghirardini L, Favero I, Gomez C, Lemaître A, Celebrano M, De Angelis C, Leo G (2016) Monolithic AlGaAs second-harmonic nanoantennas. Opt Express 24:15965–15971
18. Camacho-Morales R, Rahmani M, Kruk S, Wang L, Xu L, Smirnova DA, Solntsev AS, Miroshnichenko A, Tan HH, Karouta F, Naureen S, Vora K, Carletti L, De Angelis C, Jagadish C, Kivshar YS, Neshev DN (2016) Nonlinear generation of vector beams from AlGaAs Nanoantennas. Nano Lett 16:7191–7197
19. Liu S, Sinclair MB, Saravi S, Keeler GA, Yang Y, Reno J, Peake GM, Setzpfandt F, Staude I, Pertsch T, Brener I (2016) Resonantly enhanced second-harmonic generation using III-V semiconductor all-dielectric Metasurfaces. Nano Lett 16:5426–5432
20. Lalanne P, Yan W, Vynck K, Sauvan C, Hugonin JP (2018) Light interaction with photonic and Plasmonic resonances. Laser Photonics Rev 12:1–38
21. Bai Q, Perrin M, Sauvan C, Hugonin J-P, Lalanne P (2013) Efficient and intuitive method for the analysis of light scattering by a resonant nanostructure. Opt Express 21:27371–27382
22. Sauvan C, Hugonin JP, Maksymov IS, Lalanne P (2013) Theory of the spontaneous optical emission of nanosize photonic and plasmon resonators. Phys Rev Lett 110:1–5
23. Yan W, Faggiani R, Lalanne P (2018) Rigorous modal analysis of plasmonic nanoresonators. Phys Rev B 97:1–9
24. Wu T, Baron A, Lalanne P, Vynck K (2020) Intrinsic multipolar contents of nanoresonators for tailored scattering. Phys Rev A 011803:1–5
25. Gigli C, Wu T, Marino G, Borne A, Leo G, Lalanne P (2020) Quasinormal-mode non-Hermitian modeling and design in nonlinear Nano-optics. ACS Photonics 7:1197–1205
26. QNM solvers and toolboxes are freely available online at https://www.lp2n.institutoptique.fr/light-complex-nanostructures
27. Celebrano M, Wu X, Baselli M, Großmann S, Biagioni P, Locatelli A, De Angelis C, Cerullo G, Osellame R, Hecht B, Duò L, Ciccacci F, Finazzi M (2015) Mode matching in multiresonant plasmonic nanoantennas for enhanced second harmonic generation. Nat Nanotechnol 10:412–417
28. Ghirardini L, Carletti L, Gili V, Pellegrini G, Duò L, Finazzi M, Rocco D, Locatelli A, De Angelis C, Favero I, Ravaro M, Leo G, Lemaître A, Celebrano M (2017) Polarization properties of second-harmonic generation in AlGaAs optical nanoantennas. Opt Lett 42:559–562
29. Carletti L, Rocco D, Locatelli A, De Angelis C, Gili VF, Ravaro M, Favero I, Leo G, Finazzi M, Ghirardini L, Celebrano M, Marino G, Zayats AV (2017) Controlling second-harmonic generation at the nanoscale with monolithic AlGaAs-on-AlOx antennas. Nanotechnology 28
30. Carletti L, Marino G, Ghirardini L, Gili VF, Rocco D, Favero I, Locatelli A, Zayats AV, Celebrano M, Finazzi M, Giuseppe L, de Angelis C, Neshev DN (2018) Nonlinear goniometry by second harmonic generation in AlGaAs nanoantennas. ACS Photonics 5:4386–4392
31. Sautter JD, Xu L, Miroshnichenko AE, Lysevych M, Volkovskaya I, Smirnova DA, Camacho-Morales R, Zangeneh Kamali K, Karouta F, Vora K, Tan HH, Kauranen M, Staude I, Jagadish C, Neshev DN, Rahmani M (2019) Tailoring second-harmonic emission from (111)-GaAs nanoantennas. Nano Lett 19:3905–3911
32. Xu L, Saerens G, Timofeeva M, Smirnova DA, Volkovskaya I, Lysevych M, Camacho-morales R, Cai M, Kamali KZ, Huang L, Karouta F, Tan HH, Jagadish C, Miroshnichenko AE, Grange R, Neshev DN, Rahmani M (2020a) Forward and backward switching of nonlinear unidirectional emission from GaAs nanoantennas. ACS Nano 14:1379–1389
33. Rocco D, Gigli C, Carletti L, Marino G, Vincenti MA, Leo G, De Angelis C (2020) Vertical Second Harmonic Generation in asymmetric dielectric nanoantennas. IEEE Photonics J 12:1–7

34. Ghirardini L, Marino G, Gili VF, Favero I, Rocco D, Carletti L, Locatelli A, de Angelis C, Finazzi M, Celebrano M, Neshev DN, Giuseppe L (2018) Shaping the nonlinear emission pattern of a dielectric nanoantenna by integrated holographic gratings. Nano Lett 18:6750–6755
35. Rodríguez-fortuño FJ, Marino G, Ginzburg P, O'Connor D, Martínez A, Wurtz GA, Zayats AV (2013) Electromagnetic guided modes. Science 328:328–331
36. Müller M, Bounouar S, Jöns KD, Glässl M, Michler P (2014) On-demand generation of indistinguishable polarization-entangled photon pairs. Nat Photonics 8:224–228
37. Versteegh MAM, Reimer ME, Jöns KD, Dalacu D, Poole PJ, Gulinatti A, Giudice A, Zwiller V (2014) Observation of strongly entangled photon pairs from a nanowire quantum dot. Nat Commun 5:5298
38. Kwiat PG, Mattle K, Weinfurter H, Zeilinger A, Sergienko AV, Shih Y (1995) New high-intensity source of polarization-entangled photon pairs. Phys Rev Lett 75:4337–4341
39. Bayraktar Ö, Swillo M, Canalias C, Björk G (2016) Quantum-polarization state tomography. Phys Rev A 94:1–5
40. Wang K, Titchener JG, Kruk SS, Xu L, Chung H, Parry M, Kravchenko II, Chen Y, Solntsev AS, Kivshar YS, Neshev DN, Sukhorukov AA (2018) Quantum metasurface for multiphoton interference and state reconstruction. Science 1108:1104–1108
41. Sipahigil A, Evans RE, Sukachev DD, Burek MJ, Borregaard J, Bhaskar MK, Nguyen CT, Pacheco JL, Atikian HA, Meuwly C, Camacho RM, Jelezko F, Bielejec E, Park H, Lončar M, Lukin MD (2016) An integrated diamond nanophotonics platform for quantum-optical networks. Science 354:847–850
42. Senellart P, Solomon G, White A (2017) High-performance semiconductor quantum-dot single-photon sources. Nat Nanotechnol 12:1026–1039
43. Somaschi N, Giesz V, De Santis L, Loredo JC, Almeida MP, Hornecker G, Portalupi SL, Grange T, Antón C, Demory J, Gómez C, Sagnes I, Lanzillotti-Kimura ND, Lemaítre A, Auffeves A, White AG, Lanco L, Senellart P (2016) Near-optimal single-photon sources in the solid state. Nat Photonics 10:340–345
44. Aharonovich I, Englund D, Toth M (2016) Solid-state single-photon emitters. Nat Photonics 10:631–641
45. Tran TT, Bray K, Ford MJ, Toth M, Aharonovich I (2016) Quantum emission from hexagonal boron nitride monolayers. Nat Nanotechnol 11:37–41
46. Marino G, Solntsev AS, Xu L, Gili VF, Carletti L, Poddubny AN, Rahmani M, Smirnova DA, Chen H, Lemaître A, Zhang G, Zayats AV, De Angelis C, Leo G, Sukhorukov AA, Neshev DN (2019a) Spontaneous photon-pair generation from a dielectric nanoantenna. Optica 6:1416
47. Guo X, Zou CL, Schuck C, Jung H, Cheng R, Tang HX (2017) Parametric down-conversion photon-pair source on a nanophotonic chip. Light Sci Appl 6:1–8
48. Poddubny AN, Iorsh IV, Sukhorukov AA (2016) Generation of photon-Plasmon quantum states in nonlinear hyperbolic metamaterials. Phys Rev Lett 117:1–6
49. Stav T, Faerman A, Maguid E, Oren D, Kleiner V, Hasman E, Segev M (2018) Quantum entanglement of the spin and orbital angular momentum of photons using metamaterials. Science 361:1101–1104
50. Marino G, Gigli C, Rocco D, Lemaître A, Favero I, De Angelis C, Leo G, De Angelis C, Leo G (2019b) Zero-order second harmonic generation from AlGaAs-on-insulator metasurfaces. ACS Photonics 6:1226–1231
51. Rocco D, Gili VF, Ghirardini L, Carletti L, Favero I, Locatelli A, Marino G, Neshev DN, Celebrano M, Finazzi M, Leo G, De Angelis C (2018) Tuning the second-harmonic generation in AlGaAs nanodimers via non-radiative state optimization [invited]. Photonics Res 6:B6
52. Albella P, Poyli MA, Schmidt MK, Maier SA, Moreno F, Sáenz JJ, Aizpurua J (2013) Low-loss electric and magnetic field-enhanced spectroscopy with subwavelength silicon dimers. J Phys Chem C 117:13573–13584
53. Zywietz U, Schmidt MK, Evlyukhin AB, Reinhardt C, Aizpurua J, Chichkov BN (2015) Electromagnetic resonances of silicon nanoparticle dimers in the visible. ACS Photonics 2:913–920

54. Bakker RM, Permyakov D, Yu YF, Markovich D, Paniagua-Domínguez R, Gonzaga L, Samusev A, Kivshar Y, Lukyanchuk B, Kuznetsov AI (2015) Magnetic and electric hotspots with silicon nanodimers. Nano Lett 15:2137–2142
55. Gigli C, Marino G, Suffit S, Patriarche G, Beaudoin G, Pantzas K, Sagnes I, Favero I, Leo G (2019) Polarization- and diffraction-controlled second-harmonic generation from semiconductor metasurfaces. J Opt Soc Am B 36:E55–E63
56. FJF L, Fedotova AN, Liu S, Keeler GA, Peake GM, Saravi S, Shcherbakov MR, Burger S, Fedyanin AA, Brener I, Pertsch T, Setzpfandt F, Staude I (2018) Polarization-dependent second harmonic diffraction from resonant GaAs metasurfaces. ACS Photonics 5:1786–1793
57. Rybin MV, Filonov DS, Samusev KB, Belov PA, Kivshar YS, Limonov MF (2015) Phase diagram for the transition from photonic crystals to dielectric metamaterials. Nat Commun 6:6–11
58. De Angelis C, Leo G, Neshev DN (2020) Nonlinear meta-optics, 1st edn. CRC Press
59. Li S, Xu X, Veetil RM, Valuckas V, Kuznetsov AI (2019) Phase-only transmissive spatial light modulator based on tunable dielectric metasurface. Science 364(6445):1087–1090
60. Arbabi E, Arbabi A, Kamali SM, Horie Y, Faraji-Dana MS, Faraon A (2018) MEMS-tunable dielectric metasurface lens. Nat Commun 9
61. Smirnova D, Leykam D, Chong Y, Kivshar Y (2020) Nonlinear topological photonics. Appl Phys Rev 7
62. Xu L, Rahmani M, Ma Y, Smirnova DA, Kamali KZ, Deng F, Chiang YK, Huang L, Zhang H, Gould S, Neshev DN, Miroshnichenko AE (2020) Enhanced light–matter interactions in dielectric nanostructures via machine-learning approach. Adv Photonics 2:1

Chapter 7
Nanophotonic Circuits for Unconventional Computing Applications

Wolfram Pernice

Abstract Photonic integrated circuits allow for designing computing architectures which process optical signals in analogy to electronic integrated circuits. Therein electrical connections are replaced with photonic waveguides which guide light to desired locations on chip. Through near-field coupling, such waveguides enable interactions with functional materials placed very close to the waveguide surface. This way, photonic circuits which are normally passive in their response are able to display active functionality and thus provide the means to build reconfigurable systems. Here several approaches for implementing active photonic devices based on heterogeneous integration with phase-change materials are presented. The chapter focusses on the design of photonic circuits for information processing in non-von-Neumann architectures.

7.1 Introduction

Optical information processing holds tremendous promise because of the wide bandwidth available to optical carrier waves [1]. However, a majority of implementations involves electro-optical conversions, meaning that primary signals are created electrically and are then impregnated onto optical waves as signal carriers [2]. This process involves fast modulators and fast photodetectors and consumes significant amounts of energy. Power efficient implementations of optical information processing devices would likely circumvent detours through electronic devices and thus operate entirely in the optical domain. In order to do so, suitable platforms which enable all aspects of information processing, such as logic operation and memory storage need to be realized [3]. In this chapter, an emerging realization employing active optical materials is presented. In order to enhance the functionality of traditional nanophotonic devices, passive waveguides

W. Pernice (✉)
Institute of Physics, University of Münster, Münster, Germany
e-mail: wolfram.pernice@uni-muenster.de

M. Cesaria et al. (eds.), *Light-Matter Interactions Towards the Nanoscale*,
NATO Science for Peace and Security Series B: Physics and Biophysics,
https://doi.org/10.1007/978-94-024-2138-5_7

are equipped with nanoscale patches of phase-change materials (PCMs) [4]. These materials provide strong optical contrast when switched between amorphous and crystalline phase states. The phase-change comes with attractive properties, such as long retention times, reversible switching operation and high cyclability [5]. In addition, the change in optical properties is significantly stronger compared to alternative modulation techniques exploiting electro-optical effects, thermo-optical effects or also mechanical modulation of optical properties. The phase change can be conveniently induced all-optically with short laser pulses. Importantly, the change in optical properties is maintained in nanoscale devices and is thus compatible with nanophotonic waveguides [6].

A typical device architecture is depicted in Fig. 7.1a. The PCM element (made from the material GST) is deposited directly on to of a waveguide [7]. This way, the propagating optical pulses (red, yellow) interact with the PCM element in the evanescent near field. Because the PCM provides higher refractive index compared to the dielectric waveguide, the optical mode is pulled towards the phase change region and creates strong interaction with the light field.

A fabricated device is shown in the scanning electron microscope (SEM) image in Fig. 7.1b. The PCM cell is shown in false-color on top of the waveguide. When switching is induced, the crystalline structure of the PCM cell changes strongly.

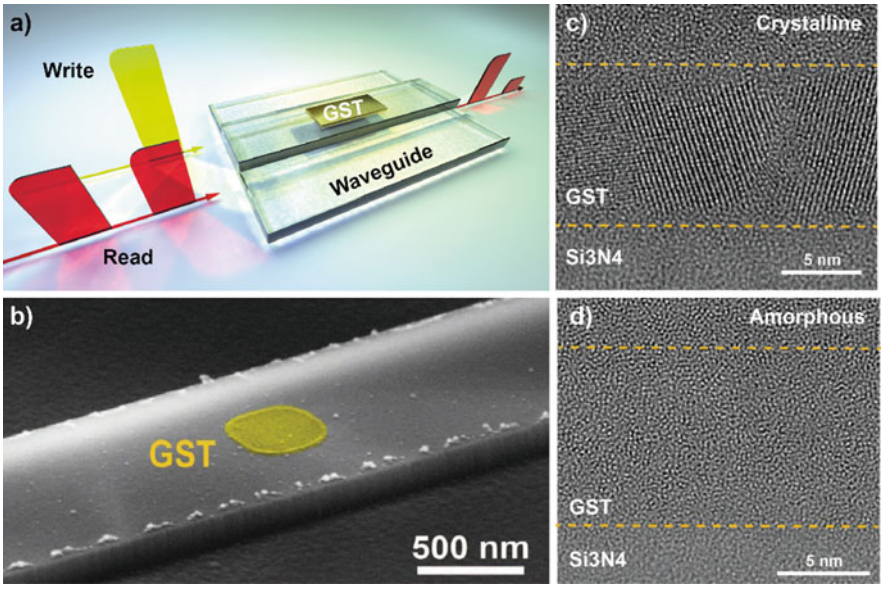

Fig. 7.1 Phase-change nanophotonic devices. (**a**) Schematic of a waveguide with integrated PCM cell. Switching and readout is performed using short optical pulses. (**b**) SEM image of a fabricated device. The PCM element is shown in false-color overlay. (**c**) TEM image of a PCM cell in the crystalline phase state, showing pronounced microcrystals in the GST section. (**d**) TEM image of a PCM cell in the amorphous phase state. No crystal structure is visible

This can be observed directly using transmission electron microscopy (TEM). Two PCM cells in the crystalline and amorphous phase are shown in Fig. 7.1c and d, respectively. In the crystalline phase, the PCM GST shows clear signatures of microcrystals, while in the amorphous phase no crystalline order is visible. In such devices the presence of the GST modulates the optical transmission in the waveguide. In the crystalline phase, the GST is highly absorptive and thus transmission past the device is strongly suppressed. In the amorphous phase, on the other hand, the absorption losses are low and thus the transmitted signal is only weakly attenuated.

Via intensity modulation, the PCM cell can be used as an optical memory, where the crystalline state is associated with a logical "0" and the amorphous state with a logical "1" as depicted in Fig. 7.1a. Importantly, the transition between both states can be induced in a semi-continuous fashion. By performing stepwise crystallization and amorphization, intermediate transmission levels can be recorded in the PCM cell [8]. This enables multi-level photonic storage and thus saving multiple bits in a single optical element. With respect to optical memories, this way the memory density of waveguide integrated devices can be strongly enhanced. In addition, access to multi-level transmission levels forms the basis of non-von-Neumann photonic devices as described in the following sections. In such devices, data processing and data storage is not carried out in physically separate locations, but rather in the same device.

7.2 Arithmetic Processing with PCM Photonic Devices

The multi-level transmission capability of waveguide integrated PCM devices enables the implementation of basic arithmetic processors. This way elementary processors such as mechanical abaci can be implemented in the optical domain. By associating the transmission levels with the beads of a mechanical abacus, basic arithmetic functions can be realized. In such a system, sliding of a mechanical bead corresponds to sending an optical pulse past the PCM cell in order to induce partial crystallization. Thus counting optical pulses is equivalent to shifting a given number of beads.

Since in a mechanical abacus several strings of beads are available, an optical abacus needs to provide multiple storage sites. This can be achieved by using an array of PCM cells such that each site corresponds to one string. Differing from a mechanical device, two-dimensional computations are thus feasible on a chip. At the same time, the array layout provides a convenient addressing scheme in row and column format as depicted in Fig. 7.2a [9]. In order to use such an approach, the PCM elements are switched not with a single optical pulse, but with two overlapping pulses. Switching within a desired PCM cell then occurs when the pulses overlap in time at the PCM site. This scheme therefore also implements an optical random access memory (ORAM) [10].

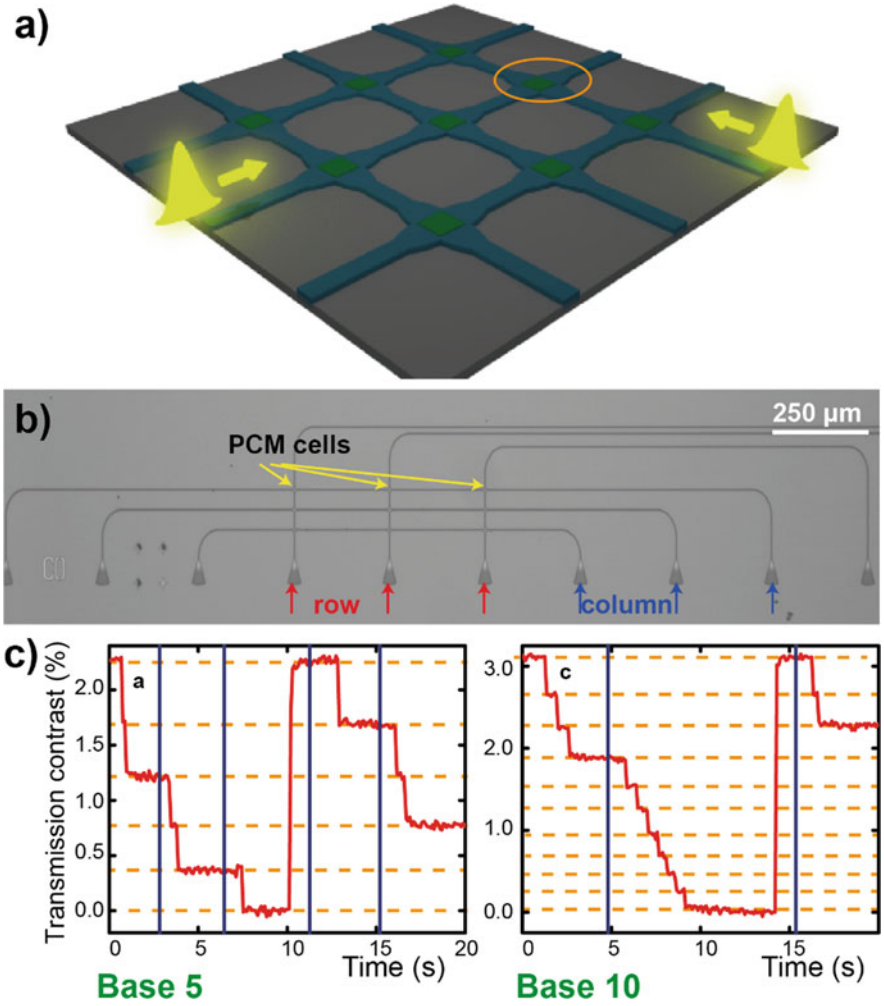

Fig. 7.2 (**a**) Schematic illustration of an optical random access memory. Rows and columns are selected as input for optical pulses. Switching within the marked PCM cell is induced when both pulses overlap in time. (**b**) SEM micrograph of a fabricated all-optical abacus with nine PCM elements. (**c**) Multi-level processing in two different bases (5, left and 10, right)

A physical implementation of an all-optical abacus is shown in the nanofabricated device in Fig. 7.2b. The photonic circuits is fabricated on a silicon nitride-on-insulator platform using electron beam lithography (EBL) and dry etching. Under optimized processing conditions high quality photonic devices with low propagation loss can be obtained. The optical abacus features nine PCM cells and thus allows for arithmetic processing of numbers with up to nine digits. Light is injected into the photonic circuit using photonic grating couplers, which are the triangular structures

visible at the bottom of the SEM image. These devices can be aligned to optical fibers to enable multi-port access to a photonic arithmetic processor. Through the fibers optical pulses can be conveniently injected.

Arithmetic operations are carried out in the device by injecting a desired number of optical pulses into an amorphized PCM cell. By choosing a desired partial crystallization level, the number of intermediate phase states can be selected and thus also the arithmetic base at the same time. This is shown for two examples in Fig. 7.2c for base 5 and base 10. When full crystallization is reached, a reset pulse is necessary to re-amorphize the PCM cell and to implement a carry-over into a neighboring PCM element. By realizing arithmetic addition as a base function, all other arithmetic functions can be carried out this way in the optical domain.

7.3 Artificial All-Optical Neural Networks

Multi-level transmission modulation enables further advanced optical processing schemes, in particular brain-inspired or neuromorphic computing approaches. This allows implementing all-optical artificial neural networks (ANNs) [11]. Such structures combine hardware mimics of neurons and synapses to interconnected networks for information processing. As with the abacus, also in ANNs data storage and data processing is carried out in the same physical location.

PCMs lend themselves in combination with nanophotonic circuits for the implementation of ANNs. The high cyclability enables many switching operations to be carried out. By exploiting multi-level crystallization, convenient weighting of input data can be performed with nonvolatile data retention. The nanoscale size of the PCM elements further enable compact implementations of artificial synapses.

Using evanescently coupled nanoscale PCM cells we have implemented functional all-optical neurosynaptic spiking networks [12]. The schematic of a single artificial optical neuron is shown in Fig. 7.3a. Plastic synapses are created by employing PCM cells as transmission modulators, thus realizing programmable weighting of the input. In order to combine the input from multiple ports wavelength division multiplexing (WDM) on different wavelengths is used to avoid interference on the summation waveguide [13]. Spike generation in dependence of a given threshold power is implemented with optical microring resonators. These devices enable realizing a power dependent threshold function by relying on the shift of the resonance of the ring when the embedded PCM cell is switched. Changing the phase state of the PCM corresponds to a change in refractive index and thus a change in the optical path length of the device. This in turn modifies the overall length of the ring resonator and thus the resonance condition. By positioning a probe optical pulse on the bottom bus waveguide going past the ring resonator precisely at one of the ring resonances, the overall transmission can be modulated in dependence of the phase state of the PCM cell.

A fabricated neuron device with four input weights is depicted in Fig. 7.3b. The neuron comprises four ring resonators for WDM, as well as four PCM cells

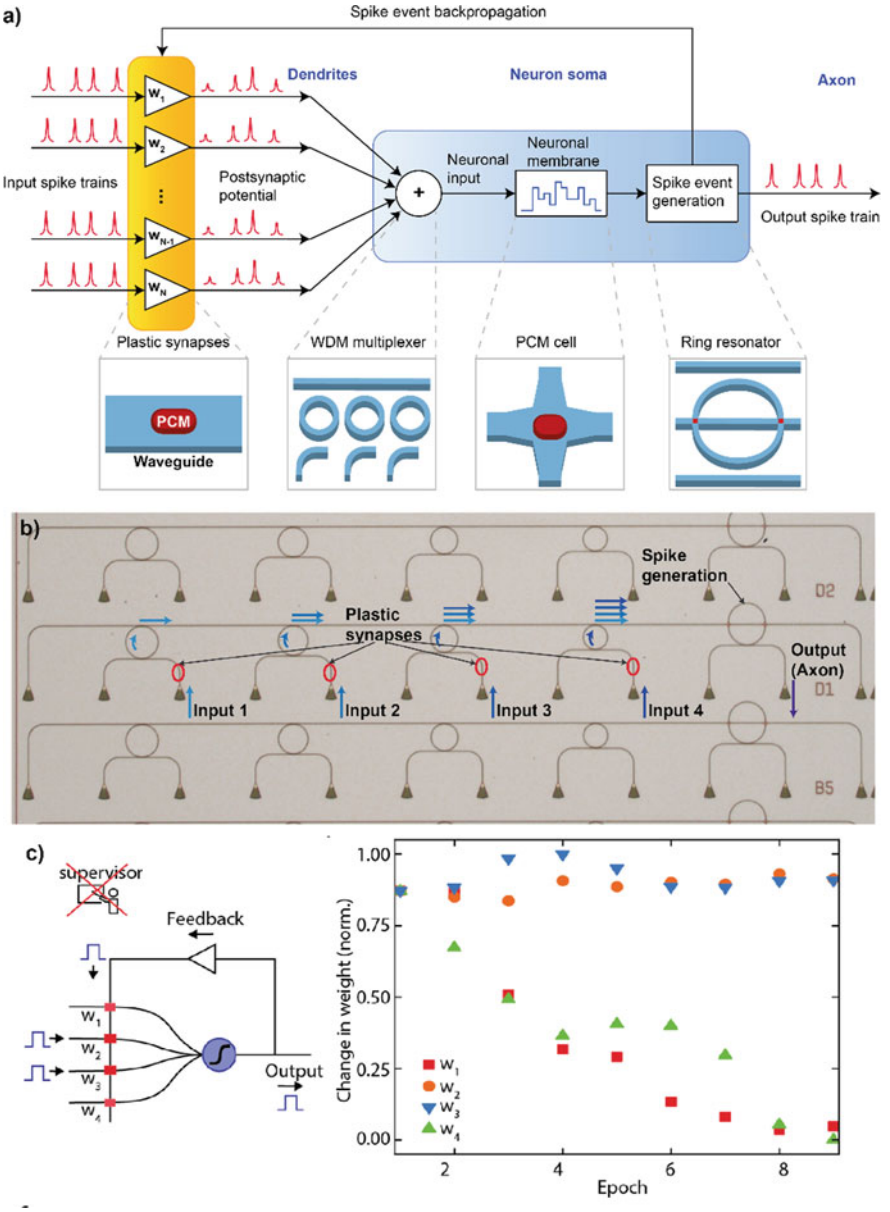

Fig. 7.3 (**a**) Schematic of an artificial all-optical neuron implemented with PCM cells. (**b**) Optical micrograph of a fabricated single neuron with four optical inputs. (**c**) Self-learning operation of the neuron with inherent optical feedback. Two of the input weights remain constant, while w1 and w1 converge towards the crystalline phase state

in the waveguides leading to the ring resonators acting as artificial synapses [14]. In addition, a crossed ring resonator with embedded PCM cell is used to implement the required spiking functionality. As PCM GST is used while the waveguides are made from silicon nitride.

The functionality of the neuron is depicted in Fig. 7.3c. The neuron can be operated either using an external programmer or with inherent optical feedback to show self-learning capability. In self-learning mode, the output pulse generated by the ring resonator is re-routed towards the input weights. Using longer pulses in the nanosecond range, partial temporal overlap with the output pulse can be achieved. This way two-pulse switching as used in the ORAM is possible to reinforce desired weighting.

In the recorded data the development of the four input weights during several training epochs is depicted. From the measurements it can be seen, that two weights converge towards the crystalline state, while the other two weights remain in the amorphous phase state at high transmission. In a four-pixel representation the neuron thus learned to recognize the image diagonal.

With more input waveguides more complex pixel representations can be created. As a proof-of-principle demonstration, letter images composed of 3x5 pixels were successfully learned by a single-layer neural network comprised of four neurons with 15 input weights each. Therefore this exemplary network can be trained to recognize the letters “A”, “B”, “C” and “D” in a reproducible fashion, all in the optical domain.

7.4 Conclusions

Phase-change nanophotonic hybrid circuits offer unique capabilities for implementing reconfigurable integrated optical devices. Particularly attractive is the capability to maintain a desired phase state without the need for continuous input power and thus nonvolatile data retention.

By integrating PCM elements directly with nanophotonic waveguides the strong optical contrast can be conveniently employed to modify the optical properties of a propagating mode. Since PCMs provide high refractive indices, nanoscale cells are sufficient to induce a significant change in the effective mode index. This can be either exploited for inducing a tunable phase shift, or for inducing tunable absorption for transmission modulation.

Combined with the toolbox of nanophotonics, a wide range of functional devices can be realized through this approach. Since nonvolatile phase state retention implies memory storage, in particular computing approaches which exploit in-memory computing can be ported conveniently to a phase-change photonic platform.

Because the phase change can furthermore be induced electrically, attractive options for mixed-mode devices come within reach. In such hybrid approaches either optical switching combined with electrical readout could be envisioned, as

well as electrical switching combined with optical readout. The latter furthermore enables combination with established electrical platforms for direct programming of phase change photonic components.

References

1. Lugt AV (1968) A review of optical data-processing techniques. Opt Acta Int J Opt 15:1
2. Alferness RC (1982) Waveguide Electrooptic Modulators. IEEE Trans Microwave Theory Tech 30:1121
3. Hutchby JA (2008) Emerging Nanoscale Memory and Logic Devices: A Critical Assessment. Computer 41:28
4. Lencer D, Salinga M, Grabowski B, Hickel T, Neugebauer J, Wuttig M (2008) A map for phase-change materials. Nat Mater 7:972
5. Wuttig M (2005) Phase-change materials: towards a universal memory? Nat Mater 4:265
6. Rios C, Hosseini P, Wright CD, Bhaskaran H, Pernice WHP (2014) On-Chip Photonic Memory Elements Employing Phase-Change Materials. Adv Mater 26:1372
7. Ríos C, Stegmaier M, Hosseini P, Wang D, Scherer T, Wright CD, Bhaskaran H, Pernice WHP (2015) Integrated all-photonic non-volatile multi-level memory. Nat Photonics 9:725
8. Li X, Youngblood N, Ríos C, Cheng Z, Wright CD, Pernice WHP, Bhaskaran H (2019) Fast and reliable storage using a 5 bit, nonvolatile photonic memory cell. Optica 6:1
9. Feldmann J, Stegmaier M, Gruhler N, Ríos C, Bhaskaran H, Wright CD, Pernice WHP (2017) Calculating with light using a chip-scale all-optical abacus. Nat Comm 8:1256
10. Raoux S, Burr GW, Breitwisch MJ, Rettner CT, Chen Y-C, Shelby RM, Salinga M, Krebs D, Chen SH, Lung HL, Lam CH (2008) Phase-change random access memory: A scalable technology. IBM J Res Dev 52:465
11. Jain AK, Mao J, Mohiuddin KM (1996) Artificial Neural Networks: A Tutorial. Computer 29:31
12. Feldmann J, Youngblood N, Wright CD, Bhaskaran H, Pernice WHP (2019) All-optical spiking neurosynaptic networks with self-learning capabilities. Nature 569:208
13. Brackett CA (1990) Dense wavelength division multiplexing networks: Principles and applications. IEEE J Sel Areas Commun 8:948
14. Cheng Z, Ríos C, Pernice WHP, Wright CD, Bhaskaran H (2017) On-chip photonic synapse. Sci Adv 3:e1700160

Chapter 8
Terahertz Light-Matter Interactions at the Nanoscale

John W. Bowen

Abstract This chapter focuses on how terahertz frequency electromagnetic radiation interacts with matter at the nanoscale. Despite the challenges posed by the relatively long wavelengths of terahertz radiation, which lie in the millimetre to sub-millimetre wavelength regime, recent developments have made it possible to use terahertz radiation to image, probe and manipulate matter at unprecedented sub-wavelength scales, with nanometre or even sub-nanometre resolution. The information gained is complementary to that obtained in other regions of the spectrum. Furthermore, strong field enhancements due to nanoscale confinement of terahertz radiation provide a new label-free tool for biosensing. In addition, a growing body of evidence suggests that terahertz radiation can be used to manipulate the functioning of biological processes at the nanoscale, potentially leading to novel clinical applications. The chapter introduces the terahertz range and its underpinning technology, as well as covering the latest research results in these areas.

Keywords Terahertz technology · Terahertz biosensing · Terahertz control · Nanoscopy · Biomolecular spectroscopy · Bioelectromagnetics

8.1 Introduction

The terahertz frequency portion of the electromagnetic spectrum covers frequencies between 100 GHz and 10 THz, corresponding to wavelengths from 3 mm to 30 μm. This places it between the microwave and infrared regions. Although the radiation is not visible, terahertz waves can propagate in well-defined beams through free space and can be controlled with the aid of mirrors and lenses. In this sense, terahertz radiation is sometimes referred to as "terahertz light". However, the wavelengths involved are orders of magnitude greater than those of visible light. Nevertheless,

J. W. Bowen (✉)
School of Biological Sciences, University of Reading, Reading, UK
e-mail: j.bowen@reading.ac.uk

M. Cesaria et al. (eds.), *Light-Matter Interactions Towards the Nanoscale*,
NATO Science for Peace and Security Series B: Physics and Biophysics,
https://doi.org/10.1007/978-94-024-2138-5_8

recent developments have made it possible to use terahertz radiation to image, probe and control matter at the nanoscale, providing information complimentary to that obtained in other regions of the electromagnetic spectrum.

Terahertz photons have energies corresponding to molecular rotations and vibrations, particularly the collective vibrational modes of large molecules and the hydrogen bond fluctuations in networks of water molecules. The energies are low enough that the radiation is non-ionising, and many visibly opaque materials become transmissive in the terahertz range, giving rise to a wide range of application areas, such as security screening [1] and imaging of artworks [2]. Additionally, terahertz spectroscopy can be used to measure the conductivity and ultrafast carrier dynamics of materials such as semiconductors and nano-materials [3]. This chapter focuses on recent attempts to extend these capabilities to the imaging and manipulation of matter at the nanometre or even sub-nanometre scale. Current indications are that this may have profound implications in, for example, label-free biosensing and lead to potential new clinical applications based around manipulating the functioning of biological processes at the nanoscale.

Following an overview of the underlying terahertz technology, the chapter will discuss the latest developments in terahertz nanoscopy, terahertz scanning tunnelling microscopy, terahertz sensing with nano-slot antennas, terahertz control over matter, nanoscale phenomena in biological systems and terahertz bioelectromagnetics.

8.2 Terahertz Technology

There are a number of ways to generate and detect terahertz radiation. Currently, the most widely adopted approach is via the generation and detection of ultrafast pulses of terahertz radiation, ultimately derived from femtosecond pulsed near-infrared lasers. Generation is most commonly achieved either using a dc-biased photoconductive switch-based antenna, which launches a short terahertz pulse after being triggered by an incident near-infrared pulse, or via a non-linear crystal which produces a short terahertz pulse derived from the difference frequencies present within the near-infrared pulse. After propagating to, and interacting with a sample, the emergent terahertz pulse can be detected either with a second, unbiased, photoconductive antenna, or with an electro-optic detector consisting of a crystal that displays the Pockels effect, a polarisation splitter and a pair of balanced photodiodes. In both cases a further near-infrared pulse derived from the femtosecond laser is used to gate the detector, so that a signal is only detected when both the terahertz and near-infrared pulses are co-incident on the detector. As the terahertz pulses are longer in duration than the near-infrared pulses, a scanning optical delay line can be used to delay the gating pulse with respect to the pulse used to pump the generator, enabling the time domain waveform of the detected pulse to be recorded. If a reference waveform with no sample present is recorded, the relative amplitude and time delay of the detected waveform after interaction with the sample can be determined. By Fourier transformation of the

pulse waveforms to the frequency domain and ratioing the sample spectrum to the reference spectrum, the frequency-dependent amplitude and phase transmission or reflection coefficients of the sample can be determined. In the case of a layered sample measured in a reflection configuration, the incident terahertz pulses give rise to a series of reflected pulses in the detected waveform corresponding to reflections from the interfaces between the sub-surface layers. The resulting waveform can be analysed to provide depth information on the internal layered structure of the sample, or individual reflection signatures can be isolated to provide spectroscopic information on particular layers. By mounting the sample on an *x*-*y* translation stage and scanning it through a tightly focussed terahertz beam, a two-dimensional image of the object can be formed. In combination with the depth information derived from the time domain waveform recorded for each pixel, a three-dimensional image of the internal structure of the sample can be reconstructed. Alternatively, the terahertz generation and detection heads can be raster scanned across a stationary object to the same effect.

The above technique gives broad spectral coverage from at least 100 GHz to 3 THz or more, depending on the exact implementation. However, there are a variety of alternative terahertz sources that emit essentially a single frequency at once, although it may be possible to sweep their output frequency over a limited bandwidth or retune them to another frequency to obtain high resolution spectroscopic information. Some of these are derived from solid-state electronic sources, such as Gunn and IMPATT oscillators, or from vacuum tube devices, such as reflex klystrons and backward wave oscillators, extended upwards in frequency from the microwave region. However, the power available from them drops off dramatically as the frequency is increased above 100 GHz. Often they may be used to pump solid-state diode-based frequency multipliers to extend their output further into the terahertz range, although with further decline in the output power.

Other sources, extended downwards in frequency from the infrared and visible regions include photomixers, which give an output at the difference frequency between two diode lasers, and quantum cascade lasers, although the latter are currently limited to frequencies above 1 THz.

Optically-pumped terahertz (or far-infrared) lasers can be tuned to emit at specific lines throughout the terahertz range, deriving from molecular transitions in whichever laser gas is used. They are, however, considerably more complicated to operate than the sources mentioned above.

Other, intense, sources of terahertz radiation include p-Ge lasers, free-electron lasers and synchrotron light sources.

Likewise, there are a variety of detectors that can be used for terahertz radiation. These include direct detectors and heterodyne receivers based on Schottky diodes, superconductor-insulator-superconductor (SIS) mixers, hot-electron bolometers, superconducting hot electron bolometers, composite bolometers, kinetic induction detectors and pyroelectric detectors. Recently, imaging arrays have also become commercially available.

The sources mentioned above can produce well-directed beams of terahertz radiation, which can propagate through free-space and be refocused using lenses

and mirrors. However, in order to keep terahertz optical systems to a convenient size, these beams are laterally confined to a few wavelengths or tens of wavelengths, leading to significant diffractive spreading as they propagate. Furthermore, any optical components have to be placed in the near-field or near to far-field transition region of the beam, meaning that more general treatments than geometrical optics have to be used in their design [4]. As a consequence of diffraction, there is a minimum spot size to which the beam can be focussed. As this is around half a wavelength, and the wavelengths of terahertz radiation are in the millimetre and sub-millimetre range, special techniques are required to reach nanometre scales.

8.3 Terahertz Nanoscopy

In 2008, Huber et al. demonstrated imaging at 2.45 THz with a spatial resolution of 40 nm [5]. This was achieved by focusing the beam from an optically-pumped terahertz laser onto the tip of an atomic force microscope (AFM) positioned over the sample. By scanning the tip over the sample, simultaneous AFM and terahertz images could be obtained of the same object. The AFM tip acted as an antenna to plasmonically concentrate the terahertz field at the apex of the tip to nanometre dimensions via the lightning rod effect. Non-linearities at the tip, dependent on the tip-to-sample distance, generate higher harmonics of the tapping frequency of the tip in the scattered terahertz signal, serving to separate the scattered field from the incident. The signal-to-noise is further improved by using a Michelson interferometer to combine a phase modulated reference beam with the scattered beam in a homodyne detection scheme. The interferometer output beam is detected with a bolometer and the output demodulated at a harmonic of the tapping frequency to yield the background-free terahertz signal amplitude. The resulting terahertz image of a nano-transistor chip was compared with an infrared image obtained using a similar scattering near-field optical microscopy technique, AFM and transmission electron microscopy images. This clearly demonstrated the unique capability of the terahertz technique to image regions of important current density within the semiconductor with a resolution of a few tens of nanometres.

Recently, alternative implementations and refinements to the technique have emerged, with a view to improving the simplicity of the set-up, the signal-to-noise ratio and the spatial resolution. In one implementation, the optically pumped laser source is replaced by a quantum cascade laser, which doubles up as both the source and detector [6]. When the scattered signal is returned to the quantum cascade laser, its amplitude and phase can be detected as a modulation of the quantum cascade laser bias voltage at a low order harmonic of the tapping frequency of the AFM tip. Imaging of the edge of a layer of gold deposited on a silicon substrate gave good correlation with the AFM image and indicated a spatial resolution of around 65 nm at 2.7 THz.

In another approach, the terahertz signal is generated and detected all electronically, utilising the 54th harmonic of a microwave synthesiser in combination with

heterodyne detection [7]. This allows the signal to be tuned over a wide range, from 0.5 to 0.75 THz, with simultaneous AFM, terahertz amplitude and phase imaging. 0.6 THz imaging of a silicon test sample has demonstrated the ability to distinguish regions of differing topography and doping density, with a conductance sensitivity of 10^{16} cm^{-3} of mobile carriers. The spatial resolution achieved was 50 nm, with a 10,000 pixel image recorded in just a few minutes acquisition time.

Work has also been directed towards improving upon the standard AFM tips by using focussed ion beam fabrication to produce tips with optimised dimensions to act as resonant terahertz antennas [8]. Tips 80 μm in length resulted in a nine-fold near-field intensity enhancement compared to standard AFM tips, which are typically 17 μm in length, and an enhancement of 10^7 compared to the incident field, when operated at 3.11 THz (a wavelength of 96.5 μm).

Similar tips have been used in a modification of the scattering probe technique to enable terahertz photocurrent nanoscopy of graphene plasmons [9]. Here, rather than detecting the terahertz radiation scattered from the tip, a terahertz-induced photocurrent generated in the graphene sample in the region under the tip is detected. Hence, the graphene layer acts as both the sample and detector in this implementation. The photocurrent is a result of placing the graphene layer, sandwiched between two layers of hexagonal boron nitride, over two metal gate regions on a quartz substrate. These gates lie side-by-side and are separated from each other by a small gap, so that half of the graphene layer is over one gate and half over the other. Through application of a bias voltage to the gates, the carrier density in the graphene on either side of the gap can be controlled. With resulting positive and negative charge densities on either side of the gap, a sharp pn junction and associated carrier density gradient is established in the graphene above the gates. Concentration of the terahertz field by the tip causes localised heating at the tip nanofocus leading to a thermoelectrically generated photocurrent as a result of the localised Seebeck effect arising from the carrier density gradient. Scanning the tip over the graphene sample enables standing waves due to terahertz graphene plasmons to be imaged and their wavelength determined. Using incident terahertz frequencies between 2.52 and 5.67 THz, the terahertz graphene plasmon dispersion curve has been plotted [9]. It was found that the graphene plasmon wavelengths in the graphene/hexagonal boron nitride heterostructure were a factor of 12 lower than those in free-standing graphene, and a factor of 70 lower than the free-space wavelength of the incident radiation. The graphene plasmon group velocity was found to be around 0.014 of the speed of light in free space, which is an order of magnitude lower than in free-standing graphene at 2.52 THz.

A rather different tip-based approach to terahertz nanoscopy is to replace the incident terahertz radiation with the near-infrared beam from a femtosecond laser and to detect the resulting terahertz pulses emitted from the sample under the tip. This is, of course, limited to samples which emit terahertz radiation in response to incident near-infrared pulses, but can provide useful information on the charge or polarization dynamics. The approach is known as Nanoscale Laser Terahertz Emission Microscopy (LTEM) [10]. LTEM was originally demonstrated without the tip [11], and achieved a spatial resolution of around 3 μm, defined by the spot

size of the near-infrared beam at the sample. In its nanoscale implementation, the introduction of the tip concentrates the incident near-infrared field at the sample, so that a tip-size-limited spatial resolution of around 20 nm has been demonstrated when imaging a gold nano-rod [10].

The techniques discussed thus far have all been based on the use of sharply pointed tips to concentrate the incident fields to achieve resolutions of a few tens of nanometers. An entirely different approach is known as reconstructive imaging. This is a super-resolution technique based on image processing rather than modifying the imaging system or developing new devices. In does not require the close approach to the sample needed in tip-based systems and can operate successfully at adjustable stand-off distances of tens of millimeters. Furthermore, three-dimensional sub-surface layer-by-layer imaging is possible and sub-nanometer spatial resolution has been claimed [12]. From the hardware point of view, all that is required is a terahertz generation and detection system, configured either for transmission or reflection measurements, and a three-axis (x, y and z) nano-positioning translation stage. The sample is typically scanned through the terahertz beam with about a 24 nm step size. This effectively creates multiple images of the same sample with sub-pixel lateral shifts, where the pixel is defined by the diffraction limited spot size. Images are also created at different depths by repositioning the sample in the beam relative to the focal plane. Inverse distance weighting interpolation is used to create a high resolution three dimensional image from this low resolution image data. In an image of Cr^3 nanoparticles on a glass slide, the smallest particle detected had a width of around 8.5 Å [13]. Three-dimensional imaging of AgI quantum dots has demonstrated the capability to extract image slices at different depths within the image for layer-by-layer inspection [13].

8.4 Terahertz Scanning Tunnelling Microscopy (THz-STM)

Rather than direct terahertz imaging of samples at the nanoscale, as discussed in the preceding section, terahertz radiation can also be used to control matter to enable ultrafast scanning tunnelling microscopy. In this approach, known as Terahertz Scanning Tunnelling Microscopy (THz-STM), an ultrafast terahertz probe pulse coupled to the scanning tip of a standard scanning tunnelling microscope (STM) is used to modulate the bias voltage between the tip and the sample, inducing tunnelling of electrons from the sample to the tip. The non-linear current-voltage characteristic of the tip-sample tunnel junction rectifies the resulting ultrafast tunnel current burst, so that it can be detected with the conventional STM electronics.

The initial demonstration of the technique additionally utilised an 800 nm optical pump pulse to induce electron trapping in an InAs nanodot, with time-resolved imaging from the THz-STM probe [14]. The time resolution could be explored by varying the delay between the pump and probe pulses and was found to be faster than 500 fs. The resulting image had a spatial resolution of 2 nm.

Refinement of the THz-STM technique has made it possible to tailor the bias and terahertz pulse so that a single electron can be removed from a selected orbital of a single molecule. Doing so modifies the Coulomb and van der Waals forces between the molecule and its substrate, setting the molecule into oscillation which can be detected by applying a second terahertz pulse after a variable delay to act as a probe (the varying distance between the molecule and the STM tip modulating the tunnel current). Hence, in this case, both the pump and probe pulses are terahertz pulses. Single molecules of pentacene and copper phtalocyanine have been imaged in this fashion with a spatial resolution of 0.6 Å and time resolution of 115 fs [15].

8.5 Terahertz Sensing with Nanoslot Antennas

Not all applications require the imaging of samples. A great deal of useful information can be gained from sensing the interaction between terahertz radiation and matter at the nanoscale without forming images, enabling the measurement of material properties and the sensing of specific molecules and viruses. However, the small size of the objects of interest compared to the wavelength present similar challenges to those encountered when conducting imaging. For example, molecular absorption cross-sections in this frequency range are very small. Fortunately, it is possible to confine the radiation through the use of narrow slots in a metal ground plane. Within the slot, the terahertz electric field is concentrated so that it interacts more strongly with small scale objects and the molecular absorption cross-section becomes significantly enhanced.

By forming an array of such slot antennas on the surface of a semiconductor sample, this field confinement enables one to probe the surface carrier dynamics of bulk semiconductors using terahertz time domain spectroscopy [16]. Without such field confinement, terahertz spectroscopy is limited to probing the bulk carrier dynamics of the semiconductor. However, the carrier dynamics at the surface differ due to surface defects, doping levels and symmetry breaking. The field confinement associated with the slot antennas is such that the terahertz penetration depth in the semiconductor sample is limited to about 20 nm for 150 nm gap width slot antennas in InP, and to about 80 nm for 500 nm gap width slot antennas in GaAs. The measured surface carrier lifetimes using this technique are markedly reduced compared to those for the bulk semiconductor.

The factor by which the molecular absorption cross-section is enhanced by a slot antenna is dependent on the width of the slot. For a 100 nm slot width, the enhancement factor is 10^3 compared to the free-space cross-section, whereas it becomes 10^5 for a 1 nm width [17]. Moreover, by changing the length of the slot, it is possible to tune the antenna so that it has a resonant frequency that matches a specific molecular absorption line, sensitising it for the detection of a specific molecule. For example, the work presented in [17] demonstrates 50 nm wide slot antennas, 90 μm in length, optimised for the detection of small amounts of the explosive RDX, and antennas 150 μm long, optimised for the detection of lactose.

These antennas were able to detect amounts of RDX deposited across their surface as small as 40 ng, which corresponds to 22 fg in the slot itself. Such small amounts are undetectable using conventional terahertz time-domain spectroscopy without the use of slot antennas.

This approach has been expanded upon for the rapid, label-free detection of biomaterials. In the situation where the materials of interest have broad spectral features in the terahertz range, it can be difficult to identify the optimal resonant frequency for the antenna design. In this case, it can be helpful to use a multi-element antenna array, comprising antennas of different lengths and thus different resonant frequencies [18]. The resonant frequency that gives the biggest response to the material of interest can then be identified empirically and an optimised single-resonance nanoslot antenna designed. Using this approach, a nano-antenna capable of sensing and distinguishing between three types of avian influenza virus (H5N2, H1N1 and H9N2) has been demonstrated [18]. The virus type was classified by taking into account the shift in the antenna resonant frequency and change in transmittance on application of the virus sample.

Where the materials of interest are known to have characteristic spectral features in the terahertz range, specific nanoslot antenna sensing chips can be designed accordingly. In this manner, it is possible to distinguish between two target materials by having one sensing chip that is sensitive to one of them, whilst being insensitive to the other, with a second sensing chip sensitive to the second material. This technique has been used to selectively discriminate and quantify trace amounts of the steroid hormones progesterone and 17α-OH-progesterone, of importance in the development and prevention of endocrine disorders [19].

Rather than simple nano-slot antennas, it is possible to use more elaborate metamaterial structures, such as split-ring resonators, in order to give more control over the resonant frequency. Detection of the viruses PRD1 and MS2 has been demonstrated with a nano-gap metamaterial, showing a sensitivity in terms of the resonant frequency shift of up to 40 GHz per virus particle in the gap area [20]. Based upon this result, the authors suggest that single virus detection would be possible if the number of metamaterial elements were reduced.

Generally, the samples in the nano-slot antenna work described in this section thus far have been drop-cast in solution onto the antennas and the solution allowed to evaporate before the terahertz measurements are conducted. This is because of the significant attenuation of terahertz radiation imposed by aqueous solutions. A nanofluidic terahertz metasensor, consisting of a metamaterial array sealed by a quartz plate suspended above its surface, has been developed to overcome this limitation [21]. Selective adenosine triphosphate (ATP) sensing by functionalization of the metamaterial resonators has been demonstrated in an aqueous environment using this structure.

8.6 Nanoscale Phenomena in Biological Systems

The use of nano-slot antennas, as described in the previous section, is particularly suited to the sensing of very small amounts of nanoscale objects. However, even without concentration of the terahertz fields to nanoscale dimensions, it is possible to use terahertz spectroscopy of bulk biological samples in solution to shed light on nanoscale phenomena and to provide a means for label-free detection.

Terahertz spectroscopy is sensitive to both the collective vibrational modes of large biomolecules and the fluctuating dynamics of the network of water molecules that surround them. It has been discovered that the presence of a biomolecule, such as a protein, influences the dynamics of the surrounding water molecules, slowing down the fluctuations in their hydrogen bonding network and modifying the terahertz absorption spectrum of the water in the process [22]. Molecular dynamics simulations have shown that the vibrational density of states (VDOS) of this hydration water moves to a higher frequency range between 2.4 and 2.7 THz, resulting in an increased VDOS and corresponding increased absorption at frequencies above 1.5 THz and a reduced VDOS and decreased absorption at lower frequencies [23]. This behaviour is consistent with experimental results.

Measurements of the terahertz absorbance of biomolecules in solution versus their concentration have indicated the concentration at which the surrounding dynamical hydration shells begin to overlap. From this, it has been possible to deduce the extent of the dynamical shell, revealing that proteins can affect water dynamics as far as at least 1 nm away from their surface [22]. This is significantly further than the static hydration shell, probed by techniques such as neutron scattering, and appears to be an important aspect in the proteins' biological functioning and interaction with other molecules. For example, terahertz spectroscopy has indicated the presence of a gradient of hydrogen bond dynamics, hypothesised to guide the long range interaction and binding of molecules in enzyme-substrate catalysis and the binding of nano-sized ice crystals to antifreeze proteins, which enable organisms to survive in sub-freezing environments [23].

Measurements have also revealed that the hydration dynamics of molecules can differ depending on their conformation and due to the presence of site-specific mutations. This opens up the possibility of label-free detection of various biological processes and has been recently demonstrated in the case of label-free detection of antibody-antigen binding in estrogen receptor alpha, an important biomarker for breast cancer diagnosis [24].

8.7 Terahertz Control over Matter

Section 8.4 has already described how terahertz radiation can be used to control the tunnelling of electrons in THz-STM. This is just one example of how terahertz radiation can control matter at the nanoscale. As terahertz field oscillations are two

orders of magnitude slower than those of optical radiation, they interact with matter in different ways. Firstly, terahertz radiation can provide resonant control over matter to drive molecular rotations, crystal lattice vibrations, electronic properties such as conductivity, and the behaviour of bound and free electrons. Secondly, the Lorentz force resulting from the terahertz magnetic field can exert a significant torque on the magnetic dipole moment of the electron spin, enabling terahertz spin control in ferromagnets and antiferromagnets. Finally, with sufficiently strong terahertz fields, non-resonant control becomes possible. This is because the strong terahertz field persists in the same direction long enough to accelerate electrons to kinetic energies around 1 eV and to free bound electrons via field ionisation. These energies are thus considerably larger than the terahertz photon energy and are comparable to semiconductor bandgap energies. Therefore, in semiconductors, it is possible to induce electron-hole pairs, impact ionisation, field ionisation of impurities and excitons, and high field electron transport. Terahertz-induced phase transitions also become possible, for example the insulator-metal transition in vanadium dioxide [25]. The terahertz field concentration techniques described earlier in this chapter in relation to nanoscopy and sensing with nanoslot antennas provide a means to achieving high field strengths, even with relatively modest table-top terahertz systems. To date, relatively little work has been done on using terahertz to control matter compared to its use in spectroscopy. The greatest body of work in this area has been in exploring the influence of terahertz radiation on biological systems; a topic covered in the following section. A comprehensive discussion of the topics mentioned above can be found in a paper by Kampfrath et al. [26].

8.8 Terahertz Bioelectromagnetics

The resonant absorption of terahertz radiation by biomolecules, such as proteins and DNA, and the surrounding water network, which can be probed through absorption spectroscopy, suggests that terahertz irradiation is also likely to be able to drive, and potentially control, changes in biological systems. The field concerned with exploring the influence of terahertz radiation on biological systems is generally referred to as terahertz bioelectromagnetics. Research in this area has implications both for defining safe exposure levels and for novel diagnostic or therapeutic applications.

Experimental work on a wide variety of biological systems has been carried out using a wide variety of terahertz sources with different characteristics and, unsurprisingly, has produced a wide variety of results. Effects seen include alterations to gene expression at the transcript and protein level, increases in membrane permeation, and modification of cellular differentiation in stem cells [27]. Many recent investigations have utilised high-intensity broadband terahertz pulses of low average power to avoid thermal effects. However, almost entirely distinct differences have been observed between thermal effects on gene expression induced by continuous wave (CW) terahertz radiation when compared to equivalent bulk

heating [28], highlighting the different mechanisms involved. Recent developments in biological techniques and bioinformatics have greatly aided this field by enabling identification and quantification of the biological effects induced by the radiation.

There is a growing body of evidence that terahertz irradiation can cause upregulation and downregulation of specific genes, depending on the frequency and dose of the radiation applied. Alterations to the expression of specific genes have been observed under irradiation with both broadband pulsed sources and single frequency CW sources throughout the terahertz range. Broadly speaking, the number of genes differentially expressed increases with the intensity of the radiation [29].

As an example, exposure of artificial human skin tissue to 1.0 μJ and 0.1 μJ terahertz pulses with a bandwidth extending up to around 2 THz for 10 minutes altered the expression of 442 and 397 genes respectively [30]. In contrast, exposure to UVA pulses modified the expression of only 290 genes. Some genes were upregulated under terahertz exposure, while others were downregulated. An extension of this work has employed bioinformatics techniques to explore the effects of this differential gene expression on gene interaction networks and specific biological signalling pathways [29]. While some genes are directly affected by terahertz radiation, others are not affected directly but are affected by perturbations in the signalling pathway resulting from up or downregulation of other genes which are directly affected by the radiation. Yet others show direct terahertz-induced changes in expression and are further modified by pathway perturbations. Taking account of the entire signalling pathway thus gives a much more complete understanding of the influence of terahertz radiation on biological functioning. This work has shown that in the case of the cytokine-cytokine receptor interaction pathway, prolonged exposure to intense pulses of terahertz radiation may lead to an inflammatory-like response in human skin. On the other hand, terahertz exposure results in downregulation of genes associated with glioma, a type of brain cancer, and suppression of the associated glioma pathway. This implies that terahertz radiation may be able to play a role in the suppression of division, differentiation and progression of cancer.

At present, the mechanisms behind these biological effects remain unclear. However, recent work has indicated that a 10 min exposure to high intensity picosecond terahertz pulses can disassemble DNA nanostructures, which had been thermodynamically assembled in a DNA origami approach [31]. Furthermore, the same work has shown that terahertz radiation can provoke the opening of short lengths of double-stranded DNA. This effect was seen for 10–20 base pair lengths, but not in 30 and 40 base pair lengths of double-stranded DNA. The observed effects were consistent with the double-stranded DNA rapidly dissociating under the influence of the terahertz pulses and then rapidly rehybridising with itself. In addition to providing new insight into biological interaction mechanisms, the authors suggest that this effect may be harnessed for externally actuating DNA nanostructures to release a therapeutic agent.

8.9 Conclusion

This chapter has described the current state-of-the-art in the sensing and manipulation of matter at the nanoscale using terahertz radiation. Even though the exploration of the terahertz part of the electromagnetic spectrum is in its infancy compared to the other regions of the spectrum, impressive results have already been gained. Despite the relative scale of the wavelengths involved, new techniques have made it possible to explore terahertz light-matter interactions at a scale many orders of magnitude smaller than the wavelength, providing a unique capability complementary to other spectral regions.

References

1. Robertson DA, MacFarlane DG, Hunter RI, Cassidy SL, Llombart N, Gandinini E, Bryllert T, Ferndahl M, Lindström H, Tenhunen J, Vasama H, Huopana J, Selkälä T, Vuotikka AJ (2017) High resolution, wide field of view, real time 340 GHz 3D imaging radar for security screening. In: Wikner DA, Robertson, DA (eds) Passive and active millimeter-wave imaging XX. Proceedings of the of SPIE, vol. 10189, 101890C
2. Jackson JB, Bowen J, Walker G, Labaune J, Mourou G, Menu M, Fukunaga K (2011) A survey of terahertz applications in cultural heritage conservation science. IEEE Trans Terahertz Sci Technol 1(1):220–231
3. Lloyd-Hughes J, Jeon T-I (2012) A review of the terahertz conductivity of bulk and nanomaterials. J Infrared Millim Terahertz Waves 33:871–925
4. Martin DH, Bowen JW (1993) Long-wave optics. IEEE Trans Microwave Theory Tech 41(10):1676–1690
5. Huber AJ, Keilmann F, Wittborn J, Aizpurua J, Hillenbrand R (2008) Terahertz near-field nanoscopy of mobile carriers in single semiconductor nanodevices. Nano Lett 8(11):3766–3770
6. Giordano MC, Mastel S, Liewald C, Columbo LL, Brambilla M, Viti L, Politano A, Zhang K, Lianhe L, Davies AG, Linfield EH, Hillenbrand R, Keilmann F, Scamarcio G, Vitiello MS (2018) Phase-resolved terahertz self-detection nearfield microscopy. Opt Express 26(14):18423–18435
7. Liewald C, Mastel S, Hesler J, Huber AJ, Hillenbrand R, Keilmann F (2018) All-electronic terahertz nanoscopy. Optica 5(2):159–163
8. Mastel S, Lundeberg MB, Alonso-González P, Gao Y, Watanabe K, Taniguchi T, Hone J, Koppens FHL, Nikitin AY, Hillenbrand R (2017) Terahertz nanofocussing with cantilevered terahertz-resonant antenna tips. Nano Lett 17:6526–6533
9. Alonso-González PJ, Nikitin AY, Gao Y, Woessner A, Lundeberg MB, Principi A, Forcellini N, Yan W, Vélez S, Huber AJ, Watanabe K, Taniguchi T, Casanova F, Hueso LE, Polini M, Hone J, Koppens FHL, Hillenbrand R (2016) Acoustic terahertz graphene plasmons revealed by photocurrent nanoscopy. Nat Nanotechnol 12:31–35
10. Klarskov P, Kim H, Colvin VL, Mittleman DM (2017) Nanoscale laser terahertz emission microscopy. ACS Photonics 4:2676–2680
11. Yamashita M, Kawase K, Otani C, Kiwa T, Tonouchi M (2005) Imaging of large-scale integrated circuits using laser terahertz emission microscopy. Opt Express 13(1):115–120
12. Rahman A, Rahman AK (2019) Nanoscale metrology of line patterns on semiconductor by continuous wave terahertz multispectral reconstructive 3-D imaging overcoming the Abbe diffraction limit. IEEE Trans Semicond Maunf 32(1):7–13

13. Rahman A, Rahman AK, Yamamoto T, Kitagawa H (2016) Terahertz sub-nanometer subsurface imaging of 2D materials. J Biosens Bioelectro 7(3):1000221
14. Cocker TL, Jelic V, Gupta M, Molesky SJ, Burgess JAJ, De Los Reyes G, Titova LV, Tsui YY, Freeman MR, Hegmann FA (2013) An ultrafast terahertz scanning tunnelling microscope. Nat Photonics 7(8):620–625
15. Cocker TL, Peller D, Yu P, Repp J, Huber R (2016) Tracking the ultrafast motion of a single molecule by femtosecond orbital imaging. Nature 539(7628):263–267
16. Choi G, Bahk Y-M, Kang T, Lee Y, Son BH, Ahn YH, Seo M, Kim D-S (2017) Terahertz nanoprobing of semiconductor surface dynamics. Nano Lett 17:6397–6401
17. Park H-R, Ahn KJ, Han S, Bahk Y-M, Park N, Kim D-S (2013) Colossal absorption of molecules inside single terahertz nanoantennas. Nano Lett 13:1782–1786
18. Lee D-K, Kang J-H, Kwon J, Lee J-S, Lee S, Woo DH, Kim JH, Song C-S, Park Q-H, Seo M (2017) Nano metamaterials for ultrasensitive terahertz biosensing. Sci Rep 7:8146
19. Lee S-H, Lee D, Choi MH, Son J-H, Seo M (2019) Highly sensitive and selective detection of steroid hormones using terahertz molecule-specific sensors. Anal Chem 91:6844–6849
20. Park SJ, Cha SH, Shin GA, Ahn YH (2017) Sensing viruses using terahertz nano-gap metamaterials. Biomed Opt Express 8(8):3551–3558
21. Shih K, Pitchappa P, Jin L, Chen C-H, Singh R, Lee C (2018) Nanofluidic terahertz metasensor for sensing in aqueous environment. Appl Phys Lett 113:071105
22. Leitner DM, Gruebele M, Havenith M (2008) Solvation dynamics of biomolecules: modeling and terahertz experiments. HFSP J 2(6):314–323
23. Nibali VC, Havenith M (2014) New insights into the role of water in biological function: studying solvated biomolecules using terahertz absorption spectroscopy in conjunction with molecular dynamics simulations. J Am Chem Soc 136(37):12800–12807
24. Li M, Chang T, Wei D, Tang M, Yan S, Du C, Cui H-L (2017) Label-free detection of anti-estrogen receptor alpha and its binding with estrogen receptor peptide alpha by terahertz spectroscopy. RSC Adv 7(39):24338–24344
25. Gray AX, Hoffmann MC, Jeong J, Aetukuri NP, Zhu D, Hwang HY, Brandt NC, Wen H, Sternbach AJ, Bonetti S, Reid AH, Kukreja R, Graves C, Wang T, Granitzka P, Chen Z, Higley DJ, Chase T, Jal E, Abreu E, Liu MK, Weng T-C, Sokaras D, Nordlund D, Chollet M, Alonso-Mori R, Lemke H, Glownia JM, Trigo M, Zhu Y, Ohldag H, Freeland JW, Samant MG, Berakdar J, Averitt RD, Nelson KA, Parkin SSP, Dürr HA (2018) Ultrafast terahertz field control of electronic and structural interactions in vanadium dioxide. Phys Rev B 98:045104
26. Kampfrath T, Tanaka K, Nelson KA (2013) Resonant and nonresonant control over matter and light by intense terahertz transients. Nat Photonics 7:680–690
27. Il'inaa IV, Sitnikova DS, Agranata MB (2018) State-of-the-art of studies of the effect of terahertz radiation on living biological systems. High Temp 56(5):789–810
28. Echchgadda I, Grundt JE, Cerna CZ, Roth CC, Payne JA, Ibey BL, Wilmink GJ (2016) Terahertz radiation: a non-contact tool for the selective stimulation of biological responses in human cells. IEEE Trans Terahertz Sci Technol 6(1):54–68
29. Hough CM, Purschke DN, Huang C, Titova LV, Kovalchuk O, Warkentin BJ, Hegmann FA (2018) Topology-based prediction of pathway dysregulation induced by intense terahertz pulses in human skin tissue models. J Infrared Milli Terahz Waves 39:887–898
30. Titova LV, Ayesheshim AK, Golubov A, Rodriguez-Juarez R, Woycicki R, Hegmann FA, Kovalchuk O (2013) Intense THz pulses down-regulate genes associated with skin cancer and psoriasis: a new therapeutic avenue? Sci Rep 3:2363
31. Greschner AA, Ropagnol X, Kort M, Zuberi N, Perreault J, Razzari L, Ozaki T, Gauthier MA (2019) Room-temperature and selective triggering of supramolecular DNA assembly/disassembly by nonionizing radiation. J Am Chem Soc 148:3456–3469

Chapter 9
An Alternative Starting Point for Electromagnetism

Ivan Fernandez-Corbaton

Abstract The aim of these lectures is to provide a simple introduction to an unconventional approach to electromagnetism. From the start, the prominent role of the electric and magnetic fields is taken over by two other fields. These fields represent the two handedness that Maxwell solutions can have. The use of this alternative set of fields has notable advantages over the electric and magnetic fields: Decoupled evolution equations, relativistic invariance, and the remarkable ability to split the two possible handedness in electromagnetism.

Keywords Maxwell equations · Riemann-Silberstein vectors · Helicity

9.1 About These Lectures

On the one hand, many of the ideas and concepts contained in these lectures are not new. The two handedness fields are Rieman-Silberstein-like combinations, and I would like to highlight the seminal works of I. Bialynicki-Birula about the Riemann-Silberstein vectors [1–3]. On the other hand, the versions of the Riemann-Silberstein vectors used in these lectures are not the ones that are typically found in the literature, and I am not aware of the existence of a gentle introduction to the formulism and its consequences, which is the main objective of these lectures.

My aim is that the lectures can be understood from a basic knowledge of electromagnetism and a few mathematical tools, namely Fourier transforms and some aspects of vector calculus. I explicitly write down even simple derivations, and, when faced with what I perceived as a choice between mathematical rigor and pedagogical value I have always opted for the latter, bluntly so in a few instances. I have intentionally not started by discussing the helicity operator and showing that it

I. Fernandez-Corbaton (✉)
Institute of Nanotechnology, Karlsruhe Institute of Technology, Karlsruhe, Germany
e-mail: ivan.fernandez-corbaton@kit.edu

M. Cesaria et al. (eds.), *Light-Matter Interactions Towards the Nanoscale*,
NATO Science for Peace and Security Series B: Physics and Biophysics,
https://doi.org/10.1007/978-94-024-2138-5_9

determines the structure of Maxwell equations. I have rather let the structure emerge naturally from Maxwell equations whey they are looked at in the right way.

9.2 An Alternative Form of Maxwell Equations

We start with Maxwell equations in vacuum assuming $\epsilon_0 = \mu_0 = 1$, or, alternatively, $c_0 = 1/\sqrt{\epsilon_0\mu_0} = 1$ and $Z_0 = \sqrt{\frac{\mu_0}{\epsilon_0}} = 1$

$$\begin{aligned} &\text{ⓐ}: \ \nabla \cdot \mathbf{E}(\mathbf{r},t) = 0, \ \partial_t \mathbf{E}(\mathbf{r},t) = \nabla \times \mathbf{H}(\mathbf{r},t), \\ &\text{ⓑ}: \ \nabla \cdot \mathbf{H}(\mathbf{r},t) = 0, \ \partial_t \mathbf{H}(\mathbf{r},t) = -\nabla \times \mathbf{E}(\mathbf{r},t), \end{aligned} \tag{9.1}$$

and manipulate them as follows

$$\begin{aligned} \frac{\text{ⓐ} + \mathrm{i}\text{ⓑ}}{\sqrt{2}}&: \nabla \cdot \left[\frac{\mathbf{E}(\mathbf{r},t) + \mathrm{i}\mathbf{H}(\mathbf{r},t)}{\sqrt{2}}\right] = 0, \\ &\partial_t \left[\frac{\mathbf{E}(\mathbf{r},t) + \mathrm{i}\mathbf{H}(\mathbf{r},t)}{\sqrt{2}}\right] = \nabla \times \left[\frac{\mathbf{H}(\mathbf{r},t) - \mathrm{i}\mathbf{E}(\mathbf{r},t)}{\sqrt{2}}\right] = -\mathrm{i}\left[\frac{\mathbf{E}(\mathbf{r},t) + \mathrm{i}\mathbf{H}(\mathbf{r},t)}{\sqrt{2}}\right], \\ \frac{\text{ⓐ} - \mathrm{i}\text{ⓑ}}{\sqrt{2}}&: \nabla \cdot \left[\frac{\mathbf{E}(\mathbf{r},t) - \mathrm{i}\mathbf{H}(\mathbf{r},t)}{\sqrt{2}}\right] = 0, \\ &\partial_t \left[\frac{\mathbf{E}(\mathbf{r},t) - \mathrm{i}\mathbf{H}(\mathbf{r},t)}{\sqrt{2}}\right] = \nabla \times \left[\frac{\mathbf{H}(\mathbf{r},t) + \mathrm{i}\mathbf{E}(\mathbf{r},t)}{\sqrt{2}}\right] = \mathrm{i}\left[\frac{\mathbf{E}(\mathbf{r},t) - \mathrm{i}\mathbf{H}(\mathbf{r},t)}{\sqrt{2}}\right]. \end{aligned} \tag{9.2}$$

We now define a new set of fields

$$\boxed{\mathbf{G}_{\pm}(\mathbf{r},t) = \frac{\mathbf{E}(\mathbf{r},t) \pm \mathrm{i}\mathbf{H}(\mathbf{r},t)}{\sqrt{2}}}, \tag{9.3}$$

and use them to re-write the equations in (9.2)

$$\begin{aligned} &\nabla \cdot \mathbf{G}_{+}(\mathbf{r},t) = 0, \ \partial_t \mathbf{G}_{+}(\mathbf{r},t) = -\mathrm{i}\nabla \times \mathbf{G}_{+}(\mathbf{r},t), \\ &\nabla \cdot \mathbf{G}_{-}(\mathbf{r},t) = 0, \ \partial_t \mathbf{G}_{-}(\mathbf{r},t) = \mathrm{i}\nabla \times \mathbf{G}_{-}(\mathbf{r},t). \end{aligned} \tag{9.4}$$

The four equations in (9.4) are equivalent to the initial Maxwell equations in (9.1). The equivalence is clear since the manipulation $\frac{\text{ⓐ}\pm\mathrm{i}\text{ⓑ}}{\sqrt{2}}$ together with the definition in Eq. (9.3) can be seen as a unitary change of basis, and unitary changes of basis do not alter the information content. This particular change of basis takes us from a description of electromagnetism based on the electric and magnetic fields, $\mathbf{E}(\mathbf{r},t)$ and $\mathbf{H}(\mathbf{r},t)$, to a description of electromagnetism based on the $\mathbf{G}_{\pm}(\mathbf{r},t)$ fields. While we have not "broken" anything with such change of basis, there is a notable

difference between the equations in (9.1) and the equations in (9.4): The new set of equations is decoupled. The $\mathbf{G}_+(\mathbf{r}, t)$ field does not depend at all on or affect the $\mathbf{G}_-(\mathbf{r}, t)$ field in any way, and vice versa. In sharp contrast, the time evolution equations in (9.1) show how the electric and magnetic fields are coupled to each other: The time evolution of $\mathbf{E}(\mathbf{r}, t)$ depends on $\mathbf{H}(\mathbf{r}, t)$, and vice versa. In this sense, while there is no change on the physical content, the form of Maxwell equations is simpler in (9.4) than in (9.1).

The $\mathbf{G}_\pm(\mathbf{r}, t)$ fields are called the Riemann-Silberstein vectors [3]. Actually, in these lectures, we will not use the typical version of Riemann-Silberstein vectors, where the electric and magnetic fields used to build them are *real-valued* fields. We will use *complex-valued* electric and magnetic fields instead. The reason for this choice will be made clear later.

9.3 The $\frac{\nabla \times}{\omega}$ Operator and $\mathbf{G}_\pm$ as *the* Polarization Description

9.3.1 From the $(\mathbf{r}, t)$ *to the* $(\mathbf{r}, \omega)$ *Domain*

One obtains a complex-valued field $\mathbf{X}(\mathbf{r}, t)$ with the following definition of its inverse Fourier transform

$$\mathbf{X}(\mathbf{r}, t) = \int_{>0}^{\infty} \frac{d\omega}{\sqrt{2\pi}} \mathbf{X}(\mathbf{r}, \omega) \exp(-\mathrm{i}\omega t), \tag{9.5}$$

where only positive frequencies are considered. Such one-sided definition is appropriate in electromagnetism because the same information is contained on both sides of the spectrum. Note that $\omega = 0$ is explicitly taken out of the integral in Eq. (9.5). This is because we are dealing with electrodynamics and need to exclude electro- and magneto-statics.

We will now use the harmonic decomposition on Eq. (9.5) to work on the equations in (9.4). Let us in particular consider the evolution equation for $\mathbf{G}_+(\mathbf{r}, t)$, and substitute $\mathbf{G}_+(\mathbf{r}, t)$ by its decomposition of the kind written in Eq. (9.5):

$$\partial_t \left[\int_{>0}^{\infty} \frac{d\omega}{\sqrt{2\pi}} \mathbf{G}_+(\mathbf{r}, \omega) \exp(-\mathrm{i}\omega t) \right] = -\mathrm{i}\nabla \times \left[\int_{>0}^{\infty} \frac{d\omega}{\sqrt{2\pi}} \mathbf{G}_+(\mathbf{r}, \omega) \exp(-\mathrm{i}\omega t) \right]. \tag{9.6}$$

After applying the ∂_t on the left-hand side, shifting the curl to the inside of the integral of the right-hand side, and moving the right-hand side onto the left-hand side, we obtain

$$\int_{>0}^{\infty} \frac{d\omega}{\sqrt{2\pi}} \left[-\mathrm{i}\omega \mathbf{G}_+(\mathbf{r}, \omega) + \mathrm{i}\nabla \times \mathbf{G}_+(\mathbf{r}, \omega) \right] \exp(-\mathrm{i}\omega t) = 0, \ \forall (\mathbf{r}, t). \tag{9.7}$$

The only way to meet Eq. (9.7) is that the term within the square-brackets is zero for all $(\mathbf{r}, \omega)$. One can reach this conclusion after thinking about how a sum of weighted harmonic functions $\alpha(\mathbf{r}, \omega)\exp(-\mathrm{i}\omega t)$ with different frequencies can add up to zero simultaneously for all positions $\mathbf{r}$ and time instances t. We therefore have that the evolution equation for $\mathbf{G}_+(\mathbf{r}, t)$ results in the following equation for $\mathbf{G}_+(\mathbf{r}, \omega)$: $\mathbf{G}_+(\mathbf{r}, \omega) = \frac{\nabla\times}{\omega}\mathbf{G}_+(\mathbf{r}, \omega)$. Very similar steps can be used to show that the set of equations in (9.4) result in:

$$\begin{aligned} \nabla \cdot \mathbf{G}_+(\mathbf{r}, \omega) = 0,\ \mathbf{G}_+(\mathbf{r}, \omega) = \frac{\nabla\times}{\omega}\mathbf{G}_+(\mathbf{r}, \omega), \\ \nabla \cdot \mathbf{G}_-(\mathbf{r}, \omega) = 0,\ \mathbf{G}_-(\mathbf{r}, \omega) = -\frac{\nabla\times}{\omega}\mathbf{G}_-(\mathbf{r}, \omega). \end{aligned} \tag{9.8}$$

These equations are another form of Maxwell equations. Let us consider just the curl equations:

$$\boxed{\frac{\nabla\times}{\omega}}\mathbf{G}_\pm(\mathbf{r}, \omega) = \pm\mathbf{G}_\pm(\mathbf{r}, \omega). \tag{9.9}$$

When we consider the object inside the box as an operator, Eq. (9.9) is telling us that:

Box 1

- There are two different kinds of solutions of Maxwell equations.
- Both kinds are eigenstates of an operator, which, in the $(\mathbf{r}, \omega)$ representation reads $\frac{\nabla\times}{\omega}$.
- The difference between the two kinds of solutions is their $\frac{\nabla\times}{\omega}$ eigenvalue, which is either $+1$ or -1.

9.3.2 *The $\frac{\nabla\times}{\omega}$ Operator*

Apparently, the operator $\frac{\nabla\times}{\omega}$ has a special role in Maxwell equations. Let us investigate some of its properties, starting by its action on electric and magnetic fields. Such action can be easily elucidated by bringing the evolution equations in (9.1) onto the $(\mathbf{r}, \omega)$ representation:

$$\frac{\nabla\times}{\omega}\mathbf{E}(\mathbf{r}, \omega) = \mathrm{i}\mathbf{H}(\mathbf{r}, \omega),\ \frac{\nabla\times}{\omega}\mathbf{H}(\mathbf{r}, \omega) = -\mathrm{i}\mathbf{E}(\mathbf{r}, \omega), \tag{9.10}$$

which shows that $\frac{\nabla\times}{\omega}$ exchanges electric and magnetic fields. In particular, this means that $\mathbf{E}(\mathbf{r}, \omega)$ and $\mathbf{H}(\mathbf{r}, \omega)$ *are not* eigenstates of $\frac{\nabla\times}{\omega}$.

If we apply $\frac{\nabla\times}{\omega}$ one more time to Eq. (9.10)

$$\begin{aligned}\frac{\nabla\times}{\omega}\frac{\nabla\times}{\omega}\mathbf{E}(\mathbf{r},\omega) &= \mathrm{i}\frac{\nabla\times}{\omega}\mathbf{H}(\mathbf{r},\omega) \overset{\text{Eq. (9.10)}}{=} \mathbf{E}(\mathbf{r},\omega),\\ \frac{\nabla\times}{\omega}\frac{\nabla\times}{\omega}\mathbf{H}(\mathbf{r},\omega) &= -\mathrm{i}\frac{\nabla\times}{\omega}\mathbf{E}(\mathbf{r},\omega) \overset{\text{Eq. (9.10)}}{=} \mathbf{H}(\mathbf{r},\omega),\end{aligned} \tag{9.11}$$

we find out that[1] $\frac{\nabla\times}{\omega}\frac{\nabla\times}{\omega} = \left(\frac{\nabla\times}{\omega}\right)^2$ is really the identity operator for solutions of Maxwell equations. This can also be seen after applying $\frac{\nabla\times}{\omega}$ to both sides of Eq. (9.9). An operator that squares to the identity has only two eigenvalues: +1 and -1. This means that the $\mathbf{G}_{\pm}(\mathbf{r},\omega)$ are all the eigenstates that $\frac{\nabla\times}{\omega}$ has for Maxwellian fields.

9.3.3 *The Meaning of* $\mathbf{G}_{\pm}$

The $\mathbf{G}_{\pm}(\mathbf{r},\omega)(\mathbf{G}_{\pm}(\mathbf{r},t))$ fields are also apparently special in the context of Maxwell equations. Let us investigate their properties by examining them for particular electromagnetic fields.

We consider a linearly-polarized plane-wave with wavevector $\mathbf{k} = [0,0,k]$

$$\mathbf{E}(\mathbf{r},\omega)\exp(-\mathrm{i}\omega t) = \hat{\mathbf{x}}\exp(\mathrm{i}kz - \mathrm{i}\omega t), \tag{9.12}$$

where $k = +\sqrt{\mathbf{k}\cdot\mathbf{k}} = \omega$ since we have set $c_0 = 1$. We use Eq. (9.10) to obtain the corresponding magnetic field applying the determinant mnemonic to compute the curl:

$$\begin{aligned}\mathrm{i}\mathbf{H}(\mathbf{r},\omega)\exp(-\mathrm{i}\omega t) &= \frac{\nabla\times}{\omega}\mathbf{E}(\mathbf{r},\omega)\exp(-\mathrm{i}\omega t) = \frac{1}{\omega}\begin{vmatrix}\hat{\mathbf{x}} & \hat{\mathbf{y}} & \hat{\mathbf{z}}\\ \partial_x & \partial_y & \partial_z\\ \exp(\mathrm{i}kz) & 0 & 0\end{vmatrix}\exp(-\mathrm{i}\omega t)\\ &= \frac{1}{\omega}\begin{bmatrix}0\\ \mathrm{i}k\exp(\mathrm{i}kz)\\ 0\end{bmatrix}\exp(-\mathrm{i}\omega t) = \mathrm{i}\hat{\mathbf{y}}\exp(\mathrm{i}kz - \mathrm{i}\omega t).\end{aligned} \tag{9.13}$$

[1] The fact that $\nabla\cdot\mathbf{E}(\mathbf{r},\omega) = \nabla\cdot\mathbf{H}(\mathbf{r},\omega) = 0$ is implicitly used.

Note that $\mathbf{H}(\mathbf{r},\omega)$ is also a linearly-polarized plane-wave. We now build $\mathbf{G}_{\pm}(\mathbf{r},\omega) = [\mathbf{E}(\mathbf{r},\omega) \pm \mathrm{i}\mathbf{H}(\mathbf{r},\omega)]/\sqrt{2}$ using Eqs. (9.12) and (9.13):

$$\begin{aligned}\mathbf{G}_{+}(\mathbf{r},\omega)\exp(-\mathrm{i}\omega t) &= \frac{\hat{\mathbf{x}}+\mathrm{i}\hat{\mathbf{y}}}{\sqrt{2}}\exp(\mathrm{i}kz-\mathrm{i}\omega t),\\ \mathbf{G}_{-}(\mathbf{r},\omega)\exp(-\mathrm{i}\omega t) &= \frac{\hat{\mathbf{x}}-\mathrm{i}\hat{\mathbf{y}}}{\sqrt{2}}\exp(\mathrm{i}kz-\mathrm{i}\omega t),\end{aligned} \tag{9.14}$$

which shows that $\mathbf{G}_{\pm}(\mathbf{r},\omega)\exp(-\mathrm{i}\omega t)$ are circularly-polarized plane-waves, specifically, $\mathbf{G}_{+}(\mathbf{r},\omega)\exp(-\mathrm{i}\omega t)$ is left-handed and $\mathbf{G}_{-}(\mathbf{r},\omega)\exp(-\mathrm{i}\omega t)$ is right-handed.

Let us now examine what happens when the initial $\mathbf{E}(\mathbf{r},\omega)\exp(-\mathrm{i}\omega t)$ is circularly-polarized:

$$\mathbf{E}(\mathbf{r},\omega)\exp(-\mathrm{i}\omega t) = \frac{\hat{\mathbf{x}}+\mathrm{i}\hat{\mathbf{y}}}{\sqrt{2}}\exp(\mathrm{i}kz-\mathrm{i}\omega t). \tag{9.15}$$

We could repeat the procedure in Eq. (9.13) to compute $i\mathbf{H}(\mathbf{r},\omega)\exp(-\mathrm{i}\omega t) = \frac{\nabla\times}{\omega}\mathbf{E}(\mathbf{r},\omega)\exp(-\mathrm{i}\omega t)$, but we can also reach the result through a shortcut. The expression for $\mathbf{E}(\mathbf{r},\omega)\exp(-\mathrm{i}\omega t)$ in Eq. (9.15) is actually identical to the one for $\mathbf{G}_{+}(\mathbf{r},\omega)\exp(-\mathrm{i}\omega t)$ in Eq. (9.14). This means that it is an eigenstate of $\frac{\nabla\times}{\omega}$ with eigenvalue 1, and hence $i\mathbf{H}(\mathbf{r},\omega)\exp(-\mathrm{i}\omega t) = \frac{\hat{\mathbf{x}}+\mathrm{i}\hat{\mathbf{y}}}{\sqrt{2}}\exp(\mathrm{i}kz-\mathrm{i}\omega t)$. The corresponding $\mathbf{G}_{\pm}(\mathbf{r},\omega)\exp(-\mathrm{i}\omega t)$ are then:

$$\mathbf{G}_{+}(\mathbf{r},\omega)\exp(-\mathrm{i}\omega t) = \left(\hat{\mathbf{x}}+\mathrm{i}\hat{\mathbf{y}}\right)\exp(\mathrm{i}kz-\mathrm{i}\omega t),\ \mathbf{G}_{-}(\mathbf{r},\omega)\exp(-\mathrm{i}\omega t) = \mathbf{0}. \tag{9.16}$$

It is straightforward to see that when the initial polarization in Eq. (9.15) is the of opposite polarization handedness ($\frac{\hat{\mathbf{x}}-\mathrm{i}\hat{\mathbf{y}}}{\sqrt{2}}$), then $\mathbf{G}_{+}(\mathbf{r},\omega)\exp(-\mathrm{i}\omega t) = \mathbf{0}$ and $\mathbf{G}_{+}(\mathbf{r},\omega)\exp(-\mathrm{i}\omega t) = \left(\hat{\mathbf{x}}-\mathrm{i}\hat{\mathbf{y}}\right)\exp(\mathrm{i}kz-\mathrm{i}\omega t)$.

In summary:

- When the electric field is a single linearly-polarized plane-wave, the magnetic field is also a single linearly-polarized plane-wave, and both $\mathbf{G}_{\pm}(\mathbf{r},\omega)$ are different than zero and circularly-polarized. $\mathbf{G}_{+}(\mathbf{r},\omega)$ is left-handed and $\mathbf{G}_{-}(\mathbf{r},\omega)$ is right-handed.
- When the electric field is a single circularly-polarized plane-wave, the magnetic fields is also circularly-polarized with the same handedness, and then, the $\mathbf{G}_{-}(\mathbf{r},\omega)(\mathbf{G}_{+}(\mathbf{r},\omega))$ vanishes for left(right)-handed polarization.

Which indicates that:

Box 2

- $\mathbf{G}_+(\mathbf{r}, \omega)$ is always left-hand polarized and $\mathbf{G}_-(\mathbf{r}, \omega)$ is always right-hand polarized.
- The $\mathbf{G}_\pm(\mathbf{r}, \omega)$, and consequently also the $\mathbf{G}_\pm(\mathbf{r}, t)$, split the two handed components of the electromagnetic field.
- The operator $\frac{\nabla\times}{\omega}$ is some kind of handedness operator, whose +1(-1) eigenvalue corresponds to fields with left(right)-handedness.

We are writing the statements in Box 2 by "extrapolating" from the analysis of a single plane-wave of particular frequency ω and momentum $\omega\hat{\mathbf{z}} = [0, 0, \omega]$. While it is obvious that the steps in Eqs. (9.12–9.16) hold for any ω, it is not so apparently obvious that they hold for any wavevector $\mathbf{k}$. But such is indeed the case, and then, by linearity, they also hold for arbitrary linear combinations of plane-waves, that is, arbitrary fields. Before showing that such is indeed the case, let us reflect on what that means with the help of Fig. 9.1.

Figure 9.1 has three panels. Each panel represents three different electromagnetic fields by the sum of the depicted plane-waves. Each plane-wave is characterized by its wavevector and its polarization handedness. The direction and length of the wavevector is represented by the long straight arrows in the figure. The polarization handedness are represented by the curved lines, and encoded by the use of blue color for left-handed and red color for right-handed. On the leftmost panel of Fig. 9.1, there are five plane-waves with different wavevectors, and all the plane-waves are left-handed. On the central panel, all of the four plane-waves are right-handed. On the rightmost panel there is a mix between left- and right-handed plane-waves.

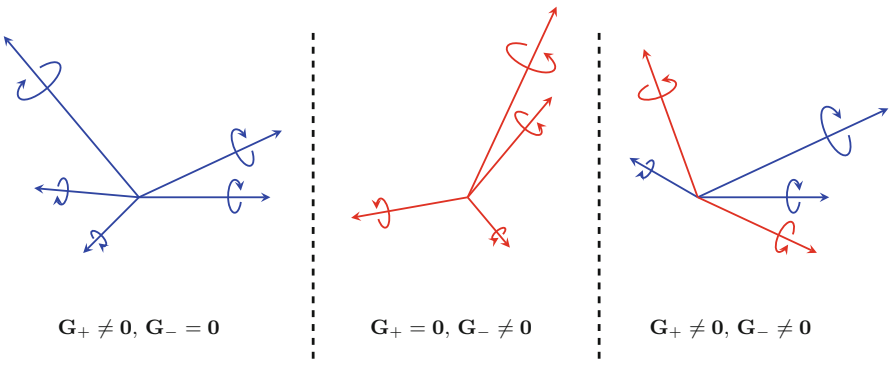

Fig. 9.1 Three different electromagnetic fields represented as the sum of the depicted plane-waves. The left-handed plane-waves are blue and the right-handed plane-waves are red. The $\mathbf{G}_\pm(\mathbf{r}, \omega)(\mathbf{G}_\pm(\mathbf{r}, t))$ have the very remarkable ability to split the two handed components of a given electromagnetic field, independently of how many different plane-waves compose it

According to Box 1, and as indicated in the figure, the $\mathbf{G}_-(\mathbf{r},\omega)(\mathbf{G}_-(\mathbf{r},t))$ corresponding to the field in leftmost panel will be zero, the $\mathbf{G}_+(\mathbf{r},\omega)(\mathbf{G}_+(\mathbf{r},t))$ corresponding to the field in the central panel will be zero, and neither of the $\mathbf{G}_\pm(\mathbf{r},\omega)(\mathbf{G}_\pm(\mathbf{r},t))$ corresponding to the field in the rightmost panel will be zero. The $\mathbf{G}_\pm(\mathbf{r},\omega)(\mathbf{G}_\pm(\mathbf{r},t))$ have the ability to split the two handedness components independently of how many different plane-waves compose the field. This is a very remarkable property.

Let us now go back to showing that the $\mathbf{G}_\pm(\mathbf{r},\omega)(\mathbf{G}_\pm(\mathbf{r},t))$ split the two polarization handedness of the electromagnetic field for any linear combination of plane-waves. We will do this by showing that $\mathbf{G}_-(\mathbf{r},\omega) = \mathbf{G}_-(\mathbf{r},t) = \mathbf{0}$ for the field corresponding to the leftmost panel of Fig. 9.1.

To such end, it is convenient to introduce the following notation for a plane-wave with wavevector $\mathbf{k}$ and handedness $\lambda = \pm 1$:

$$|\mathbf{k}\,\lambda = \pm 1\rangle \equiv \hat{\mathbf{e}}_\pm(\hat{\mathbf{k}})\exp(\mathrm{i}\mathbf{k}\cdot\mathbf{r}-\mathrm{i}\omega t) = \begin{bmatrix} \mathrm{i}\sin\phi - \lambda\cos\phi\cos\theta \\ -\mathrm{i}\cos\phi - \lambda\sin\phi\cos\theta \\ \lambda\sin\theta \end{bmatrix}\exp(\mathrm{i}\mathbf{k}\cdot\mathbf{r}-\mathrm{i}kt), \tag{9.17}$$

where $k = \omega = +\sqrt{\mathbf{k}\cdot\mathbf{k}}$, $\phi = \arctan(k_y, k_x)$, $\theta = \arccos(k_z/k)$, $\hat{\mathbf{k}}$ is the unit vector in the direction of $\mathbf{k}$, and the $\hat{\mathbf{e}}_\pm(\hat{\mathbf{k}})$ are polarization vectors corresponding to the two handedness. A plane-wave with wavevector $\mathbf{k}$ and handedness λ can be obtained by the rotation of a reference plane-wave of the same handedness and frequency [4, Eq. (8.7-1)]:

$$|\mathbf{k}\,\lambda = \pm 1\rangle = R(\hat{\mathbf{k}})|\sqrt{\mathbf{k}\cdot\mathbf{k}}\hat{\mathbf{z}}\,\lambda\rangle, \tag{9.18}$$

where $R(\hat{\mathbf{k}})$ is a rotation that brings the reference wavevector $[0, 0, \sqrt{\mathbf{k}\cdot\mathbf{k}}\hat{\mathbf{z}}]$ onto the target vector $\mathbf{k}$. The standard way of building such rotation is by a rotation along the $\hat{\mathbf{y}}$ axis by the angle θ followed by a rotation around the $\hat{\mathbf{z}}$ axis by the angle ϕ: $R(\hat{\mathbf{k}}) = R_z(\phi)\,R_y(\theta)$.

The standard reference plane-waves are

$$|k\hat{\mathbf{z}}\,\lambda\rangle \equiv \frac{-\lambda\hat{\mathbf{x}} - \mathrm{i}\hat{\mathbf{y}}}{\sqrt{2}}\exp(\mathrm{i}kz - \mathrm{i}\omega t). \tag{9.19}$$

In order for us to go forward, and since we have not introduced certain powerful algebraic tools, we will need to accept the following statement without a formal proof:

When a plane-wave of a given handedness λ is rotated, its handedness does not change.

This is intuitively easy to grap. For example, rotating your right arm does not change your right hand into a left hand. Similarly, rotating a screw does not change

the handedness of its threads. The statement that we are assuming can be formally written, using the notation $\Lambda \equiv \frac{\nabla\times}{\omega}$, as:

$$\text{If } \Lambda|\mathbf{k}\,\lambda\rangle = \lambda|\mathbf{k}\,\lambda\rangle, \text{ then } \Lambda R|\mathbf{k}\,\lambda\rangle = \lambda R|\mathbf{k}\,\lambda\rangle \text{ for any rotation } R. \tag{9.20}$$

Once we accept this, the proof is relatively easy. The electric field $\mathbf{E}$ corresponding to the leftmost panel in Fig. 9.1 can be written as the sum of five different left-hand polarized plane-waves built as in Eq. (9.18):

$$\sum_{s=1}^{5} \alpha_s R_s(\hat{\mathbf{k}}_s)|k_s\hat{\mathbf{z}}\,+\rangle, \tag{9.21}$$

where the α_s are complex numbers. Let us choose one of the five plane-waves by fixing $s = n$ so that $\mathbf{E}_n$ is $\alpha_n R_n(\hat{\mathbf{k}}_n)|k_n\hat{\mathbf{z}}\,+\rangle$. According to Eq. (9.10), its corresponding magnetic field $\mathrm{i}\mathbf{H}_n$ can be computed as $\Lambda\mathbf{E}_n$, namely

$$\Lambda\alpha_n R_n|k_n\hat{\mathbf{z}}\,+\rangle = \alpha_n \Lambda R_n|k_n\hat{\mathbf{z}}\,+\rangle \overset{\text{Eq. (9.20)}}{=} \alpha_n R_n|k_n\hat{\mathbf{z}}\,+\rangle. \tag{9.22}$$

That is $\mathbf{E}_n = i\mathbf{H}_n$, implying that $\mathbf{G}^n_+ \neq \mathbf{0}$ and $\mathbf{G}^n_- = [\mathbf{E}_n - i\mathbf{H}_n]/\sqrt{2} = \mathbf{0}$, which is true for both $(\mathbf{r}, \omega)$- and $(\mathbf{r}, t)$-dependent fields. After seeing that $\mathbf{G}^n_- = \mathbf{0}$, it is obvious that the whole $\mathbf{G}_- = \sum_{s=1}^{5} \mathbf{G}^s_-$ will be equal to zero because the analysis with $s = n$ works for any other s.

9.3.4 The Importance of Complex Fields

This is a good point to motivate the choice of complex-valued electric and magnetic fields, with harmonic decompositions of the kind in Eq. (9.5), to build the $\mathbf{G}_\pm(\mathbf{r}, t)$ in Eq. (9.3). Let us assume that we use real-valued fields instead, $\boldsymbol{\mathcal{E}}(\mathbf{r}, t)$ and $\boldsymbol{\mathcal{H}}(\mathbf{r}, t)$

$$\boldsymbol{\mathcal{G}}_\pm(\mathbf{r}, t) = \frac{\boldsymbol{\mathcal{E}}(\mathbf{r}, t) \pm \mathrm{i}\boldsymbol{\mathcal{H}}(\mathbf{r}, t)}{\sqrt{2}}. \tag{9.23}$$

The real-valued fields can be defined as the real part of their complex-valued counterparts: $\boldsymbol{\mathcal{E}}(\mathbf{r}, t) = \mathrm{Real}\{\mathbf{E}(\mathbf{r}, t)\}$, and $\boldsymbol{\mathcal{H}}(\mathbf{r}, t) = \mathrm{Real}\{\mathbf{H}(\mathbf{r}, t)\}$.

The $\boldsymbol{\mathcal{G}}_\pm(\mathbf{r}, t)$ in Eq. (9.23) are still complex, but now, since $\boldsymbol{\mathcal{E}}(\mathbf{r}, t)$ and $\boldsymbol{\mathcal{H}}(\mathbf{r}, t)$ are real we have that $\boldsymbol{\mathcal{G}}_\pm(\mathbf{r}, t)$ determine each other through complex conjugation:

$$[\boldsymbol{\mathcal{G}}_+(\mathbf{r}, t)]^* = [\boldsymbol{\mathcal{G}}_-(\mathbf{r}, t)]\,. \tag{9.24}$$

This is crucially different from the case of $\mathbf{G}_\pm(\mathbf{r}, t)$, where such connection does not exist. There is no physical law that, in general and *a priori*, ties one handedness to the other as Eq. (9.24) implies. Therefore, the $\boldsymbol{\mathcal{G}}_\pm(\mathbf{r}, t)$ are not obviously suitable

to represent the two handed components of the electromagnetic field. In particular, it can be easily shown that their point-wise squared-norms are equal

$$|\boldsymbol{\mathcal{G}}_{+}(\mathbf{r},t)|^2 = |\boldsymbol{\mathcal{G}}_{-}(\mathbf{r},t)|^2, \text{ for all } (\mathbf{r},t). \tag{9.25}$$

The clean split illustrated in Fig. 9.1 is hence not possible using the $\boldsymbol{\mathcal{G}}_{\pm}(\mathbf{r},t)$ since if one of them is zero, so must be the other, according to Eq. (9.25).

9.3.5 *The* $\mathbf{G}_{\pm}$ *Split as the Polarization Description: Generality and Invariance*

Let us go back to the $\mathbf{G}_{\pm}$ and investigate further their ability to characterize the polarization of the electromagnetic field. To such end, we start with the question of *What is polarization?*.

The polarization of a field may be defined as its non-scalar degrees of freedom. That is, those degrees of freedom that scalar fields cannot have. For example, the Higgs boson has energy, but does not have different polarization states. The electromagnetic field has scalar degrees of freedom like energy, momentum, angular momentum, and, *additionally*, can have different polarizations. Non-scalar degrees of freedom are sometimes called internal degrees of freedom. Table 9.1 lists some polarized and unpolarized fields.

Let us focus on the electromagnetic field to tackle the question of how to characterize its polarization.

When dealing with a single plane-wave, the concept of polarization is quite intuitive. Polarization is typically understood as the direction of the field oscillations in a plane transverse to the wavevector. Fixing one such plane, the linear, circular, or generally elliptical polarization of the plane-wave is identified by the geometrical figure that the "tip" of the electric field "draws" on the plane with the passing of time. This understanding of polarization, though, is quite restricted to single plane-wave cases, and not applicable in general. For example, consider the following electric field:

$$\sqrt{2}\mathbf{E}(\mathbf{r},t) = \\ \hat{\mathbf{x}}\exp\left(\mathrm{i}2\omega(z-t)\right) - \mathrm{i}\hat{\mathbf{y}}\left[\exp\left(\mathrm{i}\omega(x-t)\right) + \exp\left(\mathrm{i}2\omega(z-t)\right)\right] - \hat{\mathbf{z}}\exp\left(\mathrm{i}\omega(x-t)\right). \tag{9.26}$$

Table 9.1 Some fields have a polarization degree of freedom, i.e. a non-scalar degree of freedom, some other fields do not have it

Polarized fields	Unpolarized fields
Electromagnetic field	Temperature
Electrons	Pressure
Neutrinos	The Higgs boson
Gravitational waves	Electric charge density

It is apparent the field contains at least two different plane-waves of different frequency and wavevector directions. The previous definition of polarization cannot be applied because it is impossible to find a plane transverse to both wavevectors. We may attempt to define polarization by fixing a point $\mathbf{r}_0$ and observing the trajectory of the "tip" of the electric field $\mathbf{E}(\mathbf{r}_0, t)$ as time elapses. Or we may fix $t = t_0$ and observe the trajectory of $\mathbf{E}(\mathbf{r}, t_0)$ for some $\mathbf{r}$ in a given volume or surface. Some exercises with Eq. (9.26) quickly show the complexity of these kind of approaches. But, the fact is that the field in Eq. (9.26) is just

$$|[\omega, 0, 0] +\rangle + |[0, 0, 2\omega] +\rangle, \tag{9.27}$$

that is, it is a $\mathbf{G}_+$.

We will now argue that the $\mathbf{G}_+/\mathbf{G}_-$ split is the most general and robust way to characterize the polarization degree of freedom of the electromagnetic field.

The general applicability of $\mathbf{G}_\pm$ is already clear from the previous discussion: It applies to general linear combinations of plane-waves. Let us discuss its robustness. By that, we mean the resilience upon transformations, i.e., invariance. We have already heuristically discussed how the $\mathbf{G}_\pm$ character does not change upon rotations. The linearly-polarized states provides a counter-example. A rotation along the axis defined by the wavevector of a plane-wave transforms the two orthogonal linear polarization vectors onto each other. Linear polarizations are hence not invariant under rotations.

Let us keep using the analogy of the threads of a screw to investigate the transformation properties of the handed $\mathbf{G}_\pm$. In the same way that the threads do not change handedness when the screw is rotated, they also do not change handedness upon:

- Spatial translations: Moving the screw from point A to point B.
- Time translations: Letting time pass or moving time backwards.

So, the handedness defined by $\mathbf{G}_\pm$ is invariant under time and space translations and rotations. We only need to add the Lorentz transformations to complete the Poincaré group, that is, the group of transformations of special relativity. And we can do that. A Lorent boost, or Lorentz transformation, changes an inertial reference frame into another intertial reference frame. The new reference frame moves with a constant velocity $\boldsymbol{\beta}$ with respect to the original one. Let us consider the transformation of the electric and magnetic fields upon a Lorentz boost characterized by the real-valued 3-vector $\boldsymbol{\beta}$. The relationship between the $\mathbf{E}$ and $\mathbf{H}$ fields in the original reference frame and the $\bar{\mathbf{E}}$ and $\bar{\mathbf{H}}$ fields in the boosted reference frame is [5, Eq. (11.149)]:

$$\begin{aligned} \text{ⓐ}: \ \bar{\mathbf{E}} &= \gamma\,(\mathbf{E} + \boldsymbol{\beta} \times \mathbf{H}) - \frac{\gamma^2}{1+\gamma}\boldsymbol{\beta}\,(\boldsymbol{\beta} \cdot \mathbf{E})\,, \\ \text{ⓑ}: \ \bar{\mathbf{H}} &= \gamma\,(\mathbf{H} - \boldsymbol{\beta} \times \mathbf{E}) - \frac{\gamma^2}{1+\gamma}\boldsymbol{\beta}\,(\boldsymbol{\beta} \cdot \mathbf{H})\,, \end{aligned} \tag{9.28}$$

where $\gamma = (1 - \boldsymbol{\beta} \cdot \boldsymbol{\beta})^{-1/2}$. We now perform the same manipulation that took the equations in (9.1) to the equations in (9.2):

$$\begin{aligned} \frac{ⓐ + \mathrm{i}ⓑ}{\sqrt{2}}&: \bar{\mathbf{G}}_+ = \gamma \mathbf{G}_+ - \mathrm{i}\boldsymbol{\beta} \times \mathbf{G}_+ - \frac{\gamma^2}{1+\gamma}\boldsymbol{\beta}\,(\boldsymbol{\beta} \cdot \mathbf{G}_+) \\ \frac{ⓐ - \mathrm{i}ⓑ}{\sqrt{2}}&: \bar{\mathbf{G}}_- = \gamma \mathbf{G}_- + \mathrm{i}\boldsymbol{\beta} \times \mathbf{G}_- - \frac{\gamma^2}{1+\gamma}\boldsymbol{\beta}\,(\boldsymbol{\beta} \cdot \mathbf{G}_-)\,. \end{aligned} \tag{9.29}$$

Equation (9.29) shows that a boosts does not mix $\mathbf{G}_+$ and $\mathbf{G}_-$. Incidentally, Eq. (9.28) shows that the notions of electric and magnetic field are not relativistically invariant: A boost mixes electric and magnetic fields.

The conclusion is that the characterization of polarization by means of $\mathbf{G}_\pm$ is relativistically invariant. Actually, the $\mathbf{G}_\pm$ character is invariant under a larger group: The conformal group, which is actually the largest group of invariance of Maxwell equations [6]. Therefore, the $\mathbf{G}_\pm$ character is as robust as anything can be in electromagnetism.

9.4 An Even Simpler Form of Maxwell Equations and the $\mathrm{i}\hat{\mathbf{k}}\times$ Operator

We will now simplify Maxwell equations further by the use of the following decomposition of an $(\mathbf{r}, t)$-dependent field:

$$\begin{aligned} \mathbf{X}(\mathbf{r}, t) &= \int_{\mathbb{R}^3 - \{\mathbf{0}\}} \frac{d\mathbf{k}}{\sqrt{(2\pi)^3}}\, \mathbf{X}(\mathbf{k}) \exp\left(\mathrm{i}\mathbf{k} \cdot \mathbf{r} - \mathrm{i}kt\right) \\ &= \int_{>0}^{\infty} \frac{dk}{\sqrt{2\pi}} k^2 \left[\int_{\mathbb{S}^2} \frac{d\hat{\mathbf{k}}}{2\pi}\, \mathbf{X}(k, \hat{\mathbf{k}}) \exp(\mathrm{i}\mathbf{k} \cdot \mathbf{r}) \right] \exp(-\mathrm{i}kt), \end{aligned} \tag{9.30}$$

where, in the second line, we have split the initial $d\mathbf{k}$ integral into its radial and angular parts

$$\int_{\mathbb{R}^3 - \{\mathbf{0}\}} \frac{d\mathbf{k}}{\sqrt{(2\pi)^3}} = \int_{>0}^{\infty} \frac{dk}{\sqrt{2\pi}} k^2 \int_{\mathbb{S}^2} \frac{d\hat{\mathbf{k}}}{2\pi} = \int_{>0}^{\infty} \frac{dk}{\sqrt{2\pi}} k^2 \int_0^{\pi} d\theta \sin\theta \int_{-\pi}^{\pi} d\phi, \tag{9.31}$$

where θ and ϕ are defined below Eq. (9.17) and $\mathbb{S}^2$ is the 2-sphere in $\mathbf{k}$ space with radius k. The removal of the origin $\mathbf{k} = \mathbf{0}$ responds again to the exclusion of electro-

and magneto-statics. Recalling that $k = \omega$, and comparing Eq. (9.30) with Eq. (9.5), we establish that:

$$\mathbf{X}(\mathbf{r}, \omega) = k^2 \int_{\mathbb{S}^2} \frac{d\hat{\mathbf{k}}}{2\pi} \mathbf{X}(k, \hat{\mathbf{k}}) \exp(\mathrm{i}\mathbf{k} \cdot \mathbf{r}), \tag{9.32}$$

which we will now use to work on the equations in (9.9). To such end, we need to know what is the effect of $\frac{\nabla\times}{\omega}$ in a field $\mathbf{X}(\mathbf{r}, \omega)$ decomposed as in Eq. (9.32):

$$\begin{aligned}
\frac{\nabla\times}{\omega}\mathbf{X}(\mathbf{r}, \omega) &= k^2 \int_{\mathbb{S}^2} \frac{d\hat{\mathbf{k}}}{2\pi} \frac{\nabla\times}{\omega}\mathbf{X}(k, \hat{\mathbf{k}}) \exp(\mathrm{i}\mathbf{k} \cdot \mathbf{r}) \\
&= \frac{k^2}{\omega} \int_{\mathbb{S}^2} \frac{d\hat{\mathbf{k}}}{2\pi} \begin{vmatrix} \hat{\mathbf{x}} & \hat{\mathbf{y}} & \hat{\mathbf{z}} \\ \partial_x & \partial_y & \partial_z \\ X_x(k, \hat{\mathbf{k}}) \exp(\mathrm{i}\mathbf{k} \cdot \mathbf{r}) & X_y(k, \hat{\mathbf{k}}) \exp(\mathrm{i}\mathbf{k} \cdot \mathbf{r}) & X_z(k, \hat{\mathbf{k}}) \exp(\mathrm{i}\mathbf{k} \cdot \mathbf{r}) \end{vmatrix} \\
&= \frac{\mathrm{i}k^2}{\omega} \int_{\mathbb{S}^2} \frac{d\hat{\mathbf{k}}}{2\pi} \begin{bmatrix} X_z(k, \hat{\mathbf{k}})k_y - X_y(k, \hat{\mathbf{k}})k_z \\ -X_z(k, \hat{\mathbf{k}})k_x + X_x(k, \hat{\mathbf{k}})k_z \\ X_y(k, \hat{\mathbf{k}})k_x - X_x(k, \hat{\mathbf{k}})k_y \end{bmatrix} \exp(\mathrm{i}\mathbf{k} \cdot \mathbf{r}) \\
&= k^2 \int_{\mathbb{S}^2} \frac{d\hat{\mathbf{k}}}{2\pi} \frac{\mathrm{i}\mathbf{k}\times}{\omega}\mathbf{X}(k, \hat{\mathbf{k}}) \exp(\mathrm{i}\mathbf{k} \cdot \mathbf{r}) \\
&= k^2 \int_{\mathbb{S}^2} \frac{d\hat{\mathbf{k}}}{2\pi} \mathrm{i}\hat{\mathbf{k}} \times \mathbf{X}(k, \hat{\mathbf{k}}) \exp(\mathrm{i}\mathbf{k} \cdot \mathbf{r}).
\end{aligned} \tag{9.33}$$

The one-before-last equality can be easily verified using the expression of the cross-product between two 3-vectors.

Using Eq. (9.33), we can write Eq. (9.9) as:

$$k^2 \int_{\mathbb{S}^2} \frac{d\hat{\mathbf{k}}}{2\pi} \left[\mathrm{i}\hat{\mathbf{k}} \times \mathbf{G}_\pm(\mathbf{k}) \mp \mathbf{G}_\pm(\mathbf{k})\right] \exp(\mathrm{i}\mathbf{k} \cdot \mathbf{r}) = \mathbf{0} \text{ for all } \mathbf{r}, \tag{9.34}$$

which implies

$$\mathrm{i}\hat{\mathbf{k}} \times \mathbf{G}_\pm(\mathbf{k}) = \pm\mathbf{G}_\pm(\mathbf{k}). \tag{9.35}$$

It is clear that $\mathrm{i}\hat{\mathbf{k}}\times$ in Eq. (9.35) represents, in the $\mathbf{k}$ domain, the same operator represented by $\frac{\nabla\times}{\omega}$ in the $(\mathbf{r}, \omega)$ domain.

A very similar procedure allows to show that

$$\nabla \cdot \mathbf{G}_\pm(\mathbf{r}, \omega) = 0 \implies \mathrm{i}\mathbf{k} \cdot \mathbf{G}_\pm(\mathbf{k}) = 0, \tag{9.36}$$

and the four Maxwell equations can finally be written in $\mathbf{k}$ domain as:

$$\boxed{\mathrm{i}\mathbf{k}\cdot\mathbf{G}_{\pm}(\mathbf{k})=0,\ \mathrm{i}\hat{\mathbf{k}}\times\mathbf{G}_{\pm}(\mathbf{k})=\pm\mathbf{G}_{\pm}(\mathbf{k}).} \tag{9.37}$$

The equations in (9.37) are a very simple form of Maxwell equations. All the partial derivatives are eliminated and Maxwell equations become algebraic equations in (9.37). These are easier to interpret. For example, the $\mathrm{i}\mathbf{k}\cdot\mathbf{G}_{\pm}(\mathbf{k})=0$ conditions say that, given a wavevector $\mathbf{k}$, the polarization of the field must be orthogonal to it. There cannot be any longitudinal components along $\mathbf{k}$. We say that Maxwell solutions are transverse.

9.5 Summary

The $\mathbf{G}_{\pm}$ forms of Maxwell equations

$$\mathrm{i}\partial_t\mathbf{G}_{\pm}(\mathbf{r},t)=\pm\nabla\times\mathbf{G}_{\pm}(\mathbf{r},t)\ \ ,\nabla\cdot\mathbf{G}_{\pm}(\mathbf{r},t)=0, \tag{9.38}$$

$$\boxed{\frac{\nabla\times}{\omega}}\mathbf{G}_{\pm}(\mathbf{r},\omega)=\pm\mathbf{G}_{\pm}(\mathbf{r},\omega)\ \ ,\nabla\cdot\mathbf{G}_{\pm}(\mathbf{r},\omega)=0, \tag{9.39}$$

$$\boxed{\mathrm{i}\hat{\mathbf{k}}\times}\mathbf{G}_{\pm}(\mathbf{k})=\pm\mathbf{G}_{\pm}(\mathbf{k})\ \ ,\mathrm{i}\mathbf{k}\cdot\mathbf{G}_{\pm}(\mathbf{k})=0. \tag{9.40}$$

The conversion of the Maxwell equations from their typical form featuring electric and magnetic fields to their form featuring the $\mathbf{G}_{\pm}$ Riemann-Silberstein-like fields reveals a simple underlying structure:

The $\mathbf{G}_{\pm}$ Maxwell structure

- There are two decoupled and fundamentally different kinds of solutions of Maxwell equations: $\mathbf{G}_{+}$ and $\mathbf{G}_{-}$.
- The $\mathbf{G}_{\pm}$ are eigenstates of the operator inside the boxes in Eqs. (9.39–9.40) with corresponding eigenvalues ±1.
- The $\mathbf{G}_{\pm}$ split the handedness content of the field into the left- and right-handed components, corresponding to $\mathbf{G}_{+}$ and $\mathbf{G}_{-}$, respectively.

The $\frac{\nabla\times}{\omega}\equiv\mathrm{i}\hat{\mathbf{k}}\times$ operator is actually the well-known helicity operator. These two forms of the helicity operator are particular representations of its abstract definition. The helicity operator Λ is defined as the projection of the angular momentum operator vector $\mathbf{J}$ onto the direction of the linear momentum operator vector $\mathbf{P}$:

$$\Lambda=\frac{\mathbf{J}\cdot\mathbf{P}}{|\mathbf{P}|}. \tag{9.41}$$

Helicity is not only relevant in electromagnetism, but also in the general field of high energy physics. Essentially, helicity is one of the key operators used in the identification of physical particles and fields with the representations of the Poincaré group [7]. This identification is the basic idea behind our understanding of the standard model and its extensions.

9.6 Concluding Remarks

One can see the $\mathbf{G}_{\pm}$ forms of Maxwell equations as one of the bases for an algebraic approach to light-matter interactions. The other bases of such approach are the setting of Hilbert spaces, and the scattering operator for modeling the interaction of material objects with the electromagnetic field. With such tools, the powerful ideas of symmetries and conservation laws can be applied to light-matter interactions in a straightforward way [8]. In this regard, the advantage of considering $\mathbf{G}_{\pm}$ and the helicity operator is that helicity is the generator of a fundamental symmetry in electromagnetism: The electromagnetic duality symmetry. Helicity and duality are in the same kind of relationship as angular momentum and rotations, or linear momentum and translations. The one-to-one connection to a fundamental symmetry does not exist for other ways of characterizing polarization [9, Sec. 2.4.2]. The use of helicity and duality allows the use of symmetries and conservation laws for treating polarization in light-matter interactions [9]. Importantly, the handedness-splitting ability of $\mathbf{G}_{\pm}$ actually extends to evanescent plane-waves, which are ubiquitous in the near-fields around illuminated objects (see e.g. [9, Fig. 2.7]).

When a given formulation simplifies the theoretical description of physical phenomena, it is often the case that such formulation also helps in practical scenarios. The use of the $\mathbf{G}_{\pm}$ fields is not an exception. The practical application of the algebraic approach has lead, for example, to criteria for the optimal sensing of chiral molecules, to the symmetry conditions for zero reflection, and to a quantitative understanding of near-field directional coupling.

References

1. Bialynicki-Birula, I.: Photon wave function. Prog. Optics **36**, 245 (1996)
2. Bialynicki-Birula, I., Bialynicka-Birula, Z.: Beams of electromagnetic radiation carrying angular momentum: the Riemann–Silberstein vector and the classical-quantum correspondence. Opt. Commun. **264**(2), 342 (2006)
3. Bialynicki-Birula, I., Bialynicka-Birula, Z.: The role of the Riemann-Silberstein vector in classical and quantum theories of electromagnetism. J. Phys. A Math. Theor. **46**(5), 053001 (2013)
4. Tung, W.-K.: Group Theory in Physics. World Scientific, New Jersey (1985)
5. Jackson, J.D.: Classical Electrodynamics. Wiley, New York (1998)

6. Bateman, H.: The transformation of the electrodynamical equations. Proc. Lond. Math. Soc. s**2-8**(1), 223 (1910)
7. Wigner, E.: On unitary representations of the inhomogeneous Lorentz group. Ann. Math. **40**(1), 149 (1939)
8. Fernandez-Corbaton, I., Rockstuhl, C.: Unified theory to describe and engineer conservation laws in light-matter interactions. Phys. Rev. A **95**, 053829 (2017)
9. Fernandez-Corbaton, I., Helicity and duality symmetry in light matter interactions: Theory and applications. Ph.D. Thesis, Macquarie University (2014)

Chapter 10
Absorption, Emission, and Vacuum Fluctuations

Markus Pollnau

Abstract In the literature one finds several conflicting accounts of the phase difference of stimulated and spontaneous emission, as well as absorption, with respect to an existing (triggering) electromagnetic field. One of these approaches proposes that stimulated emission and absorption occur in phase and out of phase with their driving field, respectively, whereas spontaneous emission occurs under an arbitrary phase difference with respect to an existing field. It has served as a basis for explaining quantum-mechanically the laser linewidth, its narrowing by a factor of 2 around the laser threshold, as well as its broadening due to amplitude-phase coupling, resulting in Henry's α-factor. Assuming the validity of Maxwell's equations, all three processes would, thus, violate the law of energy conservation. In semi-classical approaches, we investigate stimulated emission in a Fabry-Pérot resonator, analyze the Lorentz oscillator model, apply the Kramers-Kronig relations to the complex susceptibility, understand the summation of quantized electric fields, and quantitatively interpret emission and absorption in the amplitude-phase diagram. In all cases, we derive that the phase of stimulated emission is 90° in lead of the driving field, and the phase of absorption lags 90° behind the transmitted field. Also spontaneous emission must obey energy conservation, hence it occurs with 90° phase in lead of an existing field. These semi-classical findings agree with recent experimental investigations regarding the interaction of attosecond pulses with an atom, thereby questioning the physical explanation of the laser linewidth and its narrowing or broadening.

M. Pollnau (✉)
Advanced Technology Institute, University of Surrey, Guildford, UK
e-mail: m.pollnau@surrey.ac.uk

M. Cesaria et al. (eds.), *Light-Matter Interactions Towards the Nanoscale*,
NATO Science for Peace and Security Series B: Physics and Biophysics,
https://doi.org/10.1007/978-94-024-2138-5_10

10.1 Introduction

Einstein exploited a semi-classical rate-equation approach [1] including the rates of stimulated and spontaneous emission and absorption to provide the physical foundation of Planck's law of blackbody radiation [2], thereby predicting the existence of stimulated emission. By assuming conservation of energy and momentum, Einstein showed that an incident electromagnetic field at frequency ν triggers a two-level atom in its excited state to emit an additional electromagnetic field with an energy $h\nu$ that equals the energy gap between the two levels, such that the energy of the incident field increases by this energy during the interaction. The emitted field has the same frequency, the same direction, and the same polarization as the incident field, hence it is emitted into the same optical mode. Einstein did not specify the phase difference between the incident and emitted electromagnetic field.

In the literature, three different accounts of this phase difference can be found.

(i) The semi-classical Lorentz oscillator model [3] predicts that stimulated emission is in quadrature, i.e., 90° out of phase with the incident field [4–7].
(ii) Quantum-optically stimulated and spontaneous emission are both described by the same creation operator [8], hence either both processes must occur with the same phase difference or the phase difference is not explicitly considered when applying the creation operator.
(iii) The amplitude-phase diagram of Fig. 10.1a proposes that stimulated emission is in phase with the incident field (red solid arrows), whereas according to Lax [9], Haken [10], Henry [11], and others spontaneous emission occurs at an arbitrary phase angle θ with the incident field (red dashed-dotted arrow).

Despite their obvious incompatibility concerning the phase aspect, all three models have been applied to understand important optical phenomena. Model (i) has been exploited to derive the Kramers-Kronig relations [15, 16] between susceptibility and absorption. In a simple rate-equation approach equivalent to Einstein's [1] without phase considerations, i.e., in line with model (ii), the power behavior of semiconductor lasers around the laser threshold has been described [17]. A combination of models (ii) and (iii) has been applied to calculate quantum-mechanically the fundamental laser linewidth and its reduction compared to the Schawlow-Townes linewidth [12] by an additional factor of two around laser threshold [9, 10, 13]. Model (iii) has served to justify this reduction of laser linewidth around the laser threshold [9–11]. Spontaneous emission induces amplitude and phase fluctuations (projection onto the axes with $\theta_a = 0° - 180°$ and $\theta_p = \pm 90°$, respectively), of which the latter constitute the quantum noise that determines the fundamental laser linewidth, whereas the former are damped out in a laser, thereby reducing the laser linewidth by a factor of 2. It has also served to derive Henry's α-factor, which quantifies broadening of the laser linewidth due to amplitude-phase coupling via the refractive index [11]. Here, we propose a consistent semi-classical picture of the phase aspect in emission and absorption [14, 18].

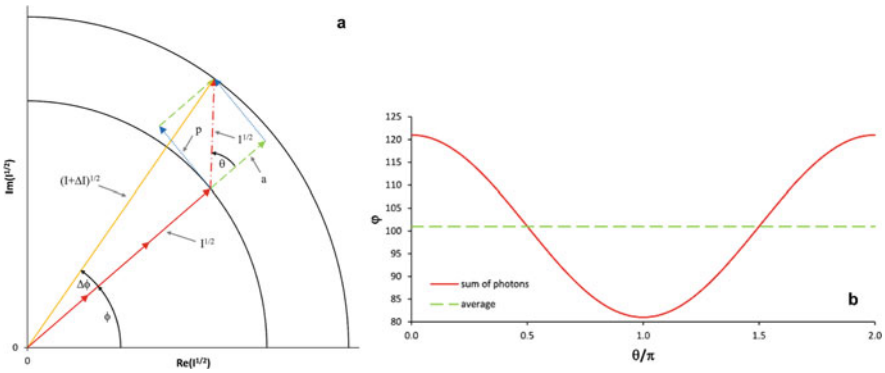

Fig. 10.1 (**a**) Amplitude-phase diagram visualizing the interpretation of quantum noise and laser linewidth by Lax [9], Haken [10], and Henry [11]. Quantum noise in a laser is said to be induced by adding with an arbitrary phase difference θ a spontaneously emitted photon (red dashed-dotted arrow) of intensity 1 to the intra-cavity laser field (red solid arrows) of intensity I and phase ϕ, resulting in an intra-cavity laser field of intensity $I + \Delta I$ (orange solid arrow) and inducing a phase shift $\Delta\phi$. Below laser threshold all phase differences θ are proposed to generate noise, whereas, above laser threshold, amplitude fluctuations a ($\theta = 0$ or π, i.e., the projection of noise onto the direction of the green dashed arrow) are rapidly damped out by relaxation oscillations, and only phase fluctuations p ($\theta = \pm\pi/2$, i.e., the projection of noise onto the direction of the blue dotted arrow) contribute to noise, thereby reducing the laser linewidth compared to the Schawlow-Townes linewidth [12] by a factor of 2 [9–11, 13]. (**b**) Number φ of photons resulting from the interference according to Eq. (10.1) between one photon and 100 photons (red solid curve) versus phase difference θ and medium of 101 photons averaged over all θ (green dashed line). (Figure taken from Ref. [14])

10.2 Interference and Energy Conservation

By use of the term "photon" we will solely refer to the fundamental energy unit $h\nu$ that corresponds to the quantized energy of one photon. The parameter φ represents the number of these energy units called photons that is present in a classical electromagnetic field. The conservation of energy requires that an emission or absorption process by a two-level atom changes the value of φ by ± 1 energy unit $h\nu$.

Based upon Maxwell's equations, superposition of two co-propagating electromagnetic waves at the same frequency ν, with electric-field amplitudes E_1 and E_2 and a phase difference θ, yields the intensity

$$\varphi \propto I_{1+2} = \frac{c\varepsilon_0}{2}\left|\vec{E}_1 + \vec{E}_2\right|^2 = \frac{c\varepsilon_0}{2}\left[|E_1|^2 + 2\,|E_1 E_2|\cos(\theta) + |E_2|^2.\right] \tag{10.1}$$

ε_0 is the vacuum permittivity and c is the speed of light in the medium of refractive index n. For $\cos(\theta) \neq 0$, the interference term does not vanish and the law of energy conservation is obviously violated. Two fields with $E_1 = E_2$ constructively

(destructively) interfere to produce four (zero) times the intensity of each field alone. When adding a field representing one photon ($E_2 \propto 1^{1/2} = 1$) to a field representing 100 photons ($E_1 \propto 100^{1/2} = 10$), then averaged over all phase angles, $\overline{\cos}\,(\theta) = 0$, the expected energy of 101 photons emerges, whereas constructive (destructive) interference yields the energy of 121 (81) photons; see Fig. 10.1b. In the absence of a source or drain, energy can only be conserved if the opposite interference occurs in another location of the optical system, i.e., constructive or destructive interference never occurs alone!

Let us analyze the processes in Fig. 10.1a with respect to energy conservation. If stimulated emission occurred in phase with the incident field, $\cos(\theta) = 1$, then according to Eq. (10.1) each stimulated-emission event would generate an excess of photons, thereby violating the law of energy conservation. If spontaneous emission occurred at an arbitrary phase angle, then, according to Eq. (10.1), each spontaneous-emission event would either generate or annihilate extra photons [Fig. 10.1b], and in the amplitude-phase diagram [Fig. 10.1a] the added intensity ΔI would not correspond to the intensity generated by one photon. As pointed out by Henry [11], only when averaging over many spontaneous-emission events, $\overline{\cos}\,(\theta) = 0$, energy would be conserved [Fig. 10.1b]. Since energy must be conserved, this interpretation of stimulated and spontaneous emission is obviously questionable.

10.3 Stimulated Emission in a Fabry-Pérot Resonator

The problem of energy conservation manifests itself in a fundamentally important optical system, the Fabry-Pérot resonator. In Fig. 10.2a, a monochromatic external light source continuously launches light into a resonator whose only losses are the outcoupling losses through its two mirrors. A steady state of light launched into, circulating inside, and emitted from the resonator is established, described by the Airy distributions [19].

$$\begin{aligned}
A_{circ} &= I_{circ}/I_{laun} = \frac{1}{\left(1-\sqrt{R_1R_2}\right)^2+4\sqrt{R_1R_2}\sin^2(\Delta\phi_{RT}/2)} \\
A'_{trans} &= I_{trans}/I_{inc} = (1-R_1)\,(1-R_2)\,A_{circ} \\
A'_{back} &= I_{back}/I_{inc} = (1-R_1)^2 R_2 A_{circ} \\
A'_{refl} &= I_{refl}/I_{inc} \\
&= \left[\left(\sqrt{R_1}-\sqrt{R_2}\right)^2 + 4\sqrt{R_1R_2}\sin^2\left(\Delta\phi_{RT}/2\right)\right] A_{circ} \\
A'_{trans} &+ A'_{refl} = \left(I_{trans} + I_{refl}\right)/I_{inc} = 1,
\end{aligned} \tag{10.2}$$

where r_i and $R_i = |r_i|^2$ are the amplitude and intensity reflectivity of mirror i, respectively. $\Delta\phi_{RT}$ is the phase shift accumulated over one round trip. The different electric fields are displayed in Fig. 10.2a; their intensities are $I \propto |E|^2$, and their

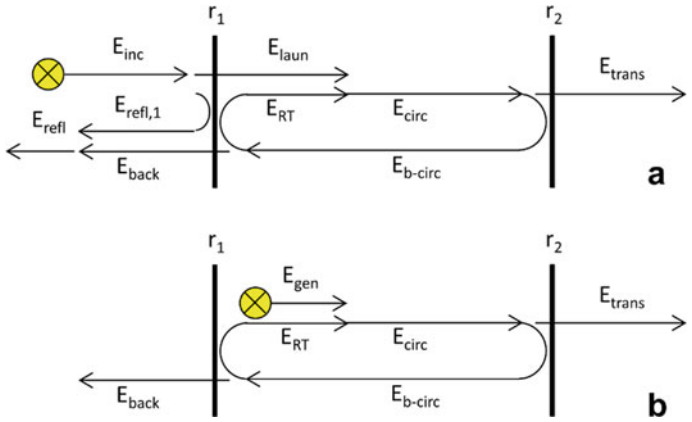

Fig. 10.2 Schematic of a Fabry-Pérot resonator and the relevant electric fields E for (**a**) light launched from outside [19] and (**b**) light generated inside the resonator. (Figure taken from Ref. [14])

spectral dependencies are given by the Airy distributions A with respect to the launched intensity or $A^{'}$ with respect to the incident intensity [19]. For arbitrary.

$\Delta\phi_{RT}$ the energy is conserved, $A'_{trans} + A'_{refl} = 1$, because the interference between E_{RT} and E_{laun} is compensated by the opposite interference between $E_{refl,1}$ and E_{back}.

Now we move the light source into the resonator [Fig. 10.2b]. Let us assume that the light source is a pumped inverted medium that continuously generates E_{gen} via stimulated emission triggered by E_{RT}, resulting in the combined field E_{circ}. For simplicity, we neglect spontaneous emission and assume that several stimulated-emission processes can occur simultaneously in different lateral regions of the gain sheet without influencing each other. Furthermore, for comparison with Fig. 10.2a, we assume a race-track resonator with unidirectional light propagation, such that the backward-circulating field $E_{b\text{-}circ}$ does not penetrate the active medium and the stimulated-emission process is uni-directional. If stimulated emission occurred "in phase" and we pumped the medium to a desired inversion, such that in Fig. 10.2a and b the same field $E_{gen} = E_{laun}$ interfered constructively with E_{RT} at the resonance frequency ν_q, then the same steady state of light generated, circulating inside, and emitted from the resonator would be established and the same fields E_{trans} and E_{back} would be emitted in both situations. However, since in Fig. 10.2b E_{back} cannot destructively interfere, because there is no $E_{refl,1}$, the constructive interference is not compensated for. Therefore, if the phase shift $\Delta\phi_{em}$ potentially induced by stimulated emission between E_{RT} and E_{circ} equals zero, energy is not conserved.

If stimulated emission occurred in phase, $\Delta\phi_{em} = 0$, the law of energy conservation would be violated; e.g., for $R_1 = R_2 = 0.7$, 5.7 times the light generated by stimulated emission would be emitted through both mirrors. Also for all phase shifts $\Delta\phi_{em} \neq 0$ energy is not conserved, except for one specific value of $\Delta\phi_{em}$ for

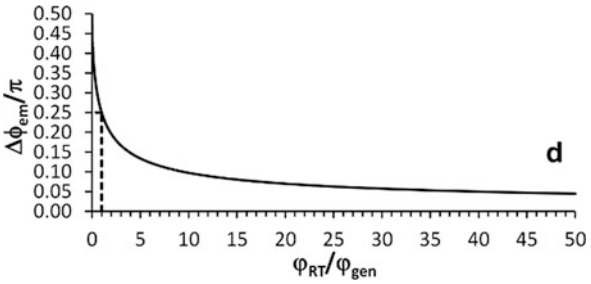

Fig. 10.3 Phase shift $\Delta\phi_{em}$ induced by stimulated emission as a function of the ratio $\varphi_{RT}/\varphi_{gen}$. For $\varphi_{RT}/\varphi_{gen} = 1$ one obtains $\Delta\phi_{em} = \pi/4$ (dashed lines). (Figure taken from Ref. [14])

each value of $(R_1R_2)^{1/2}$. To ensure energy conservation, the condition [14].

$$\tan(\Delta\phi_{em}) = \sqrt{\frac{1-\cos^2(\Delta\phi_{em})}{\cos^2(\Delta\phi_{em})}} = \sqrt{\frac{1-R_1R_2}{R_1R_2}} \tag{10.3}$$

must be fulfilled. The phase shift $\Delta\phi_{em}$ induced by stimulated emission differs from zero and depends on R_1 and R_2. We convert this reflectivity dependence to a photon dependence. Since each intensity is proportional to the corresponding photon number, the ratio between the numbers φ_{RT} of photons triggering stimulated emission and φ_{gen} of photons generated by stimulated emission equals the Airy distribution A_{RT}, from which we derive the phase shift [14]:

$$\tan(\Delta\phi_{em}) = \sqrt{\varphi_{gen}/\varphi_{RT}}. \tag{10.4}$$

The final result of Eq. (10.4) is shown in Fig. 10.3. Only for an infinite ratio $\varphi_{RT}/\varphi_{gen}$ is the induced phase shift $\Delta\phi_{em}$ zero. The smaller the number of photons triggering stimulated emission and the larger the number of photons generated, the further the induced phase shift $\Delta\phi_{em}$ increases to $\pi/2$. If one photon triggers stimulated emission of one photon, then $\Delta\phi_{em} = \pi/4$. Since the second angle in the vector diagram comprising the fields E_{RT}, E_{gen}, and E_{circ} is also known, the phase difference between triggering and stimulated field equals [14].

$$\theta = \pi - \arctan\sqrt{\varphi_{gen}/\varphi_{RT}} - \arctan\sqrt{\varphi_{RT}/\varphi_{gen}} = \pi/2. \tag{10.5}$$

In resonance, stimulated emission occurs with a 90° phase difference between driving and generated field, its direct consequence being the phase shift $\Delta\phi_{em}$ of Eq. (10.4) between driving and transmitted field. For this derivation we have only assumed the validity of Maxwell's equations and the law of energy conservation.

10.4 Lorentz Oscillator Model

The Lorentz oscillator model describes the motion of electrons with electric charge e and mass m_e, bound as a cloud with electron density N_e within an atom, as a damped harmonic oscillation with an angular resonance frequency ω_0 and gain/damping rate constant γ_e (positive for stimulated emission, negative for absorption) displaced by a distance x from its rest position by an external driving electric field E_{ext} oscillating with angular frequency ω_{ext}. The magnetic force is neglected. Its mathematical treatment is equivalent to that of a mechanical spring oscillator. The linear second-order ordinary differential equation of motion is solved, yielding the atomic polarization P_e and phase difference θ between the driving electric field and the polarization:

$$\begin{aligned} &m_e\ddot{x}(t) + 2\gamma_e m_e \dot{x}(t) + \omega_0^2 m_e x(t) = -eE_{ext}\exp(-i\omega_{ext}t) \\ &P_e = -N_e e x(t) = \frac{N_e e^2/m_e}{\omega_0^2-\omega_{ext}^2-i2\gamma_e\omega_{ext}} E_{ext}\exp(-i\omega_{ext}t+\theta) \\ &\tan(\theta) = \frac{2\gamma_e\omega_{ext}}{\omega_0^2-\omega_{ext}^2}. \end{aligned} \tag{10.6}$$

The same phase difference θ as from the Lorentz oscillator model in Eq. (10.6) obtains from the Kramers-Kronig relations [15, 16] between the real part (susceptibility) χ_e' and the imaginary part (gain or absorption) χ_e'' of the complex susceptibility χ_e (Fig. 10.4):

$$\begin{aligned} P_e &= \varepsilon_0\chi_e E_{ext}\exp(-i\omega_{ext}t+\theta) \\ \chi_e &= \chi_0\frac{\omega_0^2}{\omega_0^2-\omega_{ext}^2-i2\gamma_e\omega_{ext}}, \quad \chi_0 = \frac{N_e e^2}{\varepsilon_0 m_e\omega_0^2} \\ \chi_e' &= \chi_0\frac{-(\omega_0^2-\omega_{ext}^2)\omega_0^2}{(\omega_0^2-\omega_{ext}^2)^2+(2\gamma_e\omega_{ext})^2} \\ \chi_e'' &= \chi_0\frac{2\gamma_e\omega_{ext}\omega_0^2}{(\omega_0^2-\omega_{ext}^2)^2+(2\gamma_e\omega_{ext})^2} \\ \tan(\theta) &= \frac{\chi_e''}{\chi_e'} = \frac{2\gamma_e\omega_{ext}}{\omega_0^2-\omega_{ext}^2}. \end{aligned} \tag{10.7}$$

As is well known from mechanical oscillators, when the driving frequency ω_{ext} is significantly lower (higher) than the resonance frequency ω_0, the oscillation is in (out of) phase with the driving field. In resonance, the phase difference θ crosses the value of $\pi/2$ (Fig. 10.4). The emitted electric field is generated in phase with the dipole oscillation, and stimulated emission is 90° in lead of the triggering field. Likewise, in resonant absorption the phase difference between the atomic oscillation and the transmitted field is $\theta = -\pi/2$, i.e., the atomic oscillation lags 90° behind. This simple derivation confirms that in stimulated emission the emissive part of the generated dipole field is in quadrature with the driving electromagnetic field [5–8].

Consequently, in a resonant stimulated-emission process the interference term in Eq. (10.1) vanishes, the two individual intensities add up, and the energy is conserved. For exactly this reason, Einstein was allowed to neglect interference in his semi-classical rate-equation derivation [1] of Planck's law [2].

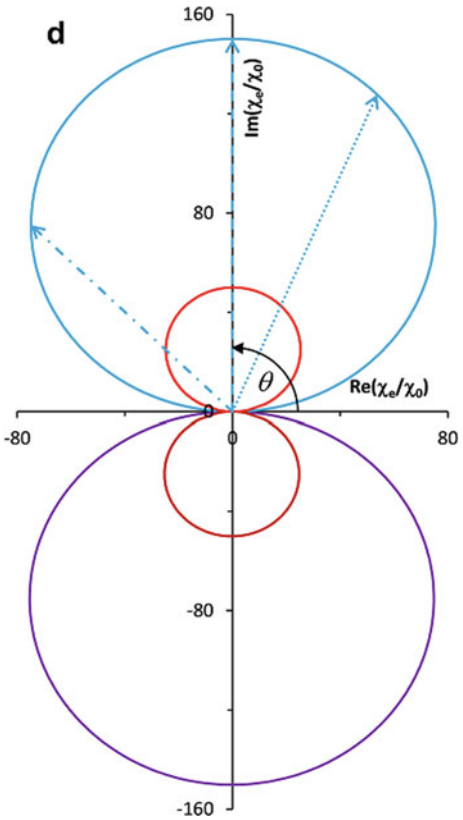

Fig. 10.4 Complex susceptibility χ_e, calibrated to χ_0, for $\gamma_e = \pm 0.00333\ \omega_0$ (blue curves) and $\gamma_e = \pm 0.01\ \omega_0$ (red curves) in stimulated emission (upper part) and absorption (lower part). For the examples of $\gamma_e = \pm 0.00333\ \omega_0$, the arrows indicate the situations of $(\omega_{ext} - \omega_0)/\omega_0 = -1.38 \times 10^{-3}$, 0 (resonance), and 3.34×10^{-3}, resulting in $\theta = 3/8\pi$ (dotted arrow), $\pi/2$ (resonance, dashed arrow), and $3/4\pi$ (dashed-dotted arrow), respectively. The phase difference in resonance of $\theta = \pi/2$ is indicated by the black curved arrow, which points in the direction of increasing ω_{ext}. (Figure taken from Ref. [14])

10.5 Quantized Electric Fields

Assuming an incident electromagnetic field containing the energy of $\varphi_{ext} = 1$ photon, the build-up of a larger electromagnetic field by consecutive stimulated emission of electromagnetic fields, each containing the energy of $\varphi_{gen} = 1$ photon, is displayed in Fig. 10.5b. The total phase shift accumulated by the consecutive stimulated emission of $n - 1$ photons by one initial photon with an arbitrary phase, resulting in an electromagnetic wave containing n photons, amounts to

$$\Delta\phi_n = \sum_{i=1}^{n-1} \Delta\phi_{em,i} = \sum_{i=1}^{n-1} \arctan\left(1/\sqrt{i}\right) \quad \text{for} \quad n \geq 1, \tag{10.8}$$

The total phase shift of Eq. (10.8) establishes a relation among all these states.

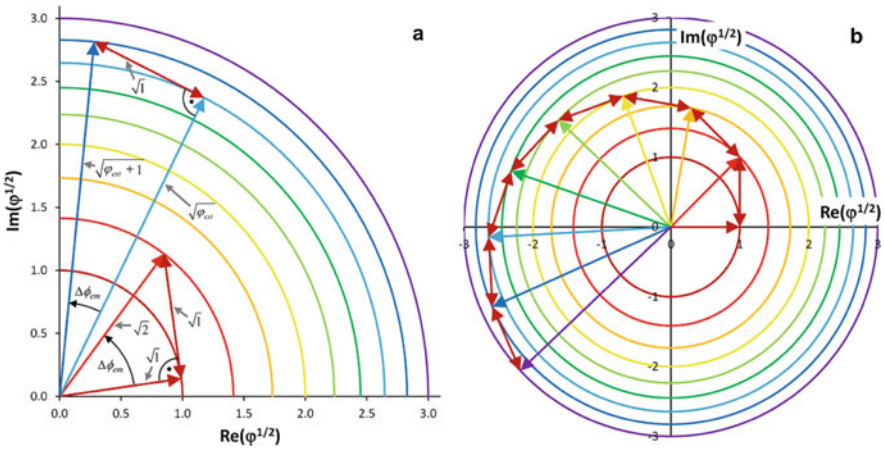

Fig. 10.5 (**a**) Quadrant of the amplitude-phase diagram illustrating the process of stimulated emission (with the dark-red arrows of the emitted field pointing towards the upper left): a field of φ_{ext} photons triggers an atom in its excited state to emit $\varphi_{em} = 1$ photon, in the two situations of (i) $\varphi_{ext} = 1$ and (ii) $\varphi_{ext} = 7$. In both situations, the indicated right angle is $90° = 180° - \theta$, hence $\theta = 90°$. The color code denotes the amplitude in units of $\varphi^{1/2}$, from $\varphi = 1$ photon (dark red) to $\varphi = 9$ photons (violet). The same diagram holds true for absorption (with the dark-red arrows of the absorbed field pointing toward the lower right). (**b**) Build-up of a light beam by the consecutive addition of single photons in the amplitude-phase diagram. (Figure taken from Ref. [14])

Simultaneous independent stimulated emission of several photons, $\varphi_{gen} > 1$, induces a phase shift $\Delta\phi_{em}$ in Eq. (10.4) that is smaller than the phase shift $\Delta\phi_n$ of Eq. (10.8) accumulated by consecutive stimulated emission of single photons:

$$\Delta\phi_{em}\,(\varphi_{em} > 1) < \Delta\phi_n\,(n = \varphi_{em} > 1)\,, \tag{10.9}$$

For investigating the Fabry-Pérot resonator above, we assumed a simultaneous independent stimulated emission of several photons into the same mode. It is an interesting question whether this assumption is physically justified. If true, the total phase shift induced when building up a light beam depends on the way the photons are generated, consecutively or simultaneously. If not true, i.e., the simultaneous emission of several photons within the same mode is correlated, such that these photons must obey the law of energy conservation also with respect to each other, then the total phase shift of Eq. (10.8) establishes a unique relation between all photon numbers φ.

When an electromagnetic field that was generated by individual atomic emission processes triggers stimulated emission of another electromagnetic field by an atom, it requires only two ingredients for a correct quantization, namely, (i) each individual amplitude must be proportional to the square root $\sqrt{\varphi}$ of an integer photon number φ, and (ii) the phase difference must be $\theta = 90°$, the automatic consequence being the phase shift $\Delta\phi_{em}$ of Eq. (10.4) between driving and transmitted field.

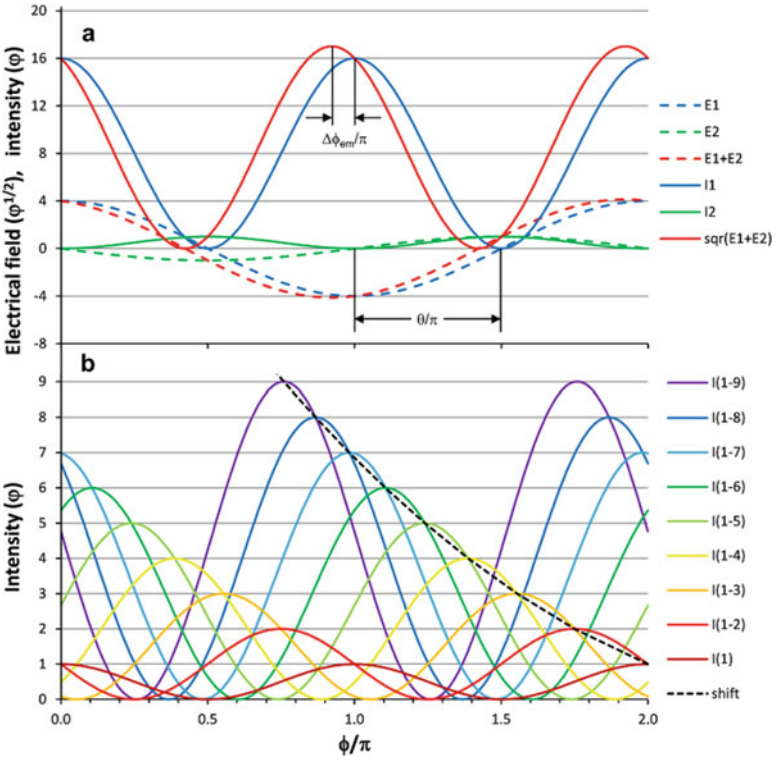

Fig. 10.6 (**a**) Example of the summation according to Eq. (10.1) of two electric fields of amplitudes equivalent to $\varphi^{1/2} = 4$ and 1, with a phase difference of $\theta = \pi/2$. The phase shift $\Delta\phi_{em} = 0.1476\ \pi$ is equal to Eq. (10.8), and the energy is conserved, as $16 + 1 = 17$ photons emerge. (**b**) Consecutive addition of single photons to an existing electromagnetic field. Intensity of the light beam in units of φ. The black dashed line calculated from Eq. (10.9) indicates the phase shift $\Delta\phi_n = \Sigma\ (\Delta\phi_{em})$ accumulated with increasing number φ of photons. (Figure taken from Ref. [14])

An example of $\varphi_{ext} = 16$ photons triggering the emission of $\varphi_{gen} = 1$ photon is illustrated in Fig. 10.6a, its result being quantitatively equivalent to the same process when displayed in the amplitude-phase diagram, as shown for other photon numbers Fig. 10.5a. The build-up of an electromagnetic field containing φ photons by consecutive stimulated emission of electromagnetic fields containing the energy of single photons is displayed in Fig. 10.6b, its result being quantitatively equivalent to Fig. 10.5b.

10.6 Summary

Whatever aspect we have discussed semi-classically, (i) Maxwell's equations and the resulting interference term in the superposition of electromagnetic waves, (ii) energy conservation in a Fabry-Pérot resonator, (iii) the Lorentz oscillator model, (iv) the Kramers-Kronig relations applied to the complex susceptibility, (v) the amplitude-phase diagram, or (vi) simply adding up sine waves in a quantized electric-wave picture, we have arrived at the conclusion that stimulated and spontaneous emission both occur under a 90° phase difference with the incident field.

Acknowledgments The author acknowledges financial support by the ERC Advanced Grant "Optical Ultra-Sensor" No. 341206 from the European Research Council.

References

1. Einstein A (1917) Phys Z 18:121
2. Planck M (1901) Ann Phys 309:553
3. Lorentz HA (1880) Ann Phys 245:641
4. Sargent M III, Scully MO, Lamb WE Jr (1993) Laser physics, 6th edn. Westview Press, Boulder, Oxford, pp 34–42
5. Milonni PW (1976) Phys Rep 25:1
6. Cray M, Shih ML, Milonni PW (1982) Am J Phys 50:1016
7. Milonni PW, Eberly JH (1988) Lasers. Wiley, New York, pp 27–33
8. Glauber RJ (1963) Phys Rev 131:2766
9. Lax M (1967) Phys Rev 160:290
10. Haken H (1970) "Laser Theory," Vol. XXV/2c of Encyclopedia of Physics. Springer, Berlin, Heidelberg
11. Henry CH (1982) IEEE J Quantum Electron 18:259
12. Schawlow AL, Townes CH (1958) Phys Rev 112:1940
13. Hempstead RD, Lax M (1967) Phys Rev 161:350
14. Pollnau M (2018) Optica 5:465
15. Kronig R d L (1926) J Opt Soc Am 12:547
16. Kramers HA (1927) "La diffusion de la lumière par les atoms," in Atti del Congresso Internazionale del Fisica, Transactions of Volta Centenary Congress. Como 2:545–557
17. Siegman AE (1986) Lasers. University Science Books, Mill Valley, pp 510–524
18. Pollnau M (2019) Appl Phys B Lasers Opt 125:25
19. Ismail N, Kores CC, Geskus D, Pollnau M (2016) Opt Express 24:16366

Chapter 11
Nd^{3+} Ion as a Structural Probe in Studies of Selected Oxide Host Lattices: Coupling the Low-Temperature High-Resolution Spectroscopic Techniques with Microscopy

M. Guzik, G. Boulon, Y. Guyot, E. Tomaszewicz, M. Bieza, J. Legendziewicz, J. Pejchal, A. Yoshikawa, P. Sobota, and M. Sobota

Abstract In this paper we present the relationships between structural and spectroscopic investigations of neodymium ion dopant (Nd^{3+}) in selected oxide host lattices with particular highlighting its role as a structural probe. The main goal is to get precious information about the symmetry and activator's environment in the following different oxide host lattices like cubic Lu_2O_3 sesquioxide and molybdate compounds of tetragonal scheelite-type $CdMoO_4$, monoclinic/cubic $La_2Mo_2O_9$ (LAMOX) as well as cubic Y_6MoO_{12}, we met during research of new transparent ceramics. This choice gives us the opportunity to point out the usefulness of two techniques: the low-temperature high-resolution techniques applied to the $^4I_{9/2} \rightarrow {}^2P_{1/2}$ (around 432 nm) and $^4I_{9/2} \rightarrow {}^4F_{3/2}$ (around 875 nm) absorption transitions at 4.2 K and site-selective tuneable laser spectroscopy with OPO and Ti:Sapphire laser sources, applied to the $^4F_{3/2} \rightarrow {}^4I_{9/2}$ (around 900 nm) and $^4F_{3/2} \rightarrow {}^4I_{11/2}$ (around 1064 nm) emission transitions at 77 K. We hope that the results presented at the School will help the students to know how important is the role played by Nd^{3+} dopant not only as laser ion in near the infrared spectral region but also as structural probe for host lattices.

M. Guzik (✉) · M. Bieza · J. Legendziewicz · P. Sobota · M. Sobota
Faculty of Chemistry, University of Wrocław, Wrocław, Poland

G. Boulon · Y. Guyot
Institut Lumière Matière (ILM), UMR5306 CNRS- Université Claude Bernard Lyon1, Université de Lyon, Villeurbanne, France

E. Tomaszewicz
Department of Inorganic and Analytical Chemistry, West Pomeranian University of Technology, Szczecin, Poland

J. Pejchal · A. Yoshikawa
Institute for Materials Research (IMR), Tohoku University, Sendai, Japan

M. Cesaria et al. (eds.), *Light-Matter Interactions Towards the Nanoscale*,
NATO Science for Peace and Security Series B: Physics and Biophysics,
https://doi.org/10.1007/978-94-024-2138-5_11

Keywords Nd^{3+} ion · Oxide host lattices · Transparent ceramics · Structural probe · Optical materials

11.1 Introduction

Rare earth (RE)-doped oxide materials have been the subject of interest for many years as they found many applications in the optical field as laser materials, phosphors or scintillators. The search for new solid-state lasers is still very current since over half of the last century and even 50 years after the discovery of the first ruby laser, solid-state lasers mainly based on metal transition ions (3d configuration) and rare earth ions (4f configuration) used as oscillators or amplifiers are continuing to be a very prosperous field. Nd^{3+} ion has been extensively used in the laser crystals since it has abundant pumping levels, a 4-level scheme and both relatively high absorption and emission cross-sections. In addition, the absorption peak at around 805 nm matches well with the wavelength of the laser diode pump source.

Among a lot of laser crystals, two hosts emerged for various industrial, medical and scientific applications: rare earth (Nd, Yb, Er)-doped yttrium aluminum garnet $Y_3Al_5O_{12}$ so-called YAG, and tunable Ti-doped Al_2O_3, so-called Ti–sapphire, emitting laser output in near IR and visible/UV after second or third harmonic generation. The main reason of the large development of these crystals was due to high thermal conductivity, chemical stability, ease of machining, and excellence in laser energy-conversion efficiency. However, limitations exist with single crystals which are grown from the melt, suffering from drawbacks such as optical inhomogeneity caused by stress and faceting during crystal growth, segregation of the dopant from the host depending on the crystal growth speed increasing from Liquid Phase Epitaxy, Czochralski, Kyropoulos and Micro-Pulling-Down techniques used [1]. Finally, crystal growths are expensive and are characterized by low productivity due to high temperature processing.

An important breakthrough happened in 1995 when Ikesue has shown equivalent results on the laser output of Nd^{3+}:YAG crystal and Nd^{3+}:YAG transparent ceramics [2]. Requirements for laser ceramics are very restrictive and rely on lack of optical scattering and perfect homogeneity, so that before 1995, everyone considered that ceramic material cannot be used for laser, because the optical quality of conventional ceramics is quite low. Nowadays, Nd:YAG transparent ceramic has been demonstrated more than 100 kW of output power at 1064.2 nm [3]. Consequently, rare earth-doped polycrystalline transparent ceramic lasers appear as a new generation of solid-state laser materials, especially for high-power laser systems for which large-scale laser materials are needed. The extended capabilities of the ceramic laser materials compared with the single crystals (easier fabrication, larger size), increase compositional versatility, higher doping concentrations with controlled profile, higher mechanical strength, overall production cost and higher productivity) have offered potential for extension of the performances of solid-state lasers [4, 5].

The development of these ceramic materials for applications in laser sources, phosphors under blue LED pumping and scintillators are the ultimate aim of material technology widely used in industrial, medical, military and scientific applications [6, 7], so that it is a huge challenge of optical material scientists to develop new transparent polycrystalline ceramics used with a performance equal or even better than that of conventional single crystals [8]. As to prepare polycrystalline transparent ceramics two conditions should be fulfilled: the compounds have to crystallize in the cubic system (or if not the grain size must be in the order of tens of nanometers to avoid the birefringence effect) and nearly no residual porosity or second phase should remain, therefore the choice of a host is a very important aspect for developing new optical materials.

Nonetheless, until now, only a few types of transparent optical ceramics doped with rare earth (RE) ions are known. The most well-known are garnets (Nd^{3+} and Yb^{3+}-doped $Y_3Al_5O_{12}$ for laser sources [9–11], Ce^{3+} – doped $Y_3Al_5O_{12}$ [12] and $Lu_3Al_5O_{12}$ [13, 14] for scintillators), sesquioxides (Nd^{3+} and Yb^{3+}-doped Y_2O_3, Sc_2O_3, Nd^{3+} and Yb^{3+}-doped Lu_2O_3 for laser sources [5, 15–22] and fluorides (Yb^{3+}-doped CaF_2 also for laser sources) [23, 24] and Nd^{3+}, Yb^{3+}-co-doped SrF_2 laser ceramics) [25].

Most of the above-mentioned compositions were already well-known optical materials in the form of RE-doped single crystals or polycrystalline powders. Moreover, the object of several experiments is $MgAl_2O_4$ spinel, which in an un-doped transparent ceramic form are finding applications in civil and military engineering [26]. However, as one can see from the literature, introducing Ln^{3+} ions into $MgAl_2O_4$ host lattice and obtaining a homogenous phase-pure transparent ceramic is a very difficult task [27, 28]. Other transparent optical ceramics with cubic structures are also known in laser applications such as Cr^{2+} or Fe^{2+}-doped (ZnSe) selenides [29] and Nd^{3+} or Pr^{3+}-doped perovskite-type BMT ($Ba(MgZrTa)O_3$ [30–32].

For many years Nd^{3+}-doped YAG single crystals have been extensively studied and widely used for high-power lasers. However, compared with Nd^{3+}:YAG, Nd^{3+}-doped tungstate crystals have many outstanding properties such as relatively weak concentration quenching. Especially, $KGd(WO_4)_2$ (KGW) and $KY(WO_4)_2$ (KYW) tungstates doped with Nd^{3+}, Er^{3+} and Yb^{3+} rare-earth ions show high potential for light generation or amplification. Tungstates and molybdates doped with rare earth (RE) ions have attracted considerable attention due to their excellent luminescent properties [33–35].

Also Yb^{3+}:KGW and Yb^{3+}:KYW crystals are used as lasing materials to generate ultra-short high power pulses and can be used as ultra-short pulse amplifiers. These crystals are one of the best materials for high-power thin disk lasers. Laser action has also been demonstrated in thulium and holmium-doped $KGd(WO_4)_2$ and thulium-doped $KYb(WO_4)_2$ crystals [36, 37]. Also, we should not forget that the first continuously operating crystal laser doped with Nd^{3+} ions, reported in 1961, based on calcium tungstate ($CaWO_4$). In turn, simply molybdates and tungstates belong to important families of inorganic materials used in the optical field due to their potential applications. The most investigated groups are $CaWO_4$ and $MgWO_4$

(as phosphors), as well as $ZnWO_4$, $CdWO_4$ and $PbWO_4$ (as scintillators). Great interest of tungstates and molybdates is a result of their special properties such as high chemical stability, good mechanical strength and thermal properties. This is why for many years we are very involved in studies of new compositions from this family to find efficient optical materials and especially new transparent ceramics of rare earth-doped tungstates and molybdates of cubic structure. For these families, we are interested in the most known Nd^{3+} laser dopant.

In this article, we present to NATO School participants, some relationships between structural and spectroscopic results selected among rare earth ions, not with the usual Eu^{3+} or Yb^{3+} probe ions but with Nd^{3+} ions embedded in various oxide crystal lattices used in our research to find new transparent ceramics. The oxide hosts are characterized by the following structures: cubic Lu_2O_3, tetragonal scheelite-type $CdMoO_4$, monoclinic/cubic $La_2Mo_2O_9$ (LAMOX) as well as cubic Y_6MoO_{12}. This choice gives us the opportunity to point out the usefulness of, both, low-temperature high-resolution techniques like absorption spectroscopy at 4.2 K and site-selective tuneable laser spectroscopy at 77 K and, in addition for some of them, the coupling with microscopy techniques.

11.2 Experimental Section

11.2.1 Sample Preparation

Growth of Cubic Nd^{3+}-Doped Lu_2O_3 Single Crystal by Micro-pulling-down Technique (μ-PD) Nd^{3+}-doped Lu_2O_3 single crystals have been grown by the μ-PD method [19, 38, 43, 44]. As starting materials was Lu_2O_3 and Nd_2O_3 powders with 99.99% purity were used. The growth was performed in the micro-pulling-down apparatus with radio frequency inductive heating in rhenium crucible with circular die of 5 mm in diameter and five capillary nozzles, which was placed on rhenium after heater and zirconia pedestal. The double-layer zirconia shielding was used for thermal insulation. A mixture of Ar and H_2 gases was used as growth atmosphere. The H_2 concentration was 3%, which is sufficient to prevent rhenium from being oxidized at high temperatures. The gas flow was kept at 1 l/min. The crucible with the starting material was heated up to the Lu_2O_3 melting temperature, which is around 2400 °C. Then, the Lu_2O_3 single crystal seed was brought into contact with the melt coming through the nozzles due to capillary action. The crystal was pulled at a pulling rate of 0.09 mm/min.

Preparation Micro-powdered Samples of Three Types of Nd^{3+}-Doped Molybdates by Solid-State Reaction

Tetragonal $Cd_{1-3x}Nd_{2x}\square_xMoO_4$. The micro-crystalline $Cd_{1-3x}Nd_{2x}\square_xMoO_4$ solid solutions containing different concentrations of Nd^{3+} ions up to $x = 0.25$ crystallizing in the tetragonal structure were prepared from $CdMoO_4$ and $Nd_2(MoO_4)_3$ according the procedure described previously [39]. The preparation

of $Cd_{1-3x}Nd_{2x}\square_xMoO_4$ (later labeled as Nd^{3+}-doped $CdMoO_4$) can be briefly described by the following equation:

$$(1–3x)\,CdMoO_4(s)_{(s)} + xNd_2(MoO_4)_{3(s)} = Cd_{1-3x}Nd_{2x}\square_xMoO_{4(s)} \qquad (11.1)$$

where the symbol □ denotes cationic vacancies.

The $CdMoO_4$ and $Nd_2(MoO_4)_3$ mixed in appropriate ratios were sintered in static air, in corundum crucible with following heating sequence: 750 °C (12 h), 800 °C (12 h), 850 °C (12 h), 900 °C (12 h), and 950 °C (12 h).

Monoclinic/Cubic $La_{2-x}Nd_xMo_2O_9$ The microcrystalline Nd^{3+}-doped $La_2Mo_2O_9$ molybdates were synthesized from commercial metal oxides of lanthanum oxide, neodymium oxide and molybdenum oxide employing the method described previously [40, 41]. Preparation of the $La_{2-x}Nd_xMo_2O_9$ solid solutions (later labeled as Nd^{3+}-doped $La_2Mo_2O_9$) can be described by the following equation:

$$(1 - x/2)\ La_2O_{3(s)} + x/2\ Nd_2O_{3(s)} + 2\ MoO_{3(s)} = La_{2-x}Nd_xMo_2O_{9(s)} \qquad (11.2)$$

In case of these solid solutions the heat treatment was slightly higher and the obtained mixtures were heated in ceramic crucibles in air in the following cycles: 550 °C (12 h), 600 °C (12 h), 650 °C (12 h), 700 °C (12 h) and 750 °C (12 h), 800 °C (12 h), 900 °C (12 h), and 1000 °C (3×12 h).

Cubic $Y_{6-x}Nd_xMoO_{12}$ To obtain the $Y_{6-x}Nd_xMoO_{12(s)}$ (later labeled as Nd^{3+}-doped Y_6MoO_{12}) crystallizing in the cubic structure much higher temperature of annealing was applied. As shown our previous studies to obtain pure phase solid solutions we have to go up to 1550 °C. The details of the synthesis were reported in [42].

Weighed in appropriate molar ratios (stoichiometric) $Nd_2O_3/Y_2O_3/MoO_3$ mixtures of oxides were heated in corundum crucibles, in air, in the following stages: 550 °C (6 h), 600 °C (6 h), 700 °C (6 h), 800 °C (12 h), 1000 °C (12 h), 1200 °C (12 h), 1400 °C (12 h), 1500 °C (6 h) and 1550 °C (3 × 6 h).

The synthesis can be described by the following equation:

$$(3 - x/2)\ Y_2O_{3(s)}\ + MoO_{3(s)} + x/2\ Nd_2O_{3(s)} = Y_{6-x}Nd_xMoO_{12(s)} \qquad (11.3)$$

11.2.2 Techniques for Analysis

Scanning Electron Microscopy (SEM) Scanning electron microscopy studies were carried out on Hitachi S-3400 N equipped with an energy dispersive X-ray spectroscopy (EDX) EDAX analyzer. The powders were coated with thin gold alloy layer to facilitate conductivity.

Emission Measurements Fluorescence measurements were performed at room temperature and 77 K (in a nitrogen quartz dewar). A tuneable laser (EKSPLA

OPO NT342B, 7 ns, 10 Hz) was used. The fluorescence was collected with an optical fiber and analysed with the help spectrometer equipped with a 1200 l/mm grating blazed at 500 nm, coupled to intensified charge coupled device (ICCD) camera (Shamrock 303 and iStar from Andor Technology). For some emission spectra under site selective excitation the measurements were performed under CW titanium sapphire laser with the help of an ANDOR iDus InGaAs CCD camera following a Shamrock 500i monochromator equipped with a 900 l/mm grating blazed at 1300 nm. For excitation in the CT (Mo^{6+}-O^{2-}) band, laser diode LD (laser power 200 mW) with line of 405 nm was used. Emission spectra were recorded at room and liquid nitrogen temperature (77 K). For comparative measurements of the integral intensity, a LED source at 590 nm was used.

Luminescence Decay Measurements The luminescence decay curves were recorded under pulsed laser excitation (OPO laser, EKSPLA NT342, 10 Hz, 7 ns), the fluorescence intensity around 1.06 μm being detected with a R1767 Hamamatsu photomultiplier through a HRS1 Jobin-Yvon monochromator equipped with a 1 μm blazed grating and coupled to a LECROY LT 342 digital oscilloscope. The luminescence decay curves were recorded at RT and 77 K.

11.3 Energy Level Diagram of Nd^{3+} Ion in Solids

The Nd^{3+}-doped YAG is by far the most commonly used type of commercial solid state laser. It possesses a combination of properties uniquely favorable for laser operation: very hard, high transparency, high thermal conductivity (un-doped crystal: 13 W m^{-1} K^{-1} and 11 W m^{-1} K^{-1} with 1%Nd^{3+} ion) and isotropic optical properties. The highest quality of crystals are grown by Czochralski (CZ) technique.

The optical properties of Nd^{3+} ion are determined by the transitions inside the $4f^3$ shell. The structure of the energy-level-free Nd^{3+} ion is determined by the electrons' Coulomb interactions with the nucleus and with each other, and also with the spin and orbitals moments of the electrons. The lowest Nd^{3+} ion energy level belongs to a ^4I_J atomic state. This means that 3 electrons of the Nd^{3+} ion being on the 4f shell, have a total spin moment S of 3/2 ($2S + 1 = 4$) and orbital moment of $L = 6$.

As a result of the spin-orbital interaction, the 4f multiplet is split into 4 levels with total moment J from L-S = 6–3/2 = 9/2 up to L + S = 6 + 3/2 = 15/2.

All levels of the free ion in crystals split as a consequence of the Stark effect arising from the crystal field. Each term is split into J + 1/2 components, in particular $^4I_{9/2}$ into 5, $^4I_{11/2}$ into 6, $^4I_{13/2}$ into 7, $^4I_{15/2}$ into 8. Energy splitting between components lies in the range of few tens of cm^{-1}. The energy levels of a free Nd^{3+} ion and the splitting of the lowest ^4I_J levels and $^4F_{3/2}$ of the Nd^{3+} ion with various spin-orbits and Stark splitting by the crystal field in a YAG crystal are shown in Fig. 11.1. The Stark splitting is only shown for levels which participate to laser generation.

The Nd^{3+} four-level scheme for laser generation for Nd^{3+}-doped YAG is presented in Fig. 11.2.

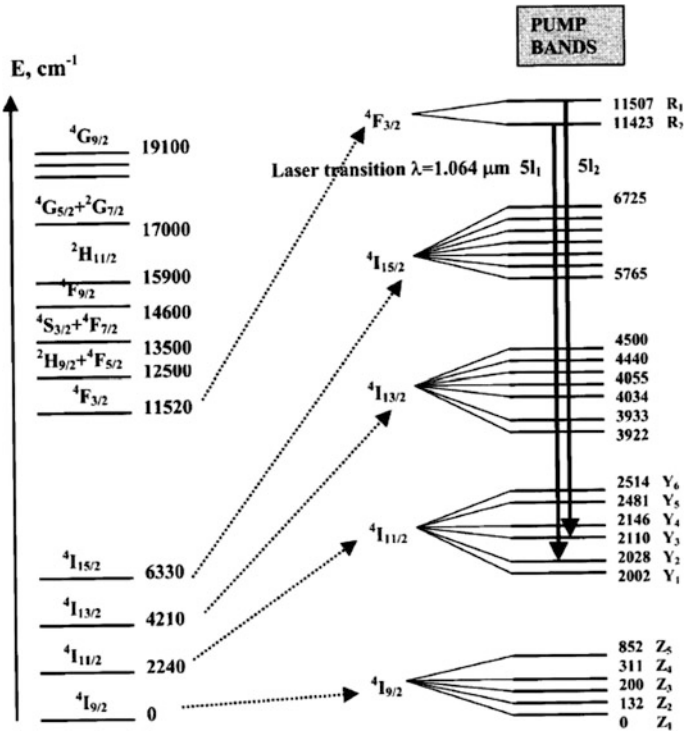

Fig. 11.1 Energy level diagram of the free ion and the splitting of the Nd^{3+} ion inside the crystal field of YAG [45]

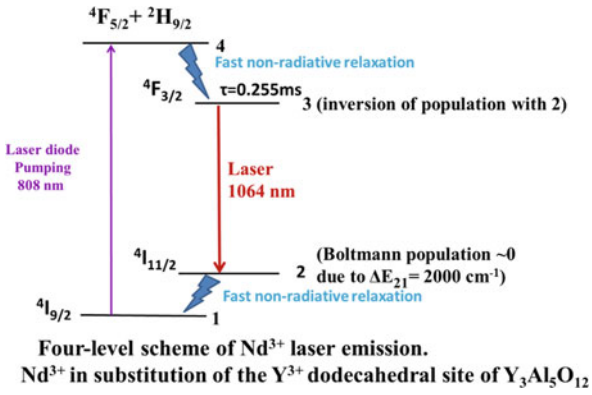

Fig. 11.2 An ideal four-level scheme for Nd^{3+} ion

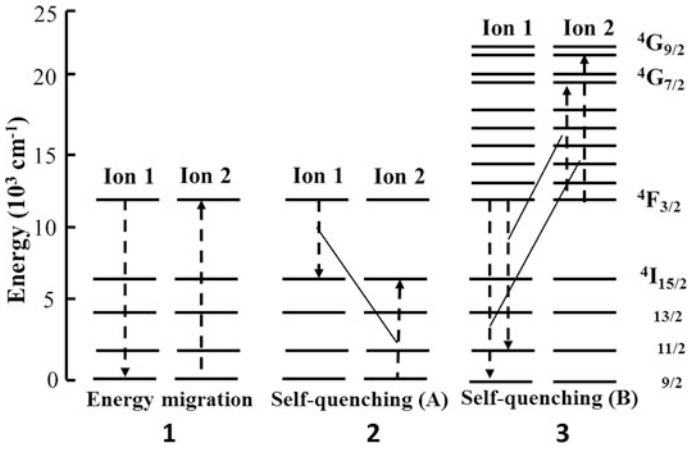

Fig. 11.3 Several resonant energy transfer processes between energy levels of Nd^{3+} ions: (1) Diffusion by resonant energy transfer, (2) self-quenching by cross relaxation, (3) self-quenching by up-conversion cross relaxation

11.4 Various Energy-Transfer Processes with Nd^{3+} Ions

When the concentration increases, indeed several processes are in competition, a photon trapping leading to an increase of the lifetime value (self-trapping according to the process 1 in Fig. 11.3) and Nd^{3+}- Nd^{3+} interactions which can reduce the decay times (self-quenching in according to processes 2 and 3 in Fig. 11.3). As an example, in Nd^{3+}-doped YPO_4, YVO_4 and $YAsO_4$, the main process described in the literature is the cross-relaxation mechanism according to two possible de-excitation schemes: $[^4F_{3/2},^4I_{9/2}] \rightarrow [^4I_{15/2},^4I_{15/2}]$, corresponding to an interaction between one Nd^{3+} ion in the $^4F_{3/2}$ state and another Nd^{3+} ion in the $^4I_{9/2}$ state. When the interactions occur, as there is a relatively good resonance between the energy levels, the final states for the two ions are $^4I_{15/2}$ and both ions reach the fundamental state by non-radiative de-excitation. Sometimes the same process occurs with the assistance of the lattice phonons when the transitions are not in good resonances [46].

11.5 Nd^{3+} Ion in the Host as a Structural Probe

As it was mentioned above the Nd^{3+} ion is one of the most efficient for solid-state lasers in crystals and glasses due to the intense $^4F_{3/2} \rightarrow {}^4I_{11/2}$ emission at around 1.06 μm but can also be used as a probe for local ordering due to the close relation between its spectroscopic properties and the local structure at the ion site. The absorption spectra of Nd^{3+} ion in the visible and IR regions involves parity

forbidden f–f transitions from the $^4I_{9/2}$ ground state to the various excited states. According to the Judd–Jorgensen statement, the f–f transitions which obey $\Delta J = 2$, $\Delta L = 2$ selection rules are the most sensitive to the lanthanide ion environment, and are commonly referred to as hypersensitive ones. The Nd^{3+} $^4I_{9/2} \rightarrow {}^4G_{5/2}$ absorption transition satisfies the above criteria, and therefore its intensity is often used as a probe of structural changes, similar to the $^4I_{9/2} \rightarrow {}^4F_{5/2}$ transition in the IR region, which also partially satisfies the selection rule for "hypersensitive transition".

In practice the energy of the $^2G_{7/2}$ term is very close to that of the $^4G_{5/2}$ one, thus at room temperature the $^4I_{9/2} \rightarrow {}^4G_{5/2}$, $^2G_{7/2}$ transitions must be analyzed together. Based on the intensity ratio of the $^4I_{9/2} \rightarrow {}^4G_{5/2}$, $^2G_{7/2}$ and $^4I_{9/2} \rightarrow {}^4F_{7/2}$, $^4S_{3/2}$, $^4I_{9/2} \rightarrow {}^4F_{5/2}$, $^2H_{9/2}$ transitions in the IR region one can conclude about the symmetry of compounds. For the high symmetry systems, such as O_h and D_{4h}, the intensities of these two transitions in the IR region are about half of those of the $^4I_{9/2} \rightarrow {}^4G_{5/2}$, $^2G_{9/2}$ transitions, while in low symmetry environments the ratio is significantly higher. Since at 4.2 K (liquid helium temperature) only the lowest Stark component of this multiplet is populated, the number of components of the Kramer's doublet $^4I_{9/2} \rightarrow {}^2P_{1/2}$ transition is consisted with the number of metal sites in the crystal structure.

It is well known from the group theory consideration that the $^4F_{3/2}$ multiplet is split into two Kramer's doublets since the number of components correlates with J + 1/2 levels for one site. Thus, at low temperature, 5 emission lines for the $^4F_{3/2} \rightarrow {}^4I_{9/2}$ transition, 6 for $^4F_{3/2} \rightarrow {}^4I_{11/2}$ and 7 for $^4F_{3/2} \rightarrow {}^4I_{13/2}$ one should be observed, respectively [39].

11.6 Examples of Nd^{3+} Ions in Different Host Lattices

11.6.1 Cubic Nd^{3+}-Doped Lu_2O_3 and Its Two C_{3i} and C_2 Symmetry Sites

Actually, one of our research program is dealing with the Lu_2O_3 refractory sesquioxide, which has been suggested to be a potential laser host when doped by Nd^{3+} rare earth ions since a long time, possessing the highest thermal conductivity (12.5 W/m/K) and the lowest phonon energy (391 cm^{-1}) in comparison with YAG (10.8 W/m/K and 700 cm^{-1}, respectively). However, it is extremely difficult to grow Lu_2O_3 single crystal using conventional crystal growth methods because of its high melting point (2490 °C) [47]. It is much easier to fabricate Lu_2O_3 into a ceramic structure since the sintering temperature is about 700 °C lower than its melting point, and no expensive crucible is required [19, 22, 48, 49]. As a result, spectroscopic data of Nd^{3+} laser ions are needed in Lu_2O_3 host, either as single crystal or as ceramics. Materials we have analyzed and compared are either Nd^{3+}-doped Lu_2O_3 single crystals grown by the μ-Pulling Down method [47] or Nd^{3+}-doped Lu_2O_3

ceramics fabricated by the non-conventional method Spark Plasma Sintering (SPS) [19, 20] for which we have also shown laser outputs. The main goal of this article is to compare the spectroscopic data of Nd^{3+} ions occupying C_{3i} and C_2 sites of the sesquioxide structure not only in Nd^{3+}-doped Lu_2O_3 ceramics as recently reported [19] but also in Nd^{3+}-doped Lu_2O_3 single crystals.

Structure of Sesquioxides and Effect of Nd^{3+} Dopant The well-known structure Ln_2O_3 (Ln = Y, Lu, Sc) sesquioxides belongs to the bixbyite type $[^{VI}A_2]$ $[^{IV}O_3]$, which is body-centred cubic, space group $Ia\overline{3}$ with Z = 16. The cubic lattice parameters of 10.391 Å. This type of structure offers two available independent cations sites for the Lu^{3+} atoms with local symmetries C_2 (non-centrosymmetric) and C_{3i} or S_6 (centrosymmetric), each of them with six-fold coordination [47]. The ratio of C_2 to C_{3i} is 3:1, that is, 32 cations in a unit cell in which 24 occupy C_2 sites and 8 occupy C_{3i} sites. The O^{2-} anions occupy the 48 general positions. The X-ray single crystal structure determination of Lu_2O_3 sesquioxide and of polycrystalline transparent ceramic fabricated by the unconventional spark plasma sintering (SPS) method was reported in [47]. Due to the small difference of ionic radii, trivalent Nd^{3+} (0.983 Å) dopant ions can substitute Lu^{3+} (0.861 Å) ions of the same valence, with a slight distortions in the crystal field. The distribution of the nearest neighbor cations around each C_2 and C_{3i} sites create several possibilities of Nd^{3+} pairs.

Table 11.1 shows the smallest distances between both the C_2 nearest neighbors and the C_{3i} nearest neighbors for Y_2O_3 [50]. Clearly, we assume comparable values for Lu_2O_3. Direct spectra of pairs are experimentally observed only by doping with Yb^{3+} ions characterized by the simplest energy level diagram but not with Nd^{3+} ones having too many energy levels in the UV and visible ranges avoiding any evidence of cooperative luminescence. At around 500 nm we have observed the cooperative luminescence spectra of Yb^{3+} ions in crystals mentioned [38], when the shortest distances between rare earth cations are less than around 4 Å. The same effect, which should be inferred with Nd^{3+} ions in Lu_2O_3 has been detected by the presence of satellite lines in the foot of the Nd^{3+} 0-phonon absorption lines [50, 51]. Indeed, the creation of Nd^{3+} pairs leads to shifts of absorption lines from isolated Nd^{3+} ions lines mainly due to ionic radii misfit between Nd^{3+} and Lu^{3+} host ions. The Nd^{3+}-doped Lu_2O_3 ceramics and crystals show quite well-resolved spectral

Table 11.1 Distribution of expected Nd^{3+} (or Yb^{3+}) nearest neighbors of C_2 (3/4) and C_{3i} (1/4) site symmetries in Y_2O_3 [50]

	Numbers of sites	Distances (Å)
C_2-C_2	4	3.54
	4	4.01
	2	5.30
	4	5.34
C_2-C_{3i}	2	3.52
	2	3.99
C_{3i}-C_2	6	3.52
	6	3.99
C_{3i}-C_{3i}	6	5.30

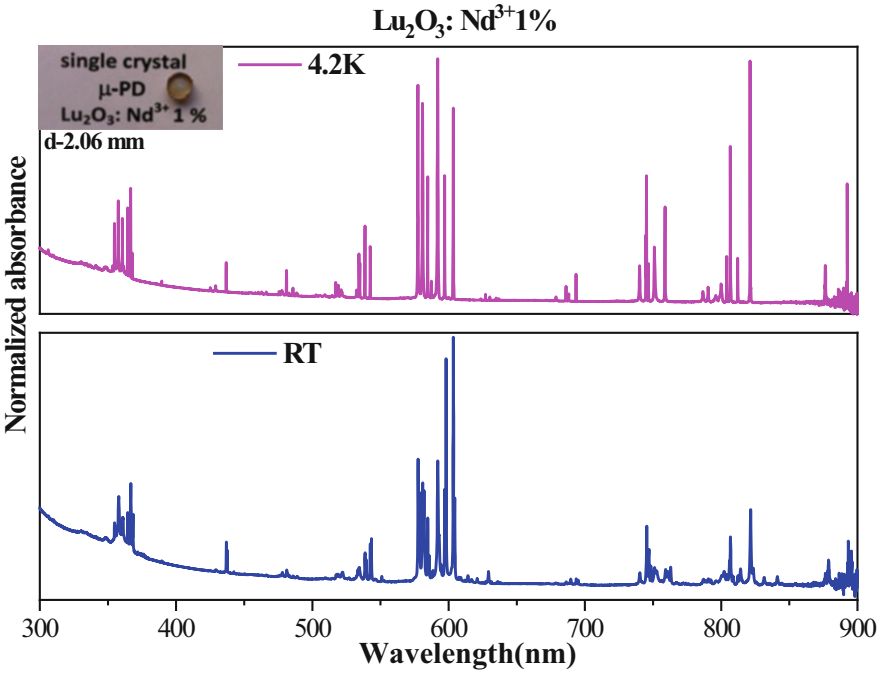

Fig. 11.4 Absorption spectra of 1% Nd^{3+}-doped Lu_2O_3 crystal recorded at 4.2 K (upper panel) and room temperature (bottom panel)

satellites for all the main Nd^{3+} 0-phonon absorption lines with energy shift from the isolated ion lines up to10 cm^{-1} [19].

Absorption Spectra

Figure 11.4 presents all absorption transitions from the ground $^4I_{9/2}$ state to the excited states observed for 1% Nd^{3+}-doped Lu_2O_3 crystal in the spectra recorded at room temperature and 4.2 K. On spectra recorded at both temperatures very narrow bands with almost linear structure are observed. Clearly Much better splitting can be seen at low temperature. Such narrow lines indicate the very ordered nature of the crystal structure.

The Nd^{3+} absorption spectra of the first $^4I_{9/2} \rightarrow {}^4F_{3/2}$, $^4I_{9/2} \rightarrow {}^4F_{5/2}$, $^2H_{9/2}$ usual transitions in the near infrared at room temperature and 4.2 K for 1% Nd^{3+}-doped Lu_2O_3 ceramic and 1% Nd^{3+}-doped Lu_2O_3 crystal are shown in Fig. 11.5.

Especially at RT, these line positions allow to know the pumping wavelengths of the laser material under laser diodes. In a previous work the laser output of 1% Nd^{3+}-doped Lu_2O_3 ceramic have been successfully obtained under 805–806 nm pumping, it means under excitation of the $^4I_{9/2}$ (Z_1, Z_2) $\rightarrow {}^4F_{5/2}$ transition [20]. The same spectroscopic parameters have been measured for both 1% Nd^{3+}-doped Lu_2O_3 ceramic and 1% Nd^{3+}-doped Lu_2O_3 crystal.

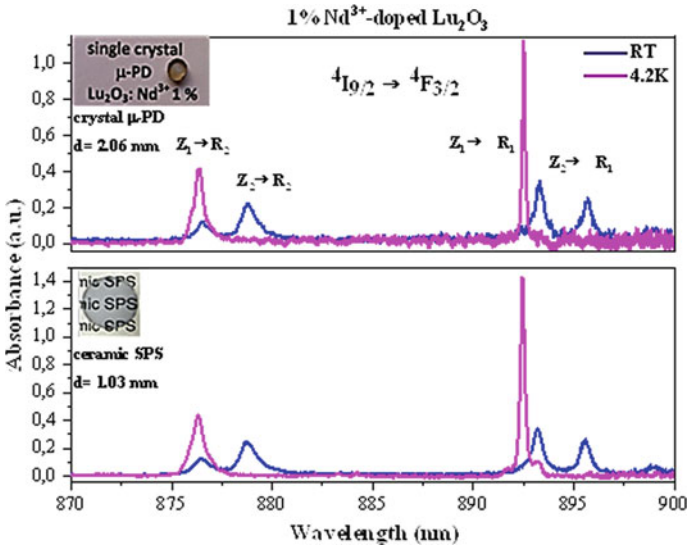

Fig. 11.5 $^4I_{9/2} \rightarrow {}^4F_{3/2}$ absorption lines at 4 K and RT of the most populated C_2 sites in 1% Nd^{3+}-doped Lu_2O_3 ceramic (upper panel) and 1% Nd^{3+}-doped Lu_2O_3 crystal (bottom panel). Insert is the photo of the corresponding samples

Moreover, we have selected, in Fig. 11.6 the 0-phonon absorption line of the two lowest $^4F_{3/2}$ (11,205 cm^{-1}, 892.5 nm) excited level, which have a simple Stark structure. As the Nd^{3+} *J* manifolds in all these sites are split in *J* + *1/2* Stark levels it is easy to assign the doublet structure of the $^4F_{3/2}$ level in Fig. 11.6b).

For $^4I_{9/2} \rightarrow {}^4F_{5/2}$; $^2H_{9/2}$ transitions, the assignment is not so easy due to the mixing of both $^4F_{5/2}$ and $^2H_{9/2}$ levels (presented in [38]). In addition, we also have chosen the 0-phonon absorption line of the $^2P_{1/2}$ energy level of high energy at 436.7 nm (22,899 cm^{-1}, 436.7 nm), which has been selected because it is not split by the crystal field (see Fig. 11.6).

For C_2 centers the inter-Stark transitions are mainly of electric-dipole induced type, while the lines associated to C_{3i} centers with inversion correspond to magnetic-dipole transitions. Consequently, the optical transitions recorded in absorption spectra are associated with electric-dipole induced type transitions of the C_2 non-centrosymmetric centers of much higher probability than magnetic-dipole transitions of C_{3i} symmetrical center with the additional argument that the population is three times higher than those of the C_{3i} centers. We were not able to record any absorption transitions of the C_{3i} centers. The magnetic dipole absorption lines of the C_{3i} sites are hidden in the noisy signal between 882 nm and 891 nm at both RT and 4 K. As we will see it in the next section, this is possible to reveal the emission of C_{3i} sites at 77 K under selective laser excitation od a Ti-Sapphire laser.

This analysis has allowed the detection of weak shoulders or satellites at the foot of each 0-phonon absorption lines in Fig. 11.6. In paper [38] we reported detailed

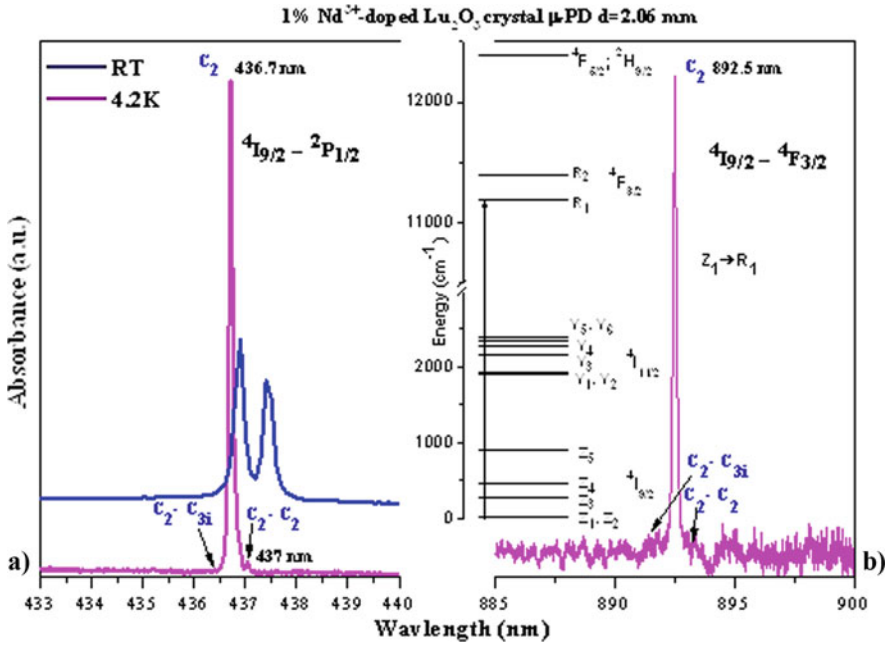

Fig. 11.6 High resolution spectra of the un-split $^4I_{9/2} \rightarrow {}^2P_{1/2}$ absorption lines at 4 K and at RT of the most populated C_2 sites in 1% Nd^{3+}-doped Lu_2O_3 crystal (**a**) and of the $^4I_{9/2} \rightarrow {}^4F_{3/2}$ ($Z_1 \rightarrow R_1$) absorption lines at 4 K of the most populated C_2 sites in 1% Nd^{3+}-doped Lu_2O_3 (**b**). For both transitions the C_2 sites of C_2-C_2 and C_2-C_{3i} pairs are assigned

analysis of satellite lines. The energy shift of each satellite from the 0-phonon line is roughly 10 cm^{-1}. The intensity ratio the two satellites is around 2:1 between Stokes side and Anti-Stokes side and has already been observed by Lupei in 1%Nd^{3+}-doped Y_2O_3 ceramic [50]. The situation is really similar for all transitions.

What is the origin of these two satellites? We have to take into account of the distribution of possible Nd^{3+} neighbor ions as indicated in Table 11.1. In the first sphere at around 4 Å as justified before, around one C_2 site occupied by Nd^{3+} ion, there are mainly two groups composed of 4 C_2 sites at 3.54 Å and 2 C_{3i} sites at 3.52 Å, so that clearly C_2 site population should contribute to the highest intensity of the Stokes side. The result will be the same if we take into account of 4 C_2 sites at 3.54 Å and 4 at 4.01 Å and 2 C_{3i} sites at 3.52 Å and 2 at 3.99 Å. The ratio of 2:1 is then well interpreted. In this hypothesis, the Stokes side is assigned to C_2-C_2 pairs. Naturally, C_{3i} sites of the smallest population should contribute to the satellite of the smallest intensity. Then, the Anti-Stokes side could be assigned to C_2-C_{3i} pairs. Another argument in favor of this assignment is the observation of the C_{3i} site at higher energy than the C_2 site by site selective laser excitation in the next paragraph.

When comparing spectra in Figs. 11.5 and 11.6, the first observation is the narrowest linewidths of crystals as compared with ceramics and also the highest

intensity of the C_2-C_2 pairs in ceramics with respect to C_2-C_{3i} ones in crystals indicating a greater disorder of pairs in ceramics [38].

Emission Spectra Under Selective Excitation

The emission spectra of rare earth-doped sesquioxides at RT reported in the literature [19, 20] concern mainly the most populated C_2 site. In order to know more not only on C_2 but also on C_{3i} sites and on C_2-C_2 and C_2-C_{3i} pairs, we have also applied site selective laser spectroscopy to Nd^{3+} ions in Lu_2O_3 ceramics. A systematic sweep of the excitation wavelength with a tunable Ti-sapphire laser in the spectral range of the $Z_1 \rightarrow R_1$ and $Z_1 \rightarrow R_2$ of the $^4I_{9/2} \rightarrow {}^4F_{3/2}$ transition, as it was shown in Fig. 11.5, has been used to perform emission spectra for each 0.15 nm step between 870 nm and 900 nm.

As an example Figs. 11.7a) presents site selective spectroscopy results at recorded 77 K and in Fig. 11.7b) the energy level diagram corresponding to the emission spectra observed in Fig. 11.7a). We precise the different excitations of C_2 or C_{3i} sites and C_2 belonging either to C_2- C_2 or C_2-C_{3i} pairs as well as the nature of the transition ($Z_1 \rightarrow R_1$ or $Z_1 \rightarrow R_2$):

- $Z_1 \rightarrow R_1$ of C_2 (892.5 nm),
- $Z_1 \rightarrow R_2$ of C_2 (876 nm),
- $Z_1 \rightarrow R_1$ of C_{3i} (884.4 nm).
- $Z_1 \rightarrow R_2$ of C_{3i} (871.2 nm),

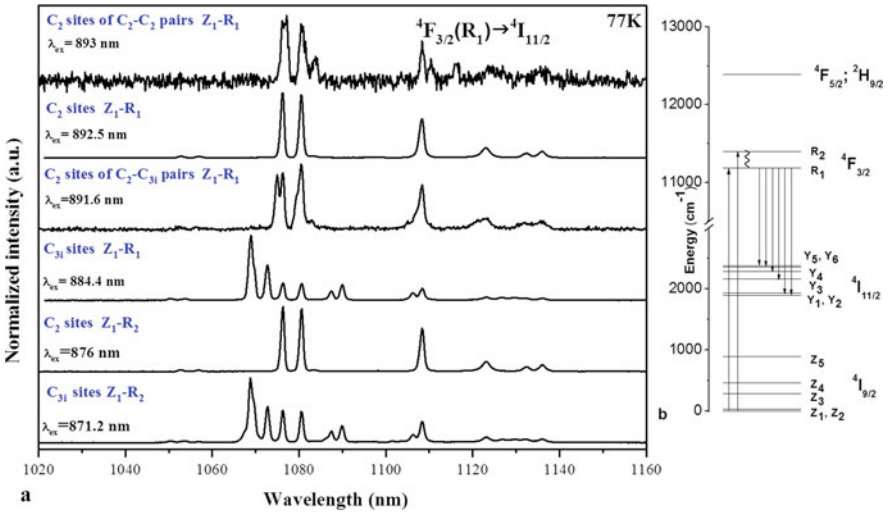

Fig. 11.7 (**a**) $^4F_{3/2}$ (R_1) $\rightarrow {}^4I_{11/2}$ normalized emission spectra at 77 K of C_2, C_{3i} sites, C_2-C_2 and C_2-C_{3i} pairs respectively, into excitations either by $Z_1 \rightarrow R_1$ or by $Z_1 \rightarrow R_2$ transitions. C_2 and C_{3i} emission lines are well resolved. (**b**) Energy level diagram corresponding to the emission spectra observed in (**a**)

– $Z_1 \rightarrow R_1$ of C_2 from C_2- C_2 pairs (893 nm),
– $Z_1 \rightarrow R_1$ of C_{3i} from C_2- C_{3i} pairs (891.6 nm),

Consequently, Fig. 11.7 shows unambiguously the presence of two C_2 and C_{3i} sites under selective excitation whereas the absorption spectra in, Fig. 11.5 points out only C_2 lines. Any signal of the C_{3i} the $^4I_{9/2} \rightarrow {}^4F_{3/2}$ absorption in the spectral range of 892–895 nm is undetectable. The pumping results at 77 K around R_1 and R_2 levels of the lowest $^4F_{3/2}$ excited state indicate two distinct ranges of 892.8 nm (11,201 cm^{-1}) for C_2 and 883.7 nm (11,316 cm^{-1}) for C_{3i}, that allows the evaluation of the $^4I_{9/2} \rightarrow {}^4F_{3/2}$ (R_1) gap between C_2 and C_{3i} sites to 116 cm^{-1}. The Nd^{3+} energy level diagram had already been drawn for ceramics in [19] and it is the same for crystals.

It is easy to assign the 6 Stark components of the $^4F_{3/2}$ (R_1) $\rightarrow {}^4I_{11/2}$ transition at 77 K as a result of $J = 11/2$ manifold split in $J + 1/2$ Stark levels. Into direct excitation by 892.5 nm (R_1) and 876 nm (R_2) in C_2 sites, all the emission spectra in Fig. 11.7 are characterized by 6 expected components at 1076.2 nm, 1080.6 nm, 1108.3 nm, 1123.2 nm, 1132.6 nm, 1136.2 nm respectively, whereas into direct excitation by 884.4 nm (R_1) and 871.2 nm (R_2) in C_{3i} sites, 6 other components are systematically observed in the shorter wavelengths at 1069 nm, 1072.6 nm, 1087.5 nm, 1090 nm, 1106.2 nm, 1127.2 nm. Let us remind that the two first lines of C_2 sites at 1076.2 nm and 1080.6 nm are the two components previously observed in the laser output of the 1% Nd^{3+}-doped Lu_2O_3 ceramics [20]. In addition, we show the emission spectra of the C_2 sites belonging either to C_2-C_2 or C_2-C_{3i} pairs.

New lines are observed either on the longer wavelength side of C_2-C_2 pairs and the shorter wavelength side of C_2-C_{3i} pairs with respect of the 0-phonon line as also additional lines of the regular C_2 sites.

The red shift of the C_2- C_2 pair spectrum (1077 nm, 1083.7 nm, 1110.6 nm, 1116.4 nm are detected as additional lines of the six lines of C_2 sites) and the blue shift of the C_2-C_{3i} pair spectrum (1075.1 nm, 1079.4 nm, 1082.8 nm, 1105.3 nm, 1121.6 nm, 1127.3 nm are detected as additional lines of the six lines of C_2 sites) are coherent with the spectroscopic properties of both C_2 and C_{3i} sites. This is the evidence of the energy transfer between C_{3i} and C_2 sites at least at 77 K, so that we bring another view on the interpretation of the energy transfer expected only between C_2 sites of Nd^{3+} ions in Y_2O_3 ceramic, as it has been seen by the strong quenching of the $^4F_{3/2}$ decays [52].

In Fig. 11.7 the intensities have been normalized and to be precise we should compare each intensity. As expected, the emission from C_2 sites associated with electric-dipole induced type transitions shows the highest intensity, almost two orders of magnitude higher than magnetic-dipole transitions of C_{3i}. The emission intensity from C_2 of C_2-C_{3i} or C_2-C_2 pairs is still much weaker than that of C_{3i}. This is another evidence of the much higher sensitivity of the emission technique under powerful laser pumping with respect to the absorption technique to detect multi-sites in luminescent materials.

Two C_2 and C_{3i} Symmetry Sites in Nd^{3+} − Doped Lu_2O_3 Ceramics or Crystals

Two C_2 and C_{3i} symmetry sites were first observed in Bi^{3+} mercury-like ions in

Bi^{3+}-doped sesquioxides [53, 54] and the position of absorption and emission bands were confirmed in Bi^{3+}-doped Y_2O_3 by ab initio simulation first on the C_{3i} site [55] and then on both C_2 and C_{3i} sites [56].

Concerning trivalent rare earth ions two C_2 and C_{3i} symmetry sites have been observed in Eu^{3+}-doped Y_2O_3 and Gd_2O_3 polycrystals [57], Eu^{3+}-doped Lu_2O_3 polycrystals [58], Yb^{3+} and Nd^{3+}-doped nanostructured Lu_2O_3 [59, 60], Yb^{3+}-doped Lu_2O_3 crystal [61, 62] and more recently on Sm^{3+}-doped Y_2O_3, Lu_2O_3, Sc_2O_3 and YAG ceramics [63, 64]. Systematically, the C_{3i} energy levels of rare earth ions are always located on the higher energy side with respect of C_2 levels, like it is for Nd^{3+}-doped Lu_2O_3 ceramics with a gap of 115 cm^{-1} between $^4F_{3/2}$ (R_1) levels, giving sense to our assignment. Due to extreme similarity between spectra of ceramics and crystals this observation can be also applied to Nd^{3+}-doped Lu_2O_3 crystals.

11.6.2 Vacancied Scheelite-Type Structure $Cd_{1-3x}Nd_{2x}\square_xMoO_4$ Molybdates: Double Distribution of Nd^{3+} Sites with D_{2d} Point Symmetry Slightly Deformed

Molybdates $MMoO_4$ (M = Ca, Sr, Ba, Pb and Cd) adopt the tetragonal scheelite-type structure with space group $I4_1/a$ and form a wide class of materials in different application fields such as scintillator detectors, luminescence photoconductivity, and photocatalysis [65–68]. Due to a large X-ray absorption coefficient and efficient scintillation yield, they have been applied in medical detecting X-rays and γ-rays [69]. The multi-purpose applications of the scheelite oxide systems are due to the possibility of their appearance in several phases with different structural types. They can crystallize in the scheelite structure $I4_1/a$, Z = 4 (No. 88), pseudoscheelite structure *Pnma*, Z = 4 (No. 62), zircon structure $I4_1/amd$, Z = 4 (No. 141), M-fergusonite structure $I2/a$, Z = 2 (No. 15) and M-fergusonite structure $2_1/c$, Z = 2 (No. 14) [70]. Simple scheelite phase (e.g. $M^{II}M^{VI}O_4$, M^{VI} = Mo, W) has eight symmetry elements; a body-centered tetragonal unit cell and four formula units (Z = 4). Each M^{VI} atom is surrounded by four equivalent oxygen ions in T_d symmetry and each $M^{II}O_8$ cation shares corners with eight adjacent $M^{VI}O_4$ tetrahedra. It was observed that incorporating trivalent ions as La^{3+} into the matrix resulted in a significant improvement of the optical transmission, radiation hardness and other spectroscopic properties of $PbWO_4$ crystals [71, 72].

A peculiar aspect of rare-earth applications is not to introduce a high concentration of doping ions with the most stable RE^{3+} oxidation state. So, we realized that incorporation of RE^{3+} ions into the $CdMoO_4$ matrix could be very interesting task in searching of the optical and laser materials with improved optical parameters.

Structure When RE^{3+} ions are incorporated in the $PbMO_4$ or $CdMO_4$ (M = Mo, W) lattice, on a regular lattice, it must be accompanied by a charge-compensating

defect. Substitution of divalent Cd^{2+} by trivalent Nd^{3+} cations leads to the formation of cationic vacancies in the framework due to the charge compensation: $3Cd^{2+} - 2Nd^{3+} + \square$ vacancy and creates some disordering what in consequence leads to improving of the luminescence intensity. The $\square$ vacancy concentration dependence brings some originality to this research program in optical materials [39, 73, 74].

The structure of $Cd_{1-3x}Nd_{2x}\square_xMoO_4$ is based on the scheelite-type structure of $CdMoO_4$. We succeeded to precisely define the number of vacancies presented for the first time. The density of each solid solution slightly increased with decreasing concentrations of optically active ion. The difference between a value of experimental and calculated density for each $Cd_{1-3x}Nd_{2x}\square_xMoO_4$ solid solution was also observed. This fact confirms partial occupancy of cationic positions by Nd^{3+} in the scheelite structure and presence of vacancies in the framework. Each Mo^{6+} ion is surrounded by four equivalent O^{2-} ion at distances of 1.75 Å in approximately a tetrahedral symmetry. Each Cd^{2+} ion is surrounded by eight O atoms at distances of 2.40 Å and 2.44 Å in approximately an octahedral symmetry. The Cd^{2+} cations in $CdMoO_4$ can be substituted by trivalent ones. As we presented in [39] the phases show a random distribution of Nd^{3+} and the distance between the Cd^{2+}/Nd^{3+} ions is equal to 3.908 Å.

In case of this $Cd_{1-3x}Nd_{2x}\square_xMoO_4$ microcrystalline solid solutions the product crystallizes in a compact form with an average size of about 1–10 μm. The particles are well separated and the grain boundaries between the micro- crystals can be clearly seen.

Spectroscopic Analysis of $Cd_{1-3x}Nd_{2x}\square_xMoO_4$

Evidence of Nd^{3+} Multi-sites -confirmation from the Absorption Spectra. Figure 11.8 presents the absorption spectra at 4.2 K of $Cd_{0.9268}Nd_{\mathbf{0.0488}}\square_{\mathbf{0.0244}}MoO_4$ (5 mol% Nd^{3+}) in the spectral range from 400 to 900 nm (UV-VIS and NIR). These spectra show 4f–4f transitions with crystal field (C.F.) fine structure in the range of all transitions. At 4.2 K the absorption bands should be narrower than at room temperature and this behavior is well observed for $Cd_{1-3x}Nd_{2x}\square_xMoO_4$ solid solutions [39]. All the absorption lines are assigned to the transitions from the $^4I_{9/2}$ ground state to $^2P_{1/2}$ (433 nm), $^2G_{11/2} + {}^2P_{3/2} + {}^2D_{3/2} + {}^2G_{9/2}$ (480 nm), $^4G_{9/2}$, $^4G_{7/2}$, $^3K_{13/2}$ (530 nm), $^4G_{5/2}$, $^2G_{7/2}$ (580 nm), $^2H_{11/2}$ (630 nm), $^4F_{9/2}$ (683 nm), $^4F_{7/2} + {}^4S_{3/2}$ (750 nm), $^2H_{9/2} + {}^4F_{5/2}$ (807 nm), $^4F_{3/2}$ (875 nm). Figure 11.9 shows the absorption spectra at 4.2 K of $Cd_{0.9268}Nd_{0.0488}\square_{0.0244}MoO_4$ (5 mol% Nd^{3+}) in the spectral range of the $^4I_{9/2} \rightarrow {}^2P_{1/2}$ transition. At room temperature three components at 432.5 nm (23,121 cm^{-1}), 435 nm (22,988 cm^{-1}), 437 nm (22,883 cm^{-1}) corresponding to the $^4I_{9/2} \rightarrow {}^2P_{1/2}$ transition are clearly visible. At 4.2 K the lines at 435 and 437 nm disappear because they represent the transitions from the higher energy Stark component (Z_2) of the $^4I_{9/2}$ ground state of Nd^{3+} ion. The line localized at 432.5 nm splits into two well resolved components at 432.4 nm (23,127 cm^{-1}) and 432.7 nm (23,110 $cm^{-1)}$, with a splitting of 17 cm^{-1} and a full width at half maximum (FWHM) of this absorption line equals to 27 cm^{-1}. This

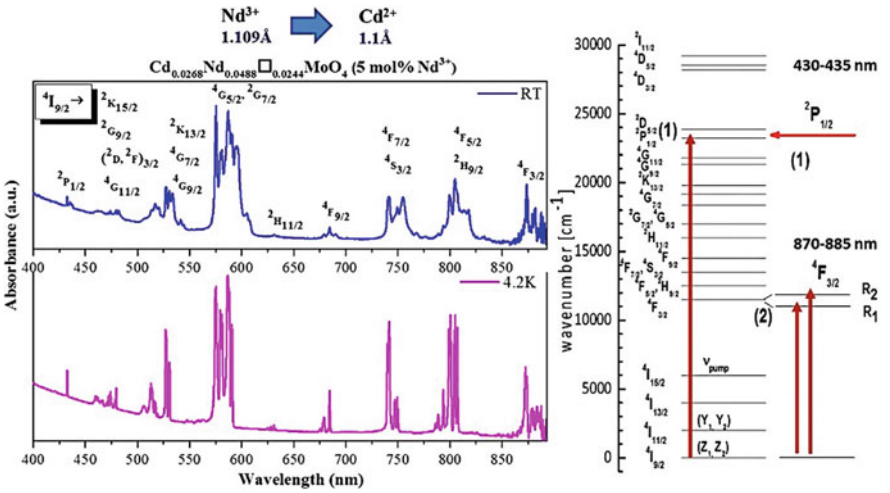

Fig. 11.8 Absorption spectra of $Cd_{0.9268}Nd_{0.0488}\square_{0.0244}MoO_4$ (5 mol% Nd^{3+}) recorded at room temperature and 4.2 K and energy level scheme for Nd^{3+} ion with particular emphasis on the $^4I_{9/2} \rightarrow {}^2P_{1/2}$ and $^4{}_{9/2} \rightarrow {}^4F_{3/2}$ transitions which simple Stark structure can play a role as a structural probe

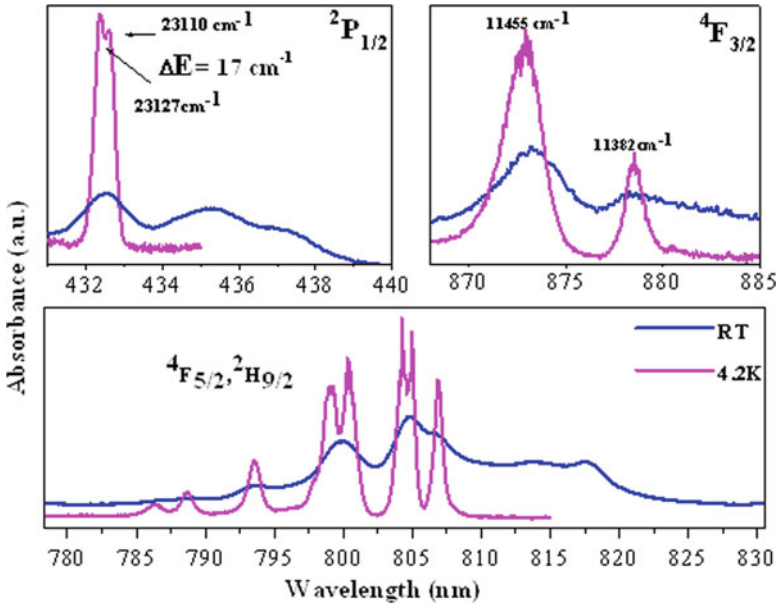

Fig. 11.9 Selected transitions ($^4I_{9/2} \rightarrow {}^2P_{1/2}$, $^4I_{9/2} \rightarrow {}^4F_{3/2}$, $^4I_{9/2} \rightarrow {}^4F_{5/2}$, $^2H_{9/2}$) of the absorption spectra of $Cd_{0.9268}Nd_{0.0488}\square_{0.0244}MoO_4$ (5% Nd^{3+}) recorded at room temperature and 4.2 K

indicates clearly two main Nd^{3+} distributions of sites in the lattice with D_{2d} point symmetry with slightly lowering symmetry.

In case of studied here $Cd_{1-3x}Nd_{2x}\square_xMoO_4$ phase the Nd^{3+} ions substitute only the Cd^{2+} ions, so that three Cd^{2+} are replaced by two Nd^{3+} ions with the creation of one vacancy, the FWHM = 27 cm^{-1} of the $^4I_{9/2} \rightarrow {}^2P_{1/2}$ absorption line is much narrower than in $Cd_{0.25}Gd_{0.50}\square_{0.25}WO_4$ and $CdY_2W_2O_{10}$ tungstates, what means that less disorder is observed in the lattice [75].

Another important observation is the easy substitution of Cd^{2+} ion (ionic radius = 1.1 Å for CN = 8) by Nd^{3+} ions (ionic radius 1.109 Å for CN = 8). In Fig. 11.9 another selected absorption lines like $^4I_{9/2} \rightarrow {}^4F_{3/2}$ of $Cd_{0.9268}Nd_{0.0488}\square_{0.0244}MoO_4$ (5 mol% Nd^{3+}) at room and 4.2 K are shown. The $^4I_{9/2} \rightarrow {}^4F_{3/2}$ transition also attracted our interest, because of two components expected at 4.2 K for one site. We observed two broad components, one at 873 nm (11,455 cm^{-1}) and second one at 878.5 nm (11,382 cm^{-1}), that gives the value of $^4F_{3/2}$ state C.F. splitting equals to 73 cm^{-1}. We did not observe a subtle splitting of the $^4I_{9/2} \rightarrow {}^4F_{3/2}$ transition for the two types of expected sites but only the broadening of each component.

The highest intensity is observed for the hypersensitive $^4I_{9/2} \rightarrow {}^4G_{5/2}$, $^2G_{7/2}$ transitions because of lowering of occupied Nd^{3+} site symmetry. Thus on the base of the intensity ratio between two bands in the IR spectral range (725–778 nm) and (778–838 nm) and the $^4I_{9/2} \rightarrow {}^4G_{5/2}$, $^2G_{7/2}$ one (550–617 nm) presented in Fig. 11.8 one can conclude that symmetry of Nd^{3+} ion in our compound is rather high.

The broadening of the absorption lines corresponding to the $^4I_{9/2} \rightarrow {}^4F_{5/2}$, $^2H_{9/2}$ transition in 780–830 nm spectral range reveals suitable absorption channels for the laser diode pumping. Important parameters for laser application are the absorption and emission cross-sections.

It is well-known that large cross-section provides effective absorption of the excitation radiation. This parameter was determined by many authors to classify laser behavior of different Nd^{3+}-doped materials among which for well-known commercial laser materials. As some kind on standard one can use the absorption cross-section equal to 0.77×10^{-19} cm^2 for Nd^{3+} doped YAG commercial laser material [75].

Confirmation from the Emission Spectra Under excitation at λ_{ex} = 588 nm (by LED) into the $^4G_{5/2}$, $^2G_{7/2}$ multiplet all the samples show a strong emission from the $^4F_{3/2}$ level to the three terms: $^4I_{9/2}$ (850–950 nm), $^4I_{11/2}$ (1040–1100 nm), and $^4I_{13/2}$ (1310–1420 nm) of the ^4I_J. The intensity of emission from Nd^{3+} ion is higher at 77 K than at room temperature as well as the emission bands are narrowing. Among all compounds under investigation the highest emission intensity is shown by the material containing 3 mol% of Nd^{3+} ions. In the spectra recorded at 4.2 K, in all spectral ranges the number of Stark components is also higher than that expected for the compound with one symmetry site due to the double distribution of Nd^{3+} ions [39].

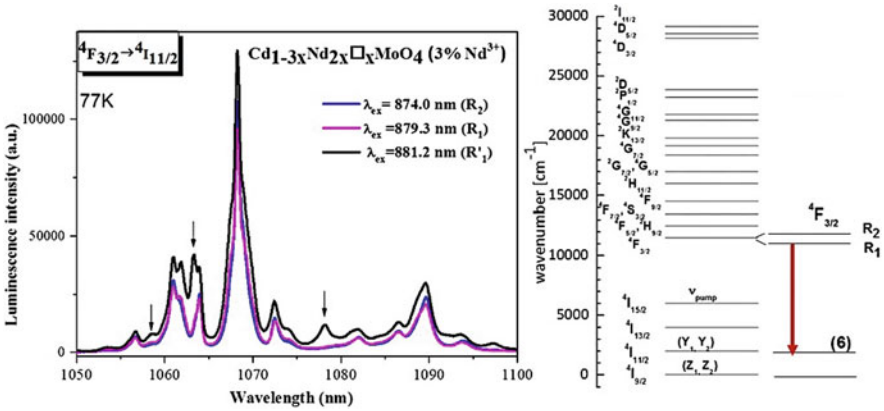

Fig. 11.10 Emission spectra of $Cd_{0.9556}Nd_{0.0296}\square_{0.0148}MoO_4$ (3 mol% of Nd^{3+}) recorded at 77 K under different excitation line of Ti-Sapphire laser

Figure 11.10 presents emission spectra of $Cd_{0.9556}Nd_{0.0296}\square_{0.0148}MoO_4$ (3 mol% of Nd^{3+}) recorded at 77 K under different excitation lines of Ti-Sapphire laser. The number of Stark components is varing when the excitation wavelength is changing, confirming the distribution of Nd^{3+} ion in more than one non-equivalent site in the lattice (additional components are indicated in Fig. 11.9 by arrows).

To check the possibility of applying our compounds as laser materials in the future, it would be useful to compare them to the well-known YAG:Nd^{3+} laser materials. Figure 11.11a) shows the commercial LED emission spectrum with a maximum at 588 nm used to pump the $^4I_{9/2} \rightarrow {}^4G_{5/2}$, $^2G_{7/2}$ hypersensitive absorption transitions of the two samples: micro-crystalline $Cd_{0.9268}Nd_{0.0488}\square_{0.0244}MoO_4$ (3 mol% of Nd^{3+}) and the powdered single crystal of YAG:Nd^{3+}, both recorded at room temperature. We see that the broad band-width of the LED source, around 13 nm, is well adapted for the excitation of both $Cd_{1-3x}Nd_{2x}\square_xMoO_4$ and YAG:Nd^{3+} samples. In Fig. 11.11b) we have compared the emission spectra of 0.8 at% Nd^{3+}-doped $Y_3Al_5O_{12}$ (YAG:Nd^{3+}) and $Cd_{0.9268}Nd_{0.0488}\square_{0.0244}MoO_4$ (3 mol% of Nd^{3+}) under LED excitation. The emission bands in the spectral region 800–1500 nm for YAG: Nd^{3+} are sharper and better resolved than for Nd^{3+}-doped $CdMoO_4$ but they are not as broad as in the case the Nd^{3+}-doped $La_2Mo_2O_9$ molybdates, presented in the next section. The comparison of the integral intensities of transitions for both types of compounds shows values eight and half times (for $^4F_{3/2} \rightarrow {}^4I_{9/2}$ transition) and nine times (for $^4F_{3/2} \rightarrow {}^4I_{11/2}$ transition) higher for the $Cd_{1-3x}Nd_{2x}\square_xMoO_4$ than for YAG:Nd^{3+}. Here, we decided to use the 3 mol% Nd^{3+}-doped $CdMoO_4$ sample which showed the most intense luminescence just to give some idea of the relative emission of $Cd_{1-3x}Nd_{2x}\square_xMoO_4$ and YAG:Nd^{3+}, recorded under non selective excitation in the broad hypersensitive absorption band.

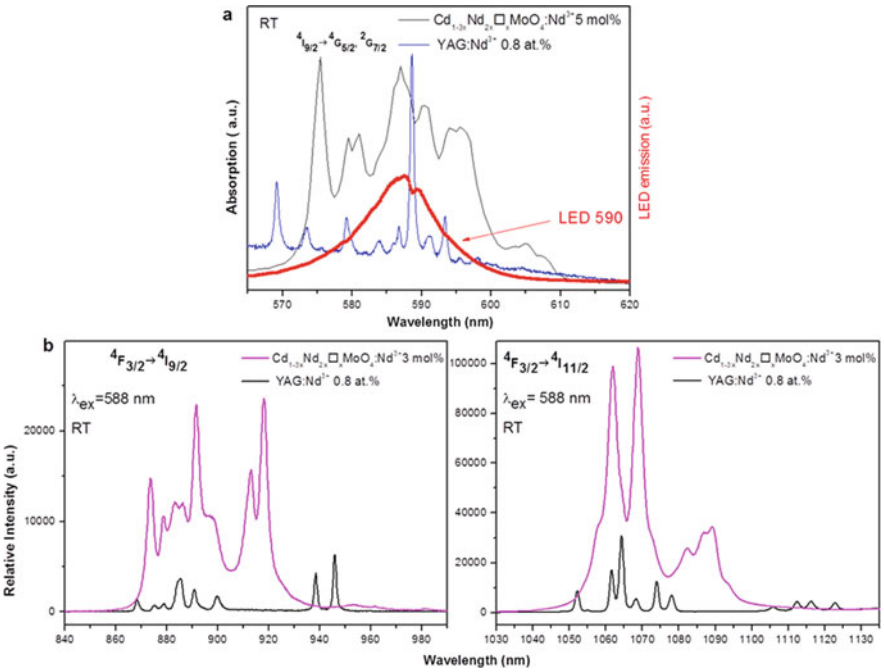

Fig. 11.11 Justification of the use of the commercial LED 590 with maximum intensity at 588 nm to pump $Cd_{0.9268}Nd_{0.0488}\square_{0.0244}MoO_4$ (5 mol% Nd^{3+}) and 0.8 at.% Nd^{3+}-doped $Y_3Al_5O_{12}$ (YAG) samples which are characterized by absorption spectra at room temperature. (**a**). Emission spectra of $Cd_{0.9556}Nd_{0.0296}\square_{0.0148}MoO_4$ (3 mol% of Nd^{3+}) and 0.8 at.% of Nd^{3+}-doped $Y_3Al_5O_{12}$ (YAG:Nd^{3+}) recorded at room temperature, $\lambda_{ex} = 588$ nm of LED. Figure presents the $^4F_{3/2} \rightarrow {}^4I_{9/2}$ and $^4F_{3/2} \rightarrow {}^4I_{11/2}$ transitions, respectively (**b**)

The result obtained for our samples indicates that $Cd_{1-3x}Nd_{2x}\square_xMoO_4$ could be especially promising for an ultra-short pulse laser generation [39].

Luminescence Decay Times Figure 11.12 presents the luminescence decay profiles with calculated values of decay times for $Cd_{1-3x}Nd_{2x}\square_xMoO_4$ with different Nd^{3+} (0.1–66.67 mol%) concentration recorded at room temperature. The decay curves were obtained under laser pulsed excitation at 808 nm (12,376 cm^{-1}) in the $^4I_{9/2} \rightarrow {}^4F_{5/2} + {}^2H_{9/2}$ absorption transition and the luminescence was monitored at 1064 nm. No dependence on the excitation wavelength is observed. As one can see, the curves for all samples exhibit the non-exponential character due to the energy transfer between the Nd^{3+} ions distributed in the two main non-equivalent sites at short times. At longer times, the curves are represented by straight lines in the log scale. A lifetime of about 92 μs fitted for the lowest concentration (0.1 mol%) at room temperature should be close to the radiative lifetime. At low temperatures the values of lifetimes are slightly higher (95 μs for 0.1 mol%). When the concentration increases then the values of fluorescence lifetimes decrease drastically (from 92 to 3.5 μs at RT and from 95 to 5.6 μs at 77 K) illustrating the fluorescence quenching

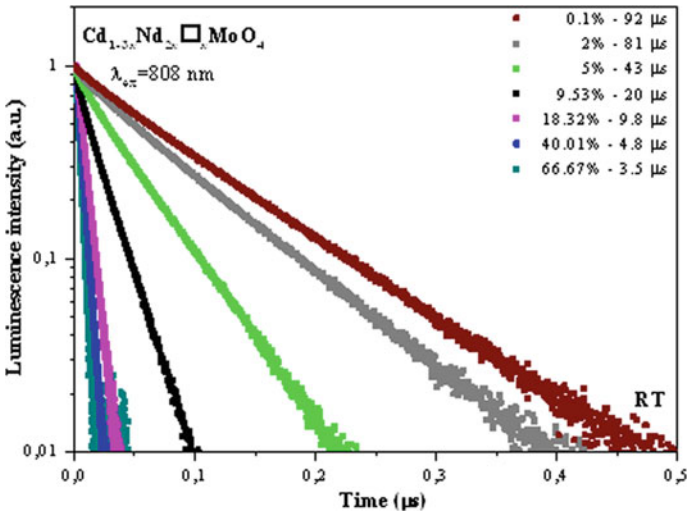

Fig. 11.12 Decay curves of the fluorescence from $^4F_{3/2}$ for the $Cd_{1-3x}Nd_{2x}\square_xMoO_4$ solid solutions, recorded at room temperature, $\lambda_{ex} = 808$ nm, $\lambda_{em} = 1064$ nm

due to different types of energy transfers, both between molybdate group and Nd^{3+} ions and also between Nd^{3+} ions themselves, by usual up/down-conversion and cross-relaxation mechanisms due to the high number of Nd^{3+} levels in the visible and UV ranges, according the schemes in Fig. 11.3.

11.6.3 Monoclinic/Cubic $La_{2-x}Nd_xMo_2O_9$ Micro-powders: Disordered Structure and Multisite Character

As it states in the literature, until now the compounds from the $La_2Mo_2O_9$ (LAMOX) family has been examined only as oxide ion conductors. Additionally, a catalytic activity of nanoscaled powder was studied [76, 77]. The crystal structure of the LAMOX materials based on $La_2Mo_2O_9$ dilanthanum dimolybdate, has been a subject of continuous investigations since more than 40 years, when it was synthesized for the first time by Fournier et al. by using conventional solid-state technique [78]. The compound presents a reversible phase transformation at 580 °C from a low-temperature monoclinic form (α-$La_2Mo_2O_9$) to a high-temperature modification β-$La_2Mo_2O_9$, which has a cubic structure, derived from the β-$SnWO_4$ one [79, 80]. However, several possible substitutions on both cationic [81] and anionic [82] sites of $La_2Mo_2O_9$ stabilize the high temperature β-form.

This is why this material is considered by us as promising in our research program devoted to fabrication of transparent optical sintered ceramics basing on cubic tungstates or molybdates. In addition lack in the literature the reports

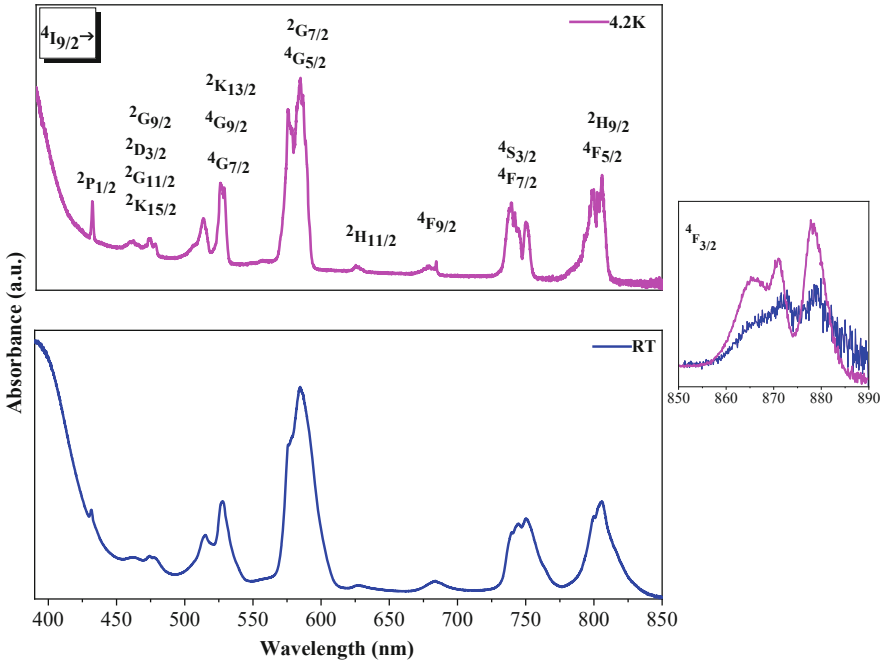

Fig. 11.13 Absorption spectra of 10% Nd^{3+}-doped $La_2Mo_2O_9$ recorded at room temperature and 4.2 K

on the optical properties for RE^{3+}-doped LAMOX were the motivation of these studies, which should have the double character of studies for applications and also fundamental research.

Structure The patterns obtained for low and high-concentrated samples are similar because the structure of α-$La_2Mo_2O_9$ is derived from the β-$La_2Mo_2O_9$ by oxide ion ordering of lattice distortions. Monoclinic distortion in α-$La_2Mo_2O_9$ often leads to splitting of characteristic peaks, such as those corresponding to the pseudo-cubic (111), (211) and (321) reflections. In particular, the (321) reflection id highly sensitive to monoclinic distortion.

The cubic symmetry of the substituted samples is presented by the single reflection of (321). Taking into account above, for low-concentration doped samples the powder diffraction patterns agree with the diffraction lines of the α-$La_2Mo_2O_9$ monoclinic form (ICSD 172479).

For more concentrated compositions, the agreement with the high-temperature cubic structure of $La_2Mo_2O_9$ (ICSD 420672) was observed. Pure high-temperature cubic phase only appears starting from concentration of 50% Nd^{3+} ion [40, 41]. The shape of the pseudo-cubic peak (231) at 47.5–48° 2Theta allows to detect the change of the structure with increasing of the Nd^{3+} doping level in the investigated LAMOX solid solutions. According to the studies reported by Evans

et al., α-$La_2Mo_2O_9$ possesses the monoclinic cell with the following parameters: a = 14.325(3) Å, b = 21.482(4) Å, c = 28.585(6) Å and β = 90.40(3), space group $P2_1$, Z = 48. This 2 x 3 x 4 superstructure corresponds to the cubic high-temperature β-form. Given the cell dimensions and symmetry, the crystal structure of α-phase contains a remarkable 312 crystallographically independent atoms: 48 La, 48 Mo and 216 O. Crystallographically unique La atoms have coordination shell containing between 6 and 12 oxygen atoms with 30 out of the 48 independent La atoms being nine-coordinate [83]. More accurate information on existing research on α-$La_2Mo_2O_9$ and β-$La_2Mo_2O_9$ forms we reported in [40, 41].

Absorption Spectra Figure 11.13 shows the absorption spectra in the visible and near infrared at room and low temperature (4.2 K) recorded for monoclinic 10% Nd^{3+}-doped $La_2Mo_2O_9$ and contain characteristic for Nd^{3+} ion transitions from the $^4I_{9/2}$ ground state to the excited states. The most intense band with a maximum located at 584 nm corresponds to the hypersensitive $^4I_{9/2} \rightarrow {}^4G_{5/2}, {}^2G_{7/2}$ transitions. The intensity ratio between two bands in the NIR spectral ranges 710–778 nm and 778–838 nm and that in the range 550–617 nm equal to 1:2 indicating high symmetry of the system. When the concentration of Nd^{3+} is increasing this ratio changes reaching almost 1:1 for 60% of activator [40, 41]. Observed variation suggests that symmetry of the system is reduced when samples are richer in Nd^{3+}. The bands observed in the room-temperature absorption spectra are relatively broad what suggests disordering of the active ions in the structure. At liquid helium temperature the absorption bands are better resolved. Due to depopulation of the crystal field components of the $^4I_{9/2}$ ground state multiplet, all bands occurring in the absorption spectra become slightly narrower with decreasing temperature. However, even at low temperature the splitting of the bands is not as good as it was observed for high-symmetry systems presented in two previous paragraphs. In case of Nd^{3+}-doped $La_2Mo_2O_9$ it is very important that the substitution of La^{3+} by Nd^{3+} takes place. Both ions possess the same valence and similar ionic radii *i.e.* Nd^{3+} ion 1.163 Å (CN = 9) is slightly smaller than La^{3+} 1.216 Å (CN = 9). For this type of molybdates, the absorption bands corresponding to the $^4I_{9/2} \rightarrow {}^2P_{1/2}$ transition (not present here), both at room as well as at low temperature, possess only one component. However, this band is relatively large (85 cm^{-1}) and asymmetric, even at 4.2 K. In turn, for $^4I_{9/2} \rightarrow {}^4F_{3/2}$ doublet two components should be observed at 4.2 K. The low temperature absorption spectra of monoclinic 10% Nd^{3+}-doped $La_2Mo_2O_9$ reveals well resolved lines which correspond to $^4I_{9/2}(Z_{1,2}) \rightarrow {}^4F_{3/2}(R_2)$ and $^4I_{9/2}(Z_{1,2}) \rightarrow {}^4F_{3/2}(R_1)$, respectively. Also here the bands are broad what allow us to conclude about the second perturbed site of the Nd^{3+} ion in this lattice. To separate Stark components in $^4F_{3/2}$ (R_1) and $^4F_{3/2}$ (R_2) of each Nd^{3+} site it is necessary using site-selective laser excitation and monitoring the emission intensity, what will be presented in next section.

For monoclinic polymorph, it is known from the literature [83] that crystallographically unique La atoms have the coordination shell containing between 6 and 12 oxygen atoms with 30 out of the 48 independent La atoms being nine-coordinate giving rise a great number of Nd^{3+} non-equivalent centers in substitution of the

two main distribution of two La^{3+} polyhedra. These multi-centers are manifested by broad line-widths of both $^4I_{9/2} \rightarrow {}^2P_{1/2}$ and $^4I_{9/2} \rightarrow {}^4F_{3/2}$ absorption transitions. Because of very complex structure of $La_2Mo_2O_9$ and lack of detailed information about La–O bonding (there is only information that this bonding change in the cubic phase 2.3–2.93 Å) it is very difficult to discuss the problem. Also, the single crystals for this composition have not been obtained until now, so lack of detailed information about the structure make impossible any discussion about the metal–oxygen bonding.

Luminescence Spectra Low-concentrated monoclinic samples showed a strong emission from the $^4F_{3/2}$ level to the three terms $^4I_{9/2}$ (850–940 nm), $^4I_{11/2}$ (1055–1120 nm) and $^4I_{13/2}$ (1320–1420 nm) of the ^4I_J multiplet with maxima at 918 nm (10,893 cm^{-1}), 1064.86 nm (9390 cm^{-1}) and 1341.81 nm (7453 cm^{-1}) (not presented here, reported 40, 41]). For all samples the most intense transition is $^4F_{3/2} \rightarrow {}^4I_{11/2}$ which shows five peaks. The most intense peak is located at high energy and intensities of the other lines decrease, gradually shifting to longer wavelengths. The intensity of emission from the Nd^{3+} ion in this molybdate matrix is higher at 77 K than at room temperature. Even if at liquid helium temperature the emission bands, similar to the absorption bands, should be narrower, here, the widths of the bands at room and low temperature remain the same. in the spectra recorded at room and liquid nitrogen temperature. For the band corresponding to the $^4F_{3/2} \rightarrow {}^4I_{9/2}$ transition (~900 nm) one can distinguish more than five lines (the number for the completely removed degeneracy of the $^4I_{9/2}$ level). Therefore, the number of Stark components is higher than that expected for the compound with only one symmetry site.

In the high-resolution emission spectra recorded at 77 K eight components can be observed for the $^4F_{3/2} \rightarrow {}^4I_{9/2}$ transition, and the presence of additional weak peaks indicates Nd^{3+} ions occupying another position in the structure. Among all compounds under investigation the highest emission intensity is shown by the material containing 3% Nd^{3+} ions, both at 77 K, as well as at room temperature. For the highly concentrated samples very low emission intensity at room temperature, even with a tunable Ti–sapphire laser ($\lambda_{ex} = 872$ nm) was observed.

As it was expected for the cubic compounds with high concentration of Nd^{3+} ions, a very strong concentration quenching process takes place due to the clustering effect of Nd^{3+} ions. Presented in the previous paragraph absorption spectra allow to conclude on multi-sites in Nd^{3+}-doped $La_2Mo_2O_9$ micro-crystalline solid solutions. The confirmation of this supposition one can find in low-temperature site-selective excitation spectra into the $^4F_{3/2}$ doublet with using a Ti-sapphire laser pumping source. To record those spectra, extensive tuning of excitation was used. As an example, the emission spectra of 3% Nd^{3+}-doped $La_2Mo_2O_9$ recorded at 77 K under different excitation lines of the Ti-sapphire laser is presented in Fig. 11.14. A comparison of the splitting and the position of the bands corresponding to the $^4F_{3/2} \rightarrow {}^4I_{11/2}$ transition reveals the significant differences. One can distinguish at least three different emission spectra. This effect can also be seen for different excitations by a laser diode around $\lambda_{ex} = 808$ nm (not presented here).

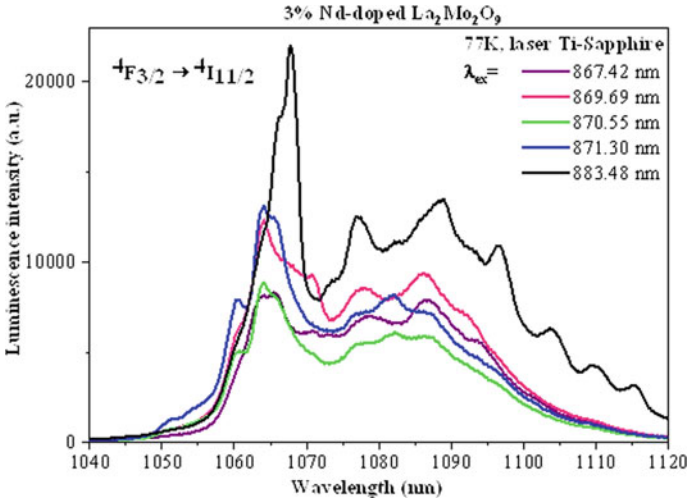

Fig. 11.14 Emission spectra of 3% Nd^{3+} − doped $La_2Mo_2O_9$ recorded at 77 K under Ti-Sapphire laser excitation

In turn, Fig. 11.15 shows the comparison of the emission spectra of 0.8% Nd^{3+}-doped $Y_3Al_5O_{12}$ (YAG:Nd^{3+}) and 3% Nd^{3+}-doped $La_2Mo_2O_9$ recorded at room temperature under Xe lamp excitation at $\lambda_{ex} = 590$ nm. The emission bands in the spectral region 800–1500 nm for YAG:Nd^{3+} are sharper and better resolved, while for Nd^{3+}-doped $La_2Mo_2O_9$ they are very broad. The comparison of the integral

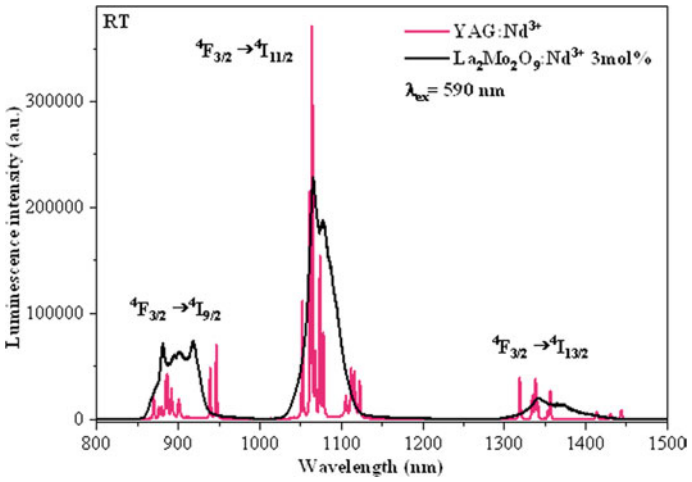

Fig. 11.15 Comparison of the emission spectra of 0.8% Nd^{3+}-doped $Y_3Al_5O_{12}$ (YAG:Nd^{3+}) and 3% Nd^{3+}-doped $La_2Mo_2O_9$ recorded at room temperature under LED excitation at $\lambda_{ex} = 590$ nm

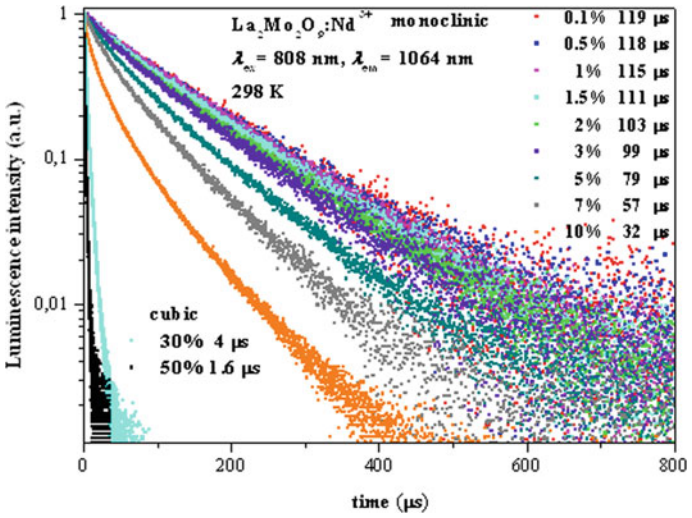

Fig. 11.16 Luminescence decays at room temperature of Nd^{3+} $^4F_{3/2}$ meta-stable level at $\lambda_{em} = 1064$ nm) for monoclinic (0.1, 0.5, 1, 1.5, 2, 3, 5, 7 and 10% of Nd^{3+}) and cubic (30% and 50% of Nd^{3+}) samples, $\lambda_{ex} = 808$ nm

intensities of the transitions for both types of compounds shows values five times (for $^4F_{3/2} \rightarrow {}^4I_{9/2}$ transition) and four times (for $^4F_{3/2} \rightarrow {}^4I_{11/2}$ transition) higher for the molybdates than for YAG:Nd^{3+}. This result indicates that the large emission spectral widths of Nd^{3+}-doped $La_2Mo_2O_9$ could be especially promising for an ultra-short pulse laser generation.

Luminescence Decays Figure 11.16 presents the Nd^{3+} ion concentration dependence of luminescence decay profiles for monoclinic and cubic Nd^{3+}-doped $La_2Mo_2O_9$ samples recorded at room temperature. The decay curves were obtained under laser pulsed excitation at 808 nm in the $^4F_{5/2} + {}^2H_{9/2}$ absorption levels, by monitoring of $^4F_{3/2} \rightarrow {}^4I_{11/2}$ transition at 1064 nm. Confirmed by the values of calculated lifetimes strong concentration quenching of luminescence when the amount of Nd^{3+} ion in the sample is increasing is clearly shown in Fig. 11.16. The decay curve recorded for the lowest concentration (0.1%) is almost exponential with a fitted lifetime of about 119 µs both at room temperature and 77 K (not presented here) and corresponds to the radiative lifetime. When concentration increases, decays become strongly non-exponential. At RT the values of fluorescence lifetimes varied from about 100 µs for the low concentration samples to 32 µs for the compounds containing 10% of Nd^{3+} ions. The decay curves were recorded also at low temperature where values of the integrated lifetimes are slightly higher, what is typical. As it was mentioned before the cubic Nd^{3+}-doped $La_2Mo_2O_9$ exist when concentration of active ion is high, what unfortunately is connected with strong concentration quenching process confirmed in Fig. 11.16 by the luminescence decay curves and lifetimes values obtained for 30% (4 µs) and 50% (1.4 µs) of

Nd^{3+} ions. Decreasing of the lifetimes originates from higher Nd^{3+} doping level but not from the change of structure (monoclinic–cubic), however the change of crystallographic system is a consequence of existence of the bigger amount of the Nd^{3+} in the structure. The non-exponential character is enhanced at the highest concentration pointing at the fluorescence quenching due to the well-known energy transfer between the Nd^{3+} ions by usual up/ down conversion and cross-relaxation mechanisms between the great numbers of Nd^{3+} levels. Discussed in the previous sections multisite character of Nd^{3+} ion in $La_2Mo_2O_9$ structure is manifesting also by the curved shape of the luminescence decays resulting from energy transfer processes betweenNd^{3+} ions.

Please remind the shape of the curves for discussed for $Cd_{1-3x}Nd_{2x}\square_xMoO_4$ represent much ordered structure and two only slightly distorted symmetry sites. The concentration quenching was also present but the decay curves were exponential. The real difficulty of the spectroscopic analysis of Nd^{3+}-doped LAMOX comes from the lack of precise structural data, which could be improved by the growth of single crystals of both monoclinic and cubic phases with the hope to get laser materials and the advantage to have the possibility to transform the cubic phase into transparent ceramics.

11.6.4 Cubic Nd^{3+}-Doped Y_6MoO_{12} – Two Aspects: Multisite Character and Detection of Nd^{3+}-Y_2O_3 Phase Contamination

Y_6MoO_{12} was the next promising matrix for realization our project to achieve new transparent optical ceramics. Only few articles on RE^{3+}-doped Y_6MoO_{12} as optical materials can be found in the literature. In 2016 Li et al. described photoluminescence properties and energy transfer in nano-crystalline Eu^{3+}-doped Y_6MoO_{12} which caught the attention as a phosphor [84]. Recently, we reported the studies on structural and spectroscopic properties of Yb^{3+}-doped Y_6MoO_{12} obtained by high temperature solid state reaction [85]. One can find also the articles on Sm^{3+} [86] or Si^{4+}/Pr^{4+} co-doped Y_6MoO_{12} as inorganic pigments with high NIR reflectance [87]. At last, there is also one paper where Nd^{3+}-doped yttrium molybdate were analysed for high NIR reflective nano-pigments [88]. But there is no deep structural and spectroscopic research for application as optical materials. Moreover, as no single crystal of RE^{3+}-doped Y_6MoO_{12} exists, the exact structure is not well-known. This is why, very extensive fundamental investigations focused on the influence of the synthesis route on the morphology and spectroscopic properties of Nd^{3+}-doped cubic Y_6MoO_{12} molybdate solid solutions have been performed. The samples with various concentration of Nd^{3+} optical activator (0.07–10 mol%) in the form of nano-crystalline powders obtained by the combustion method at 600 °C/3 h (grain size 5–10 nm) and annealed at 800 and 1050 °C (grain size 10–20 nm and 35–40 nm, respectively) were prepared [42]. Obtained samples were

compared with micro-powders synthesized by high-temperature solid state reaction at 1550 °C (grain size was 4–5 μm), having regard to the potential application as optical materials.Here, we would like to present only the case of the micro-powders obtained by solid state reaction.

Structure The synthesis route can play a critical role to modify the materials properties, and also control both composition, structure or microstructure. It is exactly the case of Y_6MoO_{12}. When the samples are prepared by wet chemical method the phase transformation in Y_6MoO_{12} can be observed. For the samples obtained by combustion method the body-centered cubic (b.c.c.) phase $Ia\bar{3}$ exists in the temperature range 600 up to1200°C, then undergoes the phase transformations through rhombohedral $R\bar{3}$ (from 1300 °C) to face-centered cubic (f.c.c) $Fm\bar{3}m$ one (between 1500 °C and 1550 °C). Detailed analysis has been reported by us recently [42]. In contrary, no phase transformation was observed during time consuming multi-stage many hours heating preparation of micro-powders in high-temperature solid state reaction. The face-centered cubic face appears for Y_6MoO_{12} molybdate only at 1550 °C [42]. The diffraction patterns of samples obtained in such way correspond to high-temperature cubic phase of Y_6MoO_{12} (PDF #30–1456) and no phase transformation is observed with increasing of concentration of Nd^{3+} ion. Pure cubic phase was confirmed also by lattice parameters calculation for all the samples. According to the same valence of Nd^{3+} ion as the Y^{3+} one and quite similar ionic radii (for Y^{3+} r = 0.96 Å, CN = 7 and for Nd^{3+} r = 0.983 Å, CN = 6 and r = 1.109 Å CN = 8) we supposed that the substitution of Y^{3+} ions by the Nd^{3+} ones will be quite easy and will not bring a big perturbation in the structure. However, as it will be shown in the section devoted to spectroscopic studies, a disordered structure was observed [42].

Morphology In the next step, the analysis of morphology and particle size performed by TEM and SEM techniques for all the samples leads to conclusion that samples are homogenous with grains of average grain size is around 4–5 μm. However, it is possible also to find smaller grains of about 800 nm or bigger of about 7–8 μm, which are in fact the clusters formed from smaller grains. However, on some micrographs of micro-powders from solid state reaction one can notice very sporadically small clusters made from grains with slightly different morphology. As an example, in Fig. 11.17 such a fragment in big magnification is presented. To confirm the chemical composition and purity of Nd^{3+}- doped Y_6MoO_{12} micro-powders the EDS analysis was used. The presence of four elements, *i.e.* Y, Mo, Nd and O was indicated. Practically for all grains the concentration of elements stays on the same level, indicating the homogeneity of the samples. However, EDS analysis performed for the grains with slightly different morphology, as shown in Fig. 11.17, indicated that in these clusters the concentration of Mo^{6+} ion is smaller than in the regular grains of Nd^{3+}-doped Y_6MoO_{12} phase and at the same time the concentration of Y^{3+} ion is higher (Table 11.2). In our opinion, this result could point on the presence of very small quantities of Nd^{3+}-doped Y_2O_3 in the sample. It should be emphasized here, that no traces of Y_2O_3 were detected during very careful

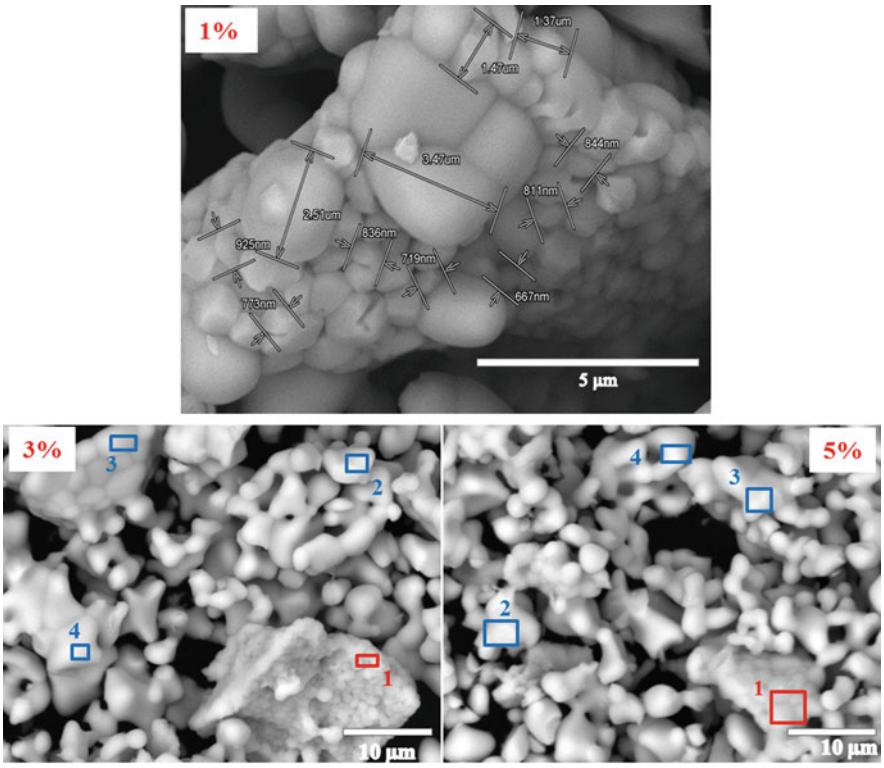

Fig. 11.17 SEM micrographs of 1,3,5% Nd^{3+}-doped Y_6MoO_{12} solid solutions in the form of micro-powders prepared by high-temperature solid state reaction at 1550 °C

Table 11.2 Results of the EDS elemental analysis in the measurement points labeled as 1,2,3 and 4 in Fig. 11.17

Elements	O	Y	Mo	Nd	Elements	O	Y	Mo	Nd
Expected [at%]	63.16	30.63	5.26	0.95	Expected [at%]	63.16	30.63	5.26	0.95
Point 1	72.06	25.79	1.83	0.32	Point 1	71.88	22.44	4.69	1.00
Point 2	75.25	18.87	5.28	0.60	Point 2	73.80	19.99	5.25	0.96
Point 3	70.69	22.72	5.86	0.74	Point 3	76.16	17.16	5.28	1.40
Point 4	71.24	22.21	5.83	0.73	Point 4	76.96	16.77	5.10	1.17

structural analysis by XRD technique, which confirmed absolutely pure cubic phase of the solid solutions under investigations.

As we will show later the emission spectra under site selective excitation for Nd^{3+}-doped Y_2O_3, the site selective spectroscopy allowed us to confirm our supposition about the presence of some traces of Y_2O_3 in Nd^{3+}-doped Y_6MoO_{12} micro-powdered samples.

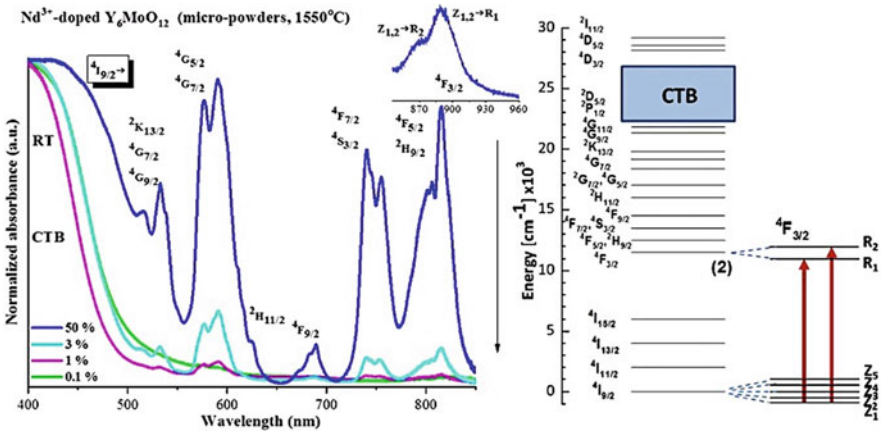

Fig. 11.18 Absorption spectra at RT for Nd^{3+}-doped Y_6MoO_{12} micro-crystalline powders obtained by reaction in the solid state at 1550 °C

Absorption Spectra Figure 11.18 presents the absorption spectra at RT of Nd^{3+}-doped Y_6MoO_{12} micro-crystalline powders in the spectral range from 400 to 900 nm (VIS and NIR). All absorption lines are assigned to the transitions from the $^4I_{9/2}$ ground state to the excited states. The transition from $^4I_{9/2}$ ground state to $^2P_{1/2}$ excited state at around 425 nm, used as a structural probe, is not observed for Nd^{3+}-doped Y_6MoO_{12} molybdates due to the fact that it is covered by the low-lying CTB with a maximum at 380 nm, between orbitals 2p of O^{2-} and 4d of Mo^{6+}. In the entire spectral range for all concentrations the spectra consists of broad weakly resolved bands. The insert in Fig. 11.18 presents the $^4I_{9/2} \rightarrow {}^4F_{3/2}$ transition, which can play a role as a structural probe due to the doublet of the $^4F_{3/2}$ state. For $^4I_{9/2} \rightarrow {}^4F_{3/2}$ transition, two maxima can be distinguished on a very wide band, due to both the nano-size of grains and the disorder of the Y_6MoO_{12} molybdate, composed of two Stark components R_1 and R_2 of the $^4F_{3/2}$ level, located at 867.8 nm ($Z_{1,2} \rightarrow R_2$) and 888.6 nm ($Z_{1,2} \rightarrow R_1$), respectively, assuming Z_1 and Z_2 very closed. The energy gap of the $^4F_{3/2}$ doublet was estimated as 253 cm^{-1}. The most intense band in the spectra with a maximum at and 590.7 nm corresponds to the hypersensitive $^4I_{9/2} \rightarrow {}^4G_{5/2}, {}^2G_{7/2}$ transitions. It is clearly visible that the intensity ratio between two bands in the NIR spectral ranges 710–778 nm and 778–838 nm and that in the range 550–617 nm changes with increasing Nd^{3+} concentration. For the sample doped with small amount of Nd^{3+} ion the ratio equal to 1:2 indicates high symmetry of the system, while it changes and becomes almost 1:1 with increasing of the Nd^{3+} concentration in the host lattice. Just like before observed variation suggests that symmetry of the system is reduced when one adds more and more activator ions into the matrix.

In conclusion, absorption broad bands confirm Nd^{3+} multisites and then the disordered structure of Nd^{3+}-doped Y_6MoO_{12} network appears with the presence

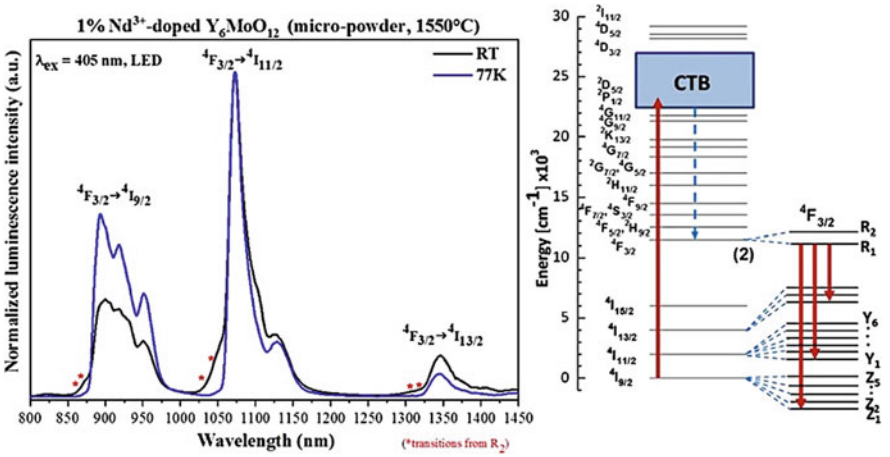

Fig. 11.19 Room and low temperature emission spectra of 1 mol% Nd^{3+}-doped Y_6MoO_{12} micro-crystalline powder (obtained at 1550 °C). Non-selective excitation by LED source, $\lambda_{ex} = 405$ nm into the charge transfer band (CTB)

of several polyhedra of coordination around Nd^{3+} ions when six Y^{3+} ions are substituting by much bigger Nd^{3+} ones.

Luminescence Properties Luminescent properties of micro-crystalline Nd^{3+}-doped Y_6MoO_{12} were studied by using non-selective excitation sources i.e. LED into the charge transfer band (CTB) and site selective excitation by using the high resolution of the tunable Ti:Sapphire laser to excite directly into f-f level of Nd^{3+} ion.

Emission Spectra Under Non-selective Excitation Figure 11.19 presents room and low temperature emission spectra of 1 mol% Nd^{3+}-doped Y_6MoO_{12} micro-crystalline powder (obtained at 1550 °C) under excitation by LED, $\lambda_{ex} = 405$ nm into the charge transfer band (CTB). As we can see, three broad bands corresponding to the transitions from R_1 Stark component of $^4F_{3/2}$ excited level to the three lower levels i.e. $^4I_{9/2}$ (850–975 nm), $^4I_{11/2}$ (1025–1175 nm) and $^4I_{13/2}$ (1300–1400 nm) were observed. For all samples the most intense transition is $^4F_{3/2} \rightarrow {}^4I_{11/2}$ one, which possesses two well visible maxima located at 1072.2 and 1128.2 nm, the third component at 1101.5 nm visible in the form of broadening of the most intense band. For $^4F_{3/2} \rightarrow {}^4I_{9/2}$ transition four components are clearly formed at 893.1, 901.4, 917.8, 952 nm, while for $^4F_{3/2} \rightarrow {}^4I_{11/2}$ transition only one visibly formed maximum at 1347 nm is observed. The highest peak is the highest energetic one and intensities of other lines decrease, gradually shifting to longer wavelengths. At room temperature some weak shoulders of the bands before each maximum of three main transitions in the spectral region 857.2–876.3 nm, 1031.5–1054.4 nm and 1296.1–1321.5 nm (marked in the Figure as red stars) are corresponding to the transitions from R_2 Stark component of $^4F_{3/2}$ excited level to the levels of the ground state.

These bands are disappearing at 77 K, what confirm that they represent the transition from the higher energy Stark component of the $^4F_{3/2}$ excited state of one Nd^{3+} site. Together with a lowering of the temperature to the liquid nitrogen one, the emission bands stay very broad, bandwidths are practically unchanged at RT and 77 K, what points out a big large disorder in the structure.

Emission Spectra Under Site Selective Excitation Site selective spectroscopy technique was performed at 77 K for the micro-crystalline sample (obtained at 1550 °C) with the small concentration of 0.5% Nd^{3+} ion. Figure 11.20a) presents the spectral region from 870 to 920 nm and the $^4F_{3/2} \rightarrow {}^4I_{9/2}$ transition under different excitation lines (806–822 nm) of tunable Ti:Sapphire laser into the $^4F_{5/2}$ and $^2H_{9/2}$ levels. Figure 11.20b) shows the spectral region from 1050 to 1090 nm of $^4F_{3/2} \rightarrow {}^4I_{11/2}$ transition under different excitation lines from 874 to 896 nm into $^4F_{3/2}$ level. In Fig. 11.20a), one can see that changing the excitation line leads to excite different sites of Nd^{3+} ions and to shift the position of the maxima around 885 nm. The envelop of all these lines forms a wide band, as it was observed in Fig. 11.19 under non-selective excitation. The same interpretation can be made in Fig. 11.20b). According to the group theory, the $^4F_{3/2}$ multiplet splits into Kramer's doublet and $^4I_{9/2}$ splits into 5 levels so that 5 peaks should appear between the $^4F_{3/2}$ lowest level and the $^4I_{9/2}$ ground state when the degeneracy is completely removed. In case of Nd^{3+}-doped Y_6MoO_{12} providing the exact number of components of $^4F_{3/2} \rightarrow {}^4I_{9/2}$ transition is impossible, but the observed phenomena without a doubt confirms the inhomogeneous distribution of Nd^{3+} ions in the Y_6MoO_{12} host lattice. In turn, very narrow well-resolved maxima at 892.2, 894.7 and 914.2 nm that appear after excitation at 891.5 nm originated from traces of Nd^{3+}-doped Y_2O_3 present in 0.5% Nd^{3+}-doped Y_6MoO_{12}. Very similar results were obtained for the $^4F_{3/2} \rightarrow {}^4I_{11/2}$ transition in the spectral range 1050–1090 nm, where under excitation with different lines (874–896 nm) of tunable Ti:Sapphire laser into the $^4F_{3/2}$ level different Nd^{3+} sites emit and then form a wide band with shifted maxima. Narrow lines located at 1073.7 nm and 1078.1 nm originated from traces of Nd^{3+}-doped Y_2O_3 present in 0.5% Nd^{3+}-doped Y_6MoO_{12}. An excellent proof for this hypothesis is presented in Fig. 11.21.

Evidence of Some Traces of Nd^{3+}-Doped Y_2O_3 from the Emission Spectra Under Site Selective Excitation Thanks to the high resolution of the tunable Ti:Sapphire laser at $\lambda_{ex} = 891.5$ nm ($Z_1 \rightarrow R_1$), a very well-resolved emission spectrum was recorded. The good quality of obtained results allowed us to designate energies for individual levels (see Fig. 11.21). An accurate analysis of the designated energies and comparison with the energies reported by Kaminski [89] for Nd^{3+}-doped Y_2O_3 ($^4F_{9/2}$: 0, 29, 267, 447, 643 cm^{-1}; $^4F_{11/2}$: 1897, 1935, 2147,2271, 2331, 2359 cm^{-1}; $^4F_{13/2}$: 3814, 3840, 4093 cm^{-1} and $^4F_{3/2}$: 11208, 11,404 cm^{-1}) allowed us without any doubt to confirm the presence of some traces of Nd^{3+}-doped Y_2O_3 in this molybdate. Most probably this observation is a result of the starting decomposition of Y_6MoO_{12} into Y_2O_3 and MoO_3 at temperature above 1500 °C, followed by a sublimation of MoO_3, even with an amount lower than 1% to obtain cubic Y_6MoO_{12}. Such effect has already observed with the similar composition of

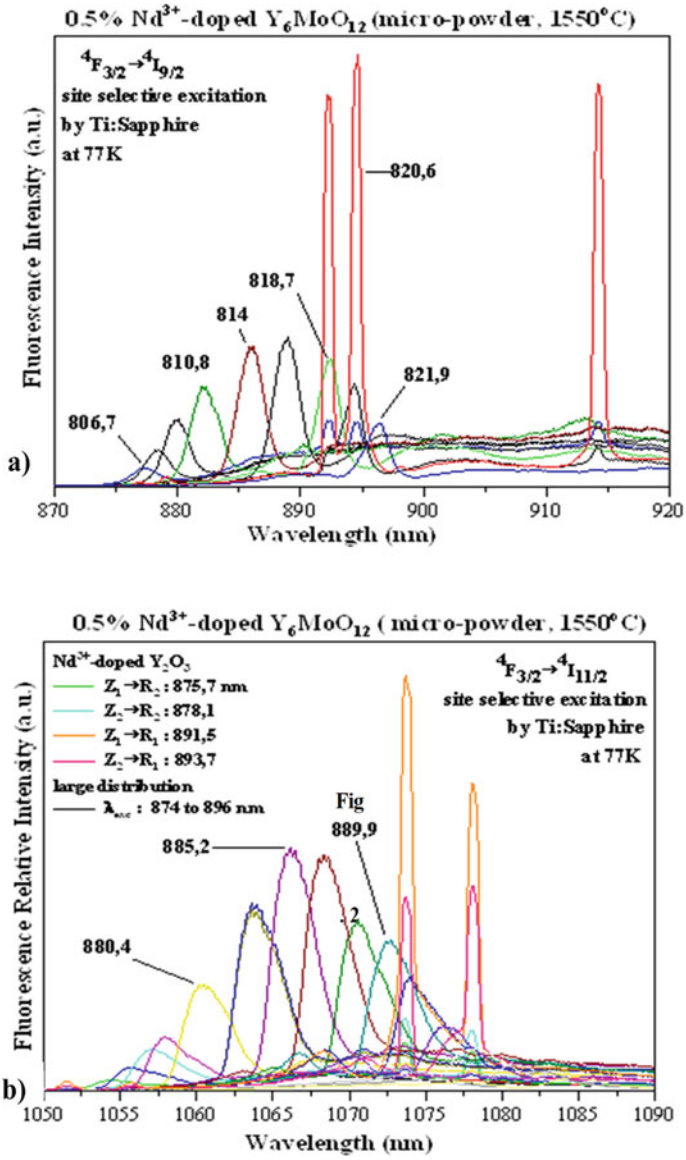

Fig. 11.20 Low temperature emission spectra of 0.5 mol% Nd^{3+}-doped Y_6MoO_{12} microcrystalline powder (obtained at 1550 °C) under site selective excitation by using of the high resolution of the tunable Ti:Sapphire laser. Figure (**a**) presents the $^4F_{3/2} \rightarrow {}^4I_{9/2}$ transition in the spectral range 870–920 nm and (**b**) the $^4F_{3/2} \rightarrow {}^4I_{11/2}$ one in the spectral range 1050–1090 nm

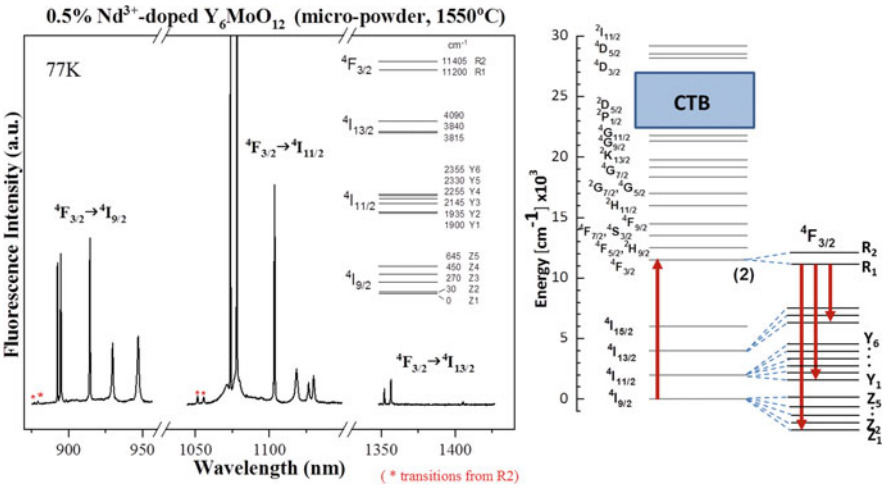

Fig. 11.21 Low temperature emission spectra of traces of Nd^{3+}-doped Y_2O_3 in 0.5 mol% Nd^{3+} – doped Y_6MoO_{12} micro-crystalline powder (obtained at 1550 °C) under site selective excitation thanks to the high resolution of the tunable Ti:Sapphire laser at $\lambda_{ex} = 891.5$ nm

Yb_6MoO_{12} [90]. We should emphasize here the powerful use of the site selective excitation with the tunable Ti: Sapphire laser of high resolution with respect to XRD technique to detect some traces of Y_2O_3 phase in the host compound.

Decays Curves of Nd^{3+}-Doped Y_6MoO_{12} and of Nd^{3+}-Doped Y_2O_3 Phase Decay measurements with calculated integrated luminescence decay times of the $^4F_{3/2}$ excited state of Nd^{3+} ions in cubic Y_6MoO_{12} micro-powdered solid solutions were performed at room temperature and at 77 K under the site selective excitation of a pulsed OPO laser at $\lambda_{ex} = 595$ nm. The monitored emission was $\lambda_{em} = 1070$ nm of the $^4F_{3/2} \rightarrow {}^4I_{11/2}$ transition, that is to say the laser transition if the sample is used as laser material. Figure 11.22 presents decays curves collected at room temperature. As we can see it, the decay curves are not exponential. For the samples with the Nd^{3+} ion concentrations lower that 2 mol% the non-exponentiality is the result of the multisite effect and for higher concentrations there is a strong concentration quenching due to the energy transfer between Nd^{3+} ions recorded at room temperature and 77 K. Practically in all cases the decay times are longer at low temperature.

The strong concentration quenching is confirmed by decreasing the values of luminescence decay times from 146 μs for 0.1 mol% to 19 μs for 5 mol%.

As we already proved it in the previous paragraph, we confirm the micro-crystalline obtained by solid state reaction at 1550 °C contains the traces of Nd^{3+}-doped Y_2O_3 for which the decay curves are seen in Fig. 11.23 into selective excitation in coherence with the radiative lifetime of bulky 0.1% Nd^{3+}-doped Y_2O_3 of 310 μs [52].From the detection of this new phase on rare earth-doped yttrium

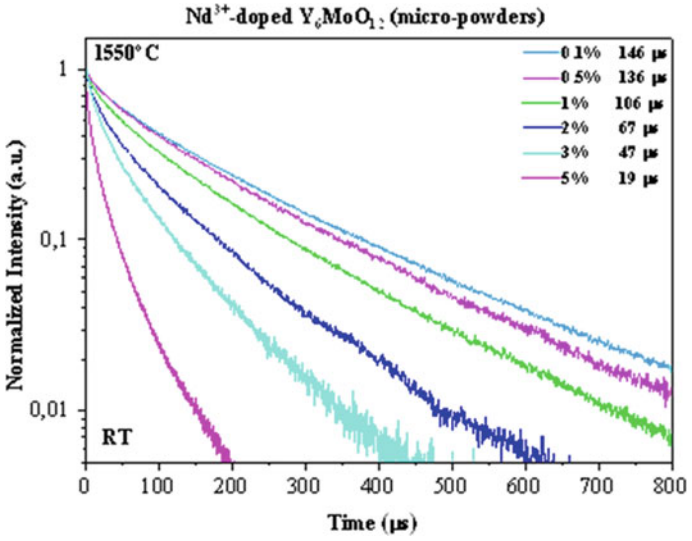

Fig. 11.22 Room temperature decays curves of the $^4F_{3/2}$ excited state for Nd^{3+}- doped Y_6MoO_{12} under site selective excitation of a pulsed OPO pulsed laser at $\lambda_{ex} = 595$ nm. The monitored emission is $\lambda_{em} = 1070$ nm of the $^4F_{3/2} \rightarrow {}^4F_{11/2}$ transition

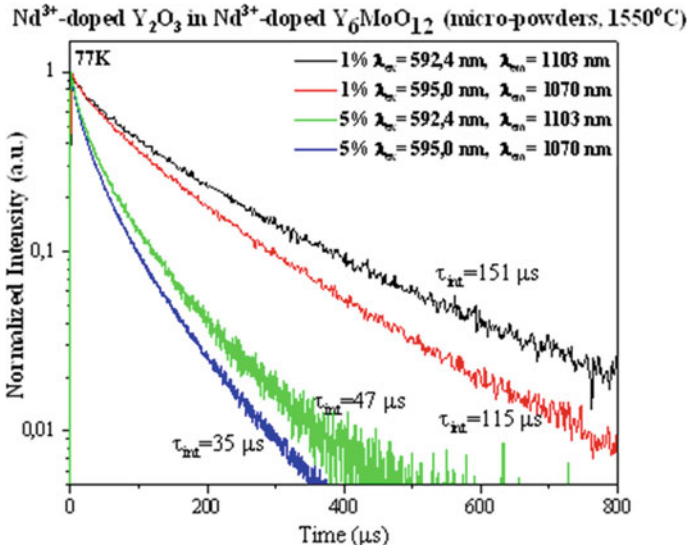

Fig. 11.23 The concentration quenching observed for Nd^{3+}-doped Y_2O_3 in 1 mol% and 5 mol% Nd^{3+}-doped Y_6MoO_{12}. Site selective excitation has been applied with a pulsed OPO pulsed laser either at $\lambda_{ex} = 592{,}4$ nm or $\lambda_{ex} = 595$ nm by monitoring the $^4F_{3/2} \rightarrow {}^4F_{11/2}$ transition either at $\lambda_{em} = 1070$ nm or $\lambda_{em} = 1103$ nm

oxides which is generally not reported in literature by XRD diagram, one can suggest to check them by site selective spectroscopy to be sure of the purity of the studied phase.

11.7 Summary

Some examples of Nd^{3+} probe ions embedded in various oxide crystal lattices, which have been used during our research of new transparent ceramics, have been analyzed in detail. Each of the following structures like cubic Lu_2O_3 sesquioxide, tetragonal scheelite-type $CdMoO_4$, monoclinic/cubic $La_2Mo_2O_9$ as well as cubic Y_6MoO_{12} pointed out specific local symmetries and even a parasitic phase for the last one. This choice gives us the opportunity to show the great interest of, both, low-temperature high-resolution techniques like absorption spectroscopy at 4.2 K and site-selective tuneable laser spectroscopy at 77 K and, in addition for some of them, to show also the coupling with microscopy techniques. The main conclusions can be summarized as follows:

In cubic Lu_2O_3, the selective laser technique has been powerful to reveal both Nd^{3+} C_2 and C_{3i} isolated centers. However, optical transitions are mainly recorded from C_2 non-centro symmetric centers, associated with electric-dipole induced type transitions of much higher probability than magnetic-dipole transitions of C_{3i} symmetry center with the additional argument that the population is three times higher than those of the C_{3i} centers. In addition of the C_2 sites, the C_2-C_2 and C_2-C_{3i} pairs have been detected. An important result is the location of the $^4F_{3/2}$ (R_1) level of C_{3i} sites at 116 cm^{-1} of higher energy than that of C_2 sites. This evaluation has confirmed a general one with rare earth (Eu^{3+}, Sm^{3+}, Yb^{3+})-doped sesquioxides.

For synthesized via solid state reaction $Cd_{1-3x}Nd_{2x}\square_xMoO_4$ stable solid solution crystallizing in a tetragonal symmetry with the space group $I4_1/a$ we succeeded to precise vacancy compositions. Absorption and emission spectra suggest presence of at least a double distribution of Nd^{3+} sites with D_{2d} point symmetry slightly deformed, most probably due to two main positions of $\square$ cationic vacancies around Nd^{3+} pairs. Promising optical parameters have been evaluated.

As an example, in tetragonal 5%-doped $Cd_{1-3x}Nd_{2x}\square_xMoO_4$ with $N_0 = 6.5 \times 10^{20}$ Nd^{3+} ions per cm^3, the absorption cross-section is equal to 1.44×10^{-19} cm^2 (at $\lambda = 804.8$ nm), which is a value twice higher than that of Nd:YAG (0.77 x 10^{-19} cm^2) with $N_0 = 1.1 \times 10^{20}$ Nd^{3+} ions per cm^3. Under commercial LED excitation at 588 nm used to pump the $^4I_{9/2} \rightarrow {}^4G_{5/2}$, $^2G_{7/2}$ hypersensitive absorption transitions, well adapted for the excitation of both 3 mol% Nd^{3+}-doped $Cd_{1-3x}Nd_{2x}\square_xMoO_4$ and 0.8 at% Nd^{3+}-doped $Y_3Al_5O_{12}$ optimized samples, the comparison of the integral emission intensities of the transitions shows values eight and half times (for $^4F_{3/2} \rightarrow 4I_{9/2}$ transition) and nine times (for $^4F_{3/2} \rightarrow 4I_{9/2}$

transition) higher and with broader lines for the molybdates than for YAG:Nd^{3+} as a probe of the interest of this material.

Much broader both absorption and emission bands observed for Nd^{3+}-doped $La_2Mo_2O_9$ (LAMOX) solid solutions suggest quite big disordering of the active ions in the structure. The number of components observed mainly for $^4I_{9/2} \rightarrow {}^4F_{3/2}$ absorption transitions at 4.2 K suggests that Nd^{3+} ion in this lattice occupy at least two main distributions of sites, both in monoclinic structure as well as in cubic one precisely in relationships with two LaO_8 and LaO_7 polyhedra. The multisite character was also confirmed in the high resolution site selective emission spectra, where the number of Stark components is higher than that expected for the compound with the lowest symmetry site. Indeed, the comparative analysis of the luminescence properties reveals only subtle differences in the shape of the emission lines when the structure changes from monoclinic to cubic one. Under commercial LED excitation at 588 nm used to pump the $^4I_{9/2} \rightarrow {}^4G_{5/2}$, $^2G_{7/2}$ hypersensitive absorption transitions, well adapted for the excitation of both 3% Nd^{3+} (3.2 x 10^{20} ions/cm^3) Nd^{3+}-doped $La_2Mo_2O_9$ and 0.8% Nd^{3+} (1.1 x 10^{20} ions/cm^3)-doped $Y_3Al_5O_{12}$ optimized samples, the comparison of the integral emission intensities of the transitions shows values five times (for $^4F_{3/2} \rightarrow {}^4I_{9/2}$ transition) and four times (for $^4F_{3/2} \rightarrow {}^4I_{11/2}$ transition) higher for the molybdates than for YAG:Nd^{3+} as a probe of the interest of this material.

Site selective spectroscopy technique with using different excitation lines of the tunable Ti:Sapphire laser into the $^4F_{5/2}$ and $^2H_{9/2}$ levels and the $^4F_{3/2}$ level at 77 K applied for Nd^{3+}-doped Y_6MoO_{12} micro-crystalline solid solutions obtained at 1550 °C allowed us to let appear the different emitting Nd^{3+} multisite. A very important result was obtained in this compound thanks to the use of the selective laser excitation: in addition to the broad lines, very narrow lines were also observed under a specific excitation line evidencing traces of Nd^{3+}- doped Y_2O_3 phase interpreted as starting from the decomposition of Y_6MoO_{12} into Y_2O_3 and MoO_3 at temperature above 1500 °C, followed by a sublimation of MoO_3. Also, the multisite effect in Nd^{3+}-doped Y_6MoO_{12} and the traces of Nd^{3+}-doped Y_2O_3 were confirmed by the analysis of the luminescence lifetimes and not pointed out by the usual XRD technique.

Both short lifetimes and high emission intensities observed for molybdates under instigation suggest that the compounds investigated here could be especially promising for an ultra-short pulse laser generation.

The real difficulty of the spectroscopic analysis of Nd^{3+}-doped molybdates comes from the lack of precise structural data, which could be improved by the growth of single crystals with the hope to get laser materials and the advantage to have the possibility to transform the cubic phase into transparent ceramics.

Acknowledgements The research was supported by the National Science Centre of Poland (NCN) under grant HARMONIA 8 No UMO-2016/22/M/ST5/00546. This work was also developed within the scope of the project POLONIUM from the Polish National Agency for Academic Exchange (NAWA) as well as the Ministries of Europe and Foreign Affairs (MEAE) and Higher Education, Research and Innovation (MESRI), for scientific exchange between Institute Light

Matter (iLM), University Claude Bernard Lyon1 in France and Faculty of Chemistry, University of Wroclaw in Poland. Also help of the French Embassy in Warsaw (French Government scholarship for research stages of M. Guzik, M. Sobota and P. Sobota) at UCBLyon1 is gratefully acknowledged.

References

1. Chani VI, Yoshikawa A, Fukuda T (1999) Growth of $Y_3Al_5O_{12}$: Nd fiber crystals by micro-pulling-down technique. J Cryst Growth 204:155–162
2. Ikesue A, Furusato I, Kamata KJ (1995) Fabrication of polycrystalline, transparent YAG ceramics by a solid-state reaction method. Am Ceram Soc 78:225–228
3. Bishop B (2009) Northrop Grumman scales new heights in electric laser power achieves 100 kW from a solid-state lase. Globe Newswire
4. Lupei V (2009) Ceramic laser materials and the prospect for high power lasers. Opt Mater 31(5):701–706
5. Sanghera J, Kim W, Villalobos G, Shaw B, Baker C, Frantz J, Sadowski B, Aggarwal I (2013) Ceramic laser materials: past and present. Opt Mater 35:693–699
6. Ikesue A, Aung YL, Lupei V (2013) Ceramic lasers. Cambridge University, New York
7. Kong LB, Huang Y, Que W, Zhang T, Li S, Zhang J, Dong Z, Tang D (2015) Transparent ceramics. Springer
8. Goldstein A, Krell A (2016) Transparent ceramics at 50: progress made and further prospects. J Am Ceram Soc 99(10):3173–3197
9. Esposito L, Epicer T, Serantoni M, Piancastelli A, Alderighi D, Pirri A, Toci G, Vannini M, Anghel S, Boulon G (2012) Integrated analysis of non-linear loss mechanisms in Yb:YAG ceramics for laser applications. J Eur Ceram Soc 32:2273–2281
10. Yagi H, Yanagitani T, Takaichi K, Ueda K, Kaminskii AA (2007) Characterizations and laser performances of highly transparent Nd^{3+}:$Y_3Al_5O_{12}$ laser ceramics. Opt Mater 29:1258–1262
11. Epicier T, Boulon G, Zhao W, Guzik M, Jiang B, Ikesue A, Esposito L (2012) Spatial distribution of the Yb^{3+} rare earth ions in $Y_3Al_5O_{12}$ and Y_2O_3 optical ceramics as analyzed by TEM. J Mater Chem 22:18221–18229
12. Zhao W, Anghel S, Mancini C, Amans D, Boulon G, Epicier T, Shi Y, Feng XQ, Pan YB, Chani V, Yoshikawa A (2011) Ce^{3+} dopant segregation in $Y_3Al_5O_{12}$ optical ceramics. Opt Mater 33:684–687
13. Pejchal J, Babin V, Beitlerova A, Kucerkova R, Panek D, Barta J, Cuba V, Yamaji A, Kurosawa S, Mihokova E, Ito A, Goto T, Nikl M, Yoshikawa A (2016) Luminescence and scintillation properties of $Lu_3Al_5O_{12}$ nanoceramics sintered by SPS method. Opt Mater 53:54–63
14. Li J, Sah S, Groza M, Pan Y, Burger A, Kenarangui R, Chen W (2017) Optical and scintillation properties of Ce^{3+}-doped LuAG and YAG transparent ceramics: a comparative study. J Am Ceram Soc 100:150–156
15. Lu J, Takaichi K, Uematsu T, Shirakawa A, Musha M, Ueda K, Yagi H, Yanagitani T, Kaminskii AA (2002) Promising ceramic laser material: highly transparent Nd^{3+}:Lu_2O_3 ceramic. Appl Phys Lett 81(23):4324–4326
16. Fukabori A, Chani V, Pejchal J, Kamada K, Yoshikawa A, Ikegami T (2011) Fundamental optical constants of Nd-doped Y_2O_3 ceramic and its scintillation characteristics. Opt Mater 34:452–456
17. Futami Y, Yanagida T, Fujimoto Y, Pejchal J, Sugiyama M, Kurosawa S, Yokota Y, Ito A, Yoshikawa A, Goto T (2013) Optical and scintillation properties of Sc_2O_3, Y_2O_3 and Lu_2O_3 transparent ceramics synthesized by SPS method. Radiat Meas 55:136–140
18. An L, Ito A, Zhang J, Tang D, Goto T (2014) Highly transparent Nd^{3+}:Lu_2O_3 produced by spark plasma sintering and its laser oscillation. Opt Mater Express 4(7):1420–1426

19. Alombert-Goget G, Guyot Y, Guzik M, Boulon G, Ito A, Goto T, Yoshikawa A, Kikuchi M (2015) Nd^{3+}-doped Lu_2O_3 transparent sesquioxide ceramics elaborated by the spark plasma sintering (SPS) method. Part 1: structural, thermal conductivity and spectroscopic characterization. Opt Mater 41:3–11
20. Toci G, Vannini M, Ciofini M, Lapucci A, Piri A, Ito A, Goto T, Yoshikawa A, Ikesue A, Alombert-Goget G, Guyot Y, Boulon G (2015) Nd^{3+}-doped Lu_2O_3 transparent sesquioxide ceramics elaborated by the spark plasma sintering (SPS) method. Part 2: first laser output results and comparison with Nd^{3+}-doped Lu_2O_3 and Nd^{3+}-Y_2O_3 ceramics elaborated by a conventional method. Opt Mater 41:12–16
21. Krsmanović Whiffen RM, Bregiroux D, Viana B (2017) Nanostructured Y_2O_3 ceramics elaborated by spark plasma sintering of nanopowder synthesized by PEG assisted combustion method: the influence of precursor morphological characteristics. Ceram Int 43:15834–15841
22. Sanghera J, Kim W, Villalobos G, Shaw B, Baker C, Frantz J, Sadowski B, Aggarwal I (2012) Ceramic laser materials. Materials 5:258–277
23. Sh Akchurin M, Basiev TT, Demidenko AA, Doroshenko ME, Fedorov PP, Garibin EA, Gusev PE, Kuznetsov SV, Krutov MA, Mironov IA, Osiko VV, Popov PA (2013) CaF_2:Yb laser ceramics. Opt Mater 35:444–450
24. Aubry P, Bensalah A, Gredin P, Patriarche G, Vivien D, Mortier M (2009) Synthesis and optical characterizations of Yb-doped CaF_2 ceramics. Opt Mater 31:750–753
25. Li W, Mei B, Song J (2015) Nd, Yb^{3+}-co-doped SrF_2 laser ceramics. Opt Mater 47:108–111
26. du Merac MR, Kleebe H-J, Mueller MM, Reimanis IE (2013) Fifty years of research and development coming to fruition; unraveling the complex interactions during processing of transparent magnesium aluminate ($MgAl_2O_4$) spinel. J Am Ceram Soc 96(11):3341–3365
27. Valiev D, Khasanov O, Dvilis E, Stepanov S, Polisadova E, Paygin V (2018) Luminescent properties of $MgAl_2O_4$ ceramics doped with rare earth ions fabricated by spark plasma sintering technique. Ceram Int 44(17):20768–20773
28. Chen CF, Doty Ronald FP, Houk JT, Loutfy Heather RO, Volz M, Yang P (2010) Characterizations of a hot pressed polycrystalline spinel:Ce scintillator. J Am Ceram Soc 93(8):2399–2402
29. Mirov S, Fedorov V, Moskalev I, Martyshkin D, Kim C (2010) Progress in Cr^{2+} and Fe^{2+} doped mid-IR laser materials. Laser Photonics Rev 4:121–141
30. Higashi Y, Nakao H, Shirakawa A, Ueda K, Kaminskii AA, Kuretake S, Kintaka Y, Murayama K, Tanaka N (2015) Femtosecond mode-locked Nd^{3+}-doped Ba (Zr,Mg,Ta)O_3 ceramic laser. Opt Lett 40(16):3818–3821
31. Kuretake S, Tanaka N, Kintaka Y, Kageyama K, Nakao H, Shirakawa A, Ueda K, Kaminskii AA (2014) Nd-doped Ba(Zr,Mg,Ta)O_3 ceramics as laser materials. Opt Mater 36(3):645–649
32. Wen Z, Ma C, Zhao C, Tang F, Cao Z, Cao Z, Yuan X, Cao Y (2018) Fabrication and optical properties of Pr^{3+} −doped Ba (Sn, Zr,Mg,Ta)O_3 transparent ceramic phosphor. Opt Lett 43(11):2438–2441
33. Boulon G, Metrat G, Muhlstein N, Brenier A, Kokta MR, Kravchik L, Kalisky Y (2003) Efficient diode-pumped Nd:$KGd(WO_4)_2$ laser grown by top nucleated floating crystal metho**d**. Opt Mater 24:377–383
34. Brenier A, Bourgeois F, Metrat G, Muhlstein N, Boulon G (2001) Spectroscopic properties at 1.351 μm of Nd^{3+}-doped $KY(WO_4)_2$ and $KGd(WO_4)_2$ single crystals for Raman conversion. Opt Mater 16:207–211
35. Merat G, Muhlstein N, Brenier A, Boulon G (1997) Growth by the induced nucleated floating crystal (INFC) method and spectroscopic properties of $KY_{1-x}Nd_x(WO_4)_2$ laser materials. Opt Mater 8:75–82
36. Silvestre O, Pujol MC, Gueell F, Aguilo M, Diaz F, Brenier A, Boulon G (2007) Crystal growth and spectroscopic analysis of codoped (Ho,Tm):$KGd(WO_4)_2$. Appl Phys B Lasers Opt 87(1):111–117
37. Pujol MC, Guell F, Mateos X, Gavalda J, Sole R, Massons J, Aguilo M, Diaz F, Boulon G, Brenier A (2002) Crystal growth and spectroscopic characterization of Tm^{3+}-doped $KYb(WO_4)_2$ single crystals. Phys Rev B Condens Matter 66(14):144304-1–144304-8

38. Guzik M, Alombert-Goget G, Guyot Y, Pejchal J, Yoshikawa A, Ito A, Goto T, Boulon G (2016) Spectroscopy of C_{3i} and C_2 sites of Nd^{3+}-doped Lu_2O_3 sesquioxide either as ceramics or crystal. J Lumin 169:606–611
39. Guzik M, Tomaszewicz E, Guyot Y, Legendziewicz J, Boulon G (2015) Structural and spectroscopic characterizations of new $Cd_{1-3x}Nd_{2x}\square_xMoO_4$ scheelite-type molybdates with vacancies as potential optical materials. J Mater Chem C 3:4057–4069
40. Guzik M, Bieza M, Tomaszewicz E, Guyot Y, Boulon G (2014) Development of Nd^{3+}-doped monoclinic Dimolybdates $La_2Mo_2O_9$ as optical materials. Z Naturforsch 69b:193–204
41. Guzik M, Bieza M, Tomaszewicz E, Guyot Y, Zych E, Boulon G (2015) Nd^{3+} dopant influence on the structural and spectroscopic properties of microcrystalline $La_2Mo_2O_9$ molybdate. Opt Mater 41:21–31
42. Sobota M, Sobota P, Bieza M, Guzik M, Tomaszewicz E, Guyot Y, Boulon G (2019) Influence of synthesis route and grain size on structural and spectroscopic properties of cubic Nd^{3+}-doped Y_6MoO_{12} nano and micro-powders as optical materials. Opt Mater 90:300–314
43. Novoselov A, Yoshikawa A, Fukuda T (2004) The micro-pulling-down method: fast and economic solution for materials screening. Curr Top Cryst Growth Res 7:87–111
44. Yoshikawa A, Nikl M, Boulon G, Fukuda T (2007) Challenge and study for developing of novel single crystalline optical materials using micro-pulling-down method. Opt Mater 30:6–10
45. Zagumennyi AI, Mikhailov VA, Shcherbakov IA (2004) Rare earth ion lasers –Nd^{3+}. In: Webb CE, Jones JDC (eds) Handbook of laser technology and applications, vol. II: laser design ad laser systems. Institute of Physics Publishing, Bristol\Philadelphia
46. Guillot-Noël O, Viana B, Bellamy B, Gourier D, Zogo-MBoulou GB, Jandl S (2000) Spectroscopic evidence of inhomogeneous distribution of Nd^{3+} in YVO_4, YPO_4 and $YAsO_4$ crystals. Opt Mater 13:427–437
47. Guzik M, Siczek M, Lis TA, Pejchal J, Yoshikawa A, Ito A, Goto T, Boulon G (2014) Structural investigations of Lu_2O_3 as single crystal and polycrystalline transparent ceramic. Cryst Growth Des 14:3327–3334
48. Ikesue A (2002) Polycrystalline Nd:YAG ceramics lasers. Opt Mater 19:183–187
49. Sanghera J, Bayya S, Villalobos G, Kim W, Frantz J, Shaw B, Sadowski B, Miklos R, Baker C, Hunt M, Aggarwal I, Kung F, Reicher D, Peplinski S, Ogloza A, Langston P, Lamar C, Varmette P, Dubinskiy M, Sandre LDE (2011) Transparent ceramics for high-energy laser systems. Opt Mater 33:511–518
50. Lupei A, Lupei V (2003) RE^{3+} pairs in garnets and sesquioxides. Opt Mater 24:181–189
51. Boulon G, Lupei V (2007) Energy transfer and cooperative processes in Yb^{3+}-doped cubic sesquioxide laser ceramics and crystals. J Lumin 125:45–54
52. Lupei A, Lupei V, Taira T, Sato Y, Ikesue A, Gheorghe C (2003) Energy transfer processes of Nd^{3+} in Y_2O_3 ceramics. J Lumin 102–1032:72–76
53. Boulon G (1971) Photoluminescence processes in bismuth ion activated polycrystalline rare earth oxides and orthovanadates, J. Phys. (Paris) 32, 333–347; Boulon, G.; Pedrini, C.; Guidoni, M.; Pannel, Ch.: kinetics of the bismuth(3+) ion luminogenic centers in crystals, J. Phys.(Paris) 36(3), 267–278 (1975)
54. Boulon G, Gaume-Mahn F, Pedrini C, Jacquier B, Janin J, Curie D (1973) Luminescence processes in bismuth (3+) centers. Lumin Cryst Mol Solut:530–537
55. Schamps J, Flament JP, Real F, Noiret I (2003) Ab initio simulation of photoluminescence: Bi^{3+} in Y_2O_3 (S_6 site). Opt.Mater 24:221–230
56. Réal F, Ordejón B, Vallet V, Flament J-P, Schamps J (2009) Improvement of the *ab initio* embedded cluster method for luminescence properties of doped materials by taking into account impurity induced distortions: the example of Y_2O_3:Bi^{3+}. J Chem Phys 131:194501–194517
57. Buijs M, Meyerink A, Blasse G (1987) Energy transfer between Eu^{3+} ions in a lattice with two different crystallographic sites:Y_2O_3:Eu^{3+}, Gd_2O_3:Eu^{3+} and Eu_2O_3. J Lumin 37:9–20
58. Zych E, Karbowiak M, Domagala K, Hubert S (2002) Analysis of Eu emission from different sites in Lu_2O_3. J Alloys Compd 341:381–384

59. Daldosso M, Sokolnicki J, Kepinski L, Legendziewicz J, Speghini A, Bettinelli M (2007) Preparation and optical properties of nanocrystalline Lu_2O_3:Eu^{3+} phosphors. J Lumin 120–123:858–861
60. Legendziewicz J, Sokolnicki J (2008) Spectroscopy and structural characteristic of Yb^{3+} and Nd^{3+} ions doped nanostructured Lu_2O_3 and sol–gel derived silica host materials. J Alloys Compd 451:600–605
61. Petermann K, Huber G, Forniasero L, Kuch S, Mix E, Peters V, Basun SA (2000) Rare-earth-doped sesquioxides. J Lumin 87–89:973–975
62. Guyot Y, Guzik M, Alombert-Goget G, Pejchal J, Yoshikawa A, Ito A, Goto T, Boulon G (2015) Assignment of Yb^{3+} energy levels in the C_2 and C_{3i} centers of Lu_2O_3 sesquioxide either as ceramics or ascrystal. J Lumin 170:513–519
63. Lupei A, Lupei V, Gheorghe C (2013) Electronic structure of Sm^{3+} ions in YAG and cubic sesquioxide ceramics. Opt Mater 36:419–424
64. Gheorghe C, Lupei A, Voicu T, F.M., C. (2014) Emission properties and site occupation of Sm^{3+} ion doped Lu_2O_3 translucent ceramics. J Alloys Compd 588:388–393
65. Minowa M, Itakura K, Moriyama S, Ootani W (1992) Measurement of the property of cooled Lead Molybdate as a scintillator. Nucl Instrum Methods Phys Res, Sect A 320:500–503
66. Sczancoski JC, Bomio MDR, Cavalcante LS, Joya MR, Pizani PS, Varela JA, Longo E, Li S, Andrés JA (2009) Morphology and blue photoluminescence emission of $PbMoO_4$ processed in ConventionalHydrothermal. J Phys Chem C 113:5812–5822
67. Hizhnyi YA, Nedilko SG (2003) Investigation of the luminescent properties of pure and defect Lead tungstate crystals by electronic structure calculations. J Lumin 102−103:688–693
68. Kudo, Steinberg MA, Bard J, Campion A, Fox MF, Mallouk TE, Webber SE, White JM (1990) Photoactivity of ternary Lead-group VIB oxides for hydrogen and oxygen evolution. Catal Lett 5:61–66
69. Chernov S, Deych R, Grigorieva L, Millers D (1997) Luminescence and transient optical absorption in $CdWO_4$. Mater Sci Forum 239:299
70. Godlewska P, Tomaszewicz E, Macalik L, Hanuza J, Ptak M, Tomaszewski PE, Maczka M, Ropuszynska-Robak P (2013) Correlation between the structural and spectroscopic parameters for $Cd_{1-3x}Gd_{2x}\square_xMoO_4$ solid solutions where, denotes cationic vacancies. Mater Chem Phys 139:890–896
71. Kobayashi M, Usuki Y, Ishii M, Yazawa T, Hara K, Tanaka M, Nikl M, Nitsch K (1997) Improvement in transmittance and decay time of PbWO4 scintillating crystals by La-doping. Nucl Instrum Methods Phys Res, Sect A 399:261
72. Kobayashi M, Yazawa T, Hara K, Tanaka M, Nikl M, Baccaro S, Cecilia A, Diemoz M, Dafinei I (1998) Improvement in radiation hardness of $PbWO_4$ scintillating crystals by La-doping. Nucl Instrum Methods Phys Res, Sect A 404:149–156
73. Guzik M, Tomaszewicz E, Guyot Y, Legendziewicz J, Boulon G (2015) Eu^{3+} luminescence from different sites in a scheelite-type cadmium molybdate red phosphor with vacancies. J Mater Chem C 3:8582–8594
74. Guzik M, Tomaszewicz E, Guyot Y, Legendziewicz J, Boulon G (2016) Spectroscopic properties, concentration quenching and Yb^{3+} site occupations in vacancied scheelite-type molybdates. J Lumin 169:755–764
75. Guzik M, Tomaszewicz E, Guyot Y, Legendziewicz J, Boulon G (2012) Structural and spectroscopic characterizations of two promising Nd-doped monoclinic or tetragonal laser tungstates. J Mater Chem 22:14896
76. Georges S, Goutenoire F, Altorfer F, Sheptyakov D, Fauth F, Suard E, Lacorre P (2003) Thermal, structural and transport properties of the fast oxide-ion conductors $La_{2x}R_xMo_2O_9$ (R=Nd, Gd, Y). Solid State Ionics 161:231–241
77. Kuang W, Fan Y, Yao K, Chen Y (1998) Preparation and characterization of ultrafine rare earth molybdenum complex oxide particles. J Solid State Chem 140:354–360
78. Fournier JP, Fournier J, Kohlmuller R (1970) Étude de systèmes La_2O_3-MoO_3, Y_2O_3-MoO_3 et des phases Ln_6MoO_{12}. Bull Soc Chim Fr 12:4277

79. Lacorre P, Retoux R (1997) First direct synthesis by high energy ball milling of a new lanthanum Molybdate. J Solid State Chem 132:443–446
80. Goutenoire F, Isnard O, Retoux R, Lacorre P (2000) Crystal structure of $La_2Mo_2O_9$ a new fast oxide-ion conductor. Chem Mater 12:2575–2580
81. Goutenoire F, Isnard O, Suard E, Bohnke O, Laligant Y, Retoux R, Laccore P (2011) Structural and transport characteristics of the LAMOX family of fast oxide-ion conductors, based on lanthanum molybdenum oxide $La_2Mo_2O_9$. J Mater Chem 11:119–124
82. Arulraj A, Goutenoire F, Tabellout M, Bohnke O, Lacorre P (2002) Synthesis and charaterization of the anionic conductor system $La_2Mo_2O_{9-0.5x}F_x$ (x=0.02-0.3). Chem Mater 14:2492
83. Evans IR, Howard JAK, Evans JSO (2005) The crystal structure of α-$La_2Mo_2O_9$ and the structural origin of the oxide ion migration pathway. Chem Mater 17:4074–4077
84. Li H, Pu X, Yin J, Wang X, Yao S, Noh HM, Jeong JH (2016) Effect of crystallite size and crystallinity on photoluminescence properties and energy transfer of Y_6MoO_{12}:Eu. J Am Ceram Soc 99(3):954–961
85. Bieza M, Guzik M, Tomaszewicz E, Guyot Y, Boulon G (2017) Cubic Yb^{3+}-activated Y_6MoO_{12} micro-powder e optical material operating in NIR region. Opt Mater 63:3–12
86. Zhang X, Zhang Y, Gong H, Zhao X, Wang C, Zhu H (2013) Synthesis, characterization and optical properties of $Y_{6-x}Sm_xMoO_{12+\sigma}$ composite/compounds pigments with high near-infrared reflectance. Adv Mater Res 602-604:102–106
87. George G, Vishnu VS, Reddy MLP (2011) The synthesis, characterization and optical properties of silicon and praseodymium doped Y_6MoO_{12} compounds: environmentally benign inorganic pigments with high NIR reflectance. Dyes Pigments 88:109–115
88. Zhao X, Zhang Y, Huang Y, Gong H, Zhao J (2015) Synthesis and characterization of neodymium doped yttrium molybdate high NIR reflective nano pigments. Dyes Pigments 116:119–123
89. Kaminskii AA (1996) Crystaline lasers: Pysical processes and operating schemes. CRS Press
90. Schildhammer D, Fuhrmann G, Petschnig L, Penner S, Kogler M, Gotsch T, Schaur A, Weinberger N, Saxer A, Schottenberger H, Huppertz H (2016) Synthetic access to cubic rare earth molybdenum oxides $RE_6MoO_{12-\delta}$ (RE = Tm–Lu) representing a new class of ion conductors. Chem Mater 28:7487–7495

Chapter 12
Research of Efficient and Fast Scintillator Garnet Crystals: The Role of Ce^{4+} in Ce^{3+}, Mg^{2+}-Co-Doped $Gd_3Al_2Ga_3O_{12}$ from Spectroscopic and XANES Characterizations

Georges Boulon, Y. Guyot, Małgorzata. Guzik, G. Dantelle, D. Testemale, S. Kurosawa, K. Kamada, and A. Yoshikawa

Abstract In this lecture, two main goals have been shown: first, the state-of-art of the inorganic scintillator materials used for many important applications and, secondly, the illustration of the dynamics of this field by giving spectroscopic and scintillation properties of the most advanced oxide scintillator Ce^{3+}, Mg^{2+}-co-doped $Gd_3Al_2Ga_3O_{12}$ (GAGG) garnet host, grown by using both the micro-pulling-down (μ-PD) and the Czochralski methods at the Tohoku University, Sendai. The adopted strategy for optimization of garnet scintillator composition in both, the defect engineering and band gap engineering of this research program gives us the opportunity to discuss on the role of Ce^{4+} ion which has always been a challenge for Ce^{3+}-doped luminescent crystals. By analogy with the approach used for commercial Ce^{3+}, Mg^{2+}-co-doped-doped orthosilicates as Lu_2SiO_5 (LSO) and $(Lu_{1-x}Y_x)_2SiO_5$ (LYSO), we confirm the creation of stable Ce^{4+} oxidation state and we evaluate the Ce^{3+}/Ce^{4+} ratio of concentrations in Ce^{3+}, Mg^{2+}-co-doped $Gd_3Al_2Ga_3O_{12}$ (GAGG) garnet by XANES spectroscopy analysed at the Ce L_{III} threshold of the European Synchrotron Radiation Facility (ESRF) in Grenoble.

G. Boulon (✉) · Y. Guyot
Institut Lumière Matière (ILM), UMR5306 CNRS-UCB Lyon1, Université de Lyon, Villeurbanne, France
e-mail: georges.boulon@univ-lyon1.fr

M. Guzik
Faculty of Chemistry, University of Wroclaw, Wroclaw, Poland

G. Dantelle · D. Testemale
Institut NEEL, CNRS/UGA UPR2940, Grenoble, France

ESRF, European Synchrotron Radiation Facility, Grenoble, France

S. Kurosawa · K. Kamada · A. Yoshikawa
Institute for Material Research (IMR), Tohoku University, Sendai, Miyagi, Japan

M. Cesaria et al. (eds.), *Light-Matter Interactions Towards the Nanoscale*,
NATO Science for Peace and Security Series B: Physics and Biophysics,
https://doi.org/10.1007/978-94-024-2138-5_12

Keywords Fast scintillator · Ce^{3+} and Ce^{4+} dopants · Garnet crystals · Optical spectroscopy · XANES spectroscopy

12.1 Introduction

There is no direct detector of gamma rays, so that fast scintillator materials are needed to convert high energy radiation to UV-visible range. These spectral transformers of energy, combined with photodetectors (PM photomultipliers and photon avalanche diodes), convert also high energy photons and accelerated particles. Scintillators are categorized into liquid (water) at Kamiokande (Japan) to detect neutrinos, organic with a low light yield and mostly inorganic solids in usual applications of both, medical imaging techniques, computed tomography, nuclear cameras, gas exploration and in the advanced homeland security related techniques. Many properties are desired, such as high density, a high stopping power, a high efficiency for converting the energy of incident radiation into scintillation photons, a short rise time and a fast decay fallowing timing in PET coincidence measurements; an appropriate emission range at room temperature matching the spectral sensitivity of detectors, transparency to its own scintillation light and finally should be as cheap as possible [1]. Actually, the best scintillators are based on Ce^{3+} dopant in inorganic crystals, emitting 5d-4f transitions in the near UV and visible range with high yield, for which the parity-allowed electric dipole 5d-4f transitions have larger oscillator strengths and shorter radiative lifetimes than the 4f-4f transitions of the trivalent rare earth ions. In the last two decades, great R&D effort brought several new Ce^{3+}-doped material systems, namely the Ce^{3+}-doped orthosilicates as Gd_2SiO_5 (GSO), Lu_2SiO_5 (LSO), $(Lu_{1-x}Y_x)_2SiO_5$ (LYSO), pyrosilicates based on $RE_2Si_2O_7$ (RE = Lu, Y,Gd) and most recently LaX_3 (X = Cl, Br) single crystal hosts [2–12].

The main goal of this lecture delivered at Erice's School is to show, with the concern of a pedagogical way, the approach applied at IMR, Sendai, on Ce^{3+}-doped oxide materials based on garnet structure for scintillator applications. Indeed, garnet crystals are promising candidates due to well-mastered technology already developed for laser hosts and other applications. In addition, as the optimization of garnet scintillators needs to be co-doped with Ce^{3+} and Mg^{2+} cations, we also demonstrate the importance of the presence of Ce^{4+} in these garnets we have confirmed by XANES characterization.

12.2 Strategy for Optimization of Garnet Scintillator Composition in the Defect Engineering and Band Gap Engineering

Garnet structure single crystals of $\{A_3\}[B_2](C_3)O_{12}$ formula show a good optical transparency, are not hygroscopic and are easily doped by trivalent Ce^{3+} rare-earth cation in the $\{A_3\}$ dodecahedral site (Fig. 12.1). As an example, the intense yellow emission of Ce^{3+}-doped $Y_3Al_5O_{12}$ (YAG) is very well-known and used in white light-emitting diodes under excitation by a blue diode.

Especially, the Ce^{3+}-doped $Lu_3Al_5O_{12}$ (LuAG) single crystal was shown to be a prospective scintillator material with a relatively high density of 6.7 g/cm^3, a fast scintillation response of about 60–80 ns, due to the $5d^1$-4f radiative transition of Ce^{3+} providing the emission around 500–550 nm easily detected by PMs, and light yield of about 25,000 photons/MeV [13].

However, the Ce^{3+} $5d^1 \rightarrow 4f$ luminescence is quenched in these garnets because of positioning of the Ce^{3+} 5d states in the host conduction band, which is a well-known problem in luminescent materials. At this point we should remind some interpretation of the interaction of high energy excitation with luminescent centers in insulators [2].

The scintillation processes can be divided into schematical stages as seen in Fig. 12.2:

(i) conversion of the absorbed high energy photon by the material creating a primary electron by photoelectric effect (below approximately a few hundred

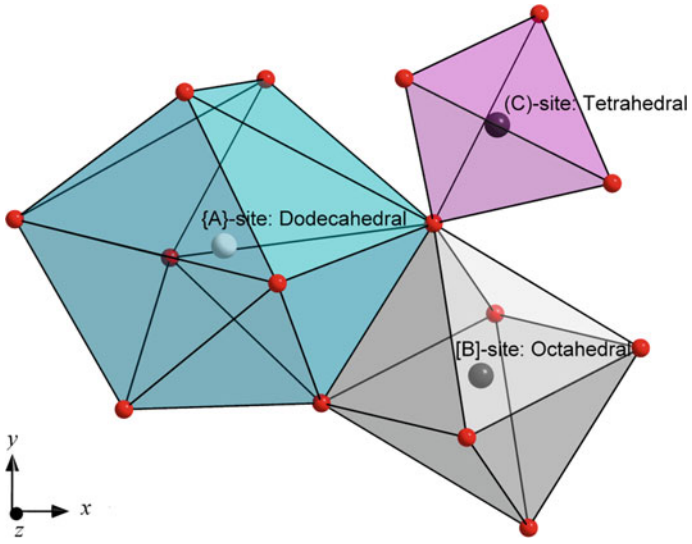

Fig. 12.1 Structure of $\{A_3\}[B_2](C_3)O_{12}$ stoichiometric garnets ($Ia\bar{3}d$ space group)

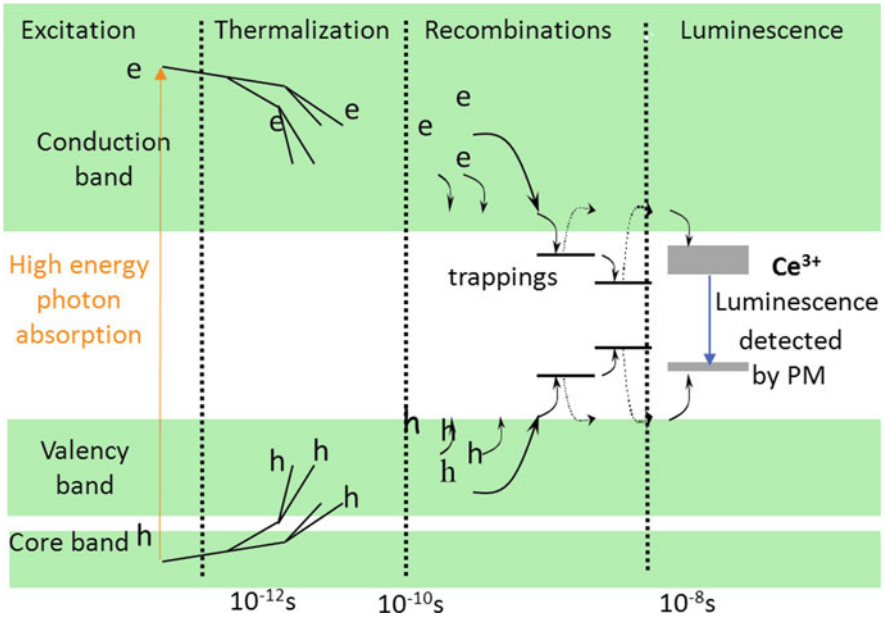

Fig. 12.2 Scintillation processes in insulators characterized by a wide band gap of few eV between the valency band and the conduction band. Time scale have been mentioned

keV), then Compton scattering (from a few hundred keV to 8000 keV) and electron-hole pair (e-h) production and their thermalization,

(ii) diffusion of (e–h) pairs according to $Ce^{3+} + e^- + h^+$ (hole trapping) $\rightarrow Ce^{4+} + e^-$ (electron trapping) $\rightarrow$ leading to Ce^{3+} in an excited state $(Ce^{3+})^*$ (Fig. 12.3) and trapping effects of an electron by non-radiative recombination due to the presence of defects. In Ce^{3+}-doped LuAG, the shallow electron traps associated to antisite Lu_{Al} defects are typical defects in the melt-grown garnet crystals [14, 15], responsible for major part of slow decay components.

(iii) radiative recombination 5d $\rightarrow$ 4f by the luminescent Ce^{3+} dopant,

(iv) finally, $Ce^{3+} + h^+ \rightarrow Ce^{4+}$ corresponding again to an hole trapping for another cycle.

Indeed, scintillation performance of Ce^{3+}-doped LuAG is strongly degraded by shallow electron traps which delay an energy delivery to the Ce^{3+} emission centers and give rise to intense slow components in the scintillation response [16].

Then, the main objective of the strategy consists to eliminate these unwanted traps by working out the ideal chemical formula of the garnet composition. Improvement of the properties of scintillators from the composition of the multi-component Ce^{3+}-doped $(Gd\text{-}Lu)_3(Ga\text{-}Al)_5O_{12}$ garnet leads to a successful result [17–19]. The substitution phenomena in the garnet structure of Al^{3+} sites with Ga^{3+} ones and of Lu^{3+} sites with Gd^{3+} ones have been studied by solidification of corresponding stoichiometric melts taking advantage of flexibility, time saving,

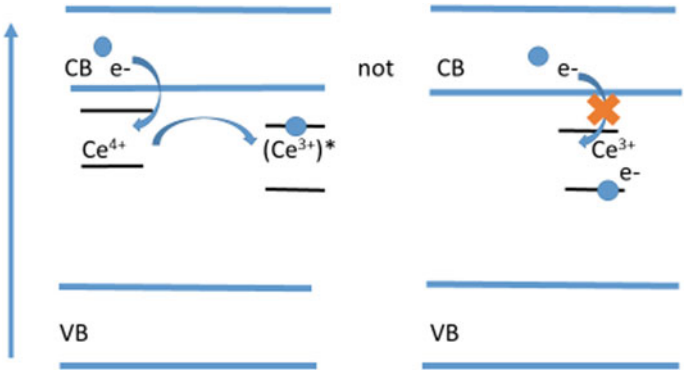

Fig. 12.3 Mechanism of trapping of an electron (blue circle) from the conduction band to Ce^{4+} ion for which levels are localized in the band gap, giving rise to the Ce^{3+} ion in an excited state $(Ce^{3+})^*$ (at left side). In order to well understand the process with Ce^{4+} ion, let's say that an electron from the conduction band can't occupy the 5d excited state of the Ce^{3+} state, since for this Ce^{3+} ion, an electron is already in the 4f ground state (at right side)

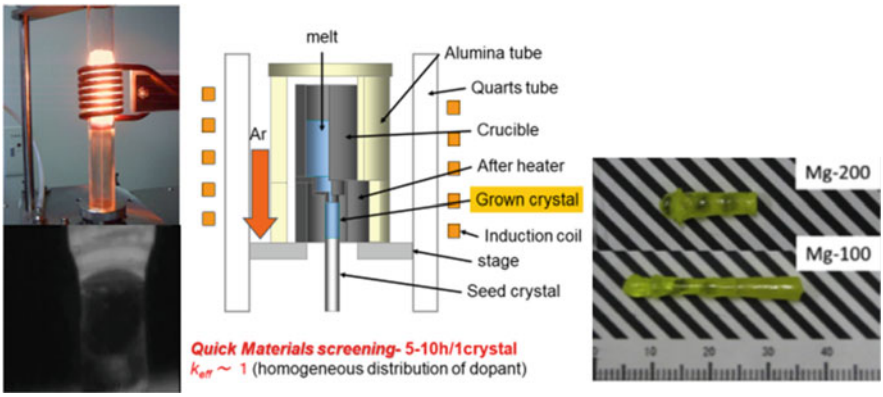

Fig. 12.4 Crystal growth of garnet crystals by the micro-pulling-down technique and examples of Ce^{3+}, Mg^{2+}-co-doped GAGG single crystals grown by K. Kamada at IMR (Sendai, Japan)

and cost-effective character of the micro-pulling-down technique (Fig. 12.4) [20]. Then, the Czochralski (Cz) technique (Fig. 12.5) is used for larger crystals when the formula is known.

It has been demonstrated by combination of the «band-gap engineering» and «$5d^1$-level positioning» strategies, using the Ga^{3+} and Gd^{3+} alloying into the LuAG structure, it is possible to diminish a negative effect of shallow traps mentioned above and to keep a sufficient energy gap between the $5d^1$ excited state level of Ce^{3+} and the bottom of the conduction band to prevent an unwanted thermally induced excited-state ionization at room temperature [21]. Consequently, an enormous enhancement of the light yield is obtained for tailored material compositions. Doped by Ce^{3+}, the Gd^{3+} and Ga^{3+} rich host compositions of Ce^{3+}-doped $Gd_3Al_2Ga_3O_{12}$

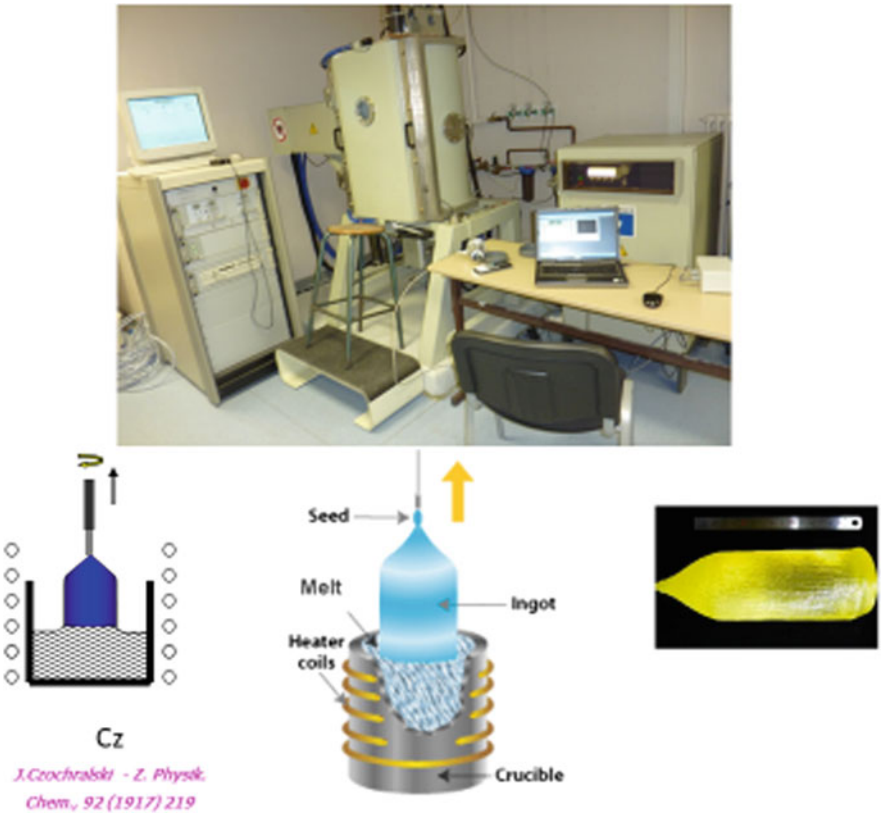

Fig. 12.5 Crystal growth of garnets by the Czochralski technique. Set-up of K. Lebbou at ILM, Lyon, France. Example of 2 inch size 1% Ce^{3+}-doped $Gd_3Al_2Ga_3O_{12}$ (GAGG) garnet single crystal grown by K. Kamada at IMR, Tohoku University, Sendai, Japan

(GAAG) single crystal show amazingly high light yield up to 50,000 photon/MeV which is the value exceeding by 30–40% the best Ce^{3+}-doped LYSO materials ever seen and decay time∼ 90 ns at emission around 520 nm and density of 6.63 g/cm^3 [15, 16].

The result of material design and tailoring is shown in Fig. 12.6: adjusting the Ga content enables one toadmixture lowers further the position of the $5d^1$ level of Ce^{3+} acting on it in an opposite way with respect to the Ga admixture, which secures sufficient separation of the 5d1 level from the bottom of the conduction band of the host even for Ga-rich compositions [17].

Another important scintillation performance has to be analyzed. This is the improvement of scintillation by co-doping with divalent alkali earth ions had been already shown in Ce activated scintillators such as, Ce, Ca^{2+}-co-doped LSO and Ce, Ca^{2+}-co-doped LYSO [22, 23].

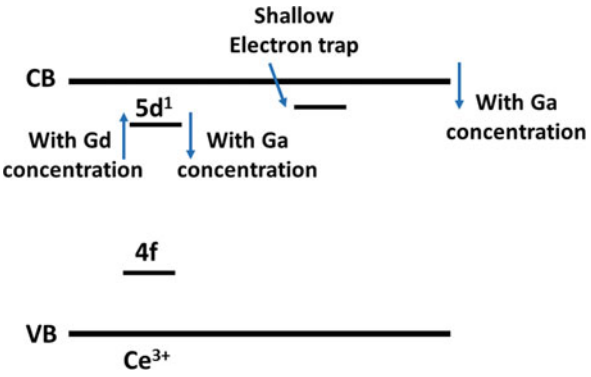

Fig. 12.6 Strategy of the defect engineering and band gap engineering. Evolution of the Ce^{3+} energy levels and shallow traps in the band gap related to Ce^{3+}-doped garnet crystals. VB and CB are abbreviations of valence and conduction bands, respectively

In order to still improve the time response properties and the light yield of several types of garnet scintillators like Ce^{3+}-doped $Lu_3Al_5O_{12}$ (LuAG) single crystals and ceramics [24], and Ce^{3+}-doped $Gd_3Al_2Ga_3O_{12}$ (GAAG) [25–28], an approach has been made by co-doping with divalent alkali earth elements such as Ca^{2+} and Mg^{2+} ions, changing the Ce^{3+} valence state into the Ce^{4+} one by the charge compensation mechanism which achieves charge neutrality:

$$Gd^{3+} + Gd^{3+} \rightarrow Mg^{2+} + Ce^{4+}$$

Such centers create another fast radiative recombination pathway working in parallel with the classical mechanism based on the stable Ce^{3+} centers. Ce^{4+} can be seen as a pre-prepared ion ready to trap a free electron directly from the conduction band leading to excited Ce^{3+} and their radiative recombination. In co-doped crystals, it has been seen that oxygen vacancies decrease, IR absorption spectra and thermoluminescence spectra vanished meaning a decreasing of traps below the conduction band. In this lecture, such an approach has been mainly shown by selecting Ce, Mg^{2+}-co-doped GAGG single crystal [29] for which crystal growths, spectroscopic properties and assignment of scintillation mechanisms are presented as below.

12.3 Crystal Growth and Spectroscopic Properties of Ce^{3+}-Doped GAGG and Ce, Mg^{2+}-Co-Doped GAGG Single Crystals

12.3.1 Crystal Growth

We analysed here 4 single crystals: 0.5% Ce^{3+}-doped GAGG, 1% Ce^{3+}-doped GAGG, 1% Ce^{3+}, 0.1% Mg^{2+}-co-doped GAGG and 0.5% Ce^{3+}, 0.5% Mg^{2+}-co-doped GAGG grown by the Czochralski (Cz) method with a radio frequency

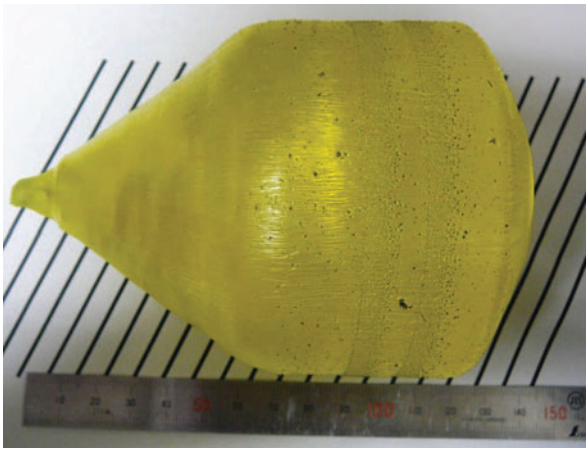

Fig. 12.7 Garnet single crystal: 3 inch diameter of 1% Ce^{3+}, 0.1% Mg^{2+}-co-doped $Gd_3Al_2Ga_3O_{12}$ (GAGG) garnet single crystal grown by the Czochralski (Cz) method at IMR, Tohoku University, Sendai, Japan

heating system. Typical growth rates were 0.9 mm/min and the diameter was around 75 mm. Crystals were grown from a 150 mm diameter Ir crucible under the N_2 with 1% O_2 atmosphere. The seed crystals were <100> oriented Ce^{3+}-doped GAGG crystals. Figure 12.7 presents 3 in. size of Ce^{3+}, Mg^{2+}-co-doped GAGG single crystal. Plates of 5 mm × 5 mm × 1 mm were cut and polished for the absorption and luminescence spectra measurements, while the rest of the rods were used for the chemical composition analyses. Quantitative chemical analyses of the crystals for the Mg, Ce, Al, Ga and Gd content along the radius and growth direction were performed by the Electron Probe Micro Analysis (EPMA; JXA-8621MX, JEOL). The Mg concentration in the crystal was determined by the Inductively Coupled Plasma Atomic Emission Spectroscopy (ICP-AES) [28].

12.3.2 Absorption Spectra

The absorption spectra of 0.5% Ce^{3+}-doped GAGG and 0.5% Ce^{3+}, 0.5% Mg^{2+}-co-doped GAGG crystals are presented in Fig. 12.8. We clearly see the two first Ce^{3+} 4f ($^2F_{5/2}$) → $5d^1$ (E′1) and 4f ($^2F_{5/2}$) → $5d^1$ (E″1) absorption bands at roughly 450 and 340 nm, respectively, the Gd^{3+} 4f $^8S_{7/2}$ → ^6P_J, ^6I_J absorption lines and, especially in the co-doped crystal, the strong absorption band assumed to be the Ce^{4+} charge transfer band (CTB) below 320 nm.

We have mentioned the $4f^7$ ($^8S_{7/2}$➔^6P_J,^6I_J) absorption lines of Gd^{3+} ion and the two first 4f ($^2F_{5/2}$) → $5d^1$ (E'_1) and 4f ($^2F_{5/2}$) → $5d^1$ (E''_1) absorption bands of Ce^{3+} ion.

This CTB is assigned from the oxygen 2p orbitals of the valence band to the Ce^{4+} 4f orbitals by analogy with Ce^{3+}, Mg^{2+}/Ca^{2+}-co-doped LYSO [22, 23] and also with Ce^{3+}, Mg^{2+}-co-doped $Lu_3Al_5O_{12}$ (LuAG) ceramics [24]. The hole in the maximum of this broad absorption band at around 275 nm corresponds to the

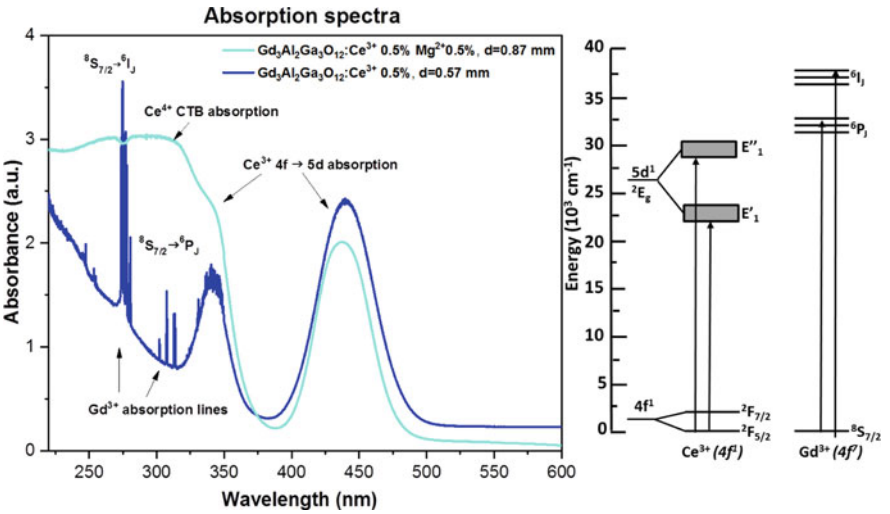

Fig. 12.8 Absorption spectra at room temperature of the 0.5% Ce^{3+}-doped GAGG and 0.5% Mg^{2+}, 0.5% Ce^{3+}-co-doped GAGG crystals. 3 types of absorption are recorded: CTB of Ce^{4+}, $4f^7 \rightarrow 4f^7$ of Gd^{3+} ion and $4f^1 \rightarrow 5d^1$ of Ce^{3+} ion. On the right, simplified energy level diagrams for both Gd^{3+} and Ce^{3+} ions

resonant energy transfer between the Gd^{3+} $^6I_J \rightarrow {}^8S_{7/2}$ emission lines and the Ce^{4+} charge transfer broad absorption band which corresponds as a result to a non-radiative energy transfer since Ce^{4+} centers do not emit [29].

12.3.3 Radioluminescence

Radioluminescence spectra under excitation by X-rays from CuKα of the Ce^{3+}-doped GAGG and Ce^{3+}, Mg^{2+} co-doped GAGG are shown in Fig. 12.9. This broad visible band is indeed composed of the two usual transitions $5d^1$ (E′1) → 4f ($^2F_{5/2}$) and $5d^1$ (E′1) → 4f ($^2F_{7/2}$) splitted by around 2000 cm^{-1} according to the energy level diagram represented at the right side of Fig. 12.9.

It is important to mention the decrease of the Ce^{3+} emission intensity by Mg^{2+} co-doping as a result of the probable creation of Ce^{4+} in these crystals and then the reduction of Ce^{3+} active centers [28].

12.3.4 Scintillation Decays

Scintillation decays of the $5d^1$ (E′1) excited level from the $5d^1$ (E′1) → 4f ($^2F_{5/2}$) and $5d^1$ (E′1) → 4f ($^2F_{7/2}$) visible broad bands of 1% Ce^{3+}-doped GAGG (0%

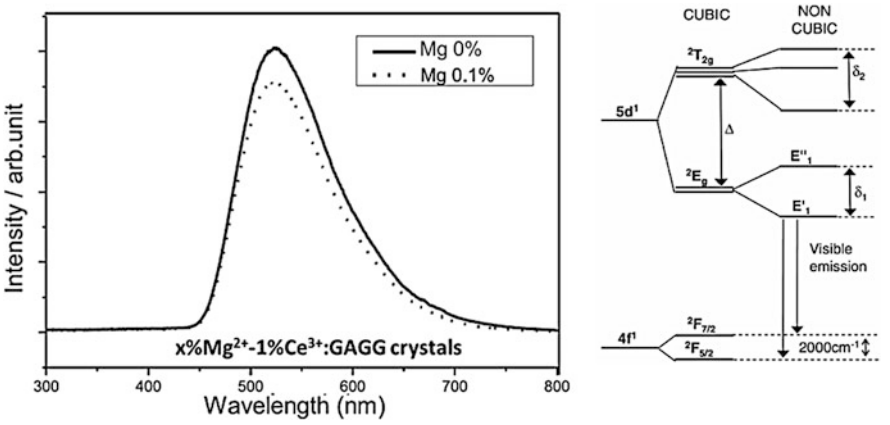

Fig. 12.9 Radioluminescence spectra at room temperature of the $5d^1$ (E′1) → 4f ($^2F_{5/2}$) and $5d^1$ (E′1) → 4f ($^2F_{7/2}$) transitions of Ce^{3+} in 1% Ce^{3+}:GAGG (0% Mg^{2+}) and 0.1% Mg^{2+}, 1% Ce^{3+}-co-doped GAGG crystals. Excitation by X-rays, CuKa, 40 kV, 30 mA. On the right, a complete diagram of Ce^{3+} energy levels is shown with the splitting of the ground state and the first $5d^1$ excited state

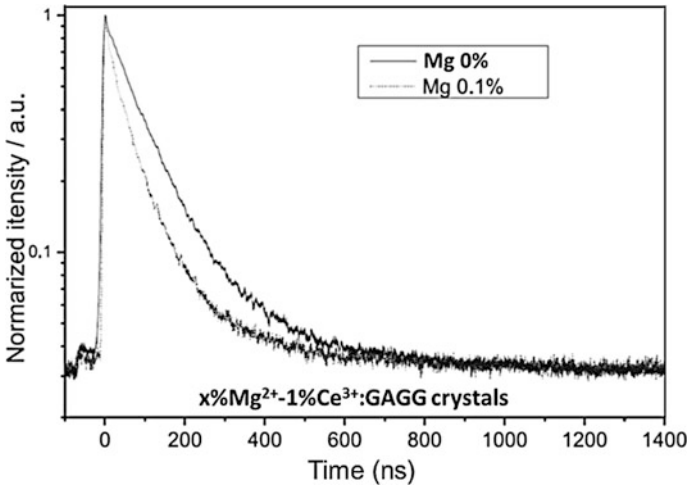

Fig. 12.10 Shortening of the scintillation decay at room temperature of the $5d^1$ (E′1) excited level from the $5d^1$ (E′1) → 4f ($^2F_{5/2}$) and $5d^1$ (E′1) → 4f ($^2F_{7/2}$) visible broad bands of the 1% Ce^{3+},0.1% Mg^{2+} co-doped GAGG crystal with respect of 1% Ce^{3+}-doped GAGG (0% Mg^{2+}) crystal, under excitation by ^{137}Cs radio-isotope (662 keV)

Mg) and 1% Ce^{3+},0.1% Mg^{2+} co-doped GAGG crystals under excitation by ^{137}Cs radio-isotope (662 keV) are shown in Fig. 12.10.

Decay profiles can be fitted by two exponentials, corresponding to the fast and slow radiative recombination of the Ce^{3+} emitting centers. The most prominent observation is the shortening of the scintillation decay-time after Mg^{2+} co-doping.

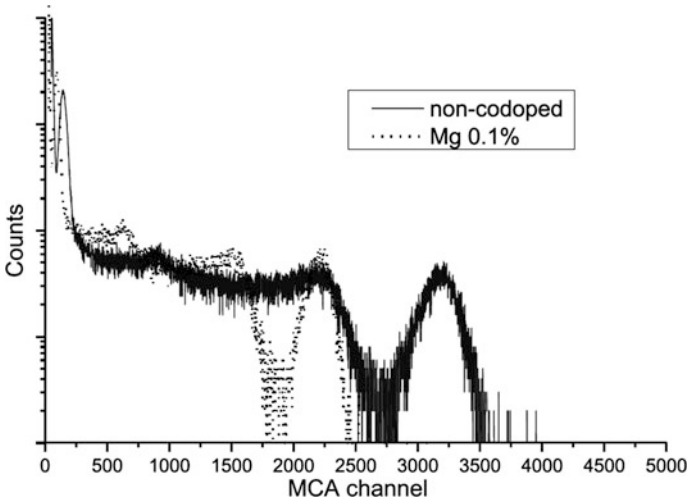

Fig. 12.11 Energy spectra of 1% Ce^{3+}-doped GAGG and 1% Ce^{3+}, 0.1% Mg^{2+} co-doped GAGG crystals. Excitation by 137Cs radioisotope (662 keV)

Without Mg^{2+}, 1% Ce^{3+}-doped GAGG is characterized by 92.2 ns decay time (81%) and in 1% Ce^{3+}, 0.1% Mg^{2+} co-doped GAGG 58% the scintillation decay time was enormously accelerated and decreased down to 45.2 ns (58%) and 135 ns (42%) [28].

12.3.5 Gamma-Ray Response

The Pulse height spectra of 1%Ce^{3+}-doped GAGG and 1% Ce^{3+}, 0.1% Mg^{2+}co-doped GAGG excited by 662 keV gamma-ray of 137Cs at room temperature and measured using the PMT are shown in Fig. 12.11. Light output was decreasing with increasing Mg^{2+} concentration. Light yield of the co-doped sample showed 79% (44,000 photon/MeV) of light output comparing with Ce^{3+}-doped GAGG standard (56,000 photon/MeV) [28].

12.3.6 Time Resolution

The timing resolution for a pair of 3 mm × 3 mm × 3 mm size samples were conducted using the Si-PMs. Timing resolution was improved from 452 ps in 1% Ce^{3+}-doped GAGG to 196 ps in 1% Ce^{3+}, 0.1% Mg^{2+} co-doped GAGG (Fig. 12.12). At the same set-up LYSO standard (Saint Gobain) showed 180 ps of timing resolution. Obtained results indicated promising potential of 1% Ce^{3+}, 0.1% Mg^{2+}

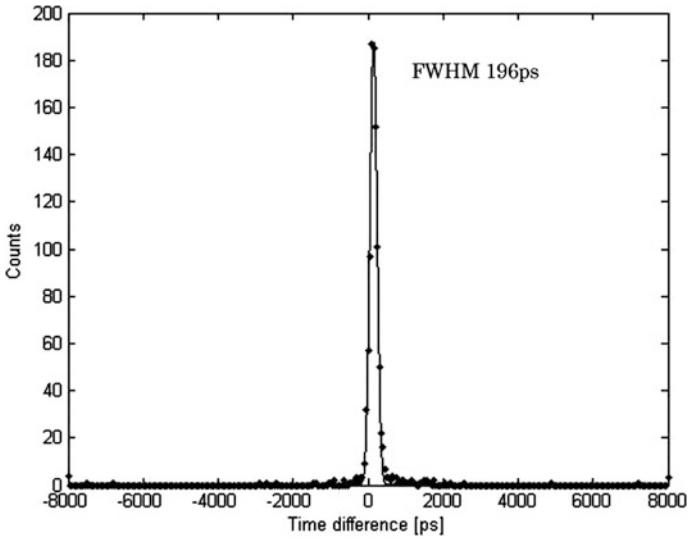

Fig. 12.12 Timing resolution measurement in 1% Ce^{3+}, 0.1%Mg^{2+} co-doped GAGG crystal

co-doped GAGG for application of positron emission tomography (PET) [28]. Consequently, the previous results show that the most advanced garnet scintillator appear to be 1% Ce^{3+},0.1% Mg^{2+} co-doped GAGG crystal which performs better than other garnet like Ce^{3+}-doped GAGG and also Ce^{3+}, Ca^{2+}-co-doped GAGG crystals.

12.4 Role of Ce4+ Cations in the Scintillation Mechanism

The presence of Ce^{4+} ions in Ce^{3+}-doped materials has always been a big issue. Ce^{4+} is unwanted in phosphors but it is researched as well for Ce^{3+}-doped orthosilicates as for Ce^{3+}-doped garnets applied for scintillators. As a result, Ce^{4+} ions are stabilized by the addition of Mg^{2+} divalent ions [25–28].

We should precise the role of Ce^{4+} in the scintillation mechanism, confirm the real presence evaluate the Ce^{3+}/Ce^{4+} ratio by another technique than the optical absorption in UV range. The first basic work showing the presence of Ce^{4+} has been published in 1992 by Rotmann on Ce^{3+}, Ca^{2+}-co-doped YAG [30]. Optically, it has been determined that the cerium can change valence state between Ce^{3+} and Ce^{4+} when annealed in an atmosphere of reducing and oxidizing gases, respectively. Under cathodoluminescence, the Ce^{3+} ion emission is seen even when only Ce^{4+} is present in the oxidized crystal and it was interpreted as an electron first entering a Ce^{4+} in an upper excited 5d state, thereby converting it *temporarily* to Ce^{3+}, followed by the standard 5d → 4f emission of Ce^{3+} at 550 nm.

Then, in 2013, Blahuta & *al* [27] proposed, a new scintillation mechanism under ionizing irradiation involving Ce^{4+} ions in Ce^{3+}-Mg^{2+}/Ca^{2+}-co-doped LYSO single crystals [23].

Nowadays, in co-doped materials, the evidence of Ce^{4+} is admitted for the sequential charge capture of an electron-hole pair by Ce^{3+} according to:

$Ce^{3+} + e^- + h^+$ (hole trapping) $\rightarrow$ $Ce^{4+} + e^-$ (electron trapping) $\rightarrow$ leading to Ce^{3+} in an excited state $(Ce^{3+})^*$ (as it can be seen in Fig. 12.3) $\rightarrow$ $Ce^{3+} + h\nu$ (radiative de-excitation) $\rightarrow$ $Ce^{3+} + h^+ \rightarrow Ce^{4+}$ (hole trapping again for another cycle).

Then, there is a continuous process of capturing a hole from the valency band.

As a result, Ce^{4+} ions are stabilized by the addition of Mg^{2+}/Ca^{2+} divalent ions [14, 18, 20, 21]. Such centers create another fast radiative recombination pathway working in parallel with the classical mechanism based on the stable Ce^{3+} centers. It means the skipping of the first hole trapping stage could result in acceleration of the decay by suppression of slow components [31]. This observation has to be combined with the favorable position of the shallow levels below the conduction band leading to slow components of the decay. The main purpose of the Mg^{2+}/Ca^{2+}-co-dopant as analyzed by Melcher's group was to limit the formation of vacancies (Vo) that were detrimental in term of afterglow level [25, 26].

12.5 Evidence and Evaluation of Stable Ce^{4+} Ions by XANES Technique in Ce^{3+}, Mg^{2+}-Co-Doped GAGG

Previous articles considered that the charge transfer absorption band located at 260 nm is the probe of the presence of Ce^{4+} ions in Ce^{3+}, Mg^{2+}/Ca^{2+}-co-doped LYSO single crystals [23] and Ce^{3+}, Ca^{2+}-co-doped GAGG [22, 28]. This hypothesis seems in agreement with the creation of Ce^{4+} ions due to the introduction of divalent ions as Ca^{2+} and Mg^{2+}. However, the quantitative values of the Ce^{3+}/Ce^{4+} concentration ratio in Ce^{3+}, Mg^{2+}-co-doped GAGG have never been measured. Therefore, our goal is firstly focused on the confirmation of the presence of Ce^{4+} ions in this crystal and secondly on the evaluation of the Ce^{3+}/Ce^{4+} ratio measured by the X-ray Absorption Near Edge Spectroscopy (XANES) at the Ce L_{III} threshold which is another effective technique able to distinguish unambiguously the Ce^{3+} and Ce^{4+} oxidation states. Measurements have been made at the European Synchrotron Radiation Facility (ESRF) in Grenoble performed in High Energy Resolution Fluorescence-Detected (HERFD) mode at the Fame-UHD beamline. The photon energy was scanned from 5.68 to 5.85 keV using a Si (220) double-crystal monochromator. A glove box filled with helium was used between the samples, the crystal analyzer spectrometer and the detector, to avoid partial beam absorption by the air. The signal was recorded with a five-Ge (331) crystal analyzer and a Vortex-Ex detector. The beam size was $300 \times 100\ \mu m^2$ (horizontal

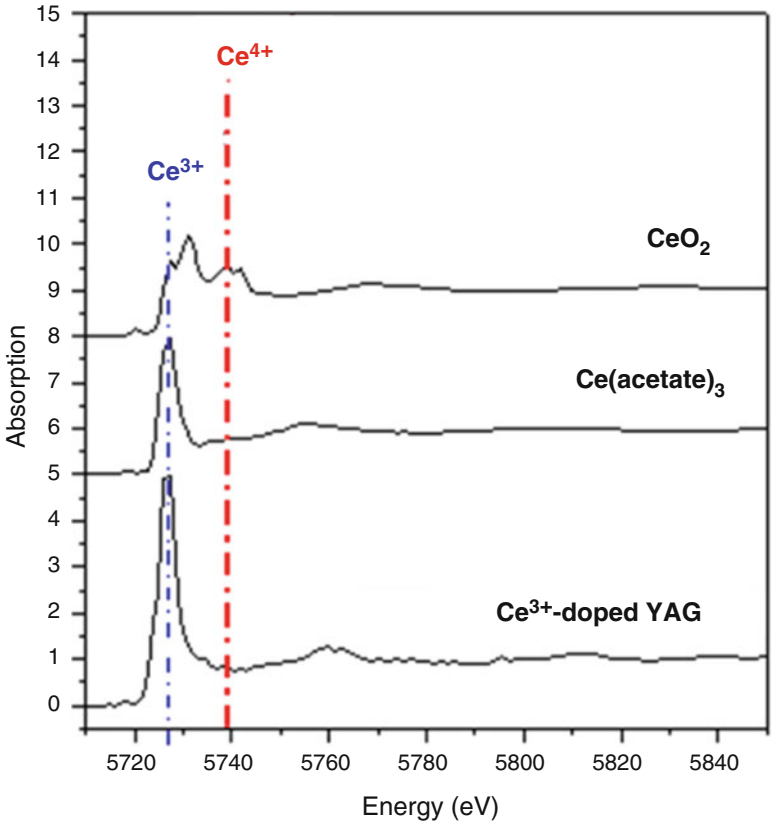

Fig. 12.13 The XANES spectroscopy at the Ce L_{III} threshold. X-ray absorption spectra of Ce^{3+} and Ce^{4+} are different. CeO_2 is chosen as a reference for Ce^{4+} (peak at 5738 eV) and either $Ce(acetate)_3$ or 0.5%Ce^{3+}-doped YAG are chosen as a reference for Ce^{3+} (peak at 5727 eV)

x vertical FWHM). The energy calibration was done using the CeO_2 spectrum. The Ce^{3+}/Ce^{4+} ratio was determined by linear combination of XANES spectra of standards, *i.e.* nano-CeO_2 as a reference for Ce^{4+} and another Ce^{3+}-doped YAG single-crystal as a reference for Ce^{3+} [32]. The experimental data were analyzed using the *Demeter/Athena* software [33]. We also have evaluated the Ce^{3+}/Ce^{4+} ratio by withdrawing ratio dependence of XANES spectra corresponding to different values of this ratio and compared with the experimental ones [29]. The Ce L_{III} threshold XANES spectra of $Ce(acetate)_3$ and Ce^{3+}-doped YAG as Ce^{3+} trivalent reference (characteristic peak at 5727 eV) and CeO_2 as Ce^{4+} tetravalent reference (characteristic peak at 5738 eV) are shown in Fig. 12.13. These two lines are enough dispersed to characterize each oxydation state.

The XANES experimental data can be seen for 0.5% Ce^{3+}-doped GAGG and 0.5% Ce^{3+}, 0.5% Mg^{2+}-co-doped GAGG garnet single-crystals in Figs. 12.14 and 12.15, respectively. It is clear that we observe Ce^{4+} reference at 5738 eV, in 0.5%

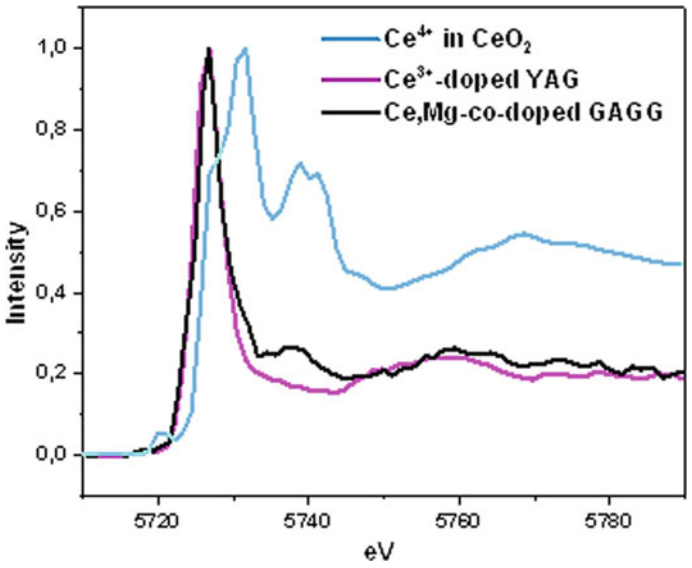

Fig. 12.14 Experimental Ce L_{III}-edge XANES spectra of 0.5%Ce^{3+}, 0.1%Mg^{2+}-co-doped GAGG garnet single crystal (black curve). The XANES spectra of the Ce^{4+} ion in CeO_2 (blue curve) and 0.5%Ce^{3+}-doped YAG (pink curve) are used as references

Ce^{3+},0.5% Mg^{2+}-co-doped GAGG like in CeO_2 (Fig. 12.14), whereas 0.5% Ce^{3+}-doped GAGG contains only Ce^{3+} ions detected by the peak at 5727 eV (Fig. 12.15). Both crystals contain both Ce^{4+} and Ce^{3+} ions well observed by the peak at 5727 eV.

The estimation of the Ce^{3+}/Ce^{4+} ratio (80/20) in the spectra is the result of the linear combination fit method of the two Ce^{4+} and Ce^{3+} references. We also have chosen to evaluate the Ce^{3+}/Ce^{4+} ratio from simulation of XANES concentration dependences [29] and the Ce^{3+}/Ce^{4+} ratio value of 82.5/17.5 has been found. Then, the two methods give the same order of magnitude of the Ce^{3+}/Ce^{4+} ratio value, considering an error of roughly 10% on the Ce^{4+} value.

XANES spectra of Ce^{3+}, Mg^{2+}-co-doped GAGG garnet single-crystal confirms the role of stable Ce^{4+} in the scintillation process and obviously the absence of stable Ce^{4+} in the crystals without any Mg^{2+}, as expected.

Indeed, we have always to take into account of the competition in the scintillation mechanism between the creation of Ce^{4+} and the presence of the shallow electron traps and deeper traps in the crystal lattice of garnet. These traps capture electrons from the conduction band and contribute to extend component in scintillation decay. It is difficult at this point to evaluate each contribution of Ce^{4+} ion and traps to the fastest component of scintillation response as it was shown in Fig. 12.5. It is only clear that Ce^{3+}, Mg^{2+}-co-doped GAGG shows lower afterglow and thermo-stimulated luminescence intensity [34] and there is an improvement of fast

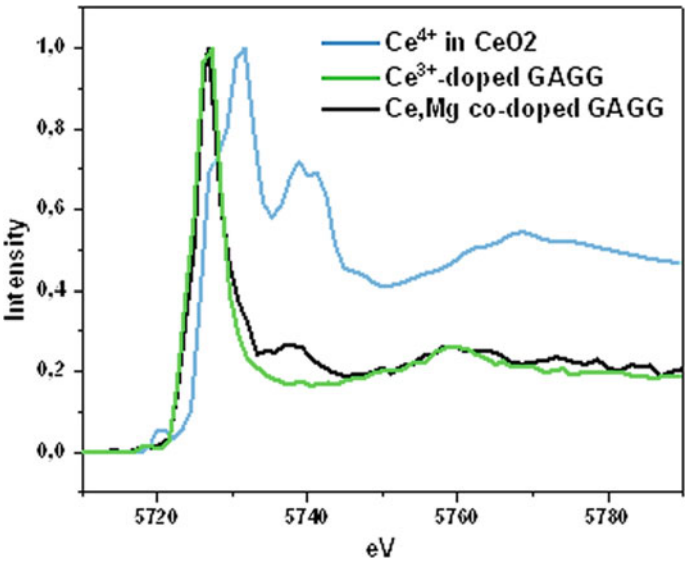

Fig. 12.15 Comparison between experimental Ce L_{III}-edge XANES spectra of 0.5%Ce^{3+}, 0.1%Mg^{2+}-co-doped GAGG garnet single crystal (black curve) and of 0.5%Ce^{3+}-doped GAGG garnet single crystal (green curve). The XANES spectra of the Ce^{4+} ion in CeO_2 (blue curve) is used as reference. 0.5%Ce^{3+}-doped GAGG contains only Ce^{3+} ion, any Ce^{4+} ion

performances from the creation of Ce^{4+} in agreement with the ideas developed in this research.

12.6 Conclusions

This lecture has shown the main spectroscopic properties and the strategy for optimization of garnet scintillator composition of the most advanced oxide Ce^{3+}, Mg^{2+}-co-doped $Gd_3Al_2Ga_3O_{12}$ (GAGG) host, grown at the Tohoku University, Sendai, by both the micro-pulling-down and Czochralski techniques. This crystal is promising for applications which require fast-timing resolution and high light yield such as PET. The co-doping of Ce^{3+} ion by Mg^{2+} one has revealed the creation of Ce^{4+} ion, assigned first from the charge transfer absorption band in UV, due to charge compensation effect, occurring in the scintillation mechanisms, in addition of the usual Ce^{3+} ion, like in commercial Ce^{3+}, Mg^{2+}-co-doped LYSO orthosilicate oxydes. The presence and then the role played by the stable Ce^{4+} ion for the scintillation mechanisms has been demonstrated by XANES spectroscopy at the Ce L_{III} threshold of the European Synchrotron Radiation Facility (ESRF) in Grenoble. In addition, the estimation of the Ce^{3+}/Ce^{4+} ratio measured by a linear combination fit method is 80/20 and 82.5/17.5 by the simulation of Ce^{4+} curves.

While Ce^{4+} ion is unwanted in photoluminescence inorganic crystals due to the UV charge transfer absorption band, it appears to be an essential ion for scintillation mechanisms.

References

1. Knoll GF (2010) Radiation detection and measurement, 4th edn. Wiley, New York
2. Nikl M, Yoshikawa A (2015) Recent R&D trends in inorganic single-crystal scintillator materials for radiation detection. Adv Opt Mater 3(4):463–481
3. Melcher C, Schweitzer JS (1992) Cerium-doped lutetium orthosilicate: a fast, efficient new scintillator. IEEE Trans Nucl Sci 39(4):502–505
4. Kapusta M, Szupryczynski P, Melcher CL, Moszynski M, Balcerzyk M, Carey AA (2005) Nonproportionality and thermoluminescence of LSO:Ce. IEEE Trans Nucl Sci 52(4):1098–1104
5. Spurrier MA, Szupryczynski P, Carey AA, Melcher CL (2008) Effects of Ca^{2+} co-doping on the scintillation properties of LSO:Ce. IEEE Trans Nucl Sci 55(3):1178–1182
6. Lecoq P, Korzhik M (2002) New inorganic scintillation materials development for medical imaging. IEEE Trans Nucl Sci 49(4):1651–1654
7. Moszynski M, Wolski D, Ludziejewski T, Kapusta M, Lempicki A, Brecher C (1997) Properties of the new LuAP:Ce scintillator. Nucl Instrum Methods Phys Res A 385:123–131
8. Weber S, Christ D, Kurzeja M, Engels R, Kemmerling G, Halling H (2003) Comparison of LuYAP, LSO, BGO as scintillators for high resolution PET detectors. IEEE Trans Nucl Sci 50(5):1370–1372
9. Conti M (2009) State of the art and challenges of time-of-flight PET. Phys Med 25:1–11
10. Shah KS, Glodo J, Klugerman M, Moses WW, Derenzo SE, Weber MJ (2003) $LaBr_3$:Ce scintillators for gamma-ray spectroscopy. IEEE Trans Nucl Sci 50(6):2410–2413
11. Kramer KW, Dorenbos P, Gudel HU, van Eijk CWE (2006) Development and characterization of highly efficient new cerium doped rare earth halide scintillator materials. J Mater Chem 16:2773–2278
12. Alekhin M, de Haas J, Khodyuk I, Krämer K, Menge P, Ouspenski V, Dorenbos P (2014) Improvement of gamma-ray energy resolution of $LaBr_3$:Ce^{3+} scintillation detectors by Sr^{2+} and Ca^{2+} co-doping. Appl Phys Lett 104:161915–161918
13. Nikl M, Yoshikawa A, Kamada K, Nejezchleb K, Mares J, Blazez K (2013) Development of LuAG-based scintillator crystals. A review. Progr Cryst Growth Charact Mater 59:47–72
14. Lupei V, Lupei A, Tiseanu C, Georgescu S, Stoicescu C, Nanau P (1995) High-resolution optical spectroscopy of YAG: Nd: A test for structural and distribution models. Phys Rev B 51:8–17
15. Stanek CR, McClellan KJ, Levy MR, Grimes RW (2006) Extrinsic defect structure of $RE_3Al_5O_{12}$ garnets. Phys Status Solidi B 243:R75–R77
16. Nikl M, Vedda A, Fasoli M, Fontana I, Laguta V, Mihokova E, Pejchal J, Rosa J, Nejezchleb K (2007) Shallow traps and radiative recombination processes in $Lu_3Al_5O_{12}$:Ce single crystal scintillator. Phys Rev B 76(19):195121
17. Kamada K, Endo T, Tsutumi K, Yanagida T, Fujimoto Y, Fukabori A (2011) Composition engineering in cerium-doped $(Lu,Gd)_3(Ga, Al)_5O_{12}$ single-crystal scintillators. Cryst Growth Des 11:4484–4490
18. Kamada K, Yanagida T, Endo T, Tsutumi K, Usuki Y, Nikl M (2012) 2 inch diameter single crystal growth and scintillation properties of $Ce:Gd_3Al_2Ga_3O_{12}$. J Cryst Growth 352:88–90
19. Kamada K, Kurosawa S, Prusa P, Nikl M, Kochurikhin V, Endo T, Tsutumi K, Sato H, Yokota Y, Sugiyama K, Yoshikawa A (2014) Cz grown 2-in. size $Ce:Gd_3(Al, Ga)_5O_{12}$ single crystal; relationship between Al, Ga site occupancy and scintillation properties. Opt Mater 36:1942–1945

20. Yoshikawa A, Nikl M, Boulon G, Fukuda T (2007) Challenge and study for developing of novel single crystalline optical materials using micro-pulling-down method. Opt Mater 30:6–10
21. Raukas M, Basun SA, van Schaik W, Yen WM, Happek U (1996) Luminescence efficiency of cerium doped insulators: the role of electron transfer processes. Appl Phys Lett 69:3300–3305
22. Spurrier MA, Szupryczynski P, Yang K, Carey AA, Melcher CL (2008) Effects of Ca^{2+} co-doping on the scintillation properties of LSO:Ce. IEEE Trans Nucl Sci 55:1178–1182
23. Blahuta S, Bessiere A, Viana B, Dorenbos P, Ouspenski V (2013) Evidence and consequences of Ce^{4+} in LYSO:Ce,Ca and LYSO:Ce,Mg single crystals for medical imaging applications. IEEE Trans Nucl Sci 60:3134–3141
24. Liu S, Feng X, Zhou Z, Nikl M, Shi Y, Pan Y (2014) Effect of Mg^{2+} co-doping on the scintillation performance of LuAG:Ce ceramics. Phys Status Solidi RRL 8:105–109
25. Tyagi M, Meng F, Koschan M, Donnald S, Rothfuss H, Melcher CL (2013) Effect of codoping on scintillation and optical properties of Ce doped $Gd_3Ga_3Al_2O_{12}$ scintillator. J Phys D Appl Phys 46:475302–475307
26. Wu Y, Meng F, Li Q, Koschan M, Melcher CL (2014) Role of Ce^{4+} in the scintillation mechanism of co-doped $Gd_3Ga_3Al_2O_{12}$: Ce. Phys Rev Appl 2:044009
27. Kamada K, Nikl M, Kurosawa S, Beitlerova A, Nagura A, Shoji Y, Pejchal J, Ohashi Y, Yokota Y, Yoshikawa A (2015) Alkali earth co-doping effects on luminescence and scintillation properties of Ce-doped $Gd_3Al_2Ga_3O_{12}$ scintillator. Opt Mater 41:6
28. Kamada K, Shoji Y, Kochurikhin V, Nagura A, Okumura S, Yamamoto S, Yeom JY, Kurosawa S, Pejchal J, Yokota Y, Ohashi Y, Nikl M, Yoshino M, Yoshikawa A (2016) Large size Czochralski growth and scintillation properties of Mg^{2+} co-doped Ce:$Gd_3Ga_3Al_2O_{12}$. IEEE Trans Nucl Sci 63(2):443
29. Dantelle G, Boulon G, Guyot Y, Testemale D, Guzik M, Kurosawa S, Kamada K, Yoshikawa A (2019) Research of efficient fast scintillators. Evidence and XANES characterization of Ce^{4+} in Ce^{3+}, Mg^{2+}-co-doped $Gd_3Al_2Ga_3O_{12}$ garnet crystals. Phys Status Solidi B 257:1900510–1900518
30. Rotman SR, Tuller HL, Warde C (1992) Defect-property correlations in garnet crystals. VI. The electrical conductivity, defect structure, and optical properties of luminescent calcium and cerium-doped yttrium aluminum garnet. J Appl Phys 71:1209–1214
31. Derdzyan MV, Hovhannesyan KL, Yeganyan AV, Sargsyan RV, Novikov A, Petrosyan AG, Dujardin C (2018) Dissimilar behavior of YAG:Ce and LuAG:Ce scintillator garnets regarding Li^+ co-doping. CrystEngComm 20:1520–1526
32. Tella M, Auffan M, Brousset L, Morel E, Proux O, Chanéac C, Angeletti B, Pailles C, Artells E, Santaella C, Rose J, Thiéry A, Bottero J-Y (2015) Chronic dosing of a simulated pond ecosystem in indoor aquatic mesocosms: fate and transport of CeO_2 nanoparticles. Environ Sci Nano 2:653–663
33. https://bruceravel.github.io/demeter/
34. Chewpraditkul W, Pattanaboonmee N, Sakthong O, Wantong K, Chewpraditkul W, Yoshikawa A, Kamada K, Kurosawa S, Szczesniak T, Moszynski M, Babin V, Nikl M (2019) Scintillation properties of $Gd_3Al_2Ga_3O_{12}$:Ce, Li and $Gd_3Al_2Ga_3O_{12}$:Ce, Mg single crystal scintillators: a comparative study. Opt Mater 92:181

Part II
Short Seminars

Chapter 13
Refractive Index Sensing by Phase Shift Cavity Ringdown Spectroscopy

Rana M. Armaghan Ayaz, Yigit Uysalli, Nima Bavili, Berna Morova, M. Imran Cheema, and Alper Kiraz

Abstract Cavity ring down spectroscopy is a sensitive optical detection technique but it makes use of expensive electronics and data fitting algorithm. Both of these factors put a limitation on its performance for sensing applications. In this study cost effective and easy to use phase shift cavity ring down spectroscopy (PS-CRDS) technique, has been demonstrated for refractive index sensing. A refractive index sensor consisting of a tapered single mode optical fiber and two fiber Bragg gratings (FBGs) is proposed. In this sensing methodology, an intensity modulated laser beam centered at 1550 nm from a DFB laser is scanned at a narrow wavelength range and cavity modes are excited. Later the phase shift corresponding to these cavity modes is measured using a lock-in amplifier. Sucrose solutions of various concentrations are used for performance analysis of the refractive index sensing device. The resultant limit of detection (LOD) came out to be ~6.4×10^{-6} refractive index units (RIUs), which can be improved further by using thinner fiber tapers or fiber Bragg gratings with higher reflectivity.

Keywords Tapered optical fiber · Fiber bragg gratings · Phase shift cavity ringdown spectroscopy · Refractive index

13.1 Introduction and Experimental Method

In classical CRDS systems, ring down time τ is extracted by applying exponential fit to the output from the optical cavity and which is later related to the cavity losses

R. M. Armaghan Ayaz · Y. Uysalli · N. Bavili · B. Morova · A. Kiraz
Department of Physics, KOÇ University,İstanbul, Turkey

M. I. Cheema · A. Kiraz (✉)
Department of Electrical Engineering, Lahore University of Management Sciences (LUMS), Lahore, Pakistan
e-mail: akiraz@ku.edu.tr

M. Cesaria et al. (eds.), *Light-Matter Interactions Towards the Nanoscale*,
NATO Science for Peace and Security Series B: Physics and Biophysics,
https://doi.org/10.1007/978-94-024-2138-5_13

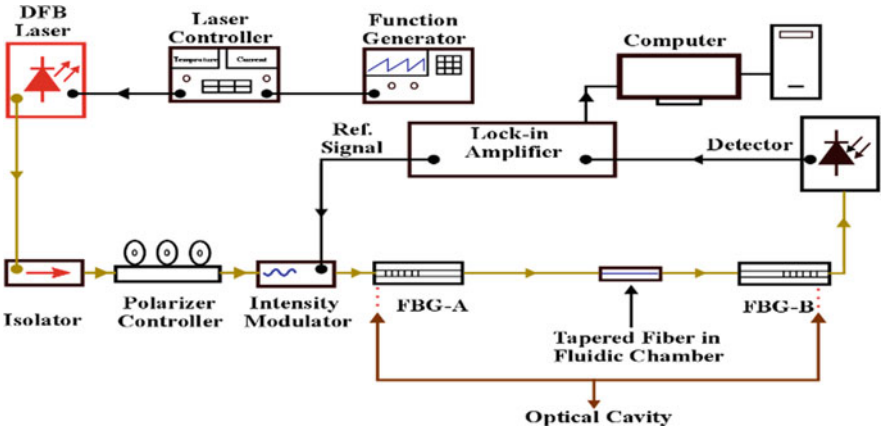

Fig. 13.1 Experimental setup for refractive index measurement

[1, 2]. But CRDS is an expensive technique and application of fitting algorithms to find ring down time also makes it unsuitable for real time sensing purposes [3].

Phase shift cavity ring down spectroscopy (PS-CRDS) is a reasonable alternative for the real time sensing applications that utilizes the experimental setup as shown in Fig. 13.1. In PS-CRDS, an intensity modulated light at f_m frequency serves as the input to the cavity and phase shift is measured between the input and output from the cavity with the help of lock-in detection [4] given as $\Phi = -\arctan(2\pi f_m \tau)$. In this way, any parameter affecting ring down time can be sensed. By using this methodology, we sensed the change in refractive index (RI) of sucrose solution in deionized (DI) water. Our results showed the limit of detection (LOD) around ~6.4×10^{-6} refractive index units (RIUs).

This limit of detection is an improvement over that has been achieved by using conventional, amplified, and gain-clamped CRDS employing fiber loop resonators [5].

13.2 Results and Discussions

For determining the sensitivity of the system, different concentrations of sucrose solution in (DI) water were used as a test liquid. The pattern of phase change with the change of solution concentration can be seen in Fig. 13.2a for taper fiber with 3.2 μm taper waist diameter. For the consecutive concentration steps as shown in Fig. 13.2, LODs came out to be 6.4848×10^{-6}, 7.1537×10^{-6}, 6.3912×10^{-5}, 1.0480×10^{-5} and 9.1360×10^{-6} RIUs.

The sensitivity curve obtained from the switching experiment for increasing and decreasing the sucrose solution concentration can be seen in Fig. 13.2b. The calculated sensitivity was around 198.682°/% for sucrose solution. These LODs and

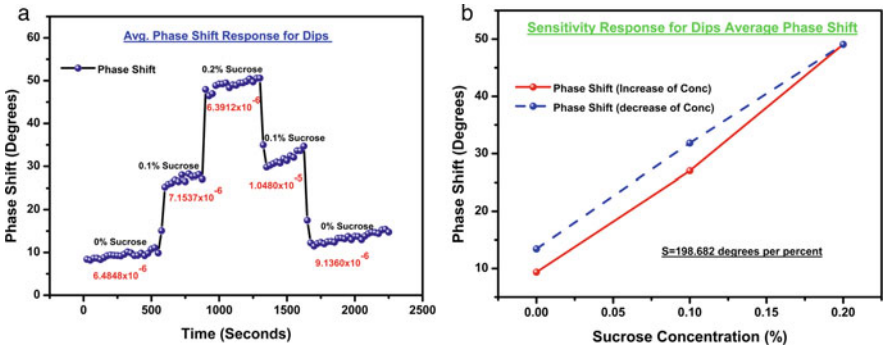

Fig. 13.2 (**a**) Change of phase shift with the change of sucrose solution concentration with LOD in terms of RIUs for each step (**b**) sensitivity curve obtained for increasing (red line solid) and decreasing (blue line dotted) the sucrose solution concentration

sensitivity can be further enhanced with thinner fiber tapers or fiber Bragg gratings having higher reflectivity.

13.3 Conclusion

We reported a highly sensitive refractive index sensor based on phase shift cavity ring down spectroscopy. This sensor is able to reach limit of detection up to 6.4×10^{-6} refractive index units (RIUs) with sensitivity around 198.682°/% for sucrose concentration in DI water. This value is expected to improve further by using thinner taper diameters and FBGs with higher reflectivity. The proposed sensor can also be used for air or water contamination detection and biological sensing.

References

1. O'Keefe A, Deacon DAG (1988) Cavity ring-down optical spectrometer for absorption measurements using pulsed laser sources. Rev Sci Instrum 59(12):2544–2551
2. Berden G, Engeln R (eds) (2009) Cavity ring-down spectroscopy: techniques and applications. Wiley, Chichester
3. Tong Z, Wright A, McCormick T, Li R, Oleschuk RD, Loock H-P (2004) Phase-shift fiber-loop ring-down spectroscopy. Anal Chem 76(22):6594–6599
4. Engeln R, von Helden G, Berden G, Meijer G (1996) Phase shift cavity ring down absorption spectroscopy. Chem Phys Lett 262(1–2):105–109
5. Sharma K, Abdul Khudus MIM, Alam SU, Bhattacharya S, Venkitesh D, Brambilla G (2018) Comparison of detection limit in fiber-based conventional, amplified, and gain-clamped cavity ring-down techniques. Opt Commun 407:186–192

Chapter 14
Hyperpolarizability of Plasmonic Nanostructures: A Method to Quantify the SHG Emission from a Metasurface

Joshua Baxter, Antonio Calà Lesina, and Lora Ramunno

Abstract We present a method for calculating the second harmonic generation from a nonlinear plasmonic metasurface. We first calculate the hyperpolarizability of the nanostructure by considering the electron dynamics through the hydrodynamic model. We then use the hyperpolarizability to drive the emission from a distribution of independent dipoles. And finally, we sum these contributions in the far-field to obtain the SHG emission from the metasurface.

Keywords FDTD · Nonlinear plasmonic metasurfaces · Computational electromagnetism

14.1 Calculating SHG from a Plasmonic Metasurface

To model the nonlinear processes in plasmonic nanoparticles, we use the hydrodynamic plasma model [1]:

$$nm\left(\frac{\partial}{\partial t} + (\mathbf{u}\cdot\nabla) + \gamma\right)\mathbf{u} = ne(\mathbf{E} + \mathbf{u}\times\mathbf{B}) - \nabla\frac{\delta G[n]}{\delta n}, \tag{14.1}$$

J. Baxter (✉) · L. Ramunno
Department of Physics and Centre for Research in Photonics, University of Ottawa, Ottawa, ON, Canada
e-mail: jbaxt089@uottawa.ca

A. Calà Lesina
Department of Physics and Centre for Research in Photonics, University of Ottawa, Ottawa, ON, Canada

Faculty of Mechanical Engineering (Institut für Transport- und Automatisierungstechnik), Hannover Centre for Optical Technologies, and Cluster of Excellence PhoenixD, Leibniz Universität Hannover, Hannover, Germany

M. Cesaria et al. (eds.), *Light-Matter Interactions Towards the Nanoscale*,
NATO Science for Peace and Security Series B: Physics and Biophysics,
https://doi.org/10.1007/978-94-024-2138-5_14

where **u** represents the free electron velocity, **E** and **B** the electric and magnetic fields respectively, γ the damping coefficient, n is the free electron density, m is the electron mass, and $G[n]$ is the Thomas-Fermi energy functional. This model is implemented in our in-house FDTD software [2], where we track the current density $J = -en\mathbf{u}$ and the electron density via Gauss's Law. We calculate the nonlinear dipole moment using FDTD by simulating the excitation of a single nanoparticle by a narrow band plane wave (such that the fundamental and second harmonic response are distinguishable). We then calculate the effective nonlinear dipole moment p_0 using the SHG scattered power P [3]:

$$p_0 = \sqrt{\frac{12\pi\varepsilon_0 P}{ck^4}}, \tag{14.2}$$

where k is the wavenumber, and c is the speed of light. From the nonlinear dipole moment, we calculate the hyperpolarizability β because the incident field is narrow-band [4]:

$$\beta(\omega) = \frac{2\pi}{\varepsilon_0} p_0(\omega) \left[\int E_{inc}(\omega') E_{inc}(\omega - \omega') d\omega' \right]^{-1} \tag{14.3}$$

Using the hyperpolarizability we calculate the far field electric and magnetic fields using the far field dipole formulas [3] (assuming no interaction between dipoles). After summing the far field electric and magnetic fields from all of the dipoles on the surface, we then calculate the time averaged (over the inverse repetition rate of the laser τ) Poynting vector using:

$$< \mathbf{S}(\mathbf{r}) >= \frac{1}{2\pi\tau} \int_{-\infty}^{\infty} \mathbf{E}_{far}(\mathbf{r}, \omega) \times \mathbf{H}^*_{far}(\mathbf{r}, \omega) d\omega, \tag{14.4}$$

which we integrate over the observation plane to get the SHG power.

We validate this method by calculating the SHG power from a metasurface consisting of single-sized gold nano-triangles randomly distributed on a square sample where we assuming an incident field with a Gaussian profile as shown in Fig. 14.1a. We calculate the SHG power spectrum for four metasurfaces consisting of triangles of length 146 nm, 157 nm, 168 nm, and 179 nm shown in Fig. 14.1b. Our calculations agree with experimental measurements on SHG emission from similar metasurfaces conducted from collaborators at uOttawa and Tampere University [2].

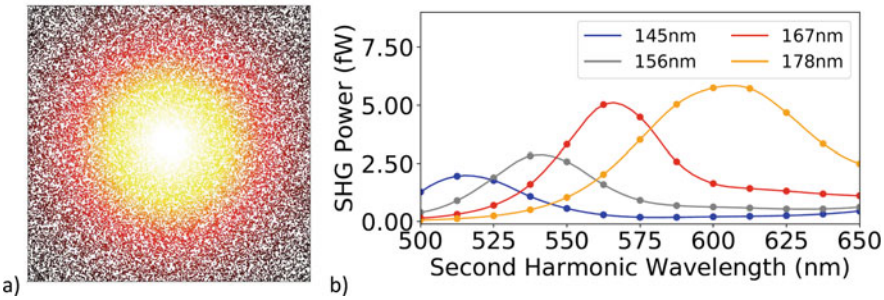

Fig. 14.1 (**a**) Nano-triangle metasurface layout where each dot represents a nano-triangle and the colour represents the electric field experienced by the nano-triangle. (**b**) SHG power spectrum for four different triangle lengths

References

1. Raza, S., et al.: Nonlocal optical response in metallic nanostructures. J. Phys. Condens. Matter **27**, 183204 (2015)
2. Bin-Alam, M.S., Baxter, J., et al.: Hyperpolarizability of plasmonic meta-atoms in metasurfaces. Nano Lett. **21**, 51–59 (2021)
3. Jackson, J.D.: Classical Electrodynamics, 2nd edn. John Wiley & Sons, Inc., New York (1975)
4. Shen, Y.R.: The Principles of Nonlinear Optics. Wiley-Interscience, Hoboken (2003)

Chapter 15
Nonlinear Up- and Down-Conversion in AlGaAs Microdisks Integrated in a Photonic Circuit

Adrien Borne, Iännis Roland, Marco Ravaro, Giuseppe Marino, Stefan Suffit, Pascal Filloux, Aristide Lemaître, Ivan Favero, and Giuseppe Leo

Abstract We report on the integration of AlGaAs whispering-gallery mode microdisks into a monolithic photonic chip as a platform for frequency conversion and non-classical state generation based on parametric nonlinear optical processes. Quasi phase-matching, resonant field enhancement and confinement ensure efficient nonlinear interactions: second-harmonic generation has been achieved with a conversion efficiency of $5\%\mathrm{W}^{-1}$, and spontaneous parametric down-conversion with a photon pair generation rate of 1.2 kHz/μW.

Keywords Nonlinear photonics · Whispering gallery-mode microresonators

15.1 Introduction

High-index-contrast optical microcavities like microdisks and microrings can combine high Q factors with sub-wavelength size, allowing for strong nonlinear light-matter interaction at low optical power. Such whispering gallery-mode (WGM) microcavities are used in an increasing set of photonic applications like microlasers, optomechanics, biosensors, optic switches, optical frequency comb generation, harmonic generation, and photon-pair generation.

Among all the materials for such high-Q WGM microcavities, two semiconductors lead the realm of photonic applications: silicon and aluminum gallium arsenide (AlGaAs). While the former benefits from advanced CMOS technology, its centrosymmetry hinders $\chi^{(2)}$ effects and motivates an increasing interest in

A. Borne (✉) · I. Roland · M. Ravaro · G. Marino · S. Suffit · P. Filloux · I. Favero · G. Leo
Matériaux et Phénomènes Quantiques, Université de Paris and CNRS, Paris, France
e-mail: adrien.borne@univ-paris-diderot.fr

A. Lemaître
Centre de Nanosciences et de Nanotechnologies, Université Paris-Sud and CNRS, Marcoussis, France

M. Cesaria et al. (eds.), *Light-Matter Interactions Towards the Nanoscale*,
NATO Science for Peace and Security Series B: Physics and Biophysics,
https://doi.org/10.1007/978-94-024-2138-5_15

AlGaAs. This III-V direct-gap semiconductor has a huge quadratic nonlinearity and has recently resulted in rapid progress in the domain of nonlinear and quantum photonics. The related state-of-the-art includes three-wave mixing in III-V-on-insulator microrings [2], and in suspended microdisks. Until very recently, the latter had only been observed with harmonic-light collection via out-of-plan scattering [3] or evanescent coupling with a tapered fiber [4, 5].

15.2 Results

We report here on the fabrication and characterization of a monolithic III-V semiconductor photonic chip, designed to perform parametric nonlinear optical processes for frequency conversion and non-classical state generation [1]. As shown on the electron-microscope image in Fig. 15.1, this chip includes a microdisk evanescently coupled to two suspended waveguides, one designed to allow light injection and collection at $\lambda_\omega = 1600\,\text{nm}$ (in red in Fig. 15.1), and the other at $\lambda_{2\omega} = 800\,\text{nm}$ (in blue in Fig. 15.1). The resonator is resonant a both λ_ω and $\lambda_{2\omega}$, and the corresponding Q-factors are of the order of 10^4 and 10^3, respectively.

Quasi phase-matching provided by the resonator geometry and material symmetry, resonant field enhancement and confinement ensure efficient nonlinear interactions. We demonstrated on the same device both second-harmonic generation (SHG) with a conversion efficiency of $5\%\text{W}^{-1}$, and spontaneous parametric down-conversion (SPDC) with a photon pair production rate of $1.2\,\text{kHz}/\mu\text{W}$.

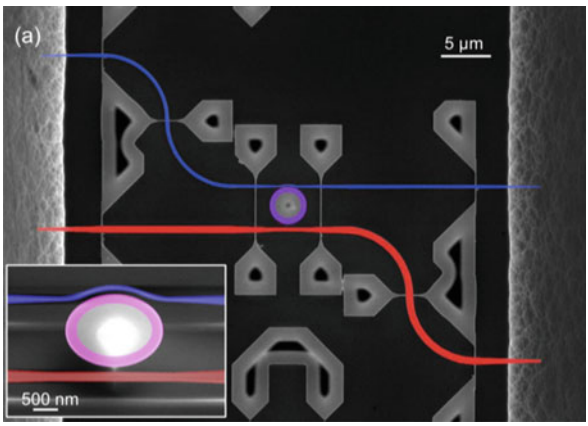

Fig. 15.1 Electron-microscope image of our photonic circuit, with the waveguides at λ_ω and $\lambda_{2\omega}$ colored in red and in blue, respectively [1]. The three-wave mixings are represented by the color gradient on the rim of the microdisk

15.3 Discussion

This monolithic device is attractive for frequency conversion, generation of dual frequency combs, and generation of separable or entangled biphoton states for quantum applications, not only in the telecom range, but also at $\lambda_\omega \simeq 2\mu m$ with higher Q GaAs devices. This work could be extended to allow spectral tuning of the generated photons, e.g. by means of temperature or voltage control.

References

1. Roland, I., Borne, A., Ravaro, M., De Oliveira, R., Suffit, S., Filloux, P., Lemaître, A., Favero, I., Leo, G.: Frequency doubling and parametric fluorescence in a four-port aluminum gallium arsenide photonic chip. Opt. Lett. **45**, 10 (2020)
2. Chang, L., Boes, A., Pintus, P., Peters, J.D., Kennedy, M., Guo, X.-W., Volet, N., Yu, S.-P., Papp, S.B., Bowers, J.E.: Strong frequency conversion in heterogeneously integrated GaAs resonators. APL Photonics **4**, 036103 (2019)
3. Roland, I., Gromovyi, M., Zeng, Y., El Kurdi, M., Sauvage, S., Bri- mont, C., Guillet, T., Gayral, B., Semond, F., Duboz, J.-Y., de Micheli, M., Checoury, X., Boucaud, P.: Phase-matched second harmonic generation with on-chip GaN-on-Si microdisks. Sci. Rep. **6**, 34191 (2016)
4. Kuo, P., Bravo-Abad, J., Solomon, G.: Second-harmonic generation using $\bar{4}$-quasi-phasematching in a GaAs whispering-gallery-mode microcavity. Nat. Commun. **5**, 3109 (2014)
5. S. Mariani, A. Andronico, A. Lemaître, I. Favero, S. Ducci, G. Leo, Second-harmonic generation in AlGaAs microdisks in the telecom range. Opt. Lett. **39**, 3062 (2014)

Chapter 16
Tuning of Phonons and Surface Phonon Polaritons

Vanessa M. Breslin, Andrea B. Grafton, Daniel C. Ratchford, Alexander J. Giles, Kenan P. Fears, Christopher R. So, D. Scott Katzer, Chase T. Ellis, Joseph G. Tischler, Joshua D. Caldwell, Adam D. Dunkelberger, and Jeffrey C. Owrutsky

Abstract Plasmonic materials can be used for surface enhanced infrared absorption, a particularly useful technique for chemical sensing applications, but these materials typically suffer from high optical losses, which result in broad optical resonances. In contrast, surface phonon polaritons (SPhPs) have much lower losses, resulting in narrower resonance bands. In particular, our group is investigating polar dielectric inorganic crystals that have mid-IR Reststrahlen bands, frequency ranges where the crystals' optical constants resemble metals and can support SPhP resonances. Currently, our efforts are focused on studying the optical properties of calcite ($CaCO_3$) crystals in the mid-IR. We have used a focused ion beam to directly nanostructure the surface of calcite in order to generate SPhPs (or more specifically for calcite, hyperbolic phonon polaritons) for sub-diffraction optical confinement of mid-IR incident light. The results of these studies will allow us to better understand how to tune these phonon polaritons in a broader spectral range with different inorganic materials and provide a basis for exploring how these resonances interact with other chemical systems.

Keywords Surface phonon polaritons · Polar dielectric · Reststrahlen band

Plasmonic Materials for Nanophotonics Plasmonic metal nanostructures display some unique and interesting optical properties and are capable of sub-diffraction

V. M. Breslin (✉) · A. B. Grafton
NRC/RAP, Washington, DC, USA
e-mail: vanessa.breslin@nrl.navy.mil

D. C. Ratchford · A. J. Giles · K. P. Fears · C. R. So · D. S. Katzer · C. T. Ellis · J. G. Tischler · A. D. Dunkelberger · J. C. Owrutsky
U.S. Naval Research Laboratory, Washington, DC, USA

J. D. Caldwell
Vanderbilt University, Nashville, TN, USA

M. Cesaria et al. (eds.), *Light-Matter Interactions Towards the Nanoscale*,
NATO Science for Peace and Security Series B: Physics and Biophysics,
https://doi.org/10.1007/978-94-024-2138-5_16

optical confinement. Consequently, they can be used to manipulate light at the nanoscale, and thus enable new opportunities for nanophotonics and enhanced material optical effects, such as near-field optics and chemical sensing. However, plasmonic materials have limitations. Their spectral range for many desirable and strong optical-material interactions is confined to the UV through near-infrared (NIR) frequencies and they have high optical losses due to fast electron scattering, which result in broad spectral bands. The optical properties at longer wavelengths (mid-IR) of plasmonic materials, including metals and doped semiconductors, limit their performance for many applications because they do not exhibit sub-diffraction optical confinement or strong field enhancement in this region.

Polar Dielectric Materials for Nanophotonics One approach that overcomes the limitations of plasmonic materials described above is to utilize surface phonon polaritons (SPhPs) of polar dielectric crystals, which rely on surface phonon oscillations, i.e. lattice vibrations. Polar dielectric materials have mid-IR Reststrahlen bands between the transverse and longitudinal optical (TO and LO) phonon bands, where they behave optically like metals but with lower optical loss. In this region they are very reflective with negative real permittivities and support SPhP resonances, which can lead to sub-diffraction light confinement and enhanced light-matter interactions similar to surface plasmon resonances in the visible. In a manner very similar to geometry tuning of localized plasmon bands, the position of SPhP bands can be tuned within the Reststrahlen band by altering the size, shape, and periodicity of the nanostructures on a material's surface. In addition to the coarse tuning that depends on the position of the Reststrahlen band for a given material, fine tuning of the SPhP resonance frequencies by size and shape can be used to position them to interact with molecular vibrations, potentially achieving more sensitive and selective IR chemical sensing applications than surface plasmon polaritons (SPPs) [1].

Surface Phonon Polaritons Supported in Semiconductor Materials Research on SPhPs has focused mainly on semiconductor materials, such as SiC [1, 2], hexagonal BN (hBN) [3], and GaN [4]. Previous work at the Naval Research Laboratory has demonstrated that cylindrical and rectangular nanopillars of SiC can support SPhP localized resonances at wavelengths within the Reststrahlen band that have incredibly narrow linewidths (7–24 cm^{-1}), which results in higher quality (Q)-factors than those observed or even the theoretical limit for localized SPP resonances [1, 2]. SiC nanostructures with relatively well-defined size, geometry, and periodicity can be fabricated with electron beam lithography for high Q SPhP resonators [1, 2]. However, not only does it remain difficult to fabricate monodisperse SiC nanoparticles, but it is also still challenging to work with other SPhP materials such as hBN [3] flakes (sub 100 um). SPhPs are a promising alternative to plasmons for infrared applications, so expanding the class of materials and also the spectral range for SPhPs is necessary for realizing their full potential.

New Materials for Nanophotonics Current efforts in our group toward expanding the reach of SPhPs to new materials are focused on studying the optical properties of

calcite ($CaCO_3$) crystals, a non-semiconductor polar dielectric material, in the mid-IR. Calcite is a naturally hyperbolic material that has upper and lower Reststrahlen bands in the mid-IR. We have observed hyperbolic phonon polariton resonances in the upper Reststrahlen band after directly nanostructuring the surface of the calcite substrates with nanohole and nanopillar arrays using a gallium focused ion beam. By changing the geometry of the calcite nanostructures, we have demonstrated that we can tune the resonances over almost the entire frequency range of the Reststrahlen band in this material.

References

1. Caldwell JD, Glembocki OJ, Francescato Y, Sharac N, Giannini V, Bezares FJ, Long JP, Owrutsky JC, Vurgaftman I, Tischler JG, Wheeler VD, Bassim ND, Shirey LM, Kasica R, Maier SA (2013) Low-loss, extreme subdiffraction photon confinement via silicon carbide localized surface phonon polariton resonators. Nano Lett 13(8):3690–3697
2. Ellis CT, Tischler JG, Glembocki OJ, Bezares FJ, Giles AJ, Kasica R, Shirey L, Owrutsky JC, Chigrin DN, Caldwell JD (2016) Aspect-ration driven evolution of high-order resonant modes and near-field distributions in localized surface phonon polariton nanostructures. Sci Rep 6(32959):1–11
3. Caldwell JD, Kretinin AV, Chen Y, Giannini V, Fogler MM, Francescato Y, Ellis CT, Tischler JG, Woods CR, Giles AJ, Hong M, Watanabe K, Taniguchi T, Maier SA, Novoselov KS (2014) Sub-diffractional volume-confined polaritons in the natural hyperbolic material hexagonal boron nitride. Nat Commun 5(5221):1–9
4. Ng SS, Hassan Z, Abu Hassan H (2008) Surface phonon polariton of wurtzite GaN thin film grown on *c*-plane sapphire substrate. Solid State Commun 145(11–12):535–538

Chapter 17
Defect-Related Optical Properties of ZnO Nanoparticles in ZnO/SiO_2 Systems

Roberta Crapanzano, Irene Villa, Barbara Di Credico, Massimiliano D'Arienzo, Mauro Fasoli, Silvia Mostoni, Roberto Scotti, and Anna Vedda

Abstract ZnO nanoparticles grown on highly porous silica with spherical and rod-like morphology were investigated by radioluminescence and photoluminescence measurements to assess the influence of intrinsic defectiveness on the optical properties. Spectroscopic analysis of ZnO/SiO_2 systems unveils defect-related luminescence and a very weak excitonic emission. The samples display peculiar optical properties with unlike intensity and energy emissions, disclosing the occurrence of inequivalent defect centers in ZnO nanoparticles supported onto silica with different morphology.

Keywords Zinc oxide · Photoluminescence · Radioluminescence · Defectiveness

17.1 Introduction

ZnO is a wide band gap semiconductor ($E_g = 3.37$ eV) with a large excitonic energy (60 meV) [1]. In addition to near-UV excitonic emission (~3.3 eV), defect-related ones are reported in the violet (~2.9 eV), blue (~2.6 eV), green (~2.2 eV), and yellow (~2.1 eV) regions of the visible spectrum [2]. Their attribution is controversial due to the complexity of ZnO defectiveness. In this study, radioluminescence (RL), photoluminescence emission (PL), and photoluminescence excitation (PLE) measurements were exploited to investigate the optical properties of ZnO/SiO_2 systems synthesized by sol-gel route [3]. ZnO nanoparticles (NPs) with 5 nm diameter were grown directly on highly porous silica NPs with two different

R. Crapanzano (✉) · I. Villa · B. Di Credico · M. D'Arienzo · M. Fasoli · S. Mostoni · R. Scotti · A. Vedda
Department of Materials Science, University of Milano-Bicocca, Milan, Italy
e-mail: r.crapanzano2@campus.unimib.it

B. Di Credico · M. D'Arienzo · S. Mostoni · R. Scotti
INSTM, University of Milano-Bicocca, Milan, Italy

M. Cesaria et al. (eds.), *Light-Matter Interactions Towards the Nanoscale*,
NATO Science for Peace and Security Series B: Physics and Biophysics,
https://doi.org/10.1007/978-94-024-2138-5_17

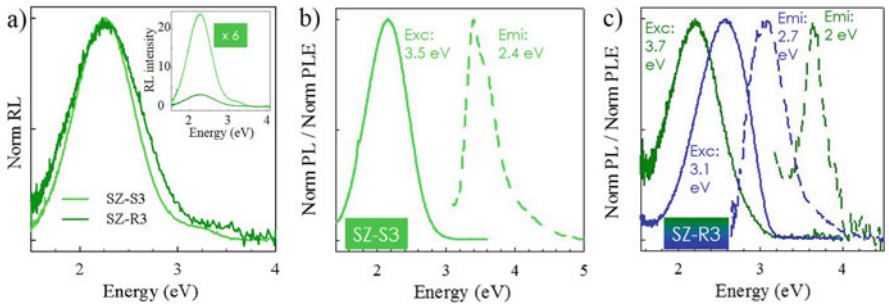

Fig. 17.1 (**a**) Normalized RL spectra of SZ-S3 and SZ-R3. For comparison, in the inset absolute RL intensities are shown. (**b, c**) Normalized PL and PLE spectra of SZ-S3 and SZ-R3, recorded at the reported excitation and emission energies, respectively

morphology: the first sample (SZ-S3) is supported onto spherical SiO_2 with 30 nm diameter, while the second one (SZ-R3) onto rod-like SiO_2 with 30 nm diameter and 150 nm length.

17.2 Results

In ZnO/SiO2, the excitonic emission was barely observed in RL measurements and not detected in the PL ones. Both under X-rays or UV light excitation, SZ-S3 and SZ-R3 disclose a greenish emission peaked at 2.2 eV (Fig. 17.1). However, SZ-S3 exhibits higher RL and PL intensities than SZ-R3 (Inset Fig. 17.1a). Differently, exciting below ZnO energy gap, only SZ-R3 displays a composite blue emission featuring two Gaussian components peaked at 2.55 and 2.82 eV (Fig. 17.1c). RL measurements were performed also at different pressures. At medium (10^{-3} mbar) and high (10^{-7} mbar) vacuum, SZ-R3 RL profile shows no differences, while SZ-S3 one presents a new emission band at 2.95 eV, whose intensity increases by pressure lowering.

RL and PL spectra of pristine spherical (S-S3) and rod-like (S-R3) silica NPs were investigated: their negligible emissions with respect to the ones of the ZnO/SiO2 systems allow the attribution of all the observed optical properties only to ZnO NPs.

17.3 Conclusions

In conclusion, this work unveils the influence of ZnO intrinsic defectiveness on its optical properties as the different RL and PL features of SZ-S3 and SZ-R3 display. In particular, it seems that the surface properties of ZnO NPs depend on the

morphology of the grown substrate [4], leading to the occurrence of inequivalent defect centers in ZnO/SiO2 systems.

References

1. Özgür Ü et al (2005) A comprehensive review of ZnO materials and devices. J Appl Phys 98:1–103
2. Djuriić AB et al (2010) ZnO nanostructures for optoelectronics: material properties and device applications. Prog Quantum Electron 34:191–259
3. Susanna A et al (2015) ZnO nanoparticles anchored to silica filler. A curing accelerator for isoprene rubber composites. Chem Eng J 275:245–252
4. Robin IC et al (2009) Compared optical properties of ZnO heteroepitaxial, homoepitaxial 2D layers and nanowires. J Cryst Growth 311:2172–2175

Chapter 18
Integrated Slot Waveguide-Based Phase Shifter

T. Grottke, W. Hartmann, C. Schuck, and W. H. P. Pernice

Abstract Here we present a slot waveguide-based phase shifter. Our device is based on the electrostatic displacement of mechanical structures, which can be achieved by applying a voltage. This leads to a change of the effective refractive index and thus to a phase shift.
Using an integrated Mach-Zehnder interferometer, this phase shift can be measured. We show that our device can generate a phase shift of $1\,\pi$ at a voltage at 7.5 V. A maximal phase shift of $1.8\,\pi$ can be achieved at 10 V. Operation and the generation of optical pulses with a frequency in the MHz range and a sub-μm pulse width is possible. Furthermore, our device operates over a large wavelength range in the near infrared regime.

18.1 Introduction

Photonic integrated circuits have gained much attention over the last years. Compared to free-space optics they have many advantages, such as robust and alignment-free circuits, scalability and a high number of devices per area. Among other components, phase shifters are one essential part of these circuits. So far, different physical mechanism have been studied: Electro optical modulators can be operated in the GHz range. However due to the small electro optic effect, long phase tuning lengths in the range of mm are required, resulting in limited scalability [1, 2]. Phase shifters based on the thermo optic effect are compact but lack cryogenic compatibility [3]. In addition, they usually have a high power consumption and suffer from thermal crosstalk. On the other hand, micro-electro-mechanical system (MEMS) based phase shifters offer decent modulation speed and loss, compact footprint, low power consumption and low half-wave voltages [4, 5]. Here, we

T. Grottke · W. Hartmann · C. Schuck · W. H. P. Pernice (✉)
Westfälische Wilhelms-Universität Münster, Münster, Germany
e-mail: Thomas.Grottke@wwu.de; wolfram.pernice@uni-muenster.de
https://www.uni-muenster.de/Physik.PI/Pernice/index.html

M. Cesaria et al. (eds.), *Light-Matter Interactions Towards the Nanoscale*,
NATO Science for Peace and Security Series B: Physics and Biophysics,
https://doi.org/10.1007/978-94-024-2138-5_18

present a MEMS phase shifter, which is based on the change of the gap width of a slot waveguide. We demonstrate a phase shift of more than 1 π and the generation of pulses with a width in the µs range.

18.2 Approach

The phase light gains by traveling a length l through a material with refractive index n is given by $\phi = 2\pi \frac{nl}{\lambda_0}$, where λ_0 is the vacuum wavelength. In free-space, one would change the length l to get a phase shift. Since this is difficult when working with integrated optics, one has to change the refractive index.

For this purpose, we make use of a slot waveguide, which consists of two rails with a high refractive index surrounding a low refractive index slot. As it can be seen in Fig. 18.1b, the refractive index depends on the slot width, meaning that in order to change this refractive index, one has to vary the slot width. In order to do so, we make use of the structure presented in figure (a). By applying a voltage to the electrodes, the free-standing electrode is displaced towards the non-free-standing electrode. Consequently, the gap between rails of the slot waveguide is increased and the effective refractive index is changed. To measure the phase shift, the phase shifter is implemented in a Mach-Zehnder interferometer. The phase shift can be estimated with $\phi \approx \frac{2\pi l_i}{\lambda_0} \frac{\partial n_{\text{eff}}}{\partial w_{\text{slot}}} V^2$, where V^2 is the applied voltage, w_{slot} is the width of the slot and l_i is the interaction length. This is the length over which a phase shift is generated.

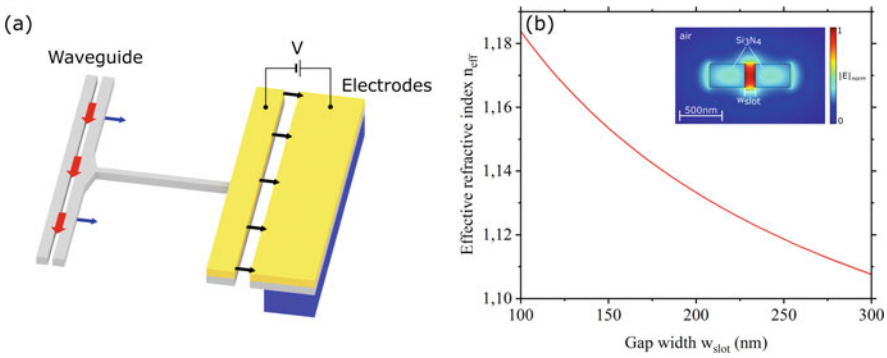

Fig. 18.1 (**a**) Schematic of the phase shifter. By applying a voltage, the free-standing electrode is pulled towards the second electrode. Thus, the slot width is increased and the effective refractive index is decreased, which results in a phase shift. (**b**) Simulated effective refractive index at $\lambda_0 = 1550$ nm

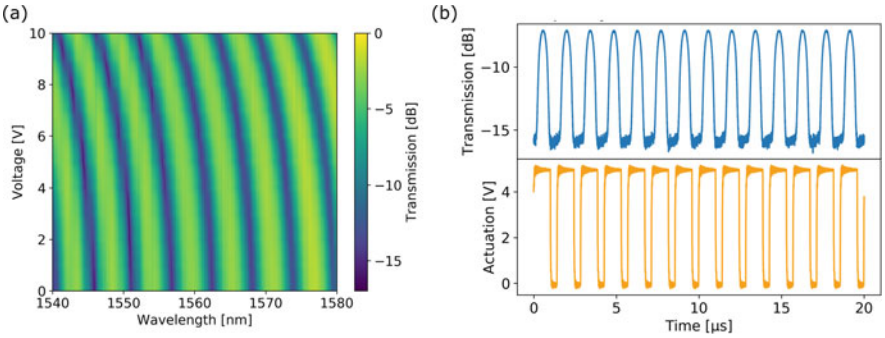

Fig. 18.2 (**a**) Spectrum of the Mach-Zehnder interferometer for different applied voltages. (**b**) Generation of optical pulses with a frequency of 700 kHz and a pulse width of 1 µs

18.3 Characterization of the Static Phase Shift

The measured spectrum of one Mach-Zehnder interferometer is shown in Fig. 18.2a. The phase shifter has a slot length of 200 µm and a slot width of 160 nm. The rails have a width of 400 nm and one of these is connected to the free-standing electrodes by two bridges. The distance between the electrodes is 600 nm. As it can be seen in Fig. 18.2a, by applying a voltage, the spectrum is shifted to smaller wavelength. A phase shift of $1\,\pi$ is reached at a voltage at 7.5 V. In addition, a maximal phase shift of $1.8\,\pi$ can be achieved at 10 V. As shown above, there is a quadratic dependency between the phase shift and the applied voltage, which is illustrated in Fig. 18.2a.

18.4 Dynamic Response of the Phase Shifter

It is also possible to generate optical pulses as shown in Fig. 18.2b. For the measurement the wavelength is set to a minimum of one of the MZI fringes. Actuation pulses with a voltage of 5 V, a frequency of 700 kHz and a pulse width of 1 µs were used. It can be seen that the phase shifter follows this actuation and optical pulses with a height of 9 dB are generated. The frequency can be increased up to 1 MHz.

References

1. Wang, C., Zhang, M., Chen, X., Bertrand, M., Shams-Ansari, A., Chandrasekhar, S., Winzer, P., Lončar, M.: Integrated lithium niobate electro-optic modulators operating at CMOS-compatible voltages. Nature **562**(7725), 101–104 (2018)
2. Ahmed, A.N.R., Nelan, S., Shi, S., Yao, P., Mercante, A., Prather, D.W.: Subvolt electro-optical modulator on thin-film lithium niobate and silicon nitride hybrid platform. Opt. Lett. **45**(5), 1112–1115 (2020)
3. Harris, N.C., Ma, Y., Mower, J., Baehr-Jones, T., Englund, D., Hochberg, M., Galland, C.: Efficient, compact and low loss thermo-optic phase shifter in silicon. Opt. Express **22**(9), 10487–10493 (2014)
4. Pruessner, M.W., Park, D., Stievater, T.H., Kozak, D.A., Rabinovich, W.S.: Broadband opto-electro-mechanical effective refractive index tuning on a chip. Opt. Express **24**(13), 13917–13930 (2016)
5. Poot, M., Tang, H.X.: Broadband nanoelectromechanical phase shifting of light on a chip. Appl. Phys. Lett. **104**(6), 061101 (2014)

Chapter 19
Radiation by a Finite-Length Electric Dipole in a Uniaxial Medium

Aamir Hayat and Muhammad Faryad

Abstract The far-field radiation pattern of a finite-length electric dipole is derived in an unbounded negative uniaxial medium (calcite). An extraordinary wave is emitted when the dipole is oriented parallel to the optic axis. Both ordinary and extraordinary waves are observed when the dipole is oriented perpendicular to the optic axis (Hayat and Faryad, OSA Continuum 2:1411–1429, 2019).

Keywords Finite-length electric dipole · Uniaxial medium

Let us assume an unbounded negative uniaxial medium with optic axis along the x-axis and let us consider a linear finite-length electric dipole of length 2 L with two different orientations with respect to the optic axis. In the first case, the dipole and the optic axis are oriented along the z-axis, i.e., parallel to each other. In the second case, the dipole is along the z-axis, i.e., perpendicular to the optic axis [1–3]. Near-fields and far-fields were derived theoretically and the results of the far-field are presented for calcite in Fig. 19.1.

In Fig. 19.1, we show the far-field radiation pattern of a dipole in a uniaxial medium (calcite) with $\epsilon_a = 2.749$, $\epsilon_b = 2.208$, $\mu_b = 1$, $\lambda_o = 0.597\ \mu m$ [3], and $L = 0.2\ \lambda_o$. The plot is given for $-\pi \leq \theta \leq \pi$ in (a). From Fig. 19.1a, it is clear that when both dipole and optic axis are oriented along the z-axis, no radiation is emitted along this direction.

The plot in Fig. 19.1b is given for $\phi = \pi/6$, $-\pi \leq \theta \leq \pi$, and we see that both ordinary and extraordinary waves are emitted when the dipole is along the z-axis and the optic axis is along the x-axis. Also, it is clear that no radiation is emitted along the direction of the optic axis, and the radiation is observed perpendicular to the direction of the optic axis. The extraordinary wave is also emitted perpendicular to the direction of the optic axis along with the ordinary wave. If we compare Figs.

A. Hayat (✉) · M. Faryad
Department of Physics, Lahore University of Management Sciences, Lahore, Pakistan
e-mail: 15120005@lums.edu.pk; muhammad.faryad@lums.edu.pk

M. Cesaria et al. (eds.), *Light-Matter Interactions Towards the Nanoscale*,
NATO Science for Peace and Security Series B: Physics and Biophysics,
https://doi.org/10.1007/978-94-024-2138-5_19

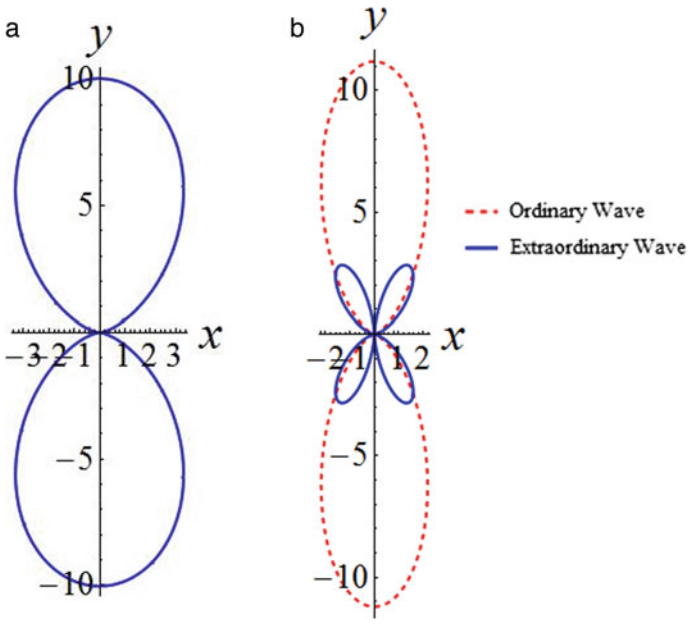

Fig. 19.1 (**a**) Far-field radiation pattern of the extraordinary wave when the dipole and the optic axis are oriented along the z-axis and (**b**) radiation pattern of the ordinary and extraordinary waves when the dipole is along the z-axis and the optic axis is along the x-axis, for a uniaxial medium (calcite) with $\epsilon_a = 2.749$, $\epsilon_b = 2.208$, $\mu_b = 1$, $\lambda_o = 0.597$ μm [3], and $L = 0.2\ \lambda_o$. The plot is given for $-\pi \leq \theta \leq \pi$ in (a) and, for $\phi = \pi/6$, $-\pi \leq \theta \leq \pi$ in (**b**)

19.1a, b, we see that in Fig. 19.1a only the extraordinary wave is emitted, whereas in Fig. 19.1b both the ordinary and extraordinary waves are emitted.

References

1. Hayat A, Faryad M (2019) On the radiation from a Hertzian dipole of a finite length in the uniaxial dielectric medium. OSA Continuum 2(4):1411–1429
2. Faryad M, Lakhtakia A (2018) Infinite-space dyadic green functions in electromagnetism. IOP Concise Physics, Bristol
3. Yariv A, Yeh P (1984) Optical waves in crystals, propagation and control of laser radiation. Wiley, Hoboken
4. Chen HC (1983) Theory of electromagnetic waves: a coordinate-free approach. McGraw-Hill, New York

Chapter 20
How Integrated Photonics Can Help to Understand Our Brain

Corinna Kaspar, Julia Lehrich, and Wolfram H. P. Pernice

Abstract The functionality of the central nervous system including the human brain is extremely complex and still gives rise to many questions. The driving force behind the huge interest in a deeper understanding of the same is not only neuroscientists and physicians with the urge to be able to cure neural disorders. In addition, artificial neural networks, which are inspired by the human brain, become more powerful tools for information processing.

In the last decade, optogenetics opened up new possibilities to control cells in living tissue. Channelrhodopsin expressing nerve cells can be directly and selectively stimulated on a time scale of milliseconds. This is achieved by means of light, which is absorbed by channelrhodopsin and thus leads to a modulation of the conductance of the ion channel in the cell membrane. In this way, the investigation of neural activity including processes such as synaptic transmission and plasticity is facilitated (Schoenenberger et al., Exp Physiol 96:34–39, 2010). In particular, the mechanisms involved in short-term plasticity, which is the constant modulation of synaptic strength on a time scale of seconds, have not been extensively studied and remain unclear (Regehr, Cold Spring Harb Perspect Biol 4:a005702, 2012).

Here, we present an approach how to investigate precisely the time-, use- and frequency-dependence of short-term plasticity even at the level of a single synapse. For this, an integrated photonic network serves as a platform for the growth of nerve cells. With the help of polymer-pen lithography, the photonic components are locally biofunctionalised so that the formation of synapses at selected spots is controlled. Light propagates in waveguides to these spots and interacts with the cells, which enables a stimulation of individual neurons or even single synapses in a regulated manner. At the same time, the evanescent field at the surface of the waveguides is used for total internal reflection fluorescence microscopy (Diekmann et al., Nat Photonics 11, 322–328, 2017; Tinguely et al., Opt Express 25(22), 27678–27690,

C. Kaspar · J. Lehrich · W. H. P. Pernice (✉)
University of Muenster, Muenster, Germany
e-mail: corinna.kaspar@wwu.de; corinna.kaspar@uni-muenster.de; wolfram.pernice@uni-muenster.de

M. Cesaria et al. (eds.), *Light-Matter Interactions Towards the Nanoscale*,
NATO Science for Peace and Security Series B: Physics and Biophysics,
https://doi.org/10.1007/978-94-024-2138-5_20

2017). Hence, fluorescent labels, which indicate synaptic release events or a firing of a neuron, can be excited and the synaptic response can be optically read out. In this way, we can optically analyse synaptic activity and investigate short-term plasticity in an unprecedented manner.

Keywords Optogenetics · Synaptic plasticity · Waveguide TIRF microscopy

References

1. Schoenenberger P, Schärer Y-PZ, Oertner TG (2010) Channelrhodopsin as a tool to investigate synaptic transmission and plasticity. Exp Physiol 96(1):34–39
2. Regehr WG (2012) Short-term presynaptic plasticity. Cold Spring Harb Perspect Biol 4:a005702
3. Diekmann R, Helle OI, Oie CI, McCourt P, Huser TR, Schüttpelz M, Ahluwalia BS (2017) Chip-based wide field-of-view nanoscopy. Nat Photonics 11:322–328
4. Tinguely J-C, Helle OI, Ahluwalia BS (2017) Silicon nitride waveguide platform for fluorescence microscopy of living cells. Opt Express 25(22):27678–27690

Chapter 21
Polarized and Diffracted Second Harmonic Generation from Semiconductor Metasurfaces

Giuseppe Marino, Carlo Gigli, Davide Rocco, Ivan Favero, Aristide Lemaître, Costantino De Angelis, and Giuseppe Leo

Abstract We demonstrate polarization, phase, and amplitude control of second harmonic generation in diffractive all-dielectric nonlinear metasurfaces.

Keywords Nonlinear metasurfaces · Mie resonances · Nanophotonics · Second-harmonic generation · All-dielectric nanophotonics · Fourier imaging

21.1 Introduction

Semiconductor metasurfaces are two-dimensional arrangements of nanoresonators recently studied for their potentials in shaping polarization, phase and amplitude of both linear and harmonic light waves. Up to date, their reported nonlinear optical properties have been dominated by the local features of the individual nanoresonators [1–3]. However, collective responses typical of either Mie-resonant metamaterials or photonic crystals can potentially boost the control over such optical properties.

G. Marino (✉) · C. Gigli · I. Favero · G. Leo
Matériaux et Phénomènes Quantiques, Université Paris Diderot & CNRS, Paris, France
e-mail: giuseppe.marino@univ-paris-diderot.fr; giuseppe.leo@univ-paris-diderot.fr

D. Rocco
Department of Information Engineering, Università degli Studi di Brescia & INO-CNR, Brescia, Italy

A. Lemaître · C. De Angelis
Centre de Nanosciences et de Nanotechnologies, CNRS, Université Paris-Saclay, Palaiseau, France

M. Cesaria et al. (eds.), *Light-Matter Interactions Towards the Nanoscale*,
NATO Science for Peace and Security Series B: Physics and Biophysics,
https://doi.org/10.1007/978-94-024-2138-5_21

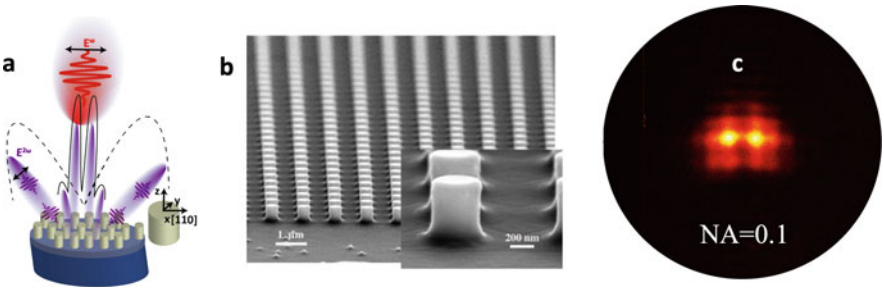

Fig. 21.1 (**a**) Schematic of the AlGaAs-on-AlOx metasurface, with FF input field at normal incidence (red) and SH interference pattern (violet): solid line represents a cut plane of the grating lobes at SH, while the dashed line represents a cut plane of the SHG from the isolated nanoresonator. (**b**) SEM image of the fabricated metasurface. With h = 400 nm, r = 195 nm and p = 1025 nm. (**c**) Measured radiation pattern of reflected SHG from AlGaAs-on-AlOx metasurface within NA = 0.1

21.2 Results

In this work, we demonstrate the generation of second harmonic with zero-order diffraction from quadratically nonlinear metasurfaces, made out of AlGaAs-on-AlOx nanocylinders with spatial period comparable with a pump wavelength in the optical telecom range [4]. Upon normal incidence of the pump beam, we demonstrate that the modulation of Mie- resonances via Bragg scattering at both fundamental and second harmonic frequencies results in a constructive diffraction of the second harmonic light into the zero order, based on effective optical properties. This zero-order second harmonic (SH) diffraction results in a 50-fold increase of the detected harmonic power within a solid angle of 5° (see Fig. 21.1). Moreover, 90% of the incident polarization is converted in the SH cross-polarized component, in contrast to around 40% measured previously for isolated nano-antennas [5–8]. This is achieved by a stronger coupling of the incident light with the metasurface resonances at both fundamental and harmonic frequencies with respect to the original Mie-resonances of the isolated constituents. In addition, upon pumping a polarization-gradient $\chi^{(2)}$ metasurface with varying incident polarizations, highly horizontal and diagonal linear polarized zero-order SH states can be achieved [8].

21.3 Conclusion

Our results demonstrate that higher control of polarization, phase, and amplitude of the harmonic wavefront can be achieved in diffractive all-dielectric nonlinear metasurfaces, with applications for on-axis optical imaging.

References

1. Wang L, Kruk SS, Koshelev KL, Kravchenko II, Luther-Davies B, Kivshar YS (2018) Nonlinear wavefront control with all-dielectric metasurfaces. Nano Lett 18:3978–3984
2. Vabishchevich PP, Liu S, Sinclair MB, Keeler GA, Peake GM, Brener I (2018) Enhanced second-harmonic generation using broken symmetry III–V semiconductor Fano metasurfaces. ACS Photon 5:1685–1690
3. Löchner FJ, Fedotova AN, Liu S, Keeler GA, Peake GM, Saravi S, Shcherbakov MR, Burger S, Fedyanin AA, Brener I (2018) Polarization-dependent second harmonic diffraction from resonant GaAs metasurfaces. ACS Photon 5:1786–1793
4. Marino G, Gigli C, Rocco D, Lemaître A, Favero I, De Angelis C, Leo G (2019) Zero-order second harmonic generation from AlGaAs-on-insulator metasurfaces. ACS Photon 6(5):1226–1231
5. Gili VF, Carletti L, Locatelli A, Rocco D, Finazzi M, Ghirardini L, Favero I, Gomez C, Lemaitre A, Celebrano M, De Angelis C, Leo G (2016) Monolithic AlGaAs second-harmonic nanoantennas. Opt Expr 24:15965–15971
6. Camacho-Morales R, Rahmani M, Kruk S, Wang L, Xu L, Smirnova DA, Solntsev AS, Miroshnichenko A, Tan HH, Karouta F, Naureen S, Vora K, Carletti L, De Angelis C, Jagadish C, Kivshar YS, Neshev DN (2016) Nonlinear generation of vector beams from AlGaAs nanoantennas. Nano Lett 16:7191–7197
7. Liu S, Sinclair MB, Saravi S, Keeler GA, Yang Y, Reno J, Peake GM, Setzpfandt F, Staude I, Pertsch T (2016) Resonantly enhanced second-harmonic generation using III–V semiconductor all-dielectric metasurfaces. Nano Lett 16:5426–5432
8. Gigli C, Marino G, Suffit S, Patriarche G, Beaudoin G, Pantzas K, Sagnes I, Favero I, Leo G (2019) Polarization- and diffraction-controlled second harmonic generation from semiconductor metasurfaces. JOSA B 36(7):E55–E64

Chapter 22
Simple Multidimensional Two-Fluid Plasma Model Solver Based on PseudoSpectral Time-Domain Method

Benoit Morel, Remo Giust, Kazem Ardaneh, Remi Meyer, and Francois Courvoisier

Abstract We present a 3D hydrodynamic code solving the two-fluid plasma model. This code is simple to implement and adapted for simulations of short-pulse laser interactions with plasma. The code gave excellent results for several well-known problems of plasma physics.

Keywords Two-fluid plasma model · 3D hydrodynamic code · PSTD

22.1 The Two-Fluid Plasma Model

The interaction of laser beam with a plasma has turned out to be a remarkably rich topic in physics: X-Ray sources, laser-plasma accelerators, inertial fusion, nonlinear plasmonics [1]. However, the fundamental understanding of a large range of physical phenomena requires precise numerical simulations. Hydro-codes are known to well describe dense collisional plasmas. The starting point of a hydro-code is the two-fluid plasma model [2], which means solving Maxwell equations together with Euler equations describing the plasma dynamics (density, mean velocity, local temperature of electron and ion fluids). However, stable and precise two-fluid plasma hydro-code are often based on Riemann solvers [3], which are exceedingly complex for most non-expert groups.

B. Morel (✉) · R. Giust · K. Ardaneh · R. Meyer · F. Courvoisier
Institut FEMTO-ST, Université de Bourgogne Franche-Comté, CNRS, Besançon, France
e-mail: benoit.morel@femto-st.fr

M. Cesaria et al. (eds.), *Light-Matter Interactions Towards the Nanoscale*,
NATO Science for Peace and Security Series B: Physics and Biophysics,
https://doi.org/10.1007/978-94-024-2138-5_22

22.2 Numerical Algorithm

Here we report on the development of a new technique to solve this difficult problem for multidimensional hydro-codes. Our algorithm is based on a composite scheme mixing Lax-Friedrichs and Lax-Wendroff schemes to solve Euler equations, and on PseudoSpectral Time-Domain (PSTD) method to solve Maxwell's curl equations. Furthermore, the source term of fluid equations is integrated with a standard fourth-order Runge-Kutta scheme. The technical implementation of this approach is simple because it does not require complex mathematical techniques other than Fast Fourier Transform (FFT) and finite differences. In addition, we have integrated the Bhatnagar-Gross-Krook collision model.

22.3 Validation of the Code

Our code was validated against several difficult problems. First, the fluid equations solver was validated with the Rayleigh-Taylor instability problem [4]. The full two-fluid plasma code was then used to retrieve most of the well-known plasma physics problems: dispersion relations of unmagnetized plasmas, mode conversion in oblique incidence, reflection on over-critical plasmas and wakefield generation via ponderomotive force. Figure 22.1a shows the numerical dispersion diagram obtained for the excitation of longitudinal waves. The analytic and numerical results shows an excellent agreement, even for the longitudinal ion plasma wave where analytics describe the high- and low-frequency asymptotic regimes. Furthermore, Fig. 22.1b shows the expected absorption for a laser pulse reflection on over-critical plasma density ramp.

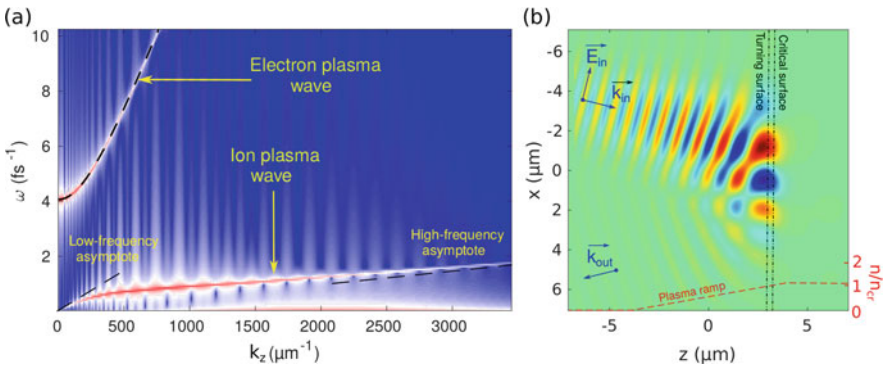

Fig. 22.1 (**a**) Dispersion diagram (ω,k_z) in logarithm scale for longitudinal waves in a warm plasma with light ions ($m_{ion} = 25\, m_{electron}$). Black dashed lines correspond to the analytical dispersion relations for ion and electron plasma waves. (**b**) E_x laser field component representation during reflection on over-critical plasma ramp

To conclude, we developed a two-fluid plasma hydro-code which is very easy to implement. This is a robust and simple manner to perform simulations of laser-plasma interaction.

References

1. Kauranen, M., Zayats, A.V.: Nonlinear plasmonics. Nat. Photonics **6**, 737–748 (2012). https://doi.org/10.1038/nphoton.2012.244
2. Gibbon, P.: Short Pulse Laser Interactions with Matter. Imperial Colloege Press, London (2005). https://doi.org/10.1142/p838
3. Shumlak, K., Loverich, J.: Approximate Riemann solver for the two-fluid plasma model. J. Comput. Phys. **187**, 620–638 (2003). https://doi.org/10.1016/S0021-9991(03)00151-7
4. Youngs, D.L.: Numerical simulation of turbulent mixing by Rayleigh-Taylor instability. J. Sci. Comput. **12**, 32–44 (1984). https://doi.org/10.1016/0167-2789(84)90512--8

Chapter 23
Volumetric, Glass-Based Luminescent Nanocomposites Produced Using the NPDD Method

Rafał Nowaczyński, Marcin Gajc, Hańcza B. Surma, Piotr Paszke, Kamil Szlachetko, Piotr Piotrowski, and Dorota A. Pawlak

Abstract NanoParticle Direct Doping (NPDD) (Gajc and Pawlak, Adv Funct Mater 23:3443, 2013) is a method developed in the Institute of Electronic Materials Technology in Warsaw that allows fabrication of volumetric composites based on low-melting-point glass matrices doped with various kinds of nanoparticles (NPs), including metallic plasmonic NPs and Quantum Dots (QDs). It is based on a Micro-Pulling down method, in which dry powders of the matrix and dopants are mixed together, heated until the matrix melts and then pulled in a form of a rod.

Here we show that it is possible to obtain composite material doped with silver NPs with diameter of 20 nm, based on a sodium borophosphate dielectric glass (NBP), which is transparent over wide range of wavelengths and exhibits melting temperature of ca. 750 °C (Gajc and Pawlak, Adv Funct Mater 23:3443, 2013). It results in Localized Surface Plasmon Resonance (LSPR) peak visible on the absorbance spectrum of the material with maximum at 405 nm. It is also possible to co-dope the composite with QDs. Addition of Ag NPs results in the enhancement of the 510 nm excitonic emission from CdTe QDs compared to the material doped only with QDs.

The NPDD method allows us to combine different types of NPs. Even after co-doping simultaneously with hydrophilic CdTe QDs (λ_{em} = 730 nm) and hydrophobic, core-shell CdSe/ZnS QDs (λ_{em} = 530 nm) material exhibits dual-

R. Nowaczyński (✉)
Faculty of Materials Science and Engineering, Warsaw University of Technology, Warsaw, Poland

Faculty of Chemistry, University of Warsaw, Warsaw, Poland
e-mail: rafal.nowaczynski.dokt@pw.edu.pl; r.nowaczynski@cent.uw.edu.pl

P. Paszke · K. Szlachetko · P. Piotrowski
Faculty of Chemistry, University of Warsaw, Warsaw, Poland

D. A. Pawlak
Faculty of Chemistry, University of Warsaw, Warsaw, Poland

Institute of Electronic Materials Technology, Warsaw, Poland

M. Gajc · H. B. Surma
Institute of Electronic Materials Technology, Warsaw, Poland

M. Cesaria et al. (eds.), *Light-Matter Interactions Towards the Nanoscale*,
NATO Science for Peace and Security Series B: Physics and Biophysics,
https://doi.org/10.1007/978-94-024-2138-5_23

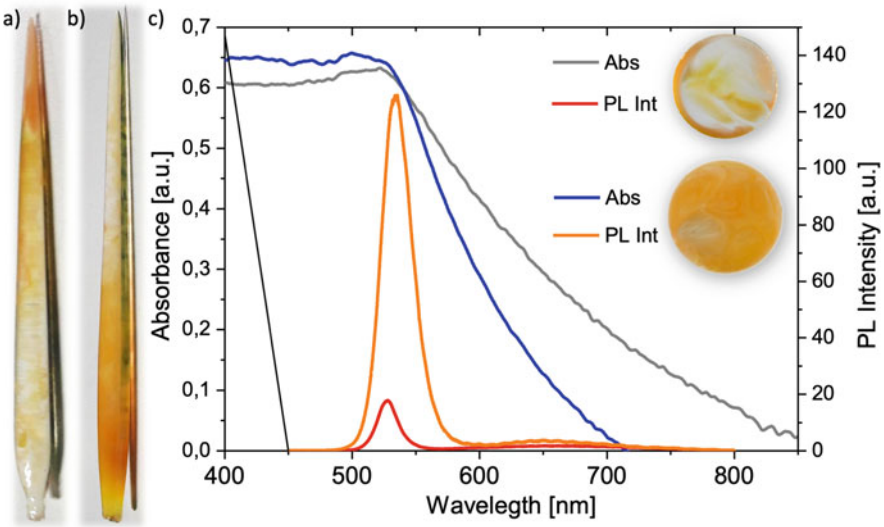

Fig. 23.1 (**a**) NBP glass rod doped with 0.3 wt.% of ZnCdSeS QDs, added to the initial glass matrix as a dry powder. (**b**) NBP glass rod doped with 0.3 wt.% of ZnCdSeS QDs, added to the initial glass matrix trough dispersion in toluene. (**c**) Absorbance and PL intensity spectra of obtained materials along with cross-sections of rods. Low homogeneity – QDs added as a dry powder, high homogeneity – QDs dispersed in toluene

wavelength photoluminescence (Nowaczynski and Pawlak Part Part Syst Charact 36:1800124, 2018). This versatility of the method can potentially allow us to construct a material doped with Ag NPs, QDs and rare-earth ions, especially Pr^{3+} to achieve narrowband Pr luminescence with laser diode excitation at wavelengths that are not absorbed well by the Pr itself. However, quality and homogeneity of composites has to be improved, which can be achieved by modification of the initial powder preparation process, like QDs dispersion in toluene prior to mixing with glass powder (Fig. 23.1).

Keywords NanoParticle direct doping · Quantum dots · Plasmonic nanoparticles

Acknowledgments The authors thank the MAESTRO Project (2011/02/A/ST5/00471) operated by National Science Centre for support of this work. This project was supported financially by the TEAM programme of the Foundation for Polish Science (No. TEAM/2016-3/29), co-financed by the European Union under the European Regional Development Fund.

References

1. Gajc M, Pawlak DA et al (2013) Nanoparticle direct doping: novel method for manufacturing three-dimensional bulk Plasmonic nanocomposites. Adv Funct Mater 23:3443
2. Nowaczynski R, Pawlak DA et al (2018) Manufacturing of volumetric glass–based composites with single- and double-QD doping. Part Part Syst Charact 36:1800124

Chapter 24
Hybrid Optical Nanocavities for Reflective Displays

Stefano Rossi and Magnus Jonsson

Abstract We present a new type of optical metal-insulator-metal nanocavities that provide a tunable reflection peak in the visible and corresponding reflective structural coloration. The system may be particularly useful for reflective displays in color. The integration with conductive electrochromic polymers in a hybrid structure may allow active tunability of the cavity.

Keywords Nanocavity · Reflective displays · Conductive polymers

24.1 Introduction

Metasurfaces based on plasmonic systems or optical nanocavities can control light at the nanoscale, allowing a broad range of effects including structural coloration. Their strong localized resonant coupling of the incident light allows the use of flat and nanometric thin structures, which typically have much longer-term stability than organic dyes or pigments. A Fabry-Perot (FP) cavity, formed by two mirrors separated by a transparent spacer layer, can provide structural coloration, although with limited quality of the reflection peak. The colors typically need to be improved by modification of the structure, for example, using plasmonic nanoholes as top mirror [1, 2]. Other studies have replaced the top mirror with a broadband absorber [3, 4]. Interference between incident and reflected light creates a node at the position of the absorber for certain wavelengths, which therefore are not absorbed and instead form a proper reflection peak. Here, we investigate a hybrid version between these two concepts, by adding a broadband absorber on top of a Fabry-Perot cavity.

S. Rossi (✉) · M. Jonsson
Laboratory of Organic Electronics, Linköping University, Norrköping, Sweden
e-mail: stefano.rossi@liu.se

M. Cesaria et al. (eds.), *Light-Matter Interactions Towards the Nanoscale*,
NATO Science for Peace and Security Series B: Physics and Biophysics,
https://doi.org/10.1007/978-94-024-2138-5_24

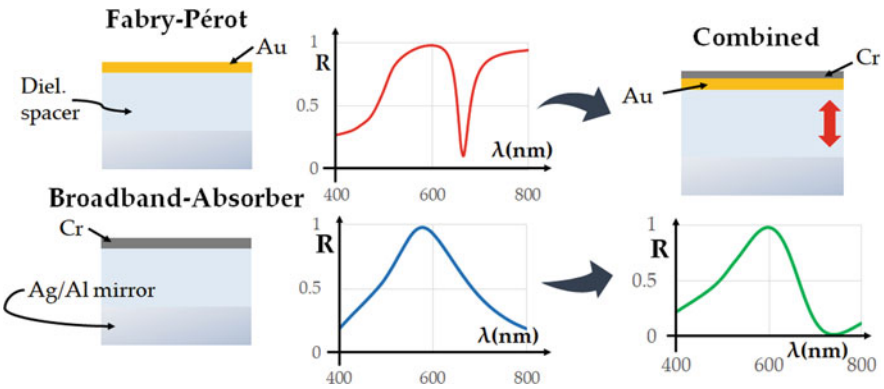

Fig. 24.1 Comparison between the Fabry-Pérot and broadband absorber-based nanocavities (on the left) with the combined structure. The spectra are simulated for the same dielectric thickness and mirror, while optimizing the top film thickness

24.2 Results

The FP cavity used silver as bottom mirror and a semitransparent gold layer as top mirror. As absorber, we used chromium, which has similar values of the real and imaginary part of the refractive index and provides uniform absorption across the visible spectral range. In addition, chromium was selected because of its good availability and ease of thermal evaporation. Figure 24.1 shows the reflectance for the final structure and for the two individual concepts (only gold or only chromium as top layer). The single FP cavity cannot efficiently cover the entire visible in reflection, due to its absorptive nature. In contrast, the broadband-absorber cavity is the best choice for reflective colors, forming a single reflection peak, but it suffers from high reflection tails. Since the FP absorption dip is red-shifted from the reflection peak of the corresponding broadband absorber-cavity, the two cavities can be combined. We found that the hybrid system with both mirror and absorber gave an overall better result in terms of chromaticity by lowering the tails of the reflection peak in the red region. The structure provided a reflective peak that could be tuned in the entire visible spectrum just by changing the dielectric thickness.

24.3 Conclusions

The presented hybrid optical cavity does not require nanostructuring and can therefore be easily fabricated by various methods at large scale. Based on the superior chromaticity and easy color tuning, the concept may find particular use for

reflective displays in color, for which the use of conductive electrochromic polymers may be used to control the plasmonic excitation by changing their redox states [1, 2, 5].

References

1. Xiong K et al (2016) Electronic paper: plasmonic metasurfaces with conjugated polymers for flexible electronic paper in color. Adv Mater 28(45):10103–10103
2. Xiong K et al (2017) Switchable plasmonic metasurfaces with high chromaticity containing only abundant metals. Nano Lett 17(11):7033–7039
3. Hong J et al (2015) Continuous color reflective displays using interferometric absorption. Optica 2(7):589
4. Liu F et al (2018) Tunable reflective color filters based on asymmetric Fabry–Perot cavities employing ultrathin Ge 2 Sb 2 Te 5 as a broadband absorber. Appl Opt 57(30):9040
5. Peng J et al (2019) Scalable electrochromic nanopixels using plasmonics. Sci Adv 5(5):1–9

Chapter 25
Laser-Irradiated Nanostructures for Intracellular Delivery

Weilu Shen and Eric Mazur

Abstract Diseases and disorders arise when cells begin to malfunction. In order to advance basic research in diseases and develop therapeutics, it is vital to understand and fix mechanisms at the cellular level. However, a challenge in the biomedical field is the direct delivery of such revolutionary cargoes into the cellular cytoplasm with three key features: viability of the cells, throughput of the cells for therapeutic applications, and efficiency of the tool. We present three different laser-activated large-area nanostructured substrates for dynamic intracellular delivery of large biomolecules in the kDa range. All three substrate platforms are excited by 11-ns laser pulses of 1064 nm wavelength to create transient pores in cells that allow materials in the environment to diffuse into the cytoplasm before the phospholipid bilayer membrane seals.

Keywords Biophotonics · Cargo delivery · Nanomaterials

In the emerging field of nanomedicine, it is important to deliver biologically interesting cargo and molecules directly into relevant cells. In order to change the characteristics of cells, we must be able to manipulate biological functions through the delivery of cargoes such as proteins, antibodies, and genetic materials. Proteins can be delivered into the cytosol to manipulate the expressed traits of cells. Genetic materials such as small interfering RNA can be delivered to manipulate gene expression. With the development of CRISPR-cas9, gene-editing can be used for gene-therapy treatments. Current established methods such as electroporation, viral techniques, and liposomal reagents each come with respective strengths and weaknesses that fit different application needs [1]. These are summarized in Table 25.1:

We recently developed a delivery method using the laser-activation of polymer substrates to perform effective cargo delivery. We fabricate and characterize laser-

W. Shen (✉) · E. Mazur
Harvard University, Cambridge, MA, USA
e-mail: weilu_shen@g.harvard.edu

M. Cesaria et al. (eds.), *Light-Matter Interactions Towards the Nanoscale*,
NATO Science for Peace and Security Series B: Physics and Biophysics,
https://doi.org/10.1007/978-94-024-2138-5_25

Table 25.1 Toxicity, efficiency, and throughput of current methods used in delivering cas9

Method	Toxicity	Efficiency	Throughput	*In vivo*
Lipid	Medium	Medium	High	No
Electroporation	High	High	High	No
Viral transfection	Medium	High	High	Yes
Optotransfection	Low	High	Low	No
Plasmonic substrates	Low	High	High	?

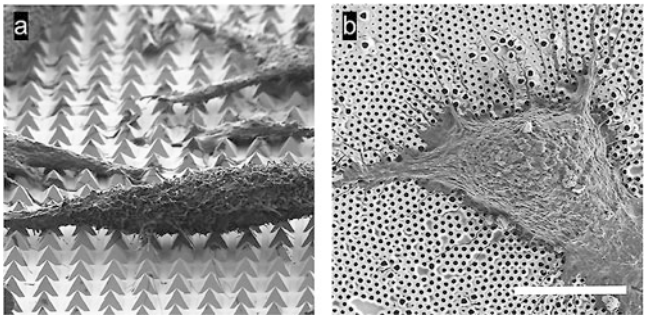

Fig. 25.1 (**a**) Shows a tilted SEM image of chemically fixed HeLa CCl2 cells on gold thin-film pyramids. A scale bar is not provided due to the detection angle but as a reference, the base length of each pyramid is 2.4 μ. (**b**) Shows a chemically fixed cell on self-assembled nanocavities Scale bar for b and c represent 10 μ

activated polymers, with the aim of better equipping the biomedical field with novel *in vitro* and *in vivo* cargo-delivery methods that harness laser-activated materials.

We also present two other types of laser-based cargo delivery platforms which utilize thermoplasmonic effects: (1) gold nanopyramid arrayed substrates created with a cost-effective method of large-area photolithography and template-stripping, a plasmonically optimized device which efficiently delivers cargoes ranging in size from 0.6 to 2000 kDa to cells with high viability (of up to 98%). The technique is also high-throughput, treating 50,000 cells per minute. There were minimal residual fragments after laser-irradiation, unlike other plasmonic delivery methods using gold nanoparticles. Figure 25.1a shows a tilted SEM image of the device [2–4]. (2) Dense arrays of colloidal self-assembled nanocavities were thermally coated with 50 nm of titanium to create large macroscopic areas that can efficiently convert near-infrared laser light into heat. Figure 25.1b shows a top-down SEM image of the self-assembled device. The substrate array geometry facilitates successful optoporation and cargo delivery. This colloidal substrate does not require cleanroom fabrication facilities that the gold nanopyramids do and are able to deliver the membrane-impermeable calcein green dye molecules into the cellular cytoplasm at an efficiency of 78% and at a throughput rate of 30,000 cells per minute. 87% of the cells survive treatment [5].

All three substrate platforms are excited by 11-ns laser pulses of 1064 nm wavelength to create transient pores in cells. Adherent cell lines such as HeLa and

Panc-1 are grown on the substrates, and pores only form on the cells in the localized regions excited with nanosecond laser pulses—thus, allowing treatment selectivity within a population. The medium surrounding the cell contains the delivery cargo in solution, and cargoes diffuse into the cell before the transient pores are sealed. We use fluorescence imaging and flow cytometry to quantify the delivery efficiency and viability in a reproducible manner. Our light-activated substrate platforms can deliver important material directly into cells, furthering the field of nanomedicine in a cost-effective manner. Further details and data can be seen in the reference materials pertaining to thermoplasmonic intracellular delivery.

References

1. Lino CA, Harper JC, Carney JP, Timlin JA (2018) Delivering CRISPR: a review of the challenges and approaches delivering. Drug Deliv 25(1):1234–1257
2. Saklayen N, Huber M, Madrid M, Nuzzo V, Vulis DI, Shen W, Nelson J, McClelland AA, Heisterkamp A, Mazur E (2017) Intracellular delivery using nanosecond-laser excitation of large-area plasmonic substrate. ACS Nano 11(4):3671–3680
3. Madrid M, Saklayen N, Shen W, Huber M, Vogel N, Mazur E (2018) Laser-activated self-assembled thermoplasmonic nanocavity substrates for intracellular delivery. ACS Appl Biomater 1(6):1793–1799
4. Saklayen N, Kalies S, Madrid M, Nuzzo V, Huber M, Shen W, Sinanan-Singh J, Heinemann D, Heisterkamp A, Mazur E (2017) Analysis of poration-induced changes in cells from laser-activated plasmonic substrates. Biomed Opt Express 8(10):4756–4771
5. Raun A, Saklayen N, Zgrabik C, Shen W, Madrid M, Huber M, Hu E, Mazur E (2018) A comparison of inverted and upright laser-activated titanium nitride micropyramids for intracellular delivery. Sci Rep 8(1):15595

Chapter 26
Integrated Photonics for Infrared Spectroscopy

Maik Stappers, Nico Gruhler, and Wolfram H. P. Pernice

Abstract Integrated photonics enables the mass production of stable and reliable optic experiments. By interfacing integrated photonic circuits with molecules cheap and yet reliable and stable spectrometers can be build. In this work we show, that silicon be used to fabricate integrated waveguides and resonators for the mid infrared wavelength range.

Keywords Mid-IR · Integrated photonics · SOI · Silicon

26.1 Introduction

In this work integrated photonic waveguides are presented, that are able to guide light in a wavelength range from 6.8 μm to 8.2 μm. The propagation losses of these waveguides were investigated using the cut-back method and were derived from the quality factor of ring resonators, coupled evanescently to the waveguide. The wavelength range around 8 μm is especially interesting, because many molecules show characteristic absorption spectra in this range. Measuring these spectra allows the identification of the molecules. Therefore, it is called "Fingerprint Region". Modern Infrared spectrometers for detecting certain molecules such as explosives or drugs often use free space optics, making them hard to align and stabilize properly. Integrating these spectrometers onto a chip promises an enhanced stability and reliability. Utilizing the mass fabrication possibilities of the semiconductor industry allows a cheap production of such integrated photonic circuits.

M. Stappers (✉) · N. Gruhler · W. H. P. Pernice
Münster University, CeNTech – Center for Nanotechnology, Münster, Germany
e-mail: m.stappers@uni-muenster.de
https://www.uni-muenster.de/Physik.PI/Pernice/

M. Cesaria et al. (eds.), *Light-Matter Interactions Towards the Nanoscale*,
NATO Science for Peace and Security Series B: Physics and Biophysics,
https://doi.org/10.1007/978-94-024-2138-5_26

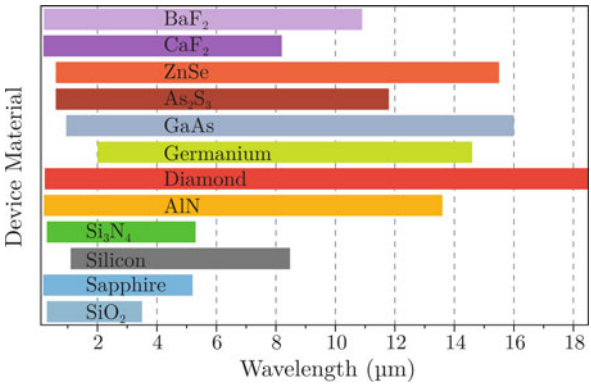

Fig. 26.1 Transparency region of materials often used for IR components and integrated photonic circuits [1]

26.2 Material Platform

Most of today's integrated photonic circuits are designed to operate at telecom wavelength (around 1550 nm) or in the visible range. In order to build photonic structures that operate at 8 µm first a suitable material platform needs to be found. As can be seen in Fig. 26.1 silicon and diamond are suitable candidates for Mid-IR integrated photonics, as they are transparent in this range and can also be structured by standard semiconductor industry processes like reactive ion etching.

26.3 Fabrication and Results

Silicon typically comes in the form of silicon-on-insulator wafers. On this platform the silicon layer for the devices is deviced from the silicon substrate by a buried oxide layer made from SiO_2. As this material is opaque to Mid-IR radiation, it needs to be removed from beneath the structure. Thus, the structures need to be underetched using hydrofluoricacid. The final structures can be seen in Fig. 26.2. A transmission spectrum of a waveguide is shown in Fig. 26.3. It can clearly be seen that the used silicon waveguides are only transparent up to 8.2 µm. Nevertheless, the transparency range of the Silicon Waveguides is enough to warrant further investigation into the Integration of Mid-IR Spectrometers in Silicon.

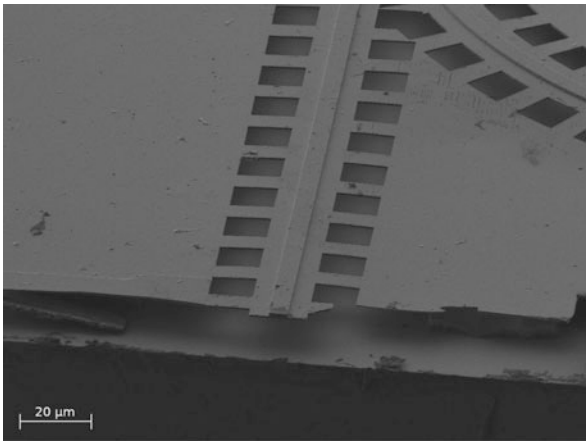

Fig. 26.2 SEM micrograph of the fabricated suspended silicon structure for Mid-IR photonics

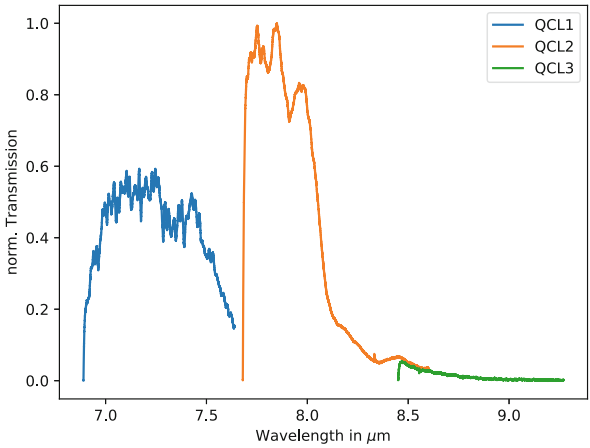

Fig. 26.3 Transmission spectrum through a long Mid-IR waveguide made from suspended silicon. The curve is normalized to it's maximum

Reference

1. Gruhler, N.: Near-Field Coupling in Hybrid Integrated Photonic Circuits. PhD Thesis. University of Muenster (2018)

Chapter 27
Self-Organized Nanostructures Obtained by Bottom-Up Methods as Plasmonic Materials and Metamaterials for VIS and IR Applications

Kamil Szlachetko, Monika Tomczyk, Piotr Piotrowski, Katarzyna Sadecka, Pawel Osewski, Aneta Antolik, and Dorota Anna Pawlak

Abstract Plasmonic materials (Barnes WL, Nature 424:824, 2003) and metamaterials (Smith, Science 305:788–792, 2004) are novel and promising fields for application in photonics, optics and optoelectronics. Engineering of structural and intrinsic properties of the materials lead to achieve controllable light-matter interactions. However, unusual properties of these materials strongly depend on structural features of the media; therefore, novel efficient methods of manufacturing are still sought. Here, we demonstrate our approach to fabricate both plasmonic composites and metamaterials in the melt-based Directional Solidification of Eutectics (DSE) method and advantages resulting from its use (Pawlak, Adv Funct Mater 20(7):1116–1124, 2010).

The presented method opens broad possibilities in the development of novel materials with unusual electromagnetic responses. For example, combining biaxial matrix with uniaxial crystal leads to narrowband and switchable light filtering (Osewski et al, Adv Opt Mater 8(7):1901617, 2020), doping dielectric matrices with plasmonic nanoparticles allows us to achieve tunable Localized Surface Plasmon Resonances in the visible (Sadecka, Opt Express 23(15):19098–19111, 2015) and infrared range (Osewski et al, Adv Opt Mater 8(7):1901617, 2020), and enhanced Raman scattering, which allows us to recognize structural features of the studied matter beyond the diffraction limit (Szlachetko K., Piotrowski P., Nanophotonics 9(14):4309-4317, 2020). A co-doping eutectics with rare earth ions causes enhanced

K. Szlachetko (✉) · M. Tomczyk · P. Piotrowski · D. A. Pawlak
Faculty of Chemistry, University of Warsaw, Warsaw, Poland
e-mail: kszlachetko@chem.uw.edu.pl

K. Sadecka · P. Osewski · A. Antolik · D. A. Pawlak
Łukasiewicz Research Network – Institute of Microelectronics and Photonics, Warsaw, Poland

M. Cesaria et al. (eds.), *Light-Matter Interactions Towards the Nanoscale*,
NATO Science for Peace and Security Series B: Physics and Biophysics,
https://doi.org/10.1007/978-94-024-2138-5_27

photoluminescence and up-conversion, which could be utilized for example in solar energy conversion cells or optoelectronic devices.

Keywords Self-organization · Eutectics · Composites · Plasmonics · Metamaterials

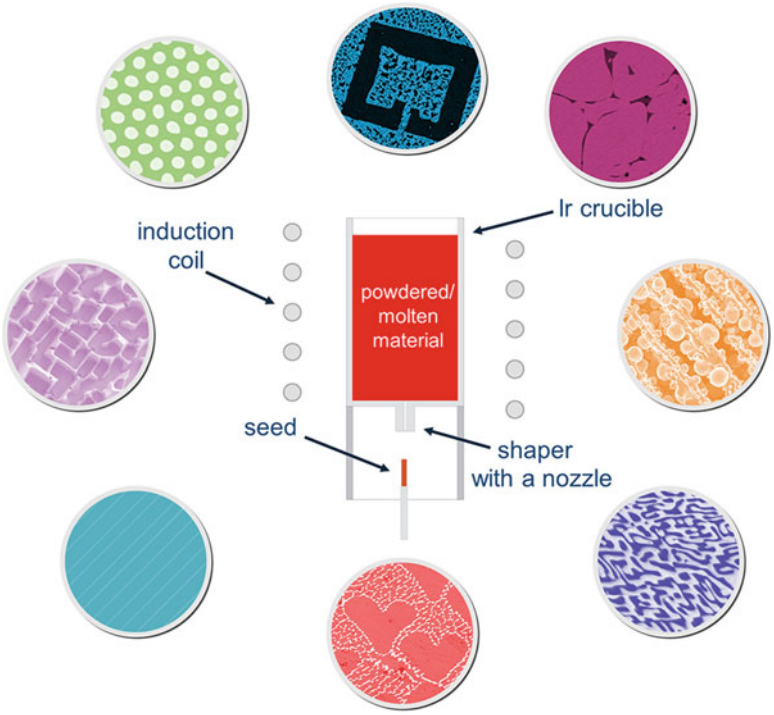

Fig. 27.1 A scheme of the directional solidification of eutectics (DSE) method based on the micro-pulling down system and examples of eutectic structures obtained within it

Acknowledgments This project was supported financially by the TEAM programme of the Foundation for Polish Science (No. TEAM/2016-3/29), co-financed by the European Union under the European Regional Development Fund. The authors thank also the National Science Centre for HARMONIA Project (2013/10/M/ST5/00650) and MAESTRO Project (2011/02/A/ST5/00471) and the Air Force Office for Scientific Research of the US NOE Project (14RT0477).

References

1. Barnes WL et al (2003) Surface plasmon subwavelength optics. Nature 424(6950):824
2. Smith DR et al (2004) Metamaterials and negative refractive index. Science 305(5685):788–792
3. Pawlak DA et al (2010) How far are we from making metamaterials by self-organization? The microstructure of highly anisotropic particles with an SRR-like geometry. Adv Funct Mater 20(7):1116–1124
4. Osewski P et al (2020) New self-organization route to tunable narrow-band optical filters and polarizers demonstrated with ZnO-$ZnWO_4$ eutectic composite. Adv Opt Mater 8(7):1901617
5. Sadecka K et al (2015) Temperature and atmosphere tunability of the nanoplasmonic resonance of a volumetric eutectic-based Bi_2O_3-Ag metamaterial. Opt Express 23(15):19098–19111
6. Szlachetko K, Piotrowski P et al (2020) Selective surface enhanced Raman scattering (SERS) in a bulk nanoplasmonic eutectic composite Bi_2O_3-Ag. Nano 9(14):4309–4317

Part III
Poster Presentations

Chapter 28
Few-Femtosecond Plasmon Transients Probed with nm-Scale Sensitivity

Béla Lovász, Péter Sándor, Zsuzsanna Pápa, Bálint Éles, Balázs Bánhegyi, Péter Rácz, Christine Prietl, Joachim R. Krenn, and Péter Dombi

Abstract Full spatiotemporal resolution of the evolution of plasmonic fields is a major goal in plasmonics in order to investigate the buildup and decay of collective electron phenomena. Here, we demonstrate few-femtosecond probing of plasmon transients uniquely combined with nm-scale sensitivity.

Keywords Plasmonics · Femtosecond · Photoelectrons

28.1 Introduction

Photoelectrons were shown to be sensitive tools for ultrahigh-sensitivity near-field probing [1–3]. We have shown that using this technique, plasmonic field enhancement can be experimentally measured with unprecedented surface sensitivity with the help of photoemitted and rescattering electrons [2]. It was demonstrated that the cutoff region of these photoelectron spectra is made up of electrons emitted from plasmonic hot spots of the nanoparticles [1] (Fig. 28.1).

B. Lovász · P. Sándor · Z. Pápa · B. Éles · B. Bánhegyi (✉) · P. Rácz · P. Dombi
Wigner Research Centre for Physics, Budapest, Hungary

ELI-ALPS, ELI-HU Nonprofit Kft., Szeged, Hungary
e-mail: banhegyi.balazs@wigner.hu

C. Prietl · J. R. Krenn
Institut für Physik, Karl-Franzens-Universitaet, Graz, Austria

M. Cesaria et al. (eds.), *Light-Matter Interactions Towards the Nanoscale*,
NATO Science for Peace and Security Series B: Physics and Biophysics,
https://doi.org/10.1007/978-94-024-2138-5_28

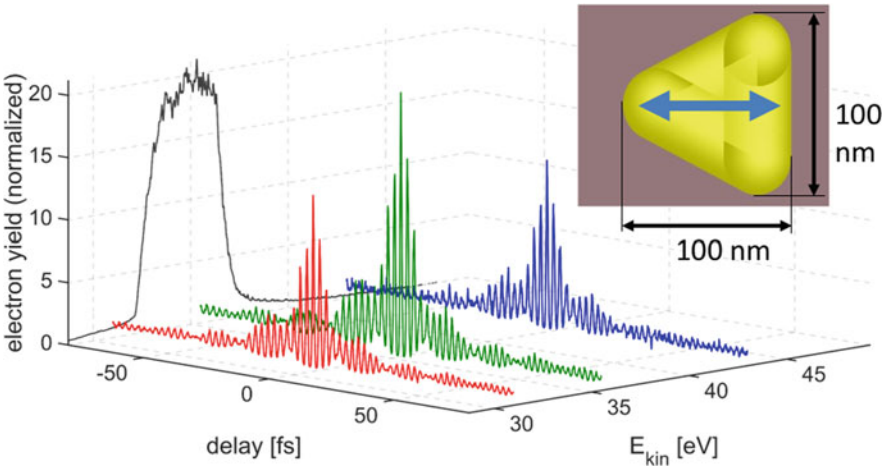

Fig. 28.1 Designed gold triangle, measured photoelectron spectrum and reconstructed electron-autocorrelations for different kinetic energy regions

28.2 Results

If we use femtosecond pulses made up of ~1.5 eV photons for this measurement, the photoelectron generation is highly nonlinear and it can serve as a basis for time-resolved probing of near-fields in a spatially highly selective manner. In contrast to a previous experiment [3], by filtering for a certain kinetic energy range of photoemitted electrons, we can limit the measurement for rescattering electrons resulting in a sub-nm surface sensitivity [2] and selectivity for plasmonic hot spots.

References

1. Rácz P, Pápa Z, Márton I et al (2017) Measurement of nanoplasmonic field enhancement with ultrafast photoemission. Nano Lett 17:1181–1186
2. Budai Z, Pápa IM et al (2018) Plasmon-plasmon coupling probed by ultrafast, strong-field photoemission with <7 Angström sensitivity. Nanoscale 10:16261–16267
3. Marsell E, Losquin A et al (2015) Nanoscale imaging of local few-femtosecond near-field dynamics within a single plasmonic nanoantenna. Nano Lett 15:6601

Chapter 29
Simulating Small Metallic Nanoparticles in FDTD: Nonlocal Correction to the Drude Model

Joshua Baxter, Antonio Calà Lesina, and Lora Ramunno

Abstract The classical Drude model fails to accurately predict the optical response of metal particles with sizes less than 10 nm due to nonlocality. A nonlocal correction can be added to the Drude model, and implemented in the finite-difference time-domain (FDTD) method.

Keywords FDTD · Nonlocality · Computational electromagnetism

29.1 Nonlocal Optical Response

The classical Drude model is commonly used to model the free electron response in plasmonic nanoparticles and is given by:

$$\frac{\partial^2 \mathbf{P}}{\partial t^2} + \gamma \frac{\partial \mathbf{P}}{\partial t} = \varepsilon_0 \omega_p^2 \mathbf{E}. \tag{29.1}$$

where $\mathbf{P}$ is the polarization field, $\mathbf{E}$ is the electric field, γ is the damping coefficient, and ω_p is the plasma frequency. This model breaks down when particles are less than 10 nm in size due to spacial nonlocality. This manifests itself as a blue shift of

J. Baxter (✉) · L. Ramunno
Department of Physics and Centre for Research in Photonics, University of Ottawa, Ottawa, ON, Canada
e-mail: jbaxt089@uottawa.ca

A. Calà Lesina
Department of Physics and Centre for Research in Photonics, University of Ottawa, Ottawa, ON, Canada

Faculty of Mechanical Engineering (Institut für Transport- und Automatisierungstechnik), Hannover Centre for Optical Technologies, and Cluster of Excellence PhoenixD, Leibniz Universität Hannover, Hannover, Germany

M. Cesaria et al. (eds.), *Light-Matter Interactions Towards the Nanoscale*,
NATO Science for Peace and Security Series B: Physics and Biophysics,
https://doi.org/10.1007/978-94-024-2138-5_29

the particle absorption resonance frequency with decreasing size and a broadening of the resonance peak [1].

To correct the classical theory and to model the free electron response, we use the hydrodynamic plasma model [1] where we apply the Thomas-Fermi energy functional given by $\frac{\delta G[n]}{\delta n} = \frac{h^2}{2m}\left(\frac{3}{8\pi}\right)^{2/3} n^{2/3}(\mathbf{r}, t)$. As we are interested only in the linear response, we remove all nonlinear terms from the hydrodynamic model and use the continuity equation $\partial n/\partial t = -1/e\nabla \cdot \partial \mathbf{P}/\partial t$, to derive the nonlocal Drude model:

$$\frac{\partial^2 \mathbf{P}}{\partial t^2} + \gamma \frac{\partial \mathbf{P}}{\partial t} - \beta^2 \nabla(\nabla \cdot \mathbf{P}) = \varepsilon_0 \omega_p^2 \mathbf{E}, \tag{29.2}$$

where β is proportional to the Fermi velocity of the metal. This is Eq. 29.1 with a nonlocal correction term. We implemented Eq. 29.2 in our in-house FDTD electromagnetic software [2] along with the Generalized Nonlocal Optical Response model (GNOR) which adds electron diffusion to the model [1]. We replace β^2 with $\beta^2 + D\gamma + D\partial/\partial t$ in Eq. 29.2, where D is the diffusion coefficient. Whereas GNOR accounts for both the shift and broadening the resonance peak, the simpler nonlocal Drude model only accounts for the shift. The normalized absorption spectra for nanospheres on a cabon film are plotted in Fig. 29.1a using GNOR. This result can be compared to experiments [3] with excellent agreement. A further benefit of these models is the reduction of staircasing artifacts at rounded material interfaces that plague FDTD due to it's rectangular mesh. This is demonstrated in Fig. 29.1b.

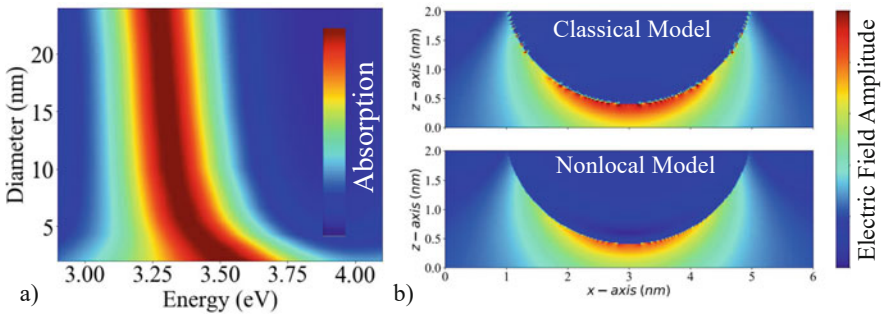

Fig. 29.1 (**a**) Normalized absorption spectra from silver nanospheres with diameters ranging from 2 nm–54 nm. (**b**) Electric field amplitude distribution near the surface of a 4 nm silver nanosphere in vacuum at wavelength 425 nm. Staircasing artifacts are greatly reduced when using the nonlocal model

References

1. Raza, S., et al.: Nonlocal optical response in metallic nanostructures. J. Phys. Condens. Matter **27** 183204 (2015)
2. Baxter, J., et al.: Parallel FDTD modelling of nonlocality in plasmonics. IEEE Trans. Antennas. Propag. **69**(7), 3982–3994 (2021)
3. Scholl, J., et al.: Quantum Plasmon resonances of individual metallic nanoparticles. Nature **483**, 421–427 (2012)

Chapter 30
Eu^{3+} Exchange in High-Charge Synthetic Mica-2 for Radioactive Waste Storage Applications

M. T. Candela, R. Martín-Rodríguez, R. Valiente, A. C. Perdigón, S. Díaz-Moreno, and F. Aguado

Abstract High charge synthetic Na-Mica-2 has been synthesized by the *NaCl melt* method. The Na^{+} cations in the interlayer space of the clay have been exchanged with Eu^{3+} ions by a cation exchange reaction. The correct incorporation of Eu^{3+} and further characterization of its coordination environment and location within the clay, as well as its optical properties, have been studied by means of x-ray diffraction, x-ray absorption (XANES and EXAFS), thermogravimetry and luminescence. Different structural scenarios for the incorporation of europium have been proposed and evaluated.

Keywords Mica · Cation exchange · Eu^{3+}

M. T. Candela (✉)
Dpto. Física Aplicada, Universidad de Cantabria, Santander, Spain

Grupo de Nanomedicina, Universidad de Cantabria-IDIVAL, Santander, Spain
e-mail: candelamt@unican.es; marinateresa.candela@unican.es

R. Valiente
Dpto. Física Aplicada, Universidad de Cantabria, Santander, Spain

Grupo de Nanomedicina, Universidad de Cantabria-IDIVAL, Santander, Spain

R. Martín-Rodríguez · A. C. Perdigón
Dpto. QUIPRE, Universidad de Cantabria, Santander, Spain

Grupo de Nanomedicina, Universidad de Cantabria-IDIVAL, Santander, Spain

S. Díaz-Moreno
Diamond Light Source, Didcot, Oxon, UK

F. Aguado
Dpto. CITIMAC, Universidad de Cantabria, Santander, Spain

Grupo de Nanomedicina, Universidad de Cantabria-IDIVAL, Santander, Spain

M. Cesaria et al. (eds.), *Light-Matter Interactions Towards the Nanoscale*,
NATO Science for Peace and Security Series B: Physics and Biophysics,
https://doi.org/10.1007/978-94-024-2138-5_30

30.1 Introduction

Incorporation of lanthanide ions in synthetic clay minerals, such as high-charge micas, is a promising approach to combine their cation exchange, adsorption capacities and their structural stability with the efficient sharp-line emission of lanthanides. These clays are layered systems (Fig. 30.1) which have been proposed as suitable candidates for use as efficient adsorbents for the elimination of pollutants in water and for the capture, retention and storage of radioactive waste containing actinides [1]. The effectiveness of these systems for the storage of radioactive waste depends to a large extent on the characteristics of its incorporation. In this way, the study of retention of lanthanides, which are chemically analogues to actinides, in high charge micas is a useful tool to know the physical-chemical behavior of contaminants.

Na-n Micas, with an ideal composition $Na_n[Mg_6]^{VIII}[Si_{8-n}Al_n]^{IV}O_{20}F_4$, can be synthetized by the *NaCl melt* method [2]. Lanthanide cations (Eu^{3+} in this case) are incorporated in the clay by a cation exchange reaction, where the Na^+ cations present in the interlayer space are exchanged by Eu^{3+}. When the exchange is produced, different retention mechanisms are possible: they can act as inner sphere complexes or as outer sphere complexes, depending whether the lanthanide interacts with the atoms in the TOT layers or not (Fig. 30.1).

High-charge Mica-2 presents some advantages from the luminescence point of view, since it is a fluorinated and synthetic clay, and hence, it does not present undesired impurities (iron) or hydroxyl groups in its structure that could quench/deactivate the lanthanide luminescence. Also, the Al^{3+} cations homogeneously distributed in the tetrahedral sheet of the clay, act as a dispersing agent of the lanthanide ions, thus avoiding clustering that could limit luminescence

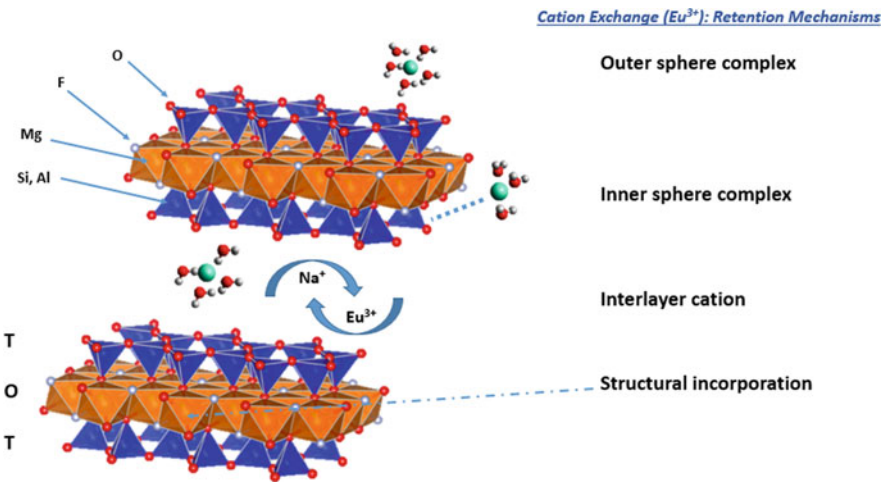

Fig. 30.1 Structural conformation of Mica-2 and scheme of lanthanides retention mechanisms

efficiency. Lastly, high-charge mica is a biocompatible material, so applications in the biomedical field, such as biosensing, imaging or drug delivery, are also possible.

30.2 Experimental

Na-Mica-2 was synthetized using the *NaCl melt* method [2] and Eu^{3+} cations were incorporated in the clay by a cation exchange reaction. X-ray diffraction (XRD) experiments were performed in a Bruker D8 Advanced diffractometer ($\lambda = 1.5418$ Å). Photoluminescence, excitation and lifetime measurements were performed using a FLSP920 spectrofluorometer (Edinburgh instruments). Thermogravimetric analysis (TG) was carried out on a Setaram Setsys evolution TG-DSC model. XAS measurements (EXAFS, XANES) were performed at Diamond Light Source synchrotron (beamline I20-Scanning) in transmission mode (Eu^{3+} L_{III} edge).

30.3 Results

Figure 30.2a shows the XRD patterns (in the 4–8.5° 2θ range) of the Mica-2 after several cation exchanges. As it can be observed, the incorporation of Eu^{3+} ions in the clay, at the expense of Na^{+} ones, is progressive, being approx. 70% after the third exchange.

The temporal evolution of the $^5D_0$ to $^7F_2$ Eu^{3+} luminescence, obtained by detecting at 610 nm after a short-pulsed excitation at 393 nm is shown in Fig. 30.2b. The decay curve, fitted to a single exponential, corroborates the fact that Eu^{3+} ions are distributed homogeneously in the clay. The resultant lifetime for Eu^{3+} in Mica-2 is 250 μs [1], which is in agreement with that of Eu^{3+} in different crystalline solids in which it is surrounded by 3 H_2O molecules [3]. From TG analysis is obtained that Eu^{3+} is surrounded of 2.9 H_2O molecules [1]. Nevertheless, a short order technique is necessary to fully elucidate the local environment of the lanthanide. For that reason, and with the help of x-ray absorption measurements, different structural scenarios for the incorporation of europium cations have been evaluated (Fig. 30.1), through data fitting and simulations. XANES spectra confirmed that the oxidation state of europium is 3+. EXAFS data analysis allowed to discard some scenarios, such as the structural incorporation, and to obtain the first coordination sphere of Eu^{3+}, which is formed by seven oxygen ions at 2.42 Å. The high coordination number agrees with that predicted for lanthanides. This result is also compatible with that provided by the TG curve and the emission and lifetime measurements of Eu^{3+}[1], as three of these seven oxygens can be due to water molecules, while the rest correspond to oxygens in the tetrahedral layer (T) of the clay. This would indicate that Eu^{3+} acts as an inner sphere complex.

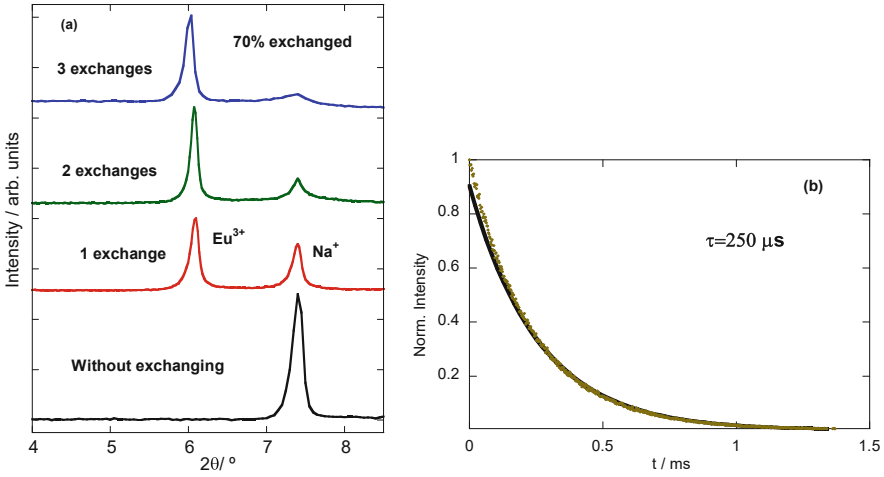

Fig. 30.2 XRD diffraction pattern of the mica after several cation exchanges, showing the incorporation of Eu^{3+} (**a**) and temporal evolution of the $^5D_0$-^7F_J Eu^{3+} luminescence ($\lambda_{exc} = 393$ nm, $\lambda_{em} = 610$ nm) for the same compound (b)

References

1. Martín-Rodríguez R, Valiente R, Aguado F, Perdigón AC (2017) Highly efficient photoluminescence from isolated Eu^{3+} ions embedded in a high-charge mica. J Mater Chem C 5:10360–10368
2. Park M, Lee DH, Choi CL, Kim SS, Kim KS, Choi J (2002) Pure Na-4-mica: synthesis and characterization. Chem Mater 14:2582–2589
3. Lezhnina M, Bentlage M, Kynast U (2011) Nanoclays: two-dimensional shuttles for rare earth complexes in aqueous solution. Opt Mater 33:1471

Chapter 31
Equivalent Circuit of the Defected Ground Structure in the Coplanar Waveguide

Artem Chernov, Victor Kazmirenko, Anton Voloshyn, and Yuriy Prokopenko

Abstract A new equivalent model of the defected ground structure for the CPW based filter is presented. The DGS is considered as a short-ended slotline which is connected in series with the ground electrodes of the CPW line. The equivalent parameters of the line, such as effective dielectric permittivity and characteristic impedance, allow to calculate S-parameters of the filter. Both effective dielectric permittivity and characteristic impedance are calculated by using the 2D finite element method which is applied to the cross section of the line. The simulation results of the proposed equivalent model are in good agreement with the 3D simulations. Such method could be applied to structures with different geometries and electro physical parameters. Also, it may be used for tunable devices with micromechanical tuning.

Keywords CPW · Defected ground structure · Slotline · Effective dielectric permittivity · Frequency tuning

31.1 Introduction

Devices with defected ground structures (DGS) are widely implemented in the communication field, both for antennas [1] and filters [2] based on the different types of the striplines. They also could be used for the tunable devices [3]. Usually, DGS is described as a resonant parallel RLC circuit. The parameters of the circuits components are extracted from the results of the simulation, thus, a huge calculation is required. In this work, a new equivalent model is proposed. Instead of traditional parallel RLC circuit, DGS is represented as a slotline inserted in the ground electrode of the CPW transmission line.

A. Chernov (✉) · V. Kazmirenko · A. Voloshyn · Y. Prokopenko
National Technical University of Ukraine "Kyiv Polytechnic Institute", Kyiv, Ukraine

M. Cesaria et al. (eds.), *Light-Matter Interactions Towards the Nanoscale*,
NATO Science for Peace and Security Series B: Physics and Biophysics,
https://doi.org/10.1007/978-94-024-2138-5_31

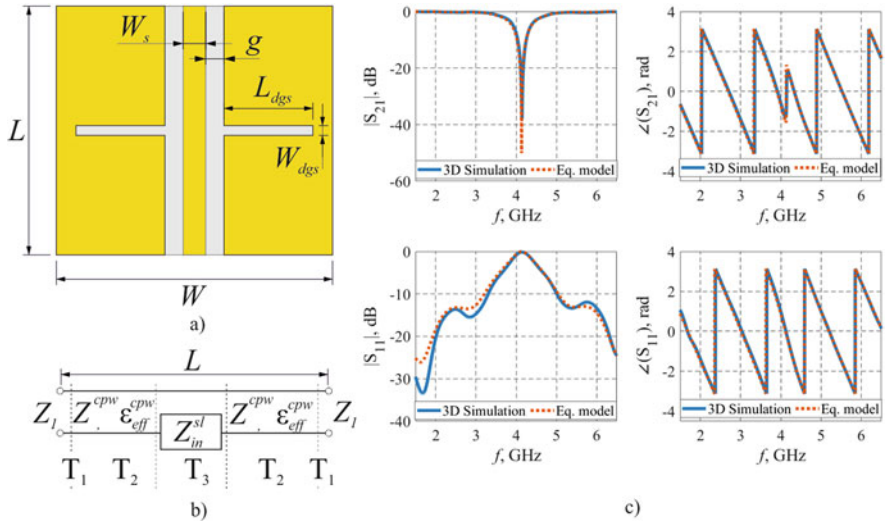

Fig. 31.1 (**a**) Structure of the CPW filter with DGS; (**b**) equivalent model; (**c**) S-parameters

31.2 Equivalent Model of the DGS Unit

The CPW transmission line with a simple DGS unit is shown in Fig. 31.1a. The DGS unit has a shape of narrow line. This DGS unit could be considered as a slotline with gap width W_{dgs}. Slotline has its own equivalent parameters, such as effective dielectric permittivity and characteristic impedance, which differ from the CPW line ones. The equivalent model of the line is shown in Fig. 31.1b, where Z^{cpw} and ε_{eff}^{cpw} are the characteristic impedance and the effective dielectric permittivity of the CPW line, respectively. Z_{in}^{sl} is the input impedance of the short-ended slotline with length L_{dgs}, and $\mathbf{T_{1\text{-}3}}$ are the transfer matrixes, which are obtained from the calculation based on the equivalent parameters of the lines. The S-parameters of the filter are derived from the **T** matrix, which is calculated by multiplying the transfer matrixes $\mathbf{T_{1\text{-}3}}$. The equivalent parameters of the CPW and slotline are calculated by using the 2D Finite Element Method. The results of the 3D simulation, performed by CST Studio, and the calculation performed by using the proposed model are shown in Fig. 31.1c.

31.3 Conclusion

The proposed equivalent model of the CPW base filter with DGS shows good agreement with 3D simulation results. The model is based on the calculation of effective parameters of the CPW and slotline via 2D FEM. Thus, the problem could

be reduced from 3D to 2D. This method has no restrictions on line's geometry and electro-physical parameters, and may be applied to micromechanically tunable devices

References

1. Liu W, Wu C, Dai Y (2011) Design of triple-frequency Microstrip-Fed monopole antenna using defected ground structure. IEEE Trans Antennas Propag 59(7):2457–2463
2. Sekar V, Entesari K (2011) Miniaturized UWB bandpass filters with notch using slow-wave CPW multiple-mode resonators. IEEE Microw Wirel Compon Lett 21(2):80–82
3. Chernov A, Prokopenko Y, Vandenbosch GAE (2017) Continuously tunable band-stop filter based on coplanar waveguide with defected ground structure. In: IEEE 37th International conference on electronics and nanotechnology (ELNANO), Kiev, pp 187–189

Chapter 32
Interstitial Light Trapping and Optical Confinement in Multijunction Solar Cells

Erin R. Cleveland, Nicole Kotulak, Stephanie Tomasulo, Phillip P. Jenkins, Alexander Mellor, Phoebe Pearce, N. J. Ekins-Daukes, and Michael K. Yakes

Abstract We recently demonstrated an ultra-thin solar cell with increased radiation tolerance as compared to a traditionally thick absorber counterpart. However, as the active region of the device was reduced so was the absorption with respect to state of the art devices. Therefore, we discuss a light trapping design, which implements nanosphere natural photolithography to fabricate a micropillared diffraction grating, combined with a transparent spacer layer and a distributed Bragg reflector. We discuss the fabrication process and illustrate the effectiveness of integrating light trapping structures for enhanced optical confinement within an ultra-thin solar cell design.

Keywords III-V solar cell · Nanosphere natural photolithography · Reactive ion etching · Surface texturing

Currently, III–V multijunction solar cells (MJSCs) are the highest efficiency photovoltaic (PV) technology for space applications. For terrestrial applications, research and development is aimed at improving the efficiency/unit cost of MJSCs. However, for space, the emphasis is on improving the efficiency at end-of-life, which require improvements for both beginning-of-life and radiation tolerance.

Traditional solar cells are typically ~3500 nm thick, owing that much of this volume is needed to absorb most of the incident light. However, if the carrier diffusion length is too short and the carriers cannot be efficiently collected, then the efficiency of the solar cell ends up suffering. In space, this problem is exacerbated

E. R. Cleveland (✉) · N. Kotulak · S. Tomasulo · P. P. Jenkins · M. K. Yakes
Naval Research Laboratory, Washington, DC, USA
e-mail: erin.cleveland@nrl.navy.mil

A. Mellor · P. Pearce
Imperial College, London, UK

N. J. Ekins-Daukes
University of New South Wales, Sydney, Australia

M. Cesaria et al. (eds.), *Light-Matter Interactions Towards the Nanoscale*,
NATO Science for Peace and Security Series B: Physics and Biophysics,
https://doi.org/10.1007/978-94-024-2138-5_32

due to high-energy irradiation, which degrades the material. In currently used InGaP/GaAs/Ge triple junctions, the GaAs middle cell has the most pronounced degradation, which limits the total current generation at the end-of-life. Recently, we demonstrated an ultra-thin GaAs solar cell (absorber thickness ~100 nm) with a drastically increased tolerance to radiation damage [1]. However, as the thickness of the active region is reduced, light trapping becomes a critical parameter for improving the efficiency of thin and ultra-thin film solar cells.

Building on existing knowledge, surface texturing is a well-known technique used to increase the optical path length of incident solar illumination by scattering light into oblique modes within the absorber layers and producing total internal reflection at the front surface of the cell; thereby producing a device that is optically thick while remaining physically thin. Several techniques have been developed to texturize surfaces in order to increase light absorption, such as metal islands, crystallographic etching, and natural photolithography. Although diffraction gratings can improve carrier collection efficiency, they can also reduce transmission and absorption within the solar cell.

A distributed Bragg reflector (DBR) is another technique used to manipulate light. It is formed by alternating multiple layers of materials with varying refractive indices. Each layer boundary causes a partial reflection of an optical wave. Within a MJSC, the stop-band of a DBR is designed to be centered on the bandwidth of a targeted subcell; thereby, reflecting photons in that bandwidth, while transmitting photons in the bandwidth of lower subcells. However, a DBR is not an effective reflector for photons with oblique trajectories. Therefore, the combination of a DBR with a textured diffraction grating would lead to leakage of oblique-trajectory photons into lower subcells.

In this paper, we present a light trapping design for a MJSC, in which the light trapping structure is positioned interstitially between two of the subcells of the device (Fig. 32.1a). The design combines a diffraction grating fabricated via nanosphere natural lithography (Fig. 32.1b), a low-index transparent spacer layer, and a DBR, which synergistically traps light inside the targeted subcell [2]. This paper will highlight processing techniques and challenges associated with fabricating a textured ultra-thin solar cell, while illustrating the effectiveness of integrating light trapping structures within an ultra-thin solar cell as an effort towards realizing high efficiency ultra-thin photovoltaic devices.

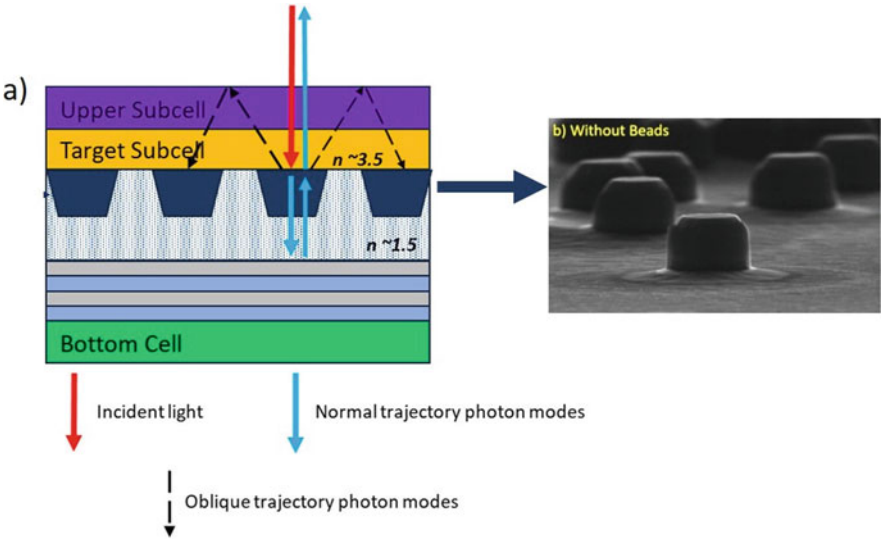

Fig. 32.1 (**a**) An interstitial light trapping design of a multijunction solar cell using the combination of (**b**) a diffraction grating, a low-index transparent spacer layer, and a distributed Bragg reflector

References

1. Hirst LC et al (2016) Intrinsic radiation tolerance of ultra-thin GaAs solar cells. APL 109
2. Mellor A, Hylton NP, Maier SA, Ekins-Daukes N (2017) Interstitial light-trapping design for multi-junction solar cells. Solar Energy Mater Sol Cells 159:212–218

Chapter 33
Nanocrystalline $NaYF_4:Pr^{3+}$ Luminescent Thermometers Using Ground and Excited State Absorption

Joanna Drabik, Artur Bednarkiewicz, Katarzyna Prorok, and Łukasz Marciniak

Abstract One of the most popular trends in the field of luminescence thermometry is the search for novel and more satisfactory materials and dopants that allow optical temperature reading with better quality. Another alternative is the use of simple compounds and dopants with the simultaneous proposition of unconventional measurement approaches.

Lanthanide ions are one of the most commonly used type of optically active ions for luminescent thermometry, due to their unique advantages like photostability with no photobleaching, high brightness as well as narrow emission and absorption lines. However, usually nanothermometers based on the optical response of lanthanides are based on the relative intensities of the two emission bands as a function of temperature, which requires the use of special optical filters that separate the appropriate spectral ranges.

Therefore, in this work, a new approach for temperature readout which involved two excitation lines was utilized. Ideally, the first excitation wavelength should result in the emission of which the intensity decreases with increasing temperature. The other one should induce the opposed effect – the resultant emission should be more intense at high temperatures than at low. Such a result can be obtained for non-resonant processes, for example for the excited state absorption, whose extreme case is the phenomenon of photon avalanche, which in turn was firstly observed in the Pr^{3+} ions (Chivian et al., Appl Phys Lett 35:124–125, 1979; Kueny et al., J Opt Soc Am B 6:639–642, 1989).

In this work, nanocrystalline $NaYF_4$ doped with Pr^{3+} ions were synthesized and characterized. The first excitation line 455 nm matched to the $^3H_4 \rightarrow {}^3P_2$ ground state absorption of Pr^{3+}, while the second one 525 nm allowed the use of the excited state absorption $^3H_5 \rightarrow {}^3P_1$. In our study, thanks to this simply approach, it was possible to define a temperature-dependent parameter as the luminescence intensity

J. Drabik (✉) · A. Bednarkiewicz · K. Prorok · Ł. Marciniak
Institute of Low Temperature and Structure Research, Polish Academy of Sciences, Wroclaw, Poland
e-mail: j.drabik@intibs.pl

M. Cesaria et al. (eds.), *Light-Matter Interactions Towards the Nanoscale*,
NATO Science for Peace and Security Series B: Physics and Biophysics,
https://doi.org/10.1007/978-94-024-2138-5_33

ratio of the same emission band but under two separate excitation lines. This type of measurement scheme already shows promising results (Marciniak et al., J Mater Chem C 6:7568–7575, 2018) and in the case of our research, $NaYF_4:Pr^{3+}$ seem to be suitable for making thermal maps with a great spatial resolution and significant sensitivity reaching 1.5–2.5%/°C in a wide temperature range.

Keywords Luminescent thermometry · Excited state absorption · Praseodymium

References

1. Chivian J, Case W, Eden D (1979) The photon avalanche: a new phenomenon in Pr3+ −based infrared quantum counters. Appl Phys Lett 35:124–125
2. Kueny A, Case W, Koch M (1989) Nonlinear-optical absorption through photon avalanche. J Opt Soc Am B 6:639–642
3. Marciniak L, Bednarkiewicz A, Elzbieciak K (2018) NIR–NIR photon avalanche based luminescent thermometry with Nd3+ doped nanoparticles. J Mater Chem C 6:7568–7575

Chapter 34
An Achiral Optical Cavity with Helicity-Preserving Modes for Enhanced Sensing of Chiral Molecules

Joshua Feis, Dominik Beutel, Julian Köpfler, Xavier Garcia-Santiago, Carsten Rockstuhl, Martin Wegener, and Ivan Fernandez-Corbaton

Abstract The two handednesses of a chiral molecule are identical in most of their physical properties yet may differ substantially in their chemical and biological effects. Circular dichroism (CD), the normalised difference between their absorption of left- and right-handed circularly polarised light, offers one of the few ways to physically distinguish them. Typically the CD of a molecule is very small though, particularly at low concentrations, which in turn means long measurement times with highly specialised devices to achieve acceptable signal-to-noise ratios. Thus a way of enhancement for the sensing of chiral molecules would be highly desirable for many chemical, medical and biological applications.

J. Feis
Institute of Applied Physics, Karlsruhe Institute of Technology, Karlsruhe, Germany

D. Beutel
Institute of Theoretical Solid State Physics, Karlsruhe Institute of Technology, Karlsruhe, Germany

J. Köpfler · M. Wegener
Institute of Applied Physics, Karlsruhe Institute of Technology, Karlsruhe, Germany

Institute of Nanotechnology, Karlsruhe Institute of Technology, Karlsruhe, Germany

X. Garcia-Santiago
Institute of Theoretical Solid State Physics, Karlsruhe Institute of Technology, Karlsruhe, Germany

JCMWave GmbH, Berlin, Germany

C. Rockstuhl
Institute of Theoretical Solid State Physics, Karlsruhe Institute of Technology, Karlsruhe, Germany

Institute of Nanotechnology, Karlsruhe Institute of Technology, Karlsruhe, Germany

I. Fernandez-Corbaton (✉)
Institute of Nanotechnology, Karlsruhe Institute of Technology, Karlsruhe, Germany

M. Cesaria et al. (eds.), *Light-Matter Interactions Towards the Nanoscale*,
NATO Science for Peace and Security Series B: Physics and Biophysics,
https://doi.org/10.1007/978-94-024-2138-5_34

However, conventional ways of enhancing light matter interaction like they've been employed previously [1] fail for CD due to the additional design requirement of having helicity-pure light on top of just strong field enhancements. A typical Fabry-Perot cavity, for example, flips the helicity of the light with each reflection and creates a perfect mix of helicities. Even though the fields might be strongly enhanced, the mixing causes there to be no difference between left- and right-handed illumination, and hence a decrease of the CD signal.

Many recent designs are based on designing scatterers that provide a helicity-preserving near-field enhancement [2]. This limits the practicability of this design though, as the enhanced fields only exist until a few hundreds of nanometers away from the scatterers and in a realistic microfluidic channel this would reduce the average enhancement factor towards near unity.

We now present a design for an achiral cavity featuring helicity-preserving modes with long lifetimes, enabling resonant CD enhancements by two orders of magnitude for cavity lengths exceeding tens of micrometers for infrared operation [3]. The cavity consists of two identical hexagonal diffracting arrays of silicon cylinders supported by finite-thickness substrates, as sketched in Fig. 34.1. The fundamental principle enabling helicity-preserving cavity modes is the fact that for reflection from a slab with an angle of incidence β, Fresnel's equations state that

$$\lim_{\beta \to \pi/2} r_{\mathrm{TE}} = -1 = \lim_{\beta \to \pi/2} r_{\mathrm{TM}}. \tag{34.1}$$

Just like how the superposition of a TE and TM wave gives circular polarisation, so helicity-pure light, this degeneracy of the reflection coefficients for TE and TM polarisation causes reflection to become helicity-preserving for the limit of grazing incidence angle [4]. Based on this, large transverse momentum modes will also be helicity-preserving. In our cavity, operation close to the diffraction limit for the periodic cylinder arrays and hence shallow diffraction angles make it possible to

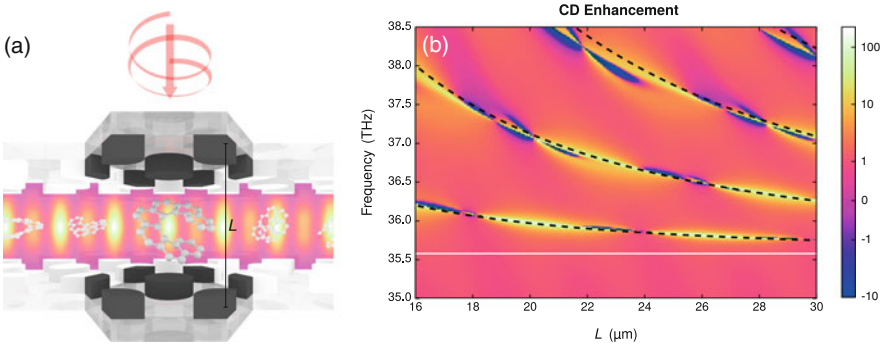

Fig. 34.1 (**a**) Sketch of the cavity. (**b**) Example for CD enhancement achieved by the cavity. The scale is linear between −1 and 1 and shows the logarithm of the absolute value of the enhancement multiplied with its sign otherwise

easily excite such a leaky large transverse momentum guided mode, allowing for strong field enhancements in the cavity while preserving the helicity of the incoming light. This in turn enables enhancement of CD signal by more than two orders of magnitude for a large quantity of chiral analyte along distinct lines (see Fig. 34.1) for infrared operation, as an example.

References

1. Armani, A.M., Kulkarni, R.P., Fraser, S.E., Flagan, R.C., Vahala, K.J.: Label-free, single-molecule detection with optical microcavities. Science **317**, 5839 (2007)
2. Graf, F., Feis, J., Garcia-Santiago, X., Wegener, M., Rockstuhl, C., Fernandez-Corbaton, I.: Achiral, helicity preserving, and resonant structures for enhanced sensing of chiral molecules. ACS Photonics **6**, 482 (2019)
3. Feis, J., Beutel, D., Köpfler, J., Garcia-Santiago, X., Rockstuhl, C., Wegener, M., Fernandez-Corbaton, I.: Helicity-preserving optical cavity modes for enhanced sensing of chiral molecules. Phys. Rev. Lett. **124** (2020)
4. Fernandez-Corbaton, I., Zambrana-Puyalto, X., Tischler, N., Vidal, X., Juan, M. L., Molina-Terriza, G.: Electromagnetic duality symmetry and helicity conservation for the macroscopic Maxwell's equations. Phys. Rev. Lett. **111**, 6 (2013)

Chapter 35
Chirp Effect on CEP-Controlled Molecular Dissociation

Saba Arife Bozpolat, Philipp Rosenberger, Marcelo F. Ciappina, Matthias F. Kling, and I. Yavuz

Abstract Intense, few-cycle laser fields enable a strong control over the electronic and nuclear dynamics of chemical reactions. Particularly, molecular dissociation in few-cycle chirp-free field has been well-understood (Yavuz et al., Phys Rev A 98:043413, 2018; Li et al., J Phys B 50:172001, 2017; Kling et al., Science 312(11262559):246–248, 2006). Going beyond this, in this study we theoretically studied the chirp effect of the intense laser pulse, as an additional controllable-parameter, on molecular dissociation using the numerical solutions of TDSE. We introduce the chirp to our equations with $\cos(\omega_0 t + \varphi_0 + \omega_0 \eta t^2/\tau^2)$ term where ω_0, φ_0, η and τ are angular frequency, phase, chirp parameter and the FWHM duration, respectively The time variation of the laser pulse is shown for chirp-free and chirped cases. For a preliminary understanding we consider the two level model first. Then we solve the time-dependent Schrödinger (TDSE) equation for full investigation. The results for two-level model is presented in Fig. 35.1 (Bozpolat et al., Phys Rev A 100:06340, 2019). We consider various chirp values in our calculations, while maintaining the temporal bandwidth, and compare our results to the case with non-chirped laser pulse. We assume that H_2^+ are populated at the peak ionization times of H_2, as found from CEP-included MO-ADK calculations. Reported dissociation probabilities are the weighted sums of these time-resolved dissociation probabilities and also vibrational wave-packets are FC-averaged.

We observed that the chirp considerably modifies the dissociation and asymmetry. Dissociation asymmetry changes sign with chirp parameter (see Fig. 35.1

S. A. Bozpolat (✉) · I. Yavuz
Department of Physics, Faculty of Arts & Science, Marmara University, Istanbul, Turkey
e-mail: saba.bozpolat@marmara.edu.tr

P. Rosenberger · M. F. Kling
Max-Planck-Institut für Quantenoptik, Garching, Germany

Department of Phyics, Ludwig-Maximillians-Universitat Munich, Garching, Germany

M. F. Ciappina
Max-Planck-Institut für Quantenoptik, Garching, Germany

ELI Beamlines, Institute of Physics of the ASCR, Prague, Czech Republic

M. Cesaria et al. (eds.), *Light-Matter Interactions Towards the Nanoscale*,
NATO Science for Peace and Security Series B: Physics and Biophysics,
https://doi.org/10.1007/978-94-024-2138-5_35

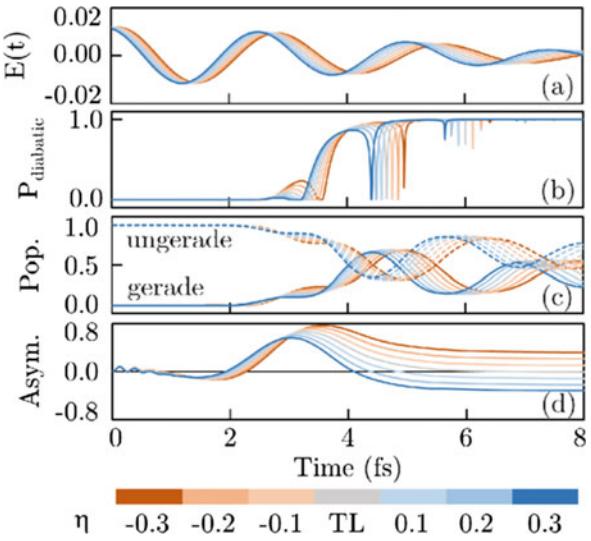

Fig. 35.1 Results for two-level model. (**a**) Laser field profiles. (**b**) Landau-Zener transition probability for avoided crossing passage. (**c**) gerade and ungerade states. (**d**) dissociation asymmetry [4]

(d)). This is due to that the gerade and ungerade states mixes one more time before electron localization freezes out for positive chirp values. Therefore the localization and asymmetry occurs opposite nuclei for positive and negative chirp parameters.

Keywords Strong interactions · Hydrogen molecule · Laser-matter interactions

References

1. Yavuz I, Schötz J, Ciappina MF, Rosenberger P, Altun Z, Lewenstein M, Kling MF (2018) Control of molecular dissociation by spatially inhomogeneous near fields. Phys Rev A 98:043413
2. Li H, Gong X, Lin K, de Vivie-Riedle R, Tong XM, Wu J, Kling MF (2017) Sub-cycle directional control of dissociative ionization of H2 in tailored femtosecond laser fields. J Phys B 50:172001
3. Kling MF, Siedschlag C, Verhoef AJ, Khan JI, Schultze M, Uphues TH, Ni Y, Uiberacker M, Drescher M, Krausz F, Vrakking MJJ (2006) Control of electron localization in molacular dissociation. Science 312(11262559):246–248
4. Bozpolat SA, Rosenberger P, Ciappina MF, Kling MF, Yavuz L (2019) Carrier-envelope-phase–controlled molecular dissociation by ultrashort chirped laser pulses. Phys Rev A 100:06340

Chapter 36
Parallelizing Direct Laser Writing: Multitasking on the Nanoscale

Pascal Kiefer, Vincent Hahn, Eva Blasco, and Martin Wegener

Abstract Many applications of direct laser writing (DLW) demand high fabrication speeds to realize complex or large structures. Due to the high precision and small feature size, DLW requires comparably long times to fill large volumes. Increasing the writing speed opens up the possibility for new structure dimensions while maintaining a high resolution. To achieve this goal, not only the scan speed of the laser focus has to be increased. By parallelizing the manufacturing process, the writing time of periodic structures decreases tremendously. Periodically arranged structures have a wide range of applications in biology and materials science, e.g. cell scaffolds [1] or metamaterials [2].

Galvanometric mirrors enable the steering of the laser beam, which is focused in the photo resist, to execute the writing process. Realizing a fast movement of the laser focus requires advanced hardware control with an FPGA to synchronize galvanometric scanners and the intensity controlling acousto-optic modulator. To assure a constante dose over a given line segment as well as sharp edges, the dynamics of the galvanometric scanners were already investigated and taken into account for writing at high speeds.

By illuminating a custom-built diffractive optical element, the generation of an array of laser foci is possible. A high illumination dose is required to induce the photopolymerization process. Therefore, distributing lasing power to multiple

P. Kiefer (✉)
Institute of Applied Physics, Karlsruhe Institute of Technology, Karlsruhe, Germany
e-mail: pascal.kiefer@kit.edu

V. Hahn · M. Wegener
Institute of Applied Physics, Karlsruhe Institute of Technology, Karlsruhe, Germany

Institute of Nanotechnology, Karlsruhe Institute of Technology, Karlsruhe, Germany

E. Blasco
Institute for Chemical Technology and Polymer Chemistry, Karlsruhe Institute of Technology, Karlsruhe, Germany

M. Cesaria et al. (eds.), *Light-Matter Interactions Towards the Nanoscale*,
NATO Science for Peace and Security Series B: Physics and Biophysics,
https://doi.org/10.1007/978-94-024-2138-5_36

foci and rapidly steering them introduces polymerisation problems. To overcome this issue, a photoresist has to be engineered that allows for printing with lower intensities. Using multi-component photoinitiating systems could lead to more sensitive photoinitiators and therefore reduce the required illumination dose to enable applications for e.g. cell scaffolds [1] or metamaterials [2].

References

1. Hippler, M., Lemma, E.D., Bertels, S., Blasco, E., Barner-Kowollik, C., Wegener, M., Bastmeyer, M.: 3D scaffolds to study basic cell biology. Adv. Mater. **31**, 26 (2019)
2. Frenzel, T., Kadic, M., Wegener, M.: Three-dimensional mechanical metamaterials with a twist. Science **358**, 6366 (2017)

Chapter 37
Waveguide-Coupled Disk Resonators Fabricated from Hexagonal Boron Nitride

Ronja Khelifa, Nikolaus Flöry, Shadi Nashashibi, Konstantin Malchow, Markus Parzefall, Achint Jain, Takashi Taniguchi, Kenji Watanabe, and Lukas Novotny

Abstract We present waveguide-coupled disk resonators fabricated from exfoliated hexagonal boron nitride (h-BN) flakes. Using standard fabrication techniques like electron beam lithography and reactive ion etching Q-factors of up to ∼600 are shown. The coupled h-BN waveguides allow in-plane light guiding and enable first steps towards on-chip photonic circuits entirely fabricated from two-dimensional (2D) materials.

Keywords Waveguide-coupled disk resonator · Hexagonal boron nitride

37.1 Introduction

The on-chip integration of photonic systems is a key challenge for applications of optoelectronic devices. 2D materials show great potential for on-chip optoelectronic devices coupled to silicon based waveguides [1]. Because of their strong in-plane and weak out-of-plane bonds, different layers of 2D materials can be stacked on top of each other, independent of their lattice constants. This technique enables the fabrication of so-called van der Waals heterostructures [2]. Fabricating such a structure that combines both, an optoelectronic device, as well as a photonic

R. Khelifa (✉) · N. Flöry · S. Nashashibi · K. Malchow · M. Parzefall · A. Jain · L. Novotny
Photonics Laboratory, ETH Zürich, Zürich, Switzerland
e-mail: khelifar@student.ethz.ch

T. Taniguchi
International Center for Materials Nanoarchitectonics, National Institute for Materials Science, Tsukuba, Japan

K. Watanabe
Research Center for Functional Materials, National Institute for Materials Science, Tsukuba, Japan

M. Cesaria et al. (eds.), *Light-Matter Interactions Towards the Nanoscale*,
NATO Science for Peace and Security Series B: Physics and Biophysics,
https://doi.org/10.1007/978-94-024-2138-5_37

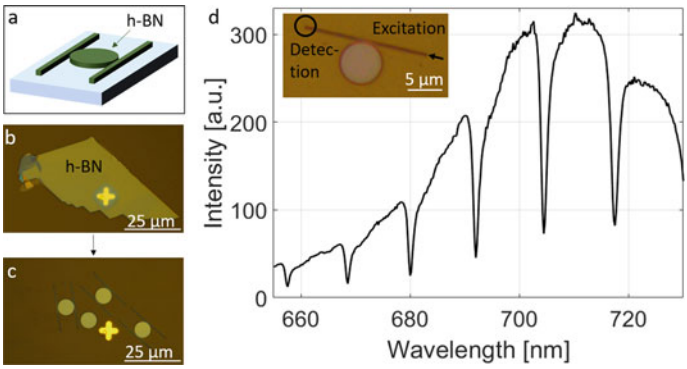

Fig. 37.1 (**a**) Schematic of a disk resonator coupled to two waveguides. Optical microscope image of an h-BN flake before (**b**) and after (**c**) pattering into waveguide coupled disk resonators. (**d**) Measured spectrum of a disk resonator coupled to one waveguide. Excitation with a tightly focused broad band source and detection as indicated in the inset. The envelope function is defined by the excitation spectrum as well as the transfer functions of the experimental setup and the waveguide

structure could enable efficient on-chip electro-optical-coupling and optical guiding. It has already been demonstrated that h-BN, a wide-bandgap insulator, can be used to fabricate photonic structures like disk resonators [3], photonic crystals [4] or ring resonators [5]. Here we discuss waveguide-coupled disk resonators as shown in the schematic in Fig. 37.1a (further progress and detailed characterization is discussed in [6]). The coupling to waveguides provides on-chip in-plane light guiding and enables the integration into photonic circuits.

37.2 Results

We use mechanically exfoliated h-BN flakes with thicknesses ranging from 100 to 300 nm (Fig. 37.1b). Disk resonators coupled to one or two waveguides are patterned by means of electron beam lithography and reactive ion etching. In Fig. 37.1c waveguide-coupled disk resonators after etching and mask removal are shown. To determine the Q-factor of such devices, one waveguide end is illuminated with a tightly focused, broad band excitation source. In Fig. 37.1d, the measured spectrum, at the other waveguide end is shown. The device consists, as shown in the inset, of a disk resonator coupled to one waveguide. From fitting the resonance peaks with Lorentzian lineshapes, Q-factors of up to ∼600 were determined.

37.3 Outlook

In future works the Q-factor can be improved by reducing the sidewall roughness of the etched structures. Recently, we have also shown the integration of other 2D materials inside waveguide-coupled disk resonators [6]. Further integration of optoelectronic devices based on van der Waals heterostructures can enable the next step towards 2D materials based on-chip photonics.

References

1. Ma, P., Flöry, N., Salamin, Y., Baeuerle, B., Emboras, A., Josten, A., Taniguchi, T., Watanabe, K., Novotny, L., Leuthold, J.: Fast $MoTe_2$ waveguide photodetector with high sensitivity at telecommunication wavelengths. ACS Photonics **5**, 1846–1852 (2018). https://doi.org/10.1021/acsphotonics.8b00068
2. Geim, A.K., Grigorieva, I.V.: Van der Waals heterostructures. Nature **499**, 419–425 (2013). https://doi.org/10.1038/nature12385
3. Ren, T., Song, P., Chen, J., Loh, K.P.: Whisper gallery modes in monolayer tungsten disulfide-hexagonal boron nitride optical cavity. ACS Photonics **5**, 353–358 (2018). https://doi.org/10.1021/acsphotonics.7b01245
4. Kim, S., Fröch, J.E., Christian, J., Straw, M., Bishop, J., Totonjian, D., Watanabe, K., Taniguchi, T., Toth, M., Aharonovich, I.: Photonic crystal cavities from hexagonal boron nitride. Nat. Commun. **9**, 2623 (2018). https://doi.org/10.1038/s41467-018-05117-4
5. Fröch, J.E., Hwang, Y., Kim, S., Aharonovich, I., Toth, M.: Photonic nanostructures from hexagonal boron nitride. Adv. Opt. Mat. **7**, 1801344 (2019). https://doi.org/10.1002/adom.201801344
6. Khelifa, R., Back, P., Flöry, N., Nashashibi, S., Malchow, K., Taniguchi, T., Watanabe, K., Jain, A., Novotny, L.: Coupling interlayer excitons to whispering gallery modes in van der Waals Heterostructures. Nano Lett. **20**, 6155–6161 (2020). https://doi.org/10.1021/acs.nanolett.0c02432

Chapter 38
Spectroscopic Properties of Vanadium Ions for Applications in Luminescent Nanothermometry

Karolina Kniec and Lukasz Marciniak

Abstract Luminescent nanothermometry is a method of temperature imaging, relying on the thermally-affected spectroscopic properties of the phosphors, including band shape, luminescent lifetime, emission intensity and spectral position, providing temperature redout in noncontact and fast manner. Due to the small size of inorganic luminescent nanothermometers and their numerous advantages, such as mechanical, chemical and thermal stability, high accuracy and photostability, they can be employed in plenty of applications, involving medicine and electronic devices, operating in wide thermal range (Marciniak et al., J Mater Chem C 4(24):5559–5563, 2016; Jaque and Vetrone, Nanoscale 4(15):4301–4326, 2012). To improve the temperature sensing capabilities of the luminophore, the luminescence of transition metal (TM) ions is used as an optical signal, revealing strong thermal-dependence (Marciniak and Bednarkiewicz, Sensors Actuators B Chem, 243:388–393, 2017). Based on this, new luminescent nanotherometer are presented, taking advantage of temperature susceptible emission of V ions, namely V^{3+}, V^{4+} and V^{5+}, being incorporated into inorganic garnet and perovskite host nanomaterials, i. e. YAG ($Y_3Al_5O_{12}$) and $LaGaO_3$, respectively (Kniec and Marciniak, Sensors Actuators B Chem, 2018; Phys Chem Chem Phys 20(33):21598–21606, 2018). It was found that three emission bands of V are present upon 266 nm of irradiation, coming from penta-, tetra- and trivalent vanadium, being located in the different parts of the nanocrystals, namely V^{5+} ions are localized mainly in the surface, where $V^{4+}$and V^{3+} in the core. The luminescence response of V-doped nanothermometers on the temperature changes can be modulated via grain size tuning, dopant concentration and synthesis conditions. Moreover each of V ions reveal different thermal-susceptibility, simultaneously influencing on the sensitivity of the nanosensor and the total colour emission of the luminophore, showing promising applicability of V-based luminescent nanothermometers.

K. Kniec (✉) · L. Marciniak
Institute of Low Temperature and Structure Research, PAS, Wrocław, Poland
e-mail: k.kniec@intibs.pl

M. Cesaria et al. (eds.), *Light-Matter Interactions Towards the Nanoscale*,
NATO Science for Peace and Security Series B: Physics and Biophysics,
https://doi.org/10.1007/978-94-024-2138-5_38

Keywords Vanadium · Luminescence · Inorganic nanocrystals · Luminescent nanothermometry

Acknowledgements The "High sensitive thermal imaging for biomedical and microelectronic application" project is carried out within the First Team programme of the Foundation for Polish Science co-financed by the European Union under the European Regional Development Fund.

References

1. Marciniak L, Bednarkiewicz A, Kowalska D, Strek W (2016) A new generation of highly sensitive luminescent thermometers operating in the optical window of biological tissues. J Mater Chem C 4(24):5559–5563
2. Jaque D, Vetrone F (2012) Luminescence nanothermometry. Nanoscale 4(15):4301–4326
3. Marciniak L, Bednarkiewicz A (May 2017) Nanocrystalline NIR-to-NIR luminescent thermometer based on Cr 3+ ,Yb 3+ emission. Sensors Actuators B Chem 243:388–393
4. Kniec K, Marciniak L (2018) The influence of grain size and vanadium concentration on the spectroscopic properties of YAG:V 3+ ,V 5+ and YAG: V, Ln 3+ (Ln 3+=Eu 3+ , Dy 3+, Nd 3+) nanocrystalline luminescent thermometers. Sensors Actuators B Chem
5. Kniec K, Marciniak L (2018) Spectroscopic properties of LaGaO 3 :V,Nd 3+ nanocrystals as a potential luminescent thermometer. Phys Chem Chem Phys 20(33):21598–21606

Chapter 39
Metallic Bar Grating with a Bistable Response

Liudmyla A. Kochetova

Abstract The area of bistability of nonlinear periodic structures has attracted much attention in recent years. The Kerr type nonlinearity in the grating is characterized by a quadratic dependence of a dielectric on an electric field inside the grating. In this work the problem of electromagnetic wave diffraction by the metallic bar grating with a defect is studied. The motivation of this research is the miniaturization of optical devices, which are controlled by the intensity of the incident field. The bistable operating regime of the grating has been demonstrated at extremely low values of the incident field intensity. Thus, the nonlinear metallic bar grating is promising for creating ultracompact filters which are controlled by the incident field intensity.

Keywords Grating · Kerr type nonlinearity · Defect mode · Bistability

39.1 Introduction

We study the problem of electromagnetic wave diffraction by the perfectly electric conducting (PEC) metallic bar grating with a defect layer (Fig. 39.1). The slits between the bars are filled by 15 dielectric layers of the same thickness Δ. All even layers except the eight layer in the slit are made of silicon with permittivity $\varepsilon_s = 12.8$. The eight layer is made of the Kerr type nonlinear dielectric with permittivity $\varepsilon_{8l} = 2.72$ and nonlinear coefficient $\varepsilon_{8n} = 1.3 \times 10^{-3}$ cm^2/kW. All odd layers in the slit are made of quartz with permittivity $\varepsilon_c = 2.1$. The bistable transmission and reflection of the wave through the grating with the nonlinear defect are obtained.

L. A. Kochetova (✉)
O. Y. Usikov Institute for Radiophysics and Electronics of NASU, Kharkiv, Ukraine

M. Cesaria et al. (eds.), *Light-Matter Interactions Towards the Nanoscale*,
NATO Science for Peace and Security Series B: Physics and Biophysics,
https://doi.org/10.1007/978-94-024-2138-5_39

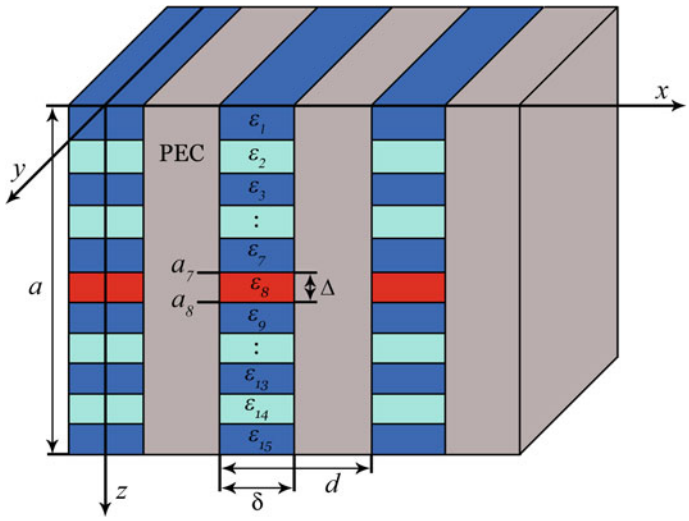

Fig. 39.1 Metallic bar grating with a nonlinear defect in 15 dielectric layers filling of its slits. The nonlinear defect is located in the slit as the eight layer

39.2 Results and Discussion

The dependence of the module of the transmission and reflection coefficients on the intensity of the incident field at $\kappa = 0.310$ are presented in Figs. 39.2a and b, respectively [1–3]. The arrows indicate the switching regime of the grating in the forward direction at $I_{inc} = 27.897$ W/cm^2 and for the opposite direction at $I_{inc} = 4.179$ W/cm^2. The figures show that when the incident field intensity is increased, we observe a jump from $|T| = 0.224$ to $|T| = 0.446$ (Fig. 39.2a) and from $|R| = 0.974$ to $|R| = 0.895$ (Fig. 39.2b). When the incident field intensity is decreased, the maximum transmission coefficient of the structure $|T| = 1.000$ becomes $|T| = 0.151$, while the value of the reflection coefficient changes from a minimum $|R| = 0.006$ to a maximum $|R| = 0.988$. The transmission and reflection resonances of the grating are obtained at the defect mode [4, 5]. We should note that the bistable operating regime of the structure with the nonlinear defect is implemented at extra low values of the intensity of the incident field $I_{inc} \approx 5 - 35$ W/cm^2.

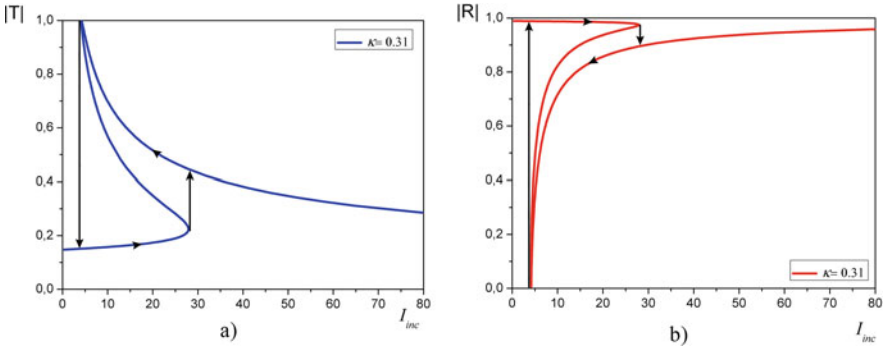

Fig. 39.2 Magnitude of the (**a**) transmission and (**b**) reflection coefficients versus intensity of the incident field

References

1. Gibbs H (1985) Optical bistability: controlling light with light. Academic, Orlando
2. Liu D, Wu L, Liu Q, Yang S, Zhou R, Xie S, Chen Z (2017) Optical bistability effect in SPP-based metallic grating containing Kerr nonlinear medium. Modern Phys Lett B 31(24):1750146
3. Kochetova L, Prosvirnin S, Tuz V (2014) Optical bistability in a grating with slits filled nonlinear media. Prog Electromag Res 35:133–139
4. Zhang J, Zhang R, Wang Y (2015) Modulation of Kerr nonlinearity on spectral characteristics for one-dimensional nonlinear defective photonic crystals. Optik 126(24):5052–5056
5. Entezar S, Karimi M, Adl H (2015) Optical isolation via one-dimensional magneto-photonic crystals containing nonlinear defect layer. Opt Commun 352:91–95

Chapter 40
Electrically Driven Optical Sources Based on van der Waals Heterostructures

Anna Kuzmina, Markus Parzefall, and Lukas Novotny

Abstract Light emitting tunnel junctions based on van der Waals (vdW) heterostructures are expected to be efficient transducers between electrical and optical signals. Using graphene as a material for one or both electrodes, out-coupling limitations to the far-field which are characteristic of metal-insulator-metal (MIM) structures could be overcome. Moreover, the presence of graphene electrodes allows for the design of an external plasmonic environment in order to modify the local density of optical states (LDOS) and thus the ratio between inelastic and elastic tunneling channels. Here we discuss our understanding of the fundamental physics underlying the inelastic tunneling process and possible approaches for engineering electronic and optical LDOS.

Keywords Tunnel junctions · Inelastic tunneling · van der Waals heterostructures

Light emission from inelastic electron tunneling (LEIT) was firstly discovered by Lambe and McCarthy [1] in vertical MIM structures. Since the majority of the further LEIT studies was also carried out using the MIM geometry, the efficiency of the light emission to the far-field was reported to be low, mostly due to the absorption inside metallic layers. Nevertheless, the mechanism of LEIT will be discussed here on the most intuitive example of two metallic electrodes.

The tunnel current through the device consists of both elastic, i.e. with energy and momentum conservation, and inelastic contributions, as it is shown in Fig. 40.1. The elastic tunneling rate functionally depends on the density of electronic states, but the magnitude of the elastic tunneling process can also be influenced by the thickness and material properties of the insulator [3]. The inelastic tunneling rate is affected by both electronic and optical density of states. Usually, an inelastic tunneling event is treated as a two-step process which consists of electron coupling to a localized

A. Kuzmina (✉) · M. Parzefall · L. Novotny
Photonics Laboratory, ETH Zürich, Zürich, Switzerland
e-mail: kuzminaa@ethz.ch

M. Cesaria et al. (eds.), *Light-Matter Interactions Towards the Nanoscale*,
NATO Science for Peace and Security Series B: Physics and Biophysics,
https://doi.org/10.1007/978-94-024-2138-5_40

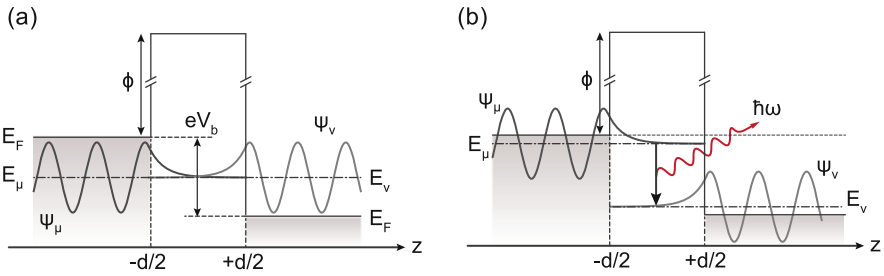

Fig. 40.1 The sketch of the electron states coupling in the case of (**a**) elastic and (**b**) inelastic tunneling process (adapted from the ref. [2])

optical mode while traversing the barrier and then radiative out-coupling to the far-field. In our device configuration the inelastic part of the tunneling current contributes to the light-emission more than other mechanisms [2], so this process is desired to be maximized.

Since the band structures of the electrodes play a major role in the tunneling process, the choice of materials with specific features in the band structure can change the performance of the device. A vertical stack consisting of two graphene electrodes separated by a few-layers-thick hexagonal boron nitride (hBN) crystal can serve as an example of this approach. Graphene with its Dirac cone band structure provides not only a way to have energy selectivity during the tunneling process but also a strict momentum conservation rule. Thus only specific transitions between states with the same momentum are allowed, which should reduce the elastic tunneling contribution and lead to a drastic increase of the inelastic tunneling rate.

Also, the electron-to-photon conversion rate highly depends on the optical DOS. Another approach for boosting the efficiency can be combining plasmonic structures with tunnel junctions to locally increase coupling to the optical modes. The main advantage of a MIM structure is the strong enhancement of the surface plasmon mode inside the gap between the electrodes. Unfortunately, a decrease in the density of optical states is the necessary cost which should be paid for the renouncement from the MIM geometry. A similar plasmonic cavity can be formed by placing graphene –h-BN– graphene junction on a golden mirror and positioning a plasmonic nanoparticle on top of the device. The described geometry allows to locally increase the coupling rate to the optical mode and to simultaneously use the nanoparticle as an optical antenna.

References

1. Lambe, J., McCarthy, S.L.: Light emission from inelastic electron tunneling. Phys. Rev. Lett. **27**, 923–925 (1976). https://doi.org/10.1103/PhysRevLett.37.923
2. Parzefall, M., Bharadwaj, P., Novotny, L.: Antenna-coupled tunnel junctions. Quantum Plasmonics 211–236 (2017). https://doi.org/10.1007/978-3-319-45820-5_10
3. Reittu, H.J.: Fermi's golden rule and Bardeen's tunneling theory. Am. J. Phys. **63**, 940–944 (1995). https://doi.org/10.1119/1.18037

Chapter 41
Hybrid Integrated Quantum Photonic Architecture Driven by a Quantum Dot Single-Photon Source

Emma Lomonte, Francesco Lenzini, Juan Loredo, Pascale Senellart, and Wolfram Pernice

Abstract We propose a proof-of-principle demonstration of a hybrid quantum photonic architecture that combines state of the art technologies for generating, manipulating, and detecting quantum states of light. An InGaAs Quantum Dot is exploited as a bright source of highly pure and indistinguishable single photons, which are demultiplexed in different spatial channels by the use of a network of Lithium Niobate on insulator (LNOI) electro-optically tunable waveguides and then injected into a Silicon Nitride chip combining low loss linear optical circuits and waveguide-integrated superconducting nanowire single-photon detectors (SNSPDs) on a same device.

Keywords Quantum photonics · Integrated optics · Single photons

41.1 Introduction

An essential requirement for the development of quantum photonic processors is the availability of efficient single-photon sources, detectors and linear optical circuits combined in a physically scalable architecture. Solid state single-photon emitters, such as Quantum Dots (QD), have emerged as the technology of choice for the realization of bright sources of single photons, while linear optical circuits implemented in lithographically patterned waveguides can offer a stable and scalable platform for the manipulation of quantum states of light, as well as the possibility of being integrated on-chip with high performance SNSPDs. Here we

E. Lomonte · F. Lenzini · W. Pernice (✉)
CeNTech - Center for Nanotechnology, Münster, Germany

SoN - Center for SoftNanoscience, Münster, Germany
e-mail: lomonte@uni-muenster.de; wolfram.pernice@uni-muenster.de

J. Loredo · P. Senellart
SCNRS, Université Paris-Sud, Université Paris-Saclay, Marcoussis, France

M. Cesaria et al. (eds.), *Light-Matter Interactions Towards the Nanoscale*,
NATO Science for Peace and Security Series B: Physics and Biophysics,
https://doi.org/10.1007/978-94-024-2138-5_41

propose an experiment which will combine these cutting-edge technologies in a hybrid quantum photonic architecture.

41.2 Proposed Architecture

Figure 41.1 reports a schematic picture of the planned experiment. An InGaAs/GaAs QD embedded in a micropillar cavity made of two distributed-Bragg-reflectors [1] is optically pumped by a pulsed laser resonant with the QD transition ($\lambda_{res} = 932$ nm). A temporal stream of photons, characterized by an extremely high purity ($g^{(2)}(0) = 0.0028 \pm 0.0012$) and an indistinguishability larger than 99% under resonant excitation [1], is injected into a 4-channel demultiplexer made of three reconfigurable directional couplers integrated on a LNOI platform. An annealed proton-exchange $LiNbO_3$ demultiplexer has been already experimentally demonstrated [2], but it suffers from the low refractive index contrast between core and cladding, thus resulting in large optical mode areas, bending radii and requiring high voltage for electro-optic switching. On the contrary, by exploiting the recently developed LNOI platform ($\Delta n > 0.7$, $r_{33} = 30$ pm/V), a device with propagation loss as low as 2.7 dB/m [3], small footprint and high switching efficiency, operating at CMOS-compatible voltages [4] can be fabricated by e-beam lithography and Ar^+ physical etching.

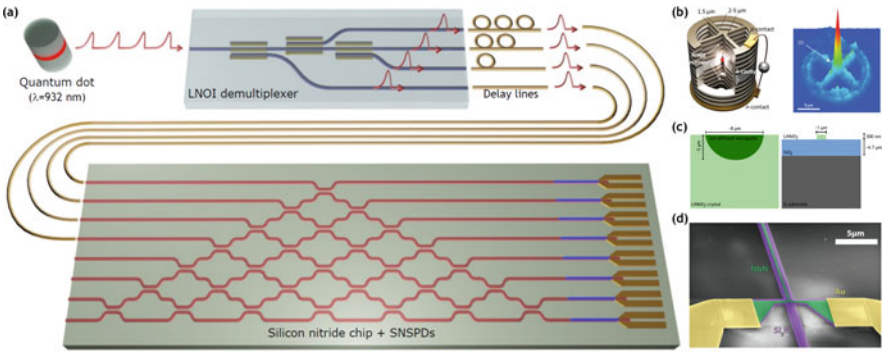

Fig. 41.1 Proposed hybrid quantum photonic architecture. (**a**) Schematic picture of the devised experiment. (**b**) QD embedded in a micropillar cavity connected to a surrounding circular frame by four one-dimensional wires. Photoluminescence map of a connected device: the bright emission at the center of the device arises from the deterministically coupled QD. (**c**) Typical sizes of a conventional LN ion-diffused waveguide (left) and a lithographically patterned waveguide on the LNOI platform (right). (**d**) Schematic picture of a SNSPD patterned on top of a Si_3N_4 waveguide. Photons travelling along the waveguide are absorbed by the superconducting nanowire. For sufficiently narrow wires the absorption of one single photon leads to the breakdown of the superconducting state, resulting in a voltage spike that can be amplified and detected by counting electronics

At the output of the demultiplexer, a set of optical fiber delay lines is used to match the different arrival times of the emitted photons, which are now coupled into four inputs of a Si_3N_4 chip, where 5 nm thick NbN superconducting nanowires are patterned on top of waveguides characterized by loss as low as 0.3 dB/cm. SNSPDs have shown on-chip detection efficiency up to $\simeq$90% for $\simeq$80 nm wide nanowires and a saturated quantum efficiency with increasing bias current [5]. This gives strong evidence that near-unitary detection efficiency can be achieved with a long enough nanowire absorbing all the incoming photons.

Efficient coupling with single mode fibers can be achieved by negative diffraction angle grating couplers [6], which image an in-plane waveguide input to an output optical fiber placed at around 120 μm above the chip. Insertion loss at the desired wavelength are about 3.6 dB. Better coupling efficiency can be obtained by locally varying the grating period and with the insertion of a metal back-reflector, by opening windows in the silicon substrate and sputtering metal, like Ag or Al.

References

1. Somaschi N (2016) Near-optimal single-photon sources in the solid-state. Nat Photonics 10(340):340–345
2. Lenzini F (2017) Active demultiplexing of single photons from a solid-state source. Laser Photonics Rev 11(3):1600297
3. Zhang M (2017) Monolithic ultra-high-Q lithium niobate microring resonator. Optica 4(12):1536–1537
4. Wang C (2018) Integrated lithium niobate electro-optic modulators operating at CMOS-compatible voltages. Nature 562(7725):101–104
5. Kahl O (2015) Waveguide integrated superconducting single-photon detectors with high internal quantum efficiency at telecom wavelength. Sci Rep 5(10941):1–11
6. Chen Y (2016) High-efficiency apodized-imaging chip-fiber grating coupler for silicon nitride waveguides. Opt Lett 41(21):5059–5062

Chapter 42
Synthesis and Cytotoxicity of $GdPO_4$: Yb^{3+}, Nd^{3+} for High Sensitivity Luminescent Nanothermometers

Kamila Maciejewska, Błażej Poźniak, Marta Tikhomirov, and Łukasz Marciniak

Keywords Synthesis · Nanoparticles · Luminescent nanothermometers

Luminescent thermometry (LT) is a technique that enables non-contact temperature measurement of the object attached to or covered by the phosphor. The temperature readout in this case relies on the analysis of the temperature dependent spectroscopic parameter of the luminescent material. This approach is especially beneficial in medicine where in-real time temperature sensing with high spatial and thermal resolution cannot be provided by any other measurement technique. However, for this type of application, the phosphor must exhibit biocompatibility and negligible cytotoxicity. Due to the above requirements, the use of metal orthophosphates seems to be the best choice due to their extraordinarily high stability in aqueous and physiological solutions. In addition, orthophosphates are characterized by a high index of refraction, resistance in acidic, neutral and alkaline environments and reveal negligible cytotoxicity [1]. However, synthetic methods are still sought for obtaining stable $REPO_4$ (RE- rare earth metal) colloidal nanoparticles. Therefore we have developed a novel, two-step synthesis method of $REPO_4$ doped with lanthanides. In this work the optical properties of $GdPO_4$ co-doped with Yb^{3+} and Nd^{3+} ions in a form of powders and aqueous colloids were investigated in terms of their potential use in the non-contact temperature sensing [2]. Moreover their potential *in vitro* application was verified by the cytotoxicity assessment onto J774.E and U2OS cell lines (Fig. 42.1).

K. Maciejewska (✉) · Ł. Marciniak
Institute of Low Temperature and Structure Research, Polish Academy of Sciences, Wrocław, Poland
e-mail: k.maciejewska@intibs.pl

B. Poźniak · M. Tikhomirov
Department of Pharmacology and Toxicology, Wrocław University of Environmental and Life Sciences, Wrocław, Poland

M. Cesaria et al. (eds.), *Light-Matter Interactions Towards the Nanoscale*,
NATO Science for Peace and Security Series B: Physics and Biophysics,
https://doi.org/10.1007/978-94-024-2138-5_42

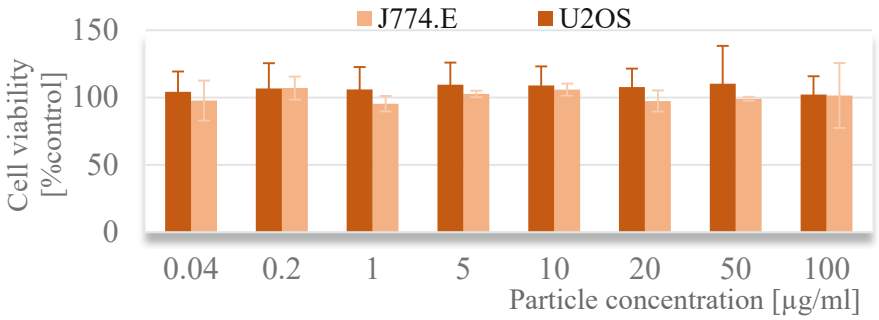

Fig. 42.1 Cytotoxicity of original synthesized orthophosphate in *U2OS and J774.E* cell line

References

1. Gavrilović T et al (2018) Particle size effects on the structure and emission of Eu^{3+}: $LaPO_4$ and $EuPO_4$ phosphors. J Lumin 195:420–429
2. Marciniak L, Prorok K, Francés-Soriano L, Pérez-Prieto J, Bednarkiewicz A (2016) A broadening temperature sensitivity range with a core–shell YbEr@YbNd double ratiometric optical nanothermometer. Nanoscale 8(9):5037–5042

Chapter 43
Programmable Generation of Arbitrary Light Field Distributions

Alfonso Nardi, Felix Tebbenjohanns, Martin Frimmer, and Lukas Novotny

Abstract We built an experimental setup consisting of two phase-only liquid crystal-based spatial light modulators to independently control amplitude, phase, and polarisation of an optical beam which is strongly focused by a microscope objective. We have furthermore implemented a method to characterize the intensity distribution in the focus with sub-wavelength resolution.

Keywords Laser beam shaping · Wavefront shaping · SLM

43.1 Introduction

Spatial light modulators (SLMs) are reconfigurable devices that allow for real-time programmable light modulation [1]. In particular, liquid crystal-based SLMs have been established as a leading technology for on-demand creation of arbitrary optical fields [2]. The availability of these powerful devices opened the path to lots of new applications for real-time structured light, like holographic optical trapping and optical tweezers [3], quantum information processing [4], microscopy [5], 3D holographic imaging [6], and laser technology [7].

In this work we show the generation of arbitrary programmable optical field distributions employing a system based on two SLMs. We intend to use the arbitrarily shaped light field to control the full three-dimensional intensity distribution of the strongly focused beam. To this aim, we built a detection system which is able to reconstruct the intensity distribution in the focus with sub-wavelength resolution.

A. Nardi (✉) · F. Tebbenjohanns · M. Frimmer · L. Novotny
Photonics Laboratory, ETH Zürich, Zürich, Switzerland
e-mail: anardi@ethz.ch

M. Cesaria et al. (eds.), *Light-Matter Interactions Towards the Nanoscale*,
NATO Science for Peace and Security Series B: Physics and Biophysics,
https://doi.org/10.1007/978-94-024-2138-5_43

43.2 Experiment

Figure 43.1a shows the experimental setup used in the present work. The setup consists of two main parts. The first part (highlighted in blue) serves to generate an arbitrary field distribution, which is then focused by a microscope objective. The second part (highlighted in green) allows us to characterize the intensity distribution

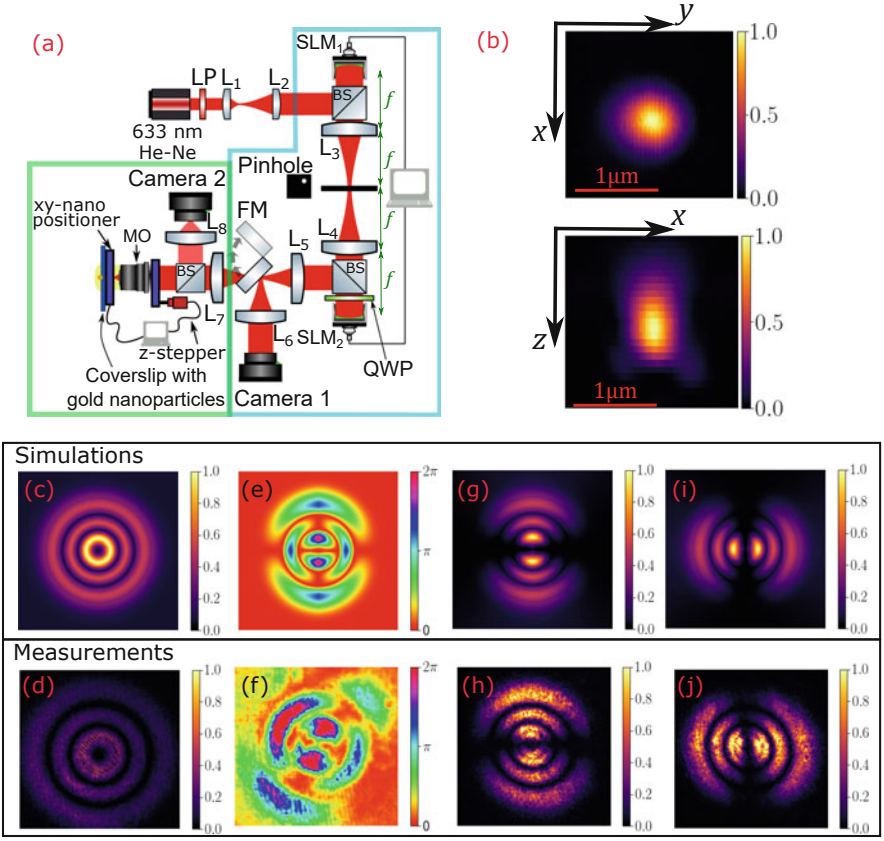

Fig. 43.1 (**a**) Experimental setup. (blue) We use a system of two SLMs to achieve amplitude, phase and polarisation spatial modulation. (green) We then strongly focus the beam with a high-*NA* objective and we collect the light scattered by scanning a gold nanoparticle through the focus. LP: linear polariser, L_{1-8} lenses, SLM: spatial light modulator, BS: beam splitter, QWP: quarter-wave plate, FM: flipping mirror, MO: microscope objective. (**b**) Reconstructed intensity distribution of a strongly focused Gaussian beam. (**c–j**) Simulations (top row) and measurements (bottom row) of a radially polarised second order Laguerre-Gaussian mode generated with the presented setup. The measurements are images of the back-focal plane of the objective taken with Camera 1. (**c**)–(**d**) Intensity distribution. (**e–f**) Phase distribution, extracted with an interferometric setup (not depicted in the sketch in subfigure a). (**g–j**) Intensity distributions when filtered with horizontal (**g–h**) or vertical (**i–j**) linear polariser

in the focus. In the first part, a 633 nm He-Ne laser is expanded with a telescope to match the aperture of the two SLMs (Meadowlark Optics P512). We employ a linear polariser to obtain a clean polarisation along the modulation axis of the SLMs. We then use the first SLM, together with a pinhole, to achieve amplitude and phase modulation [8]. Next, the beam reaches the second SLM, which, together with a quarter-wave plate, allows us to control the polarisation distribution of the generated beam [9]. Therefore, the system of the two SLMs is able to generate arbitrary light field distributions, i.e., fields with controlled amplitude, phase and polarisation. As an example, we report in Fig. 43.1c–j the generation of a radially polarised second order Laguerre-Gaussian beam. The measurements (depicted in the bottom row) are in good agreement with the simulated distributions (top row). The intensity distribution (Fig. 43.1d) is recorded with a camera placed in the backfocal plane of the microscope objective. The phase distribution (Fig. 43.1f) is extracted with an interferometric measurement (for simplicity, the interferometric setup is not reported in Fig. 43.1a). Finally, placing a linear polariser in front of the camera, we can measure the horizontally and the vertically polarized intensity distributions, which follow the expected distributions for a radially polarized field (Fig. 43.1h,j).

Finally, the beam is strongly focused by a high-*NA* objective (Nikon oil-immersion Plan Apo 100X, *NA*= 1.4). To map the intensity distribution in the focus with sub-wavelength resolution, we scan a gold nanoparticle through the focal region and measure the scattered intensity as a function of particle position. Figure 43.1b shows the three-dimensional reconstruction of the intensity distribution of a strongly focused Gaussian beam.

43.3 Conclusions and Outlook

We showed that the presented setup is able to generate light fields with arbitrary amplitude, phase and polarisation distribution, allowing us to control the full three-dimensional intensity distribution of the strongly focused beam, which is then characterized with sub-wavelength resolution using a gold particle. Arbitrary shaping of strongly focused light is used in tip-enhanced Raman measurements, where radially polarised, higher order Laguerre-Gaussian modes are used to generate a tighter focal spot with a higher longitudinal field component as compared to plane wave illumination [10]. Beam shaping has also been extensively used in single-atom trapping to obtain programmable 2D arrays of traps [11] or non-Gaussian optical potentials [12]. In analogy, it could be possible to use the present setup to study the dynamics of nanoparticles trapped by optical tweezers in non-ordinary potentials [13].

References

1. Efron, U.: Spatial Light Modulator Technology: Materials, Devices, and Applications. Marcel Dekker, New York (1995)
2. Forbes, A., Dudley, A., McLaren, M.: Adv. Opt. Photon. **8**(2), 200 (2016)
3. Giovannini, D., Romero, J., Ek, V.P., Ferenczi, G., Speirits, F., Barnett, S.M., Faccio, D., Padgett, M.J.: Science **347**(6224), 857 (2015)
4. Jack, B., Leach, J., Ritsch, H., Barnett, S.M., Padgett, M.J., Franke-Arnold, S.: New J. Phys. **11**(10), 103024 (2009)
5. Maurer, C., Jesacher, A., Bernet, S., Ritsch-Marte, M.: Laser Photonics Rev. **5**(1), 81 (2010)
6. Nehmetallah, G., Banerjee, P.P.: Adv. Opt. Photon. **4**(4), 472 (2012)
7. Burger, L., Litvin, I., Ngcobo, S., Forbes, A.: J. Opt. **17**(1), 015604 (2014)
8. Clark, T.W., Offer, R.F., Franke-Arnold, S., Arnold, A.S., Radwell, N.: Opt. Express **24**(6), 6249 (2016)
9. Beversluis, M.R., Novotny, L., Stranick, S.J.: Opt. Express **14**(7), 2650 (2006)
10. Kozawa, Y., Hibi, T., Sato, A., Horanai, H., Kurihara, M., Hashimoto, N., Yokoyama, H., Nemoto, T., Sato, S.: Opt. Express **19**(17), 15947 (2011)
11. Nogrette, F., Labuhn, H., Ravets, S., Barredo, D., Béguin, L., Vernier, A., Lahaye, T., Browaeys, A.: Phys. Rev. X **4**(2) (2014)
12. Xu, P., He, X., Wang, J., Zhan, M.: Opt. Lett. **35**(13), 2164 (2010)
13. Rondin, L., Gieseler, J., Ricci, F., Quidant, R., Dellago, C., Novotny, L.: Nat. Nanotechnol. **12**(12), 1130 (2017)

Chapter 44
Structure and Properties of LaB_6-TiB_2 Ceramic Composites Obtained by Atomization

Tetiana Soloviova, Olga Karasevska, and Petro Loboda

Abstract The structure and properties of the LaB_6-TiB_2 composite obtained by atomization were studied. The X-ray diffraction and microscopic methods were used to study phase content, diameter of the TiB_2 fibers, hardness and residual stresses in composite components. It was shown that after atomization macrostresses reduced 1.5 times, micro- and nanohardness of the phase components decreased by 10–15%, size of LaB_6 subgrains are an order of magnitude smaller than those of composites obtained by directional crystallization.

Keywords Ceramic composite · Substructure · Stresses · Eutectic alloy

44.1 Introduction

Lanthanum hexaboride (LaB_6) has both thermionic and photoelectron emissions [1]. Due to these properties, LaB_6 can be successfully used simultaneously as a high-temperature solar absorber and as an electron source in a new generation of concentrating solar thermoelectric systems. High brittleness and insufficient ductility are significant disadvantages of LaB_6 limiting its structural use. The discrepancy between the level of emission and mechanical properties of the LaB6 single crystal is eliminated by creating LaB_6-MeB_2 composite materials (Me-Ti, Zr, Hf, Ta) [2–4]. The TiB_2 has higher solar absorption than Zr, Hf, Ta borides, and its spectral deviation is lower, but higher than that of SiC, which is currently used in solar cells [5]. In addition, TiB_2 has a lower density than ZrB_2 (4.5 g/cm^3 versus 6.11 g/cm^3) and TaB_2 (12.18 g/cm^3), which is much cheaper. This is a significant advantage for use in volumetric solar absorbers fixed at a height.

T. Soloviova (✉) · O. Karasevska · P. Loboda
National Technical University of Ukraine "Igor Sikorsky Kyiv Polytechnic Institute", Kyiv, Ukraine

M. Cesaria et al. (eds.), *Light-Matter Interactions Towards the Nanoscale*,
NATO Science for Peace and Security Series B: Physics and Biophysics,
https://doi.org/10.1007/978-94-024-2138-5_44

In this work, we studied the phase composition, structure, and properties of the LaB_6-TiB_2 eutectic alloy obtained by atomization as a potential candidate for use in solar energy.

44.2 Results

Two phases are formed in atomized LaB_6-TiB_2 composites (AC): LaB_6 and TiB_2, with lattice parameters close to the equilibrium state [2, 4]. In as-grown composites (AGC), received by directional crystallization, the phase composition consists of metastable ($La_yB_{6 \pm x3}$ and $TiB_{2 \pm x4}$) and additional phases (~ 3–7%) [2, 3].

Many crystallization centers are formed during atomization, a small length of the diffusion zone reduces the size of the matrix phase, fibers and the distance between them compared to AGC. The average diameters of TiB_2 fibers in LaB_6 matrix AC decreased by 4 times (0.12 ± 0.05 μm), comparatively with AGC. With the decreasing of the TiB_2 diameter, dislocation sources reduce or absent, that leads to the increasing fibers strength.

The reciprocal space mapping data in the form of the intensity distribution of diffraction spots (Iq) in the matrix phase AC grains differs significantly from the Iq distribution of AGC. In AC the Iq distribution is not broken up into separate fragments and is similar to the distribution of Iq in the subgrains of AGC, which means the absence of multilevel misorientations. In accordance with the differences in the structure of the matrix phase of AC and AGC the residual stresses are different: 0.8 GPa and 2 GPa, respectively, and the micro- and nanohardness of AC are 10–15% higher than AGC.

44.3 Conclusion

The possibility of obtaining in thin layers a LaB_6-TiB_2 eutectic composite with an equilibrium phase composition by atomization method is shown. Homogeneity and a less disoriented substructure of the LaB_6 matrix phase, compared to as-grown composites, promote the decreasing of the residual stresses and improving of the mechanical properties of LaB_6-TiB_2 ceramic composite.

References

1. Mattox TM, Urban JJ (2018) Tuning the surface plasmon resonance of lanthanum hexaboride to absorb solar heat: a review. Materials 11(12):2473
2. Loboda PI, Soloviova TO, Bogomol YI, Remizov DO, Bilyi OI (2015) Effect of the crystallization kinetic parameters on the structure and properties of a eutectic alloy of the LaB_6–TiB_2 system. J Superhard Mater 37(6):394–401

3. Soloviova TO, Karasevska OP, Vleugels J, Loboda PI (2017) Influence of annealing on crucible-free float zone melted LaB_6-TiB_2 composites. J Alloys Compounds 729:749–757
4. Soloviova TO, Karasevska OP, Loboda PI (2019) Structure, residual stresses and mechanical properties of LaB_6–TiB_2 ceramic composites. Ceram Int 45(7):8677–8683
5. Sani E, Meucci M, Mercatelli L, Balbob A, Musa C, Licheri R, Orrù R, Cao G (2017) Titanium diboride ceramics for solar thermal absorbers. Solar Energy Mater Solar Cells 169:313–319

Chapter 45
Studies of Luminescence Properties of Eu^{3+} Ions Doped the Silicate-Substituted Apatite and Co-doped with Strontium Ions

Sara Targonska and Rafal J. Wiglusz

Abstract Nanosized silicate-substituted hydroxyapatites doped with Eu^{3+} ions were synthesized using a microwave assisted hydrothermal method and heat-treated at the temperature of 400 °C. The concentration of optically active Eu^{3+} ions was established in the range of 0.5–2.0 mol% and the concentration of strontium ions was set to be at 2 mol% in proportion to the overall molar content of calcium ions.. The structure and morphology properties were carried out by X-ray powder diffraction technique and SEM, respectively. The emission, excitation spectra and emission kinetics were measured and analyzed as a function of the concentration.

Keywords Apatite · Silicate-substitution · Co-doping Eu^{3+}/Sr^{2+} · Luminescence properties

45.1 Apatite Structure

In the structure of synthetic hydroxyapatite, the calcium, phosphate, or hydroxyl group could be replaced by different kinds of ions. In the case of the substitution, some properties might be changed, including phase stability, reactivity, bioactivity or biocompatibility as well as structural and spectral properties. Moreover, europium ion is sensitive by changes in the local environment and is often used as structural and luminescent probe. Therefore, the Eu^{3+} ion has been selected as bioimaging probe aimed at theragnostic application. Furthermore, to change the bioactivity of the obtained materials, strontium ions and silicate groups have been intentionally incorporated [1, 2].

S. Targonska (✉) · R. J. Wiglusz (✉)
Institute of Low Temperature and Structure Research Polish Academy of Sciences, Wroclaw, Poland
e-mail: s.targonska@intibs.pl; r.wiglusz@intibs.pl

M. Cesaria et al. (eds.), *Light-Matter Interactions Towards the Nanoscale*,
NATO Science for Peace and Security Series B: Physics and Biophysics,
https://doi.org/10.1007/978-94-024-2138-5_45

The silicon-substituted hydroxyapatite co-doped with Eu^{3+} ions and Sr^{2+} ions was obtained using a microwave assisted hydrothermal method. The concentration of strontium ions was set to be at 2 mol%. The concentration of europium ions were changed in the range 0.5–2.0 mol%. Both ion amounts were established in a ratio to entire calcium ions molar content. The structure of the obtained materials were determined by X-ray powder diffraction technique. Morphology properties were carried out by scanning electron microscopy (SEM).

45.2 Luminescence Properties

The emission, excitation spectra and emission kinetics were recorded and analyzed as a function of the concentration of the optically active ion (see Fig. 45.1). The luminescence spectra consist of typical transitions for Eu^{3+} ions. The decay times measurements were carried out and the average life times were calculated. The average life times of silicon-substitution hydroxyapatite doped with Eu^{3+} ions decreased with increasing of Eu^{3+} concentration and increased with heat-treating temperature increasing.

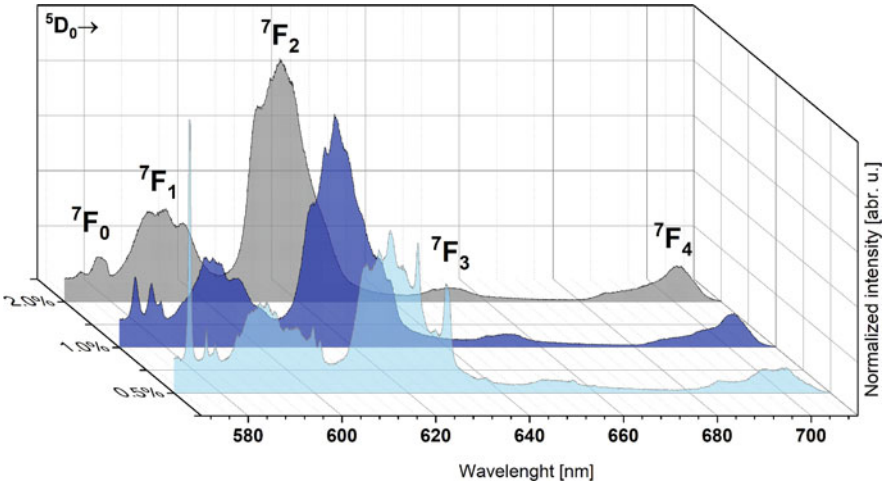

Fig. 45.1 Emission spectra of 2 mol% Sr^{2+}co-doped with x mol% Eu^{3+} doped sample as a function of Eu^{3+} ions concentration

Acknowledgements Financial support from the National Science Centre in Poland (NSC Poland) throughout the realization of the project'Preparation and characterisation of biocomposites based on nanoapatites for theranostic' (No. UMO-2015/19/B/ST5/01330) is gratefully acknowledged.

References

1. Lin K, Xia L, Li H, Jiang X, Pan H, Xu Y, Lu WW, Zhang Z, Chang J (2013) Enhanced osteoporotic bone regeneration by strontium-substituted calcium silicate bioactive ceramics. Biomaterials 34:10028–10042
2. Targonska S, Szyszka K, Rewak-Soroczynska J, Wiglusz RJ (2019) A new approach to spectroscopic and structural studies of the nano-sized silicate-substituted hydroxyapatite doped with Eu 3+ ions. Dalton Trans 48:8303–8316

Chapter 46
Bacterial Gram-Type Differentiation Accomplished with Hollow Photonic Crystal Cavities

Rita Therisod, Manon Tardif, Nicolas Villa, Pierre R. Marcoux, Emmanuel Picard, Emmanuel Hadji, David Peyrade, and Romuald Houdré

Abstract We report on the optical trapping and Gram-type differentiation of seven types of living bacteria in 2D hollow photonic crystal cavities embedded in a microfluidic layer. Excitation of the resonant cavity with a tuneable laser permitted to record multiple trapping events. The analysis of the membrane-dependent resonance frequency shift due to the electromagnetic field-bacteria coupling allowed for the Gram-type differentiation of bacteria in a fast, label-free, and non-destructive way.

Keywords Photonic crystals · Microfluidic · Bacteria · Optical trapping

R. Therisod · N. Villa (✉) · R. Houdré
Ecole Polytechnique Fédérale de Lausanne (EPFL), Institut de Physique, Lausanne, Switzerland
e-mail: nicolas.villa@epfl.ch

M. Tardif
University Grenoble Alpes CNRS, LTM – Micro and Nanotechnologies for Health, Grenoble, France

University Grenoble Alpes, CEA, INAC, PHELIQS, Laboratoire SINAPS, Grenoble, France

P. R. Marcoux
University Grenoble Alpes, CEA, LETI, Grenoble, France

E. Picard · E. Hadji
University Grenoble Alpes, CEA, INAC, PHELIQS, Laboratoire SINAPS, Grenoble, France

D. Peyrade
University Grenoble Alpes CNRS, LTM – Micro and Nanotechnologies for Health, Grenoble, France

M. Cesaria et al. (eds.), *Light-Matter Interactions Towards the Nanoscale*,
NATO Science for Peace and Security Series B: Physics and Biophysics,
https://doi.org/10.1007/978-94-024-2138-5_46

46.1 Discussion

The first step towards bacteria identification is their classification in two groups encompassing Gram positive or Gram negative types. These two classes mainly depend on the structural properties of bacteria cell wall. Here, our results concerning the study of seven types of living bacteria are presented. Those were trapped in an optical cavity consisting in a large hole in a 2D silicon photonic crystal membrane and thanks to the feedback effect induced by the trapped specimen on the optical field [1], Gram type classification was performed successfully.

Optical trapping experiments were performed as follows. Light from a tuneable source at the resonance frequency is injected in the input waveguide: the evanescent coupling between the W1 waveguide and the optical cavity results in a minimum of the detected power through the waveguide, as shown in Fig. 46.1a-black. When a bacterium is trapped, a specimen-dependent redshift in the resonance wavelength is induced and can be detected by an augmentation in the transmitted power, e. g Fig. 46.1a-green. Measurements are illustrated in Fig. 46.1b,c where the transmission recorded during a trapping event (i) together with the corresponding histogram (ii) are shown for B. subtilis (Gram +) and N. sicca (Gram −) respectively.

To further analyse the results presented in [2], statistical analysis and L^2 cross distances of the transmitted powers were carried out on a set of 9 trapping events for each type of bacterium. Results are shown in Fig. 46.2a, b respectively and allow to unambiguously differentiate the two Gram +/− families.

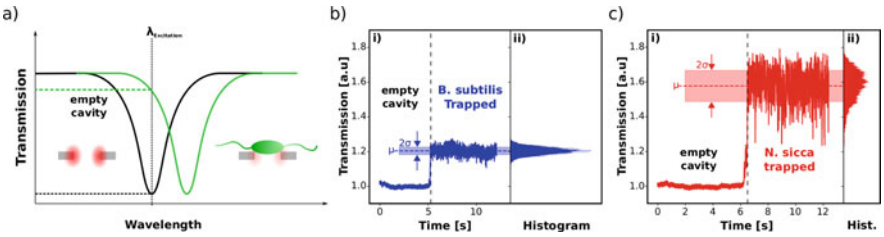

Fig. 46.1 (**a**) Illustration of the resonance wavelength shift induced by a trapped bacterium. (**b–c**) Examples of transmitted power signal recorded during a trapping event of B. subtilis and N. sicca (i) together with the corresponding histogram (ii)

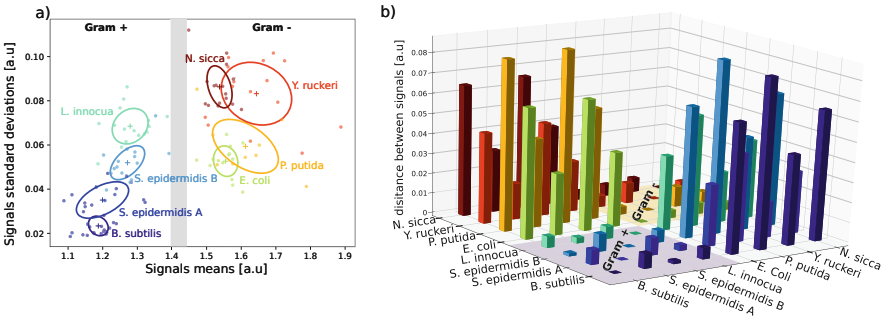

Fig. 46.2 (**a**) The standard deviations σ of all recorded trapping events are plotted in function of the corresponding mean μ. Respective ellipsoids give the standard deviation in the (μ, σ) plan. (**b**) For each couple of bacteria types (x and y axes) the L^2 distance is computed and reported on the z-axis

References

1. Descharmes, N., et al.: Observation of backaction and self-induced trapping in a planar hollow photonic crystal cavity. Phys. Rev. Lett. **110**(12), 123601 (2013)
2. Therisod, R., et al.: Gram-type differentiation of bacteria with 2D hollow photonic crystal cavities. Appl. Phys. Lett. **113**(11), 111101 (2018)

Chapter 47
Full Tunability of Whispering-Gallery-Modes in Resonators Made from Liquid-Crystal Elastomers

Simon Woska, Jannis Hessenauer, Carolin Klusmann, Matthias Migeot, Alexander Münchinger, and Heinz Kalt

Abstract Whispering-Gallery-Mode (WGM) resonators hold huge potential for various future application due to their high quality factors and low mode volumes. Hereby, their field of possible applications is further widened if the spectral position of the WGMs can be precisely and reversibly tuned. To this goal, we propose a WGM resonator entirely made from Liquid-Crystal Elastomer. These polymers undergo an anisotropic mechanical actuation under various external stimuli due to a reversible change of their molecular order. Exploiting this mechanism, the spectral position of a WGM is tuned by precisely controlling the resonator's radius using temperature as an external stimulus. The WGM's full tunability is demonstrated by means of fiber-based transmission spectroscopy.

Keywords WGM Resonators · Liquid-Crystal Elastomers · Spectral tunability

47.1 Introduction

Whispering-Gallery-Mode (WGM) resonators confine light due to total internal reflection and feature both high quality factors and low mode volumes. Therefore, they hold huge potential as building blocks for photonic devices as well as for fundamental research [1, 2]. For lots of these possible applications, a precise tunability of the spectral position of WGMs is essential. Due to that requirement, flexible photonics come into play: In WGM resonators, tuning of the spectral position of resonances can be achieved by changing the resonator's radius. To

S. Woska (✉) · J. Hessenauer · C. Klusmann · M. Migeot · A. Münchinger · H. Kalt
Institute of Applied Physics, Karlsruhe Institute of Technology, Karlsruhe, Germany
e-mail: simon.woska@kit.edu
http://www.aph.kit.edu/kalt/english/index.php
https://www.aph.kit.edu/wegener/english/index.php

M. Cesaria et al. (eds.), *Light-Matter Interactions Towards the Nanoscale*,
NATO Science for Peace and Security Series B: Physics and Biophysics,
https://doi.org/10.1007/978-94-024-2138-5_47

this end, rigid goblet-shaped PMMA resonators combined with integrated photo-responsive actuators made from Liquid-Crystal Elastomers (LCEs) were presented and showed reversible shifts of the spectral position of WGMs with varying pumping intensities [3]. In order to further enhance this tuning effect, WGM resonators completely made from LCEs were demonstrated. Investigated WGMs showed significant blue-shifts in case of optical pumping [4].

In the following, we present comparable resonators made from LCE, which are actuated using temperature as stimulus. Hereby, apart from the tunability itself, the controllability as well as the reversibility of the spectral shifts is of interest.

47.2 Methods

The demonstrated resonators were produced from Liquid-Crystal Elastomers. These polymers undergo an anisotropic mechanical actuation under various external stimuli due to a reversible change of their molecular order. The resonators were fabricated by polymerization via multi-photon absorption of a strongly focused fs-laser. The used resist hereby needs to be aligned prior to polymerization, which was done by sandwiching it between silanized cover slips [5].

The reversible actuation of the LCE was triggered using temperature as an external stimulus. The spectral position of resonant modes was investigated by means of fiber-based transmission spectroscopy near the infrared c-band. To this goal, a tapered optical fiber was brought into close proximity of the resonator to enable evanescent coupling. The transmission of the light from a wavelength-sweeping cw-laser through the fiber was investigated, where the WGMs of the resonator appear as Lorentz-shaped dips.

47.3 Results

As depicted in Fig. 47.1, the investigated WGM resonances undergo a significant red-shift of their spectral position over nearly 11 nm (and therefore more than one free spectral range) with increasing temperatures. The shift furthermore shows an approximately linear dependency with temperature and can be assigned to the simultaneously investigated change of the resonator's radius (see inset). The phase-transition temperature T_{ph} at which the molecular order of the LCE starts to change with elevating temperature can be estimated from the onset of the red-shift to be around 36 °C. Comparing these findings with the blue-shift triggered by again decreasing the temperature, an almost full reversibility of the temperature-induced tuning with a remaining hysteresis of around 2.6 nm is evident. Consequently, a full and reversible tunability of the spectral position of a WGM in a resonator entirely made from LCE is successfully demonstrated.

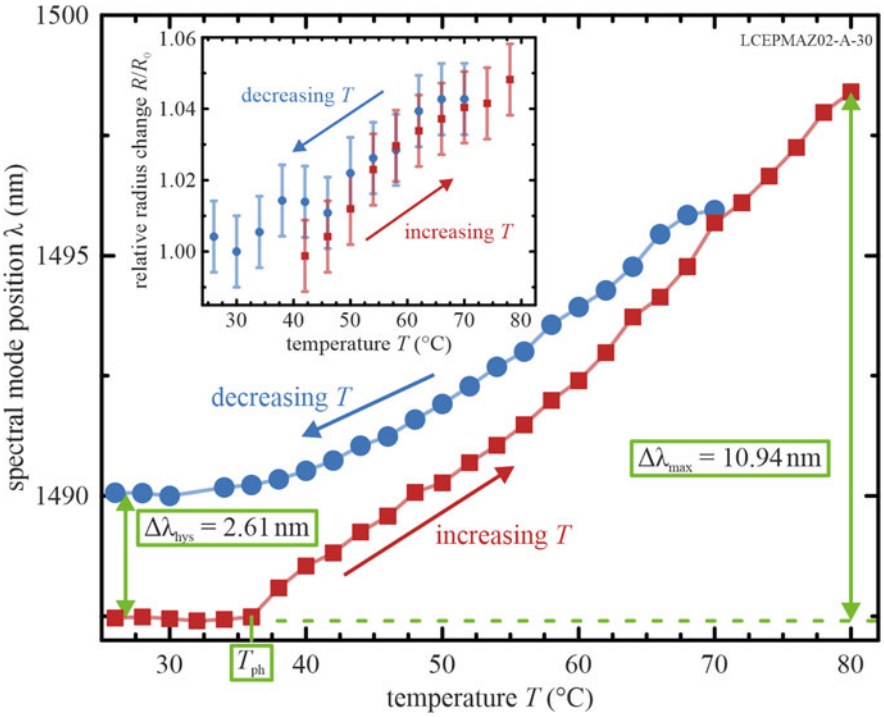

Fig. 47.1 The spectral position of a WGM at different temperatures determined from respective fiber transmission spectra is depicted. A approximately linear and mostly reversible red-shift of the resonant wavelength over more than one free spectral range with increasing temperature is evident. The wavelength tuning can be attributed to the radius change of the resonator, which is shown in the inset

47.4 Conclusion

WGM resonators entirely made from Liquid-Crystal Elastomers were produced by polymerization due to multi-photon absorption. Using temperature as an external stimulus, the resonator's radius was changed. Due to this radius change, the spectral position of a resonant WGM was precisely tuned over more than one free spectral range. The spectral tunability showed an approximately linear temperature dependency and a nearly full reversibility.

References

1. Xu, Q., Manipatruni, S., Schmidt, B., Shakya, J., Lipson, M.: 12.5 Gbit/s carrier-injection-based silicon micro- ring silicon modulators. Opt. Express **15**(2), 430–436 (2007). https://doi.org/10.1364/OE.15.000430
2. Peng, B., Özdemir, S., Lei, F., Monifi, F., Gianfreda, M., Long, G.L., Fan, S., Nori, F., Bender, C.M., Yang, L.: Parity-time-symmetric whispering-gallery microcavities. Nat. Phys. **10**, 394—398 (2014). https://doi.org/10.1038/nphys2927
3. Flatae, A.M., Burresi, M., Zeng, H., Nocentini, S., Wiegele, S., Parmeggiani, C., Kalt, H., Wiersma, D.: Optically controlled elastic microcavities. Light Sci. Appl. **4**, e282 (2015). https://doi.org/10.1038/lsa.2015.55
4. Nocentini, S., Riboli, F., Burresi, M., Martella, D., Parmeggiani, C., Wiersma, D.: Three-dimensional photonic circuits in rigid and soft polymers tunable by light. ACS Photonics **5**, 3222–3230 (2018). https://doi.org/10.1021/acsphotonics.8b00461
5. Woska, S., Münchinger, A., Beutel, D., Blasco, E., Hessenauer, J., Karayel, O., Rietz, P., Pfleging, S., Oberle, R. Rockstuhl, C., Wegener, M., Kalt, H.: Tunable photonic devices by 3D laser printing of liquid crystal elastomers. Opt. Mater. Express **10**, 2928–2943 (2020). https://doi.org/10.1364/OME.402855